



**THE UNIVERSITY
OF BIRMINGHAM**

School of Electronic and Electrical Engineering

***Finite Element-Boundary Elements Modelling of Acoustic
Scattering from Viscoelastic Anechoic Structures***

by

ALBERTO DI MEGLIO

A thesis submitted to the Faculty of Engineering
of the University of Birmingham
for the degree of
DOCTOR OF PHILOSOPHY

School of Electronic and Electrical Engineering
The University of Birmingham
January 2000

UNIVERSITY OF
BIRMINGHAM

University of Birmingham Research Archive

e-theses repository

This unpublished thesis/dissertation is copyright of the author and/or third parties. The intellectual property rights of the author or third parties in respect of this work are as defined by The Copyright Designs and Patents Act 1988 or as modified by any successor legislation.

Any use made of information contained in this thesis/dissertation must be in accordance with that legislation and must be properly acknowledged. Further distribution or reproduction in any format is prohibited without the permission of the copyright holder.

Synopsis

This research work focuses on the analysis of multi-layered, anechoic tiles for underwater applications, especially in the field of communications.

It is firstly shown how the sound absorbing properties of viscoelastic materials can be modified and enhanced by the proper use of fillers, such as lead oxide and mica. Successively, a new method for identifying the viscoelastic frequency-dependent properties of such materials from experimental data is presented. The method is based on a variational method analogous to the Hamilton Principle. It allows calculating hard-to-find properties such as the complex viscoelastic response functions and the complex Poisson ratio.

After the materials properties have been determined, it is shown how they can be incorporated into the combined finite-element-boundary element method to provide accurate numerical solutions to the acoustic scattering problem.

A tile made of three layers, a reflecting aluminium layer, an absorbing butyl rubber layer and a matching layer made of a regular grid of polyurethane cones is finally analysed in several scattering and geometrical configurations.

The scattering patterns produced by a plane wave incident on the tile are plotted, discussed and compared with experimental data obtained from in-tank scattering measurements of a model tile.

To my wife Carla:

Without your understanding support and patient love

I could not have done this

Acknowledgments

I'm in great debt to many people who encouraged, supported and helped me during this research.

Dr. Lian Sheng Wang at the School of Electronic Engineering of the University of Birmingham, who accepted the hard task to be my supervisor during the last two years of the research and without whose help and support this thesis would have never seen the light.

Prof. Rodney Coates from University of Birmingham and Mr. Marselli from Whitehead Alenia Sistemi Subacquei, who gave me the opportunity to work on the VERTLINK project, provided me with the resources I needed and encouraged me all the time.

Dr. Trevor Francis, whose work in the field of boundary element analysis was always a reference to me and whose suggestions were fundamental to the development of the WinFEBE program.

Dr. Brian Smith and Mr. Phil Atkins who patiently supervised me during part of this research.

Dr. David Foster, Mr. Frédéric Hemmer and Mr. Alberto Pace at CERN, who believed in me and supported me during the past two years and gave me the time I needed to accomplish this task.

Prof. Amalia Ercoli Finzi at the Department of Aerospace Engineering of the Politecnico di Milano for all the help in the development and refinement of the Hamilton principle optimisation method.

Many heartfelt thanks go especially to my friends and colleagues in the Acoustics and Sonar Group for their support and the many useful discussions, Mr. Richard Stoner, Dr. John Jones and Mr. Richard Mansfield.

Table of Contents

CHAPTER 1 INTRODUCTION.....	1-1
1.1. OVERVIEW.....	1-1
1.2. THE VERTLINK PROJECT	1-3
1.3. STATEMENT OF ORIGINALITY.....	1-5
1.4. THESIS CONTENTS.....	1-7
1.5. REFERENCES	1-10
CHAPTER 2 HISTORICAL BACKGROUND AND LITERATURE REVIEW	2-11
2.1. RUBBER, HIGH POLYMERS AND MATERIALS WITH MEMORY	2-11
2.2. SOUND SCATTERING: FROM BATS AND DOLPHINS TO ACOUSTIC TELEVISION.....	2-18
2.2.1. Geometrical Optics and Acoustics	2-21
2.2.2. Keller's Theory or Geometrical Theory of Diffraction (GTD).....	2-21
2.2.3. Uniform Asymptotic Theories (UTD, EUTD)	2-22
2.2.4. Luneburg-Kline Expansion	2-23
2.2.5. Physical Optics and Physical Diffraction Theory (PTD)	2-24
2.2.6. Fock's Theory.....	2-25
2.2.7. Variational Techniques.....	2-26
2.2.8. Function-Theoretic Methods: Wiener-Hopf Method.....	2-28
2.2.9. Integral Equations Methods and Numerical Methods.....	2-29
2.3. THE FINITE-ELEMENT AND BOUNDARY ELEMENT METHODS	2-30
2.4. ANALYSIS OF UNDERWATER SOUND SCATTERING FROM ABSORBING, PERIODIC AND FINITE-SIZED SURFACES	2-34
2.5. OBJECT-ORIENTED ANALYSIS AND DESIGN AND ITS APPLICATION TO FE-BE COMPUTER PROGRAMS	2-37
2.6. REFERENCES	2-39
CHAPTER 3 THE LINEAR THEORY OF VISCOELASTICITY	3-45

3.1. INTRODUCTION	3-45
3.2. NOTATIONS AND DEFINITIONS	3-46
3.2.1. <i>Points, vectors, tensors and linear transformations</i>	3-46
3.2.2. <i>Processes and histories</i>	3-46
3.2.3. <i>Convolutions</i>	3-50
3.2.4. <i>The Boltzmann operator</i>	3-51
3.3. LINEAR THEORY OF VISCOELASTICITY WITH INTEGRAL HEREDITARY LAWS.....	3-53
3.3.1. <i>Linear hereditary laws</i>	3-53
3.3.2. <i>Definition of Boltzmann laws</i>	3-55
3.3.3. <i>Constitutive relations for linearly viscoelastic materials</i>	3-57
3.3.4. <i>Constitutive equations and stress relaxation</i>	3-58
3.3.5. <i>Constitutive equations and creep laws: the inversion theorem</i>	3-61
3.3.6. <i>Response functions for isotropic materials</i>	3-63
3.3.7. <i>The fading memory hypothesis</i>	3-66
3.3.8. <i>Periodic harmonic processes and mechanical forcing</i>	3-68
3.4. DYNAMIC LINEAR VISCOELASTICITY	3-73
3.4.1. <i>Dynamic viscoelastic processes</i>	3-73
3.4.2. <i>Power and energy balance</i>	3-74
3.4.3. <i>Oscillatory displacement processes</i>	3-76
3.5. REFERENCES	3-80

CHAPTER 4 VISCOELASTIC PROPERTIES OF HARD POLYMERS: CHARACTERISATION AND EXPERIMENTAL MEASUREMENTS	4-82
4.1. INTRODUCTION	4-82
4.2. PHYSICAL PROPERTIES OF HARD POLYMERS	4-83
4.3. COMPOSITION AND PROCESSING OF THE TEST RUBBER COMPOUNDS	4-86
4.3.1. <i>The Absorbing Layer: Loaded Butyl Rubber</i>	4-86
4.3.2. <i>The Matching Layer: Loaded Polyurethane Rubber</i>	4-88
4.4. POLYURETHANE RUBBER CHARACTERISATION	4-90

4.4.1. <i>The Vibrating Reed Measurement Method</i>	4-90
4.4.2. <i>Experimental Measurements</i>	4-91
4.5. BUTYL RUBBER CHARACTERISATION.....	4-99
4.5.1. <i>Measurements of Acoustic Properties of Limited Size Panels with Parametric Sources</i>	4-99
4.5.2. <i>Experimental set-up</i>	4-101
4.5.3. <i>System calibration</i>	4-103
4.5.4. <i>Experimental Measurements</i>	4-106
4.6. DETERMINATION OF BUTYL RUBBER PROPERTIES BY PARAMETRIC OPTIMISATION	4-113
4.7. DETERMINATION OF THE VISCOELASTIC RESPONSE FUNCTIONS	4-120
4.8. CONCLUSIONS.....	4-124
4.9. REFERENCES	4-124

CHAPTER 5 ACOUSTIC RECIPROCITY THEOREMS AND THEIR APPLICATION TO PLANE

WAVE SCATTERING BY PENETRABLE OBJECTS	5-126
5.1. INTRODUCTION	5-126
5.2. THE LINEAR WAVE EQUATIONS	5-127
5.2.1. <i>The Acoustic Wave Equations in the Time Domain</i>	5-127
5.2.2. <i>Acoustic Scalar and Vector Potentials in the Time Domain</i>	5-128
5.2.3. <i>Acoustic Wave Equations in the Complex Frequency Domain (Laplace-Transform Domain)</i> ..	5-130
5.2.4. <i>Acoustic Scalar and Vector Potentials in the Complex Frequency Domain</i>	5-132
5.2.5. <i>Point Source Solutions and Green's Functions</i>	5-134
5.3. ACOUSTIC RADIATION IN HOMOGENOUS, LOSSLESS, ISOTROPIC FLUIDS	5-135
5.3.1. <i>Plane Acoustic Waves in a Homogeneous, Lossless, Isotropic Fluid</i>	5-139
5.4. THE ACOUSTIC RECIPROCITY THEOREM OF THE TIME-CONVOLUTION TYPE IN THE COMPLEX FREQUENCY DOMAIN AND ITS APPLICATION TO THE DIRECT SOURCE AND DIRECT SCATTERING PROBLEMS	5-142
5.4.1. <i>Definition of reciprocity theorem</i>	5-142
5.4.2. <i>The local and global forms of the complex frequency-domain reciprocity theorem of the time-convolution type</i>	5-144
5.4.3. <i>The Direct Source Problem</i>	5-146

5.4.4. <i>The Direct Scattering Problem</i>	5-148
5.4.5. <i>The Equivalent Surface Source Representation</i>	5-151
5.5. PLANE WAVE SCATTERING FROM A PENETRABLE, WEDGED, BOUNDED BAFFLE IN A FLUID EMBEDDING	5-153
5.5.1. <i>Problem Configuration</i>	5-153
5.5.2. <i>Far-Field Plane Wave Scattering from an Anechoic Tile by Rayleigh-Gans-Born</i> <i>Approximation</i>	5-155
5.6. REFERENCES	5-169
CHAPTER 6 THE FINITE ELEMENT-BOUNDARY ELEMENT METHOD FOR SOUND- STRUCTURE INTERACTION WITH VISCOELASTIC ELEMENTS	6-166
6.1. INTRODUCTION	6-166
6.2. FUNDAMENTALS OF THE BOUNDARY ELEMENT METHOD.....	6-169
6.2.1. <i>Basic Integral Equation</i>	6-169
6.2.2. <i>The Boundary Element Method</i>	6-174
6.3. BOUNDARY ELEMENT FORMULATION OF THE HELMHOLTZ EQUATION. ACOUSTIC RADIATION AND SCATTERING	6-183
6.4. THE NONUNIQUENESS PROBLEM	6-187
6.4.1. <i>The Partial HGF Method</i>	6-189
6.5. STRUCTURAL-ACOUSTIC COUPLING.....	6-192
6.5.1. <i>Basic Equations</i>	6-192
6.6. MODELLING OF ABSORBING STRUCTURES BY MEANS OF VISCOELASTIC ELEMENTS.....	6-196
6.7. CONCLUSIONS.....	6-201
CHAPTER 7 MODELLING OF ACOUSTIC SCATTERING FROM ANECHOIC VISCOELASTIC TILES	7-204
7.1. INTRODUCTION	7-204
7.2. THE SIMULATION ENVIRONMENT	7-206
7.3. VALIDATION OF THE METHOD.....	7-209

7.3.1. Case 1: Comparison with the Exact Modal Shapes and with the Rayleigh-Ganz-Born Solution of Sound Scattering for a Simply-Supported Square Plate	7-210
7.3.2. Case 2: Acoustic Transmission through a Clamped Epoxy-Graphite Plate Facing a Rigid Cavity	7-216
7.4. THE ANECHOIC TILE	7-220
7.5. FE-BE ANALYSIS RESULTS	7-223
7.5.1. Form Function of the Anechoic Tile.....	7-225
7.5.2. Determination of the Resonance Frequencies	7-227
7.5.3. Frequency and Polar Response at Normal Incidence on the Anechoic Side.....	7-235
7.5.4. Dispersion curves	7-241
7.5.5. Frequency and Polar Response at Normal Incidence on the Reflecting Side	7-242
7.5.6. Polar Response at the Characteristic Frequencies at Oblique Incidence on the Anechoic Side.....	7-244
7.5.7. Effects of Varying the Cone Apex Angle.....	7-251
7.6. EXPERIMENTAL COMPARISONS.....	7-254
7.6.1. The Experimental Environment.....	7-254
7.6.2. Results Comparisons.....	7-257
7.7. REFERENCES	7-261

CHAPTER 8 OBJECT-ORIENTED ANALYSIS AND DESIGN OF A FINITE ELEMENT-

BOUNDARY ELEMENT PROGRAM.....	8-263
8.1. INTRODUCTION	8-263
8.2. AN OVERVIEW OF OBJECT-ORIENTED PROGRAMMING AND DESIGN	8-265
8.3. THE UNIFIED MODELLING LANGUAGE (UML)	8-268
8.4. THE UML MODEL OF A FE-BE ANALYSIS PROGRAM.....	8-270
8.5. MODEL IMPLEMENTATION AND PROGRAM STRUCTURE	8-277
8.5.1. The Programming Language	8-277
8.5.2. The Graphics User Interface (GUI)	8-277
8.5.3. The Graphics Engine	8-280

8.5.4. <i>The Finite Element and Boundary Element Objects</i>	8-287
8.5.5. <i>The ‘Worker’ Objects and the Implementation of the FE-BE Algorithm</i>	8-289
8.6. THE SUPERCOMPUTER MODEL.....	8-291
8.6.1. <i>Client-Server Applications and Distributed Computing</i>	8-291
8.6.2. <i>The WinFEBE Console</i>	8-293
8.6.3. <i>The WinFEBE Nodes</i>	8-295
8.6.4. <i>The Communication Infrastructure</i>	8-296
8.7. CONCLUSIONS.....	8-297
8.8. REFERENCES	8-298
CHAPTER 9 SUMMARY AND FURTHER WORK.....	9-300
APPENDIX A RELATIONSHIPS AMONG COMPLEX VISCOELASTIC PARAMETERS FOR	
ISOTROPIC MATERIALS.....	306
APPENDIX B POLYMER COMPOUNDING AND PROCESSING TECHNIQUES.....	308
9.1. ELASTOMERIC POLYMERS CLASSES	309
9.2. CURE SYSTEMS AND CROSSLINKING	310
9.3. FILLERS	311
9.4. PLASTICISERS, PROCESSING AIDS AND SOFTENERS.....	312
9.5. ANTIDEGRADANTS	312
9.6. MANUFACTURING PROCESSES	313
9.7. ADHESION.....	313
9.8. MEASUREMENTS METHODS FOR HARD POLYMERS.....	314
9.8.1. <i>Young’s and Shear Moduli</i>	314
9.8.2. <i>Forced Non-Resonant Methods</i>	315
9.8.3. <i>Resonant Methods</i>	317
9.8.4. <i>Bulk and Longitudinal Bulk Moduli</i>	319
APPENDIX C TRANSDUCER EQUIVALENT AND MATCHING CIRCUIT THEORY.....	324

9.1. MATCHING CIRCUITS	324
9.2. APPLICATION TO THE 1 MHz TRANSDUCER USED IN THE MEASUREMENT TESTS	329
APPENDIX D THE TRANSFER MATRIX METHOD	337
9.1. INTRODUCTION	337
9.2. MODELLING OF PROPAGATION THROUGH STRATIFIED MEDIA INCLUDING ELASTIC, VISCOELASTIC, POROUS AND FLUID.....	338
9.3. SINGLE-LAYER TRANSFER MATRIX COEFFICIENTS FOR TWO-DIMENSIONAL PLANE WAVES.....	348
APPENDIX E THE HAMILTON PRINCIPLE OPTIMISATION METHOD	351
APPENDIX F ACOUSTIC FIELD FAR-FIELD APPROXIMATION AND RELATIONSHIPS AMONG VARIOUS FORMS OF THE GREEN FUNCTION FOR THE SCALAR AND VECTOR HELMHOLTZ EQUATION	359
9.1. ACOUSTIC FIELD FAR-FIELD APPROXIMATION	359
9.2. RELATIONSHIPS BETWEEN DIFFERENT FORMS OF THE GREEN FUNCTIONS FOR THE HELMHOLTZ EQUATION	362
9.3. REFERENCES	363
APPENDIX G	364

List of Illustrations

<i>Figure 1.1: The VERTLINK Communication System.....</i>	<i>1-4</i>
<i>Figure 1.2: The receiving unit of the VERTLINK system. The baffle is mounted around the case facing the transducer.....</i>	<i>1-4</i>
<i>Figure 2.1: Polymer strand made of a chain of cross-linked monomers (coarse and detailed computer-generated 3D image).....</i>	<i>2-13</i>
<i>Figure 2.2: Australian Navy submarine with polymer composite sonar dome.....</i>	<i>2-14</i>
<i>Figure 2.3: Omni-directional ball transducer with polyurethane shell</i>	<i>2-14</i>
<i>Figure 2.4: Echolocation and prey detection of microbats (from Microsoft Encarta 1998 Encyclopedia).....</i>	<i>2-19</i>
<i>Figure 4.1: Typical frequency and temperature pattern for hard polymers (M.W. = Molecular Weight) (reproduced from (Read 1978)).....</i>	<i>4-85</i>
<i>Figure 4.2: Loaded polyurethane samples (from left to right: glass microspheres, lead oxide in varying percentages, tungsten oxide</i>	<i>4-89</i>
<i>Figure 4.3: Block diagram of the longitudinal vibrating reed test method</i>	<i>4-90</i>
<i>Figure 4.4: Plot of storage Young's modulus vs. frequency for unloaded polyurethane rubber reduced to 25°C.....</i>	<i>4-92</i>
<i>Figure 4.5: Plot of Young's modulus loss factor vs. frequency for unloaded polyurethane rubber reduced to 25°C.....</i>	<i>4-92</i>
<i>Figure 4.6: Plot of storage Young's modulus vs. frequency for loaded polyurethane rubber. Series I: glass microspheres (logarithmic scale).....</i>	<i>4-94</i>
<i>Figure 4.7: Plot of Young's modulus loss factor vs. frequency for loaded polyurethane rubber. Series I: glass microspheres (logarithmic scale).....</i>	<i>4-94</i>
<i>Figure 4.8: Plot of storage Young's modulus vs. frequency for loaded polyurethane rubber. Series II: carbon black (logarithmic scale)</i>	<i>4-96</i>
<i>Figure 4.9: Plot of Young's modulus loss factor vs. frequency for loaded polyurethane rubber. Series II: carbon black (logarithmic scale)</i>	<i>4-96</i>
<i>Figure 4.10: Plot of storage Young's modulus vs. frequency for loaded polyurethane rubber. Series III: lead oxide (logarithmic scale).....</i>	<i>4-97</i>
<i>Figure 4.11: Plot of Young's modulus loss factor vs. frequency for loaded polyurethane rubber. Series III: lead oxide (logarithmic scale)</i>	<i>4-97</i>
<i>Figure 4.12: Plot of storage Young's modulus vs. frequency for loaded polyurethane rubber. Series IV: tungsten oxide (logarithmic scale)</i>	<i>4-98</i>

Figure 4.13: Plot of Young's modulus loss factor vs. frequency for loaded polyurethane rubber. Series IV: tungsten oxide (logarithmic scale)	4-98
Figure 4.14: Variation of loss tangent maxima with filler proportion for loaded polyurethane	4-99
Figure 4.15: Transmitter electronics and transducer set-up.....	4-102
Figure 4.16: Power spectrum of the received signal at a distance $d = 1$ m from the transducer for a secondary frequency $f_2 = 151$ kHz and primary frequencies $f_{1L} = 999$ kHz and $f_{1H} = 1150$ kHz.....	4-102
Figure 4.17: Virtual array beam pattern at a distance $d = 1$ m from the transducer for the secondary frequencies $f_2 = 97$ kHz ($f_{1L} = 1030$ kHz and $f_{1H} = 1127$ kHz) and $f_2 = 151$ kHz ($f_{1L} = 999$ kHz and $f_{1H} = 1150$ kHz).....	4-103
Figure 4.18: Power transmission loss for a 5 mm thick aluminium plate at normal incidence	4-104
Figure 4.19: Power reflection loss for a 5 mm thick aluminium plate at normal incidence.....	4-105
Figure 4.20: Power transmission loss for a 5 mm thick aluminium plate at 80 kHz as a function of incidence	4-105
Figure 4.21: Power reflection loss for a 5 mm thick aluminium plate at 80 kHz as a function of incidence	4-106
Figure 4.22: Power reflection loss as a function of frequency for a 10 mm thick butyl rubber panel at three different density values	4-107
Figure 4.23: Power transmission loss as a function of frequency for a 10 mm thick butyl rubber panel at three different density values	4-107
Figure 4.24: Power absorption loss as a function of frequency for a 10 mm thick butyl rubber panel at three different density values	4-108
Figure 4.25: Power reflection loss as a function of angle of incidence for a 10 mm thick butyl rubber panel at 40 kHz for three different density values	4-108
Figure 4.26: Power transmission loss as a function of angle of incidence for a 10 mm thick butyl rubber panel at 40 kHz for three different density values	4-109
Figure 4.27: Power reflection loss as a function of angle of incidence for a 10 mm thick butyl rubber panel at 60 kHz for three different density values	4-109
Figure 4.28: Power transmission loss as a function of angle of incidence for a 10 mm thick butyl rubber panel at 60 kHz for three different density values	4-110
Figure 4.29: Power reflection loss as a function of angle of incidence for a 10 mm thick butyl rubber panel at 80 kHz for three different density values	4-110
Figure 4.30: Power transmission loss as a function of angle of incidence for a 10 mm thick butyl rubber panel at 80 kHz for three different density values	4-111
Figure 4.31: Longitudinal bulk modulus $\lambda_L^*(\omega)$. Loaded butyl rubber compound	4-120
Figure 4.32: Shear modulus $\lambda_T^*(\omega)$. Loaded butyl rubber compound.....	4-121
Figure 4.33: Longitudinal bulk and shear loss factors. Loaded butyl rubber compound	4-121

<i>Figure 4.34: Viscoelastic Poisson ratio. Loaded butyl rubber compound.....</i>	<i>4-122</i>
<i>Figure 4.35: Viscoelastic shear response function. Loaded butyl rubber compound.....</i>	<i>4-123</i>
<i>Figure 4.36: Viscoelastic compression response function. Loaded butyl rubber compound.....</i>	<i>4-123</i>
<i>Figure 6.1: Geometrical definitions of the domain Ω with Robin (mixed) boundary conditions</i>	<i>6-170</i>
<i>Figure 6.2: Boundary points specialisation of the general integral equation for a three-dimensional domain</i>	<i>6-173</i>
<i>Figure 6.3: Curved (quadratic) elements for two- and three dimensional boundary element problems: (a) quadratic quadrilateral element; (b) quadratic triangular element; (c) quadratic two-dimensional element.....</i>	<i>6-175</i>
<i>Figure 7.1: FE-BE element size constraints as a function of frequency. The maximum linear dimension must not exceed half a wavelength in all materials</i>	<i>7-207</i>
<i>Figure 7.2: Simply-supported square plate. Exact modal shape at 40.176 kHz in vacuum ($f_{9,9}$). The square side is normalised to 1</i>	<i>7-212</i>
<i>Figure 7.3: Simply-supported square plate in air (quarter model). Maximum positive deformation along the z-axis ($\phi=-84$ deg)</i>	<i>7-213</i>
<i>Figure 7.4: Simply-supported square plate in air (quarter model). Maximum negative deformation along the z-axis ($\phi=96$ deg).....</i>	<i>7-213</i>
<i>Figure 7.5: Normalised total backscattered pressure field at 31.065 kHz in air. Comparison between the 1st-order RGB solution and the FE-BE solution.....</i>	<i>7-214</i>
<i>Figure 7.6: Normalised total backscattered pressure field at 41.725 kHz in air. Comparison between the 1st-order RGB solution and the FE-BE solution.....</i>	<i>7-215</i>
<i>Figure 7.7: Normalised total backscattered pressure field at 49.885 kHz in air. Comparison between the 1st-order RGB solution and the FE-BE solution.....</i>	<i>7-215</i>
<i>Figure 7.8: Total pressure field around the butyl rubber tile at 49.885 kHz (FE-BE solution).....</i>	<i>7-216</i>
<i>Figure 7.9: Model of the graphite-epoxy plate and acoustic cavity (quarter model).....</i>	<i>7-218</i>
<i>Figure 7.10: First mode shape at 207.5 Hz (f_{22}) of the clamped graphite-epoxy plate.....</i>	<i>7-218</i>
<i>Figure 7.11: Transmission loss for clamped graphite-epoxy panel and rigid cavity reproduced from Pates et al. (1995).....</i>	<i>7-219</i>
<i>Figure 7.12: Transmission loss for clamped graphite-epoxy panel and rigid acoustic cavity calculated with WinFEBE.....</i>	<i>7-219</i>
<i>Figure 7.13: Model of the anechoic tile. Left: upper view showing the polyurethane cones; right: side view (on a supporting base) showing the butyl rubber and aluminium layers</i>	<i>7-220</i>
<i>Figure 7.14: The VERTLINK receiver with the anechoic baffle mounted during the trial in Pilos, Greece in 1997. (a) On the quay with the dorsal stabiliser and the spacing buoys; (b) Deployment from the ship 'Neptune'</i>	<i>7-221</i>
<i>Figure 7.15: The anodised aluminium mould used to manufacture the anechoic cone layer.....</i>	<i>7-223</i>

Figure 7.16: Anechoic tile quarter model ($h = 37.5$ mm, wireframe model).....	7-224
Figure 7.17: Anechoic tile half model ($h = 37.5$ mm, $\theta_0 = 5^\circ$ - solid model).....	7-224
Figure 7.18: Cone and plane wave scattering geometry.....	7-226
Figure 7.19: Displacement response of the anechoic tile. Series (a): amplitude; series (b): phase.....	7-230
Figure 7.20: Displacement response of the anechoic tile. Series (a): amplitude; series (b): phase (continued from previous page).....	7-231
Figure 7.21: Cone tips vibration patterns ($h = 37$ mm, $f = 31.5$ kHz, $ka=1.85$). (a) Tips contours ($l = 1$); (b) tile quarter model, orthogonal projection in the x-y plane (amplification factor = $2.5e12$, — undeformed model, — deformed model).....	7-232
Figure 7.22: Modal shape at $ka = 4.45$, $\theta_l = 175^\circ$ ($\times 1.25e12$).....	7-233
Figure 7.23: Modal shape at $ka = 1.85$, $\theta_l = 165^\circ$ ($\times 2.5e12$).....	7-233
Figure 7.24: Modal shape at $ka = 1.49$, $\theta_l = 145^\circ$ ($\times 2.5e12$).....	7-234
Figure 7.25: Modal shape at $ka = 2.01$, $\theta_l = 135^\circ$ ($\times 2.5e12$).....	7-234
Figure 7.26: On-axis backscattered pressure of the anechoic tile for different values of the cone apex angle.....	7-235
Figure 7.27: Backscattered form function for the anechoic tile at different values of the cone apex angle.....	7-236
Figure 7.28: Form function polar plots at the displacement resonance frequencies ($\theta_l = 145^\circ$). Left side scattered form function amplitude; right side: total form function amplitude.....	7-237
Figure 7.29: Form function polar plots at the displacement resonance frequencies ($\theta_l = 165^\circ$). Left side: scattered form function amplitude; right side: total form function amplitude.....	7-238
Figure 7.30: Form function polar plots at the displacement resonance frequencies ($\theta_l = 175^\circ$). Left side: scattered form function amplitude; right side: total form function amplitude.....	7-239
Figure 7.31: Definition of the critical angle of reflection.....	7-240
Figure 7.32: Dispersion plots for the first four maxima of the form function: angular position (θ_l $= 145^\circ$).....	7-241
Figure 7.33: Dispersion plots for the first four maxima of the form function: pressure amplitude (θ_l $= 145^\circ$).....	7-242
Figure 7.34: Backscattered pressure with signal incident on the reflecting side.....	7-243
Figure 7.35: Form function polar plots at the resonance frequency ($\theta_l = 165^\circ$). Left side: scattered form function amplitude; right side: total form function amplitude.....	7-243
Figure 7.36: Backscattered form function at incidence $\theta_0 = 15^\circ$	7-244
Figure 7.37: Backscattered form function at incidence $\theta_0 = 30^\circ$	7-245
Figure 7.38: Backscattered form function at incidence $\theta_0 = 45^\circ$	7-245

Figure 7.39: Form function amplitude at incidence $\theta_0 = -15^\circ$. Left side: scattered field; right side: total field.....	7-246
Figure 7.40: Form function amplitude at incidence $\theta_0 = -30^\circ$. Left side: scattered field; right side: total field.....	7-247
Figure 7.41: Form function amplitude at incidence $\theta_0 = -45^\circ$. Left side: scattered field; right side: total field.....	7-248
Figure 7.42: Backscattered form function at incidence $\theta_0 = 90^\circ$	7-249
Figure 7.43: Form function amplitude at incidence $\theta_0 = -90^\circ$. Left side: scattered field; right side: total field.....	7-250
Figure 7.44: Normalised backscattered pressure Vs. frequency for $\theta_1 \sim \pi$	7-253
Figure 7.45: Normalised backscattered pressure Vs. frequency for $\theta_1 \sim \pi/2$	7-253
Figure 7.46: General schema of the experimental set up.....	7-254
Figure 7.47: Side view of the open test rig. On the left the transducers, on the right the step-motor harness with the tile.....	7-255
Figure 7.48: The open test rig on the wooden cover of the measurement tank at the School of Electronic & Electrical Engineering.....	7-255
Figure 7.49: The anechoic tile and the complete baffle used during the tests for the VERTLINK project	7-257
Figure 7.50: Backscattered form function amplitude for the model tile at normal incidence. — FE-BE, ■ experimental.....	7-258
Figure 7.51: Scattered form function amplitude for the model tile at normal incidence, $ka = 2.13$. — FE-BE, ■ experimental.....	7-259
Figure 7.52: Scattered form function amplitude for the model tile at normal incidence, $ka = 2.13$. — FE-BE, ■ experimental.....	7-259
Figure 7.53: Scattered form function amplitude for the model tile at normal incidence, $ka = 2.01$. — FE-BE, ■ experimental.....	7-260
Figure 7.54: Scattered form function amplitude for the model tile at normal incidence, $ka = 2.32$. — FE-BE, ■ experimental.....	7-260
Figure 7.55: Scattered form function amplitude for the model tile at normal incidence, $ka = 2.13$. — FE-BE, ■ experimental.....	7-261
Figure 8.1: WinFEBE splash screen (debug version).....	8-265
Figure 8.2: The main use case diagram.....	8-271
Figure 8.3: The Solve Equations use case diagram.....	8-272
Figure 8.4: The Display Subsystem use case diagram.....	8-272
Figure 8.5: The WinFEBE Remote Console class diagram	8-273

<i>Figure 8.6: The WinFEBE data structure class diagram.....</i>	<i>8-274</i>
<i>Figure 8.7: The WinFEBE Display and Graphics Engine class diagram</i>	<i>8-275</i>
<i>Figure 8.8: The WinFEBE FE-BE Algorithm class diagram.....</i>	<i>8-276</i>
<i>Figure 8.9: The WinFEBE main window displaying the data, message and model child windows</i>	<i>8-278</i>
<i>Figure 8.10: The WinFEBE model and graph windows.....</i>	<i>8-279</i>
<i>Figure 8.11: The WinFEBE material database dialog</i>	<i>8-280</i>
<i>Figure 8.12: WinFEBE Data Structure.....</i>	<i>8-281</i>
<i>Figure 8.13: The Front/Back Surface Convention.....</i>	<i>8-282</i>
<i>Figure 8.14: Projection methods: orthogonal (left) and axonometric (right).....</i>	<i>8-284</i>
<i>Figure 8.15: Viewing Parameters</i>	<i>8-284</i>
<i>Figure 8.16: The painter algorithm</i>	<i>8-287</i>
<i>Figure 8.17: The Finite Element algorithm activity diagram</i>	<i>8-290</i>
<i>Figure 8.18: The Boundary Element algorithm activity diagram</i>	<i>8-290</i>
<i>Figure 8.19: The WinFEBE computer farm (hosted by the CERN NICE Computing Infrastructure)</i>	<i>8-292</i>
<i>Figure 8.20: The WinFEBE console at start up</i>	<i>8-293</i>
<i>Figure 8.21: The WinFEBE console connected to the nodes</i>	<i>8-294</i>
<i>Figure 8.22: The WinFEBE console options dialog to add a new node</i>	<i>8-295</i>
<i>Figure 8.23: The server program communication settings</i>	<i>8-296</i>
<i>Figure A.1: Maxwell's rotating rod set-up. It is suitable for complex Young's modulus measurements from 10^{-3} to 10^3 Hz (Ferry 1980)</i>	<i>317</i>
<i>Figure A.2: Kline's suspended rod for resonant flexural vibrations measurements (Ferry 1980)</i>	<i>319</i>
<i>Figure C.1: Schematic diagram of a single resonance transducer equivalent circuit.....</i>	<i>324</i>
<i>Figure C.2: Schematic diagram of the transducer equivalent circuit at resonance with matching transformer and power source</i>	<i>327</i>
<i>Figure C.3 : Conductance Vs. Frequency for the first ceramic pair around the resonance frequency $f_s =$ 1.08 MHz (unmatched)</i>	<i>330</i>
<i>Figure C.4: Admittance plot for the first ceramic pair around the resonance frequency $f_s = 1.08$ MHz (unmatched)</i>	<i>331</i>
<i>Figure C.5: Conductance Vs. Frequency for the second ceramic pair around the resonance frequency f_s $= 1.08$ MHz (unmatched).....</i>	<i>331</i>

<i>Figure C.6: Admittance plot for the second ceramic pair around the resonance frequency $f_S = 1.08$ MHz (unmatched)</i>	<i>332</i>
<i>Figure C.7: Conductance Vs. Frequency for the first ceramic pair around the resonance frequency. Comparison between matched and unmatched response</i>	<i>335</i>
<i>Figure C.8: Admittance plot for the first ceramic pair around the resonance frequency. Comparison between matched and unmatched response</i>	<i>335</i>
<i>Figure C.9: Conductance Vs. Frequency for the second ceramic pair around the resonance frequency. Comparison between matched and unmatched response</i>	<i>336</i>
<i>Figure C.10: Admittance plot for the second ceramic pair around the resonance frequency. Comparison between matched and unmatched response</i>	<i>336</i>
<i>Figure C.11: The test parametric transducer (side view). The aluminium anodised body contains the matching transformers.....</i>	<i>337</i>
<i>Figure C.12: The test parametric transducer (front view). The piezoelectric crystals are encased in protective stycast resin</i>	<i>338</i>

List of Tables

<i>Table 4.1: Chemical formulation of uncured butyl rubber base (phr)</i>	<i>4-87</i>
<i>Table 4.2: Chemical formulation of vulcanised butyl rubber sheets (phr)</i>	<i>4-88</i>
<i>Table 4.3: Chemical formulation of loaded polyurethane rubber (phr)</i>	<i>4-89</i>
<i>Table 5-1: Acoustic impedance and admittance per length</i>	<i>5-157</i>
<i>Table 6.1: Interpolation functions for quadratic elements in two and three dimensions</i>	<i>6-177</i>
<i>Table 6.2: Interpolation functions for hexahedral quadratic elements three dimensions</i>	<i>6-194</i>
<i>Table 7.1: Memory requirements for the complete composite tile at two frequencies (FEM = Finite Element Model; BEM = Boundary Element Model)</i>	<i>7-208</i>
<i>Table 7.2: Comparison of characteristic frequencies (kHz) between analytical solution and coupled finite element-boundary element solution. Between brackets is the modal order</i>	<i>7-211</i>
<i>Table 7.3: Material properties of graphite-epoxy composite (Pates et al. 1995)</i>	<i>7-217</i>
<i>Table 7.4: Comparison of characteristic frequencies (Hz) (the values in Pates et al. (1995) are interpolated from the published graphs in the paper).....</i>	<i>7-217</i>
<i>Table 7.5: Anechoic tile resonance frequencies</i>	<i>7-229</i>
<i>Table 7.6: Transducers operative parameters (in water)</i>	<i>7-256</i>
<i>Table 8.1: UML graphical symbols.....</i>	<i>8-270</i>
<i>Table 8.2: The client-server UDP messages.....</i>	<i>8-297</i>

List of Symbols, Definitions and Abbreviations

Mathematical Operators

(f, g are scalar quantities, \mathbf{a}, \mathbf{b} are column vectors, \mathbf{M}, \mathbf{N} are $m \times n$ matrices)

$\mathbf{a} \cdot \mathbf{b}$	Scalar product	$\nabla f, \nabla \mathbf{a}$	Gradient operator
$\mathbf{a} \times \mathbf{b}$	Vector product	$\text{div } \mathbf{a}, \text{div } \mathbf{M}$	Divergence
$\mathbf{a}\mathbf{b}^T$	Transposed vector product	$\nabla^2 f$	Laplace operator
$f * g$	Convolution	\sim	Fourier transform
$f \oplus g$	Boltzmann operator	\wedge	Laplace transform

Symbols

α	attenuation	μ	Lamé coefficient
Γ	domain boundary	ν	Poisson ratio
γ	propagation vector	ξ	unit vector
δ	phase lag	ρ	density tensor
ζ	longitudinal acoustic impedance per length	ρ	scalar density
η	dynamic viscosity	Φ	mass flow density
	transverse acoustic admittance per length	Φ	injection source potential
θ	angle	ϕ	phase function
	cubic dilatation		generic process
ϑ	phase angle		scalar potential
κ	compressibility		interpolation function
Λ	scalar acoustic slowness	χ	characteristic function
λ	wavelength	Ψ	force source potential
	Lamé coefficient	ψ	vector potential
	eigenfunction	ψ	generic process
		Ω	integration domain
		ω	angular frequency
A	surface area	\mathbf{M}	mass matrix
a	radius	\mathbf{n}	normal vector
BEM	Boundary Element Model	\mathbf{p}	Laplace multipliers
\mathfrak{B}	three-dimensional body	p	pressure
\mathbf{b}	body forces	\mathbf{Q}	symmetric transformation
\mathbf{C}	complex modulus	q	weighing coefficients
\mathbf{C}	damping matrix		source distribution
c	phase velocity		flux

D	flexural rigidity	R_0	radius of curvature
\mathcal{E}	Euclidean space	R	reflection coefficient
E	strain field process		residue or error
\mathbf{E}	strain tensor	RL	reflection loss
E_I	storage Young modulus	\mathbf{r}	position vector
FEM	Finite Element Model	r	radius
f	volume force distribution	S	stress field process
f	frequency	\mathbf{S}	stress tensor
	form function	S	average deformation
\mathbf{G}, \mathbf{G}_x	relaxation response functions	s	radius
G_1, G_2	scalar relaxation response functions	\mathbf{T}	transmission matrix
		T	transmission coefficient
G	Green's function	TL	transmission loss
g	influence coefficient	t	time
J_1, J_2	scalar compliance response functions	u	displacement
	Heaviside spaces		displacement process
H, H^{ac}			potential
H	Hamilton function	V	velocity potential
h	height	\mathcal{V}	inner product space
	influence coefficient	\mathbf{v}	velocity
\mathbf{J}, \mathbf{J}_x	compliance response functions	W	virtual work
\mathbf{J}	Jacobian matrix	\mathcal{X}	generic space
J	performance functional	\mathbf{x}	material point
k	wave number		generic vector
\mathbf{K}	response function	\mathcal{Y}	generic space
\mathbf{K}	stiffness matrix	Y	acoustic admittance
\mathcal{L}	linear hereditary law	Z, Z_c	acoustic impedance
\mathbf{L}	coupling matrix		

Chapter 1

Introduction

1.1. Overview

The desire to investigate acoustic wedges and viscoelastic materials comes from the need of developing better anechoic structures for underwater applications, especially in the fields of noise control and underwater communications.

The use of wedges is not new and wooden or rubber structures have been used in many airborne and underwater applications. Nonetheless, detailed information on the performance of complex periodic structures is rather sparse.

In addition, a wide range of new materials can now be used and, in many cases, composite or complex materials can be applied in order to modify and tailor the acoustic properties for specific applications. These materials present a rather complex dependence on frequency and/or temperature and their acoustic properties can change quite considerably.

The application of exact mathematical models to the study of this kind of structures is almost inevitably made difficult by the sheer complexity of the underlying physical principles. If simple systems, such as scattering from a sphere, a cylinder, a semi-infinite wedge and so on, can be modelled by a number of mathematical theories, this approach fails when facing large periodic, multi-layered, frequency dependent systems.

However, the sort of detailed analysis sought after can be performed by means of numerical modelling techniques. These techniques, born and prospered with the modern computing machines, provide a relatively fast and reliable method to characterise complex structures. It becomes therefore possible to take into account not only their geometrical shape, but also the special properties of new, efficient, sound-absorbing materials.

It is necessary, however, to devise precise numerical methods with the ability to cope with a number of factors, some of which have already been mentioned:

- the most efficient sound absorbing materials are frequency dependent and this dependency can only be described by complex integral relationships
- the numerical model must be complemented with suitable initial and constitutive conditions, among which lie the often little known physical properties of the applied compounds
- the acoustic radiation and scattering in a fluid medium propagate from the object to infinity
- the computer codes must be time-efficient, memory efficient and provide all the required tools for a complete analysis

This research work addresses the above outlined factors with the goal to provide some of the information still missing from a detailed knowledge of the performance of complex anechoic structures.

1.2. The VERTLINK Project

This study was conducted as part of the MAST II European Communities research project MAS2-CT94-0079, code-named VERTLINK (Jones, Di Meglio *et al.* 1997).

The VERTical LINK system is an underwater telemetry and communications system developed by the Acoustics & Sonar Group of the University of Birmingham in collaboration with the Italian Whitehead Alenia Sistemi Subacquei and the Spanish Institute of Acoustics. The system collects, stores and transmits oceanographic data to an end-user. It uses a half-duplex link comprising two units - a seabed unit and a surface unit. The seabed unit, under the control of the surface unit, records data and transmits it to the surface using different levels of modulation and power. The surface unit is linked to a computer on board a survey vessel (via a physical cable) or to shore by means of a radio link, fig.1-1.

The system uses high-data rate DPSK modulation, which requires the capability of distinguishing between the different values of phase embedded in the signal. In the case of 8-DPSK, for example, the error must not exceed $\pm 22.5^\circ$ (Di Meglio 1997).

The signal received is the superposition of the direct path and the reflected signals from the sea surface and the phase errors induced by the interference of the surface path could prevent reliable recognition of the information.

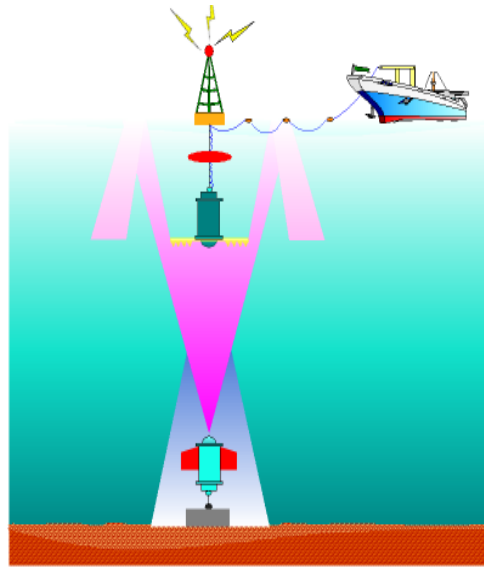


Figure 1.1: The VERTLINK Communication System

The author was involved in the project with the task of studying a suitable anechoic baffle to be mounted on a collar around the receiving unit, just above the electro-acoustic transducer (fig. 1-2) in order to reduce the interference from the surface reflected signals. Details of the analysis of the performance of the VERTLINK anechoic screen is reported in Di Meglio 1997, which can also be found in Appendix G.



Figure 1.2: The receiving unit of the VERTLINK system. The baffle is mounted around the case facing the transducer

1.3. Statement of Originality

This research work presents an original contribution to the advancement of science in two different areas, notably polymer properties characterisation and wedge scattering pattern characterisation. In addition, it provides the researchers with enhanced software tools for the detailed investigation on the acoustical and mechanical properties of structures made of viscoelastic materials.

As mentioned in the opening overview, the research work is focused on four outstanding problems:

- the description of the viscoelastic behaviour of the materials, which follows complex integral relationships
- the need for detailed information on the values of the physical properties of the materials
- the need of dealing with an infinite region of space and enabling numerical simulations, when dealing with radiation and scattering
- the need for an efficient computer program with the ability to solve the numerical problem taking into account the above mentioned issues

The first problem is solved by means of the well-established linear theory of viscoelasticity.

The classes of polymer compounds used during this research have been thoroughly investigated and their physical properties have been determined, providing detailed and previously sparsely available or utterly unavailable information on their viscoelastic properties.

Charts of longitudinal and shear complex moduli are presented, which provide novel insight into the behaviour of loaded polyurethane and butyl rubbers in the glass/rubber transition region. The effect of different fillers, both inert and chemically reactive, has been studied and performance comparisons have been produced for all the samples available.

In addition, a new method based on a variational approach has been used here for the first time to reconstruct the material properties of polymeric rubbers from a limited set of experimental data.

The second and most important contribution lies in the detailed analysis of the performance of a sound absorbing, layered, and wedged anechoic screen immersed in a heavy fluid. Information on the frequency and polar response of this kind of complex-shaped diffracting structures is scarcely available and little or no previous work has been published at the level of detail provided in this research.

The scattered acoustic field is analysed around the structure by simulations and experiments and its changes with frequency and angle of incidence are investigated. Detailed charts of the scattering patterns are provided for different acoustic and geometrical configurations.

Finally, a specific computer program has been written to solve the complex numerical problem. The program is based on the boundary element algorithm in order to be able to solve systems with boundary values at infinity. The boundary element technique is quite well established and the program implementing it for scattering from elastic objects had previously been developed within the Acoustics and Sonar Group of the University of Birmingham. However, the extension of the software to viscoelastic materials (using a rigorous linear theory approach) is herein presented for the first time. In addition, part of the code has been completely rewritten using efficient object-oriented technologies in order to take full

advantage of industry-standard, graphical computing environments, such as Windows NT and Windows 2000.

1.4. Thesis Contents

Chapter 1: This chapter. It contains a general overview of the research work, its purpose and applications and a statement of originality, which outlines the extension of the original contribution to the advancement of scientific knowledge.

Chapter 2: This chapter frames the confronted research problem in the proper historical background. It outlines the most important discoveries and the scientific milestones in the three main research areas explored here. The viscoelastic materials properties are outlined from the first uses of natural hevea rubber to the analysis of “materials with memory” and the manufacturing of modern anechoic screens. The main problems in the analysis of acoustic scattering and its application to engineering problems are then dealt with. Finally, the development of the numerical technique known as the boundary element method is outlined from its early applications to the aerospace industry to modern sound-structure interaction problems. A comprehensive literature review is presented to define the state-of-the-art of these research fields.

Chapter 3: This chapter introduces the foundations of the linear theory of viscoelasticity. The basic mathematical properties and their physical meaning are defined within a traditional integral-differential scheme based on the Volterra approach. The consequences of the so-called fading memory hypothesis on the characterisation of polymeric materials are outlined. Finally, the integral equations describing

the viscoelastic constitutive relationships are developed for the case of periodic stress-strain problems.

Chapter 4: The experimental methods used to characterise solid viscoelastic systems are herein described. A general overview of the main physical parameters and manufacturing processes is followed by the description of the special materials used during this research, loaded polyurethane and butyl rubbers. The two characterisation methods applied are then described, notably the dynamic viscoelastimeter and the time-transmit immersion method. The latter method makes also use of a parametric electro-acoustic transducer, whose basic working principle and manufacturing process are outlined. The obtained experimental results are discussed and a new method based on a variational approach is used to reconstruct the physical properties of the material from the experimental data. Finally, the viscoelastic response functions of the compounded butyl rubber are calculated in the frequency range of interest.

Chapter 5: This chapter introduces the main topic of acoustic waves scattering. The foundations of reflection and scattering of sound from solid boundaries in fluid media are outlined. An approximate analytical model of scattering from cones, cones arrays, finite size plates and their superposition is presented in order to lay down a proper reference for calibrating the numerical model presented in the following chapters.

Chapter 6: In this chapter, the core aspects of the developed numerical method are presented. First of all the combined finite element-boundary element (FE-BE) method is introduced as a means of solving complex sound-structure interaction problems. A method to overcome the problem of nonuniqueness of the solution

at certain characteristic frequencies is presented. The equations describing the kinematics and dynamics of a solid elastic body immersed in a loading fluid are outlined and their numerical form is developed. Then the viscoelastic constitutive equations presented in Chapter 3 are in turn discretised and introduced in the numerical dynamic model.

Chapter 7: The numerical method developed in Chapter 6 is applied here to the analysis of compounded sound-absorbent panels and tiles. After a short presentation of the structure of the panel, the method is calibrated against the exact results known for the simple shapes of Chapter 5. Then a complete analysis of the acoustic scattering patterns is performed as functions of frequency, angle of incidence and geometrical parameters. Experimental measurements of a model tile are presented and compared to the numerical data obtained from the combined FE-BE method.

Chapter 8: In this chapter, the software written to implement the numerical analysis method is discussed in some more details. The advantages of using the object-oriented paradigm are discussed and the object-oriented analysis and system design is presented. The structure of the program is then outlined and its most important components are described within the framework of the so-called iconic or graphic user interface provided by the Windows NT operating system. A client-server implementation of the program is presented as a way of distributing the workload on a farm of commodity PCs.

Chapter 9: The conclusions on the research carried out are drawn here. The strengths and limitations of the undertaken approach are discussed and some further enhancements proposed.

1.5. References

JONES, J.C., DI MEGLIO, A. *et al.* (1997). The design and testing of a DSP, half-duplex, vertical, DPSK communication link, *OCEAN '97 MTS/IEEE Conf. Procs.*, Halifax, Nova Scotia, Canada

DI MEGLIO, A. *et al.* (1997). Combined finite element/boundary element analysis of a viscoelastic anechoic panel for underwater applications, *OCEANS '97 MTS/IEEE Conf. Procs.*, Halifax, Nova Scotia

Chapter 2

Historical Background and Literature Review

2.1. Rubber, high polymers and materials with memory

It has long been known that material behaviour is not always elastic. Pre-Columbian Native Americans from South and Central America used rubber for balls, containers and shoes and for waterproofing fabrics. Mentioned by Spanish and Portuguese writers in the 16th century, rubber did not attract the interest of Europeans until reports about it were made (1736–51) to the French Academy of Sciences by Charles de la Condamine and François Fresneau. Pioneer research in finding rubber solvents and in waterproofing fabrics was done before 1800, but rubber was used only for elastic bands and erasers, and these were made by cutting up pieces imported from Brazil.

Joseph Priestley is credited with the discovery of its use as an eraser about 1770, thus the name rubber. The first rubber factory in the world was established near Paris in 1803, the first in England by Thomas Hancock in 1820. Hancock devised the forerunner of the rubber masticator, and in 1835, Edwin Chaffee, an American, patented a mixing mill and a calender.

In 1823, Charles Macintosh found a practical process for waterproofing fabrics, and in 1839 Charles Goodyear discovered vulcanisation, which revolutionised the rubber industry.

In the latter half of the 19th century, the demand for rubber insulation by the electrical industry and the invention of the pneumatic tyre extended the demand for rubber. In the 19th century, wild rubber was harvested in South and Central America and in Africa; most of it came from the Pará rubber tree of the Amazon basin. Despite Brazil's legal restrictions, seeds of the tree were smuggled to England in 1876. The resultant seedlings were sent to Ceylon and later to many tropical regions, especially the Malay area and Java and Sumatra, beginning the enormous Far Eastern rubber industry. Here the plantations were so carefully cultivated and managed that the relative importance of Amazon rubber diminished.

American rubber companies, as a step toward diminishing foreign control of the supply, enlarged their plantation holdings in Liberia and in South and Central America. The cutting off of Far Eastern rubber during World War II gave impetus to the development of synthetic rubber. During World War I, Germany had made a synthetic rubber that was too expensive for peacetime use. In 1927, a less costly variety was invented, and in 1931 neoprene was made, both in the United States.

German scientists developed Buna rubber just prior to World War II. When importation of natural rubber from the East Indies was cut off during World War II, the United States began large-scale manufacture of synthetic rubber, concentrating on Buna. Today synthetic rubber accounts for most of the world's rubber production.

The term *elastomer* is used to designate synthetic rubber. All rubber-like materials are polymers, which are high molecular weight compounds consisting of long chains of one or more types of molecules, such as monomers.

Vulcanisation (or curing) produces chemical links between the loosely coiled polymeric chains and elasticity occurs because the chains can be stretched and the cross-links cause them to spring back when the stress is released.

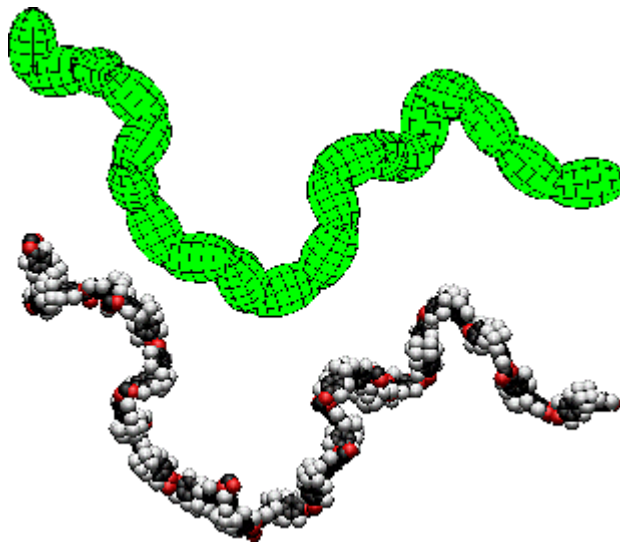


Figure 2.1: Polymer strand made of a chain of cross-linked monomers (coarse and detailed computer-generated 3D image)

Natural and synthetic rubbers elasticity, toughness, impermeability, adhesiveness, and electrical resistance make them useful as adhesives, coating compositions, fibres, moulding compounds and electrical insulators. Most elastomers are water repellent and have varying degrees of resistance to alkalis and weak acids. These properties, added to the capacity of absorbing and dissipating acoustic energy by means of a number of different internal mechanisms, make elastomers a sensible choice for many underwater applications. External protecting cases to electro-acoustic transducer backing layers, passive detection elements and sound-absorbing baffles are all examples of application of rubber compounds to acoustics.



Figure 2.2: Australian Navy submarine with polymer composite sonar dome



Figure 2.3: Omni-directional ball transducer with polyurethane shell

A number of models have been proposed to predict the behaviour of viscoelastic materials from the mathematical, mechanical and thermodynamic points of view.

Classical models of viscoelasticity were initially proposed by Maxwell, Voigt and Kelvin in the last century to modify the linear Hooke's law, which was ill suited for rubber-like materials. In the second half of the last century, the fundamental research work conducted by Boltzmann led to the development of the *superposition principle*. This principle allows the state of stress or strain in a viscoelastic material to be evaluated from the knowledge of its past deformation history.

An essential role in the development of both the mechanical theories of viscoelastic deformations and the mathematical method to deal with them was played by Volterra.

Volterra's work is associated with the birth of the modern functional analysis in particular in the field of the integral and integral-differential equations, which bear today his name. He himself explored many applications of these methods and developed such an essential concept as the hereditary behaviour of viscoelastic materials (Volterra 1913), which is a key foundation of the present research work.

Models of rubber elasticity and viscoelasticity were studied by many authors. Love (1944), Landau and Lifshitz (1959) and Treloar (1958) developed a mechanical and mathematical theory of elasticity. Green, Rivlin (1947), Noll (1958), Gurtin and Sternberg (1962) expanded the phenomenological models proposed by Boltzmann and Volterra into coherent mathematical frameworks.

Thermodynamic and statistical models of polymer elasticity were also developed by Treloar, Alfrey (1948), Tschoegl (1980) and Ferry (1980) with the increasing knowledge of chain and network configuration of high polymers.

The temperature and frequency dependence of polymer materials has also been widely studied. The frequency dependence can be quite easily derived from the Maxwell model and much experimental evidence has been given about the relationship between time and temperature for polymer mechanical properties. Earlier experimental work was carried out by Williams, Landel and Ferry (1955), who proposed the time-temperature (or frequency-temperature) superposition method now carrying their names. The method was later justified theoretically in terms of free-volume and thermodynamic relationships.

The fact that additions of 'modifiers' in the rubber matrix could change the physical properties of the material was clear since when the native Americans started mixing natural rubber and straw strands to make robust shoe soles. The modifiers used for different purposes are variable both in geometry and in properties. They go from powder-like metallic fillers to

glass and carbon fibres, from plastic spheres to iron wool, from carbon particles to air bubbles.

The research that has been so far carried out is focused on two main areas with different goals, methods and applications. On one side, the development of materials with increased strength and resistance and reduced weight for civil and aerospace applications. On the other side, the development of materials with increased sound and vibration absorption properties for civil, environmental and mechanical applications.

The second research field, which is the one we are interested in, can be further divided in two main areas. The first area deals with the prediction and determination of the modifications in material properties by addition of fillers. The second area has to do with the analysis of sound propagation and scattering within a medium filled with randomly dispersed particles.

The first experimental studies of mixed, multi-phase systems were started during the late 1950's. Extensive studies of mixed viscoelastic systems, mainly in the transition and terminal zones of the stress-frequency curve, were conducted by Becker and Oberst (1956), Blatz (1956), Landel (1958) and Ecker (1968).

A theoretical formulation relating the shear and bulk moduli of a composite with spherical inclusions to the shear and bulk moduli and Poisson's ratios of the two component materials was developed by van der Poel (1958). A number of empirical equations were also developed, such as the so-called Eilers and van Dijk formulation (Eilers 1941).

The main results of this research can be summarised by dividing the particle fillers in two classes, interacting and non-interacting substances.

In both classes, the main energy-absorption mechanism is given by the partial occupation of volume by rigid and immobile masses, whose size follows a Gaussian

distribution. The bulk modulus and energy loss increase with the filler concentration, but are essentially independent of the particle size for a given filler concentration.

In the case of interacting particles, chemical bonds can be formed between the polymer chains and the particles. These bonds, mainly surface-type van der Waals bonds, have the two-fold effect of increasing the energy required to displace the particles and of decreasing the mean distance between particles and polymer chains. They act, therefore, as additional cross-links within the polymer matrix. The size of the particles in this case plays an important role, since the strength of the bonds depends on the surface extension of the particles.

Examples of non-interacting substances are glass beads and sodium chloride particles. To the interacting class of substances there belong carbon black particles, metal oxides (lead, tungsten) and polymer beads (polyurethane).

The second aforementioned research area with the problem of evaluating the propagation parameters for a random ensemble of discrete scatterers immersed in a gaseous, fluid or solid medium. This problem arises in many applications, from elastic/viscoelastic wave propagation to quantum mechanics.

The first approximation methods were proposed in the late 1940's, early 1950's by Foldy (1945) and Lax (1952), who laid the foundations of a general probabilistic multiple scattering theory. Between 1955 and 1965, exact models for the case of scattering of longitudinal waves by spherical inclusions were presented by Ying and Truell (1956) for the static field case and by Mow (1965) for the transient response case. These models have been widely used until the 1980's, when new approaches have been presented based on variational principles (Talbot and Willis 1982), on the Kramer-Kronig relationships (Beltzer *et al.* 1983) and on the so-called effective medium theory (Gaunard and Uberall 1983). Studies of wave

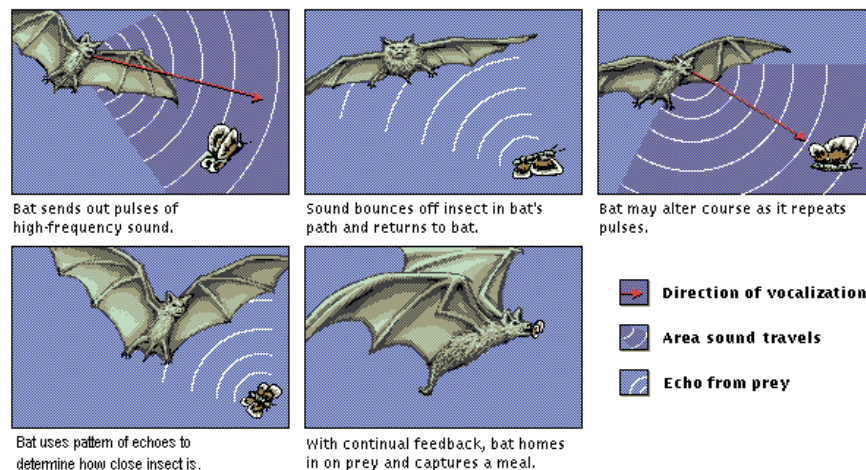
propagation in filled viscoelastic media have been carried out only in recent years, boosted by technological advances in the production of such materials for aerospace applications. An interesting example of this research can be found for example in Kim *et al.* (1994).

2.2. Sound Scattering: from Bats and Dolphins to Acoustic Television

The process of acoustic scattering and its use for recognition of the shape and properties of objects is not a human invention.

All small bats navigate and most insectivorous species target their prey by echolocation. This is the pulsed emission of high-frequency sounds that are reflected back as echoes to a bat's ears from surrounding surfaces, indicating the position, relative distance, and even the character of objects in its environment. In this sense, bats “see” acoustically. This is the basis for their ability to navigate in total darkness. The physical properties of the emitted sounds vary in characteristic ways among species. The sound pulses are generated in the larynx, and in different species are emitted either from the mouth or from nostrils.

Dolphins and other cetaceans almost constantly emit either clicking sounds or whistles. The clicks are short pulses of about 300 sounds per second, emitted from a mechanism located just below the blowhole. These clicks are used for the echolocation of objects and are resonated forward by the so-called oily melon, which is located above the forehead and acts as an acoustic lens. Echoes received at the area of the rear of the lower jaw are transmitted by a fat organ in the lower jaw to the middle ear. This echolocation system, similar to that of the bats, enables the dolphin to navigate among its companions and larger objects and to detect fish, squids, and even small shrimps.



Echolocation and Prey Detection

Bats use auditory stimuli to navigate and to locate and catch insect prey. High frequency pulses of sound emitted by the bat bounce off objects in its path and return as echoes. Different types of sensory cells in the bat's brain interpret these echoes to determine the location and some physical properties of the objects, creating a spatial "map" that governs the bat's behavior. A reflex dampens the sound of its own vocalization so it can detect the quieter sounds coming from its prey. This complex specialization is typical of most species of insectivorous microbats. Curiously, the noctuid moth uses a similar but less sophisticated adaptation to detect and evade predatory bats in the night sky.

Figure 2.4: Echolocation and prey detection of microbats (from Microsoft Encarta 1998 Encyclopedia)

Studies of wave scattering from objects of various shapes can be traced back to the works of Huygens around 1690 and Fresnel around 1820 and their development in geometrical optics (mainly in the high-frequency field). The latest applications of acoustic wave scattering can be found in many areas, from medical acoustical imaging to non-destructive testing and imaging in archaeology to seismic surveillance and space applications.

The first attempt to obtain solutions to the steady-state wave equations in the acoustic domain in the low frequency field was produced by Lord Rayleigh in 1897 (Strutt 1897). The term ‘Rayleigh scatterer’ is now applied to a body whose characteristic dimensions are small compared to the wavelength. During the first 30 years of this century, the foundations of the theory of radiation and scattering of acoustic waves were laid by Lord Rayleigh, Lamb, Love and Morse among the most active researchers.

The basic analysis method inside the Rayleigh region is based on the Rayleigh series or low-frequency expansions. The Rayleigh region is actually defined as the range of values of the wave number k for which the quantity of interest can be expanded in convergent series in positive integral powers of k . The method originally devised by Lord Rayleigh was then extended and improved by Stevenson (1953), Kleinman (1965) and Van Bladel (1963). Recent applications of this technique can be found for example in Craster (1996).

In the high-frequency field, the search for a solution to scattering problems has been more complex.

The already mentioned work of Huygens and Fresnel had clarified the relationship between ray optics and wave propagation. This relationship is especially important as the wave number k tends to infinity and on this principle are based a number of important methods such as the geometrical and physical optics and the geometrical theory of diffraction. However, more sophisticated methods are necessary to find a solution to the scattering problems in those portion of space which are not directly illuminated by the primary wave or in the transition regions between light and shadow (the penumbra regions). An overview of the most important methods applied to acoustic scattering is given here. Some general results are shown, but not fully derived and appropriate references are mentioned. One of these methods, based on the reciprocity theorem, will be addressed in some details in Chapter 5. It

will be used to find the analytic form of the solution to the scattering problem for some canonical shapes of interest in this research.

2.2.1. Geometrical Optics and Acoustics

Geometrical optics and its extension to acoustics are based on Fermat's principle that the optical/acoustical path between two points P and Q is stationary and therefore the first term of its Taylor expansion is zero. As a particular case, within a medium with constant index of refraction the path is a straight line.

This method is directly based on the work by Huygens on optical rays. It was later formalised by Kirchoff in the frame of his work about the oscillatory behaviour of light and Helmholtz successfully extended the method to electromagnetic waves. Kay and Keller (1954) improved the method to include the regions in the vicinity of the caustics, the lines where the method yields an infinite value of the field. The scalar acoustic case can be considered as a special case of the more general vector approach.

The scattered field along the reflected ray as a function of the reflected field at the surface of a body due to a given incident field was given by Fock (1965) for the first time.

2.2.2. Keller's Theory or Geometrical Theory of Diffraction (GTD)

The simple geometrical optics theory cannot explain, however, why regions that are not directly illuminated by the incident rays are not completely dark. In addition, in particular conditions also the field in the illuminated regions is not predicted correctly by this method.

During the 1950's Keller proposed and developed an extension to the geometrical optics method, which could explain these phenomena. According to Keller's method, the

Geometrical Theory of Diffraction, a new type of rays must be introduced, which are generated when the incident rays are diffracted by edges, corners and vertices of the scatterer. Similarly, diffracted rays are also generated when the incident rays hit the surface of the scatterer at a grazing angle.

The diffracted rays can penetrate the shadow region or modify the scattered field predicted by the geometrical optics method. The field can be calculated by multiplying the incident field at the point of diffraction by a diffraction coefficient. The diffraction coefficient depends only on the local properties of the field, the involved media and the boundary in the neighbourhood of the point of diffraction.

The solution of a number of simple boundary value problems with the appropriate local properties, the so-called canonical problems, conveys the amplitude of the diffracted field.

This method has been extended by Keller and others to several important cases, such as reflection, transmission and diffraction in homogeneous and inhomogeneous media (Keller 1962); diffraction by thin screens and objects with edges (Keller and Hansen 1965); diffraction by smooth convex objects (Levy and Keller 1959). In recent years, the model has been improved to include non-linear effects (Coulouvrat 1997).

2.2.3. Uniform Asymptotic Theories (UTD, EUTD)

Although GTD is a significant improvement to GO, it still has some shortcomings. It can predict the diffracted fields in regions away from the shadow boundaries, but it becomes singular in the transition regions surrounding these boundaries.

Kouyoumjian and Pathak (1974) presented a new theory, whose solutions remained bounded within the transition regions. This theory, which is valid everywhere in the space surrounding the scatterer, is called Uniform Theory of Diffraction (UTD).

The method is essentially based on a new set of diffraction coefficients obtained by multiplication of the GTD coefficients by diffraction functions that approach zero at the same rate as that at which the GTD coefficients become singular.

A general description of the method and its applications can be found for example in Mc Namare *et al.* (1990).

The UTD has been further improved to take into account non-local phenomena or non-optical incident fields (EUTD).

2.2.4. Luneburg-Kline Expansion

This asymptotic method can be used to find the high-frequency scattered field from objects of arbitrary shape. In its scalar form was introduced by Luneburg in 1944 (Luneburg 1965) as a means to solve the wave equation $(\nabla^2 + k)V = 0$ for the velocity potential V .

The method expresses the velocity potential V as an asymptotic expansion of the form:

$$V \approx e^{ik\Phi} \sum_{n=0}^{\infty} \frac{v_n}{(ik)^n} \quad k \rightarrow \infty \quad (2.1.)$$

where v_n is a function of the observation point only and Φ is an unknown phase function.

If we now insert the expansion (2.1) in the wave equation and equate to zero the coefficient of each power of k , we obtain:

$$(\nabla \Phi)^2 = 1 \quad (2.2.)$$

$$2\nabla v_n \cdot \nabla \Phi + v_n \nabla^2 \Phi = -\nabla^2 v_{n-1} \quad n = 0, 1, 2, \dots; \quad v_{-1} = 0 \quad (2.3.)$$

Eq. (2.2) is called the eiconal equation. It determines the phase function. The functions v_n are found by iteration from eq. (2.3). If s is the arc length along an optical ray from the source to the observation point, the solution for the v_n proposed by Luneburg takes the form:

$$v_n(s) = v_n(s_0) \left[\frac{G(s)}{G(s_0)} \right]^{\frac{1}{2}} - \frac{1}{2} [G(s)]^{\frac{1}{2}} \int_{s_0}^s [G(t)]^{-\frac{1}{2}} \nabla^2 v_{n-1} dt \quad (2.4.)$$

For a given scattering object, it's now possible to express the optical path s in terms of the scatterer surface and build the system of optical rays associated with the phase function satisfying the eiconal equation.

2.2.5. Physical Optics and Physical Diffraction Theory (PTD)

This method is an extension of the geometrical optics method, whereby the starting point for calculation is an explicit definition of the distribution of the scattered field on the surface of the scatterer.

The form of the surface field is assumed equal to the geometrical optics surface field:

$$\begin{aligned}
\frac{\partial V}{\partial n} &= \begin{cases} 2 \frac{\partial V^i}{\partial n} & \text{illuminated side} \\ 0 & \text{shadowed side} \end{cases} \quad (\text{Neumann condition}) \\
V &= \begin{cases} 2V^i & \text{illuminated side} \\ 0 & \text{shadowed side} \end{cases} \quad (\text{Dirichlet condition})
\end{aligned} \tag{2.5.}$$

Substitution of these surface fields (or a linear combination for surfaces with acoustic impedance) in the integral equations for the scattered field yields a representation of the far field. Since the integral equation can be solved by quadratures, this method is well suited to numerical calculation.

This method has two serious drawbacks. It cannot be used to predict the field in the shadow regions and has an inherent non-physical discontinuity of the field where illuminated and shadowed regions meet. However, the accuracy of the method in the direction of specular reflection is often very high.

2.2.6. Fock's Theory

Fock's theory (Fock 1946) is based on the principle of locality of the field in penumbra regions. The main postulate of the method is that the surface field in the transition regions between light and shadow depends only on the local curvature of the surface in the plane of incidence and on the locally plane incident wave.

Fock also estimated the width of the penumbra regions as a function of the wavelength λ and the local principal radius of curvature R_0^2 :

$$d = \sqrt{\frac{\lambda R_0^2}{\pi}} \tag{2.6.}$$

Because of the local nature of the transition region, it is therefore possible to find a set of universal solutions that can be applied to all bodies having the same local curvature near the transition region. Fock's surface field outside the transition region is equivalent to the physical optics field in the illuminated region and to a creeping wave field in the shadow region (the type of field predicted by the geometrical theory of diffraction).

The method was later extended by Weston (1965) to include transition regions with discontinuity in the local curvature (edges, corners and vertices).

2.2.7. Variational Techniques

It is known since the early work of Volterra that an integral equation can be expressed as a variational principle. This equivalence has been often exploited in many problems of mechanics, acoustic and electro-magnetic wave propagation, optimisation.

The scattered acoustic field can always be expressed as a surface integral involving the value of the field at the surface of the scatterer. The integral equations can be solved directly by means of approximation or numerical techniques (see §2.2.10) or it can be transformed into a variational principle.

The first important variational principle applied to wave scattering was developed in 1948 by Schwinger (Levine and Schwinger 1948). We can consider the inhomogenous equation:

$$\mathbf{L}g = f \tag{2.7.}$$

where \mathbf{L} is a linear symmetric operator. If $\mathbf{L} = (\nabla^2 + k^2)$, f is a known function determined by the incident field and g is the pressure or the velocity potential, eq. (2.7) represent the wave equation.

The far field solution (for example for the velocity potential) can be written as:

$$V^s(\mathbf{x}) = \frac{e^{ikx}}{kx} (f_0, g) = \frac{e^{ikx}}{kx} \int_S f_0(\mathbf{r}) g(\mathbf{r}) d\mathbf{r} \quad (2.8.)$$

where V^s is the scattered potential in the point \mathbf{x} , f_0 is the incident field and S is the surface of the scatterer. If g_0 is a velocity potential distribution compatible with the incident field, such as:

$$\mathbf{L}g_0 = f_0 \quad (2.9.)$$

it is possible to write a reciprocity theorem (reciprocity theorems will be dealt with in more depth in Chapter 5) as:

$$V^s(\mathbf{x}) = \frac{e^{ikx}}{kx} (f_0, g) = \frac{e^{ikx}}{kx} (f, g_0) \quad (2.10.)$$

from which it follows that:

$$V^s(\mathbf{x}) = \frac{e^{ikx}}{kx} \frac{(f_0, g)(f, g_0)}{(\mathbf{L}g_0, g)} \quad (2.11.)$$

Schwinger principle states that necessary and sufficient condition for eq. (2.7) and (2.9) to be satisfied is that $V^s(\mathbf{x})$ as expressed by eq. (2.11) be stationary with respect to the virtual variations of g and g_0 , δg and δg_0 respectively.

Variational techniques for solving various boundary value and energy transfer problems have been proposed by many researches. Examples can be found in Levine (1950), Goblick and Bevensee (1960), Zhe (1995).

2.2.8. Function-Theoretic Methods: Wiener-Hopf Method

An alternative method to the analysis of scattering and diffraction problems by direct solution of integral equations is the application of the functional theory and analytic functions theory. This method can be successfully applied to certain classes of diffraction problems to yield a solution in closed form.

The most important method based on this principle is known as the Wiener-Hopf method (Amerio 1986). An integral equation of the Wiener-Hopf type has the general form:

$$a\psi(x) = f(x) + \int_0^{\infty} \psi(x')K(x-x')dx' \quad x > 0 \quad (2.12.)$$

where $f(x)$ and $K(x)$ are known functions and $\psi(x)$ is unknown.

This type of equation can usually describe diffraction problems with boundary conditions on semi-infinite bodies, such as semi-infinite planes or cylinders. The Wiener-Hopf method first extends the domain of integration of eq. (2.12) from $-\infty$ to ∞ by changing the definition of the function. Application of the Fourier transformation to this new extended

equation allows obtaining a relationship between two unknown transform functions, which can then be found in closed form by function-theoretic principles.

This method has been successfully applied to many scattering, diffraction and propagation problems. Recent examples can be found in Norris and Wickham (1995), Abrahams (1996), Tamura and Nakayama (1996), Cutzach and Luneville (1998),

2.2.9. Integral Equations Methods and Numerical Methods

Integral equation methods can be derived from the integral form of the acoustic field induced on the surface of a scatterer. Equations of this kind can be derived from the reciprocity theorem and can yield approximate closed-form solutions or constitute the base for the implementation of numerical methods.

A far-field scattering solution from simple shapes was provided in analytic form by Bowman *et al.* (1969), using a method based on the complex frequency-domain integral equations. Where the shapes present a more complex structure, two approaches have been followed.

If the shapes can be decomposed in simpler parts, a linear approximation of the integral equations can be employed to develop analytic solutions by superposition. This method has been for example applied by De Hoop (Quak *et al.* 1986; De Hoop 1991) to find the far-field plane wave scattering for canonical shapes and their combinations. Both time-domain and complex frequency-domain integral equations based on reciprocity theorems were linearised by taking the first term of the Rayleigh-Gans-Born approximation, which is additive in the geometrical domains of the scatterers.

This approach will be used in this research work. The complex frequency-domain reciprocity theorems for the acoustic wave will be used in Chapter 5 to develop closed-form

solutions for the rectangular plate, the finite-height cone and their superposition in the first-order Rayleigh-Gans-Born approximation.

The second approach consists in the application of numerical quadrature methods to the integral equations of the far-field scattering. Poggio and Miller (1973) provide an extensive review of methods suitable for the solution of three-dimensional scattering problems. Fokkema and Van der Berg (1993) have successfully applied the method to low-frequency seismic applications and diffraction from submerged elastic bodies has been recently analysed by Belov *et al.* (1994).

The numerical analysis based on finite-element and boundary element techniques of the scattered acoustic field from the hard-backed viscoelastic anechoic screen will be developed in Chapters 6 and 7 and represent the second objective of this work.

2.3. The Finite-Element and Boundary Element Methods

The modern origins of the Boundary Element Method have their beginning in the use of integral equation methods roughly between 1960 and 1975 by researchers such as Jaswon, Hess, Symm, Massonnet, Shaw, Rizzo, Cruse and others. Nonetheless, the deep foundations of the method can be found in the research work about integral equations carried on during 1800s and early 1900s by Poisson, Betti, Kirchhoff, Somigliana, Fredholm, Kellogg, Kupradze, Lauricella and others.

During the period from 1960 to 1975, integral equation methods were used to find solutions for two major mechanics problems:

potential theory applied to perfect fluid flow research in the aerospace industry

acoustics research, mainly related to underwater scattering and radiation

The methods initially used in this two cases under the common name of Boundary Integral Methods (**BIM**) can generally be subdivided in two classes, even though the distinctions effectively disappear as the equivalence and commonality of the methods are recognised (Cruse and Rizzo 1975):

- *indirect methods*, whereby the physical boundaries of a system are replaced by a surface of sources or sinks, adjusting the intensity to give the same physical results as in the original problem
- *direct methods*, whereby a fundamental solution (Green's function) of the governing partial differential equation is used to satisfy the physics of the system without boundary conditions and the resulting integral equation is then solved restoring the given boundary conditions

In 1975, the first conference on the method was held at the Rensselaer Polytechnic Institution by Cruse and Rizzo (1975). The first text on the use of boundary integral equation methods was published the following year by Jaswon and Symm with the title '*Integral Equation Methods in Potential Theory and Elastostatics*' (1977).

It was only in 1977 that the name Boundary Element Method (**BEM**) was used for the first time in a conference organised by Brebbia in Southampton, UK. It is since then used to address a method of solution characterised by the element subdivision of a physical system. Under this name, a number of formulations can be found, from the classical direct and indirect methods to the 'null-field' or the embedded integral methods.

The usefulness of boundary integral methods was at first recognised in the late 1950s for the solution of all those classes of problems involving infinite boundaries. For these

problems, the classical technique based on finite differences, and even the contemporarily developing finite element method based on variational principles, were ill suited.

The validity of the method in the solution of transient acoustic scattering and time harmonic acoustic scattering was rapidly established in the early 1960s by Friedmann, Shaw, Banaugh and others. The shortcoming of nonuniqueness of the solution at certain characteristic frequencies for exterior boundary problems was recognised and studied from the late 1960s by Copley, Schenck, Burton and Miller and more recently by Piaszczyk, Klosner, Cunefare, Francis and others. Methods to overcome the problem such as CHIEF (Combined Helmholtz Integral Equation Formulation, Schenck 1968) and HGF (Helmholtz Gradient Formulation, Burton and Miller 1971) were established.

The modern use of BIM for elastostatic problems was introduced in 1967 by Rizzo by taking to the boundary the fundamental Somigliana integral approach to elasticity and was extended to elastodynamics the following year by Cruse and Rizzo (1968a 1968b).

Finally, the ever-increasing importance of stress and acoustic analysis of complex structures immersed in fluid media led the mechanical engineering community to recognise the importance of boundary integral methods. This recognition gave rise to a convergence of techniques and to the development of combined Finite-Element, Boundary-Element methods. The method was initially applied in the early work by Schenck (1968) and has lead to modern mechanical-acoustical analysis software packages, such as NASTRAN, ANSYS and the WinFEBE software presented in this research.

Integral equation methods and the Boundary Element method have been successfully used to solve several different classes of scattering problems. One of the first examples can be found in the application of retarded potentials to acoustic scattering from rigid obstacles of arbitrary shapes by Shaw (1968).

Colton and Kress (1983) published the treatise '*Integral Equation Methods in Scattering Theory*'. Seybert *et al.* (1985) developed an improved method based on the boundary integral equation approach for radiation and scattering of acoustic waves in three dimensions. More recently, new formulations of the boundary element method based on hypersingular integrals (Rêgo Silva *et al.* 1992) and mixed continuous and discontinuous elements (Rêgo Silva *et al.* 1993) have been presented.

The effect of unknown or statistically uncertain parameters in radiation and scattering problems has also been considered by application of the so-called Probabilistic Boundary Element method (PBEM). The application of PBEM to acoustic scattering from a submerged rigid sphere can be found in Daddazio and Ettouney (1991).

The coupled FE-BE method has so far been used to solve structural-acoustical interaction problems in many areas. General structural-acoustic coupling problems have been studied by Tanaka and Masuda, who have presented their results in more than one paper (see for example Tanaka and Masuda 1987). Analysis of composite panels can be found in Pates, Shirahatti and Mei (1995). Noise control has been studied by Soenarko and Seybert (1991). Kobayashi and Kawakami have applied this method to the study of the dynamic interactions between structures and viscoelastic soil (1985).

This method suffers of the same nonuniqueness problem as shown by the exterior boundary problem. The same techniques can be applied to overcome this shortcoming and the CHIEF method has often been used to this effect. In particular, the Partial HGF method developed by Harris and Amini (1990) and extended by Francis to isoparametric elements (1993) will be applied in the FE-BE schema developed in the present work for the analysis of sound scattering from viscoelastic anechoic plates (Chapter 6).

2.4. Analysis of Underwater Sound Scattering from Absorbing, Periodic and Finite-Sized Surfaces

Theoretical analysis of sound scattering from submerged shapes and gratings can be and has been performed using the methods outlined in the previous paragraph. Many examples can be found in the literature.

A most cited and used book about wave propagation covering a number of different asymptotic methods for the analysis of sound reflection and diffraction was published in 1960 by Brekhovskikh (1980). In particular Geometrical Optics, Wave Theory and Ray Theory are applied to the study of reflection and refraction of spherical waves at the interface between fluid and elastic half-spaces.

The Physical Optics method and the Kirchhoff approximation were recently applied by Thorsos (1988) and Milder (1991) to the problem of sound scattering from rough surfaces. The analysis of sound scattering from viscoelastically coated bodies has been performed by Partridge combining Physical Optics with the Deformed Cylinder Method (DCM) to obtain stable solutions at high frequencies (Partridge 1996).

Folacci *et al.* (1997) have applied the GTD theory to the study of acoustic scattering from a system of two immersed spheres, showing the effect on the scattered field due to various types of surface waves (the Stoneley wave, the Rayleigh wave and one particular Brekhovskikh wave).

The UTD model has been used by Badanin (1997) to investigate the problem of diffraction of hydroacoustic waves at the junction between two elastic plates, one of which is reinforced with a periodic set of uniform stiffeners. A general canonical problem of fluid-solid interfacial wave coupling has been investigated by Craster (1996), who proposed a

uniform asymptotic solution in the presence of mixed boundary conditions (loaded and unloaded regions, partial displacements, etc). Resonance scattering from submerged elastic spheroids has been studied by Werby and Gaunard (1990) using a special series expansion called the Watson method.

Experimental investigation and high-frequency numerical techniques have received less attention until recent years. The reasons of this lies probably in the difficulty of performing tank scattering experiments on one hand and the need for fast computers and the large data storage requirements on the other hand.

Early experimental work on underwater sound scattering was conducted in 1956 by LaCasce and Tamarkin (1956) using a sine wave surface. This work was followed in 1957 by Proud *et al.* (1957), who produced results about scattering from a wedge surface, and later by Barnard *et al.* (1966), who again investigated the sine wave grating.

In 1970, R. J. Bobber published a report titled *Underwater Electroacoustic Measurements* (Bobber 1970), where the principles of underwater panel measurements was investigated in details. Panel measurements have now become a standard method for determining the properties of passive acoustical materials and for measuring edge diffraction and scattering from rough and periodic surfaces. However most of the works published until mid 1980's were dealing with acoustically hard materials and limited frequency ranges.

In 1985, Piquette presented a method to determine the complex dynamic modulus of elastomers by inversion of acoustic scattering data obtained in water (Piquette 1985). In the same year, V. F. Humphrey applied a technique called the 'parametric source' to produce narrow-beam low-frequency pulses for in-tank panel measurements (Humphrey 1985). This technique was successfully applied to the experimental investigation of scattering (Humphrey

and Beckett 1990), edge diffraction (Humphrey and Hui 1992), wedge surfaces (Humphrey *et al.* 1993).

In 1992, backscattering from periodic surfaces was measured experimentally by Suiter using a variety of polystyrene foam gratings and compared to a Huygens-Fresnel-Kirchoff Physical Optics solution (Suiter 1992). Direct measurements of edge diffraction from soft underwater panels were conducted by Piquette (1993, 1996). Finally, measurements of acoustic backscattering from elastic cubes and irregular polyhedra were performed by Thorne *et al.* in 1997 using broadband electroacoustical transducers (Thorne *et al.* 1997).

From the numerical point of view, the Combined Finite Element-Boundary Element method (FE-BE) has been used in the past to solve the problem of acoustic scattering from submerged shapes and gratings. Acoustic radiation and scattering problems from submerged and fluid-filled objects have been recently analysed for example by Francis using the Partial HGF method (1991, 1993, 1997).

Boundary-Element analysis of the dynamics of viscoelastic materials has been conducted using fractional calculus (Xie *et al.* 1988). However, to the knowledge of this author no or very scarce results have been so far published about acoustic scattering from targets showings viscoelastic rather than elastic behaviour. Only recently, Macey *et al.* have shown the availability of some results concerning baffles constructed of PVC tubes embedded in polyurethane using the coupled FE-BE method (Macey *et al.* 1993). The preliminary work about the research presented here has been published at the OCEANS '97 Conference (Di Meglio *et al.* 1997).

2.5. Object-Oriented Analysis and Design and its Application to FE-BE

Computer Programs

The Object-Oriented programming paradigm is an evolution of the standard procedural programming methods, whereby the focus is shifted from the code to the objects that the code is written to represent. The objects (or classes) are essentially an abstract collection of methods (functions) and properties with a close mapping to functional objects taken from the real world.

The objects encapsulate the code necessary to perform all the tasks typical of real objects (the methods) and contain attributes to describe their typical appearance (the properties). New objects can be derived from existing objects using mechanisms such as inheritance and polymorphism.

It's not our goal to include here an in-depth review of the method, which is only a tool and not the target of this research work. However, it is certainly useful to outline the milestones of the object-oriented approach and to show how it has been applied to the FE and BE methods.

The concept of object-oriented programming has not always been easily understood and was very slow in gaining popularity. The first appearance of the concept of class is found in Simula 67 to give the language the capability for concurrency of objects rather than of tasks. Since Simula 67 also allowed a form of inheritance, it is considered the first object-oriented language.

Later, Alan Kay took the class concept of Simula 67 and made it the central concept of the Smalltalk programming language, first released in 1972 (Kay 1996). In Smalltalk, all data is contained in objects. The language was slow to catch on. However, Kay already envisioned that Smalltalk would work best on a small but very powerful desktop computer.

This type of computer finally began to emerge in the early 1980's. It was for this reason, and the fact that abstract data types had recently emerged in Ada and Modula-2, that attention started to be given to component reuse in terms of objects, rather than procedures.

As the popularity of the object-oriented paradigm continued to increase, designers started to add object-oriented features to existing procedural languages. In some cases, such as Turbo Pascal, the extensions were limited to a particular compiler. However, in the cases of C++ (Stroustrup 1991) and Ada 95, the new hybrid languages have gained universal acceptance. Finally, truly object-oriented programming languages started to appear, namely Object Pascal (later called Delphi) and Java. Delphi in particular is the language used to develop the WinFEBE program presented in this research (Borland 1997).

As software engineering became increasingly accepted as a true branch of engineering, the object-oriented method started to be applied not only to programming, but also to the analysis and design phases of software development. Identifiable object-oriented modelling languages began to appear between mid-1970 and the late 1980s as various methodologists experimented with different approaches to object-oriented analysis and design. The number of identified modelling languages increased from less than 10 to more than 50 during the period between 1989-1994. By the mid-1990s, these methods began to incorporate each other's techniques, and a few clearly prominent methods emerged, including the OOSE, OMT-2, and Booch '93 methods.

Finally, the development of UML began in October of 1994 when Grady Booch and Jim Rumbaugh of Rational Software Corporation began their work on unifying the Booch and OMT (Object Modelling Technique) methods.

The UML method is currently considered the *de facto* modelling language for complex software projects (Fowler and Scott 1997).

The usefulness of the object-oriented method in structural analysis programs based on the Finite Element and Boundary Element methods was acknowledged only recently.

Ohtsubo et al. (1993) developed the first object-oriented, finite-element modelling system (MODIFY) in 1993. Henrotte *et al.* (1996) have proposed a possible decomposition of the Finite Element method in terms of a library of classes designed to fit the mathematical structure of the element. Haussler Combe (1996) has applied this approach to the coupling of Finite Elements and Boundary Elements. Non-linear Finite Element classes have been developed by Dubois Pelerin and Pegon (1998).

However, none of the cited works presents a standard design approach based on the UML. Such a description of a coupled Finite Element – Boundary Element algorithm is presented in this research work as the basis for the development of the PHOEBE analysis program developed within the Acoustics and Sonar Group of the University of Birmingham. Some preliminary work based on this research has been presented at the 3rd European Conference on Underwater Acoustics (Di Meglio *et al.* 1996)

2.6. References

- ABRAHAM, I.D. (1996). Radiation and scattering of waves on an elastic half-space; A non-commutative matrix Wiener-Hopf problem. *J. Mech. Phys. Solids*, 44 (12), 2125-2154
- ALFREY, T. (1948). Mechanical behaviour of high polymers. New York: Interscience
- AMERIO, L. (1986). *Analisi matematica*, Vol. 3, *Metodi matematici e applicazioni*. Torino: UTET
- BADANIN, A.V. (1997). Diffraction of a short wave at the junction between two plates, one of which is reinforced by ribs. *PMM J. Appl. Math. Mech.*, 61 (2), 215-221
- BARNARD, G.R. *et al.* (1966). Underwater sound reflection from a pressure release sinusoidal surface. *J. Acoust. Soc. Am.*, 39, 1162-1169
- BECKER, G.W., OBERST, H. (1956). *Kolloid-Z.*, 148 (6)
- BELOV, V.G. *et al.* (1994). Application of the method of integral equations to diffraction of acoustic waves at

- elastic bodies in a layer of liquid. *Acoust. Phys.*, 40 (4), 485-496
- BELTZER, A.I. et al. (1983). On wave propagation in random particulate composites. *Int. J. Solids Struct.*, 19, 785-791
- BLATZ, P.J. (1956). *Ind. Eng. Chem.*, 48, 727
- BOBBER, R.J. (1970). Underwater electroacoustic measurements. Washington, DC: US Gov. Printing Office
- Borland International, Inc. (1997). Borland Delphi 3 (Object Pascal Language Guide). Scotts Valley CA
- BOWMAN, J.J. et al. (1969). *Electromagnetic and acoustic scattering by simple shapes*. Amsterdam: North-Holland
- BREKHOVSKIKH, L.M. (1980). *Waves in layered media*, 2nd ed. London: Academic Press
- BURTON, A.J. and Miller, G.F. (1971). The application of integral equation methods to the numerical solutions of some exterior boundary value problems. *Proc. R. Soc. London, Series A*, 323, 201-210
- COLTON, D. and KRESS, R. (1983). *Integral equation methods in scattering theory*. New York: Wiley-Interscience
- COULOUVRAT, F. (1997). Nonlinear geometrical theory of diffraction in the shadow zone. *C. R. Acad. Sc., Ser. II Fascicule B – Mech. Phys. Chim. Astr.*, 325 (2), 69-75
- CRASTER, R.V. (1996). A canonical problem for fluid-solid interfacial wave coupling. *Proc. R. Soc. London, Series A - Math. Phys. Eng. Sci.*, 452 (1996), 1695-1711
- CRUSE, T.A. and RIZZO, F.J. (1968a). A direct formulation and numerical solution of the general transient Elastodynamic problem I. *J. Math. Anal. And Appl.*, 22, 244-259
- CRUSE, T.A. and RIZZO, F.J. (1968b). A direct formulation and numerical solution of the general transient Elastodynamic problem II. *J. Math. Anal. And Appl.*, 22, 341-355
- CRUSE, T.A. and RIZZO, F.J. (1975) (eds.). *Boundary-integral equation method: computational applications in applied mechanics*, AMD-Vol. II, A.S.M.E.
- CUTZACH, P.M. and LUNEVILLE, E. (1998). Acoustic wave scattering by a semi-infinite waveguide, *C. R. Ac. Sc. - Serie I – Math.*, 326 (9), 1151-1154
- DADDAZIO, R.P. and ETTOUNEY, M.M. (1991). Probabilistic acoustic analysis. In CISKOWSKI, R.D. and BREBBIA, C.A. (eds.). *Boundary Elements Methods in Acoustics*. Southampton: Computational Mechanics Publications
- DE HOOP, T.A. (1991). Convergence criterion for the time-domain iterative born approximation to scattering by an inhomogeneous, dispersive object. *J. Opt. Soc. Am.*, 8 (8), 1256-1260
- DI MEGLIO, A. et al. (1996). PHOEBE: A 3D transducer modelling environment. *Proc. 3rd European Conference on Underwater Acoustics*, Vol. II
- DI MEGLIO, A. et al. (1997). Combined finite element-boundary element analysis of viscoelastic anechoic panels for underwater applications, *Oceans '97 MTS/IEEE Proceedings*, Vol. I
- DUBOIS PELERIN, Y. and PEGON, P. (1998). Object-oriented programming in nonlinear finite element analysis. *Comp. Struct.*, 67 (4), 225-241
- ECKER, R. (1968). *Kautsch Gummi, Kunstst.* 21 (304). Quoted in (Ferry 1980)
- EILERS, H. (1941). *Kolloid-Z.*, 97 (313)
- FERRY, J.D. (1980). *Viscoelastic properties of polymers*. New York: John Wiley & Sons, Inc.
- FOCK, V.A. (1946). The distribution of currents induced by a plane wave on the surface of a conductor. *J. Phys. USSR*, 10, 130-136
- FOCK, V.A. (1965). *Electromagnetic diffraction and propagation problems*. New York: Pergamon Press
- FOKKEMA, J.T. and Van der Berg, P.M. (1993). *Seismic applications of acoustic reciprocity*. Amsterdam:

Elsevier

FOLACCI, A. *et al.* (1997). GTD analysis of scattering by two elastic spheres. *Acustica*, 83 (1), 93-104

FOLDY, L.L. (1945). The multiple scattering of waves. *Phys. Rev.*, 67, 107-119

FOWLER, M. and SCOTT, K. (1997). UML distilled: applying the standard object modeling language. Reading MA: Addison Wesley

FRANCIS, D.T.I. (1991). Partial use of the Helmholtz Gradient Formulation to obtain unique solutions to acoustic radiation problems at characteristic frequencies, *J Sound and Vibration*, 145, 495-498

FRANCIS, D.T.I. (1993). A gradient Formulation of the Helmholtz integral equation for acoustic radiation and scattering, *J. Acoust. Soc. Am.*, 93 (4, Pt. 1), 1700-1708

FRANCIS, D.T.I. and COATES, R.F.W. Acoustic scattering from fluid-filled shells using a combined finite-element and boundary-element method, to be published in *Boundary Element Communication*

GAUNAURD, G.C. and UBERALL, H. (1983). Resonance effects and the ultrasonic effective properties of particulate composites. *J. Acoust. Soc. Am.*, 74, 305-313

GOBLICK, T.J. and BEVENSEE, R.M. (1960). Variational principles and mode coupling in periodic structures. *IRE Trans.*, MTT-8, 500-509

GURTIN, M.E. and STERNBERG, E. (1962). On the linear theory of viscoelasticity, *Arch. Rational Mech. Analysis*, 11 (4), 291-356

HARRIS, P.J. and AMINI, S. (1990). *On the Burton and Miller boundary integral formulation of the exterior acoustic problem*. School of Mathematics and Statistics, University of Birmingham, UK, Preprint 17/90

HAUSSLER COMBE, U. (1996). Coupling boundary-elements and finite-elements - A structured approach. *Comp. Meth. Appl. Mech. Eng.*, 134 (1-2), 117-134

HENROTTE, F. *et al.* (1996). An object-oriented decomposition of the FE procedure. *IEEE Trans. Magn.*, 32 (3), 1441-1444

HUMPHREY, V.F. (1985). The measurements of acoustic properties of limited size panels by use of a parametric source. *J. Sound and Vib.*, 98, 67-81

HUMPHREY, V.F. and BECKETT, C. (1990). The application of a parametric array to scattering studies in the laboratory. *Frontiers of Nonlinear Acoustics*. Elsevier, 265-270

HUMPHREY, V.F. *et al.* (1993). Measurements of the acoustic performance of materials; fibre reinforced materials and wedges. *Proc. Inst. Acoust.*, 15 (Pt. 6), 27-37

HUMPHREY, V.F. and HUI, C. Diffraction and plate wave excitation at the edge of a submerged panel, to be submitted to *J. Acoust. Soc. Am.*

JASWON, M.A. and SYMM, G.T. (1977). *Integral Equation Methods in Potential Theory and Elastostatics*. New York: Academic Press

KAY, A. (1996). The early history of SmallTalk. In BERGIN, Jr., T.J. and , GIBSON, R.G., (eds.). *History of programming languages - II*, 511-578. Reading MA: Addison-Wesley Publishing Company

KAY, I. And KELLER, J.B. (1954). Asymptotic evaluation of the field at a caustic. *J. Appl. Phys.*, 25, 876-883

KELLER, J.B. (1962). Geometrical theory of diffraction. *J. Opt. Soc. Am.*, 52, 116-130

KELLER, J.B. and HANSEN, E.B. (1965). Survey of the theory of diffraction of short waves by edges. *Acta Phys. Polon.*, 27, 217-234

KIM, J.Y. *et al.* (1994). Dispersive wave propagation in the viscoelastic matrix reinforced by elastic fibers. *J. Acoust. Soc. Am.*, 95, 1213-1222

KLEINMAN, R.E. (1965). The Rayleigh region. *Proc. IEEE*, 53, 848-856

KOBAYASHI, S. and KAWAKAMI, T. (1985). Application of BE-FE method to analysis of dynamic interactions between structures and viscoelastic soil. In BREBBIA, C.A. and MAIER G. (eds.). *Boundary*

Elements VII. 1 (6-3)-(6-12). New York: Springer-Verlag

KOUYOUMJIAN, R.G. and PATHAK, P.H. (1974). A uniform geometrical theory of diffraction for an edge in a perfectly conducting surface. *Proc. IEEE*, 62, 1448-1461

LACASCE, E.O., Jr. and TAMARKIN, P. (1956). Underwater sound reflection from a corrugated surface. *J. Appl. Phys.*, 27, 138-148

LANDAU, L.D. and LIFSHITZ, E.M. (1958). *Theory of elasticity*. London: Pergamon Press

LANDEL, R.F. (1958). *Trans. Soc. Rheol.*, 2, 53

LAX, M. (1952). The effective field in dense systems. *Phys. Rev.*, 88, 621-629

LEVINE, H. and SCHWINGER, J. (1948). On the theory of diffraction by an aperture in an infinite plane screen – I. *Phys. Rev.*, 74, 958-974

LEVINE, H. (1950). Variational principles in acoustic diffraction theory. *J. Acoust. Soc. Am.*, 22, 48-55

LEVY, B.R. and KELLER, J.B. (1959). Diffraction by a smooth object. *Comm. Pure Appl. Math.*, 12, 159-209

LOVE, A.E.H. (1944). *A Treatise on the mathematical theory of elasticity*. New York: Dover

LUNEBURG, R.K. (1965). *The mathematical theory of optics*. Berkley CA: The University of California Press

MACEY, P.C. *et al.* (1993). Scattering and transmission by plate-like baffles. In CHINNERY, P.A. (ed.). *Acoustics of advanced materials for underwater applications*. Proc. Inst. Acoust., 15 (6), 95-103

MCNAMARA, D.A. *et al.* (1990). *Introduction to the uniform theory of diffraction*. Boston: Artech House

MILDLER, D.M. (1991). An improved formalism for wave scattering from rough surfaces. *J. Acoust. Soc. Am.*, 89, 529-541

MOW, C.C. (1965). Transient response of a rigid spherical inclusion in an elastic medium. *J. Appl. Mech.*, 32, 637-642

NOLL, W. (1958). A mathematical theory of the mechanical behavior of continuous media, *Arch. Rational Mech. Analysis*, 2 (197)

NORRIS, A.N. and WICKHAM, G.R. (1995). Acoustic diffraction from the junction of two flat plates. *Proc. Roy. Soc. London - Series A – Math. Phys. Eng. Sc.*, 451 (1943), 631-655

PARTRIDGE, C. (1996). Acoustic scattering from viscoelastically coated bodies. *J. Acoust. Soc. Am.*, 99 (1), 72-78

PATES, C.S. *et al.* (1995). Sound-structure interaction analysis of composite panels using coupled boundary and finite element methods. *J. Acoust. Soc. Am.*, 98 (2,1), 1216-1221

PIQUETTE, J.C. (1985). Determination of the complex dynamic bulk modulus of elastomers by inverse scattering. *J. Acoust. Soc. Am.*, 77 (5), 1665-1673

PIQUETTE, J.C. (1993). Direct measurements of edge diffraction from soft underwater acoustic panels. *J. Acoust. Soc. Am.*, 95 (6), 3090-3099

PIQUETTE, J.C. (1996). Some new techniques for panel measurements. *J. Acoust. Soc. Am.*, 100 (5), 3227-3236

POGGIO, A.J. and MILLER, E.K. (1973). Integral equation solutions of three-dimensional scattering problems. In MITTRA, R. (ed.). *Computational techniques for electromagnetics*. London: Pergamon Press

PROUD, J.M. *et al.* (1957). Reflection of sound from a surface of saw-tooth profile. *J. Appl. Phys.*, 28, 1298-1301

QUAK, D. *et al.* (1986). Time-domain far-field scattering of plane acoustic waves by a penetrable object in the Born approximation. *J. Acoust. Soc. Am.*, 80 (4), 1228-1234

REGO SILVA, J.J. *et al.* (1992). Numerical implementation of a hypersingular boundary element formulation for acoustic radiation problems. In *Boundary Elements XIV*, 199-216. London: Computational Mechanics

Publications

- REGO SILVA, J.J. et al. (1993). A new family of continuous/discontinuous three dimensional boundary elements with application to acoustic wave propagation. *Int. J. Num. Meth. Eng.*, 36, 1661-1679
- RIVLIN, J. (1947). *J. Applied Phys.*, 18, 444
- SCHENCK, H.A. (1969). Improved integral formulation for acoustic radiation problems. *J. Acoust. Soc. Am.*, 44, 41-58
- SEYBERT, A. et al. (1985). An advanced computational method for radiation and scattering of acoustic waves in three dimensions. *J. Acoust. Soc. Am.*, 77, 362-368
- SHAW, R.P. (1968). Retarded potential approach to the scattering of elastic waves by rigid obstacles of arbitrary shapes. *J. Acoust. Soc. Am.*, 44, 745-748
- SOENARKO, B. and SEYBERT, A.F. (1991). Recent developments of the boundary element method (BEM) to noise control problems. *Proceedings Internoise 91*, Inst. Noise Control Eng., 2, 1169-1172
- STEVENSON, A.F. (1953). Solution of electromagnetic scattering problems as power series in the ratio (dimension of the scatterer)/wavelength. *J. Appl. Phys.*, 24, 1134-1142
- STROUSTRUP, B. (1991). *The C++ programming language*, 3rd ed. Reading MA: Addison Wesley
- STRUTT, J.W. [Lord Rayleigh] (1897). On the incidence of aerial and electric waves upon small obstacles in the form of ellipsoids or elliptic cylinders, and on the passage of electric waves through a circular aperture in a conducting screen. *Phil. Mag.*, 44, 28-52
- SUITER, H.R. (1992). Backscatter from periodic surfaces measured to high diffractive order. *J. Acoust. Soc. Am.*, 92 (5), 2800-2812
- TALBOT, D.R.S. and WILLIS, J.R. (1982). Variational estimates for dispersion and attenuation of waves in random composites – I. General theory and II. Isotropic composites. *Int. J. Solids Struct.*, 18, 673-698
- TAMURA, Y. and NAKAYAMA, J. (1996). Scattering and diffraction of a plane wave from a randomly rough strip. *Waves in Random Media*, 6 (4), 387-418
- TANAKA, M. and MASUDA, V. (1987). Boundary integral equation approach to structural-acoustic coupling problems. In BREBBIA, C.A. and WENDLANDS, W. (ed.). *Boundary Elements IX*. New York: Springer-Verlag
- THORNE, P.D. et al. (1997). Measurements and analysis of acoustic backscattering by elastic cubes and irregular polyhedra. *J. Acoust. Soc. Am.*, 102 (5, 1), 2705-2713
- THORSOS, E.I. (1988). The validity of the Kirchhoff approximation for rough surface scattering using a Gaussian roughness spectrum. *J. Acoust. Soc. Am.*, 83, 78-92
- TRELOAR, L.R.G. (1958). *The physics of rubber elasticity*. Oxford: Clarendon Press
- TSCHOEGL, N.W. (1980). *The theory of linear viscoelastic behaviour*. New York: Academic Press
- VAN BLADEL, J. (1963). Low frequency scattering by cylindrical bodies. *Appl. Sci. Res.*, B10, 195-202
- VAN DER POEL, C. (1958). *Rheol. Acta*, 1 (198)
- VOLTERRA, V. (1913). Sui fenomeni ereditari. *Atti Reale Accademia Lincei*, 5 (22), 529-539
- WERBY, M.F. and GAUNAURD, G.C. (1990). Resonance scattering from submerged elastic spheroids of high aspect ratios and its three-dimensional interpretation. *J. Acoust. Soc. Am.*, 88, 951-960
- WESTON, V.H. (1965). Extension of Fock theory for currents in the penumbra region. *Radio Science*, 69D, 1257-1270
- WILLIAMS, M.L. et al. (1955). *J. Am. Chem. Soc.*, 77, 3701
- XIE, K.J. et al. (1988). An investigation of wave propagation in viscoelastic media modeled by fractional derivative using boundary element method. In TANAKA, M. and CRUSE, T.A. (eds.). *Boundary Elements Methods in Applied Mechanics*, 523-531, New York: Pergamon Press

YING, C.F. and TRUELL, R. (1956). Scattering of a plane longitudinal wave by a spherical obstacle in an isotropically elastic solid. *J. Appl. Phys.*, 27, 1086-1097

ZHE, J. (1995). Variational principle and energy integrals in a complex sound intensity field. *J. Acoust. Soc. Am.*, 98 (2, Pt.1), 1163-1168

Chapter 3

The Linear Theory of Viscoelasticity

3.1. Introduction

In this chapter, the fundamental properties of linear hereditary operators are outlined and the stress-strain constitutive equations for viscoelastic materials are derived. The attention is drawn on the class of homogeneous, isotropic materials, for which special forms of the hereditary operators can be written. The viscoelastic dynamic problem is then defined on these classes of operators and materials and the solution of initial value and initial past history problems are built for the case of oscillatory processes. All the physical quantities defined in this chapter serve as foundations of the experimental and numerical analysis performed in the following chapters.

3.2. Notations and Definitions

3.2.1. Points, vectors, tensors and linear transformations

The notation used throughout this chapter follows the classic notation as outlined by Gurtin (1984) and Leitman and Fisher (1984).

Let \mathcal{E} be the three-dimensional Euclidean point space and \mathcal{V} the underlying three-dimensional inner product translation space. Elements of \mathcal{E} are called *points* and elements of \mathcal{V} are called *vectors*.

Let \mathcal{T} be the set of all linear transformations of \mathcal{V} into \mathcal{V} . \mathcal{T} is a nine-dimensional inner product space, whose elements are called *tensors*. \mathcal{T}_{sym} and \mathcal{T}_{skw} are respectively the symmetric and skew-symmetric tensor spaces.

The space generated by all linear transformations of a space \mathcal{X} into a space \mathcal{Y} is indicated by square brackets operator, $[\mathcal{X}, \mathcal{Y}]$. The space generated by all linear transformations of a space \mathcal{X} into itself is indicated simply by $[\mathcal{X}]$. By this notation, we also have that $[\mathcal{V}] \equiv \mathcal{T}$ is the second-order tensor space generated by \mathcal{V} and $[\mathcal{T}]$ is the fourth-order tensor space generated by \mathcal{T} .

3.2.2. Processes and histories

Let \mathcal{R} be the real line, \mathcal{R}_0^+ the non-negative real line and \mathcal{R}^+ the positive real line.

Let \mathcal{X} denote a point or vector space. The following definitions (as introduced by Coleman and Mizel (1966) and Noll (1958)) apply:

- (\mathcal{X})-**process** (or **process**): a function defined on \mathcal{R} with values in \mathcal{X} . If ϕ is an (\mathcal{X})-**process** and $t \in \mathcal{R}$ then $\phi(t) \in \mathcal{X}$ is called the *value* of ϕ at time t .

- **(\mathfrak{X})-history** (or **history**): a function defined on \mathfrak{R}_0^+ with values in \mathfrak{X} .
- **(\mathfrak{X})-past history** (or **past history**): a function defined on \mathfrak{R}^+ with values in \mathfrak{X} .

Given a process ϕ and a time $t \in \mathfrak{R}$, two additional restrictions are defined:

- $\phi \in \mathfrak{X}, t \in \mathfrak{R}_0^+$: $\phi^t(s) = \phi(t-s)$ is the history of ϕ up to time t
- $\phi \in \mathfrak{X}, t \in \mathfrak{R}^+$: ${}_r\phi^t(s) = \phi(t-s)$ is the past history of ϕ up to time t

We distinguish the following classes of processes. A normed vector space \mathfrak{X} is said to have:

- **finite histories**: if, and only if, some (and hence every) history of ϕ has bounded support; that is the set $\{s \in \mathfrak{R}_0^+ : \phi^t(s) \neq 0\}$ is bounded for some (and hence every) time t .
- **infinite histories**: if, and only if, it does not have finite histories.
- **bounded histories**: if, and only if, every history of ϕ is bounded; that is, for each time t there is an $M(t) \geq 0$, such that $\sup\{\|\phi^t(s)\| : s \in \mathfrak{R}_0^+\} \leq M(t)$.
- **integrable histories**: if, and only if, every history of ϕ is integrable on \mathfrak{R}_0^+ ; that is, for each time t

$$\int_0^\infty \|\phi^t(s)\| ds < \infty \quad (3.1)$$

In addition an \mathfrak{X} -process can be:

- **restricted**: if, and only if, some (and hence every) history of ϕ vanishes at infinity; that is, for some (and hence every) time t : $\lim_{s \rightarrow \infty} \phi^t(s) = 0$
- **continuous at infinity**: if, and only if, there exists an element $\overset{\infty}{\phi}$ in \mathfrak{X} , such that: $\lim_{t \rightarrow \infty} \phi^t(t) = \overset{\infty}{\phi}$
- of **Heaviside type**: if, and only if, the past history of ϕ up to time $t = 0$ vanishes; that is: $\phi(t) = 0$ for $t < 0$
- **locally integrable**: if, and only if, ϕ is integrable on every bounded subset of \mathfrak{R}

For processes of the Heaviside type it is convenient to define a set of **Heaviside classes**. Let ϕ be a process of Heaviside type and let N be a non-negative integer. Then ϕ is said to be in class H^N if, and only if, ϕ is N times continuously differentiable on \mathfrak{R}_0^+ . We write H for H^0 . If ϕ is in class H^N for every N , then ϕ is said to be in class H^∞ . In addition, a process ϕ is said to be in class H^{ac} if, and only if, ϕ is absolutely continuous on \mathfrak{R}_0^+ . The following characterisation of class H^{ac} is considered:

An (\mathfrak{X})-process ϕ of Heaviside type is in class H^{ac} if, and only if, there is an element $\overset{\circ}{\phi} \in \mathfrak{X}$ and a locally integrable function $\dot{\phi}: \mathfrak{R}_0^+ \rightarrow \mathfrak{X}$, such that

$$\phi(t) = \overset{\circ}{\phi} + \int_0^t \dot{\phi}(\tau) d\tau, \quad t \in \mathfrak{R}_0^+ \quad (3.2)$$

The element $\overset{\circ}{\phi}$ and the function $\dot{\phi}$ are uniquely determined (the latter up to a set of Lebesgue measure zero) through:

$$\overset{\circ}{\phi} = \lim_{t \rightarrow 0^+} \phi(t) \quad (3.3)$$

$$\dot{\phi}(t) = \frac{d}{dt} \phi(t) \quad (3.4)$$

for almost every t in \mathfrak{R}_0^+ .

A process ϕ in class H^{ac} is called strong if, and only if, $\dot{\phi}$ is integrable on \mathfrak{R}_0^+ . It then follows that:

A process ϕ in class H^{ac} is continuous at infinity if (but not only if) it is strong and its value at infinity is

$$\overset{\infty}{\phi} = \overset{\circ}{\phi} + \int_0^{\infty} \dot{\phi}(s) ds \quad (3.5)$$

The Heaviside unit step process h is the scalar process defined by:

$$h(t) = \begin{cases} 0 : t < 0 \\ 1 : t \geq 0 \end{cases} \quad (3.6)$$

Finally, let \mathcal{D} be a domain (open set) in \mathcal{E} with closure (close set) $\overline{\mathcal{D}}$ and let \mathcal{X} be a point or vector space. We define an (\mathcal{X}) -field as a function ϕ which maps the domain \mathcal{D} into the space \mathcal{X} , $\phi : \mathcal{D} \rightarrow \mathcal{X}$. The field is defined as a scalar field if $\mathcal{X} = \mathfrak{R}$, a vector field if $\mathcal{X} = \mathfrak{V}$, a tensor field if $\mathcal{X} = \mathfrak{T}$.

A function on $\mathcal{D} \times \mathfrak{R}$ with values in \mathcal{X} is called an (\mathcal{X}) -field process for \mathcal{D} . Given a function $\phi : \mathcal{D} \times \mathfrak{R} \rightarrow \mathcal{X}$, we can define the following two subsidiary processes:

$$\phi(t) = \phi(\cdot, t), \text{ the } (\mathcal{X})\text{-field value of the process } \phi \text{ at time } t \quad (3.7)$$

$$\phi_{\mathbf{x}} = \phi(\mathbf{x}, \cdot), \text{ the } (\mathcal{X})\text{-process at the position } \mathbf{x} \in \mathcal{D} \quad (3.8)$$

3.2.3. Convolutions

Let ϕ and ψ be scalar processes. We define formally a process $\phi * \psi$, and call it the **convolution of ϕ with ψ** , by

$$(\phi * \psi)(t) = \begin{cases} 0 : t < 0 \\ \int_0^t \phi(s) \psi(t-s) ds : t \geq 0 \end{cases} \quad (3.9)$$

The convolution (3.9) has the following properties:

1. If ϕ and ψ are in class H (or in class C on \mathfrak{R}_0^+), then (3.9) defines a scalar process $\phi * \psi$ in class H.
2. If ϕ is in class $H^{N'}$ (or in class $C^{N'}$ on \mathfrak{R}_0^+) and ψ is in class $H^{N''}$ (or in class $C^{N''}$ on \mathfrak{R}_0^+), where N' and N'' are non-negative integers, then (3.9) defines a process $\phi * \psi$ in class H^N , where $N = \min\{N', N''\}$.
3. If ϕ and ψ are locally integrable and of Heaviside type (or processes which are locally integrable on \mathfrak{R}_0^+), then (3.9) defines a scalar process $\phi * \psi$ which is locally integrable and of Heaviside type. In addition, if either ϕ or ψ is of class H (or in class C on \mathfrak{R}_0^+), then $\phi * \psi$ is of class H.

If ϕ and ψ are field processes for a domain \mathfrak{D} , the previous definition and properties still hold. Thus $\phi * \psi$ is the scalar field process for \mathfrak{D} of class H as defined by (3.9) and with the position \mathbf{x} in \mathfrak{D} held fixed:

$$(\phi * \psi)(\mathbf{x}, t) = (\phi_{\mathbf{x}} * \psi_{\mathbf{x}})(t), \quad (\mathbf{x}, t) \in \mathfrak{D} \times \mathfrak{R} \quad (3.10)$$

The definition and properties of convolution are extended to processes with values in $\mathfrak{R}, \mathfrak{V}, \mathfrak{I}, [\mathfrak{I}]$ by formal substitution of the corresponding expressions.

3.2.4. The Boltzmann operator

Let ϕ be a scalar process in class H^{ac} . It can be represented by (3.2) as

$$\phi(t) = \phi + \int_0^t \dot{\phi}(\tau) d\tau, \quad t \in \mathfrak{R}_0^+ \quad (3.2)$$

Let ψ be a scalar process and formally define the a new scalar process $\phi \oplus \psi$ by

$$(\phi \oplus \psi)(t) = \phi \psi(t) + \int_0^{\infty} \dot{\phi}(s) \psi(t-s) ds, \quad t \in \mathfrak{R} \quad (3.11)$$

Thus, the **Boltzmann operator** $\phi \oplus$ with **kernel** ϕ represents the map that assigns the process $\phi \oplus \psi$ to the process ψ .

An operator in the form of $\phi \oplus$ was originally used by Boltzmann in the study of what he called “elastic aftereffects” (Boltzmann 1870). In modern mathematical terms, the operator $\phi \oplus$ defines a Volterra integral operator with kernel ϕ for functions in the class of Heaviside processes (Volterra 1909; Burton 1983).

The Boltzmann operator has the following properties (Leitman and Fischer 1984):

Let ϕ be a process in class H^{ac} . Then the Boltzmann operator $\phi \oplus$ with kernel ϕ is a linear map in:

- The space of continuous processes with finite histories
- The space of locally integrable processes of Heaviside type
- The processes of class H

If, in addition, the process ϕ is strong, then the Boltzmann operator $\phi \oplus$ with kernel ϕ is a linear map in:

- The space of restricted continuous processes
- The space of processes with bounded histories
- The space of processes with integrable histories

Finally:

If $\phi \oplus$ is the zero map in any of the previously listed spaces, then the kernel ϕ is the zero process in H^{ac} ; that is the Boltzmann operator $\phi \oplus$ is uniquely determined by its kernel ϕ in H^{ac}

The definition and properties of the Boltzmann operator are formally extended to fields and field processes by substitution of the corresponding expressions.

3.3. Linear theory of viscoelasticity with integral hereditary laws

3.3.1. Linear hereditary laws

The concept of linear hereditary laws is fundamental to the development of a linear theory of viscoelasticity. The most important consequence of this approach is that the stress depends *linearly* and *continuously* not only upon the present state of strain as in the purely elastic case, but also upon all past values of the strain (the strain history).

Let E be an (\mathfrak{X}) -process and S be a (\mathfrak{Y}) -process, where \mathfrak{X} and \mathfrak{Y} are finite-dimensional, inner product spaces. By a linear hereditary law \mathcal{L} we mean a relation $S = \mathcal{L}[E]$ between ordered pairs of processes (E, S) defined as follows:

There exists a continuous linear functional $L: \mathcal{C}^0(\mathfrak{R}_0^+; \mathfrak{X}) \rightarrow \mathfrak{Y}$, called the **response functional** for \mathcal{L} , such that $S = \mathcal{L}[E]$ if, and only if, E is a continuous restricted (\mathfrak{X}) -process and

$$S(t) = L[E^t], \quad t \in \mathfrak{R} \quad (3.12)$$

Linear hereditary laws have the following properties:

Linearity or superposition property: if $S_1 = \mathcal{L}[E_1]$ and $S_2 = \mathcal{L}[E_2]$, then for any pair of real numbers α_1 and α_2 , $\alpha_1 S_1 + \alpha_2 S_2 = \mathcal{L}[\alpha_1 E_1 + \alpha_2 E_2]$

Time-translation invariance: let $S = \mathcal{L}[E]$; for any real number η define the translated processes E_η and S_η by

$$E_\eta(t) = E(t - \eta), \quad S_\eta(t) = S(t - \eta), \quad t \in \mathfrak{R} \quad (3.13)$$

Then, for all real numbers η , $S_\eta = \mathcal{L}[E_\eta]$

Determinism or causality: if $S_1 = \mathcal{L}[E_1]$ and $S_2 = \mathcal{L}[E_2]$ and $E_1^t = E_2^t$ for some time t , then $S_1(t) = S_2(t)$

Continuity: Let $S = \mathcal{L}[E]$. For each time t and $\varepsilon > 0$, there exists a $\delta > 0$ such that

$$\|E^t\| < \delta \text{ implies } |S(t)|_{\mathfrak{Y}} < \varepsilon$$

3.3.2. Definition of Boltzmann laws

Boltzmann laws are a special class of linear hereditary relations, which is specially suited for the study of linear viscoelastic response.

Let \mathfrak{X} and \mathfrak{Y} be two finite-dimensional inner product spaces (in what follows these spaces will essentially be stress and strain tensor spaces) and let $[\mathfrak{X}, \mathfrak{Y}]$ be the set of the linear maps of \mathfrak{X} into \mathfrak{Y} .

We define by **response function** an $([\mathfrak{X}, \mathfrak{Y}])$ -process \mathbf{K} in class H^{ac} . If \mathbf{K} is a response function, it follows from the definition of class H^{ac} that there are an element $\overset{\circ}{\mathbf{K}} \in [\mathfrak{X}, \mathfrak{Y}]$ and a function $\dot{\mathbf{K}}: \mathfrak{R}_0^+ \rightarrow [\mathfrak{X}, \mathfrak{Y}]$ such that

$$\mathbf{K}(t) = \overset{\circ}{\mathbf{K}} + \int_0^t \dot{\mathbf{K}}(s) ds, \quad t \in \mathfrak{R}_0^+ \quad (3.14)$$

The element $\overset{\circ}{\mathbf{K}} \in [\mathfrak{X}, \mathfrak{Y}]$ is the **initial response**. If \mathbf{K} is continuous at infinity, the element $\overset{\infty}{\mathbf{K}} \in [\mathfrak{X}, \mathfrak{Y}]$, given by

$$\overset{\infty}{\mathbf{K}} = \lim_{t \rightarrow \infty} \mathbf{K}(t) \quad (3.15)$$

is called the **equilibrium response**.

A response function \mathbf{K} is a strong response function only if \mathbf{K} is a strong process in class \mathbf{H}^{ac} . If \mathbf{K} is strong, it always admits the equilibrium response $\overset{\circ}{\mathbf{K}}$, but the converse is not true, since the condition is necessary, but not sufficient.

Let now \mathbf{K} be a strong response function and define a map $\mathbf{L}_{\mathbf{K}} : \mathcal{C}^0(\mathfrak{R}_0^+; \mathfrak{X}) \rightarrow \mathfrak{Y}$ by

$$\mathbf{L}_{\mathbf{K}}[H] = \overset{\circ}{\mathbf{K}}[H(0)] + \int_0^\infty \dot{\mathbf{K}}(s)[H(s)]ds \quad (3.16)$$

A linear hereditary law $\mathcal{L}_{\mathbf{K}}$ whose response functional $\mathbf{L}_{\mathbf{K}}$ is given by (3.16), for some strong response function \mathbf{K} , is called a *Boltzmann law with (strong) response function \mathbf{K}* .

From the definition (3.11) of Boltzmann operator, it follows that the hereditary law $\mathcal{L}_{\mathbf{K}}$ is a Boltzmann operator with strong kernel \mathbf{K} :

$$S = \mathcal{L}_{\mathbf{K}}[E] = \mathbf{K} \oplus E \quad (3.17)$$

or

$$S(t) = \mathbf{L}_{\mathbf{K}}[E^t] = (\mathbf{K} \oplus E)(t) \quad (3.18)$$

for every restricted continuous (\mathfrak{X}) -process E .

3.3.3. Constitutive relations for linearly viscoelastic materials

Consider a bounded domain \mathfrak{B} in \mathfrak{E} , called a **body**, and let $\mathbf{x} \in \mathfrak{B}$ be a material point in \mathfrak{B} . Let \mathbf{u} be a displacement field process for \mathfrak{B} , \mathbf{E} a strain field process and \mathbf{S} a stress field process. From the definitions introduced in [§3.1] it follows that for each $(\mathbf{x}, t) \in \mathfrak{B} \times \mathfrak{R}$ we can assume that $\mathbf{u}(\mathbf{x}, t) \in \mathfrak{V}$, $\mathbf{E}(\mathbf{x}, t) \in \mathfrak{F}$ and $\mathbf{S}(\mathbf{x}, t) \in \mathfrak{F}$.

The behaviour of the body \mathfrak{B} is said to be **linearly viscoelastic of relaxation type** at a material point \mathbf{x} if, and only if, there is a linear hereditary law $\mathcal{L}^{\mathbf{x}}$ such that the stress process $S_{\mathbf{x}}$ and the displacement process $\mathbf{u}_{\mathbf{x}}$, at the material point \mathbf{x} , are related through $\mathcal{L}^{\mathbf{x}}$ by

$$S_{\mathbf{x}} = \mathcal{L}^{\mathbf{x}}[\nabla \mathbf{u}_{\mathbf{x}}], \quad \mathbf{x} \in \mathfrak{B} \quad (3.19)$$

or equivalently by

$$S(\mathbf{x}, t) = L^{\mathbf{x}}[\nabla \mathbf{u}'(\mathbf{x}, t)], \quad (\mathbf{x}, t) \in \mathfrak{B} \times \mathfrak{R} \quad (3.20)$$

where ∇ is the gradient operator. If (3.19) or (3.20) hold at every point $\mathbf{x} \in \mathfrak{B}$, the body \mathfrak{B} is called a **viscoelastic body (of relaxation type)**.

A fundamental postulate (analogous to the purely elastic case) is the **postulate on rigid motions**:

An (infinitesimal) rigid motion of the body \mathfrak{B} up to time t results in zero stress at time t at every material point \mathbf{x} in \mathfrak{B}

The displacement gradient field process $\nabla \mathbf{u}$ can be univocally decomposed as

$$\nabla \mathbf{u} = \mathbf{E} + \mathbf{W} \quad (3.21)$$

where $\mathbf{E} \in \mathfrak{J}_{sym}$ is the (infinitesimal) symmetric strain field process and $\mathbf{W} \in \mathfrak{J}_{skw}$ is the (infinitesimal) skew-symmetric rotation field process. As a consequence of the postulate of rigid motions we have therefore:

$$\mathbf{S}_x = \mathcal{L}^x[\nabla \mathbf{u}_x] \equiv \mathcal{L}^x[\mathbf{E}_x] \quad (3.22)$$

since the hereditary law \mathcal{L}^x vanishes on the class of (\mathfrak{J}_{skw}) -processes, which are independent of the material point \mathbf{x} .

If, and only if, the relaxation law \mathcal{L}^x is independent of the material point $\mathbf{x} \in \mathfrak{B}$ the viscoelastic body \mathfrak{B} is said to be **homogeneous** and it is possible to write simply \mathcal{L} for the relaxation law \mathcal{L}^x and \mathbf{L} for the corresponding response functional \mathbf{L}^x . Otherwise \mathfrak{B} is said to be **inhomogeneous**.

3.3.4. Constitutive equations and stress relaxation

At this point we have enough elements to characterise mathematically some of the fundamental quantities describing a viscoelastic material.

Let \mathfrak{B} be a linearly viscoelastic body of relaxation type (conditions 3.19 or 3.20) with relaxation law \mathcal{L}^x satisfying the definition of Boltzmann law (3.14). It follows that there is a

response function $\mathbf{G}_x = \mathbf{G}(\mathbf{x}, \bullet)$ for each $\mathbf{x} \in \mathfrak{B}$, called the *relaxation function* at $\mathbf{x} \in \mathfrak{B}$, such that, for each $(\mathbf{x}, t) \in \mathfrak{B} \times \mathfrak{R}$, $\mathbf{G}(\mathbf{x}, t) \in [\mathfrak{I}, \mathfrak{I}_{\text{sym}}]$ and

$$\mathbf{G}(\mathbf{x}, t) = \overset{\circ}{\mathbf{G}}(\mathbf{x}) + \int_0^t \dot{\mathbf{G}}(\mathbf{x}, s) ds, \quad (\mathbf{x}, t) \in \mathfrak{B} \times \mathfrak{R}_0^+ \quad (3.23)$$

The map $\overset{\circ}{\mathbf{G}}(\mathbf{x})$ in $[\mathfrak{I}, \mathfrak{I}_{\text{sym}}]$ is the *initial elasticity* at $\mathbf{x} \in \mathfrak{B}$ and it governs the response to instantaneous changes in strain. The map $\overset{\infty}{\mathbf{G}}(\mathbf{x})$ in $[\mathfrak{I}, \mathfrak{I}_{\text{sym}}]$, given by

$$\overset{\infty}{\mathbf{G}}(\mathbf{x}) = \lim_{t \rightarrow \infty} \mathbf{G}(\mathbf{x}, t), \quad \mathbf{x} \in \mathfrak{B} \quad (3.24)$$

is the *equilibrium modulus* at $\mathbf{x} \in \mathfrak{B}$ and governs the material response at equilibrium. If, in addition, the process $\mathbf{G}_x = \mathbf{G}(\mathbf{x}, \bullet)$ is a strong response function, then it follows from (3.16), (3.18) and (3.22)

$$\mathbf{S}(\mathbf{x}, t) = \overset{\circ}{\mathbf{G}}(\mathbf{x})\mathbf{E}(\mathbf{x}, t) + \int_0^t \dot{\mathbf{G}}(\mathbf{x}, s)\mathbf{E}(\mathbf{x}, t-s)ds = (\mathbf{G} \oplus \mathbf{E})(\mathbf{x}, t), \quad (\mathbf{x}, t) \in \mathfrak{B} \times \mathfrak{R} \quad (3.25)$$

Under the hypothesis of homogeneous viscoelastic body, all quantities are independent of the material point $\mathbf{x} \in \mathfrak{B}$ and (3.25) becomes

$$\mathbf{S}(t) = \overset{\circ}{\mathbf{G}}[\mathbf{E}(t)] + \int_0^t \dot{\mathbf{G}}(s)[\mathbf{E}(t-s)]ds = (\mathbf{G} \oplus \mathbf{E})(t), \quad t \in \mathfrak{R} \quad (3.26)$$

It is easy to show that the expressions developed so far simply reduce to the elastic case if the hereditary response vanishes. Indeed, if $\mathbf{G} = h \overset{\circ}{\mathbf{G}}$ is a constant response function on \mathfrak{R}_0^+ , then (3.26) reduces to

$$\mathbf{S}(t) = \overset{\circ}{\mathbf{G}}[\mathbf{E}(t)], \quad t \in \mathfrak{R} \quad (3.27)$$

The relaxation function $\mathbf{G}(t)$ can be used to describe a phenomenon known as *stress relaxation*, which has important experimental applications. Let \mathbf{G} be a strong relaxation function with equilibrium modulus $\overset{\infty}{\mathbf{G}}$. Let $\mathbf{E} = h\mathbf{1}$ be the unit Heaviside strain process. It follows from the properties of the Boltzmann operator [§3.2.4] that \mathbf{S} is the Heaviside stress process

$$\mathbf{S}(t) = (\mathbf{G} \oplus \mathbf{E})(t) = \mathbf{G}(t) \quad (3.28)$$

with equilibrium value

$$\overset{\infty}{\mathbf{S}} = \lim_{t \rightarrow \infty} \mathbf{S}(t) = \lim_{t \rightarrow \infty} \mathbf{G}(t) = \overset{\infty}{\mathbf{G}} \quad (3.29)$$

Therefore, the relaxation function \mathbf{G} has the physical meaning of the stress resulting from a unit Heaviside strain process, which provides a direct way for its experimental evaluation.

3.3.5. Constitutive equations and creep laws: the inversion theorem

If \mathfrak{B} is a viscoelastic body, it is formally possible to define a new linear hereditary law \mathcal{L}^* for \mathfrak{B} such that the strain process \mathbf{E} is determined by the knowledge of the stress process \mathbf{S} through the dependence

$$\mathbf{E} = \mathcal{L}^*[\mathbf{S}] \quad (3.30)$$

In this case the body \mathfrak{B} is called a *linearly viscoelastic body of creep type* and \mathcal{L}^* is called a *creep law* for \mathfrak{B} .

In the following paragraph, we define the necessary and sufficient conditions for a viscoelastic body of relaxation type to be also of creep type.

Let \mathfrak{B} be a viscoelastic body of relaxation type with relaxation law \mathcal{L} ; then the hereditary law \mathcal{L}^* is a creep law for the same \mathfrak{B} if, and only if, the strain process \mathbf{E} given by $\mathbf{E} = \mathcal{L}^*[\mathbf{S}]$ satisfies $\mathbf{S} = \mathcal{L}[\mathbf{E}]$. It therefore follows that the composition $\mathcal{L}\mathcal{L}^*$ must be the identity map in the class of restricted continuous processes and \mathcal{L}^* must be the *right inverse* of \mathcal{L} . In addition, if, and only if, the map \mathcal{L} is bi-univocal, that is if, and only if, $\mathcal{L}[\mathbf{E}] = 0$ implies $\mathbf{E} = 0$, then the relationship is symmetric and $\mathcal{L}^* = \mathcal{L}^{-1}$ is the *inverse* of \mathcal{L} .

Under proper conditions (Leitman and Fischer 1984), the right inverse $\overset{*}{\mathcal{L}}$ of \mathcal{L} can be derived from \mathcal{L} . Let $\mathcal{L}_{\mathbf{G}}$ be a Boltzmann relaxation law for \mathfrak{B} as defined in (3.26)

$$\mathbf{S}(t) = \overset{\circ}{\mathbf{G}}[\mathbf{E}(t)] + \int_0^{\infty} \dot{\mathbf{G}}(s)[\mathbf{E}(t-s)]ds = (\mathbf{G} \oplus \mathbf{E})(t), \quad t \in \mathfrak{R} \quad (3.31)$$

Let then $\mathcal{L}_{\mathbf{J}}$ be a Boltzmann creep law for \mathfrak{B} with strong response function \mathbf{J} , called the *creep compliance*

$$\mathbf{E}(t) = \overset{\circ}{\mathbf{J}}[\mathbf{S}(t)] + \int_0^{\infty} \dot{\mathbf{J}}(s)[\mathbf{S}(t-s)]ds = (\mathbf{J} \oplus \mathbf{S})(t), \quad t \in \mathfrak{R} \quad (3.32)$$

$\mathcal{L}_{\mathbf{J}}$ is the creep law corresponding to the relaxation law $\mathcal{L}_{\mathbf{G}}$ if, and only if, the following two conditions are verified (Leitman and Fischer 1984)

$$\overset{\circ}{\mathbf{G}} \overset{\circ}{\mathbf{J}} = \mathbf{1} \quad (3.33)$$

$$\overset{\circ}{\mathbf{G}} \dot{\mathbf{J}}(s) + \dot{\mathbf{G}}(s) \overset{\circ}{\mathbf{J}} + (\dot{\mathbf{G}} * \dot{\mathbf{J}})(s) = 0, \quad a.e. \ s \in \mathfrak{R}_0^+ \quad (3.34)$$

The system (3.33) is satisfied if, and only if, the initial elasticity $\overset{\circ}{\mathbf{G}}$ is invertible in $[\mathfrak{F}_{\text{sym}}]$. Its inverse $\overset{\circ}{\mathbf{J}}$ is called the *initial elastic compliance*

In addition, if \mathbf{G} satisfies the stronger hypothesis of Gurtin and Sternberg's *Inversion Theorem* (Gurtin and Sternberg 1962), then the entire law $\mathcal{L}_{\mathbf{G}}$ is invertible and we have $\mathcal{L}_{\mathbf{J}} = \mathcal{L}_{\mathbf{G}}^{-1}$ and $\mathbf{J} = \mathbf{G}^{-1}$.

The results obtained so far will be of fundamental importance in the determination of the stress-strain response of viscoelastic materials from experimental data, as will be detailed in Chapter 4 of this work

3.3.6. Response functions for isotropic materials

An orthogonal tensor \mathbf{Q} is said to be a *symmetry transformation* at \mathbf{x} if, and only if

$$\mathbf{Q}L^x[\mathbf{H}]\mathbf{Q}^T = L^x[\mathbf{Q}\mathbf{H}\mathbf{Q}^T] \quad (3.35)$$

for every field history \mathbf{H} (Amerio 1985a). The collection of all orthogonal tensors that satisfy (3.35) is called the *symmetry group* at \mathbf{x} for \mathfrak{B} , $\mathfrak{S}_{\mathbf{x}}$. The group $\mathfrak{S}_{\mathbf{x}}$ is generated by the set $\{\mathbf{1}, -\mathbf{1}\}$ plus a number of proper orthogonal tensors or rotations. A body \mathfrak{B} is said to be *isotropic* at $\mathbf{x} \in \mathfrak{B}$ if, and only if, its symmetry group $\mathfrak{S}_{\mathbf{x}}$ is the full orthogonal group; otherwise \mathfrak{B} is said to be *anisotropic* at $\mathbf{x} \in \mathfrak{B}$. The materials subject of this investigation will always be considered homogeneous and isotropic at every point $\mathbf{x} \in \mathfrak{B}$.

The symmetry restriction on the response function \mathbf{L} can be seen equivalently as a restriction on the relaxation function \mathbf{G} , since the hereditary law $\mathcal{L}_{\mathbf{G}}$ is uniquely determined by \mathbf{G} , and it is possible to write

$$\mathbf{Q}\mathbf{G}(t)[\mathbf{T}]\mathbf{Q}^T = \mathbf{G}(t)[\mathbf{Q}\mathbf{T}\mathbf{Q}^T], \quad t \in \mathfrak{R}, \quad \forall \mathbf{T} \in \mathfrak{F}_{sym} \quad (3.36)$$

If the body \mathfrak{B} is isotropic, it follows (Leitman and Fischer 1984) that there are *scalar* response functions μ and λ such that

$$\mathbf{G}(t)[\mathbf{T}] = 2\mu(t)\mathbf{T} + \lambda(t)(tr\mathbf{T})\mathbf{1}, \quad t \in \mathfrak{R}, \quad \forall \mathbf{T} \in \mathfrak{F}_{sym} \quad (3.37)$$

This result is a direct extension of the elastic case and the response function μ and λ are the equivalent of the elastic Lamé moduli. The Boltzmann law (3.26) becomes

$$\begin{aligned} \mathbf{S}(t) &= 2 \overset{\circ}{\mu} \mathbf{E}(t) + 2 \int_0^\infty \dot{\mu}(s) \mathbf{E}(t-s) ds + \overset{\circ}{\lambda} (tr \mathbf{E}(t)) \mathbf{1} + \int_0^\infty \dot{\lambda}(s) (tr \mathbf{E}(t-s)) ds \mathbf{1} = \\ &= 2\mu \otimes \mathbf{E} + \lambda \otimes (tr \mathbf{E}) \mathbf{1}, \quad t \in \mathfrak{R} \end{aligned} \quad (3.38)$$

The stress tensor \mathbf{S} and strain tensor \mathbf{E} have the unique decomposition:

$$\mathbf{S} = \mathbf{S}_0 + \left(\frac{1}{3} tr \mathbf{S} \right) \mathbf{1}, \quad tr \mathbf{S}_0 = 0 \quad (3.39)$$

$$\mathbf{E} = \mathbf{E}_0 + \left(\frac{1}{3} tr \mathbf{E} \right) \mathbf{1}, \quad tr \mathbf{E}_0 = 0 \quad (3.40)$$

The traceless tensors \mathbf{S}_0 and \mathbf{E}_0 are the deviatoric stress and strain tensors. We can give relation (3.38) a more physically meaningful form by introducing the scalar response functions

$$\mathbf{G}_1 = 2\mu \quad (3.41)$$

$$\mathbf{G}_2 = 2\mu + 3\lambda \quad (3.42)$$

Using (3.31) and (3.42) the stress tensor equation (3.38) can be rewritten as

$$\mathbf{S} = \mathbf{G}_1 \oplus \mathbf{E} + \left[\frac{1}{3}(\mathbf{G}_2 - \mathbf{G}_1) \right] \oplus (\text{tr} \mathbf{E}) \mathbf{1} \quad (3.43)$$

or, equivalently

$$\mathbf{S}_0 = \mathbf{G}_1 \oplus \mathbf{E}_0 \quad (3.44)$$

$$\text{tr} \mathbf{S} = \mathbf{G}_2 \oplus \text{tr} \mathbf{E} \quad (3.45)$$

The scalar response function \mathbf{G}_1 characterises the behaviour of the material in pure shear and takes the name of *shear modulus*, whereas the response function \mathbf{G}_2 characterises the behaviour of the material in compression and takes the name of *compression modulus*.

The extension of the previous results to creep laws follows directly from [§3.3.5] under the proper conditions established by the inversion theorem. The creep relations for the relaxation expressions (3.43-3.45) are therefore

$$\mathbf{E} = \mathbf{J}_1 \oplus \mathbf{S} + \left[\frac{1}{3} (\mathbf{J}_2 - \mathbf{J}_1) \right] \oplus (\text{tr} \mathbf{S}) \mathbf{I} \quad (3.46)$$

and

$$\mathbf{E}_0 = \mathbf{J}_1 \oplus \mathbf{S}_0 \quad (3.47)$$

$$\text{tr} \mathbf{E} = \mathbf{J}_2 \oplus \text{tr} \mathbf{S} \quad (3.48)$$

3.3.7. The fading memory hypothesis

The fading memory hypothesis was first introduced by Volterra in his study of the predator-prey relationship (Volterra 1913; Volterra 1931) and later extended to other types of hereditary relations (Leitman and Mizel 1974; Fabrizio *et al.* 1995).

Physically this assumption states that the more recent past has more influence on the present value of the stress than the more distant past does. It is the expression of a continuity property at infinity for hereditary relations and has profound implications on the regular limiting behaviour of the type of Boltzmann relationships considered so far. An immediate consequence of the assumption is that, for strain histories whose present values are the same and whose past values are close (in the sense of some suitable norm), the present values of the stress are also close, even though the values of the past histories may be quite different.

Although there are different ways of including the fading memory assumption into an hereditary relationship, the approach followed here has the most direct application to the type of numerical solution introduced in Chapters 4 and 6.

Let \mathbf{G} be a strong relaxation function with equilibrium modulus \mathbf{G}^∞ . We say that a strong relaxation function has the *stress relaxation property over a space of strain processes*

if, and only if, for each strain process \mathbf{E} which is continuous at infinity, the stress process $\mathbf{S} = \mathbf{G} \oplus \mathbf{E}$ is also continuous at infinity and

$$\lim_{t \rightarrow \infty} \mathbf{S}(t) = \mathbf{G} \left[\lim_{t \rightarrow \infty} \mathbf{E}(t) \right] \quad (3.49)$$

A strong relaxation function \mathbf{G} has the relaxation property over the space of strain processes with bounded histories, which includes the piecewise continuous processes with bounded histories and therefore the Heaviside type processes. This is a sufficient condition for the validity of (3.49).

However, a more restricting condition must be employed to extend the relaxation property to the class of processes with integrable histories. A strong relaxation function \mathbf{G} has the relaxation property over the space of strain processes with integrable history if $|\dot{\mathbf{G}}|$ is *eventually monotone*¹ with

$$\lim_{t \rightarrow \infty} |\dot{\mathbf{G}}| = 0 \quad (3.50)$$

If in particular \mathbf{G} is a scalar relaxation function (as for example the scalar functions \mathbf{G}_1 and \mathbf{G}_2 of [§3.3.6]) decreasing from $\overset{\circ}{\mathbf{G}}$ to $\overset{\infty}{\mathbf{G}}$, then the condition that $|\dot{\mathbf{G}}|$ be monotone

¹ A positive function f on \mathfrak{R} is *eventually monotone* if, and only if, it is monotone on some interval of the form $[T, \infty)$.

decreasing means that $\overset{\circ}{\mathbf{G}} \leq \overset{\circ}{\mathbf{G}}^{\infty}$. Therefore, the stress corresponding to a unit Heaviside step strain *relaxes* from $\overset{\circ}{\mathbf{G}}$ to $\overset{\circ}{\mathbf{G}}^{\infty}$.

Let now \mathbf{G} have the relaxation property over a space of strain processes and let \mathbf{E}_1 and \mathbf{E}_2 be a pair of strain processes in that space, which approach each other asymptotically:

$$\lim_{t \rightarrow \infty} (\mathbf{E}_1(t) - \mathbf{E}_2(t)) = 0 \quad (3.51)$$

Then if $\mathbf{S}_1 = \mathbf{G} \oplus \mathbf{E}_1$ and $\mathbf{S}_2 = \mathbf{G} \oplus \mathbf{E}_2$ it follows from (3.49) and the linearity of the relaxation function \mathbf{G} that \mathbf{S}_1 and \mathbf{S}_2 also approach each other asymptotically:

$$\lim_{t \rightarrow \infty} (\mathbf{S}_1(t) - \mathbf{S}_2(t)) = 0 \quad (3.52)$$

If, in addition, we have the further restrictions $\overset{\circ}{\mathbf{G}} \geq \overset{\circ}{\mathbf{G}}^{\infty} > 0$ and $\dot{\mathbf{G}} \leq 0$, then the relaxation function \mathbf{G} is invertible with strong inverse $\mathbf{J} = \mathbf{G}^{-1}$ (Graffi 1982).

These results prove our initial statement about the regular behaviour at infinity of Boltzmann laws expressed by the fading memory assumption.

3.3.8. Periodic harmonic processes and mechanical forcing

We shall now examine the stress-strain hereditary relations for the case in which the strain vanishes for $t < 0$ and is periodic with time period $T \geq 0$ for $t \geq 0$. Only simple harmonic dependence will be considered, since the general problem can be solved by Fourier analysis (Achenbach 1973).

Let \mathbf{E} be a periodic strain process with amplitude $\hat{\mathbf{E}} \in \mathcal{T}_{\text{sym}}$ and circular frequency $\omega = \frac{2\pi}{T} \neq 0$:

$$\mathbf{E}(t) = \hat{\mathbf{E}} \sin(\omega t), \quad t \in \mathcal{R} \quad (3.53)$$

The stress process $\mathbf{S} = \mathbf{G} \oplus \mathbf{E}$ is also a periodic process with circular frequency ω and it is given by (Leitman and Fischer 1984)

$$\mathbf{S}(t) = \sin(\omega t) \left[\overset{\circ}{\mathbf{G}} + \hat{\mathbf{G}}_c(\omega) \right] [\hat{\mathbf{E}}] - \cos(\omega t) \left[\hat{\mathbf{G}}_s(\omega) \right] [\hat{\mathbf{E}}] \quad (3.54)$$

where $\hat{\mathbf{G}}_c$ and $\hat{\mathbf{G}}_s$ are the half-range Fourier cosine and sine transforms of $\overset{\circ}{\mathbf{G}}$ defined by:

$$\hat{\mathbf{G}}_c(\omega) = \int_0^\infty \overset{\circ}{\mathbf{G}}(s) \cos(\omega s) ds \quad (3.55)$$

$$\hat{\mathbf{G}}_s(\omega) = \int_0^\infty \overset{\circ}{\mathbf{G}}(s) \sin(\omega s) ds \quad (3.56)$$

The function $\hat{\mathbf{G}}_c$ is called the *dynamic modulus*, $-\hat{\mathbf{G}}_s$ is the *loss modulus*, the sum $\overset{\circ}{\mathbf{G}} + \hat{\mathbf{G}}_c$ the *storage modulus* and the function $\eta(\omega) = -\frac{1}{\omega} \hat{\mathbf{G}}_s(\omega)$ the *dynamic viscosity*.

Consider now a scalar relaxation function G , such that $\mathbf{S} = \mathbf{G} \oplus \mathbf{E}$. We define the *phase lag* $\delta(\omega)$ and the *loss factor* $\tan \delta(\omega)$, for each circular frequency ω , as

$$\tan \delta(\omega) = \frac{\hat{\mathbf{G}}_s(\omega)}{\mathring{\mathbf{G}} + \hat{\mathbf{G}}_c(\omega)} \quad (3.57)$$

and the stress process \mathbf{S} can be rewritten as

$$\mathbf{S}(t) = \left\{ \left[\mathring{\mathbf{G}} + \hat{\mathbf{G}}_c(\omega) \right]^2 + \left[\hat{\mathbf{G}}_s(\omega) \right]^2 \right\}^{\frac{1}{2}} \sin(\omega t - \delta(\omega)) \hat{\mathbf{E}} = \hat{\mathbf{S}} \sin(\omega t - \delta(\omega)), \quad (3.58)$$

$t \in \Re$

The phase lag is a direct consequence of the hereditary properties of viscoelastic materials. In addition, it vanishes in the high frequency limit and, in this sense, viscoelastic materials behave elastically at high frequencies.

Indeed, from the Riemann-Lebesgue lemma (Amerio 1985b), it follows that

$$\lim_{|\omega| \rightarrow \infty} \left[\mathring{\mathbf{G}} + \hat{\mathbf{G}}_c(\omega) \right] = \mathring{\mathbf{G}} \quad (3.59)$$

$$\lim_{|\omega| \rightarrow \infty} \left[\hat{\mathbf{G}}_s(\omega) \right] = 0 \quad (3.60)$$

and therefore

$$\lim_{|\omega| \rightarrow \infty} \left(\mathbf{S}(t) - \mathring{\mathbf{G}}[\hat{\mathbf{E}}] \sin(\omega t) \right) = 0, \quad t \in \Re \quad (3.61)$$

$$\lim_{|\omega| \rightarrow \infty} \delta(\omega) = 0 \quad (3.62)$$

Let now \mathbf{S} be the periodic stress tensor

$$\mathbf{S} = \hat{\mathbf{S}} \sin(\omega t) \quad (3.63)$$

and consider the strong relaxation function \mathbf{G} to be invertible with strong inverse \mathbf{J} . The corresponding strain process \mathbf{E} is also periodic with circular frequency ω and is given by

$$\begin{aligned} \mathbf{E}(t) &= (\mathbf{J} \oplus \mathbf{S})(t) = \\ &= \sin(\omega t) \left[\mathbf{J} + \int_0^\infty \dot{\mathbf{J}}(s) \cos(\omega s) ds \right] [\hat{\mathbf{S}}] - \cos(\omega t) \left[\int_0^\infty \dot{\mathbf{J}}(s) \sin(\omega s) ds \right] [\hat{\mathbf{S}}] \quad t \in \mathfrak{R} \end{aligned} \quad (3.64)$$

If we now consider the scalar Heaviside unit step process h and form the new stress process

$$\mathbf{S}' = h \hat{\mathbf{S}} \sin(\omega t) \quad (3.65)$$

the corresponding strain process is written as

$$\begin{aligned} \mathbf{E}'(t) &= (\mathbf{J} \oplus \mathbf{S}')(t) = \\ &= \sin(\omega t) \left[\mathbf{J} + \int_0^t \dot{\mathbf{J}}(s) \cos(\omega s) ds \right] [\hat{\mathbf{S}}] - \cos(\omega t) \left[\int_0^t \dot{\mathbf{J}}(s) \sin(\omega s) ds \right] [\hat{\mathbf{S}}] \quad t \in \mathfrak{R}_0^+ \end{aligned} \quad (3.66)$$

Therefore

$$\begin{aligned} \lim_{t \rightarrow \infty} (\mathbf{E}(t) - \mathbf{E}'(t)) = \\ = \lim_{t \rightarrow \infty} \left(\sin(\omega t) \left[\int_t^\infty \dot{\mathbf{J}}(s) \cos(\omega s) ds \right] [\hat{\mathbf{S}}] - \cos(\omega t) \left[\int_t^\infty \dot{\mathbf{J}}(s) \sin(\omega s) ds \right] [\hat{\mathbf{S}}] \right) = 0, \quad t \in \mathfrak{R}_0^+ \end{aligned} \quad (3.67)$$

This result, known as the *Theorem of asymptotic behaviour* (Leitman and Fischer 1984), has a fundamental application in the experimental analysis of periodic stress-strain processes, since it allows neglecting the effect of the initial step in the forcing stress process over the entire duration of the experiment.

Finally, we see that, applying the Fourier integral theorem, it is possible to recover the relaxation function \mathbf{G} from experimental measurements of the stress and strain processes. Indeed, provided that the initial elasticity $\mathring{\mathbf{G}}$ and the dynamic and loss moduli, $\hat{\mathbf{G}}_c$ and $-\hat{\mathbf{G}}_s$, are known, it follows, since \mathbf{G} is strong, that

$$\mathbf{G}(t) = \mathring{\mathbf{G}} + \frac{2}{\pi} \int_0^\infty \frac{\sin(\omega t)}{\omega} \hat{\mathbf{G}}_c(\omega) d\omega, \quad t \in \mathfrak{R}_0^+ \quad (3.68)$$

or, alternatively

$$\mathbf{G}(t) = \mathring{\mathbf{G}} - \frac{2}{\pi} \int_0^\infty \frac{\cos(\omega t) - 1}{\omega} \hat{\mathbf{G}}_s(\omega) d\omega, \quad t \in \mathfrak{R}_0^+ \quad (3.69)$$

3.4. Dynamic linear viscoelasticity

3.4.1. Dynamic viscoelastic processes

Let \mathfrak{B} be a viscoelastic body with relaxation function \mathbf{G} and density ρ , subjected to the body force \mathbf{b} . We define the *dynamic viscoelastic process* for \mathfrak{B} corresponding to \mathbf{G} , \mathbf{b} and ρ , or $\text{DVP}(\mathbf{G}, \mathbf{b}, \rho)$, as an admissible process $[\mathbf{u}, \mathbf{E}, \mathbf{S}]$ for \mathfrak{B} , such that:

- the values of \mathbf{u} , \mathbf{E} and \mathbf{S} are continuous fields of class C on the closure $\overline{\mathfrak{B}}$
- the displacement \mathbf{u} is a process of class C^2 , whose values are vector fields of class C^2 on $\overline{\mathfrak{B}}$
- on $\overline{\mathfrak{B}}$, the processes \mathbf{u} , \mathbf{E} and \mathbf{S} satisfy the linear system

$$\text{div} \mathbf{S} + \mathbf{b} = \rho \ddot{\mathbf{u}} \quad (\text{equation of motion}) \quad (3.70)$$

$$\mathbf{E} = \frac{1}{2} [\nabla \mathbf{u} + \nabla \mathbf{u}^T] \quad (\text{strain-displacement relation}) \quad (3.71)$$

$$\mathbf{S} = \mathcal{L}_{\mathbf{G}}[\mathbf{E}] = \mathbf{G} \oplus \mathbf{E} \quad (\text{Boltzmann relaxation law}) \quad (3.72)$$

Similar relationships hold for a viscoelastic body \mathfrak{B} with creep compliance \mathbf{J} .

A process $[\mathbf{u}, \mathbf{E}, \mathbf{S}]$ is said to be a *solution* for $\text{DVP}(\mathbf{G}, \mathbf{b}, \rho)$, or $\text{DVP}(\mathbf{J}, \mathbf{b}, \rho)$, corresponding to the *boundary data* $[\hat{\mathbf{u}}, \hat{\mathbf{s}}]$ on $\partial \mathfrak{B}$ if, and only if, it satisfies the boundary conditions on $\partial \mathfrak{B}$:

$$\mathbf{u} = \hat{\mathbf{u}}, \quad \text{on } \partial \mathfrak{B}_{\hat{\mathbf{u}}} \quad (3.73)$$

$$\mathbf{S} \cdot \mathbf{n} = \hat{\mathbf{s}}, \quad \text{on } \partial\mathfrak{B}_{\hat{\mathbf{s}}} \quad (3.74)$$

where $\partial\mathfrak{B}_{\hat{\mathbf{u}}}$ and $\partial\mathfrak{B}_{\hat{\mathbf{s}}}$ are the portions of boundary where Neumann and Dirichlet conditions are respectively applied.

A process $[\mathbf{v}, \mathbf{R}, \mathbf{T}]$ is said to be an initial past history up to time t_0 for \mathfrak{B} consistent with $[\hat{\mathbf{u}}, \hat{\mathbf{s}}]$, \mathbf{b} , ρ and either \mathbf{G} or \mathbf{J} if, and only if the following conditions hold (Leitman and Fischer 1984):

$$\operatorname{div} \mathbf{T} + {}_r \mathbf{b}^0 = \rho \ddot{\mathbf{v}} \quad \text{on } \mathfrak{B} \quad (3.75)$$

$$\mathbf{R} = \frac{1}{2} [\nabla \mathbf{v} + \nabla \mathbf{v}^T] \quad \text{on } \mathfrak{B} \quad (3.76)$$

$$\left\{ \begin{array}{l} \mathbf{T}(s) = \mathring{\mathbf{G}}[\mathbf{R}(s)] + \int_0^s \dot{\mathbf{G}}(\xi) [\mathbf{R}(s + \xi)] d\xi \end{array} \right. \quad (3.77)$$

$$\left\{ \begin{array}{l} \text{or} \\ \mathbf{R}(s) = \mathring{\mathbf{J}}[\mathbf{T}(s)] + \int_0^s \dot{\mathbf{J}}(\xi) [\mathbf{T}(s + \xi)] d\xi \end{array} \right. \quad \text{on } \mathfrak{B}, s \in \mathfrak{R}^+ \quad (3.78)$$

$$\mathbf{v} = {}_r \hat{\mathbf{u}}^{t_0} \quad \text{on } \partial\mathfrak{B}_{\hat{\mathbf{u}}} \quad (3.79)$$

$$\mathbf{T} \cdot \mathbf{n} = {}_r \hat{\mathbf{s}}^{t_0} \quad \text{on } \partial\mathfrak{B}_{\hat{\mathbf{s}}} \quad (3.80)$$

3.4.2. Power and energy balance

The rate at which work is done for any dynamic process on a body \mathfrak{B} by the surface forces \mathbf{s} and body forces \mathbf{b} equals the stress power plus the time rate of change of the kinetic energy. For a dynamic viscoelastic process, this statement can be written as:

$$\int_{\partial\mathfrak{B}} \mathbf{s} \cdot \dot{\mathbf{u}} dA + \int_{\mathfrak{B}} \mathbf{b} \cdot \dot{\mathbf{u}} dV = \int_{\mathfrak{B}} (\mathcal{L}_{\mathbf{G}}[\mathbf{E}]) \cdot \dot{\mathbf{E}} dV + \frac{d}{dt} \frac{1}{2} \int_{\mathfrak{B}} \rho |\dot{\mathbf{u}}|^2 dV \quad (3.81)$$

which, after substitution of the complete expression for $\mathcal{L}_{\mathbf{G}}$, becomes:

$$\begin{aligned} \int_{\partial\mathfrak{B}} \mathbf{s}(\mathbf{x}, t) \cdot \dot{\mathbf{u}}(\mathbf{x}, t) dA(\mathbf{x}) + \int_{\mathfrak{B}} \mathbf{b}(\mathbf{x}, t) \cdot \dot{\mathbf{u}}(\mathbf{x}, t) dV(\mathbf{x}) = \\ = \int_{\mathfrak{B}} \overset{\circ}{\mathbf{G}} \mathbf{E}(\mathbf{x}, t) \cdot \dot{\mathbf{E}}(\mathbf{x}, t) dV(\mathbf{x}) + \int_{\mathfrak{B}} \dot{\mathbf{E}}(\mathbf{x}, t) \cdot \int_0^\infty \dot{\mathbf{G}}(\mathbf{x}, t) \mathbf{E}(\mathbf{x}, t - \tau) d\tau dV + \\ + \frac{d}{dt} \frac{1}{2} \int_{\mathfrak{B}} \rho |\dot{\mathbf{u}}|^2(\mathbf{x}, t) dV(\mathbf{x}), \quad t \in \mathfrak{R} \end{aligned} \quad (3.82)$$

The dependence of \mathbf{G} upon the point \mathbf{x} can be removed for homogeneous materials.

A viscoelastic materials is *dissipative* if the first term in the right-end-side member of (3.81) is always non-negative:

$$\int_{\mathfrak{B}} \mathcal{L}_{\mathbf{G}}(\mathbf{x}, t) [\mathbf{E}(\mathbf{x}, t)] \cdot \dot{\mathbf{E}}(\mathbf{x}, t) dV(\mathbf{x}) = \int_{\mathfrak{B}} \mathbf{S}(\mathbf{x}, t) \cdot \dot{\mathbf{E}}(\mathbf{x}, t) dV(\mathbf{x}) \geq 0, \quad t \in \mathfrak{R}_0^+ \quad (3.83)$$

In particular, it is *strongly dissipative* if it is zero only for $\mathbf{E} \equiv 0$.

The *Theorem of displacement boundary data*, due to Edelman and Gurtin, shows that relation (3.83) is a sufficient condition for the uniqueness of the solution of the dynamic

viscoelastic problem (Carbonaro 1995). This statement stems from the fact that in this case the initial elasticity $\overset{\circ}{\mathbf{G}}$ can be proved to be symmetric and strongly elliptic² (Dallasta 1995).

3.4.3. Oscillatory displacement processes

From this section onward, we restrict our attention to oscillatory displacement processes. The interest in this kind of processes derives from a number of facts. The availability of analytical expressions for simple problems and the direct correlation with experimental data have lead to extensive research in this area. In particular, the single frequency response of viscoelastic materials is of paramount importance in underwater communications problems, through the application of Fourier analysis.

We consider an oscillatory displacement process over the viscoelastic body \mathfrak{B} at the real frequency ω :

$$\mathbf{u}(\mathbf{x}, t) = \mathbf{a}(\mathbf{x})e^{i\omega t}, \quad (\mathbf{x}, t) \in \mathfrak{B} \times \mathfrak{R} \quad (3.84)$$

The constitutive relation for strong response functions \mathbf{G} becomes³:

$$\begin{aligned} S(\mathbf{x}, t) &= \left\{ \overset{\circ}{\mathbf{G}}(\mathbf{x}) + \int_0^\infty \dot{\mathbf{G}}(\mathbf{x}, t) e^{-i\omega \tau} d\tau \right\} \frac{1}{2} (\nabla \mathbf{a}(\mathbf{x}) + \nabla \mathbf{a}(\mathbf{x})^T) e^{i\omega t} = \\ &= \mathbf{C}^*(\mathbf{x}, \omega) \mathbf{E}(\mathbf{x}, t), \quad (\mathbf{x}, t) \in \mathfrak{B} \times \mathfrak{R} \end{aligned} \quad (3.85)$$

² A tensor \mathbf{T} is said to be strongly elliptic if $\mathbf{x} \cdot \mathbf{T}(\mathbf{x}\mathbf{y}^T)\mathbf{y} > 0$, for each pair of vectors \mathbf{x} and \mathbf{y} .

³ Cf. §3.3.8

The term $\mathbf{C}^*(\mathbf{x}, \omega)$ is called **complex modulus**. It is a complex valued, frequency dependent, fourth-order tensor. Dropping the dependence upon the point \mathbf{x} , it can be rewritten in terms of its real and imaginary parts as $\mathbf{C}^*(\omega) = \mathbf{C}_1(\omega) + i\mathbf{C}_2(\omega)$, where

$$\mathbf{C}_1(\omega) = \overset{\circ}{\mathbf{G}} + \text{Re} \int_0^\infty \dot{\mathbf{G}}(\tau) e^{-i\omega\tau} d\tau = \overset{\circ}{\mathbf{G}} + \hat{\mathbf{G}}_c \quad (3.86)$$

$$\mathbf{C}_2(\omega) = \text{Im} \int_0^\infty \dot{\mathbf{G}}(\tau) e^{-i\omega\tau} d\tau = \hat{\mathbf{G}}_s \quad (3.87)$$

In the case of **plane travelling waves** propagating in the direction \mathbf{n} , we have:

$$\mathbf{a}(\mathbf{x}) = \mathbf{p} e^{-ik(\mathbf{x} \cdot \mathbf{n})}, \quad \mathbf{x} \in \mathfrak{B} \quad (3.88)$$

and

$$\mathbf{u}(\mathbf{x}, t) = \mathbf{p} e^{i[\alpha t - k(\mathbf{x} \cdot \mathbf{n})]}, \quad (\mathbf{x}, t) \in \mathfrak{B} \times \mathfrak{R} \quad (3.89)$$

The term $\mathbf{p} = \mathbf{p}_1 + i\mathbf{p}_2$ is a **complex polarisation vector** and k is a **complex wave number** defined as

$$k = \frac{\omega}{c} - i\alpha \quad (3.90)$$

where $c(\omega)$ is the frequency dependent *phase velocity* and $\alpha(\omega)$ is the frequency dependent *attenuation*.

We now look for solutions of the dynamic problem with the form of relation (3.89). The equation of motion for the oscillatory displacement field (3.84) becomes:

$$\operatorname{div}\{\mathbf{C}^*[\nabla \mathbf{a} + \nabla \mathbf{a}^T]\} = -2\rho\omega^2 \mathbf{a} \quad (3.91)$$

which yields, by substitution of (3.89), the *complex propagation condition*:

$$\mathbf{C}^*[(\mathbf{p}\mathbf{n}^T)]\mathbf{n} - \frac{\rho\omega^2}{k^2} \mathbf{p} = 0 \quad (3.92)$$

We define the frequency dependent operator $\mathbf{Q}^*(\mathbf{n})$, called the *complex acoustic tensor*, on the complex three-dimensional Euclidean vector space \mathcal{V}^* for each unit vector \mathbf{n} as:

$$\mathbf{Q}^*(\mathbf{n})\mathbf{a} = \mathbf{C}^*(\mathbf{a}\mathbf{n}^T)\mathbf{n}, \quad \mathbf{a} \in \mathcal{V}^* \quad (3.93)$$

Condition (3.92) becomes therefore:

$$\mathbf{Q}^*(\mathbf{n})\mathbf{p} - \lambda\mathbf{p} = 0 \quad (3.94)$$

where $\lambda = \frac{\rho\omega^2}{k^2}$ is a frequency dependent function, which can assume up to three different forms (given by the eigenfunctions of the matrix equation (3.94) and depending on the direction \mathbf{n}).

The analysis is from now on restricted to the case of viscoelastic isotropic materials defined in §3.3.6. Recalling the definitions of shear and compression moduli, \mathbf{G}_1 and \mathbf{G}_2 , the complex acoustic tensor is rewritten as:

$$\begin{aligned} \frac{\mathbf{Q}^*(\mathbf{n})\mathbf{a}}{\rho} &= \frac{\mathbf{C}^*[(\mathbf{a}\mathbf{n}^T)]\mathbf{n}}{\rho} = \left\{ \frac{\mathbf{G}_2^* + 2\mathbf{G}_1^*}{3\rho} \right\} (\mathbf{n}\mathbf{n}^T)\mathbf{a} + \left\{ \frac{\mathbf{G}_1^*}{2\rho} \right\} \{1 - (\mathbf{n}\mathbf{n}^T)\}\mathbf{a} = \\ &= \mathbf{K}_1^*(\mathbf{n}\mathbf{n}^T)\mathbf{a} + \mathbf{K}_2^*\{1 - (\mathbf{n}\mathbf{n}^T)\}\mathbf{a}, \quad \mathbf{a} \in \mathbf{V}^* \end{aligned} \quad (3.95)$$

where \mathbf{K}_1^* and \mathbf{K}_2^* are the *reduced longitudinal bulk modulus* and the *reduced shear modulus* respectively. The star notation means that the terms have the special complex form used in (3.86) and (3.87).

For the isotropic case, equation (3.94) has two distinct eigenfunctions:

$$\lambda(\omega) = \frac{\mathbf{G}_1^*(\omega)}{2} \quad \text{for transverse waves for which } \mathbf{p} \cdot \mathbf{n} = 0 \quad (3.96)$$

$$\lambda(\omega) = \frac{1}{3}(\mathbf{G}_2^*(\omega) + 2\mathbf{G}_1^*(\omega)) \quad \text{for longitudinal waves for which } \mathbf{p} \times \mathbf{n} = 0 \quad (3.13.)$$

Attenuation $\alpha(\omega)$ and phase velocity dispersion $c(\omega)$ can therefore be calculated from the knowledge of the shear and compression moduli or alternatively the reduced longitudinal bulk and shear moduli, provided density is known as well. The two complex polarisation vectors corresponding to the eigenfunctions (3.94) and (3.95) provide the solution to the dynamic viscoelastic problem.

3.5. References

- ACHENBACH, J.D. (1973). *Wave propagation in elastic solids*. Amsterdam: North Holland Publishing Company, Chap.1, Sect. 1.8-1.9, 37-41.
- AMERIO L. (1985a). *Analisi matematica*, Vol. III, Part A. Torino: UTET
- AMERIO L. (1985b). *Analisi Matematica*, Vol. II. Torino: UTET, 465
- BOLTZMANN, L. (1870). Zur Theorie der elastischen Nachwirkung. *Sitber. Kaiserl. Akad. Wiss., Wien Math.-Naturw.*, Kl. 70, Sect. II, 275-306
- BURTON, T.A. (1983). Volterra integral and differential equations. New York: Academic Press
- CARBONARO, B. (1995). Wave propagation, uniqueness and singularities at infinity for an unbounded linearly viscoelastic material. *Math. Mod. and Met. in App. Sc.*, 5 (8,) 1051-1078
- COLEMAN, B.D. and MIZEL, V.J. (1966). Norms and semigroups in the theory of fading memory. *Arch. Rational Mech. Anal.*, 23, 87-123
- DALLASTA, A. (1995). Stability condition for an extensive class of viscoelastic motions. *J. Elasticity*, 39 (1), 17-29
- FABRIZIO, M. et al. (1995). Internal dissipation, relaxation property and free-energy in materials with fading memory. *J. Elasticity*, 40 (2), 107-122
- GRAFFI, D. (1982). Mathematical models and waves in linear viscoelasticity. In MAINARDI, F. (ed.). *Wave propagation in viscoelastic media*. Pitman Publishing Inc., 1-27
- GURTIN, M.E. and STERNBERG, E. (1962). On the linear theory of viscoelasticity. *Arch. Rational Mech. Anal.*, 11 (4), 291-356
- GURTIN, M.E. (1984). Linear theories of elasticity and thermoelasticity. In TRUESDELL, C. (ed.). *Mechanics of Solids*, Vol. II. New York: Springer-Verlag

LEITMAN, M.J. and MIZEL, V.J. (1974). On fading memory spaces and hereditary integral equations. *Arch. Rational Mech. Anal.*, 55, 18-51

LEITMAN, M.J. and FISHER, G.M.C. (1984). The linear theory of viscoelasticity. In TRUESDALL, C. (ed.). *Mechanics of Solids*, Vol. III. New York: Springer-Verlag

NOLL, W (1958). A mathematical theory of the mechanical behavior of continuous media. *Arch. Rational Mech. Anal.*, 2, 197

VOLTERRA, V. (1909). Sulle equazioni integrodifferenziali della teoria dell'elasticità. *Atti Reale Accad. Lincei*, 18 (2), 295

VOLTERRA, V. (1913). Sui fenomeni ereditari. *Atti Reale Accad. Lincei*, 5 (22), 529-539

VOLTERRA, V. (1931). *Leçons sur la théorie mathématique de la lutte pour la vie*. Paris : Collection Borel

Chapter 4

Viscoelastic Properties of Hard Polymers: Characterisation and Experimental Measurements

4.1. Introduction

This chapter is devoted to the characterisation of the viscoelastic materials used to manufacture the anechoic baffle for the VERTLINK project.

A description of the physical characteristics of hard polymers is first given and the steps followed during the production of the special rubbers used are then described and justified.

In order to characterise completely the mechanical properties of polymers, a variety of experimental measurements is necessary. Moreover, experimental methods depend greatly on the characteristics of the substances to be studied and a large number of techniques have been devised. The two experimental set-ups chosen to test the materials used in this research are detailed: namely, the forced vibration method and the pulse-echo immersion method, the latter with parametric sound sources.

The remaining sections are dedicated to the problem of material properties identification from the experimental data. A numerical technique based on the transfer matrix approach and a set of approximated viscoelastic functions has been devised and implemented in the MATLAB macro language to solve this problem. The resulting frequency-dependent responses for the compounded butyl rubber panels are given together with an estimate of the errors involved in the procedure.

4.2. Physical Properties of Hard Polymers

When any of the dynamic functions for a particular polymer is plotted against time or frequency, it usually spans an enormous range of magnitudes with changes that can vary from very smooth to abrupt.

Inspection of the different typical zones reveals a pattern in the frequency (or time) dependence and leads to the identification of a number of behaviours characterised by different shapes (usually on a logarithmic scale).

In addition, it is found experimentally that, when measuring the values of storage and loss moduli and loss factors at a fixed frequency, they change widely with temperature. The peaks in storage modulus and loss factor can be related to particular molecular motions in the polymer structure occurring at defined temperatures for a given frequency. The peaks can be regarded as ‘damping’ effects due to the changes in free volume, molecular structure and characteristic molecular resonances.

It can be noticed that the effects of temperature and frequency on the viscoelastic behaviour act in opposing ways. At a fixed temperature the material will appear stiffer at high frequencies, since the molecular motion is slower than the changes in the forcing pressure,

whereas it will appear softer at lower frequencies, since the molecular chains have the time to reorganise themselves to follow the external load. On the other hand for a fixed frequency, high temperature will allow greater freedom in the molecular motion and vice versa.

From fig. 4.1, four different regions can be recognised (Ferry 1980; Read 1978):

- ***the glassy region***: this region can be observed at low temperature or high frequency and is characterised by rigidly networked polymer chains. The elastic moduli have high values, whereas loss is low, even though it can show one or more secondary transitions revealed by small peaks in the curve
- ***the glass-rubber transition region***: this transition marks the polymer chain undergoing long-range motions. Usually a transition frequency F_g or temperature T_g can be identified. This region is characterised by a sudden drop in the elastic moduli value and a high peak in the loss factor. This is the preferred operating region for bulk sound absorbers.
- ***the rubbery region***: in this region the long molecular chains are cross-linked in a 'coil-shaped' structure. The elastic moduli stay appreciably constant, while the loss factor curve experiences a minimum
- ***the flow region***: when the temperature or the frequency reach a new transition value T_f or F_f , the chains start undergoing translational motions relative to each other, breaking the cross-links. The material experiences a fall-off in the elastic moduli and an increase in the value of the loss factor

The simultaneous occurrence of a drop in the elastic modulus and a peak in the loss factor is a typical behaviour in all viscoelastic materials. This property is known as the

Kramer-Kronig dispersion relationship and is a consequence of the integral, Hilbert-type relationship between the real and imaginary parts of the modulus outlined in §3.1.3 (Ferry 1980).

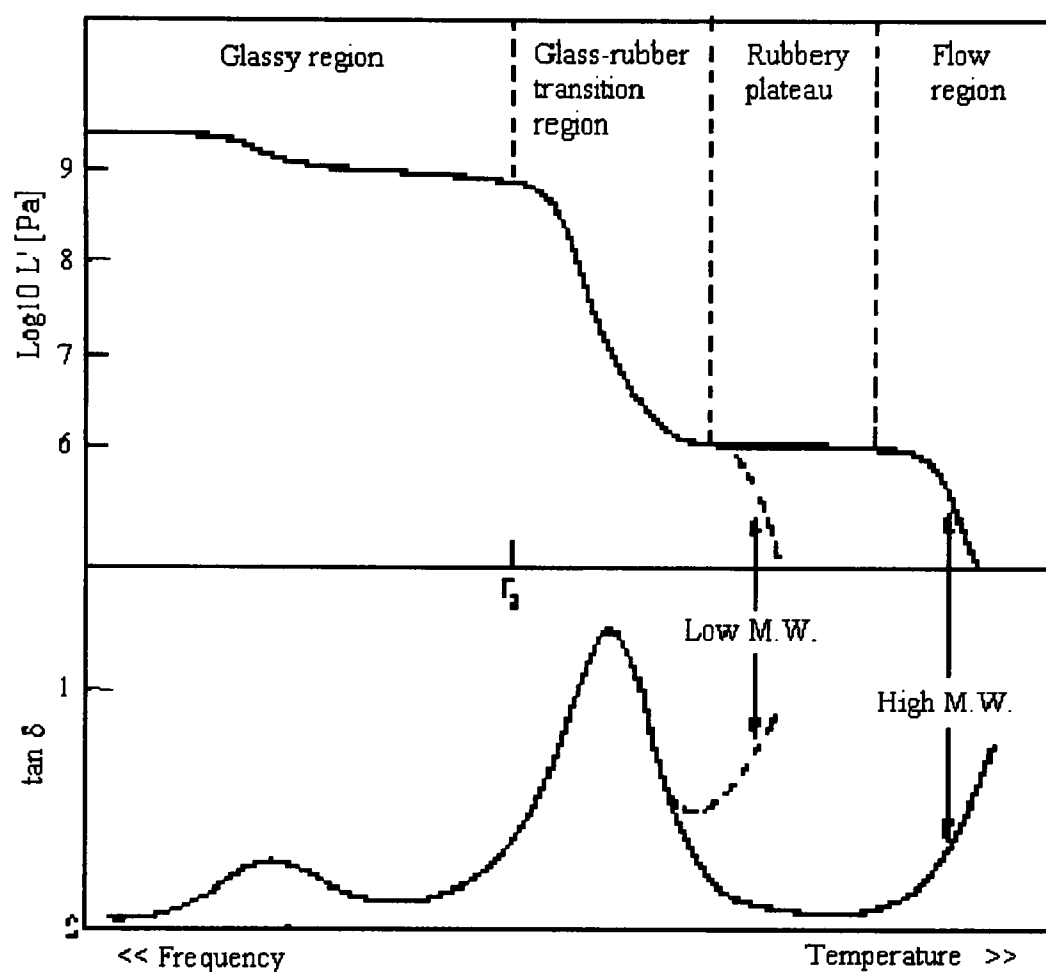


Figure 4.1: Typical frequency and temperature pattern for hard polymers (M.W. = Molecular Weight) (reproduced from (Read 1978))

The frequency range of occurrence of the transition region depends on a number of factors, among which chemical composition and temperature are the most important. In particular the higher the molecular weight, the higher the frequency. The rubber compounds here have been chosen among the class of low molecular weight methacrylate polymers (ethylene and *n*-butyl methacrylates). For these substances, the transition region falls in the operating frequency range used during this research (10 to 100 kHz) (cfr. (Ferry 1980), Table 12.1). This effect has been fine-tuned by modifying the standard behaviour with proper

amounts of heavy fillers, according to the compounding and processing factors outlined in Appendix B.

4.3. Composition and Processing of the Test Rubber Compounds

The multi-layered tile analysed in this work has been manufactured from two different rubber compounds. The first layer has the purpose of absorbing and dissipating the energy carried by the acoustic signal and it is made of loaded butyl rubber. The second layer provides a matching surface with water and it is made of loaded polyurethane rubber moulded into a grid of steep-angled cones.

The butyl rubber compound has been chosen because of its high loss factor, but it's difficult to mould into complex shapes, must be carefully compounded and vulcanised and can only be calendered into flat panels up to 1-1.5 cm thick. On the other hand, the polyurethane rubber used for the matching layer provides a lower loss factor, but has the advantage of being easily cast into complex shapes from cold-curing liquid components.

4.3.1. The Absorbing Layer: Loaded Butyl Rubber

The base butyl rubber was supplied by Exxon Chemicals Ltd as a white, uncured rubber bale (Exxon Chemical 1996). The rubber has been compounded in a low-speed milling machine, adding a number of suitable fillers to modify its mechanical properties (Suma *et al.* 1993). Finally, it's been calendered and vulcanised to form a set of black plane panels of density ranging from 1200 to 2200 kgm⁻³ in 200 kgm⁻³ increments. The chemical formulation and standard mechanical properties can be found in tables 3.1 and 3.2 (Exxon Chemical 1996; Piquette 1985).

Unvulcanised butyl rubber	ISO 2302 ASTM D 3188
Butyl	100
IRB 6	50
Zinc Oxide (NBS 370)	3
Stearic Acid (NBS 372)	1
Sulphur (NBS 371)	1.75
TMTDS (IRM 1)	1

Table 4.1: Chemical formulation of uncured butyl rubber base (phr)

Vulcanised butyl rubber	
Butyl 365	100.00
Stearic acid	0.50
Silica (Hard clay)	variable proportion to obtain desired density
Calcium carbonate	40.00
Zinc oxide	5.00
Polyethylene	6.00
Paraffin wax	4.00
S-315 carbon black	10.00
DMF (p. quinanedioxime)	6.00
Red lead (Pb3O4)	9.00
Sulphur	0.80

Table 4.2: Chemical formulation of vulcanised butyl rubber sheets (phr)

4.3.2. The Matching Layer: Loaded Polyurethane Rubber

The polyurethane rubber base was supplied by PolyMed Ltd as a two-component liquid rubber. The components are Hyperlast 200 Polyol Curative and a Hyperlast 200 Isocyanate catalyst (Polymed 1996). The base compound has been mixed with varying amounts of heavy fillers, both inert (glass microspheres) and chemically reactive substances (carbon black powder , lead oxide and tungsten oxide), to vary the mechanical properties and

increase the density (Maazouz *et al.* 1993). The mixture can easily be cold-cured at 80°C for 15 min and left to set for 60 min.

Four sets of sample bars have been produced, one for each main filler, with increasing percentage of the filler itself (Fig. 4.2). The composition can be found in Table 4.3.



Figure 4.2: Loaded polyurethane samples (from left to right: glass microspheres, lead oxide in varying percentages, tungsten oxide)

Compounded polyurethane rubber	
Hyperlast 200 Curative	100
Hyperlast 200 Isocyanate	30
S-315 Carbon Black	6.5-13-26-39
Lead Oxide (Pb3O4)	6.5-13-26-39
Tungsten Oxide	6.5-13-26-39
Glass Beads	6.5-13-26-39

Table 4.3: Chemical formulation of loaded polyurethane rubber (phr)

4.4. Polyurethane Rubber Characterisation

4.4.1. The Vibrating Reed Measurement Method

The characterisation of the loaded polyurethane rubber used in the absorbent baffle under investigation has been realised with the collaboration of the Italian Whitehead Alenia Sistemi Subacquei.

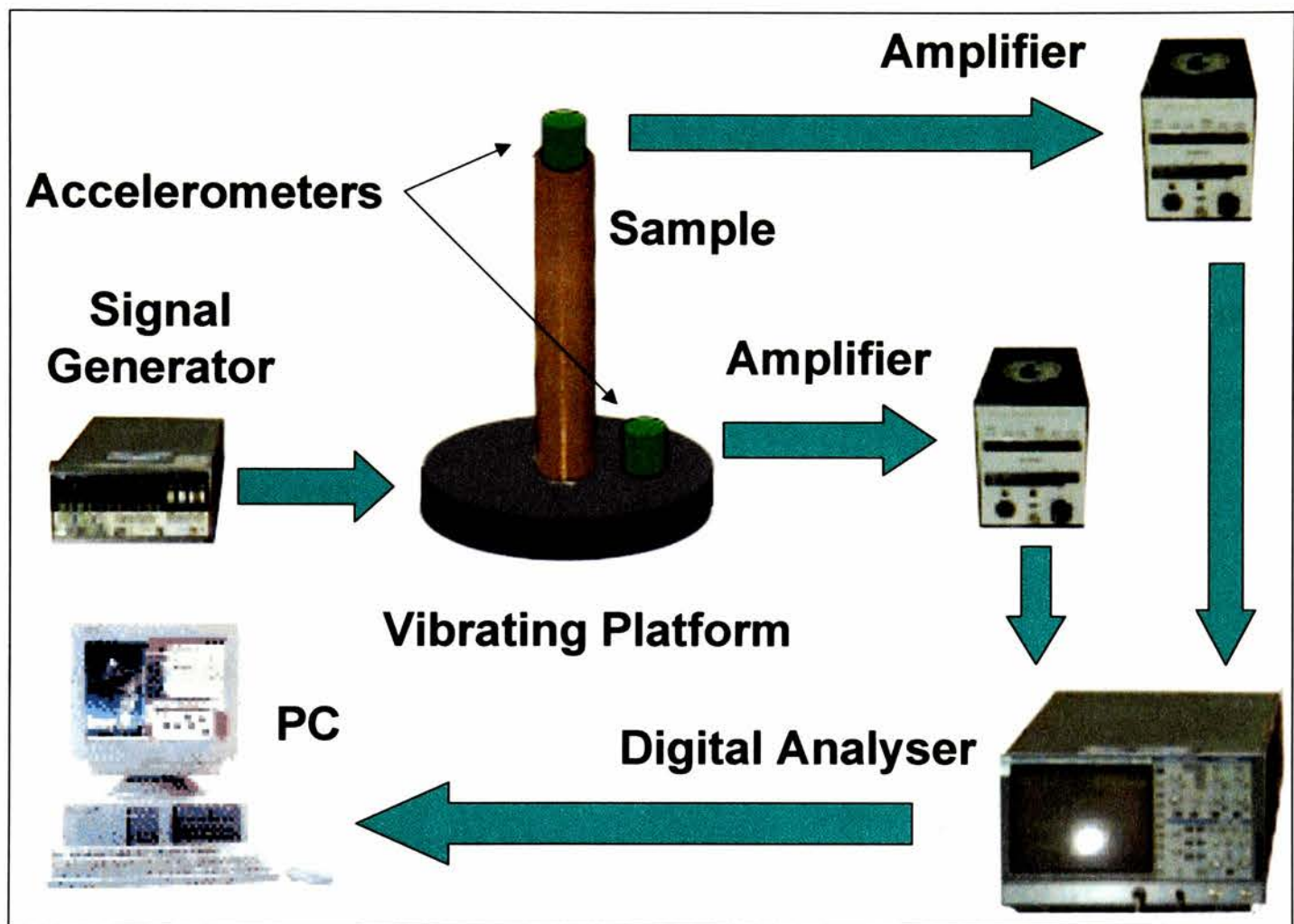


Figure 4.3: Block diagram of the longitudinal vibrating reed test method

A suitable number of rubber samples of varying composition and size have been manufactured using the method described in §4.3 (fig. 4.2). The Young's and shear moduli have been measured separately by means of two forced non-resonant methods.

The tests consist in the excitation of longitudinal and shear vibrations along a cylindrical sample of material by a vibrating head at frequencies between 1 kHz and 50 kHz.

The amplitude of the vibration is measured at the platform and at the sample top end by means of two calibrated accelerometers. The block diagram of the system is shown in fig. 4.3

A B&K 1027 signal generator transmits a continuous sinusoidal signal of given frequency to the vibrating platform. The first B&K 4374 accelerometer at the platform end of the sample is used as stress gauge, whereas the second accelerometer on the sample top end is used as strain gauge. The two signals are amplified and transmitted to a digital analyser type HP 4194A. All operations have been performed in a temperature-controlled room at 14°C.

The phase lag and complex modulus can be worked out from the two signals, either directly using the dynamic equation for long samples or from a more sophisticated multi-layer analysis, as described later in this chapter, for short samples. Indeed, in the latter case the accelerometer influences the measured values and it must be therefore taken into account as an additional layer in the system.

4.4.2. Experimental Measurements

A number of measurements have been carried out on the series of samples described in §4.2.8.2. In particular four series have been considered:

- Glass microspheres (5 to 500 μm)
- Carbon Black (S315) (300 to 400 \AA)
- Lead Oxide (300 to 400 \AA)
- Tungsten Oxide (300 to 400 \AA)

Five 120-mm long samples for each filler material have been produced with percentages of the primary substance ranging from 10% to 50% phr by weight.

The measurement system was initially tested using a sample bar made of unloaded polyurethane. The results are well in agreement with the values found in the scientific literature for cross-linked polyurethane rubber in the specified frequency range. Fig. 4.4 and 4.5 show a comparison with the experimental curves reported by Capps (1993) for unloaded polyurethane (type PR1590) of the same hardness and chemical composition.

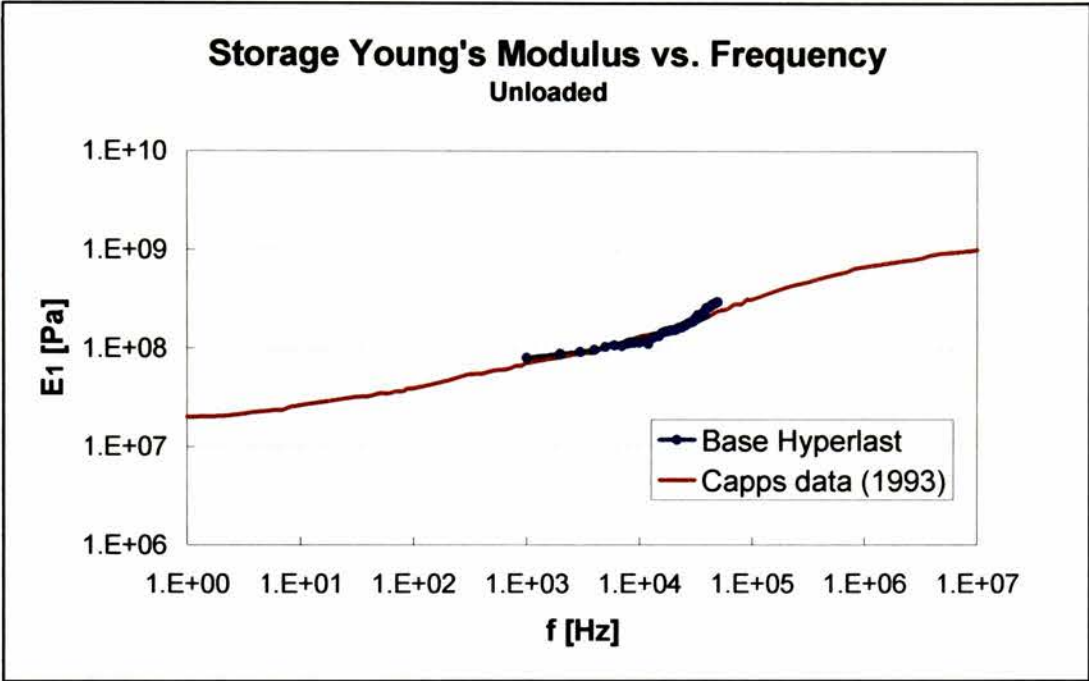


Figure 4.4: Plot of storage Young's modulus vs. frequency for unloaded polyurethane rubber reduced to 25°C

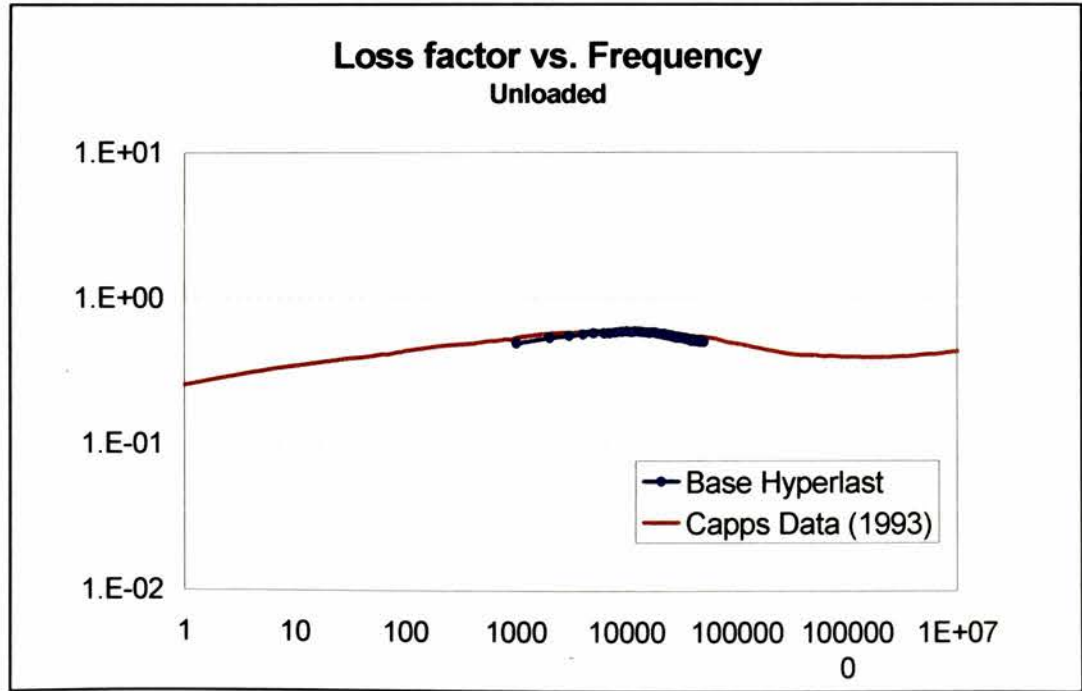


Figure 4.5: Plot of Young's modulus loss factor vs. frequency for unloaded polyurethane rubber reduced to 25°C

The storage Young's modulus E_1 experiences an increase by about one order of magnitude in the prescribed frequency range (1 Hz to 50 kHz). The maximum in the loss factor curve (or loss maximum) occurs at 14 kHz. On the left side, the storage Young's modulus conforms to the Rouse slope of $\frac{1}{2}$ (on a doubly logarithmic plot (Ferry 1980)), whereas on the right side it flattens towards the glassy plateau.

The added fillers can be split into two categories: chemically inert and chemically reactive fillers. The glass microspheres don't interact strongly with the polymer and their principal effect in the transition zone arises from the presence of rigid and immobile masses within the polymer matrix.

On the contrary, the carbon powder and metal oxides interact with the polymer chains and chemical bonds are formed between polymer molecules and filler particles.

Storage Young's modulus and loss factor for polyurethane rubber loaded with different proportions of glass microspheres are shown in figs. 4.6 and 4.7. As observed for example by Maazouz *et al.* (1993) and Landel (1958; 1961), the glass particles are large and heavy enough so that the average distance between any two microspheres is large compared to the root-mean-square separation of the polymer molecules.

The curves fall close together at low filler concentrations, especially in the higher frequency range, and move farther apart for increasing proportions.

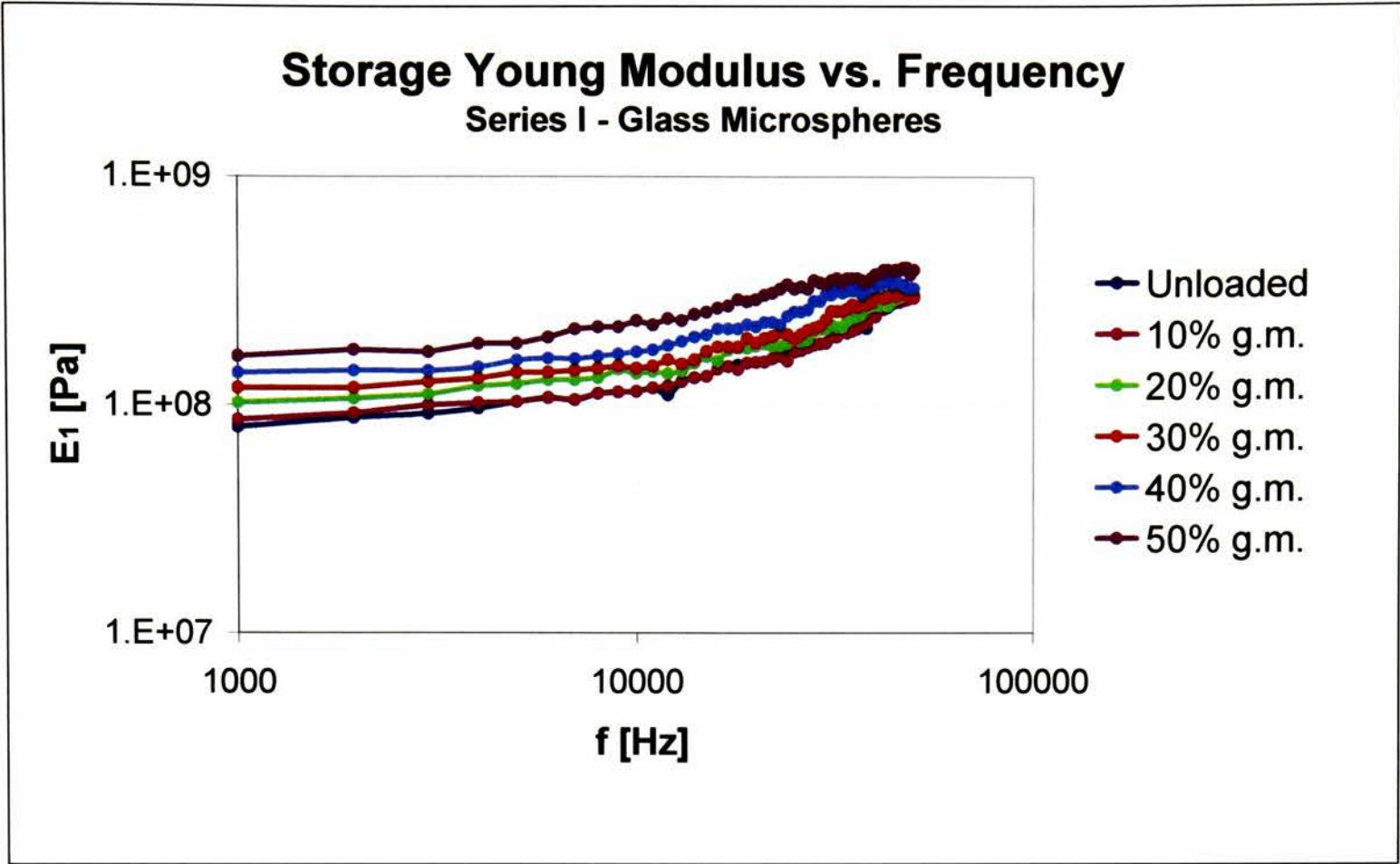


Figure 4.6: Plot of storage Young's modulus vs. frequency for loaded polyurethane rubber. Series I: glass microspheres (logarithmic scale)

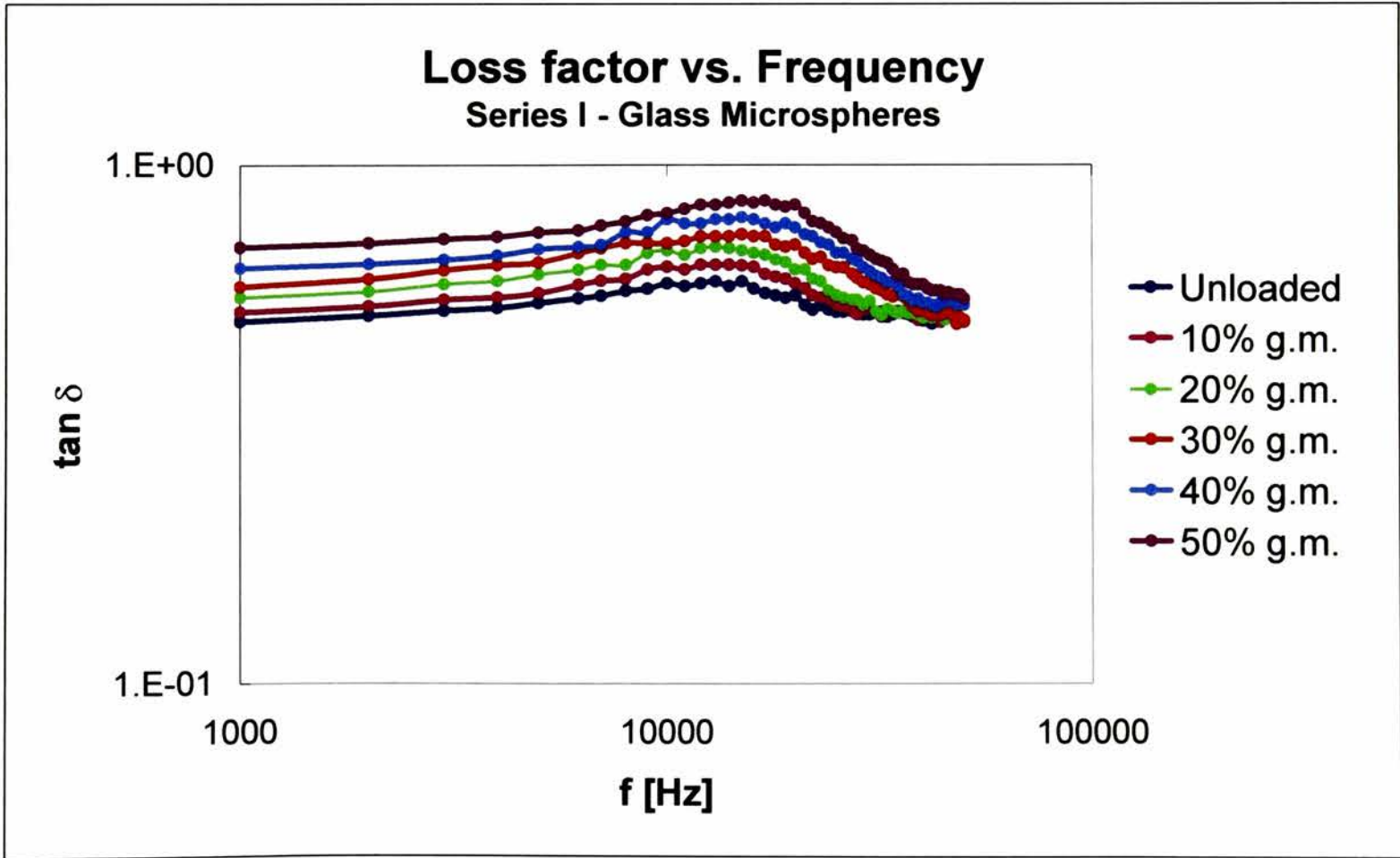


Figure 4.7: Plot of Young's modulus loss factor vs. frequency for loaded polyurethane rubber. Series I: glass microspheres (logarithmic scale)

A slight shift towards higher frequencies can be seen in the loss maxima as the filler volume fraction increases. This is a known effect, which is due to an increase in the loss maxima transition temperature and disappears if the curves are plotted using the reduced variables method (Ferry 1980). In addition, the curvature around the point of loss maximum reduces, because of the increasing sharpness of the transition zone.

When the rubber is filled with metal oxides, the behaviour is somewhat different. As already observed, the filler particles form chemical bonds with the polymer molecules. The average distance between particles is of the order of 100 Å, which is the same order of magnitude of the distance between cross-links. Segments of polymer chains form bridges between filler particles and act as additional multiple cross-links, which add to the increased rigidity of the matrix.

Both moduli and especially the loss modulus are substantially increased by the addition of the fillers. The effect increases with the increasing density of carbon powder or metal oxide. Fig. 4.8 to 4.13 show storage Young's modulus and loss factor for series II (carbon black), III (lead oxide) and IV (tungsten oxide) for different proportions of the filler substances.

While the general behaviour is the same for all three series, it is apparent that the higher the molecular weight of the filler, the higher the values of the storage modulus and loss factor. The curvature around the loss maxima isn't substantially changed, but the value of the maximum experiences a strong increase.

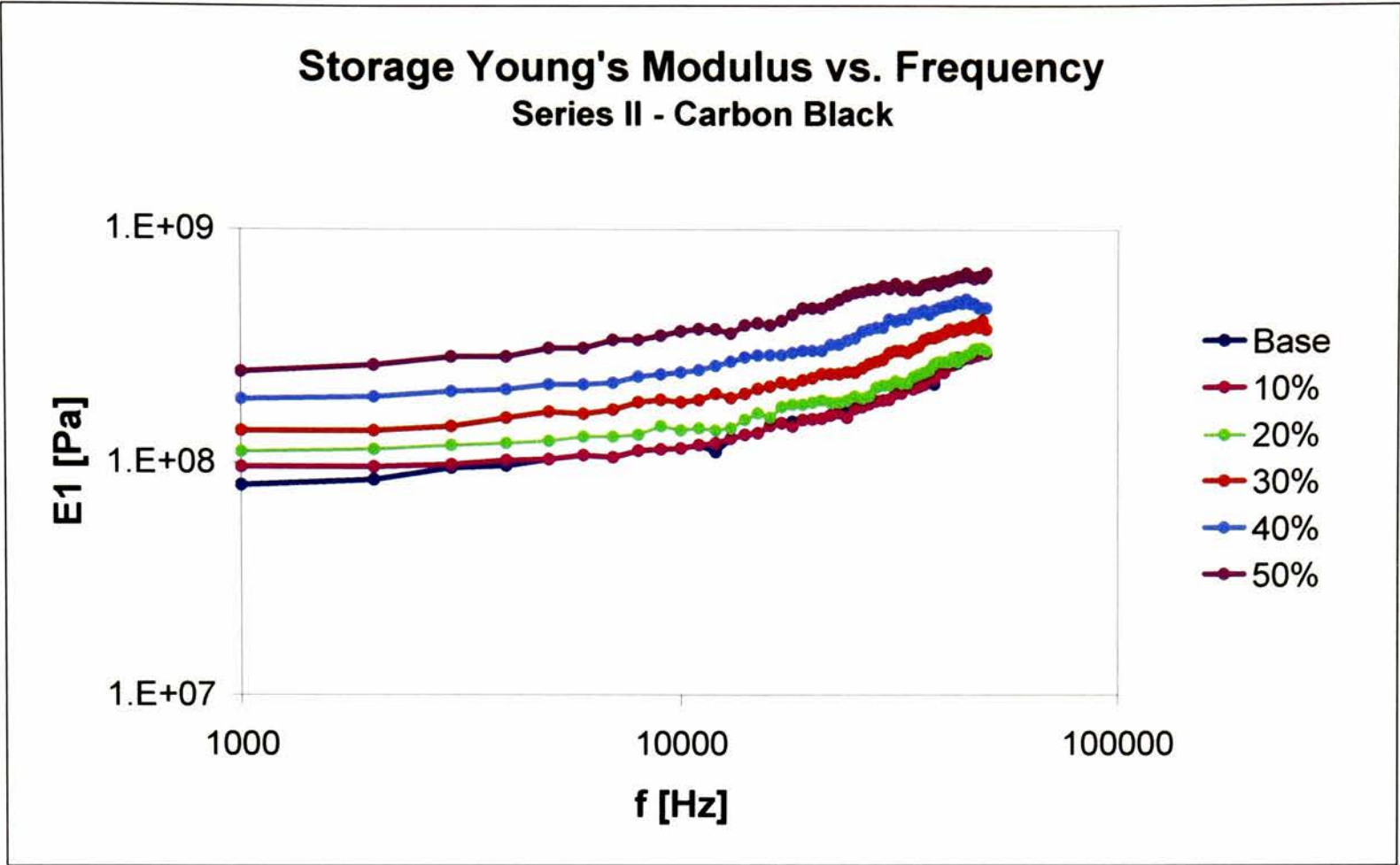


Figure 4.8: Plot of storage Young's modulus vs. frequency for loaded polyurethane rubber. Series II: carbon black (logarithmic scale)

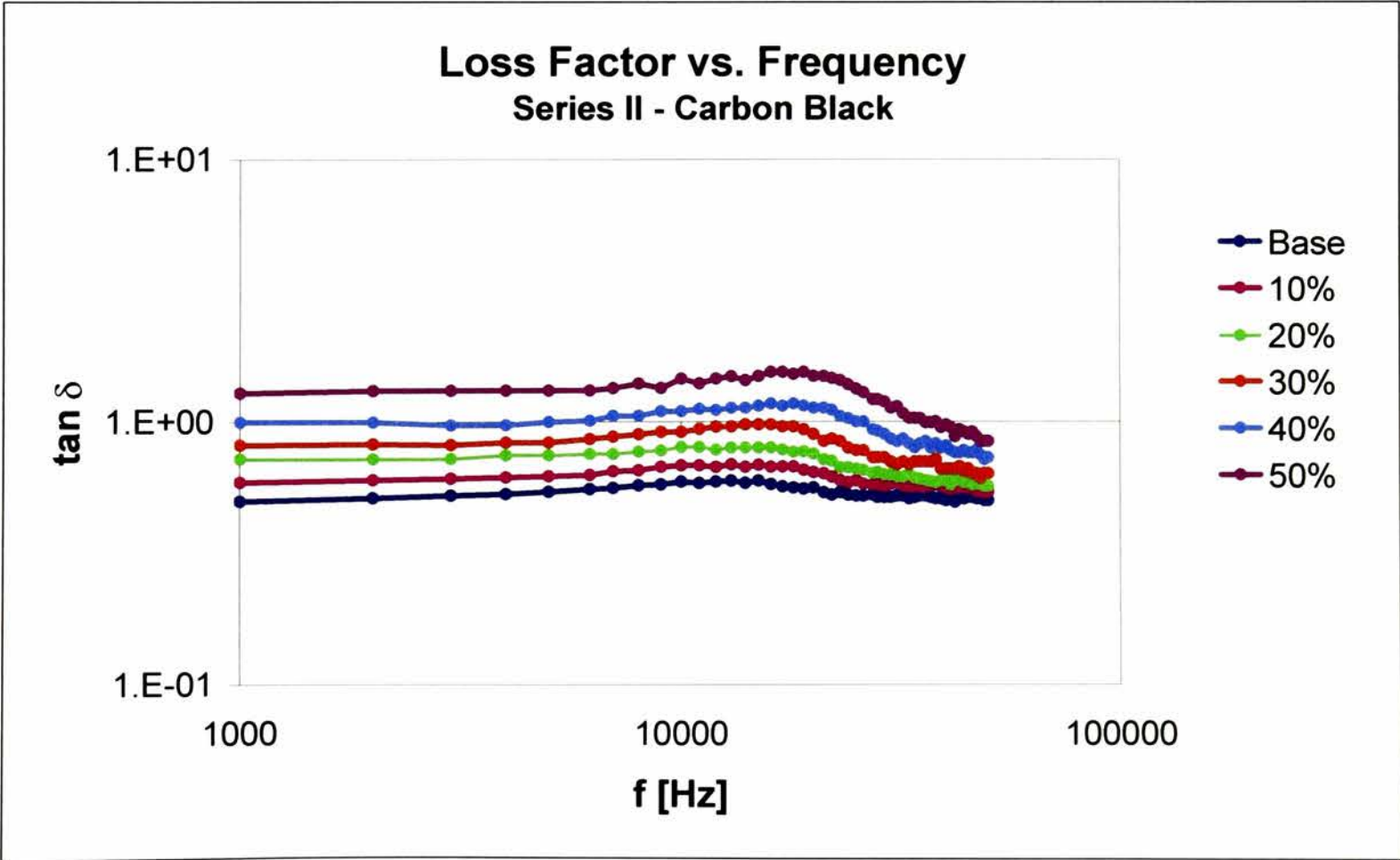


Figure 4.9: Plot of Young's modulus loss factor vs. frequency for loaded polyurethane rubber. Series II: carbon black (logarithmic scale)

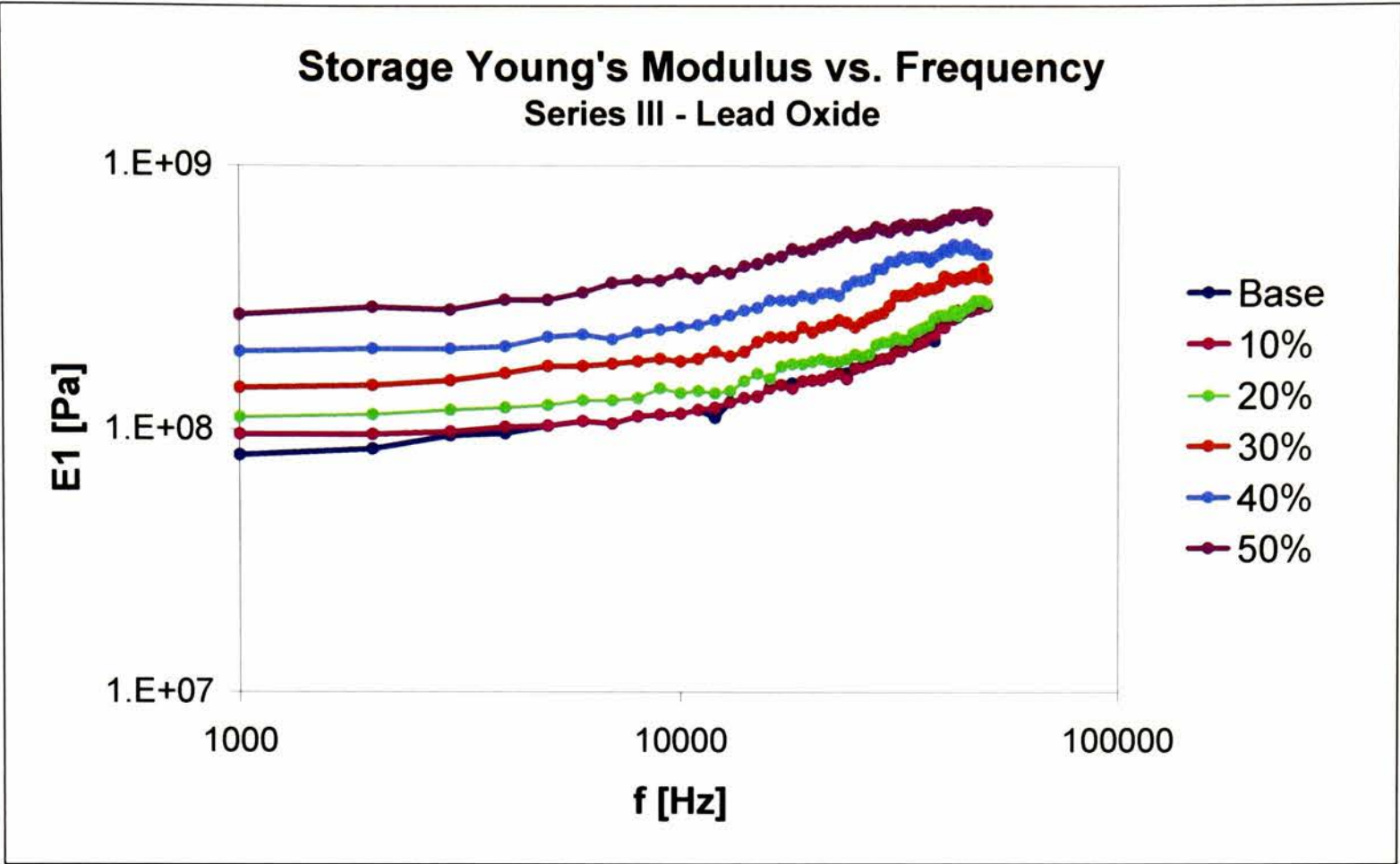


Figure 4.10: Plot of storage Young’s modulus vs. frequency for loaded polyurethane rubber. Series III: lead oxide (logarithmic scale)

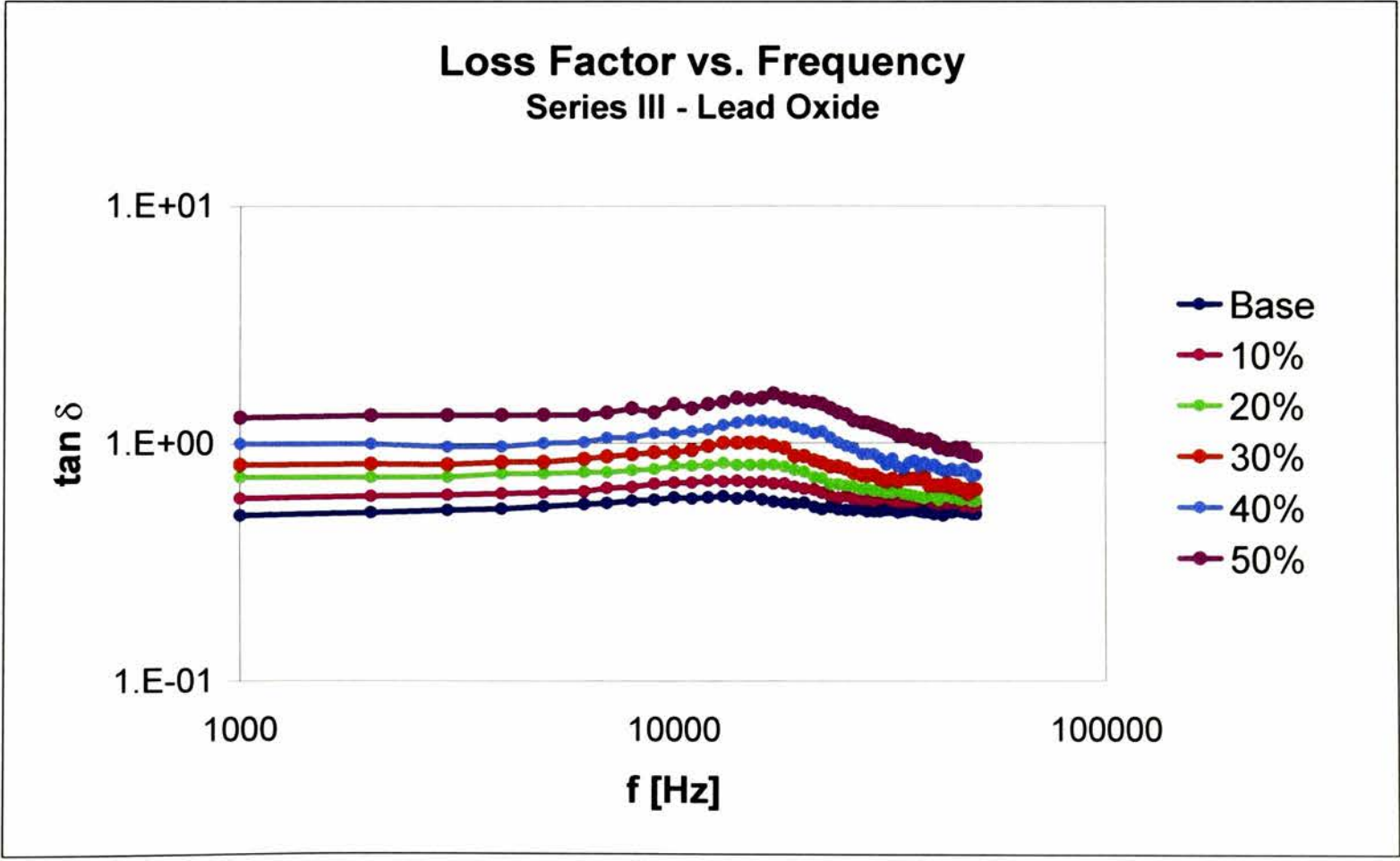


Figure 4.11: Plot of Young's modulus loss factor vs. frequency for loaded polyurethane rubber. Series III: lead oxide (logarithmic scale)

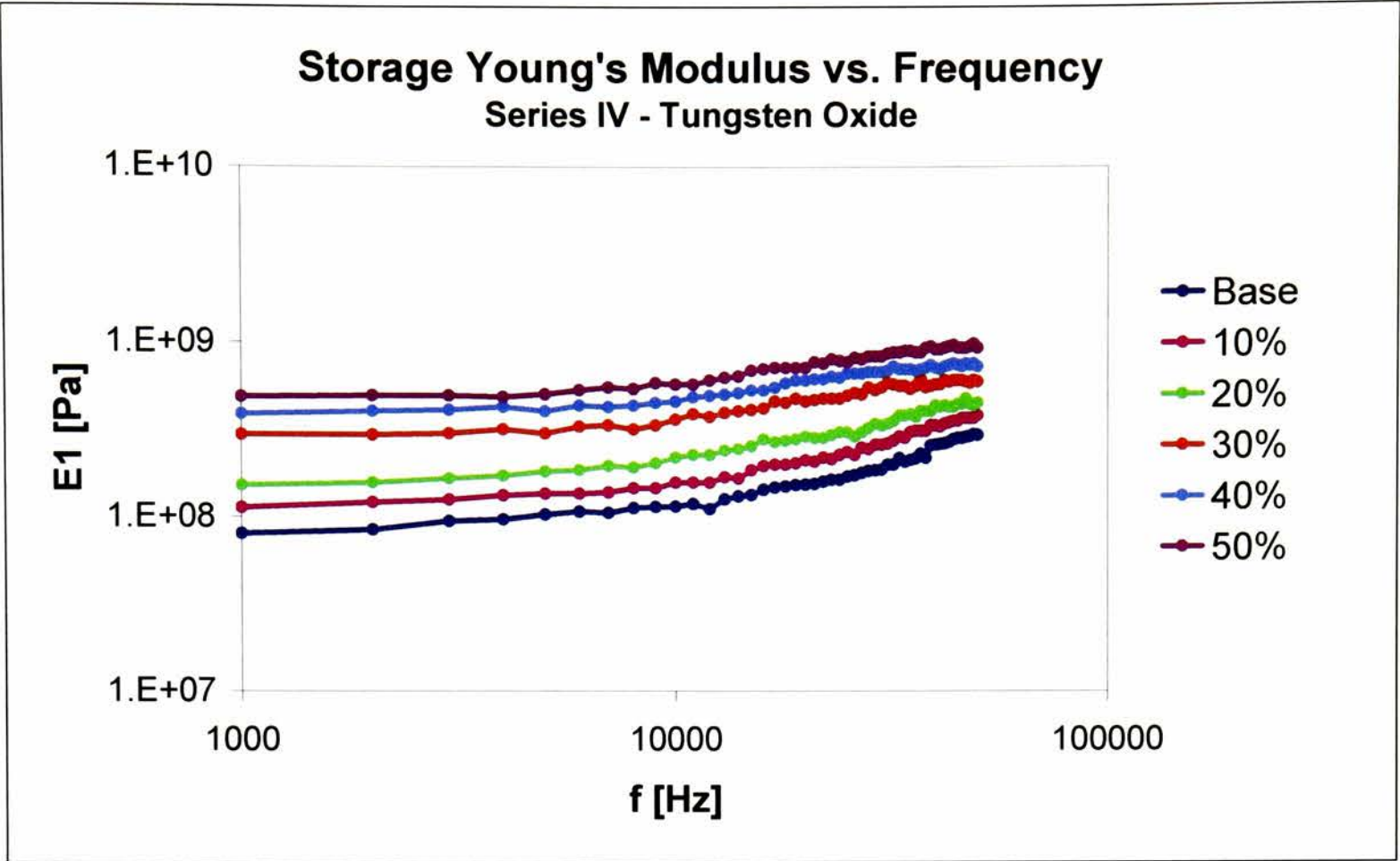


Figure 4.12: Plot of storage Young's modulus vs. frequency for loaded polyurethane rubber. Series IV: tungsten oxide (logarithmic scale)

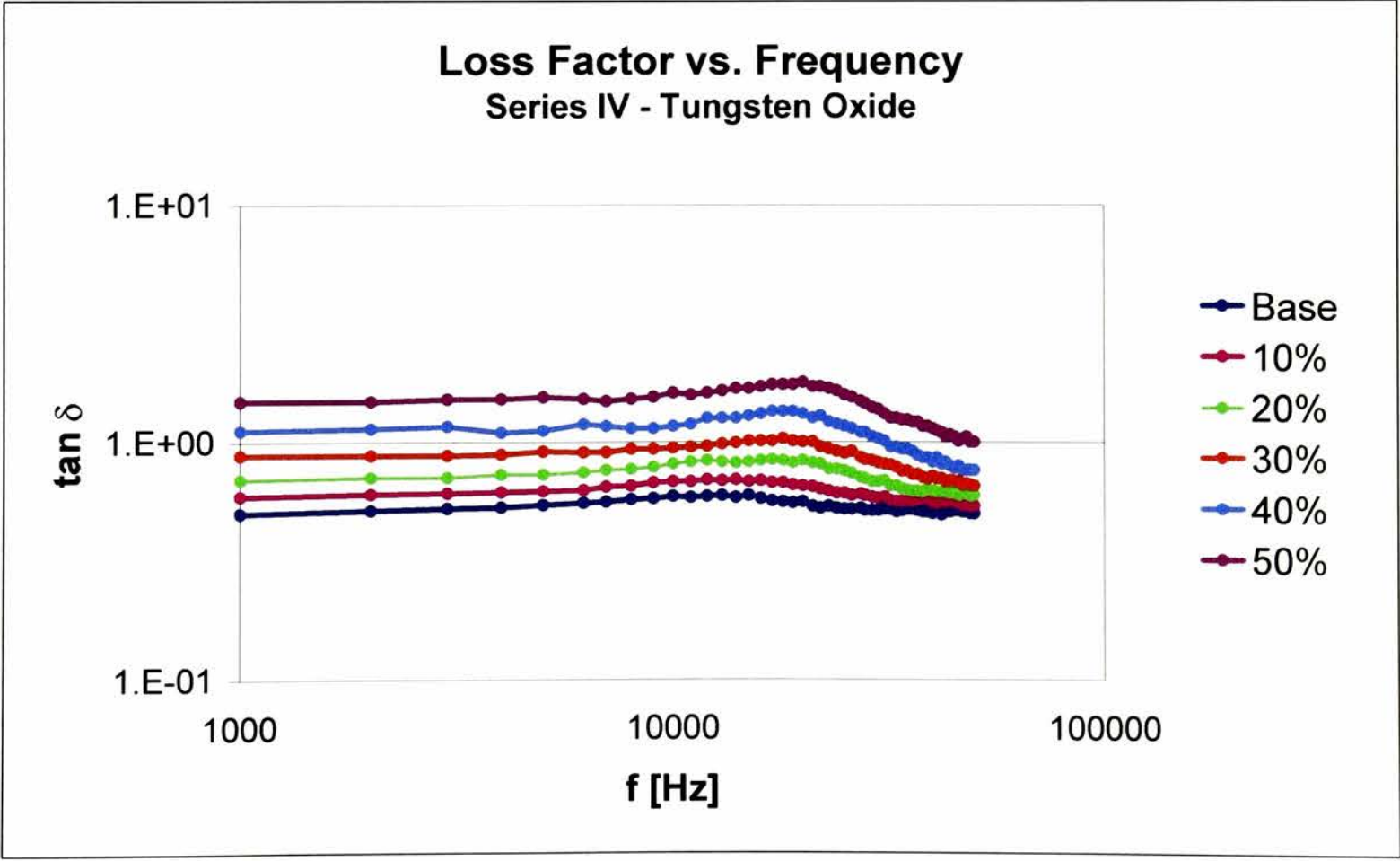


Figure 4.13: Plot of Young's modulus loss factor vs. frequency for loaded polyurethane rubber. Series IV: tungsten oxide (logarithmic scale)

Fig. 4.14 shows the variation of the loss tangent maxima for increasing proportions of the four filler substances. The increase trend in the studied range at the plot scale is close to linear for the inert glass microspheres and more decidedly non-linear for the three chemically active fillers. It can be seen that the energy dissipating effects due to chemical bonds and added rigidity increase not only with filler concentration, but also with molecular weight.

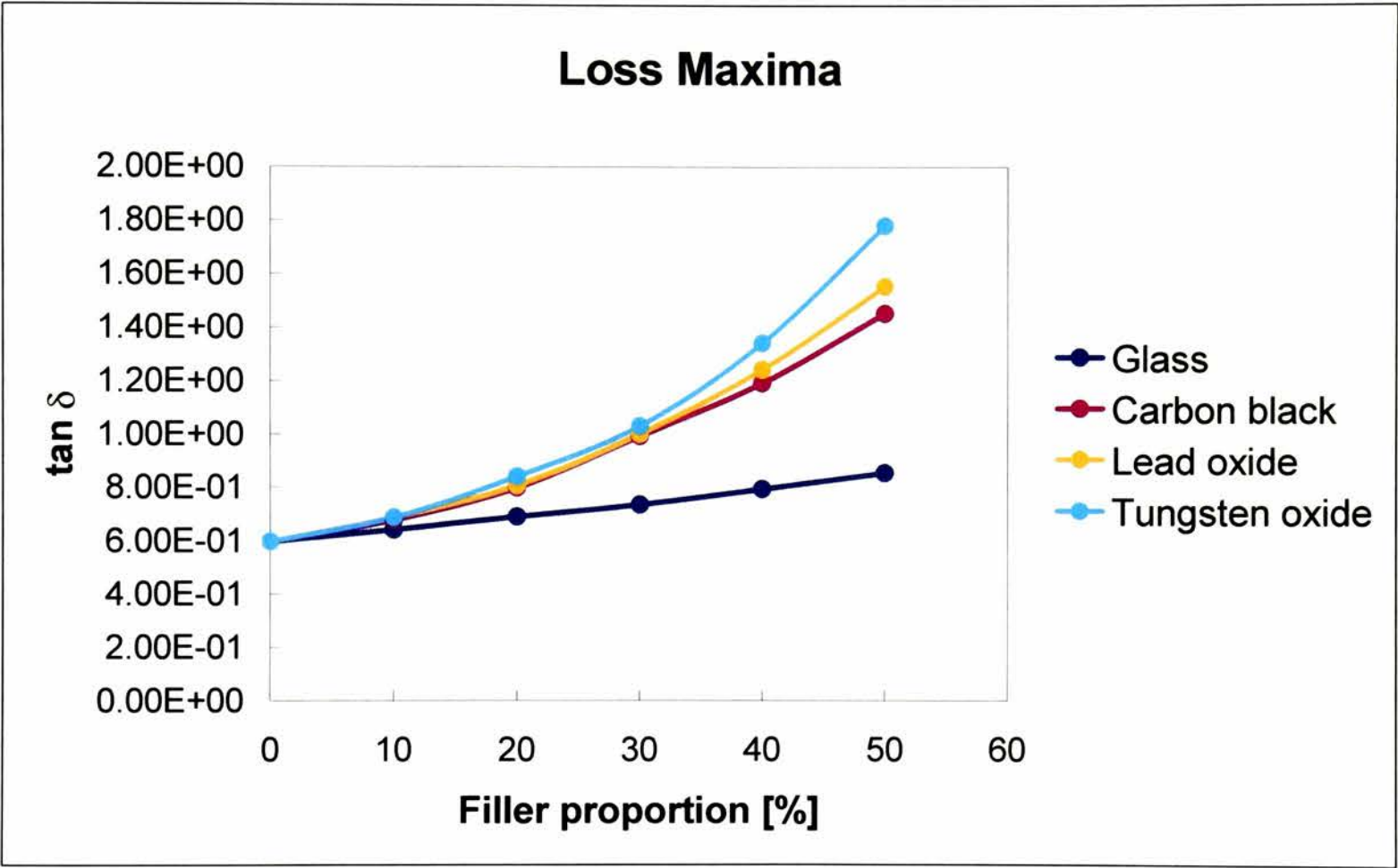


Figure 4.14: Variation of loss tangent maxima with filler proportion for loaded polyurethane

4.5. Butyl Rubber Characterisation

4.5.1. Measurements of Acoustic Properties of Limited Size Panels with Parametric Sources

One limitation of the ultrasonic immersion method (cf. Appendix B) is that high frequency sources must be used to limit the beam width of the source and avoid edge

diffraction effects from limited size panels. In addition, a large number of transducers must be employed if useful frequency range has to be covered. A method of overcoming both these limitations is the use of a parametric array.

As proposed firstly by Westervelt (1963), two high frequency primary sound waves can be used to produce a low frequency secondary sound wave as an effect of non-linearity in the propagation. The low frequency secondary source is the difference between the two main primaries and its -3dB beam width is of the same order of magnitude of the -3dB beam width of the high frequency primary sources (Smith 1992). In addition, by varying the two primary sources inside the range of useful bandwidth of the transducer, a large frequency bandwidth can be produced as a difference without the need of using a complete set of different transducers (Humphrey 1992).

The two primary frequencies can be mixed either electronically in the transmitting apparatus before the transducer or acoustically in the water using two different transducers. The pressure source level of the secondary source increases as the total primary power increases and as the square of the difference frequency itself increases. In addition, it increases with a decreasing primary frequency (Smith 1992). Consequently, the transducer used as primary source must have resonance frequency around 0.8 to 3 MHz and a fairly low Q factor to have a useful bandwidth, usually of the order of 6. It must be capable to deliver sufficient power in the water, which typically means efficiency of more than 40% with peak output electrical power of the order of 200 W (Humphrey 1992). Efficient set-up of a material testing environment has been discussed in details by Humphrey (1985) and Humphrey and Berkta (1985).

4.5.2. Experimental set-up

The described method has been used to test longitudinal and shear wave propagation and material properties of planar panels of butyl rubber. A suitable transducer has been built as described in Appendix B. The transducer is composed of four quarter-circle PZT4 ceramic crystals. The two opposing crystals are joined in parallel so to have two transducers with resonance frequency of about 1.08 MHz and $Q = 4.2$ after tuning and matching them to the power source. The two transducers can either be connected to two different channels to generate the secondary frequency acoustically or be connected to the same channel with the two primary frequencies electrically mixed. The power source is supplied by a unit capable to deliver a peak output electrical power of 200W. The schematic block diagram is shown in fig. 4.15.

The source level of the secondary signal is high enough to guarantee a good signal in the tested range between 30 to 150 kHz. The relative on-axis signal-to-noise ratio is at least 15 dB at 30 kHz and more than 35 at 150 kHz. The power spectrum output from a Lecroy digital oscilloscope for a secondary frequency $f_2 = 151$ kHz at a distance $d = 1$ m from the transducer is given in fig. 4.16. Fig. 4.17 shows the beam pattern for $f_2 = 97$ kHz and $f_2 = 151$ kHz at the same distance $d = 1$ m.

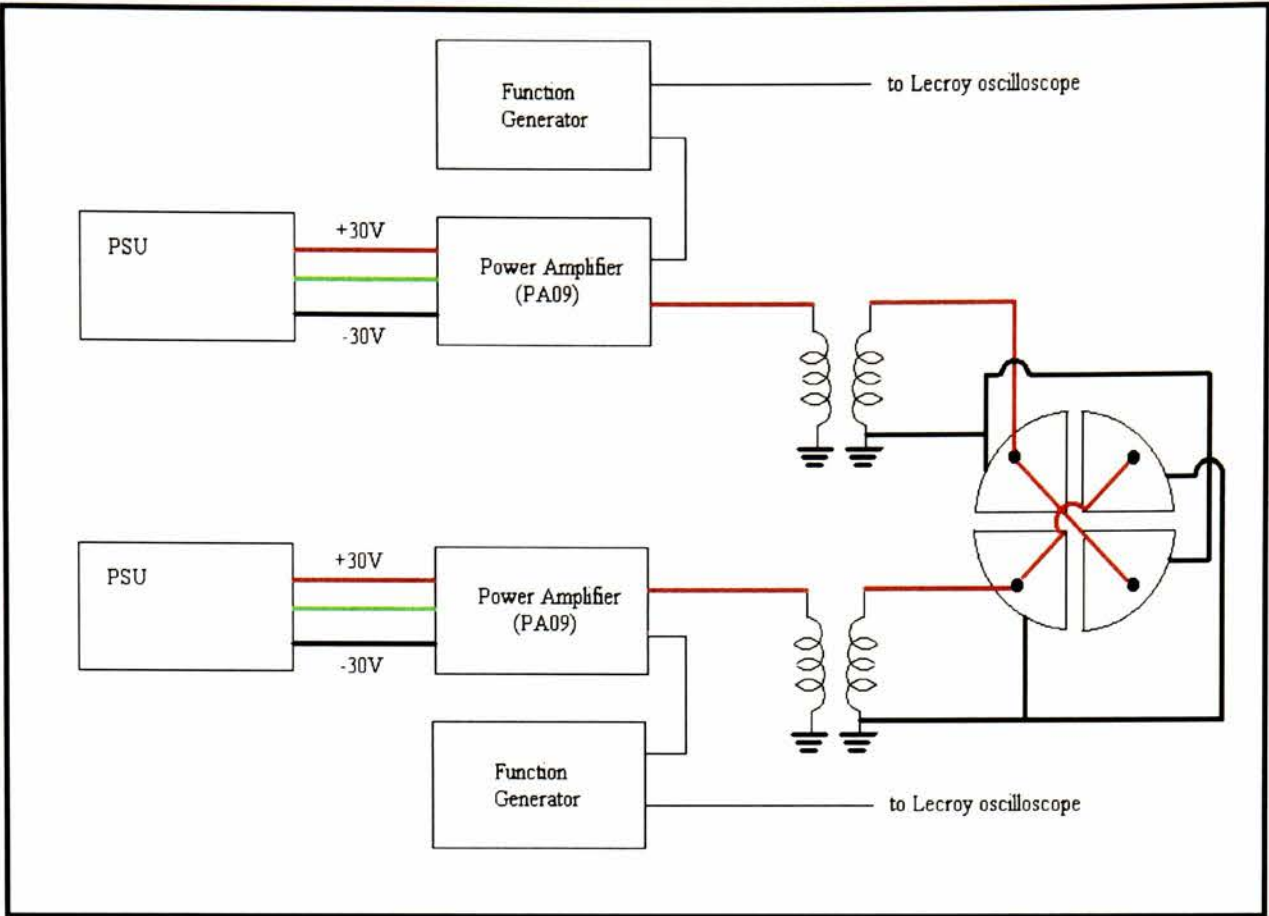


Figure 4.15: Transmitter electronics and transducer set-up

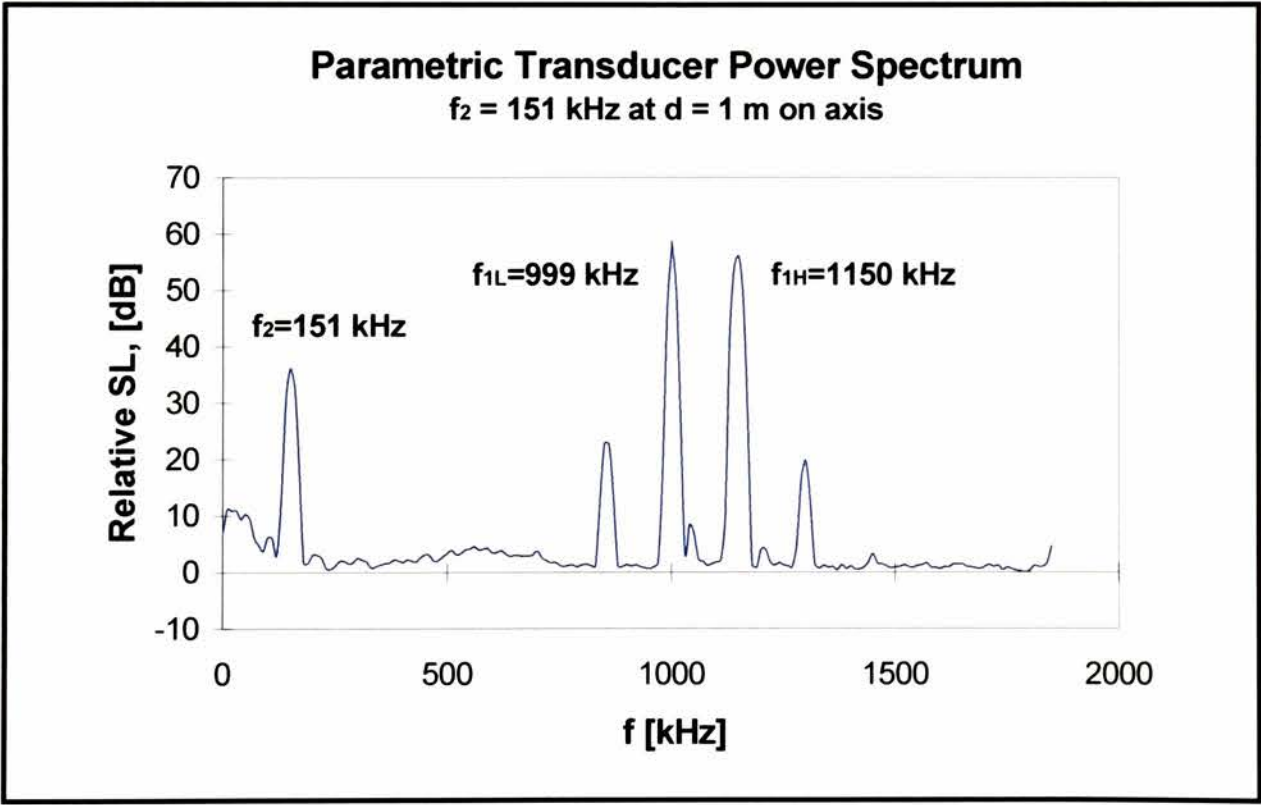


Figure 4.16: Power spectrum of the received signal at a distance $d = 1 \text{ m}$ from the transducer for a secondary frequency $f_2 = 151 \text{ kHz}$ and primary frequencies $f_{1L} = 999 \text{ kHz}$ and $f_{1H} = 1150 \text{ kHz}$

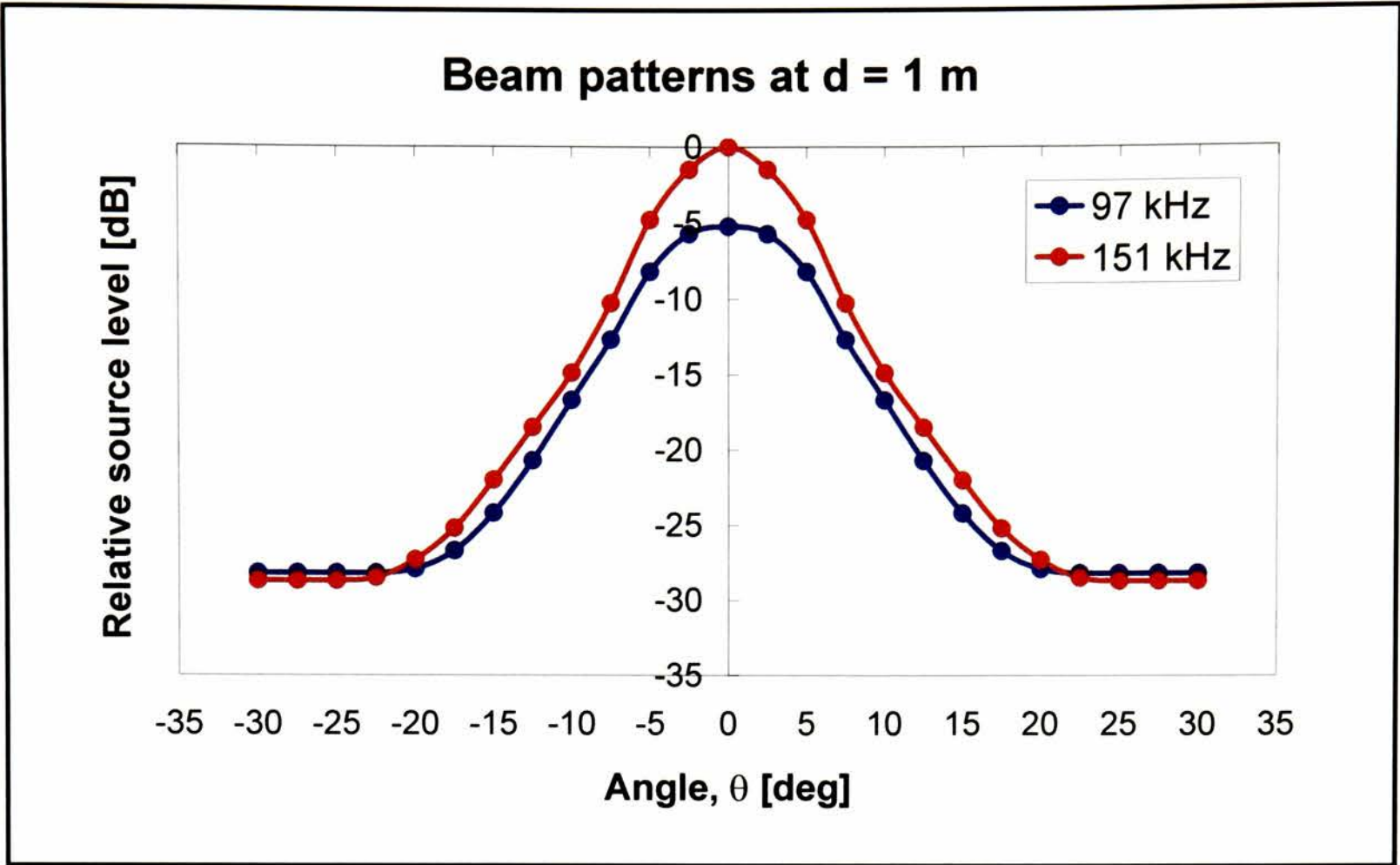


Figure 4.17: Virtual array beam pattern at a distance $d = 1$ m from the transducer for the secondary frequencies $f_2 = 97$ kHz ($f_{1L} = 1030$ kHz and $f_{1H} = 1127$ kHz) and $f_2 = 151$ kHz ($f_{1L} = 999$ kHz and $f_{1H} = 1150$ kHz)

4.5.3. System calibration

The system has been calibrated using a 600×600×5 mm aluminium reflector (photos of the test rig are shown in Chapter 7). Measurements of the reflected and transmitted pulses have been carried out using the Transmit-Time method. A B&K model 8103 hydrophone calibrated over the frequency range of interest was used. The number of cycles per pulse was set to 200 with a 20 ms repetition rate.

The reference, transmitted and reflected signals were processed by means of a Lecroy digital spectrum analyser to find the power frequency spectrum over the range of interest. The reflection and transmission coefficients were then calculated as the ratio of the Fourier spectra:

$$T(\omega) = \frac{\Phi_t(\omega)}{\Phi_{\text{Ref}}(\omega)} \quad R(\omega) = \frac{\Phi_r(\omega)}{\Phi_{\text{Ref}}(\omega)} \quad (4.1)$$

The experimental measurements are in good agreement with the analytical solution given by the transfer matrix method in the frequency range considered, for both normal (figs. 4.18, 4.19) and oblique incidence (figs. 4.20, 4.21). The behaviour of the experimental curve compared to the analytical curve is smoother in correspondence of the critical angle of total internal reflection of the longitudinal wave (see figs. 4.20, 4.21). This can be explained as the effect of the wave generated by the transducer, which cannot produce a proper plane wave (Humphrey 1985; Humphrey and Berkay 1985; Humphrey 1986). Edge diffraction effects have been reduced as much as possible by using large panels and by placing them in an asymmetrical position with respect to line of sight between the source and the receiver.

The full details of the used matrix method are given in Appendix D.

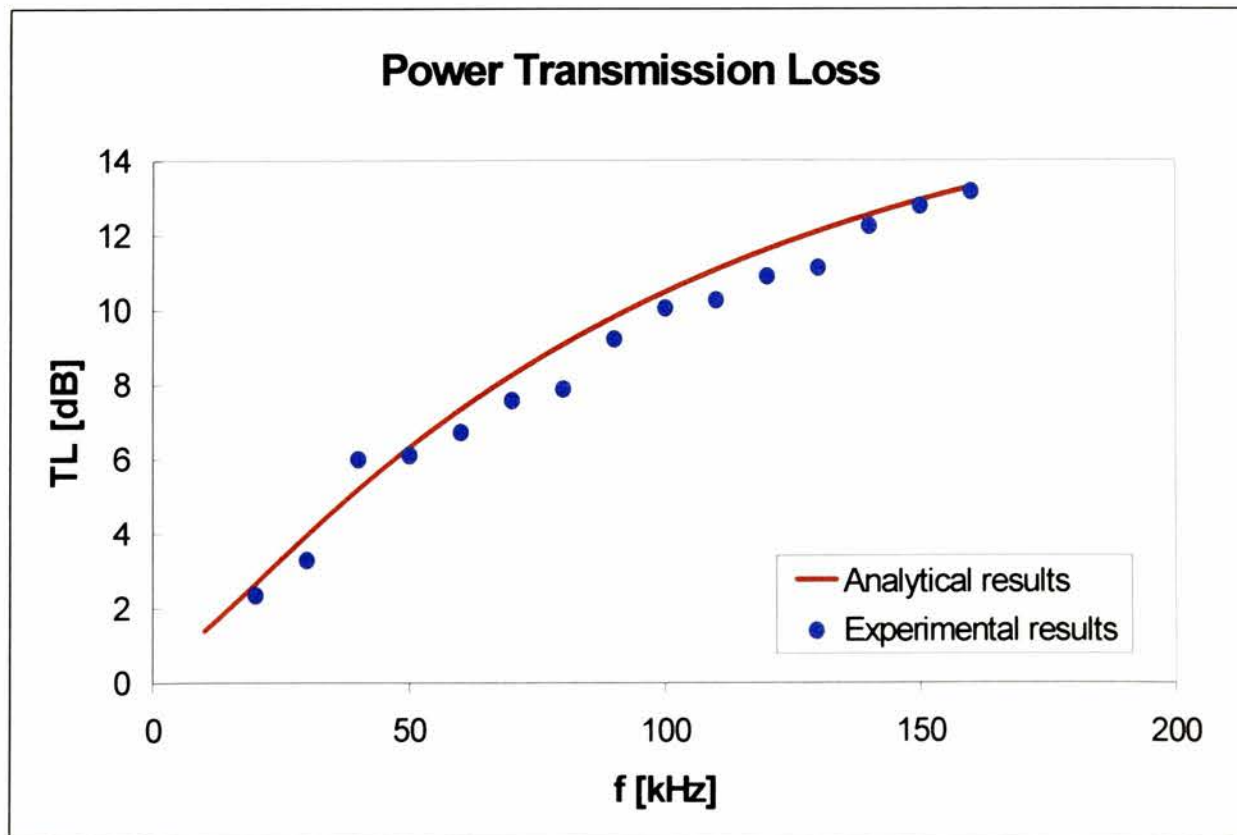


Figure 4.18: Power transmission loss for a 5 mm thick aluminium plate at normal incidence

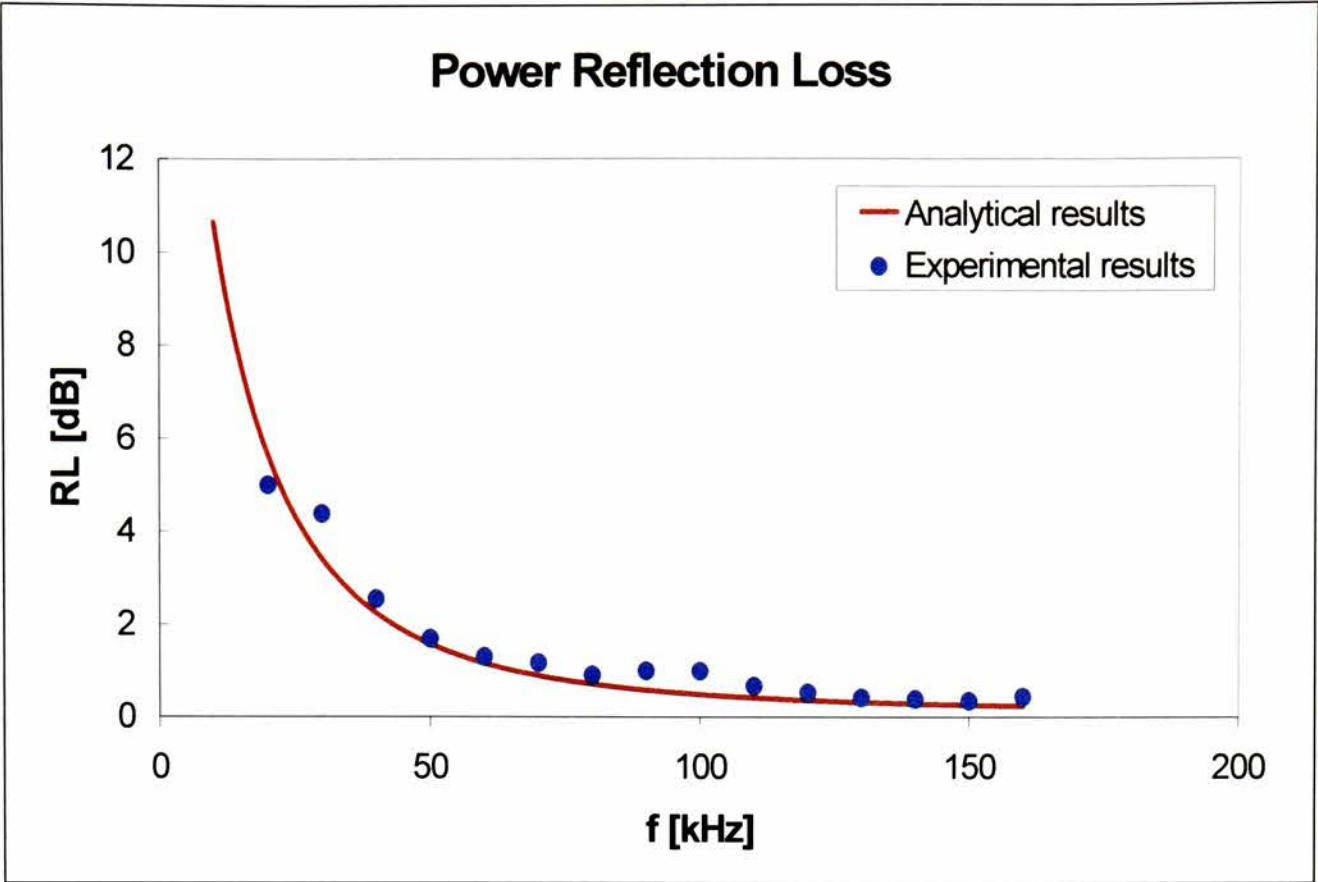


Figure 4.19: Power reflection loss for a 5 mm thick aluminium plate at normal incidence

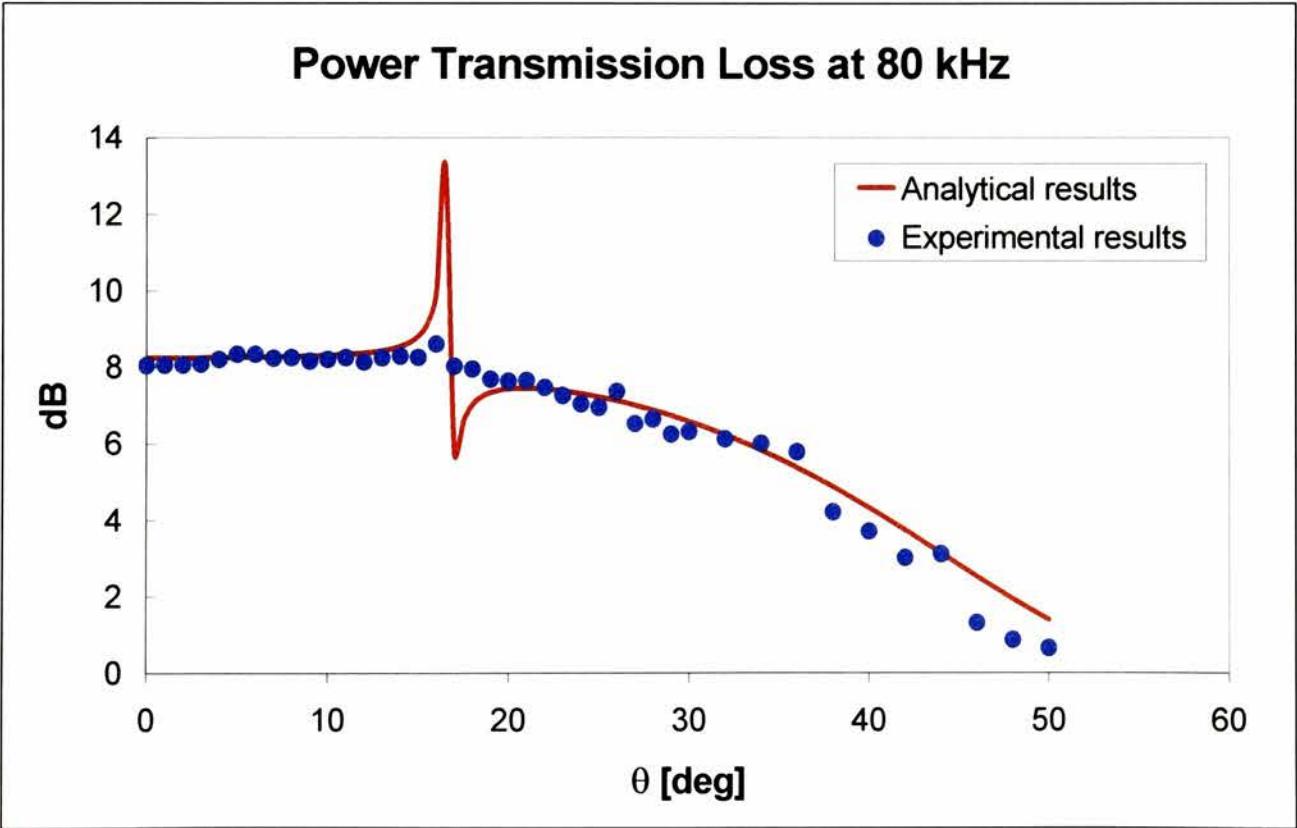


Figure 4.20: Power transmission loss for a 5 mm thick aluminium plate at 80 kHz as a function of incidence

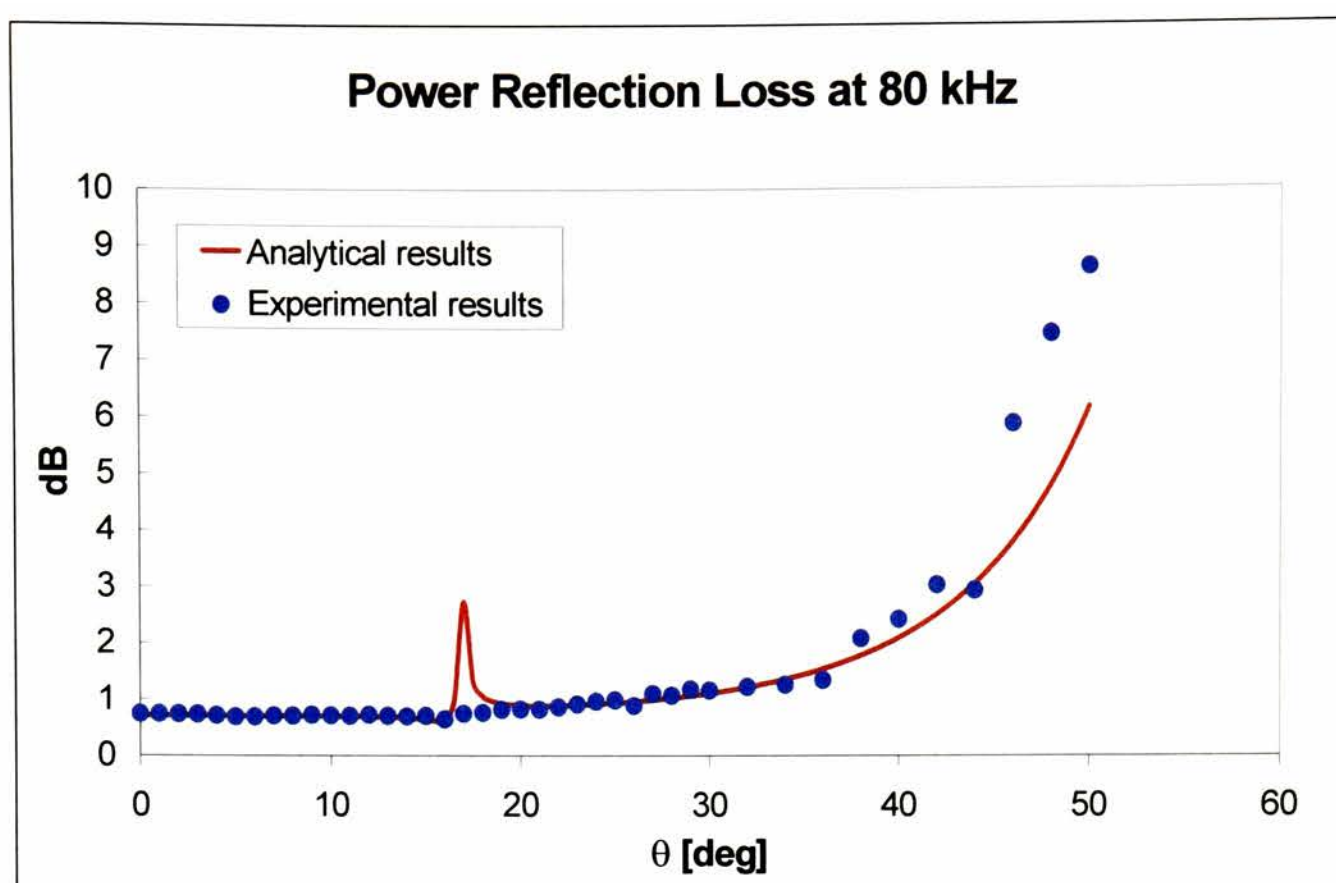


Figure 4.21: Power reflection loss for a 5 mm thick aluminium plate at 80 kHz as a function of incidence

4.5.4. Experimental Measurements

After calibration with the standard reflector, a set of measurements has been carried out on a number of 600x600x10 mm butyl rubber panels having varying density from 1200 to 2200 kgm⁻³ in 200 kgm⁻³ increments. Measurements of the reflected and transmitted signal have been obtained for both normal and oblique incidence in the frequency range 30 kHz to 130 kHz in 2 kHz steps.

The typical experimental curves are shown in figs. 4.22 to 4.30. The plots have been constructed by averaging each measurement up to 1000 times by using a Lecroy digital oscilloscope.

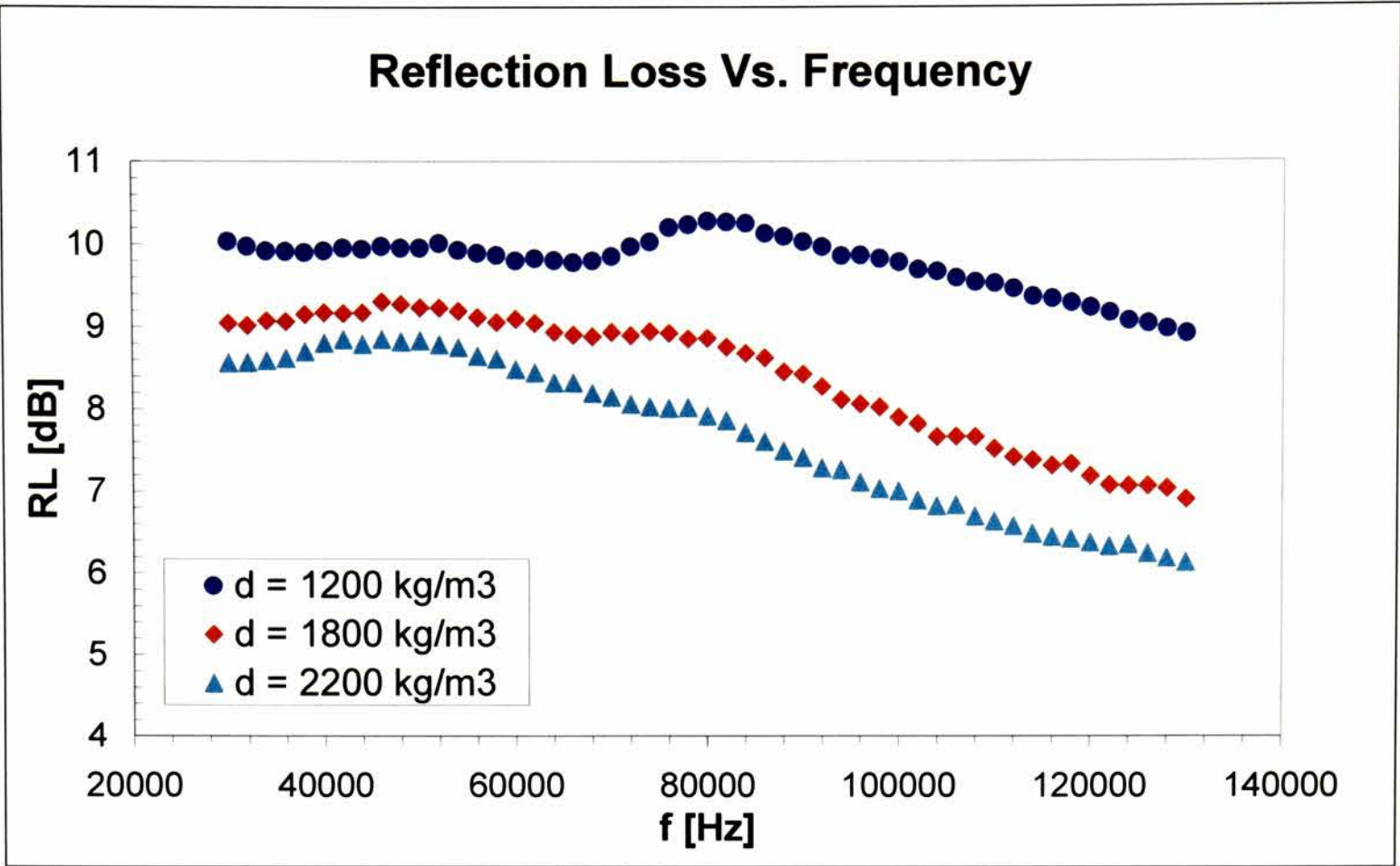


Figure 4.22: Power reflection loss as a function of frequency for a 10 mm thick butyl rubber panel at three different density values

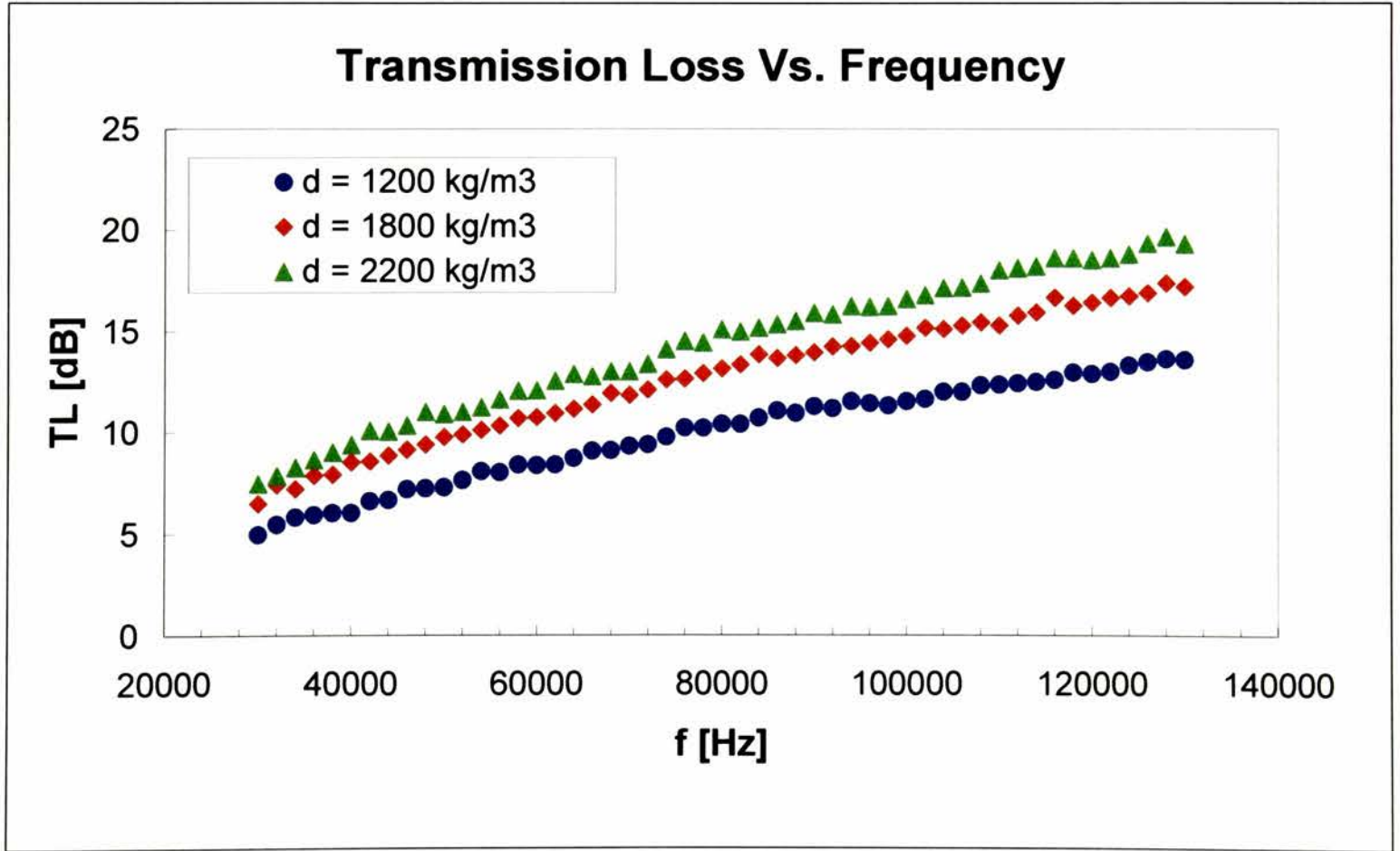


Figure 4.23: Power transmission loss as a function of frequency for a 10 mm thick butyl rubber panel at three different density values

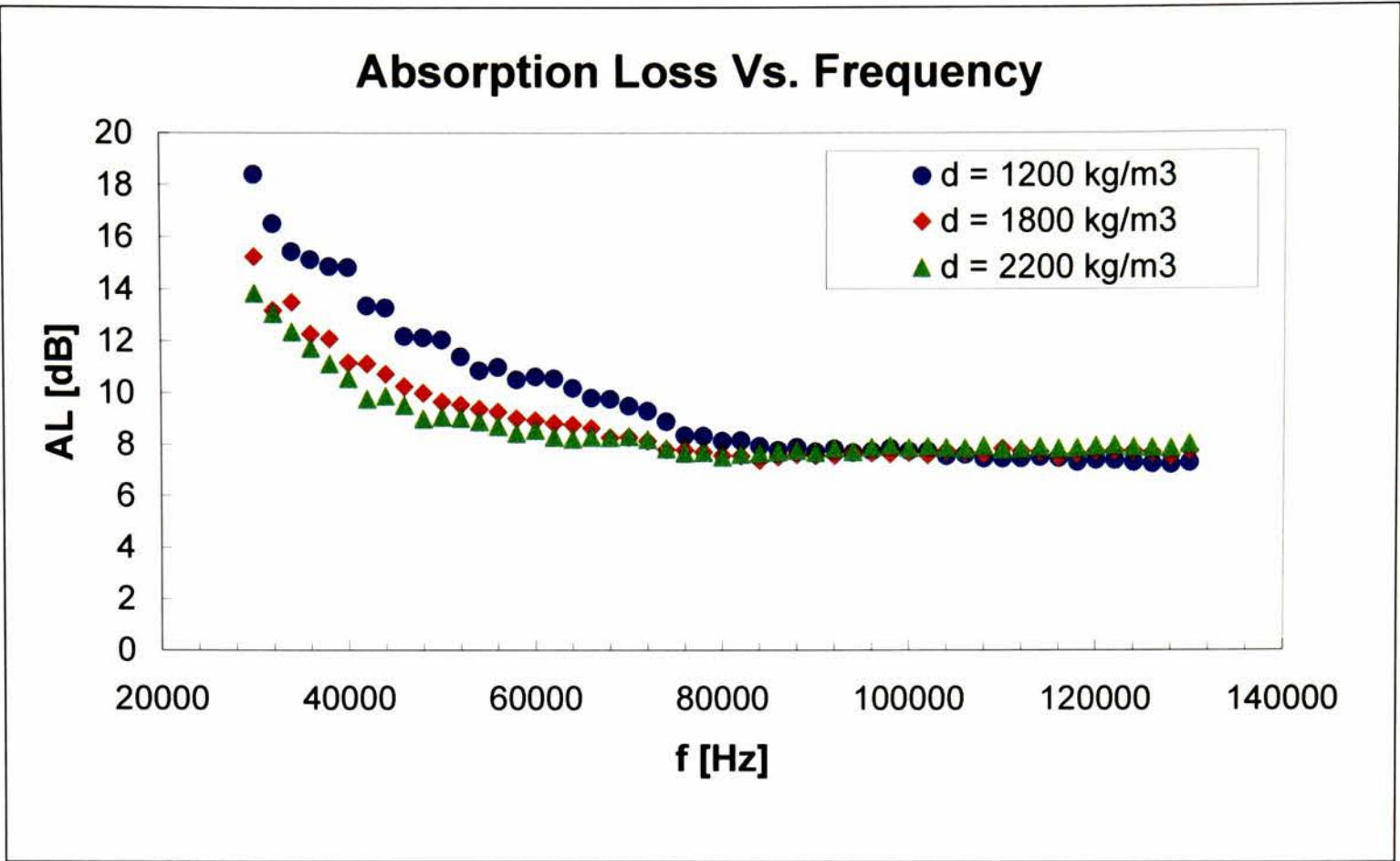


Figure 4.24: Power absorption loss as a function of frequency for a 10 mm thick butyl rubber panel at three different density values

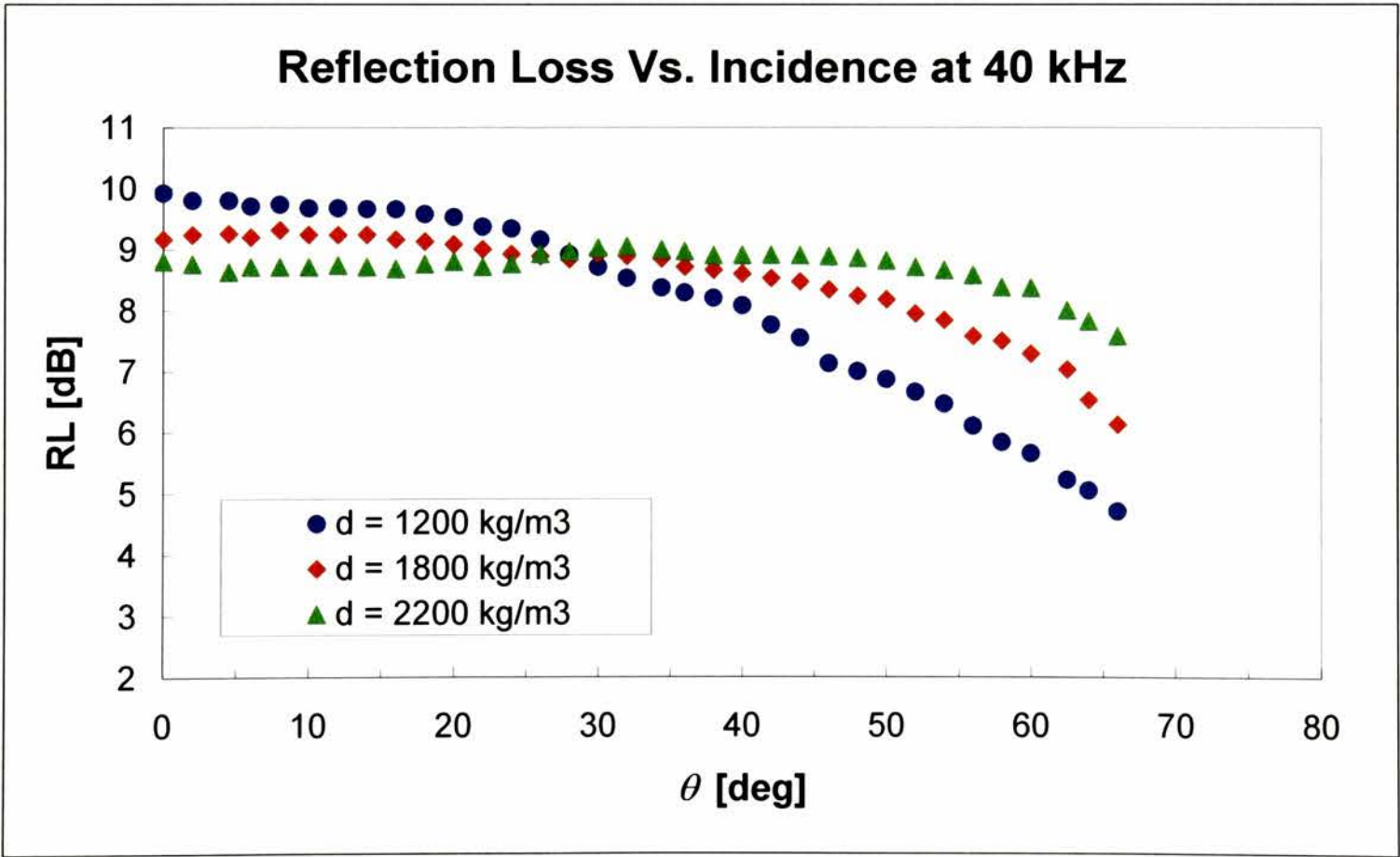


Figure 4.25: Power reflection loss as a function of angle of incidence for a 10 mm thick butyl rubber panel at 40 kHz for three different density values

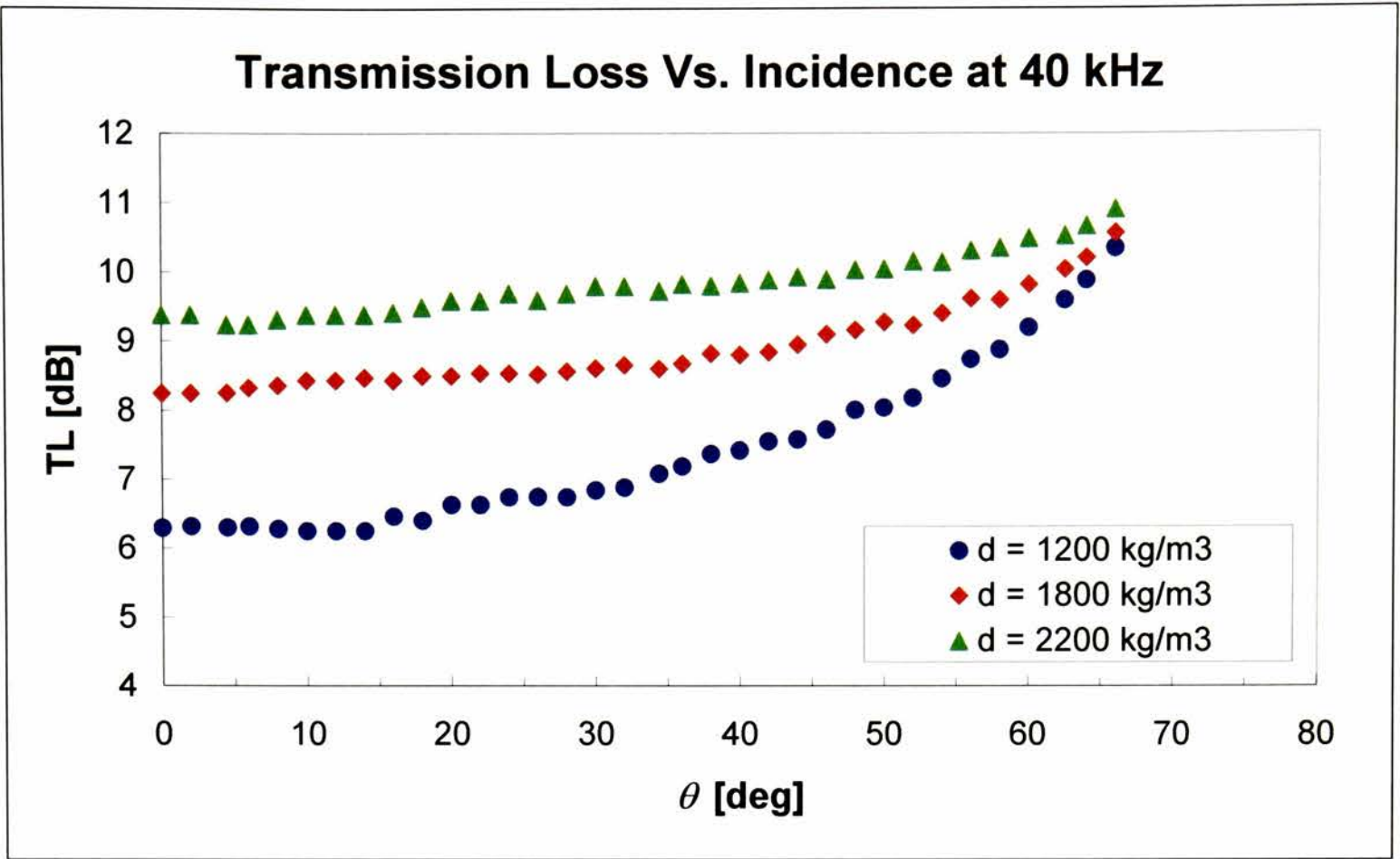


Figure 4.26: Power transmission loss as a function of angle of incidence for a 10 mm thick butyl rubber panel at 40 kHz for three different density values

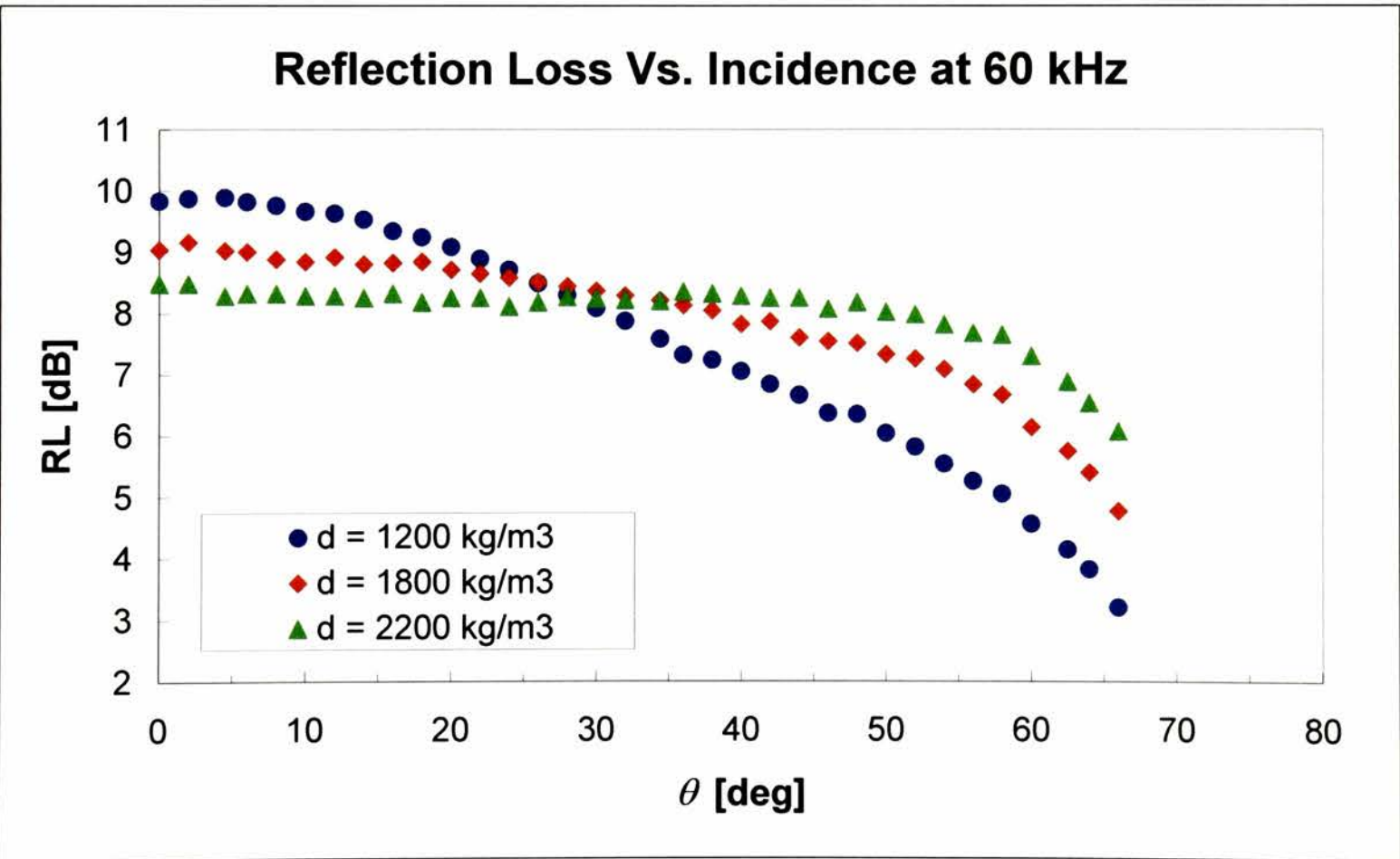


Figure 4.27: Power reflection loss as a function of angle of incidence for a 10 mm thick butyl rubber panel at 60 kHz for three different density values

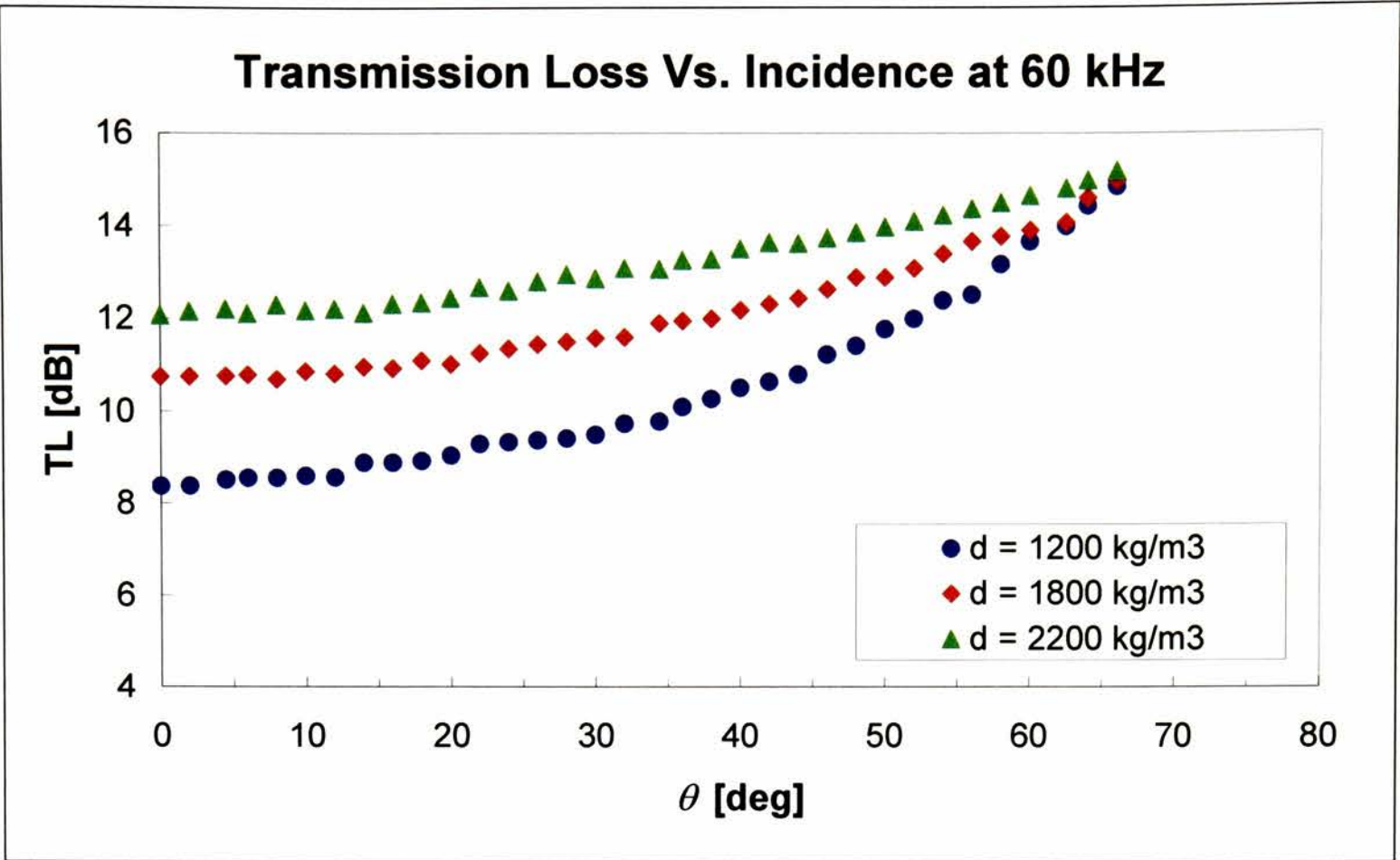


Figure 4.28: Power transmission loss as a function of angle of incidence for a 10 mm thick butyl rubber panel at 60 kHz for three different density values

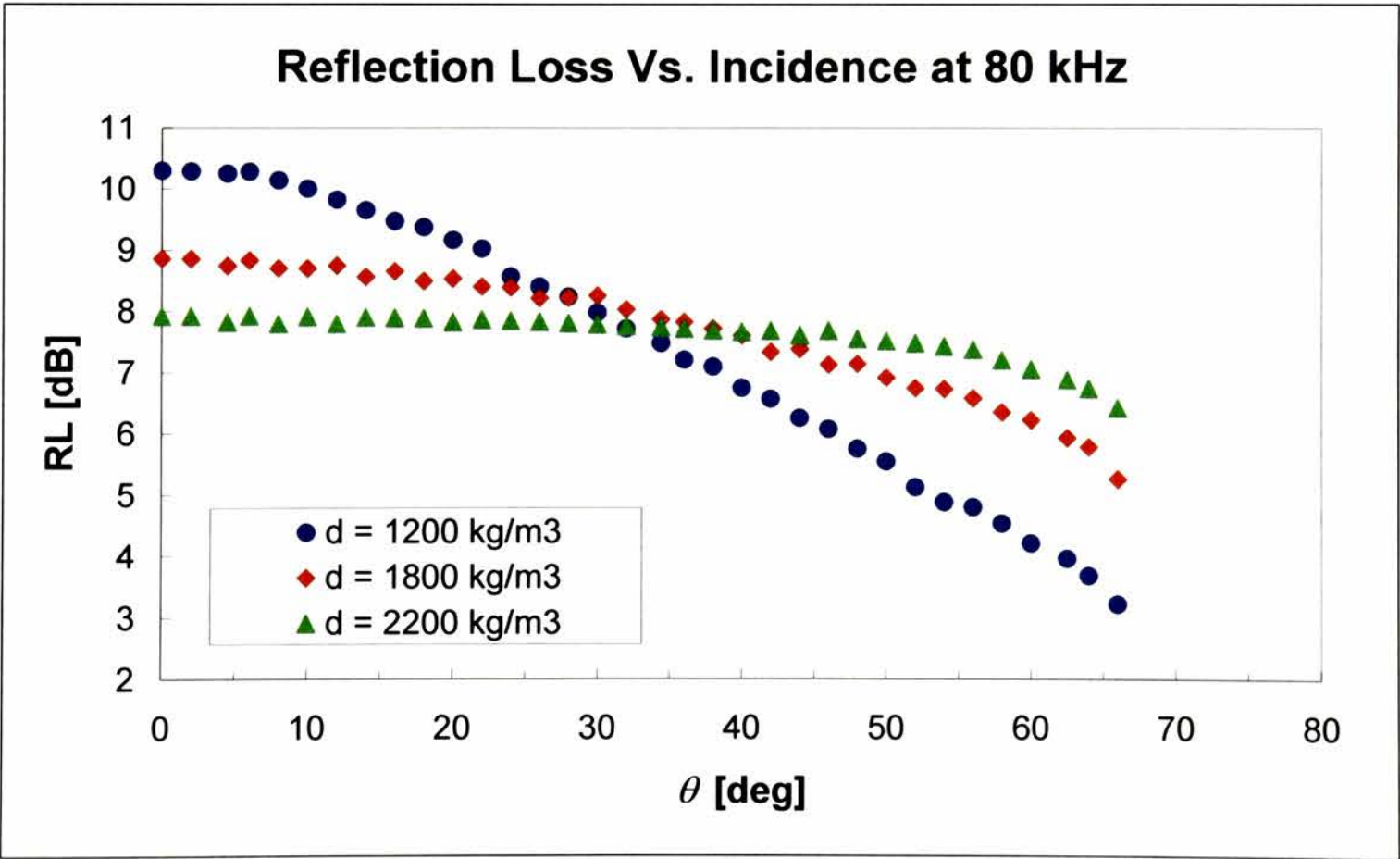


Figure 4.29: Power reflection loss as a function of angle of incidence for a 10 mm thick butyl rubber panel at 80 kHz for three different density values

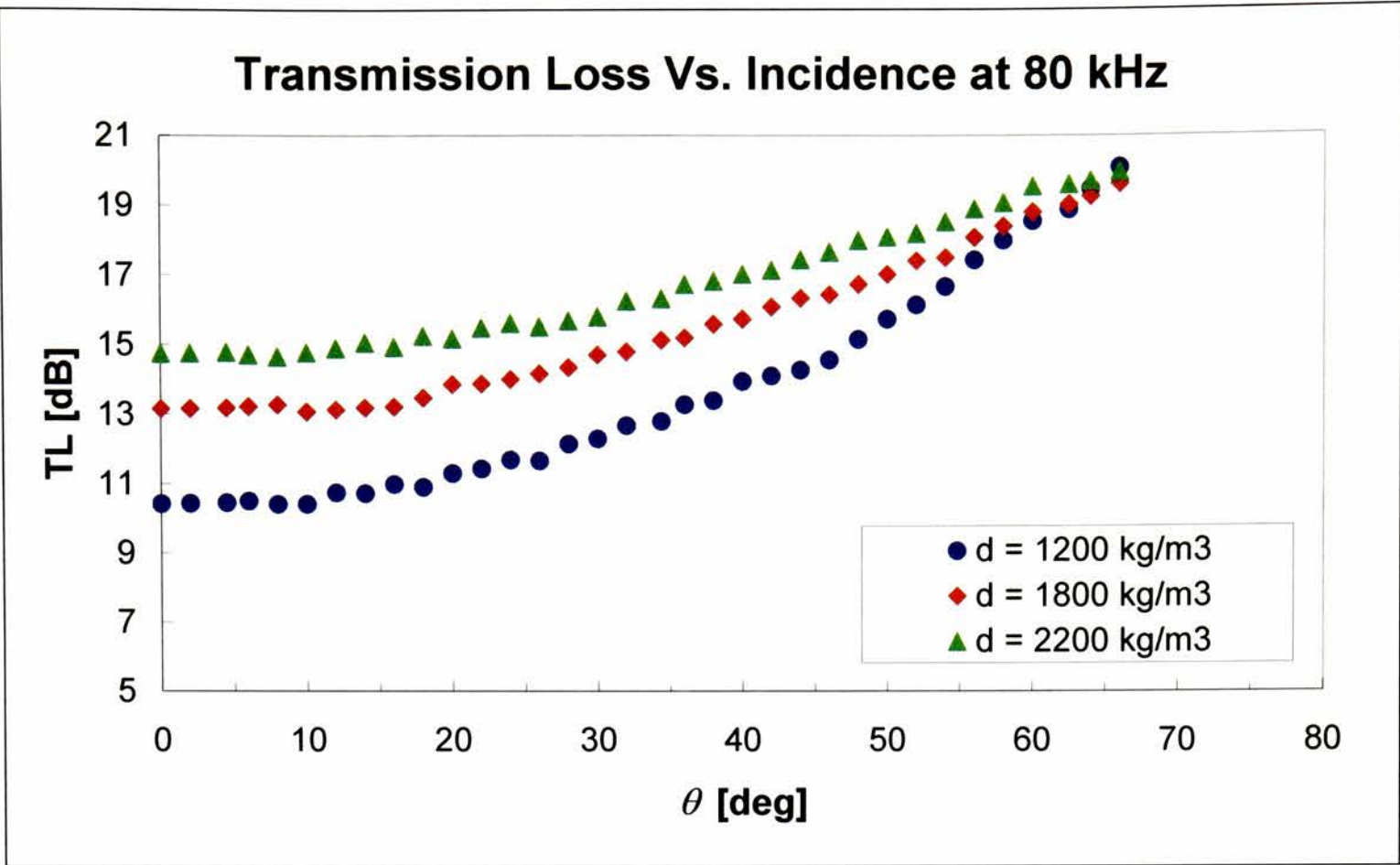


Figure 4.30: Power transmission loss as a function of angle of incidence for a 10 mm thick butyl rubber panel at 80 kHz for three different density values

The reflection and transmission losses and material absorption in terms of power as a function of frequency are plotted in figs. 4.22 to 4.24.

A first but expected conclusion is that reflection losses are higher at lower density and transmission losses are generally lower. The absorption plots in fig. 4.24 show that the increasing density leads also to increasing internal energy losses, because of friction and inertia in the molecular chains. However, these absorption mechanisms fail to work as frequency increases and as the behaviour of the material becomes more ‘rigid’.

It is possible to see from fig. 4.22 that the reflection loss curve has two local minima in the plotted range around 45 kHz and 80 kHz. The minima are more evident at lower density levels. They tend to disappear, as the material becomes more rigid because of the higher content of heavy hard clay. This behaviour, which is typical of viscoelastic materials, is

normally due to mechanical resonance phenomena in the molecular chains, triggered by different levels of energy in the forcing signal.

As the frequency of the signal increases the behaviour of the material moves towards the glassy region and the curves show a more decidedly increasing trend toward higher reflection values.

The transmission loss curves follow a decreasing trend, whose shape doesn't depend on the density.

The reflection and transmission losses as a function of angle of incidence are shown at three different frequency values in figs. 4.25 to 4.30. The chosen frequency sample values are 40 kHz, 60 kHz and 80 kHz, which are in the range of interest for the diffraction analysis to be carried out.

The plots are generally smooth and, as expected, there is no clear sign of the presence of critical angles for longitudinal and shear waves. The density has a clear effect on transmission losses, which are higher at higher values of rubber filler contents. The effect on reflection losses is less straightforward. The lower density material is less reflecting at incidence values up to about 28° to 30° and more reflecting beyond this point at all sample frequencies.

Finally, it can be seen that the reflection and the transmission curves flatten down with increasing density, showing that by increasing filler content the material becomes more locally reacting, that is independent of the angle of incidence.

4.6. Determination of Butyl Rubber Properties by Parametric Optimisation

The method used to reconstruct the physical properties of the loaded butyl rubber is an optimisation method based on the Hamilton Principle. The method was developed by the author of this research during the work for his Master Degree in Aerospace Engineering. It was originally applied to the optimisation of the dynamics of a flexible continuous system subject to an optimisation goal. A complete description of the method is given in the paper annexed in Appendix E (Di Meglio and Finzi 1997).

In the present case, the optimisation goal is that of seeking a suitable set of functional complex parameters. These parameters must be such that they minimise the difference between the measured reflection and transmission losses and the analytical values calculated from the transmission matrix schema given in Appendix D.

We assume the properties of water, the thickness of the panel and the geometry of the experiment to be known with enough precision to be considered noiseless quantities.

The function to be minimised can be derived by the propagation equation expressed in terms of the transmission matrix. Consider the complex-valued equation:

$$V_A = \mathbf{T}V_B \quad (4.2)$$

where A and B are two points in the fluid surrounding the test panel, respectively 1 m in front of and 1 m behind the panel along the line-of-sight between the acoustic source and a reference point on the panel (for example its barycentre). The panel is tilted at an arbitrary angle θ . The total transmission matrix \mathbf{T} is given by a transformation of the solid layer transmission matrix by application of two interface matrices (fluid-panel and panel-fluid) as defined in Appendix D:

$$\mathbf{T} = \mathbf{J}_{f,s} \mathbf{T}_s \mathbf{J}_{s,f} \quad (4.3)$$

where the index f refers to a fluid layer and the index s refers to a solid layer.

The vectors V_A and V_B are expressed in terms of the reflection and transmission coefficients as:

$$\begin{aligned} V_A &= \begin{pmatrix} 1+R_A \\ (1-R_A) \frac{\cos \theta}{Z_c} \end{pmatrix} \\ V_B &= \begin{pmatrix} T_B \\ T_B \frac{\cos \theta}{Z_c} \end{pmatrix} \end{aligned} \quad (4.4)$$

whereas the matrix \mathbf{T} can be expressed as a function of the circular frequency ω , the angle of incidence θ and the complex elastic moduli $G_1^*(\omega)$ and $G_2^*(\omega)$ (the complete form of the matrix elements is given in Appendix D):

$$\mathbf{T} = \mathbf{T}(G_1^*(\omega), G_2^*(\omega), \omega, \theta) \quad (4.5)$$

where the $*$ notation implies the special complex form given by relations (3.84) and (3.85).

Eq. 4.2 can be rewritten in a more compact form by forming the column vector

$$V = \begin{Bmatrix} V_A \\ V_{M2} \\ V_B \end{Bmatrix} \quad (4.6)$$

where M_2 is a point on the output face of the panel. Rearranging the elements of the matrix T to form the augmented matrix T_a , we get

$$T_a V = 0 \quad (4.7)$$

Equation 4.7 cannot be inverted to find the viscoelastic parameters from the knowledge of the reflection and transmission coefficients. In fact, even in the simplest one-dimensional model there are four complex unknowns, the two stress components σ_{13} (the shear stress) and σ_{33} (the longitudinal stress) and the two velocity components v_1 and v_3 . There are therefore eight unknowns, only seven of which are independent because of the secular equation $\det(T) = 0$. The number of known values for each frequency sample in this case is only four, namely the complex reflection and transmission loss parameters expressed as amplitude and phase with respect to the reference value.

We can overcome this problem by applying the method of parametric identification to find a best-fit solution.

If we substitute in eq. 4.7 the experimental values of the reflection and transmission coefficients, we have the approximate residual form:

$$T_a(G_1^*(\omega), G_2^*(\omega), \omega, \theta) V_e(\omega, \theta) = R \quad (4.8)$$

where R would be zero if $G_1^*(\omega)$ and $G_2^*(\omega)$ were the exact pair of functions of the material and the given experimental values of the reflection and transmission coefficients were exact noiseless quantities.

The set of optimisation parameters can be provided directly by the two response functions $G_1^*(\omega)$ and $G_2^*(\omega)$. Alternatively, it's more convenient to use a set of functions of the frequency ω that can be directly used in the expression of the elements of \mathbf{T} as defined in Appendix D. Such a set is for example given by the two eigenfunctions defined in §3.4.3 for oscillatory displacement processes:

$$\lambda_L^*(\omega) = \frac{\rho\omega^2}{k_L^{*2}} = \frac{1}{3}(G_2^*(\omega) + 2G_1^*(\omega)) = \mathbf{L}^* \quad \text{Longitudinal bulk modulus}$$

$$\lambda_T^*(\omega) = \frac{\rho\omega^2}{k_T^{*2}} = \frac{G_1^*(\omega)}{2} = \mathbf{G}^* \quad \text{Tangential (shear) modulus}$$

For a given angle of incidence, we can write:

$$L(\lambda^*, \omega) = \mathbf{T}_a(\lambda^*(\omega), \omega) V(\omega) \quad (4.9)$$

where λ^* is the vector whose elements are λ_L^* and λ_T^* .

In order to minimise the value of equation 4.9, we can now build a scalar performance functional for the optimisation process in the given frequency range as (the superscript * is understood):

$$\mathbf{J}(\lambda) = F(V(\omega_b)) + \int_{\Omega} q^T L(\lambda, \omega) d\omega \quad (4.10)$$

where q is an unknown vector of weighing coefficients and $F(V(\omega_b))$ is scalar function of boundary conditions:

$$F(V(\omega_b)) = V(\omega_f) - V_f + V(\omega_i) - V_i \quad (4.11)$$

If we now define a new set of complex-valued Lagrange multipliers p , we can introduce the experimental values as an explicit constraint in the minimisation process. We have:

$$p^T [V(\omega) - V_e(\omega)] = 0 \quad (4.12)$$

where $V_e(\omega)$ is a vector of interpolation functions over the value of $V(\omega)$ in each interval.

Finally, we define the Hamilton optimisation function, H , as

$$H(\lambda, p, q, \omega) = q^T L(\lambda, \omega) + p^T V(\omega) \quad (4.13)$$

If we introduce the Hamilton function (4.13) in the performance functional and take (4.12) into account, we obtain:

$$J(\lambda) = F(V(\omega_b)) + \int_{\Omega} [H(\lambda, p, q, \omega) - p^T V_e(\omega)] d\omega \quad (4.14)$$

The optimisation problem becomes then one of finding the optimisation functions $\bar{\lambda}$ that minimise the performance functional $J(\lambda)$ over a class Λ of admissible functions:

$$J(\bar{\lambda}) = \min_{\lambda \in \Lambda} J(\lambda) \quad (4.15)$$

where the class Λ of admissible functions for the minimisation problem is equivalent to the class of strong response functions for Boltzmann laws, as defined in §3.3.2 and following paragraphs.

We consider now the variation of the optimisation functions:

$$\lambda(\omega) = \bar{\lambda}(\omega) + \delta\lambda(\omega) \quad (4.16)$$

and the corresponding variations of the propagation vectors and the performance functional:

$$V(\omega) = \bar{V}(\omega) + \delta V(\omega) \quad (4.17)$$

and

$$J(\lambda) = J(\bar{\lambda} + \delta\lambda) \quad (4.18)$$

The necessary condition for $\bar{\lambda}$ to be the desired optimal functions is that the 1st-order variation $\delta J(\bar{\lambda})$ of the difference $\Delta J(\bar{\lambda}) = J(\bar{\lambda} + \delta\lambda) - J(\bar{\lambda})$ be zero. We can therefore write

the following optimisation condition for the residual equation (4.8) (the functional dependence on the variables inside round brackets has been dropped for brevity and is implicitly understood):

$$\begin{aligned}\delta J(\lambda) &= \int_{\Omega} \left\{ \left[\frac{\partial H}{\partial V} \right]^T \delta V + \left[\frac{\partial H}{\partial p} \right]^T \delta p + \left[\frac{\partial H}{\partial q} \right]^T \delta q + \left[\frac{\partial H}{\partial \lambda} \right]^T \delta \lambda - V_e^T \delta p \right\} d\omega = \\ &= \int_{\Omega} \left\{ [q^T \mathbf{T}_a + p^T] \delta V + V^T \delta p + \mathbf{T}_a V \delta q + \left[q^T \frac{\partial L}{\partial \lambda} V \right] \delta \lambda - V_e^T \delta p \right\} d\omega\end{aligned}\quad (4.19)$$

where we have taken into account that the virtual variation $\delta\omega$ is zero, since the experiment configuration is fixed.

Since the virtual variations of the independent variables are by definition independent and different from zero, condition 4.19 represents a system of four vector equations in the four unknown vectors V (system state), p , q (system co-state) and λ (optimisation parameters):

$$\left\{ \begin{aligned} \int_{\Omega} [\mathbf{T}_a q + p] d\omega &= 0 \\ \int_{\Omega} [V - V_e] d\omega &= 0 \\ \int_{\Omega} \mathbf{T}_a V d\omega &= 0 \\ \int_{\Omega} \left[q^T \frac{\partial \mathbf{T}_a}{\partial \lambda} V \right] d\omega &= 0 \end{aligned} \right. \quad (4.20)$$

The system of equations 4.20 can now be solved numerically in the given frequency range. In this case, the system has been solved by applying an algorithm written using the Matlab macro-language based on the non-linear Newton-Raphson method.

4.7. Determination of the viscoelastic response functions

The viscoelastic parameters obtained from the optimisation process are given in figs. 4.31 to 4.34 for the panel of density $\rho = 1800 \text{ kg m}^{-3}$. As could be expected, it has been found that the viscoelastic moduli are independent from the angle of incidence, since the material is isotropic.

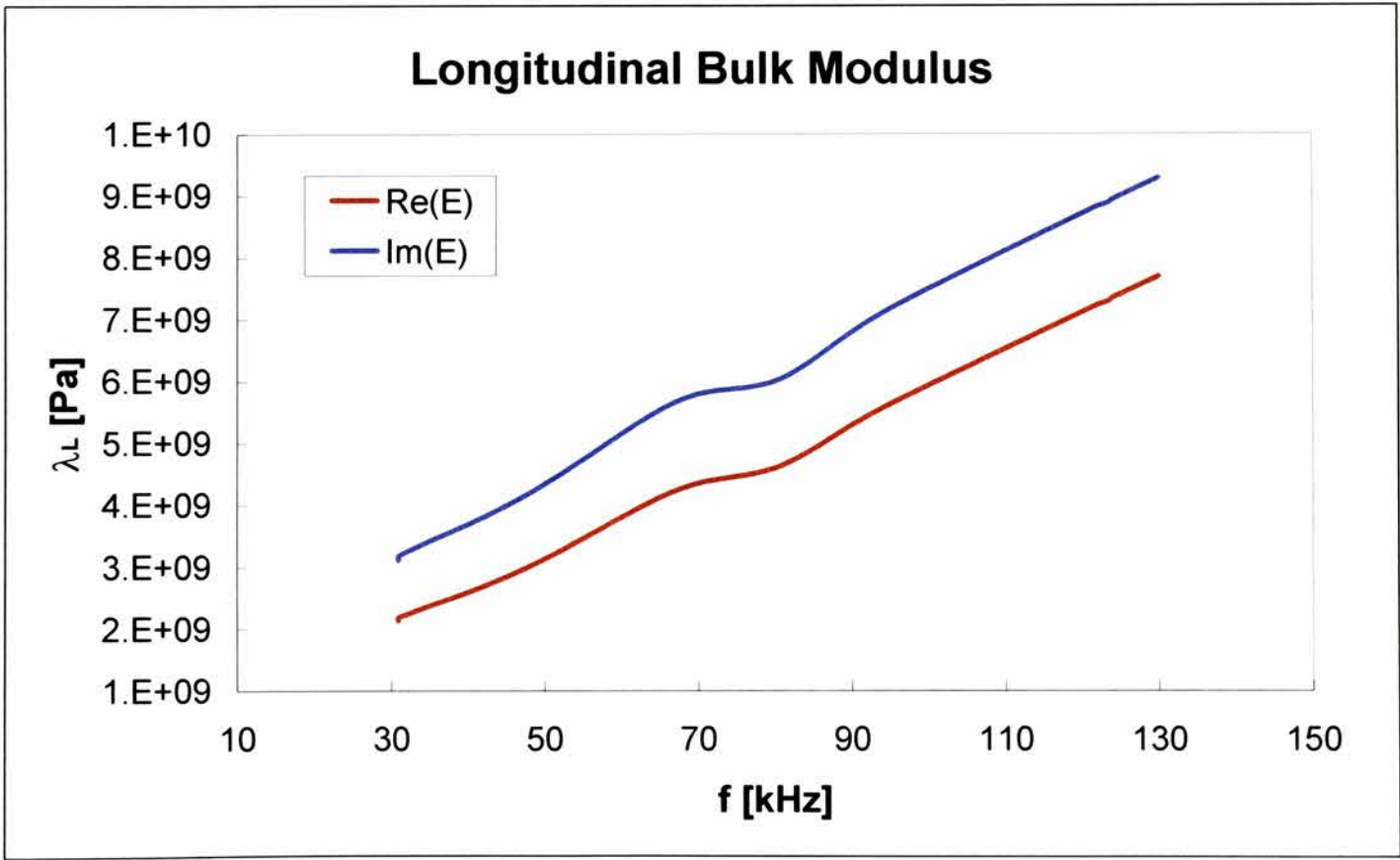


Figure 4.31: Longitudinal bulk modulus $\lambda_L^*(\omega)$. Loaded butyl rubber compound

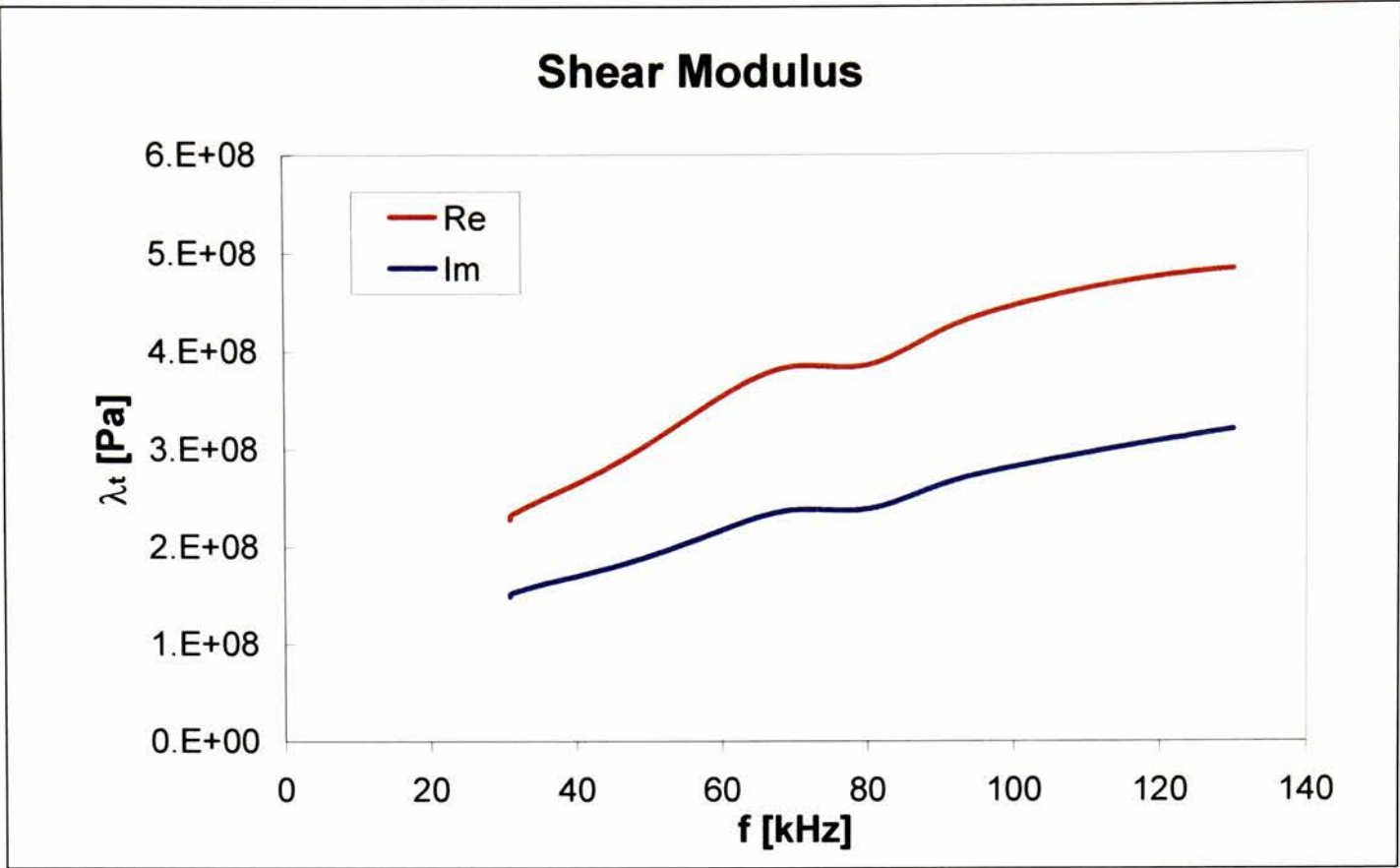


Figure 4.32: Shear modulus $\lambda_t^*(\omega)$. Loaded butyl rubber compound

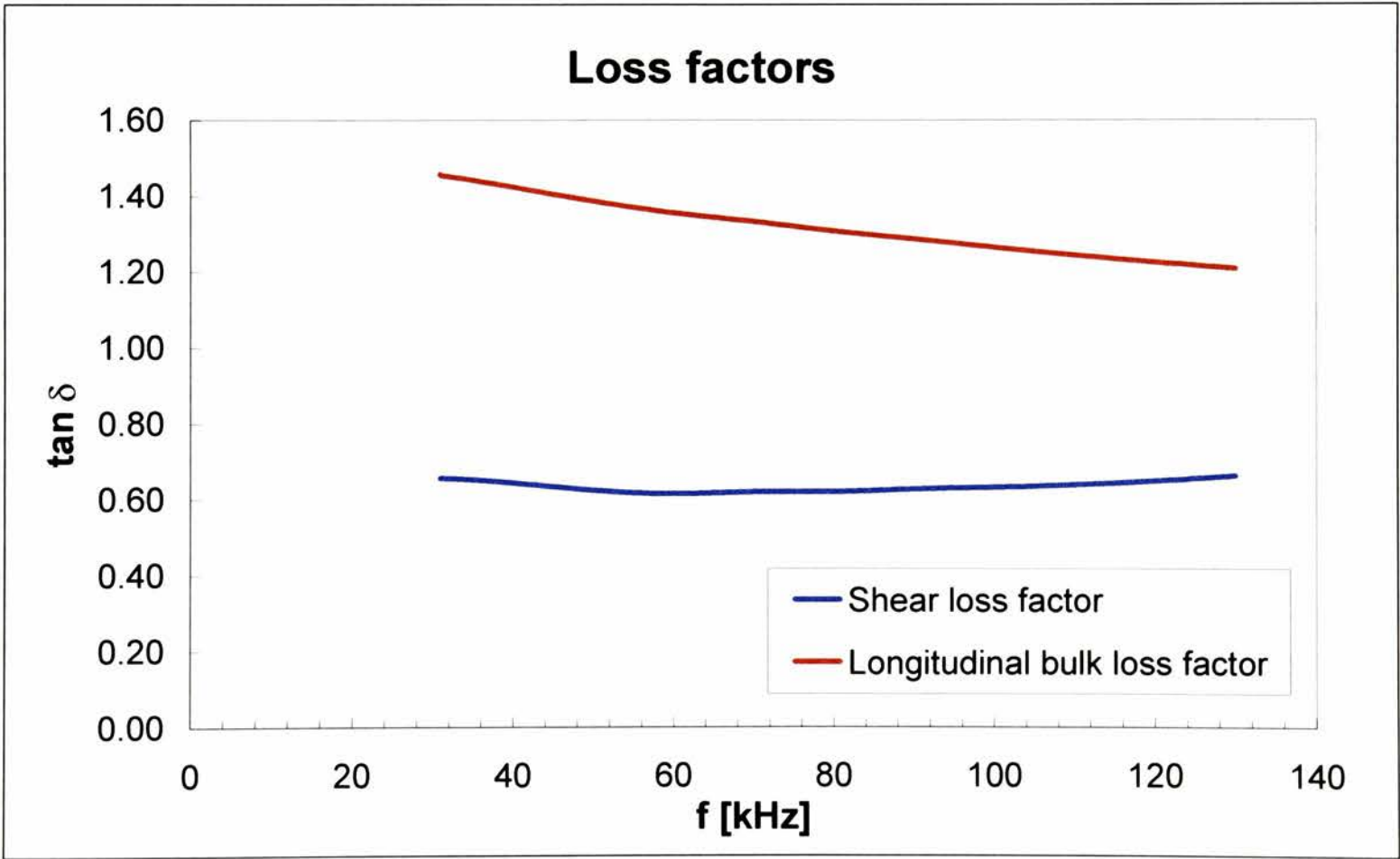


Figure 4.33: Longitudinal bulk and shear loss factors. Loaded butyl rubber compound

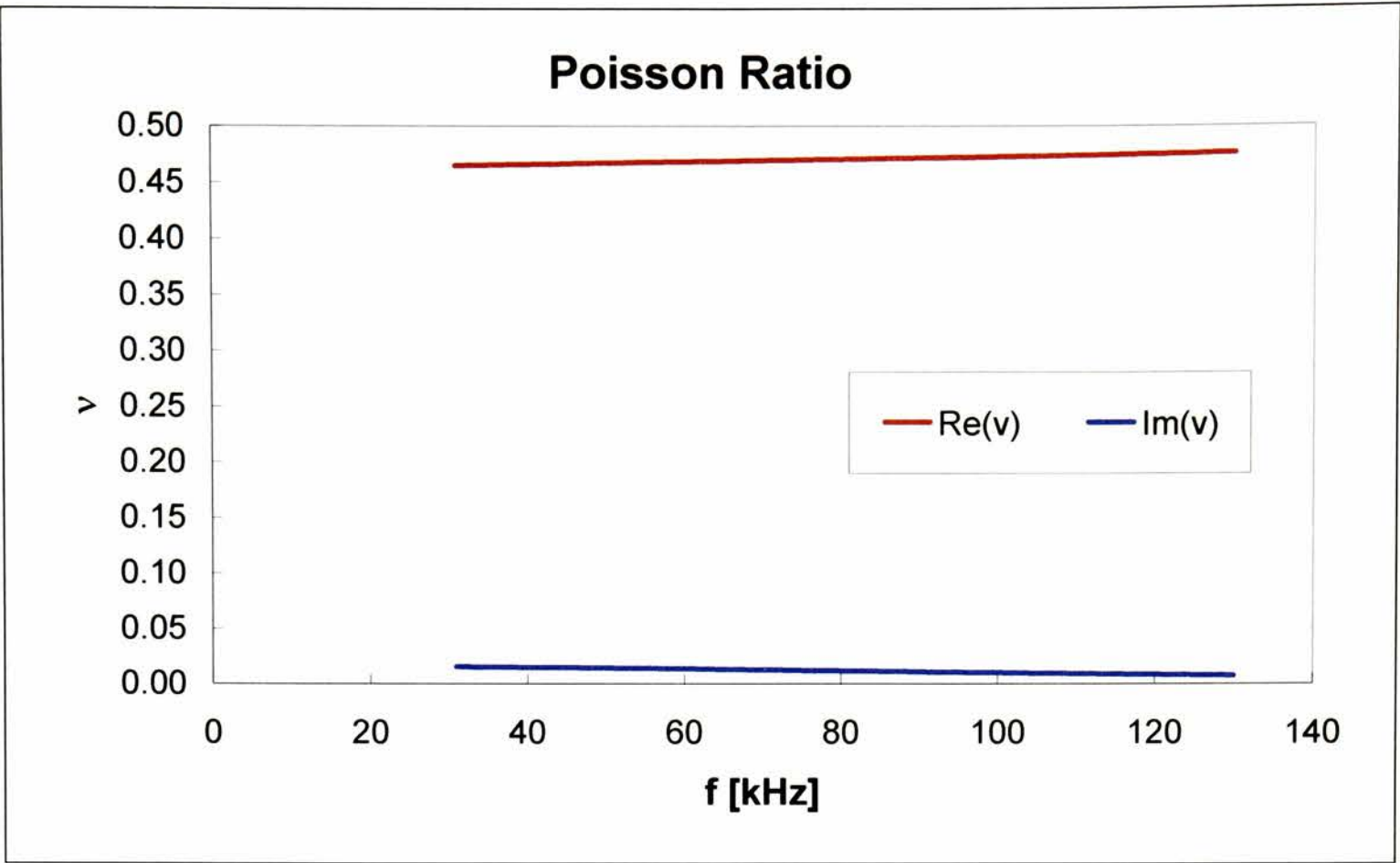


Figure 4.34: Viscoelastic Poisson ratio. Loaded butyl rubber compound

It is now possible to compute the viscoelastic response functions from the knowledge of the viscoelastic parameters using once more eqs. 3.94 and 3.95. The viscoelastic shear modulus G_1^* and the viscoelastic compression modulus G_2^* are shown in figs. 4.35 and 4.36 respectively.

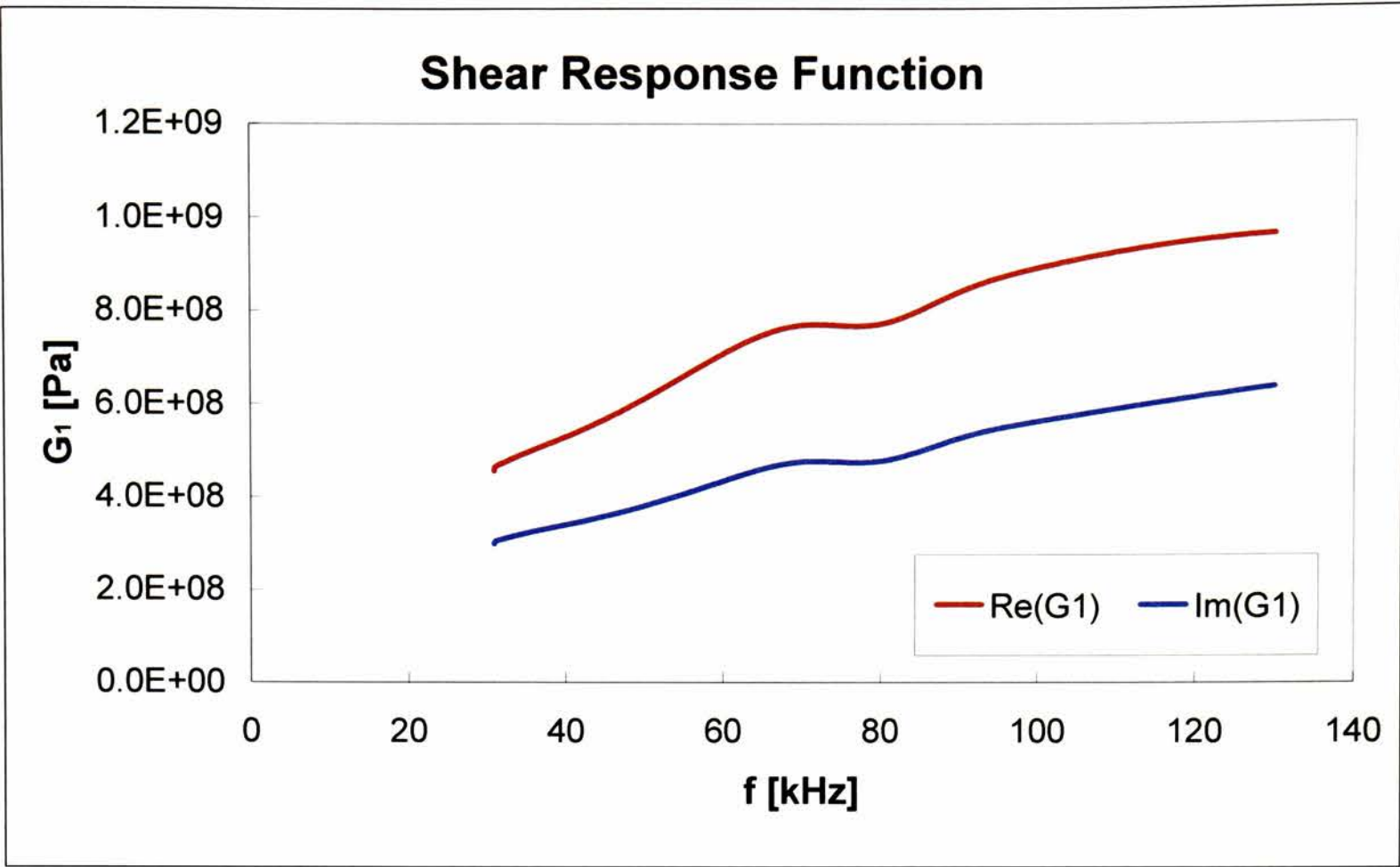


Figure 4.35: Viscoelastic shear response function. Loaded butyl rubber compound

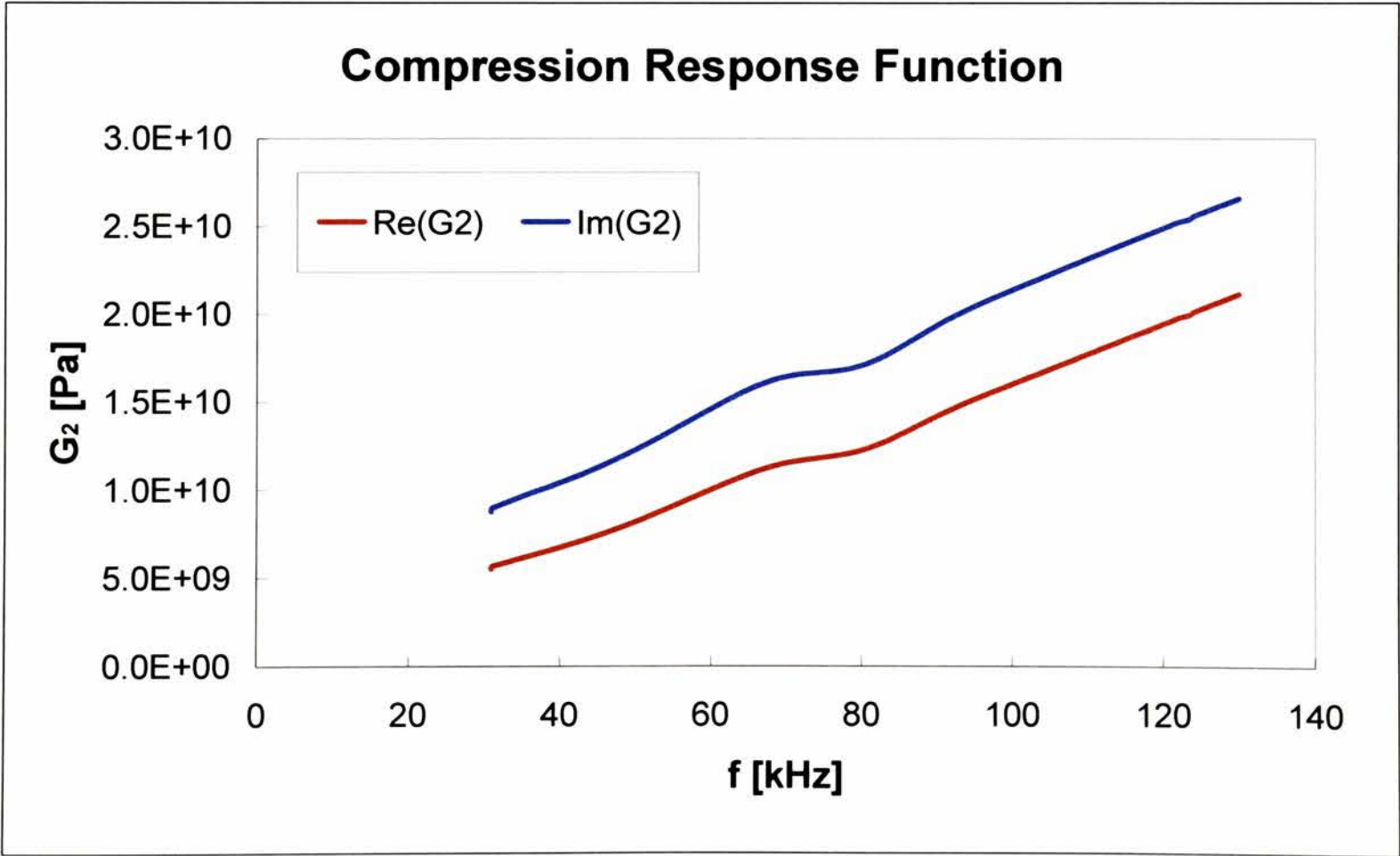


Figure 4.36: Viscoelastic compression response function. Loaded butyl rubber compound

4.8. Conclusions

In this chapter, a thorough analysis of the compounded viscoelastic materials used for the manufacturing of the scattering targets has been performed. Two different types of materials have been considered, notably a loaded polyurethane rubber, easy to compound and cast, and a loaded butyl rubber, showing marked viscoelastic properties.

The different methods used to characterise the material properties of the rubbers have been presented with particular attention to the immersion method with parametric acoustic sources, especially suited for the experimental analysis of panels and baffles.

A novel algorithm has been presented to reconstruct the viscoelastic properties of the material under investigation from limited experimental data and the complete viscoelastic response functions of the loaded butyl rubber have been computed within the frequency range of interest.

This data will be provide the basis for the determination of the viscoelastic constitutive relations used in Chapters 6 and 7 to produce the viscoelastic finite element schema.

4.9. References

- BREKHOVSKIKH, L.M. (1980). *Waves in layered media*, 2nd ed. New York: Academic Press, Inc
- CAPPS, R.N. (1993). *Elastomeric materials for acoustical applications*. Orlando FL: NRL
- DI MEGLIO, A. and FINZI, A.E. (1997). Minimum time control of flexible spacecraft by Hamilton's principle. *Meccanica*, 32 (6), 555-565
- Exxon Chemical Ltd. (1996). Technical sheet
- FERRY, J.D. (1980). *Viscoelastic properties of polymers*. New York: John Wiley & Sons, Inc.
- HSU, D.K. and HUGHES, M.S. (1992). Simultaneous ultrasonic velocity and sample thickness measurement and application in composites. *J. Acoust. Soc. Am.*, 92, 669-675
- HUMPHREY, V. (1986). The influence of the plane wave spectrum of a source on measurements of the transmission coefficient of a panel. *J. Sound Vib.*, 108, 261-272
- HUMPHREY, V.F. (1985). The measurement of acoustic properties of limited size panels by use of a parametric source. *J. Sound Vib.*, 98 (1), 67-81
- HUMPHREY, V.F. (1992). Non-linear acoustic as a laboratory tool. *Proc. Inst. Acoust.*, 14 (3), 99-113

- HUMPHREY, V.F. and BERKTAY, H.O. (1985). The transmission coefficient of a panel measured with a parametric source. *J. Sound Vib.*, 101,(1), 85-106
- HUMPHREY, V.F. *et al.* (1993). Measurements of the acoustic performance of materials: fibre reinforced materials and wedges. *Proc.Inst. Acoust.*, 15 (6), 27-37
- LANDEL, R.F. (1958). *Trans. Soc. Rheol.*, 2 (53)
- LANDEL, R.F. (1961). *J. Am. Rocket Soc.*, 31 (599)
- MAAZOUZ, A. *et al.* (1993). Hybrid-particulate composites based on an epoxy matrix, a reactive rubber, and glass-beads: morphology, viscoelastic, and mechanical properties. *J. of App. Polymer Sc.*, 50, 615-626
- PEIRLINCKX, L. *et al.* (1993). Identification of parametric models for ultrasonic wave propagation in the presence of absorption and dispersion. *IEEE Trans. Ultrasonics, Ferroelectricity and Freq. Control*, 40, 302-312
- PIQUETTE, J.C. (1985). Determination of the complex dynamic bulk modulus of elastomers by inverse scattering. *J. Acoust. Soc. Am.*, 5, 1665
- Polymed Ltd. (1996). Technical sheet
- READ, B.E. (1978). *The determination of dynamic properties of polymer and composites*. Bristol: Adam Hilger Ltd.
- ROKHLIN, S.I. and WANG, W. (1992). Double through-transmission bulk wave method for ultrasonic phase velocity measurement and determination of elastic constants of composite materials. *J.Acoust. Soc.Am.*, 91, 3303-3312
- SMITH, B.V. (1992). Introduction to non-linear acoustics and the parametric array. *Proc. Inst. Acoust.*, 14 (3), 1-25
- SUMA, N. *et al.* (1993). Improved mechanical properties of NR/EPDM and NR/Butyl blends by precuring EPDM and butyl. *J. of App. Polymer Sc.*, 49, 549-557
- THOMPSON, R.B. and GRAY, T.A. (1983). Analytical diffraction corrections to ultrasonic scattering measurements. In THOMPSON, O.D. and CHIMENTI, D.E. (eds.). *Review of progress in quantitative nondestructive evaluation 2*. New York: Plenum, 567-586
- WESTERVELT, P.J. (1963). Parametric acoustic array. *J. Acoust. Soc. Am.*, 35, 535-537
- ZHOU, D. *et al.* (1996). Identification of parametric models for ultrasonic double transmission experiments on viscoelastic plates. *J. Acoust. Soc. Am.*, 99 (3), 1446-1458

Chapter 5

Acoustic Reciprocity Theorems and their Application to Plane Wave Scattering by Penetrable Objects

5.1 Introduction

The acoustic reciprocity theorems and the systems of dynamic equations that can be derived from their application are the starting point for the computation of acoustic fields by means of numerical or integral equation approach. The understanding of the structure of the theorems, especially the time convolution form, is therefore paramount in the development of the finite element – boundary element method outlined in this research.

In this chapter, the linear equations of acoustics are introduced. The time-domain form of the equations is first presented and then their complex frequency domain form is derived.

The general principles of acoustic radiation from sources in unbounded, homogenous and isotropic fluids are presented and the special case of plane acoustic waves is then dealt with.

Building on the basic wave equations in the complex frequency form, the acoustic reciprocity theorems are derived with particular attention to the time convolution form. This theorem is then applied to the direct scattering problem from penetrable objects in an unbounded, homogenous and isotropic fluid embedding.

Finally, an analytic approximate solution to the scattering problem is derived for the geometrical configuration of interest in this research, namely the anechoic baffle.

5.2 The Linear Wave Equations

5.2.1 The Acoustic Wave Equations in the Time Domain

We consider the linear form of the dynamics of a fluid subjected to small-amplitude variations of the distribution of pressure around an equilibrium position and of the mass flow density in a stationary flow.

Under these assumptions, the equations of acoustics in the time domain have the form:

$$\begin{cases} \nabla p + \frac{\partial \Phi}{\partial t} = f \\ \text{div } \mathbf{v} - \frac{\partial \theta}{\partial t} = q \end{cases} \quad (5.1)$$

where, for a lossless, instantaneously reactive fluid:

$p = p(\mathbf{x}, t)$	pressure
$\mathbf{v} = \mathbf{v}(\mathbf{x}, t)$	velocity
$\Phi = \Phi(\mathbf{x}, t) = \rho(\mathbf{x})\mathbf{v}(\mathbf{x}, t)$	mass flow density
$\rho = \rho(\mathbf{x})$	density tensor
$\theta = \theta(\mathbf{x}, t) = -\kappa(\mathbf{x})p(\mathbf{x}, t)$	cubic dilatation
$\kappa = \kappa(\mathbf{x})$	compressibility
$\mathbf{f} = \mathbf{f}(\mathbf{x}, t)$	volume force distribution
$q = q(\mathbf{x}, t)$	source distribution

5.2.2 Acoustic Scalar and Vector Potentials in the Time Domain

We consider now two special cases of equations (5.1.). In the first case, a lossless, locally reacting fluid is subjected to a source distribution $q=q(\mathbf{x}, t)$ in the absence of volume forces, which produces the wave motion $\{p, \mathbf{v}\} = \{p^q, \mathbf{v}^q\}$. In the second case, the same fluid is subjected to a volume force distribution $\mathbf{f}=\mathbf{f}(\mathbf{x}, t)$ in the absence of injection sources, which produces the wave motion $\{p, \mathbf{v}\} = \{p^f, \mathbf{v}^f\}$.

The equations of acoustics for the first case have the form:

$$\begin{cases} \nabla p^q + \rho \frac{\partial \mathbf{v}^q}{\partial t} = 0 \\ \text{div } \mathbf{v}^q + \kappa \frac{\partial p^q}{\partial t} = q \end{cases} \quad (5.2)$$

The system of simultaneous equations (5.2.) can be solved for the pressure p^q and velocity \mathbf{v}^q as:

$$\begin{cases} p^q = \frac{\partial \varphi}{\partial t} \\ \mathbf{v}^q = -\rho^{-1} \nabla \varphi \end{cases} \quad (5.3)$$

where $\varphi = \varphi(\mathbf{x}, t)$ is the *acoustic scalar potential*, solution of the second-order differential equation:

$$\kappa \frac{\partial^2 \varphi}{\partial t^2} - \text{div} (\rho^{-1} \nabla \varphi) = q \quad (5.4)$$

The equations of acoustics for the second case have the form:

$$\begin{cases} \nabla p^f + \rho \frac{\partial \mathbf{v}^f}{\partial t} = \mathbf{f} \\ \text{div} \mathbf{v}^f + \kappa \frac{\partial p^f}{\partial t} = 0 \end{cases} \quad (5.5)$$

The system of simultaneous equations (5.5.) can be solved for the pressure p^f and velocity \mathbf{v}^f as:

$$\begin{cases} p^f = -\kappa^{-1} \text{div} \psi \\ \mathbf{v}^f = \frac{\partial \psi}{\partial t} \end{cases} \quad (5.6)$$

where $\psi = \psi(\mathbf{x}, t)$ is the *acoustic vector potential*, solution of the second-order differential equation:

$$\rho \frac{\partial^2 \psi}{\partial t^2} - \nabla (\kappa^{-1} \operatorname{div} \psi) = f \quad (5.7)$$

The total acoustic field is obtained from superposition of the two fields. The total pressure and velocity distributions have therefore the form:

$$\begin{cases} p = \frac{\partial \phi}{\partial t} - \kappa^{-1} \operatorname{div} \psi \\ \mathbf{v} = \frac{\partial \psi}{\partial t} - \rho^{-1} \nabla \phi \end{cases} \quad (5.8)$$

5.2.3 Acoustic Wave Equations in the Complex Frequency Domain (Laplace-Transform Domain)

If the configuration of interest is linear and time-invariant, it is often preferable to express the corresponding equations in the frequency domain, rather than in the time domain.

By carrying out the Laplace transformation (Amerio 1985) of the equations of acoustics, it is possible to eliminate the time t and derive a set of equations in the space \mathbf{x} and the Laplace parameter s . The parameter s is in general a complex parameter. However, by taking $s = j\omega$, the class of steady-state, sinusoidally varying wave fields with angular frequency ω can be described.

If we apply the Laplace transformation to the equations (5.1.), we obtain the following form of the complex frequency-domain acoustic wave equations:

$$\begin{cases} \nabla \hat{p} + s \hat{\Phi} = \hat{f} + e^{-st_0} \Phi_0 \\ \operatorname{div} \hat{\mathbf{v}} - s \hat{\Theta} = \hat{q} - e^{-st_0} \theta_0 \end{cases} \quad (5.9)$$

where Φ_0 and θ_0 represent the contribution of a non-vanishing acoustic field at $t = t_0$, which can be taken to be zero for our purposes.

For a lossless, instantaneously reactive fluid, we have:

$$\begin{cases} \hat{\Phi} = \hat{\Phi}(\mathbf{x}, s) = \rho(\mathbf{x})\hat{\mathbf{v}}(\mathbf{x}, s) \\ \hat{\theta} = \hat{\theta}(\mathbf{x}, s) = -\kappa(\mathbf{x})\hat{p}(\mathbf{x}, s) \end{cases} \quad (5.10)$$

Equations (5.9.) can be therefore rewritten as:

$$\begin{cases} \nabla \hat{p} + s\rho\hat{\mathbf{v}} = \hat{\mathbf{f}} + e^{-st_0}\Phi_0 \\ \text{div } \hat{\mathbf{v}} + s\kappa\hat{p} = \hat{q} - e^{-st_0}\theta_0 \end{cases} \quad (5.11)$$

or

$$\begin{cases} \nabla \hat{p} + \hat{\zeta}\hat{\mathbf{v}} = \hat{\mathbf{f}} + e^{-st_0}\Phi_0 \\ \text{div } \hat{\mathbf{v}} + \hat{\eta}\hat{p} = \hat{q} - e^{-st_0}\theta_0 \end{cases} \quad (5.12)$$

where the terms $\hat{\zeta}$ and $\hat{\eta}$ are given by:

$$\begin{aligned} \hat{\zeta} &= \hat{\zeta}(\mathbf{x}, s) = s\rho(\mathbf{x}) \quad (\text{longitudinal acoustic impedance per length}) \\ \hat{\eta} &= \hat{\eta}(\mathbf{x}, s) = s\kappa(\mathbf{x}) \quad (\text{transverse acoustic admittance per length}) \end{aligned} \quad (5.13)$$

5.2.4 Acoustic Scalar and Vector Potentials in the Complex Frequency Domain

The complex frequency-domain acoustic potential can be derived in the same way as their time-domain counterparts. In the following, we assume the acoustic field to be zero at $t = t_0$.

We consider again the two special cases of the equations of acoustics (5.12.). In the first case, a lossless, locally reacting fluid is subjected to a source distribution $\hat{q} = \hat{q}(\mathbf{x}, s)$ in the absence of volume forces, which produces the wave motion $\{\hat{p}, \hat{\mathbf{v}}\} = \{\hat{p}^q, \hat{\mathbf{v}}^q\}$. In the second case, the same fluid is subjected to a volume force distribution $\hat{f} = \hat{f}(\mathbf{x}, s)$ in the absence of injection sources, which produces the wave motion $\{\hat{p}, \hat{\mathbf{v}}\} = \{\hat{p}^f, \hat{\mathbf{v}}^f\}$.

The equations of acoustics for the first case have the form:

$$\begin{cases} \nabla \hat{p}^q + \hat{\zeta} \hat{\mathbf{v}}^q = 0 \\ \text{div } \hat{\mathbf{v}}^q + \hat{\eta} \hat{p}^q = \hat{q} \end{cases} \quad (5.14)$$

The system of simultaneous equations (5.14.) can be solved for the pressure \hat{p}^q and velocity $\hat{\mathbf{v}}^q$ as:

$$\begin{cases} \hat{p}^q = s \hat{\phi} \\ \hat{\mathbf{v}}^q = -s \hat{\zeta}^{-1} \nabla \hat{\phi} \end{cases} \quad (5.15)$$

where $\hat{\phi} = \hat{\phi}(\mathbf{x}, s)$ is the *acoustic scalar potential*, solution of the second-order differential *acoustic scalar Helmholtz equation*:

$$s\hat{\eta}\hat{\phi} - \text{div} (s\hat{\zeta}^{-1}\nabla\hat{\phi}) = \hat{q} \quad (5.16)$$

The equations of acoustics for the second case have the form:

$$\begin{cases} \nabla\hat{p}^f + \hat{\zeta}\hat{\mathbf{v}}^f = \hat{\mathbf{f}} \\ \text{div} \hat{\mathbf{v}}^f + \hat{\eta}\hat{p}^f = 0 \end{cases} \quad (5.17)$$

The system of simultaneous equations (5.17.) can be solved for the pressure \hat{p}^f and velocity $\hat{\mathbf{v}}^f$ as:

$$\begin{cases} \hat{p}^f = -s\hat{\eta}^{-1}\text{div} \hat{\psi} \\ \hat{\mathbf{v}}^f = s\hat{\psi} \end{cases} \quad (5.18)$$

where $\hat{\psi} = \hat{\psi}(\mathbf{x}, s)$ is the *acoustic vector potential*, solution of the second-order differential *acoustic vector Helmholtz equation*:

$$s\hat{\zeta}\hat{\psi} - \nabla (s\hat{\eta}^{-1}\text{div} \hat{\psi}) = \hat{\mathbf{f}} \quad (5.19)$$

The total acoustic field is obtained from superposition of the two fields. The total pressure and velocity distributions have therefore the form:

$$\begin{cases} \hat{p} = s\hat{\phi} - s\hat{\eta}^{-1}\text{div} \hat{\psi} \\ \hat{\mathbf{v}} = s\hat{\psi} - s\hat{\zeta}^{-1}\nabla\hat{\phi} \end{cases} \quad (5.20)$$

5.2.5 Point Source Solutions and Green's Functions

The two volume source distributions $\hat{\mathbf{f}}$ (force sources) and \hat{q} (injection sources) that produce the acoustic field can be expressed in a useful form if we consider them as the continuous superposition of point sources located in each point $\mathbf{x} \in \mathcal{D}$, where \mathcal{D} is the spatial support domain of the distributed sources.

We make use of the property of the Dirac delta function to 'pick up' the value of a given function in a given point (sifting property) and write:

$$\begin{cases} \hat{q}(\mathbf{x}, s) = \int_{\mathbf{x}' \in \mathcal{D}} \delta(\mathbf{x} - \mathbf{x}') \hat{q}(\mathbf{x}', s) dV \\ \hat{\mathbf{f}}(\mathbf{x}, s) = \int_{\mathbf{x}' \in \mathcal{D}} \delta(\mathbf{x} - \mathbf{x}') \hat{\mathbf{f}}(\mathbf{x}', s) dV \end{cases} \quad (5.21)$$

We now consider the scalar and vector (tensorial) Helmholtz equations (5.16.) and (5.19.) for a unit injection point source and a unit force point source respectively:

$$s\hat{\eta}\hat{G}^\varphi - \text{div} \left(s\hat{\zeta}^{-1} \nabla \hat{G}^\varphi \right) = \delta(\mathbf{x} - \mathbf{x}') \quad (5.22)$$

$$s\hat{\zeta}\hat{\mathbf{G}}^\psi - \nabla \left(s\hat{\eta}^{-1} \text{div} \hat{\mathbf{G}}^\psi \right) = \delta(\mathbf{x} - \mathbf{x}') \quad (5.23)$$

If the scalar function $\hat{G}^\varphi(\mathbf{x}, \mathbf{x}', s)$ and the tensor function $\hat{\mathbf{G}}^\psi(\mathbf{x}, \mathbf{x}', s)$ are solutions of equations (5.22.) and (5.23) respectively, then equations (5.16.) and (5.19.) are satisfied by:

$$\hat{\phi}(\mathbf{x}, s) = \int_{\mathbf{x}' \in \mathcal{D}} \hat{G}^\varphi(\mathbf{x}, \mathbf{x}', s) \hat{q}(\mathbf{x}', s) dV \quad (5.24)$$

and

$$\hat{\psi}(\mathbf{x}, s) = \int_{\mathbf{x}' \in \mathcal{D}} \hat{\mathbf{G}}^\psi(\mathbf{x}, \mathbf{x}', s) \hat{\mathbf{f}}(\mathbf{x}', s) dV \quad (5.25)$$

The functions $\hat{G}^\varphi = \hat{G}^\varphi(\mathbf{x}, \mathbf{x}', s)$ and function $\hat{\mathbf{G}}^\psi = \hat{\mathbf{G}}^\psi(\mathbf{x}, \mathbf{x}', s)$ are the complex frequency-domain scalar and tensorial Green's function.

5.3 Acoustic Radiation in Homogenous, Lossless, Isotropic Fluids

To solve the acoustic radiation problem, we need at this point to find the expression of the two acoustic field quantities, the acoustic pressure p and the particle velocity \mathbf{v} . We consider the case of a field generated by sources in a homogenous, lossless, isotropic fluid.

For a homogenous, isotropic fluid, the constitutive relationships (5.13.) take the form:

$$\begin{aligned} \hat{\zeta} = \hat{\zeta}(s) &= s\rho \quad (\text{longitudinal acoustic impedance per length}) \\ \hat{\eta} = \hat{\eta}(s) &= s\kappa \quad (\text{transverse acoustic admittance per length}) \end{aligned} \quad (5.26)$$

and the equations of acoustics can be written as:

$$\begin{cases} \nabla \hat{p} + \hat{\zeta} \hat{\mathbf{v}} = \hat{\mathbf{f}} \\ \text{div } \hat{\mathbf{v}} + \hat{\eta} \hat{p} = \hat{q} \end{cases} \quad (5.27)$$

To solve the system of equations (5.27) we can apply the Fourier transform in the spatial support \mathcal{R}^3 of \mathbf{x} . This step allows us to transform the spatial derivatives of pressure and velocity into algebraic products.

The Fourier transforms of the acoustic field quantities are:

$$\begin{cases} \tilde{p}(jk, s) = \int_{x \in \mathcal{R}} \hat{p}(x, s) e^{jk \cdot x} dV \\ \tilde{v}(jk, s) = \int_{x \in \mathcal{R}} \hat{v}(x, s) e^{jk \cdot x} dV \end{cases} \quad (5.28)$$

where

$$\mathbf{k} = k_1 \mathbf{i}_1 + k_2 \mathbf{i}_2 + k_3 \mathbf{i}_3 \quad (5.29)$$

is the *acoustic wave number vector*.

Equations (5.27.) are transformed to the \mathbf{k} -space form:

$$\begin{cases} -jk\tilde{p} + \hat{\zeta}\tilde{v} = \tilde{f} \\ -jk \cdot \tilde{v} + \hat{\eta}\tilde{p} = \tilde{q} \end{cases} \quad (5.30)$$

where \tilde{f} and \tilde{q} are the Fourier transforms of \hat{f} and \hat{q} respectively.

The algebraic system of equations (5.30.) can now be solved for \tilde{p} and \tilde{v} and gives:

$$\begin{cases} \tilde{p} = \tilde{G}(\hat{\zeta}\tilde{q} + jk \cdot \tilde{f}) \\ \tilde{v} = \hat{\zeta}^{-1}\tilde{f} + jk\tilde{G}\tilde{q} - \hat{\zeta}^{-1}kk^T\tilde{G}\tilde{f} \end{cases} \quad (5.31)$$

where

$$\tilde{G} = \frac{1}{|\mathbf{k}|^2 + \hat{\eta}\hat{\zeta}} \quad (5.32)$$

We can now inverse transform the function $\tilde{G}(j\mathbf{k}, s)$ to obtain the Green's function of the scalar Helmholtz equation in the complex frequency domain:

$$\hat{G}(\mathbf{x}, s) = \frac{1}{(2\pi)^3} \int_{\mathbf{k} \in \mathbb{R}^3} \tilde{G}(j\mathbf{k}, s) e^{-j\mathbf{k} \cdot \mathbf{x}} dV = \frac{1}{(2\pi)^3} \int_{\mathbf{k} \in \mathbb{R}^3} \frac{e^{-j\mathbf{k} \cdot \mathbf{x}}}{|\mathbf{k}|^2 + \hat{\zeta}\hat{\eta}} dV \quad (5.33)$$

Equation (5.33.) can be evaluated by transforming the Cartesian co-ordinates into spherical co-ordinates in \mathbf{k} -space with centre at $\mathbf{k} = 0$ and the polar axis along \mathbf{x} (see for example De Hoop 1995). The application of this co-ordinate transformation yields after integration with respect to the spherical co-ordinates φ and θ .

$$\hat{G}(\mathbf{x}, s) = \frac{1}{4\pi^2 j|\mathbf{x}|} \int_{k=-\infty}^{k=\infty} \frac{e^{jk|\mathbf{x}|}}{k^2 + \hat{\zeta}\hat{\eta}} k dk \quad |\mathbf{x}| \neq 0 \quad (5.34)$$

where $k = \pm(\mathbf{k} \cdot \mathbf{k})^{1/2}$.

The integral in the right-hand side member can be evaluated by analytic continuation of the integrand in the complex plane and application of the method of residues (Amerio 1985).

We obtain the following form of the Green's function:

$$\hat{G}(\mathbf{x}, s) = \frac{e^{-(\hat{\zeta}\hat{\eta})^{1/2}|\mathbf{x}|}}{4\pi|\mathbf{x}|} \quad |\mathbf{x}| \neq 0 \quad (5.35)$$

By carrying out the inverse Fourier transform of equations (5.31.) and taking into account function (5.35.), we finally obtain the integral-differential form of the complex frequency-domain acoustic field quantities:

$$\begin{cases} \hat{p} = \hat{\zeta} \int_{\mathbf{x}' \in \mathcal{D}} \hat{G}(\mathbf{x} - \mathbf{x}', s) \hat{q}(\mathbf{x}', s) dV - \text{div} \left(\int_{\mathbf{x}' \in \mathcal{D}} \hat{G}(\mathbf{x} - \mathbf{x}', s) \hat{\mathbf{f}}(\mathbf{x}', s) dV \right) \\ \tilde{\mathbf{v}} = \hat{\zeta}^{-1} \tilde{\mathbf{f}} - \nabla \left(\int_{\mathbf{x}' \in \mathcal{D}} \hat{G}(\mathbf{x} - \mathbf{x}', s) \hat{q}(\mathbf{x}', s) dV \right) + \hat{\zeta}^{-1} \nabla \left(\text{div} \int_{\mathbf{x}' \in \mathcal{D}} \hat{G}(\mathbf{x} - \mathbf{x}', s) \hat{\mathbf{f}}(\mathbf{x}', s) dV \right) \end{cases} \quad (5.36)$$

Equation (5.36.) can be rewritten in a more compact form by introducing the volume injection source scalar potential $\hat{\Phi} = \hat{\Phi}(\mathbf{x}, s)$ and the force source vector potential $\hat{\Psi} = \hat{\Psi}(\mathbf{x}, s)$:

$$\begin{cases} \hat{p} = \hat{\zeta} \hat{\Phi} - \text{div} \hat{\Psi} \\ \tilde{\mathbf{v}} = \hat{\zeta}^{-1} \tilde{\mathbf{f}} - \nabla \hat{\Phi} + \hat{\zeta}^{-1} \nabla \text{div} \hat{\Psi} \end{cases} \quad (5.37)$$

where

$$\begin{cases} \hat{\Phi}(\mathbf{x}, s) = \int_{\mathbf{x}' \in \mathcal{D}} \hat{G}(\mathbf{x} - \mathbf{x}', s) \hat{q}(\mathbf{x}', s) dV \\ \hat{\Psi}(\mathbf{x}, s) = \int_{\mathbf{x}' \in \mathcal{D}} \hat{G}(\mathbf{x} - \mathbf{x}', s) \hat{\mathbf{f}}(\mathbf{x}', s) dV \end{cases} \quad (5.38)$$

The final form of the solution to the acoustic radiation problem in a homogeneous, isotropic fluid in the complex frequency domain can be in principle found by carrying out the

integrals and differentials terms in equations (5.38.). For all but the simplest configurations, a closed-form solution cannot be easily found and these operations are performed by means of numerical methods (see for example Chadli *et al.* 1994).

5.3.1 Plane Acoustic Waves in a Homogeneous, Lossless, Isotropic Fluid

If the fluid medium under investigation is source free, the equations of acoustics (5.27.) can be written as:

$$\begin{cases} \nabla \hat{p} + \zeta \hat{\mathbf{v}} = 0 \\ \text{div } \hat{\mathbf{v}} + \hat{\eta} \hat{p} = 0 \end{cases} \quad (5.39)$$

The non-trivial solutions of this system of homogeneous equations take the name of *plane waves*.

We look for a particular solution of system (5.39.) of the form:

$$\begin{cases} \hat{p} = \hat{P} e^{-\hat{\gamma} \cdot \mathbf{x}} \\ \hat{\mathbf{v}} = \hat{\mathbf{V}} e^{-\hat{\gamma} \cdot \mathbf{x}} \end{cases} \quad (5.40)$$

where \hat{P} and $\hat{\mathbf{V}}$ are the plane wave *amplitudes* and $\hat{\gamma}$ is the *propagation vector*. By substitution of (5.40.) in (5.39.) we therefore obtain the algebraic system of equations:

$$\begin{cases} -\hat{\gamma} \hat{P} + \zeta \hat{\mathbf{V}} = 0 \\ -\hat{\gamma} \cdot \hat{\mathbf{V}} + \hat{\eta} \hat{P} = 0 \end{cases} \quad (5.41)$$

For equations (5.41.) to have a non-trivial solution, we have to find the particular value of the propagation vector $\hat{\gamma}$ that satisfies the system secular equation:

$$\begin{vmatrix} -\hat{\gamma} & \hat{\zeta} \\ \hat{\eta} & -\hat{\gamma} \end{vmatrix} = |\hat{\gamma}|^2 - \hat{\eta}\hat{\zeta} = 0 \quad (5.42)$$

Equation (5.42.) is called the wave *dispersion equation*. For all arbitrary values of $\hat{\gamma}$ satisfying the dispersion equation, the corresponding solutions $\{\hat{P}, \hat{V}\}$ of equations (5.39.) and (5.41.) constitute the general class of *non-uniform plane waves*.

If in addition the propagation vector can be expressed as:

$$\hat{\gamma} = \hat{\gamma}\hat{\xi} \quad (5.43)$$

where $\hat{\gamma} = (\hat{\eta}\hat{\zeta})^{1/2}$ is a scalar propagation coefficient and $\hat{\xi}$ is a unit vector along the direction of propagation of the wave, then we have the class of *uniform plane waves*.

In this latter case, we can write the analytic form of the uniform plane wave equation as:

$$\begin{cases} -\hat{\xi}\hat{P} + \hat{Z}\hat{V} = 0 \\ -\hat{\xi} \cdot \hat{V} + \hat{Y}\hat{P} = 0 \end{cases} \quad (5.44)$$

where

$$\left\{ \begin{array}{ll} \hat{Z} = \left(\frac{\hat{\zeta}}{\hat{\eta}} \right)^{1/2} & \text{scalar acoustic impedance} \\ \hat{Y} = \hat{Z}^{-1} = \left(\frac{\hat{\eta}}{\hat{\zeta}} \right)^{1/2} & \text{scalar acoustic admittance} \end{array} \right. \quad (5.45)$$

Finally, we can use the isotropic lossless of form (5.26.) of the constitutive relations to derive two important physical parameters of the fluid medium:

$$\hat{\gamma} = \left(\hat{\eta} \hat{\zeta} \right)^{1/2} = s(\kappa \rho)^{1/2} = s\Lambda = \frac{s}{c} \quad (5.46)$$

where

$$\left\{ \begin{array}{ll} \Lambda = (\kappa \rho)^{1/2} & \text{scalar acoustic slowness} \\ c = (\kappa \rho)^{-1/2} & \text{scalar acoustic wave speed} \end{array} \right. \quad (5.47)$$

The complete form of the acoustic field quantities together with their asymptotic far-field representation is given in Appendix F.

5.4 The Acoustic Reciprocity Theorem of the Time-Convolution Type in the Complex Frequency Domain and its Application to the Direct Source and Direct Scattering Problems

5.4.1 Definition of reciprocity theorem

We now consider two admissible states A and B of a linear fluid. Each state is characterised by its own set of physical parameters and source distributions. Both states refer to the same support domain $\mathcal{D} \subset \mathbb{R}^3$. The domain \mathcal{D} can be bounded with boundary $\partial\mathcal{D}$ or unbounded with $\partial\mathcal{D} \rightarrow \infty$.

A reciprocity theorem is defined as a specific relationship interrelating the acoustic wave field quantities in the two states A and B described below. This reciprocity relationship can be described in different forms, according to the type of domain and operator used (De Hoop 1995). In particular, the theorem can be expressed in the time domain or the complex frequency domain and can be of the time-convolution type or the time-correlation type.

In this section the complex frequency-domain reciprocity theorem of the time-convolution type will be derived and discussed. The other forms of the theorem can be derived by application of the inverse Laplace transform and a time inversion operation.

We consider the equations of acoustics for the two states A and B:

$$\begin{cases} \nabla \hat{p}^A + \hat{\zeta}^A \hat{\mathbf{v}}^A = \hat{\mathbf{f}}^A \\ \text{div } \hat{\mathbf{v}}^A + \hat{\eta}^A \hat{p}^A = \hat{q}^A \end{cases} \quad (5.48)$$

and

$$\begin{cases} \nabla \hat{p}^B + \hat{\zeta}^B \hat{\mathbf{v}}^B = \hat{\mathbf{f}}^B \\ \operatorname{div} \hat{\mathbf{v}}^B + \hat{\eta}^B \hat{p}^B = \hat{q}^B \end{cases} \quad (5.49)$$

Equations (5.48.) and (5.49.) can be complemented by suitable boundary conditions if discontinuities or impenetrable boundaries are present in the support domain \mathcal{D} .

If the domain \mathcal{D} is unbounded, the acoustic field quantities outside an arbitrarily large sphere are taken to be of the form (see Appendix F):

$$\begin{cases} \hat{p}^A = \hat{p}^{\infty A}(\boldsymbol{\zeta}, s) \frac{e^{-\hat{\gamma}_0 |\mathbf{x}|}}{4\pi |\mathbf{x}|} \\ \hat{\mathbf{v}}^A = \hat{\mathbf{v}}^{\infty A}(\boldsymbol{\zeta}, s) \frac{e^{-\hat{\gamma}_0 |\mathbf{x}|}}{4\pi |\mathbf{x}|} \end{cases} \quad (5.50)$$

and

$$\begin{cases} \hat{p}^B = \hat{p}^{\infty B}(\boldsymbol{\zeta}, s) \frac{e^{-\hat{\gamma}_0 |\mathbf{x}|}}{4\pi |\mathbf{x}|} \\ \hat{\mathbf{v}}^B = \hat{\mathbf{v}}^{\infty B}(\boldsymbol{\zeta}, s) \frac{e^{-\hat{\gamma}_0 |\mathbf{x}|}}{4\pi |\mathbf{x}|} \end{cases} \quad (5.51)$$

where the asymptotic quantities \hat{p}^∞ and $\hat{\mathbf{v}}^\infty$ satisfy the plane wave equations (5.41.).

5.4.2 The local and global forms of the complex frequency-domain reciprocity theorem of the time-convolution type

We consider now a special quantity called the *local interaction* quantity built upon the time convolution in the complex frequency domain of the acoustic field quantities of states A and B in the form:

$$\text{div} [\hat{p}^A(\mathbf{x}, s) \hat{\mathbf{v}}^B(\mathbf{x}, s) - \hat{p}^B(\mathbf{x}, s) \hat{\mathbf{v}}^A(\mathbf{x}, s)] \quad (5.52)$$

The name of the theorem stems from the fact that the time-convolution operator in the complex frequency domain is the product operator of the transforms.

We can further expand quantity (5.52.) by carrying out the divergence of the products:

$$\begin{aligned} \text{div} [\hat{p}^A(\mathbf{x}, s) \hat{\mathbf{v}}^B(\mathbf{x}, s) - \hat{p}^B(\mathbf{x}, s) \hat{\mathbf{v}}^A(\mathbf{x}, s)] &= \\ &= \text{div} [\hat{p}^A(\mathbf{x}, s) \hat{\mathbf{v}}^B(\mathbf{x}, s)] - \text{div} [\hat{p}^B(\mathbf{x}, s) \hat{\mathbf{v}}^A(\mathbf{x}, s)] = \\ &= \nabla \hat{p}^A(\mathbf{x}, s) \cdot \hat{\mathbf{v}}^B(\mathbf{x}, s) + \hat{p}^A(\mathbf{x}, s) \text{div} \hat{\mathbf{v}}^B(\mathbf{x}, s) + \\ &\quad - \nabla \hat{p}^B(\mathbf{x}, s) \cdot \hat{\mathbf{v}}^A(\mathbf{x}, s) - \hat{p}^B(\mathbf{x}, s) \text{div} \hat{\mathbf{v}}^A(\mathbf{x}, s) \end{aligned} \quad (5.53)$$

Incorporating equations (5.48.) and (5.49.) in expression (5.53.) we finally have:

$$\begin{aligned} \text{div} [\hat{p}^A(\mathbf{x}, s) \hat{\mathbf{v}}^B(\mathbf{x}, s) - \hat{p}^B(\mathbf{x}, s) \hat{\mathbf{v}}^A(\mathbf{x}, s)] &= \\ &= [\hat{\zeta}^B(\mathbf{x}, s) - \hat{\zeta}^A(\mathbf{x}, s)] \hat{p}^A(\mathbf{x}, s) \cdot \hat{\mathbf{v}}^B(\mathbf{x}, s) - [\hat{\eta}^B(\mathbf{x}, s) - \hat{\eta}^A(\mathbf{x}, s)] \hat{p}^A(\mathbf{x}, s) \hat{p}^B(\mathbf{x}, s) + \\ &\quad + \hat{f}^A(\mathbf{x}, s) \cdot \hat{\mathbf{v}}^B(\mathbf{x}, s) + \hat{p}^A(\mathbf{x}, s) \hat{q}^B(\mathbf{x}, s) - \hat{f}^B(\mathbf{x}, s) \cdot \hat{\mathbf{v}}^A(\mathbf{x}, s) - \hat{p}^B(\mathbf{x}, s) \hat{q}^A(\mathbf{x}, s) \end{aligned} \quad (5.54)$$

Equation (5.54.) is the *local form* of the complex frequency-domain acoustic reciprocity theorem of the time-convolution type. The terms in the RHS can be given a

physical interpretation. The first two terms represents the physical differences in the media for state A and state B. This contribution vanishes if $\hat{\zeta}^B(\mathbf{x}, s) = \hat{\zeta}^A(\mathbf{x}, s)$ and $\hat{\eta}^B(\mathbf{x}, s) = \hat{\eta}^A(\mathbf{x}, s)$ for all frequencies s in the support of equation (5.54.). In this case, the two fluids in state A and B are called adjoint. The last four terms represent the effect of the sources and vanishes if the media are source free.

Equation (5.54.) relates quantities in the same point \mathbf{x} of space. We can integrate the equation over its support \mathcal{D} to obtain a global form of the reciprocity theorem. By enforcing appropriate continuity conditions in the domain \mathcal{D} and applying Gauss' divergence theorem to the LHS, we obtain:

$$\begin{aligned} \int_{\mathbf{x} \in \partial \mathcal{D}} [\hat{p}^A(\mathbf{x}, s) \hat{\mathbf{v}}^B(\mathbf{x}, s) - \hat{p}^B(\mathbf{x}, s) \hat{\mathbf{v}}^A(\mathbf{x}, s)] \cdot \mathbf{n} dA = \\ = \int_{\mathbf{x} \in \mathcal{D}} \left\{ [\hat{\zeta}^B(\mathbf{x}, s) - \hat{\zeta}^A(\mathbf{x}, s)] \hat{\mathbf{v}}^A(\mathbf{x}, s) \cdot \hat{\mathbf{v}}^B(\mathbf{x}, s) - [\hat{\eta}^B(\mathbf{x}, s) - \hat{\eta}^A(\mathbf{x}, s)] \hat{p}^A(\mathbf{x}, s) \hat{p}^B(\mathbf{x}, s) \right\} dV + \\ + \int_{\mathbf{x} \in \mathcal{D}} \left[\hat{\mathbf{f}}^A(\mathbf{x}, s) \cdot \hat{\mathbf{v}}^B(\mathbf{x}, s) + \hat{p}^A(\mathbf{x}, s) \hat{q}^B(\mathbf{x}, s) - \hat{\mathbf{f}}^B(\mathbf{x}, s) \cdot \hat{\mathbf{v}}^A(\mathbf{x}, s) - \hat{p}^B(\mathbf{x}, s) \hat{q}^A(\mathbf{x}, s) \right] dV \end{aligned} \quad (5.55)$$

where \mathbf{n} is a unit vector normal to the boundary $\partial \mathcal{D}$. This form of the reciprocity theorem holds in the whole of domain \mathcal{D} even in the presence of acoustically impenetrable parts or other penetrable objects by virtue of explicit or implicit continuity conditions on the field quantities along the boundaries. In addition the LHS vanishes when the boundary $\partial \mathcal{D}$ coincides with the boundary of an acoustically impenetrable object or the domain \mathcal{D} is unbounded and the radiation conditions at infinity are satisfied.

5.4.3 The Direct Source Problem

The reciprocity theorem expressed in equation (5.55.) can be applied to the problem of determining the acoustic field quantities in a medium of given physical properties $\{\xi, \hat{\eta}\} = \{\xi(\mathbf{x}, s), \hat{\eta}(\mathbf{x}, s)\}$ produced by a given source distribution $\{\hat{q}, \hat{f}\} = \{\hat{q}(\mathbf{x}, s), \hat{f}(\mathbf{x}, s)\}$. This problem is generally referred to as the *direct source problem*.

We consider a domain \mathcal{D} , unbounded or bounded with acoustically impenetrable boundary $\partial\mathcal{D}$ as defined in section §5.4.1. The source distribution has support in a subdomain $\mathcal{I} \subseteq \mathcal{D}$.

We set the state A as the state generated by the source distribution

$$\begin{cases} \{\hat{p}^A, \hat{v}^A\} = \{\hat{p}(\mathbf{x}, s), \hat{v}(\mathbf{x}, s)\} & \mathbf{x} \in \mathcal{D} \\ \{\hat{q}^A, \hat{f}^A\} = \{\hat{q}(\mathbf{x}, s), \hat{f}(\mathbf{x}, s)\} & \mathbf{x} \in \mathcal{I} \\ \{\xi^A, \hat{\eta}^A\} = \{\xi(\mathbf{x}, s), \hat{\eta}(\mathbf{x}, s)\} & \mathbf{x} \in \mathcal{D} \end{cases} \quad (5.56)$$

The state B is calculated from the application of equation (5.55.). If we choose the fluid B to be the adjoint of the fluid in state A, only the last four terms in the RHS of the equation are relevant. In addition, we can separate the calculation of the field quantities in state B by choosing an appropriate source distribution.

We start by choosing:

$$\begin{cases} \{\hat{p}^B, \hat{v}^B\} = \{\hat{p}^{\hat{q}^B}(\mathbf{x}, \mathbf{x}', s), \hat{v}^{\hat{q}^B}(\mathbf{x}, \mathbf{x}', s)\} \\ \{\hat{q}^B, \hat{f}^B\} = \{\hat{a}(s)\delta(\mathbf{x} - \mathbf{x}'), 0\} \\ \{\xi^B, \hat{\eta}^B\} = \{\xi(\mathbf{x}, s), \hat{\eta}(\mathbf{x}, s)\} \end{cases} \quad (5.57)$$

where $\hat{q}^B(\mathbf{x}, \mathbf{x}', s) = \hat{a}(s)\delta(\mathbf{x} - \mathbf{x}')$ is a point source of volume injection in the point \mathbf{x}' acting on the point \mathbf{x} and $\hat{a}(s)$ is an arbitrary scalar function of s .

Inserting relations (5.56.) and (5.57.) in equation (5.55.) and rearranging the terms to isolate the pressure distribution \hat{p} we obtain:

$$\hat{a}(s)\hat{p}(\mathbf{x}', s) = \int_{\mathbf{x} \in \mathcal{V}} \left[\hat{p}^{\hat{q}^B}(\mathbf{x}, \mathbf{x}', s) \hat{q}(\mathbf{x}, s) - \hat{\mathbf{v}}^{\hat{q}^B}(\mathbf{x}, \mathbf{x}', s) \cdot \hat{\mathbf{f}}(\mathbf{x}, s) \right] dV \quad \mathbf{x}' \in \mathcal{D} \quad (5.58)$$

Now, remembering the definition of Green's functions (5.24.) and (5.25.) and inserting them into equation (5.55.), we obtain (see Appendix F for the details):

$$\hat{p}(\mathbf{x}', s) = \int_{\mathbf{x} \in \mathcal{V}} \left[\hat{G}^{\hat{p}\hat{q}}(\mathbf{x}', \mathbf{x}, s) \hat{q}(\mathbf{x}, s) + \hat{G}^{\hat{p}\hat{f}}(\mathbf{x}', \mathbf{x}, s) \cdot \hat{\mathbf{f}}(\mathbf{x}, s) \right] dV \quad \mathbf{x}' \in \mathcal{D} \quad (5.59)$$

The two Green's function $\hat{G}^{\hat{p}\hat{q}}$ and $\hat{G}^{\hat{p}\hat{f}}$ are respectively the acoustic pressure generated in the point \mathbf{x}' by a point source of volume injection at the point \mathbf{x} and the acoustic pressure generated in the point \mathbf{x}' by a point source of volume force at the point \mathbf{x} .

In the same way, we choose now:

$$\begin{cases} \{\hat{p}^B, \hat{\mathbf{v}}^B\} = \{\hat{p}^{\hat{f}^B}(\mathbf{x}, \mathbf{x}', s), \hat{\mathbf{v}}^{\hat{f}^B}(\mathbf{x}, \mathbf{x}', s)\} \\ \{\hat{q}^B, \hat{\mathbf{f}}^B\} = \{0, \hat{b}(s)\delta(\mathbf{x} - \mathbf{x}')\} \\ \{\hat{\xi}^B, \hat{\eta}^B\} = \{\hat{\xi}(\mathbf{x}, s), \hat{\eta}(\mathbf{x}, s)\} \end{cases} \quad (5.60)$$

where $\hat{\mathbf{f}}^B(\mathbf{x}, \mathbf{x}', s) = \hat{\mathbf{b}}(s)\delta(\mathbf{x} - \mathbf{x}')$ is a point source of volume force in the point \mathbf{x}' acting on the point \mathbf{x} and $\hat{\mathbf{b}}(s)$ is an arbitrary vector function of s .

Inserting relations (5.56.) and (5.60.) in equation (5.55.) and rearranging the terms to isolate the fluid velocity $\hat{\mathbf{v}}$ we obtain:

$$\hat{\mathbf{b}}(s) \cdot \hat{\mathbf{v}}(\mathbf{x}', s) = \int_{\mathbf{x} \in \mathcal{V}} \left[\hat{p}^{\hat{\mathbf{f}}^B}(\mathbf{x}, \mathbf{x}', s) \hat{q}(\mathbf{x}, s) + \hat{\mathbf{v}}^{\hat{\mathbf{f}}^B}(\mathbf{x}, \mathbf{x}', s) \cdot \hat{\mathbf{f}}(\mathbf{x}, s) \right] dV \quad \mathbf{x}' \in \mathcal{D} \quad (5.61)$$

Now, remembering the definition of Green's functions (5.24.) and (5.25.) and inserting them into equation (5.55.), we obtain (see Appendix F for the details):

$$\hat{\mathbf{v}}(\mathbf{x}', s) = \int_{\mathbf{x} \in \mathcal{V}} \left[\hat{\mathbf{G}}^{\hat{\mathbf{v}}\hat{q}}(\mathbf{x}', \mathbf{x}, s) \hat{q}(\mathbf{x}, s) + \hat{\mathbf{G}}^{\hat{\mathbf{v}}\hat{\mathbf{f}}}(\mathbf{x}', \mathbf{x}, s) \hat{\mathbf{f}}(\mathbf{x}, s) \right] dV \quad \mathbf{x}' \in \mathcal{D} \quad (5.62)$$

The two Green's function $\hat{\mathbf{G}}^{\hat{\mathbf{v}}\hat{q}}$ and $\hat{\mathbf{G}}^{\hat{\mathbf{v}}\hat{\mathbf{f}}}$ are respectively the particle velocity generated in the point \mathbf{x}' by a point source of volume injection at the point \mathbf{x} and the acoustic pressure generated in the point \mathbf{x}' by a point source of volume force at the point \mathbf{x} .

5.4.4 The Direct Scattering Problem

The reciprocity theorem expressed in equation (5.55.) is now applied to the problem of determining the acoustic field quantities in a medium of given physical properties $\{\hat{\xi}, \hat{\eta}\} = \{\hat{\xi}(\mathbf{x}, s), \hat{\eta}(\mathbf{x}, s)\}$, called the *embedding*, produced by a given source distribution $\{\hat{q}, \hat{\mathbf{f}}\} = \{\hat{q}(\mathbf{x}, s), \hat{\mathbf{f}}(\mathbf{x}, s)\}$ when an acoustically penetrable object, called the *scatterer*, is present. This problem is generally referred to as the *direct scattering problem*.

We consider a bounded or unbounded domain \mathcal{D} with boundary $\partial\mathcal{D}$ as defined in section §5.4.1. The source distribution has support in a subdomain $\mathcal{I} \subset \mathcal{D}$, whereas the scatterer occupies a subdomain $\mathcal{B} \subset \mathcal{D}$ with $\mathcal{B} \cap \mathcal{I} = \emptyset$.

We can express the total acoustic field present in this configuration as the superposition of an incident field generated by the given source distribution in the absence of the scatterer and a scattered field generated by the presence of the scatterer:

$$\begin{cases} \{\hat{p}^i, \hat{v}^i\} = \{\hat{p}^i(\mathbf{x}, s), \hat{v}^i(\mathbf{x}, s)\} \\ \{\hat{p}^s, \hat{v}^s\} = \{\hat{p}^s(\mathbf{x}, s), \hat{v}^s(\mathbf{x}, s)\} \\ \{\hat{p}, \hat{v}\} = \{\hat{p}^i(\mathbf{x}, s) + \hat{p}^s(\mathbf{x}, s), \hat{v}^i(\mathbf{x}, s) + \hat{v}^s(\mathbf{x}, s)\} \end{cases} \quad \mathbf{x} \in \mathcal{D} \quad (5.63)$$

The scatterer shows a finite contrast in the physical properties with respect to the fluid medium in the subdomain \mathcal{B} , whereas the contrast is zero outside the subdomain \mathcal{B} :

$$\{\hat{\zeta}^s - \hat{\zeta}, \hat{\eta}^s - \hat{\eta}\} = \{0, 0\} \quad \mathbf{x} \in (\mathcal{D} - \mathcal{B}) \quad (5.64)$$

The incident acoustic field is calculated by application of equations (5.59.) and (5.62) to the given source distribution and it's considered known. Since there are no sources in the subdomain \mathcal{B} occupied by the scatterer and the total and incident acoustic fields are generated only by the sources in the subdomain \mathcal{I} , we can write the following relationships:

$$\begin{cases} \nabla \hat{p} + \hat{\zeta}^s \hat{v} = 0 \\ \text{div } \hat{v} + \hat{\eta}^s \hat{p} = 0 \end{cases} \quad \mathbf{x} \in \mathcal{B} \quad (5.65)$$

and

$$\begin{cases} \nabla \hat{p}^i + \hat{\zeta} \hat{\mathbf{v}}^i = 0 \\ \operatorname{div} \hat{\mathbf{v}}^i + \hat{\eta} \hat{p}^i = 0 \end{cases} \quad \mathbf{x} \in \mathcal{B} \quad (5.66)$$

Inserting equations (5.65.) and (5.66.) in the expression of the total acoustic field equation (5.63.), we obtain the following expression for the scattered acoustic field:

$$\begin{cases} \nabla \hat{p}^s + \hat{\zeta} \hat{\mathbf{v}}^s = -(\hat{\zeta}^s - \hat{\zeta}) \hat{\mathbf{v}} = \hat{\mathbf{f}}^s \\ \operatorname{div} \hat{\mathbf{v}}^s + \hat{\eta} \hat{p}^s = -(\hat{\eta}^s - \hat{\eta}) \hat{p} = \hat{q}^s \end{cases} \quad \mathbf{x} \in \mathcal{B} \quad (5.67)$$

Equations (5.67.) can be given a physical meaning by observing that the scattered acoustic field is generated by injection sources \hat{q}^s and force sources $\hat{\mathbf{f}}^s$ produced by the contrast of physical properties. In addition, since both the incident field and the total field are generated by the source distribution in the subdomain \mathcal{I} , the scattered field is necessarily source free in this subdomain. It follows:

$$\begin{cases} \nabla \hat{p}^s + \hat{\zeta} \hat{\mathbf{v}}^s = \hat{\mathbf{f}} \\ \operatorname{div} \hat{\mathbf{v}}^s + \hat{\eta} \hat{p}^s = \hat{q} \end{cases} \quad \mathbf{x} \in \mathcal{D} \quad (5.68)$$

where

$$\begin{cases} \hat{\mathbf{f}} = 0 & \mathbf{x} \in (\mathcal{D} - \mathcal{B}) \\ \hat{\mathbf{f}} = -(\hat{\zeta}^s - \hat{\zeta})\hat{\mathbf{v}} & \mathbf{x} \in \mathcal{B} \end{cases} \quad (5.69)$$

$$\begin{cases} \hat{q} = 0 & \mathbf{x} \in (\mathcal{D} - \mathcal{B}) \\ \hat{q} = -(\hat{\eta}^s - \hat{\eta})\hat{p} & \mathbf{x} \in \mathcal{B} \end{cases}$$

Finally, by using sources (5.69.) to find the generated scattered field by application of equations (5.59.) and (5.62.) for the direct source problem, we arrive at the system of integral equations:

$$\begin{cases} \hat{p}^s(\mathbf{x}', s) = \int_{\mathbf{x} \in \mathcal{B}} [\hat{G}^{\hat{p}\hat{q}}(\mathbf{x}', \mathbf{x}, s) \hat{q}^s(\mathbf{x}, s) + \hat{G}^{\hat{p}\hat{f}}(\mathbf{x}', \mathbf{x}, s) \cdot \hat{\mathbf{f}}^s(\mathbf{x}, s)] dV & \mathbf{x}' \in \mathcal{D} \\ \hat{\mathbf{v}}^s(\mathbf{x}', s) = \int_{\mathbf{x} \in \mathcal{B}} [\hat{G}^{\hat{v}\hat{q}}(\mathbf{x}', \mathbf{x}, s) \hat{q}^s(\mathbf{x}, s) + \hat{G}^{\hat{v}\hat{f}}(\mathbf{x}', \mathbf{x}, s) \hat{\mathbf{f}}^s(\mathbf{x}, s)] dV & \mathbf{x}' \in \mathcal{D} \\ \hat{\mathbf{f}}^s = -(\hat{\zeta}^s - \hat{\zeta})(\hat{\mathbf{v}}^i + \hat{\mathbf{v}}^s) & \mathbf{x} \in \mathcal{B} \\ \hat{q}^s = -(\hat{\eta}^s - \hat{\eta})(\hat{p}^i + \hat{p}^s) & \mathbf{x} \in \mathcal{B} \end{cases} \quad (5.70)$$

System (5.70.) can be solved for the four unknowns $\hat{p}^s, \hat{\mathbf{v}}^s, \hat{\mathbf{f}}^s$ and \hat{q}^s , generally by application of numerical methods. An approximate analytical solution for a geometrical configuration similar to the one analysed in this research will be investigated in the next section.

5.4.5 The Equivalent Surface Source Representation

We consider now the same case as for the direct source problem, but applied to a subdomain \mathcal{B} in the domain \mathcal{D} (eventually coincident with the whole of the Euclidean space \mathbb{R}^3). The subdomain \mathcal{B} has the acoustically penetrable surface boundary $\partial\mathcal{B}$. In this case, the contribution from the LHS of eq. (5.55) doesn't vanish.

If we repeat the same steps as for the direct source problem and retain the contribution from the surface integral in eq. (5.55), we are lead to the following expressions for the acoustic wave field in the domain \mathfrak{B} (De Hoop 1995):

$$\begin{aligned} \chi_{\mathfrak{B}}(\mathbf{x}')\hat{p}(\mathbf{x}', s) = & \int_{\mathbf{x} \in \mathfrak{B}} \left[\hat{G}^{\hat{p}\hat{q}}(\mathbf{x}', \mathbf{x}, s)\hat{q}(\mathbf{x}, s) + \hat{G}^{\hat{p}\hat{f}}(\mathbf{x}', \mathbf{x}, s) \cdot \hat{f}(\mathbf{x}, s) \right] dV + \\ & - \int_{\mathbf{x} \in \partial\mathfrak{B}} \left[\hat{G}^{\hat{p}\hat{q}}(\mathbf{x}', \mathbf{x}, s)\hat{v}(\mathbf{x}, s) \cdot \mathbf{n} + \hat{G}^{\hat{p}\hat{f}}(\mathbf{x}', \mathbf{x}, s) \cdot \hat{p}(\mathbf{x}, s)\mathbf{n} \right] dA \quad \mathbf{x}' \in \mathcal{D} \end{aligned} \quad (5.71)$$

and

$$\begin{aligned} \chi_{\mathfrak{B}}(\mathbf{x}')\hat{v}(\mathbf{x}', s) = & \int_{\mathbf{x} \in \mathfrak{B}} \left[\hat{G}^{\hat{v}\hat{q}}(\mathbf{x}', \mathbf{x}, s)\hat{q}(\mathbf{x}, s) + \hat{G}^{\hat{v}\hat{f}}(\mathbf{x}', \mathbf{x}, s)\hat{f}(\mathbf{x}, s) \right] dV \\ & - \int_{\mathbf{x} \in \partial\mathfrak{B}} \left[\hat{G}^{\hat{v}\hat{q}}(\mathbf{x}', \mathbf{x}, s)[\hat{v}(\mathbf{x}, s) \cdot \mathbf{n}] + \hat{G}^{\hat{v}\hat{f}}(\mathbf{x}', \mathbf{x}, s)\hat{p}(\mathbf{x}, s)\mathbf{n} \right] dA \quad \mathbf{x}' \in \mathcal{D} \end{aligned} \quad (5.72)$$

where \mathbf{n} is the normal to the boundary $\partial\mathfrak{B}$ pointing outside \mathfrak{B} ,

$\chi_{\mathfrak{B}}(\mathbf{x}') = \left\{ 1, \frac{1}{2}, 0 \right\}$ for $\mathbf{x}' \in \{\mathfrak{B}, \partial\mathfrak{B}, \mathfrak{B}'\}$ is the characteristic function of the set \mathfrak{B} and

$\mathfrak{B}' = \mathcal{D} - (\mathfrak{B} \cup \partial\mathfrak{B})$ is the complement of the set \mathfrak{B} .

Finally, if we apply this reciprocity theorem to the subdomain \mathfrak{B}' when the sources that generate the acoustic field are in \mathfrak{B} , we have the expressions:

$$\chi_{\mathfrak{B}'}(\mathbf{x}')\hat{p}(\mathbf{x}', s) = \int_{\mathbf{x} \in \partial\mathfrak{B}} \left[\hat{G}^{\hat{p}\hat{q}}(\mathbf{x}', \mathbf{x}, s)\hat{v}(\mathbf{x}, s) \cdot \mathbf{n} + \hat{G}^{\hat{p}\hat{f}}(\mathbf{x}', \mathbf{x}, s) \cdot \hat{p}(\mathbf{x}, s)\mathbf{n} \right] dA \quad \mathbf{x}' \in \mathcal{D} \quad (5.73)$$

and

$$\chi_{\mathcal{B}}(\mathbf{x}')\hat{\mathbf{v}}(\mathbf{x}', s) = \int_{\mathbf{x} \in \partial\mathcal{B}} \left[\hat{\mathbf{G}}^{\hat{\mathbf{v}}\hat{\mathbf{q}}}(\mathbf{x}', \mathbf{x}, s) [\hat{\mathbf{v}}(\mathbf{x}, s) \cdot \mathbf{n}] + \hat{\mathbf{G}}^{\hat{\mathbf{v}}\hat{\mathbf{p}}}(\mathbf{x}', \mathbf{x}, s) \hat{p}(\mathbf{x}, s) \mathbf{n} \right] dA \quad \mathbf{x}' \in \mathcal{D} \quad (5.74)$$

Eqs. (5.73) and (5.74) are the equivalent surface source representations of the direct source problem in the complex frequency-domain. These equations are equivalent to eqs. (5.59) and (5.62) respectively. They are the starting point for the derivation of the boundary-element formulation of the Helmholtz equation for radiation and scattering problems. In particular eq. (5.73) will be used in Chapter 6 to derive the numerical solution to the direct scattering problem from the viscoelastic anechoic tile.

5.5 Plane Wave Scattering from a Penetrable, Wedged, Bounded Baffle in a Fluid Embedding

5.5.1 Problem Configuration

We consider a lossless, isotropic, homogenous embedding in the domain $\mathcal{D} = \mathbb{R}^3$. The material properties of the embedding are represented by its density ρ and its compressibility κ . A penetrable scatterer is immersed in the embedding and occupies the domain $\mathcal{B} \subset \mathcal{D}$ with boundary surface $\partial\mathcal{B}$ and material properties $\{\zeta^s, \eta^s\} = \{\zeta^s(\mathbf{x}, s), \eta^s(\mathbf{x}, s)\}$.

The total acoustic field is given by the superposition of the scattered field and the incident field. The incident field is given by an acoustic plane wave (see equation (5.41.) and (5.46.)) travelling in the direction of the unit vector $\hat{\alpha}$ with normalised pulse shape $\hat{a}(s)$.

$$\begin{cases} \hat{p}^i = \hat{P}\hat{a}(s)e^{-\frac{s}{c}\mathbf{a}\cdot\mathbf{x}} \\ \hat{\mathbf{v}}^i = \hat{V}\hat{a}(s)e^{-\frac{s}{c}\mathbf{a}\cdot\mathbf{x}} \end{cases} \quad (5.75)$$

The scattered field is given by the contrast source representation equation (5.70.):

$$\begin{cases} \hat{p}^s(\mathbf{x}', s) = \int_{\mathbf{x} \in \mathcal{B}} [\hat{G}^{\hat{p}\hat{q}}(\mathbf{x}', \mathbf{x}, s) \hat{q}^s(\mathbf{x}, s) + \hat{G}^{\hat{p}\hat{f}}(\mathbf{x}', \mathbf{x}, s) \cdot \hat{\mathbf{f}}^s(\mathbf{x}, s)] dV & \mathbf{x}' \in \mathcal{D} \\ \hat{\mathbf{v}}^s(\mathbf{x}', s) = \int_{\mathbf{x} \in \mathcal{B}} [\hat{G}^{\hat{\mathbf{v}}\hat{q}}(\mathbf{x}', \mathbf{x}, s) \hat{q}^s(\mathbf{x}, s) + \hat{G}^{\hat{\mathbf{v}}\hat{f}}(\mathbf{x}', \mathbf{x}, s) \hat{\mathbf{f}}^s(\mathbf{x}, s)] dV & \mathbf{x}' \in \mathcal{D} \\ \hat{\mathbf{f}}^s = -(\hat{\zeta}^s - s\rho\delta)(\hat{\mathbf{v}}^i + \hat{\mathbf{v}}^s) & \mathbf{x} \in \mathcal{B} \\ \hat{q}^s = -(\hat{\eta}^s - s\kappa)(\hat{p}^i + \hat{p}^s) & \mathbf{x} \in \mathcal{B} \end{cases} \quad (5.76)$$

where the corresponding contrast source distributions in the domain $\mathcal{B} \subset \mathcal{D}$ are given by equations (5.69.) by substitution of the material properties of the fluid embedding.

Finally, in the far-field region equations (5.76.) can be approximated by their far-field expansions (see Appendix F), which give:

$$\begin{cases} \hat{p}^s(\mathbf{x}', s) = \hat{p}^{s\infty}(\boldsymbol{\xi}, s) \frac{e^{-\frac{s}{c}|\mathbf{x}'|}}{4\pi|\mathbf{x}'|} \left(1 + O(|\mathbf{x}'|^{-1})\right) & \mathbf{x}' \in \mathcal{D}, \quad |\mathbf{x}'| \rightarrow \infty, \quad \mathbf{x}' = |\mathbf{x}'|\boldsymbol{\xi} \\ \hat{\mathbf{v}}^s(\mathbf{x}', s) = \hat{\mathbf{v}}^{s\infty}(\boldsymbol{\xi}, s) \frac{e^{-\frac{s}{c}|\mathbf{x}'|}}{4\pi|\mathbf{x}'|} \left(1 + O(|\mathbf{x}'|^{-1})\right) & \mathbf{x}' \in \mathcal{D}, \quad |\mathbf{x}'| \rightarrow \infty, \quad \mathbf{x}' = |\mathbf{x}'|\boldsymbol{\xi} \\ \hat{\mathbf{f}}^s = -(\hat{\zeta}^s - s\rho\delta)(\hat{\mathbf{v}}^i + \hat{\mathbf{v}}^s) & \mathbf{x} \in \mathcal{B} \\ \hat{q}^s = -(\hat{\eta}^s - s\kappa)(\hat{p}^i + \hat{p}^s) & \mathbf{x} \in \mathcal{B} \end{cases} \quad (5.77)$$

with

$$\left\{ \begin{array}{l} \hat{p}^{s\infty} = s\rho\hat{\Phi}^{s\infty} + \frac{s}{c}\xi \cdot \Psi^{s\infty} \\ \hat{v}^{s\infty} = (\rho c)^{-1} \xi \hat{p}^{s\infty} \\ \hat{\Phi}^{s\infty}(\xi, s) = \int_{\mathbf{x}' \in \mathcal{B}} \hat{q}^s(\mathbf{x}, s) e^{\frac{s}{c}\xi \cdot \mathbf{x}} dV \\ \hat{\Psi}^{s\infty}(\xi, s) = \int_{\mathbf{x}' \in \mathcal{B}} \hat{f}^s(\mathbf{x}, s) e^{\frac{s}{c}\xi \cdot \mathbf{x}} dV \end{array} \right. \quad (5.78)$$

5.5.2 Far-Field Plane Wave Scattering from an Anechoic Tile by Rayleigh-Gans-Born Approximation

The scattering configuration outlined in the previous section can be used to find an approximate solution to the scattering problem from simple geometrical shapes and their superposition. The method presented here has been previously investigated by Quak *et al.* (1986), but it's applied here for the first time to the anechoic tile configuration.

The method consists in finding an analytical solution to the scattering problem by an iterative procedure called the Neumann expansion. We start by considering the explicit form of the total scattered field derived from equations (5.76.):

$$\left\{ \begin{array}{l} \hat{p}(\mathbf{x}', s) = \hat{p}^i(\mathbf{x}', s) - \int_{\mathbf{x} \in \mathcal{B}} \left\{ \hat{G}^{\hat{p}\hat{q}}(\mathbf{x}', \mathbf{x}, s) [\hat{\eta}^s(\mathbf{x}, s) - s\kappa] \hat{p}(\mathbf{x}, s) + \right. \\ \quad \left. + \hat{G}^{\hat{p}\hat{f}}(\mathbf{x}', \mathbf{x}, s) [\hat{\zeta}^s(\mathbf{x}, s) - s\rho\delta] \hat{v}(\mathbf{x}, s) \right\} dV \quad \mathbf{x}' \in \mathcal{D} \\ \hat{v}(\mathbf{x}', s) = \hat{v}^i(\mathbf{x}', s) - \int_{\mathbf{x} \in \mathcal{B}} \left\{ \hat{G}^{\hat{v}\hat{q}}(\mathbf{x}', \mathbf{x}, s) [\hat{\eta}^s(\mathbf{x}, s) - s\kappa] \hat{p}(\mathbf{x}, s) + \right. \\ \quad \left. + \hat{G}^{\hat{v}\hat{f}}(\mathbf{x}', \mathbf{x}, s) [\hat{\zeta}^s(\mathbf{x}, s) - s\rho\delta] \hat{v}(\mathbf{x}, s) \right\} dV \quad \mathbf{x}' \in \mathcal{D} \end{array} \right. \quad (5.79)$$

Equations (5.79.) constitute a system of linear integral equations of the second kind in the two unknown \hat{p} and \hat{v} . The iterative procedure is initialised by setting:

$$\begin{cases} \hat{p}^{[0]}(\mathbf{x}', s) = \hat{p}^i(\mathbf{x}', s) & \mathbf{x}' \in \mathcal{D} \\ \hat{v}^{[0]}(\mathbf{x}', s) = \hat{v}^i(\mathbf{x}', s) & \mathbf{x}' \in \mathcal{D} \end{cases} \quad (5.80)$$

whereas the $(n+1)^{\text{st}}$ recursive term of the expansion is given by

$$\begin{cases} \hat{p}^{[n+1]}(\mathbf{x}', s) = - \int_{\mathbf{x} \in \mathcal{R}} \left\{ \hat{G}^{\hat{p}\hat{q}}(\mathbf{x}', \mathbf{x}, s) [\hat{\eta}^s(\mathbf{x}, s) - s\kappa] \hat{p}^{[n]}(\mathbf{x}, s) + \right. \\ \quad \left. + \hat{G}^{\hat{p}\hat{f}}(\mathbf{x}', \mathbf{x}, s) [\hat{\zeta}^s(\mathbf{x}, s) - s\rho\delta] \hat{v}^{[n]}(\mathbf{x}, s) \right\} dV & \mathbf{x}' \in \mathcal{D} \\ \hat{v}^{[n+1]}(\mathbf{x}', s) = - \int_{\mathbf{x} \in \mathcal{R}} \left\{ \hat{G}^{\hat{v}\hat{q}}(\mathbf{x}', \mathbf{x}, s) [\hat{\eta}^s(\mathbf{x}, s) - s\kappa] \hat{p}^{[n]}(\mathbf{x}, s) + \right. \\ \quad \left. + \hat{G}^{\hat{v}\hat{f}}(\mathbf{x}', \mathbf{x}, s) [\hat{\zeta}^s(\mathbf{x}, s) - s\rho\delta] \hat{v}^{[n]}(\mathbf{x}, s) \right\} dV & \mathbf{x}' \in \mathcal{D} \end{cases} \quad n = 0, 1, 2, \dots \quad (5.81)$$

It can be shown (Quak *et al.*, 1986) that, if the series are convergent, then the solution to the scattering problem is given by:

$$\begin{cases} \hat{p}(\mathbf{x}', s) = \sum_{n=0}^{\infty} \hat{p}^{[n]}(\mathbf{x}', s) & \mathbf{x}' \in \mathcal{D} \\ \hat{v}(\mathbf{x}', s) = \sum_{n=0}^{\infty} \hat{v}^{[n]}(\mathbf{x}', s) & \mathbf{x}' \in \mathcal{D} \end{cases} \quad (5.82)$$

The n^{th} term of the Neumann expansion is called the n^{th} Rayleigh-Gans-Born approximation.

We derive now the explicit analytic form of the first-order Rayleigh-Gans-Born approximation of the far-field scattering solution in the case of a harmonic plane wave incident on an anechoic tile. The geometrical configuration of the tile is represented in Fig. 5.1. It consists of the superposition of a square plate with a regular grid of circular cones of finite height. The scatterer is assumed homogenous and isotropic. The material behaviour is

approximated by an equivalent fluid model, whereby the isotropic inertia relaxation function $\hat{\mu}(s)$ is considered constant and equal to the mass density ρ and the coupling between compression and shear is neglected, so that the compressibility relaxation function $\hat{\chi}(s)$ can be written as the inverse of the viscoelastic bulk modulus $K^*(s)$. This behaviour is of course not exact, but it holds for the first-order approximation case.

In the case of butyl rubber, the frequency-dependent material properties have been determined in Chapter 4 (§4.7) and the coefficient of compressibility $\hat{\chi}(s)$ is plotted in Fig. 5.2 for $s = i\omega$. The scatterer is immersed in water, whose properties are given in Table 5.1.

Acoustic impedance and admittance per length ($s=i\omega$)			
Water		Butyl Rubber	
$\hat{\zeta}(s) = s\rho$	$\rho = 1\text{e}^3 \text{ kg m}^{-3}$	$\hat{\zeta}(s) = s\hat{\mu}(s)$	$\mu = \rho = 1.8\text{e}^3 \text{ kg m}^{-3}$
$\hat{\eta}(s) = s\kappa$	$\kappa = 4.45\text{e}^{-10} \text{ Pa}^{-1}$	$\hat{\eta}(s) = s\hat{\chi}(s)$	(see Fig. 5.2)

Table 5-1: Acoustic impedance and admittance per length

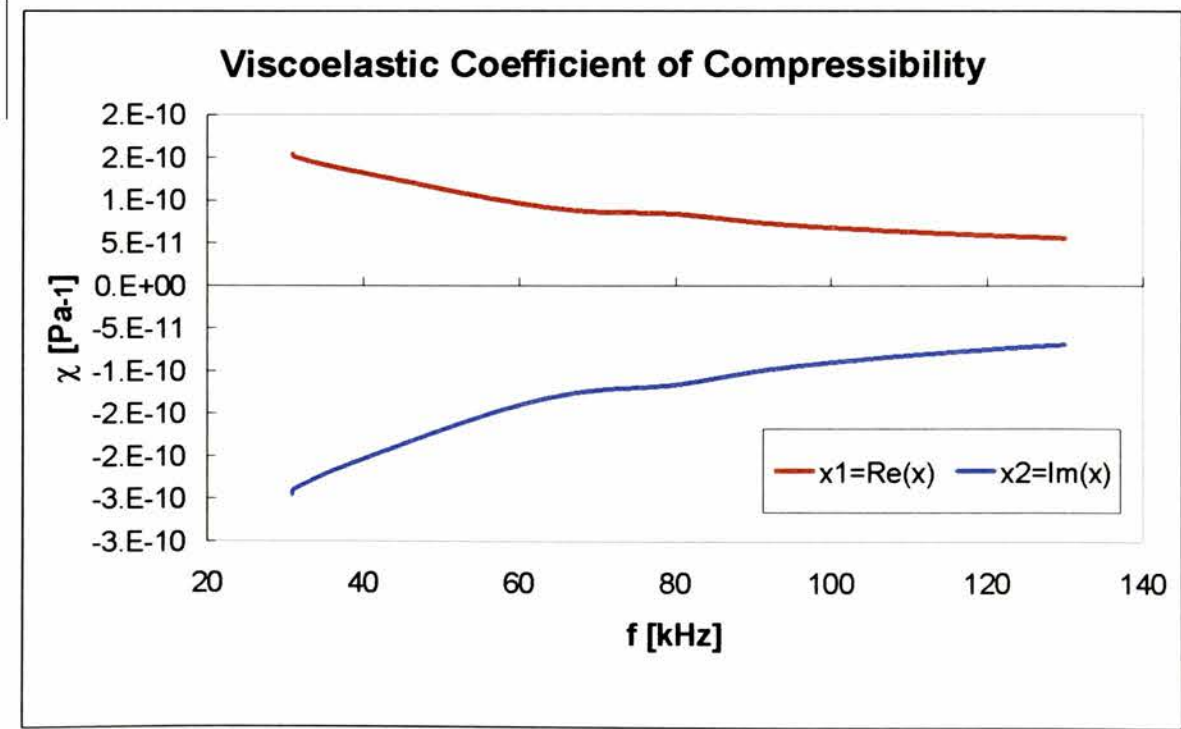


Fig. 5.1: Butyl rubber coefficient of compressibility, $\hat{\chi}(i\omega) = \hat{\chi}_1(\omega) + i\hat{\chi}_2(\omega)$

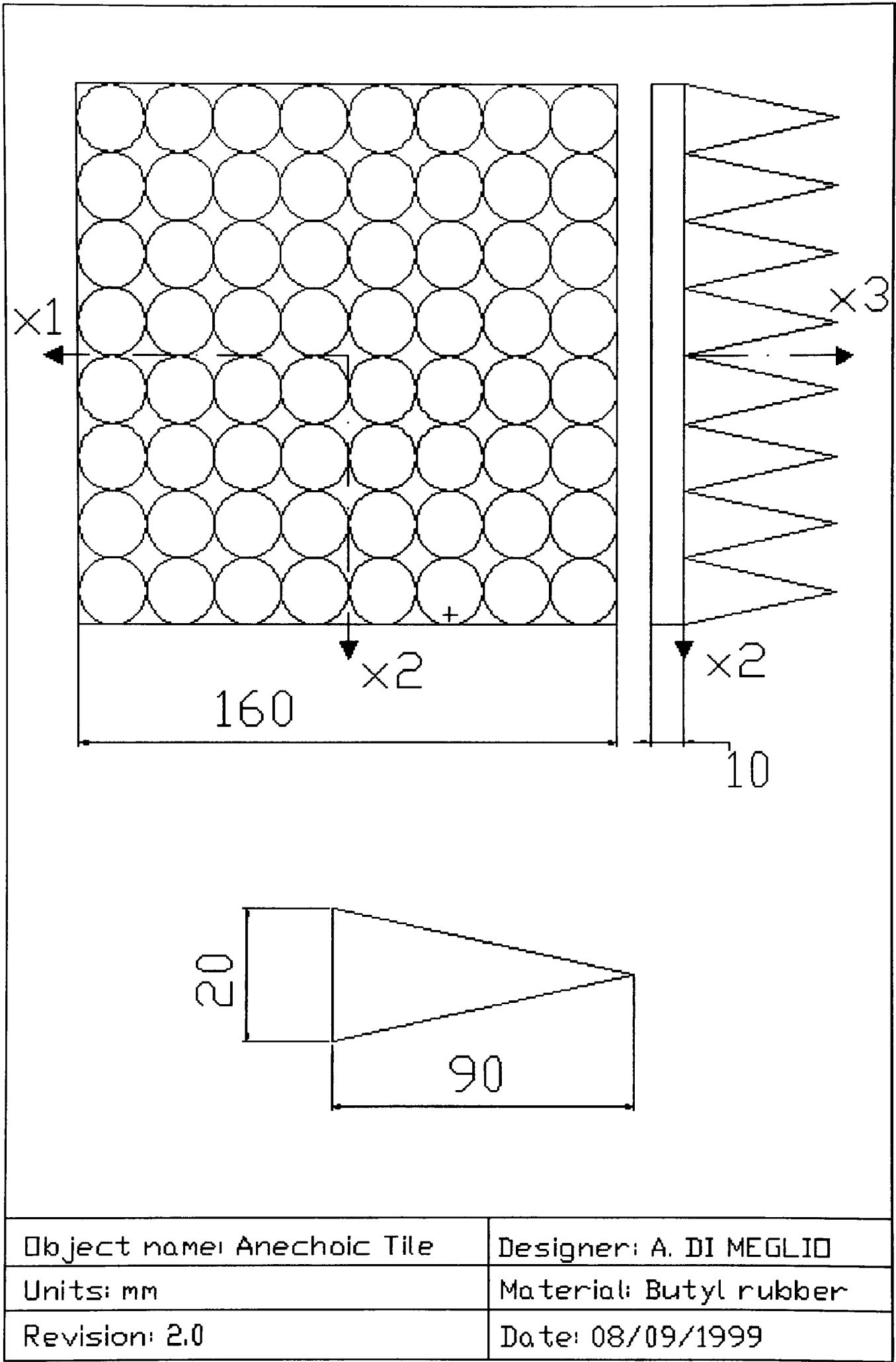


Fig. 5.2: Geometrical configuration of the anechoic tile

The expression for the scattered acoustic quantities in the far-field, first-order Rayleigh-Gans-Born approximation can be derived from equations (5.78.), (5.79.) and (5.80.) together with the plane wave equations (5.75.) (see Appendix F for the details):

$$\begin{cases} \hat{p}^{so}(\xi, s) = -Pc^{-2} \left[\hat{\lambda}^x \left(\frac{\xi}{c} - \frac{\alpha}{c}, s \right) + \xi^T \hat{\Lambda}^\mu \left(\frac{\xi}{c} - \frac{\alpha}{c}, s \right) \alpha \right] \\ \hat{v}^{so}(\xi, s) = (\rho c)^{-1} \hat{p}^{so}(\xi, s) \xi \end{cases} \quad (5.83)$$

where ξ is the direction of observation and α is the direction of propagation of the incident plane wave and

$$\begin{cases} \hat{\lambda}^x(\mathbf{u}, s) = s^2 \hat{a}(s) \left[\frac{\hat{\chi}(s)}{\kappa} - 1 \right] \hat{Y}(\mathbf{u}, s) \\ \hat{\Lambda}^\mu(\mathbf{u}, s) = s^2 \hat{a}(s) \left[\frac{\hat{\mu}(s)}{\rho} - 1 \right] \delta \hat{Y}(\mathbf{u}, s) \end{cases} \quad (5.84)$$

The term

$$\hat{Y}(\mathbf{u}, s) = \int_{\mathbf{x} \in \mathfrak{B}} e^{s\mathbf{u} \cdot \mathbf{x}} dV \quad (5.85)$$

is the *complex frequency-domain shape factor* of the domain \mathfrak{B} occupied by the scatterer.

The anechoic tile shape factor can be calculated by adding the shape factors of the single constituent parts, namely the rectangular plate and the cones. By integration of equation (5.85.) over the appropriate domains, we obtain (see Fig. 5.1):

Rectangular plate ($2a_1 \times 2a_2 \times 2a_3$)

$$\hat{Y}(\mathbf{u}, s) = 8a_1 a_2 a_3 \frac{\sinh(sa_1 u_1)}{sa_1 u_1} \frac{\sinh(sa_2 u_2)}{sa_2 u_2} \frac{\sinh(sa_3 u_3)}{sa_3 u_3} e^{s\mathbf{u} \cdot \mathbf{d}} \quad (5.86)$$

Circular cone ($r \times h$)

$$\hat{Y}(\mathbf{u}, s) = \frac{2\pi r h e^{s\mathbf{u} \cdot \mathbf{d}}}{s(u_1^2 + u_2^2)^{1/2}} \int_{\varphi=0}^{2\pi} \frac{1}{2\pi} \cos(\varphi) \left\{ \frac{e^{s[r(u_1^2 + u_2^2)^{1/2} \cos(\varphi) + hu_3]}}{s[r(u_1^2 + u_2^2)^{1/2} \cos(\varphi) + hu_3]} - \frac{e^{s[r(u_1^2 + u_2^2)^{1/2} \cos(\varphi) + hu_3]} - 1}{s^2[r(u_1^2 + u_2^2)^{1/2} \cos(\varphi) + hu_3]^2} \right\} d\varphi \quad (5.87)$$

where \mathbf{d} is a translation vector from the centre of the co-ordinate system to the reference centre of each constituent part and the integrals are evaluated at the reference centre of each part.

The far-field scattered acoustic quantities have been calculated using the MATLAB macro language and are plotted for various cases in Figs. 5.4 to 5.14. The incident field direction of propagation is $\boldsymbol{\alpha} = \{0, 0, -1\}$ in all graphs (which corresponds to the -90° direction) and the field is impinging on the cone tips. Graphs of the scattered pressure amplitude and of the normal and tangential components of the velocity amplitude are given for a number of frequencies in the range of interest. If not specified, the fields quantities are given in the plane $\{x_I=0\}$.

The effect of the grid of cones can be seen from Fig. 5.6. The backward scattered pressure amplitude is greatly reduced as compared to the simple plate configuration.

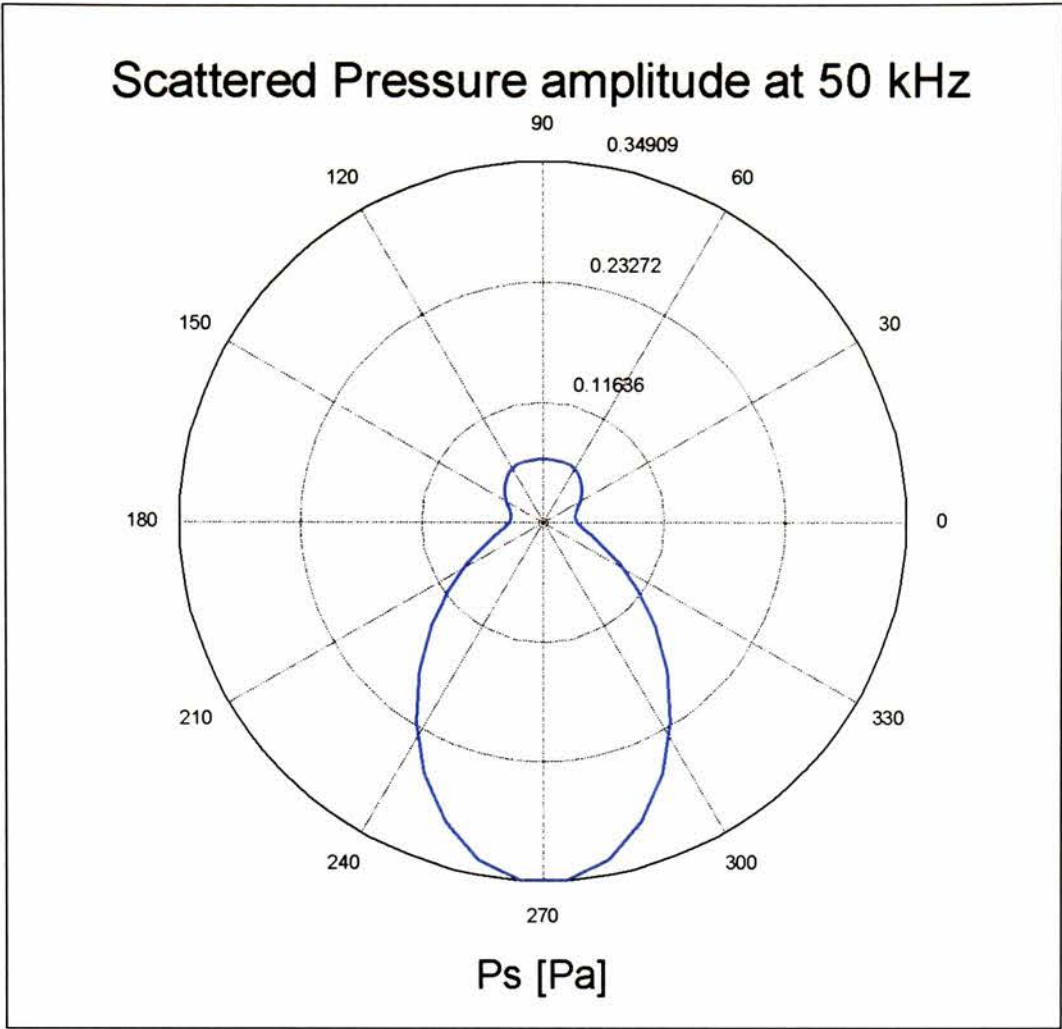


Fig. 5.3: Scattered pressure amplitude for the anechoic baffle at 50 kHz

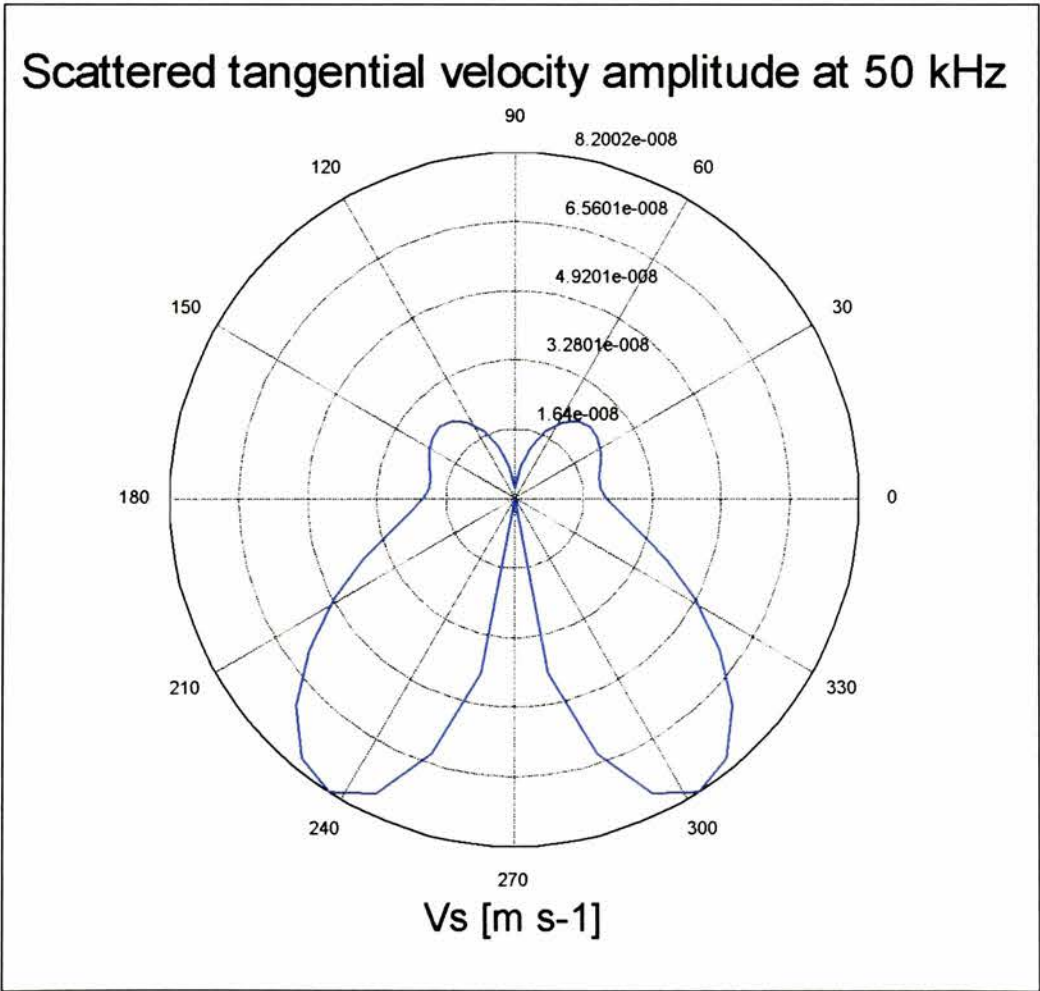


Fig. 5.4: Scattered tangential velocity amplitude for the anechoic baffle at 50 kHz

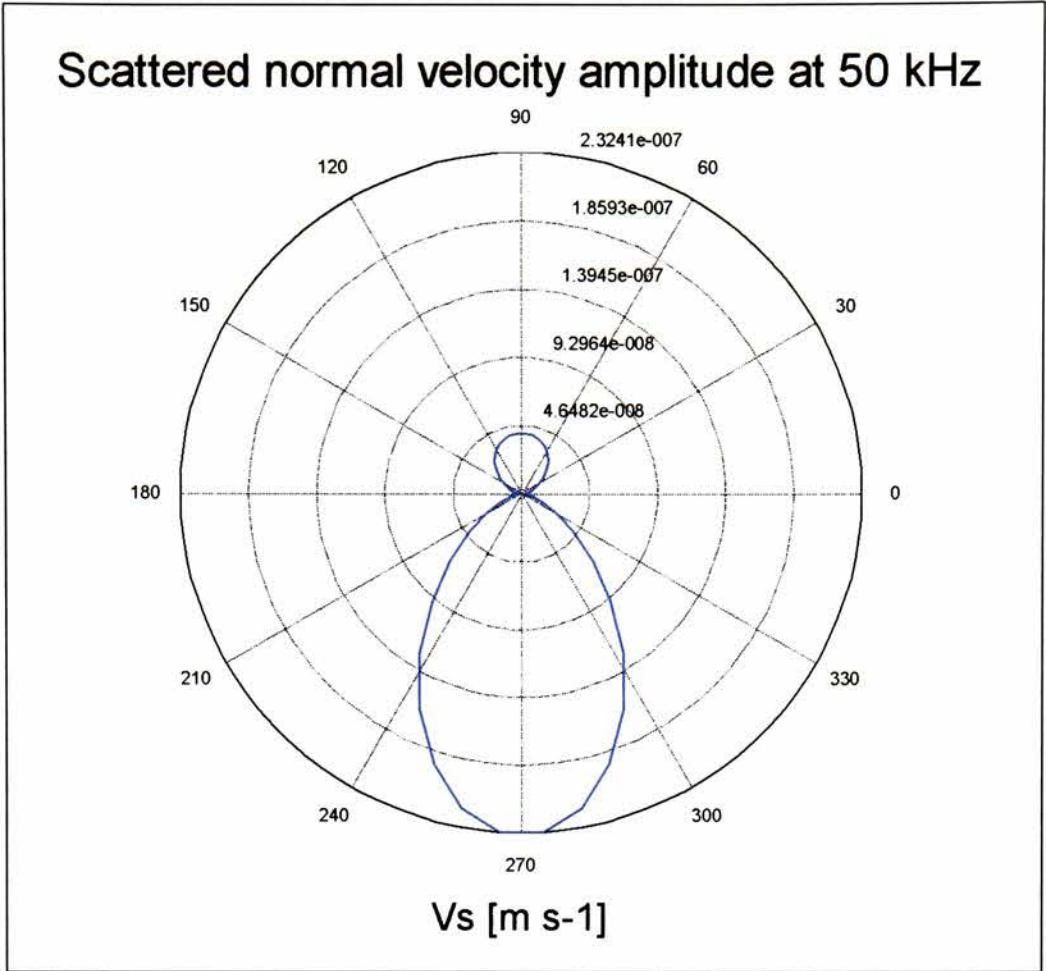


Fig. 5.5: Scattered normal velocity amplitude for the anechoic baffle at 50 kHz

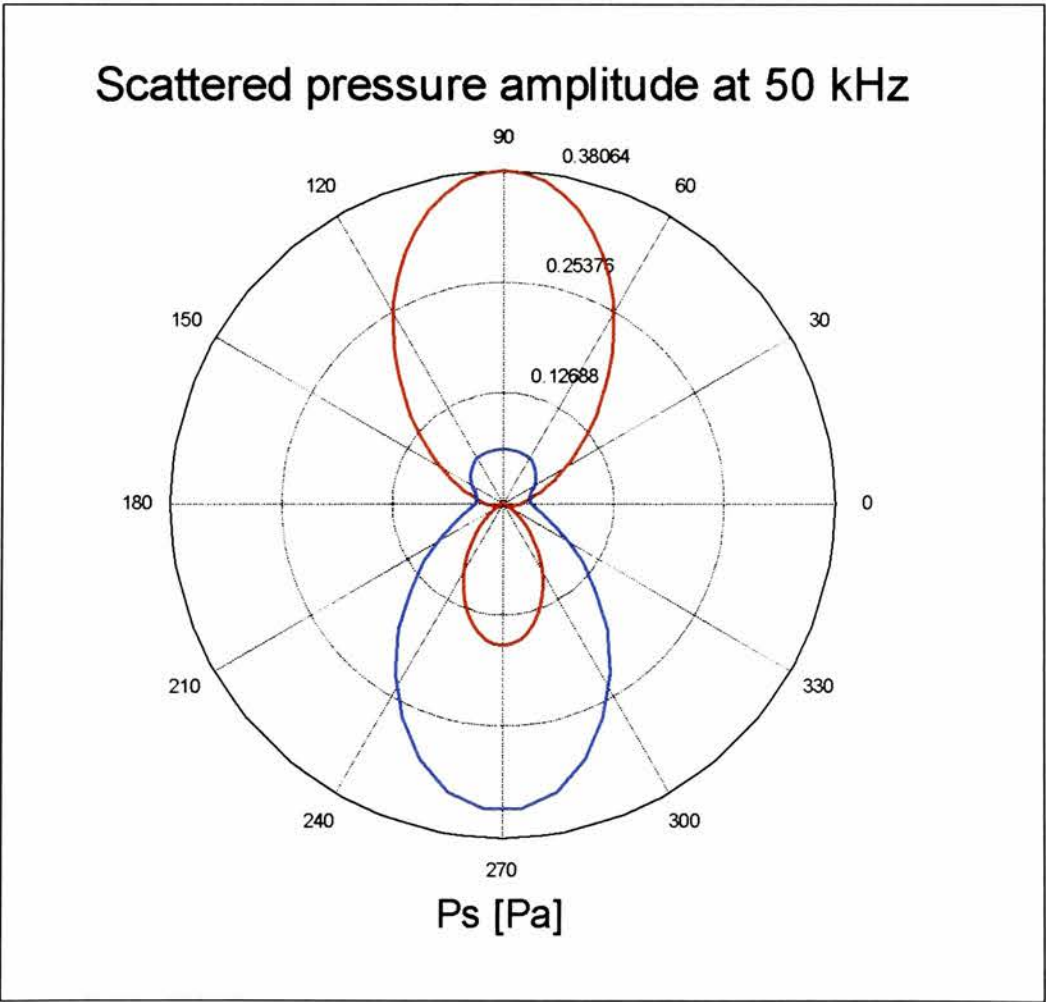


Fig. 5.6: Comparison of scattered pressure amplitude of the anechoic baffle (—) and a simple plate baffle (—) at 50 kHz

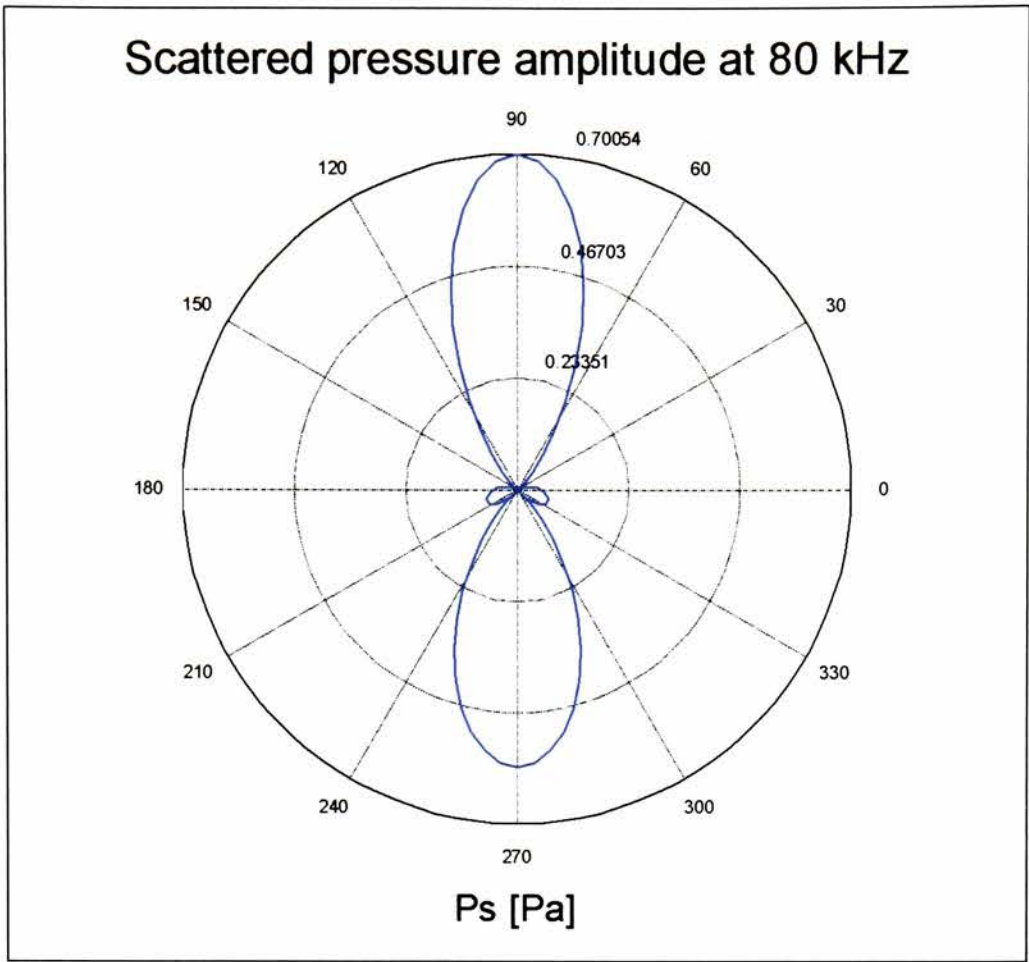


Fig. 5.7: Scattered normal velocity amplitude for the anechoic baffle at 80 kHz

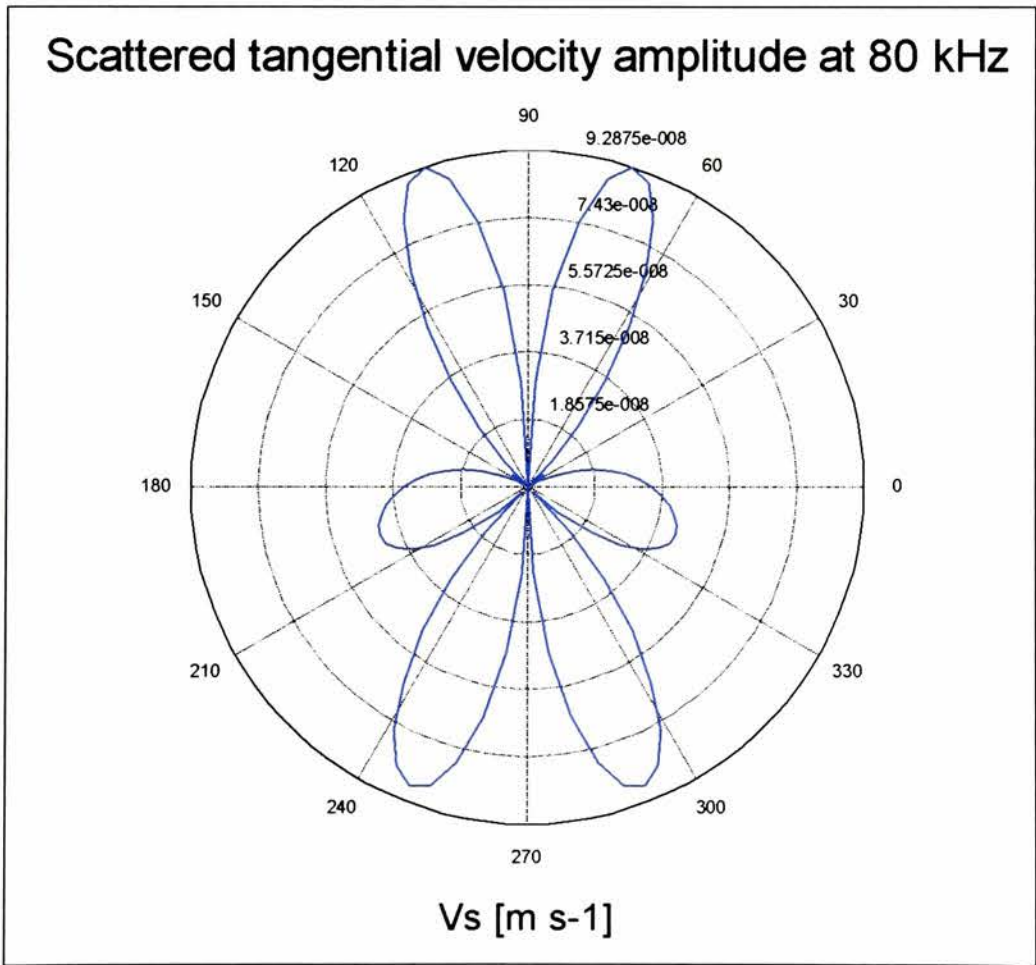


Fig. 5.8: Scattered tangential velocity amplitude of the anechoic baffle at 80 kHz

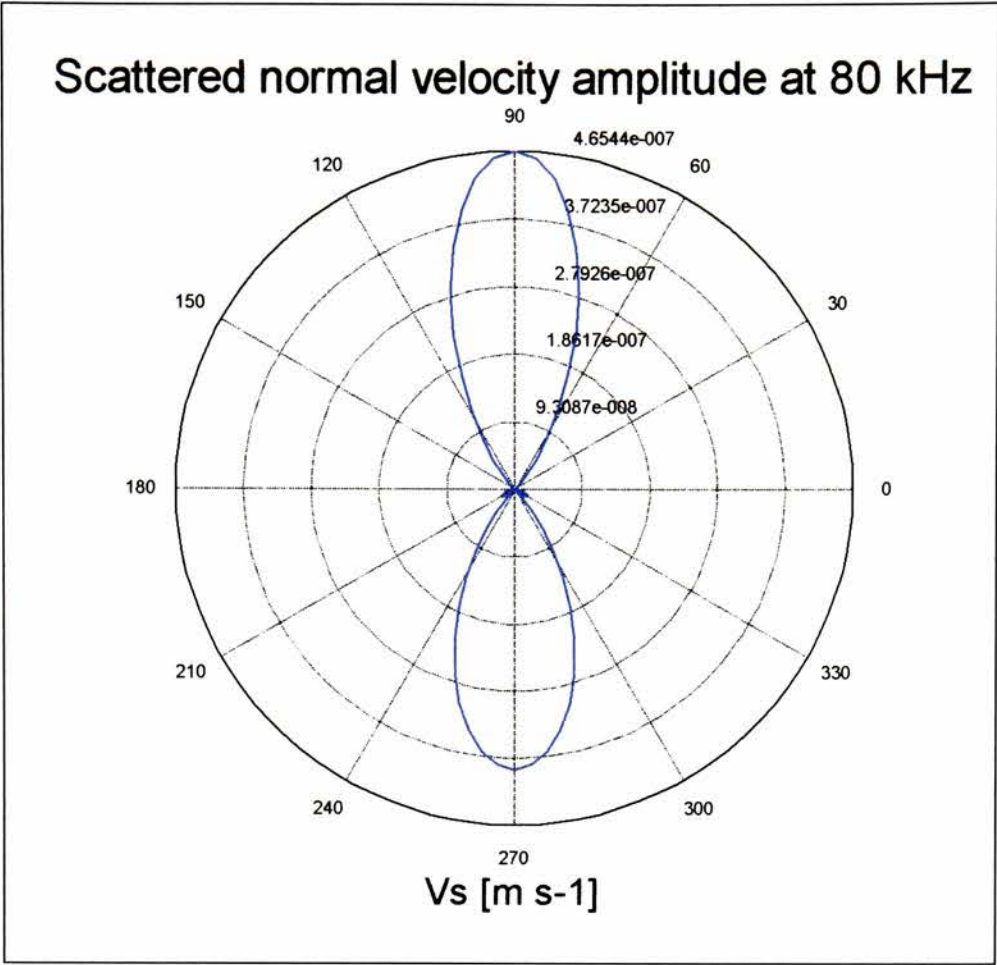


Fig. 5.9: Scattered normal velocity amplitude for the anechoic baffle at 80 kHz

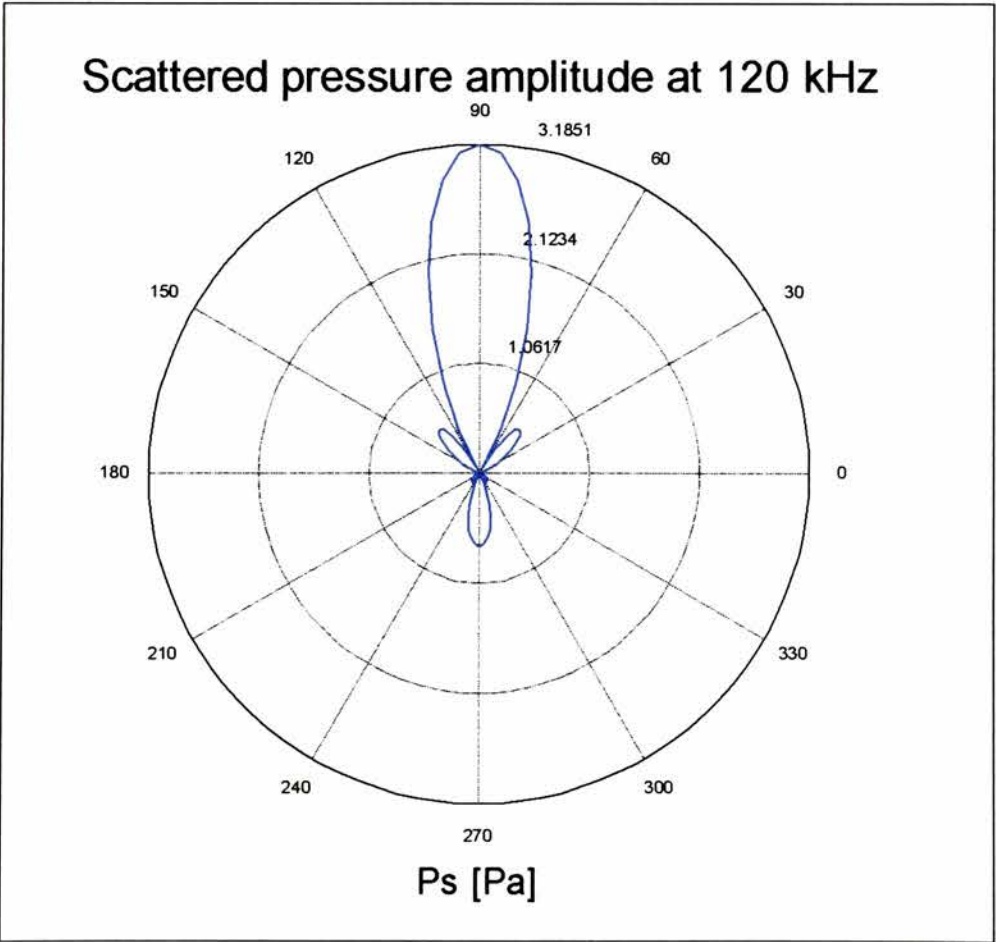


Fig. 5.10: Scattered pressure amplitude of the anechoic baffle at 120 kHz

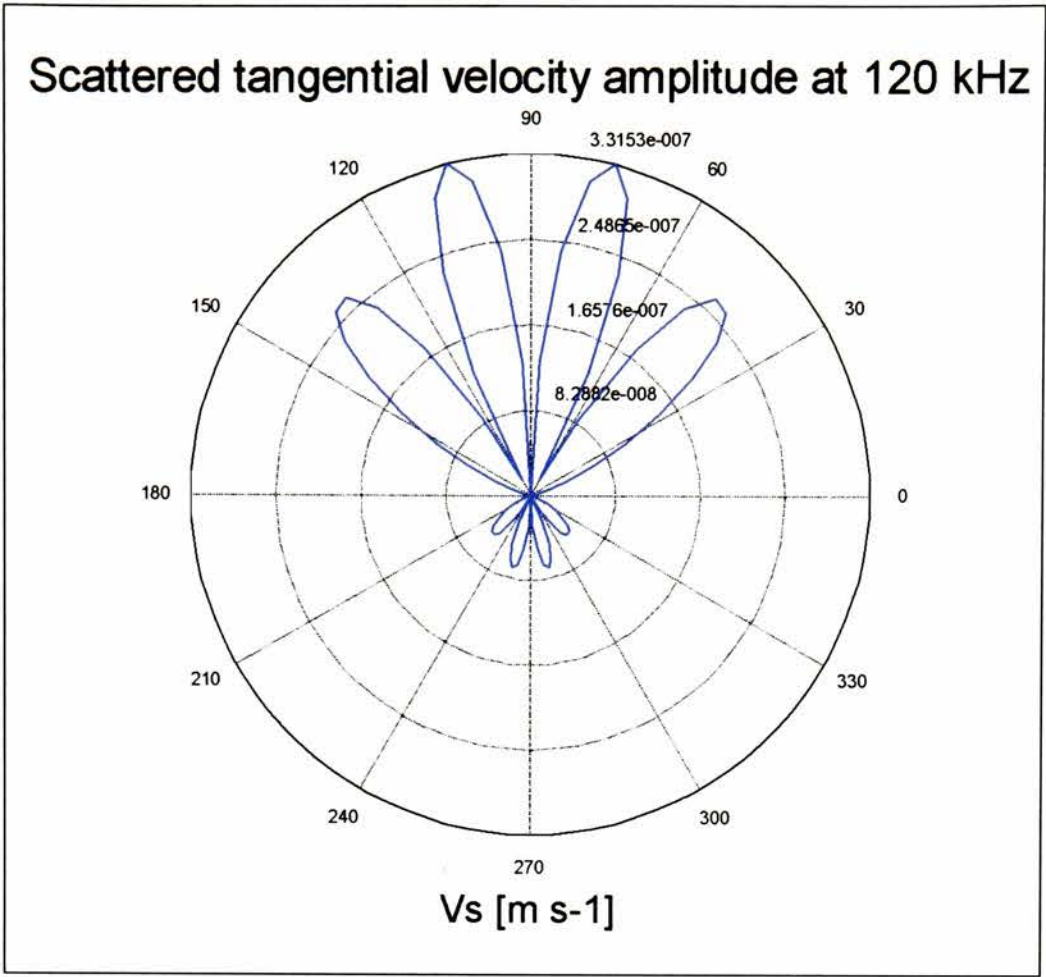


Fig. 5.11: Scattered tangential velocity amplitude for the anechoic baffle at 120 kHz

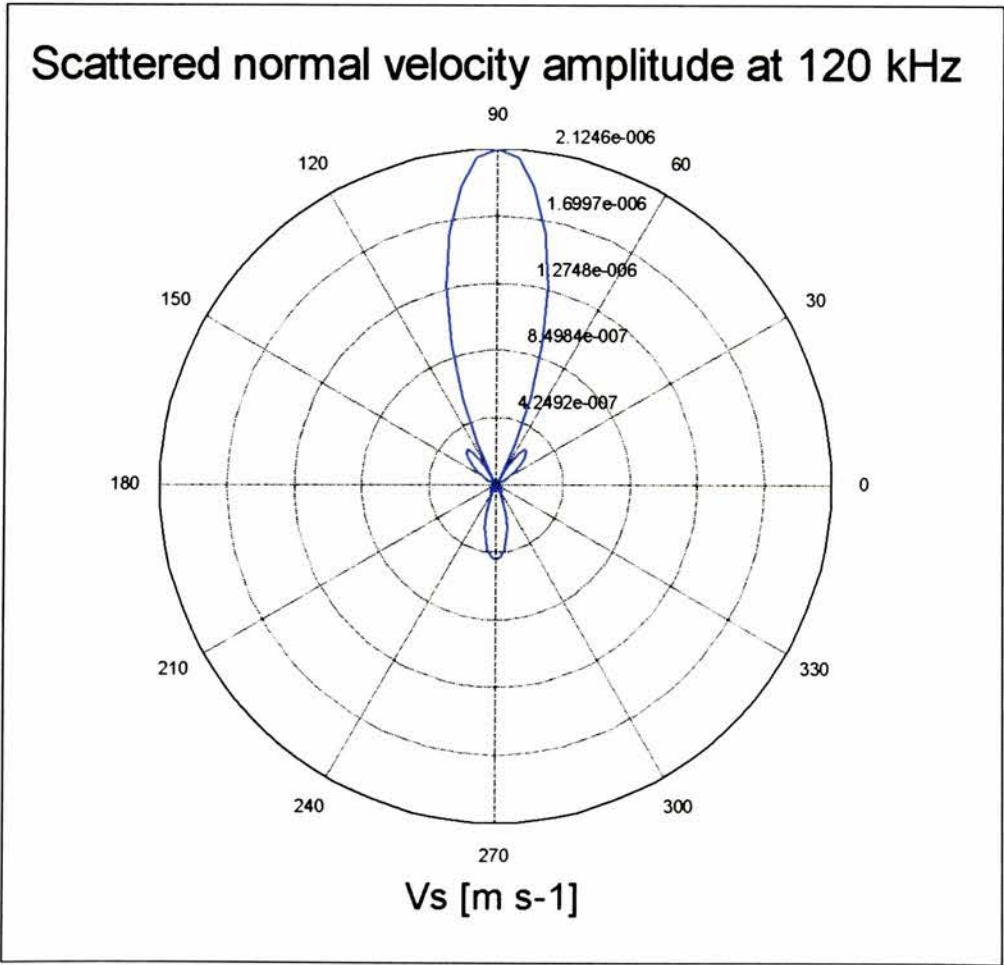


Fig. 5.12: Scattered normal velocity amplitude for the anechoic baffle at 120 kHz

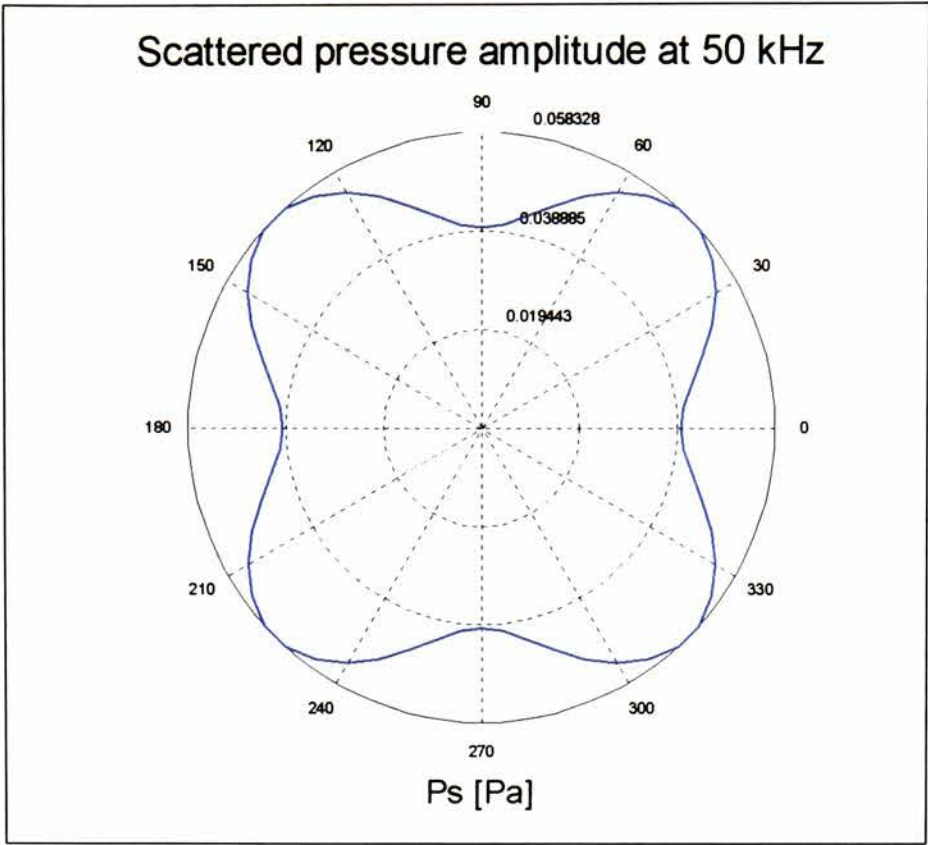


Fig. 5.13: Scattered pressure amplitude for the anechoic baffle at 50 kHz in the horizontal plane $\{x_3=0\}$

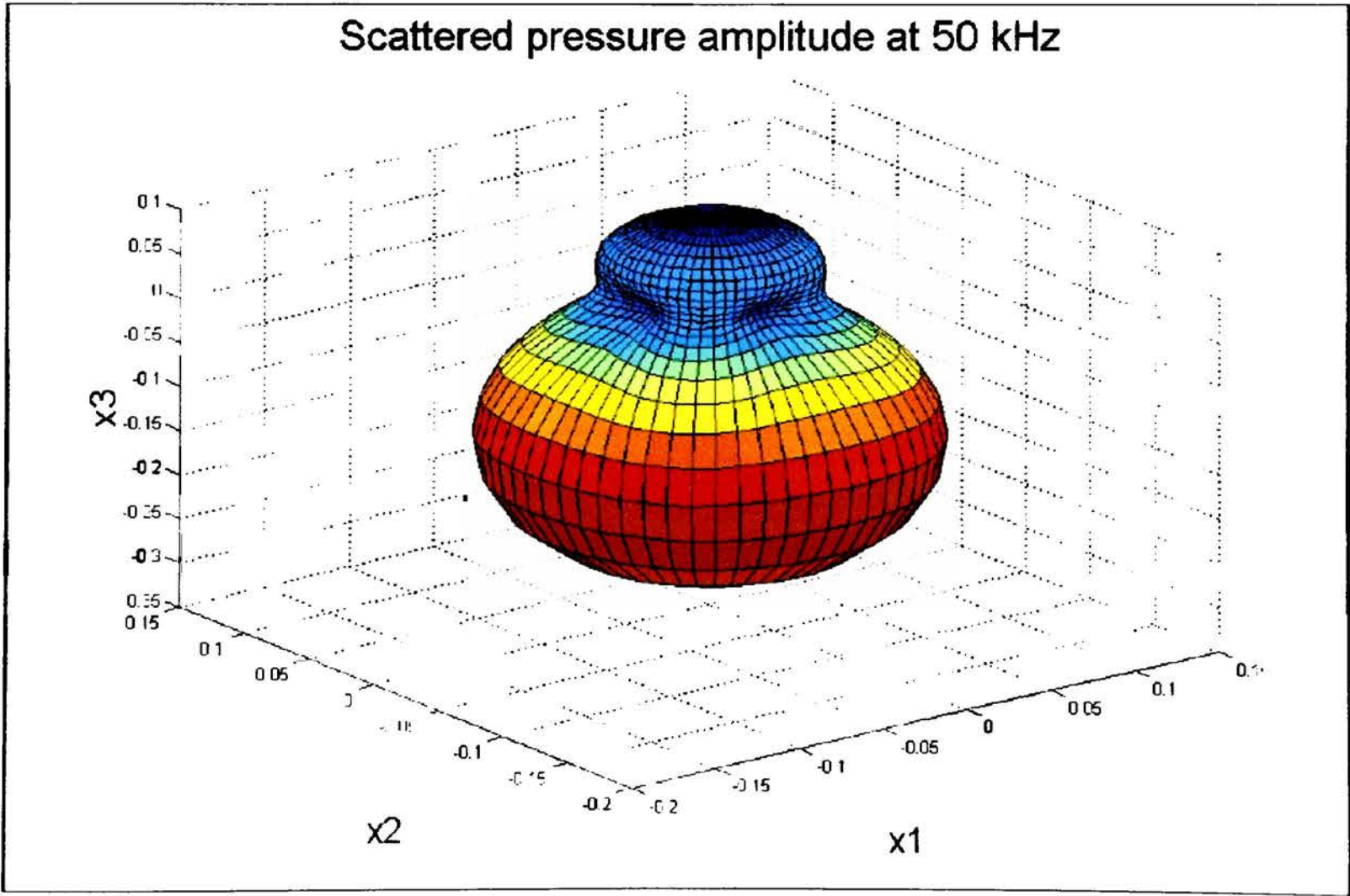


Fig. 5.14: Scattered pressure amplitude for the anechoic baffle at 50 kHz

The dependence of the backward scattered field on the cone tip angle is shown in Fig. 5.15. The curves are of course only valid in the first-order Rayleigh-Gans-Born approximation, but provide a qualitative insight of the relationship. Similar curves are reported for acoustic and electromagnetic scattering from soft and hard cones by Bowman *et al.* (1969). The same behaviour at small angles has also been reported by Babich (1996), although his results refer to rigid cones. These curves are analysed in more details in Chapter 7, when we discuss the dependence of the scattered field on the cone tip angle.

The configuration studied in this chapter has a cone tip semi-aperture of 12.5°. It can be seen that this configuration shows a minimum in the backward scattered pressure at a frequency of 47 kHz. This was indeed in the range of operating frequencies of the VERTLINK system for which the baffle was initially developed.

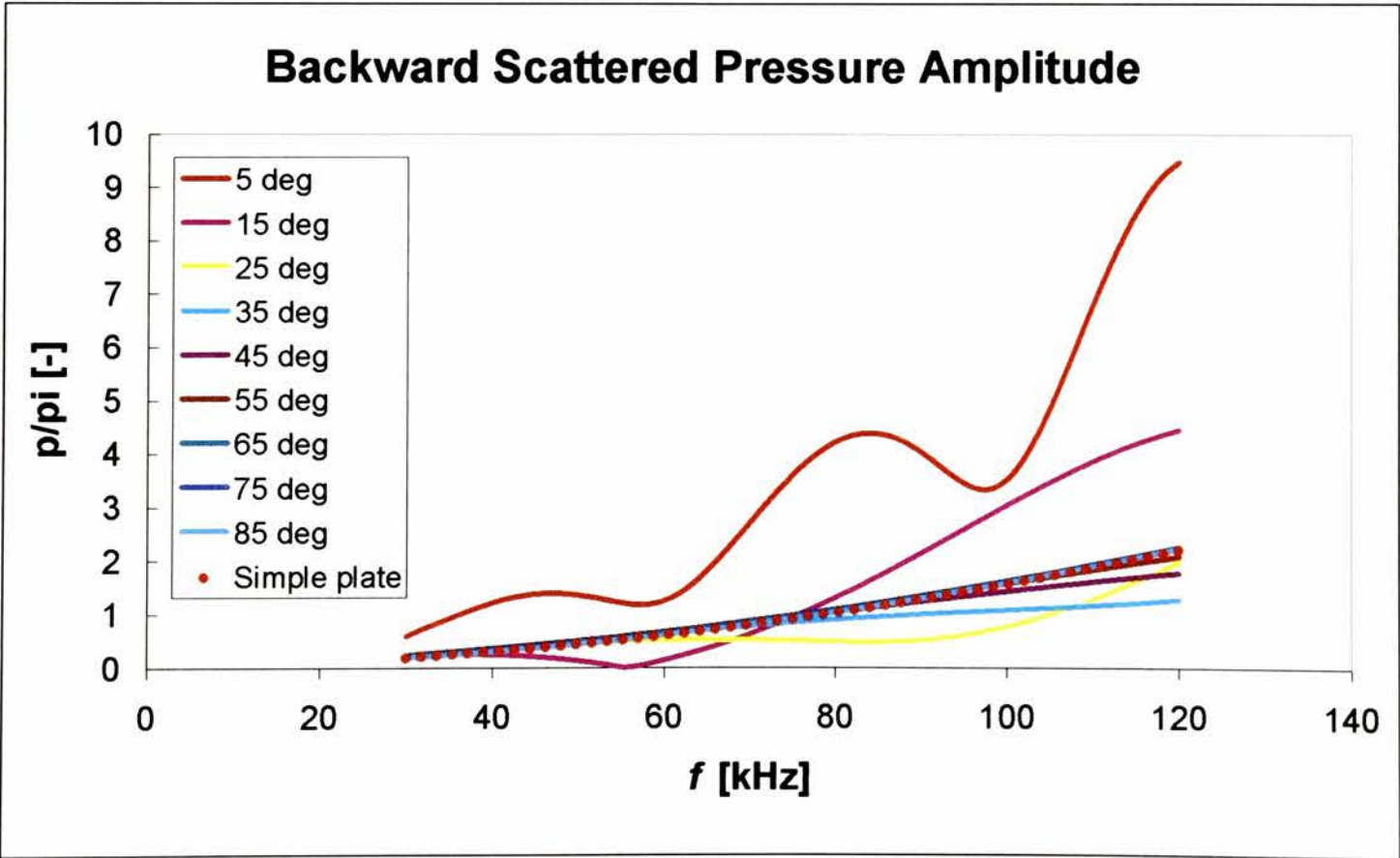


Fig. 5.15: Normalised backscattered pressure amplitude for the anechoic baffle – Dependence on cone tip angle (the values correspond to the semi-angle $\vartheta = \arctg \frac{r}{h}$)

5.6 References

- AMERIO L. (1985). *Analisi Matematica*, Vol. II. Torino: UTET, 465
- BABICH V.M. (1996). The diffraction of a high-frequency acoustic wave by a narrow-angle absolutely rigid cone of arbitrary shape. *PMM J. APP. Math. Mech.*, 60 (1), 67-73
- BOWMAN et al. (1969). *Electromagnetic and Acoustic Scattering by Simple Shapes*. Amsterdam: North-Holland Publishing Company
- CHADLI S.L. et al. (1994). Numerical Modelisation of the Scattering of an Acoustic Wave from a Wedge Immerse in a Fluid. *Journal de Physique IV, Colloque C5*, 4, C5-701-704
- DE HOOP, T.A. (1995). *Handbook of Radiation and Scattering of Waves*. London: Academic Press
- QUAK, D. et al. (1986). Time-Domain Farfield Scattering of Plane Acoustic Waves by a Penetrable Object in the Born Approximation. *J. Acoust. Soc. Am.*, 80 (4), 1228-1234

Chapter 6

The Finite Element-Boundary Element Method for Sound-Structure Interaction with Viscoelastic Elements

6.1. Introduction

The modern origins of the Boundary Element Method have their beginning in the use of integral equation methods roughly between 1960 and 1975 by researchers such as Jaswon, Hess, Symm, Massonnet, Shaw, Rizzo, Cruse and others. Nonetheless the deep foundations of the method can be found in the research work about integral equations carried out during 1800s and early 1900s by Poisson, Betti, Kirchoff, Somigliana, Fredholm, Kellogg, Kupradze and others.

During the period 1960 to 1975 integral equation methods were used to find solutions for two major mechanics problems:

- potential theory applied to perfect fluid flow research in the aerospace industry
- acoustics research, mainly related to underwater scattering and radiation

The methods initially used in this two cases under the common name of Boundary Integral Methods (**BIM**) can generally be subdivided in two classes, as now understood, even though the distinctions effectively disappear as the equivalence and commonality of the methods are recognised (Cruse and Rizzo 1975):

- *indirect methods*, whereby the physical boundaries of a system are replaced by a surface of sources or sinks, adjusting the intensity to give the same physical results as in the original problem
- *direct methods*, whereby a fundamental solution (Green's function) of the governing partial differential equation is used to satisfy the physics of the system without boundary conditions and the resulting integral equation is then solved restoring the given boundary conditions

In 1975 the first conference on the method was held at the Rensselaer Polytechnic Institution by Tom Cruse and Frank Rizzo (1975) and the first text on the use of boundary integral equation methods was published the following year by M.A. Jaswon and G.T. Symm with the title '*Integral Equation Methods in Potential Theory and Elastostatics*' (1977).

It was only in 1977 that the name Boundary Element Method (**BEM**) was used for the first time in a conference organised by C.A. Brebbia in Southampton, UK and is since then used to address a method of solution characterised by the element subdivision of a physical

system. Under this name a number of formulations can be found, from the classical direct and indirect methods to the ‘null-field’ or the embedded integral methods.

The usefulness of boundary integral methods was at first recognised in the late 1950s for the solution of all those classes of problems involving infinite boundaries, for which the classical technique based on finite differences and even the contemporarily developing finite element method based on variational principles were ill suited.

The validity of the method in the solution of transient acoustic scattering and time harmonic acoustic scattering was rapidly established in the early 1960s by Friedmann, Shaw, Banaugh and others and the shortcoming of nonuniqueness of the solution at certain characteristic frequencies for exterior boundary problems was recognised and studied from the late 1960s by L.G. Copley, H.A. Schenck, A.J. Burton and G.F. Miller and more recently by C.M. Piaszczyk, J.M. Klosner, K.A. Cunefare, D.T.I. Francis and others. Methods to overcome the problem such as CHIEF (Combined Helmholtz Integral Equation Formulation) and HGF (Helmholtz Gradient Formulation) were established.

The modern use of BIM for elastostatic problems was introduced in 1967 by F. Rizzo by transforming the fundamental Somigliana domain integral approach to elasticity into an equivalent boundary form and was extended to elastodynamics the following year by T. Cruse and F. Rizzo.

Finally the ever increasing importance of stress analysis in non-conventional materials such as polymers and composites immersed in fluid media led the mechanical engineering community to recognise the importance of boundary integral methods and gave rise to a convergence of techniques and to the development of combined Finite-Element, Boundary-Element methods from the early work of H.A. Schenck to the modern stress and radiation

analysis software packages, such as NASTRAN, ANSYS and the PHOEBE 3D software developed for this research.

In this chapter the fundamentals of the boundary element method are outlined and then applied to the solution of the Helmholtz equation for scattering problems. It is shown how the acoustic boundary element model can be coupled to a finite element model of the scatterer to provide the necessary boundary condition to the scattering problem. Finally, the viscoelastic finite element to be used in the model is derived from the viscoelastic constitutive relationships presented in Chapter 3 and incorporated in the complete FE-BE model.

6.2. Fundamentals of the Boundary Element Method

6.2.1. Basic Integral Equation

The most general way of deducing the starting boundary integral equation required by the method is based on the principle of weighted residuals. We consider as a starting point the Laplace equation in a two or three-dimensional domain Ω :

$$\nabla^2 u = 0 \quad \text{in } \Omega \quad (6.1)$$

with the following boundary conditions on Γ (fig. 6.1):

$$(I) \text{ Essential (Dirichlet) conditions: } u = \bar{u} \quad \text{on } \Gamma_1 \quad (6.2)$$

$$(II) \text{ Natural (Neumann) conditions: } q = \frac{\partial u}{\partial n} = \bar{q} \quad \text{on } \Gamma_2 \quad (6.3)$$

where n is the outward normal to the boundary $\Gamma = \Gamma_1 + \Gamma_2$ and the overbars indicate known values.

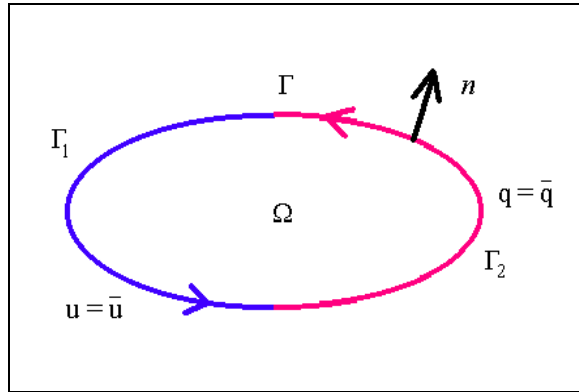


Figure 6.1: Geometrical definitions of the domain Ω with Robin (mixed) boundary conditions

Instead of looking for an exact solution for the function u , we seek an approximate solution of the form:

$$u = \sum_{j=1}^N u_j \varphi_j \quad (6.4)$$

where the φ_j 's are a set of linearly independent functions called interpolation or shape functions and the u_j 's are the nodal values of the field variable u or its derivative.

The introduction of the approximation for u and its derivatives in the governing equation produces an error, unless the approximate relationships can represent the exact solution. The errors in the domain Ω and on the boundary Γ can be represented by error functions or *residuals*, given by:

$$\begin{aligned}
R &= \nabla^2 u \neq 0 \\
R_1 &= u - \bar{u} \neq 0 \\
R_2 &= q - \bar{q} \neq 0
\end{aligned} \tag{6.5}$$

where u and q are the approximate values given by eq. (6.4.) and its derivative respectively.

In principle the errors introduced by approximating the solution u can be minimised by taking the internal product of the residuals with a weighting function u^* and its normal derivative $q^* = \frac{\partial u^*}{\partial n}$ on Γ , as follows (Brebbia and Ciskowski 1991):

$$\int_{\Omega} R u^* d\Omega = \int_{\Gamma_2} R_2 u^* d\Gamma - \int_{\Gamma_1} R_1 u^* d\Gamma \tag{6.6}$$

or

$$\int_{\Omega} (\nabla^2 u) u^* d\Omega = \int_{\Gamma_2} (q - \bar{q}) u^* d\Gamma - \int_{\Gamma_1} (u - \bar{u}) u^* d\Gamma \tag{6.7}$$

Integrating twice by parts yields:

$$\int_{\Omega} (\nabla^2 u^*) u d\Omega = - \int_{\Gamma_2} \bar{q} u^* d\Gamma - \int_{\Gamma_1} q u^* d\Gamma + \int_{\Gamma_2} u q^* d\Gamma + \int_{\Gamma_1} \bar{u} q^* d\Gamma \tag{6.8}$$

The domain integral in the left-hand side must now be transformed into a boundary integral. This can be done using the fundamental solution of Laplace equation as a weighting function. The fundamental solution in this case represents the field generated by a unit source acting at a point x_i and satisfy the following Poisson equation:

$$\nabla^2 u^* + \Delta_i = 0 \quad (6.9)$$

where Δ_i is the Dirac delta function. Since the integral of the product of the delta function times any other function is the value of the second function in x_i (sifting property) we have:

$$\int_{\Omega} (\nabla^2 u^*) u \, d\Omega = \int_{\Omega} (-\Delta_i) u \, d\Omega = -u_i \quad (6.10)$$

and eq. (6.8.) can be rewritten as:

$$u_i + \int_{\Gamma_2} u q^* \, d\Gamma + \int_{\Gamma_1} \bar{u} q^* \, d\Gamma = \int_{\Gamma_2} \bar{q} u^* \, d\Gamma + \int_{\Gamma_1} q u^* \, d\Gamma \quad (6.11)$$

The fundamental solution for isotropic media in a three dimensional domain is:

$$u_* = \frac{1}{4\pi r} \quad (6.12)$$

and in a two dimensional domain it is:

$$u^* = \frac{1}{2\pi} \ln\left(\frac{1}{r}\right) \quad (6.13)$$

where r is the distance of a boundary point from the nodal point x_i .

On the boundary Γ eq. (6.11.) must be properly specialised. The most direct way to find the correct form of the equation is taking a point x_i on the boundary Γ augmented by a hemisphere in a three-dimensional domain or a semicircle in a two dimensional domain, whose centre is the point x_i itself (Fig. 6.2.).

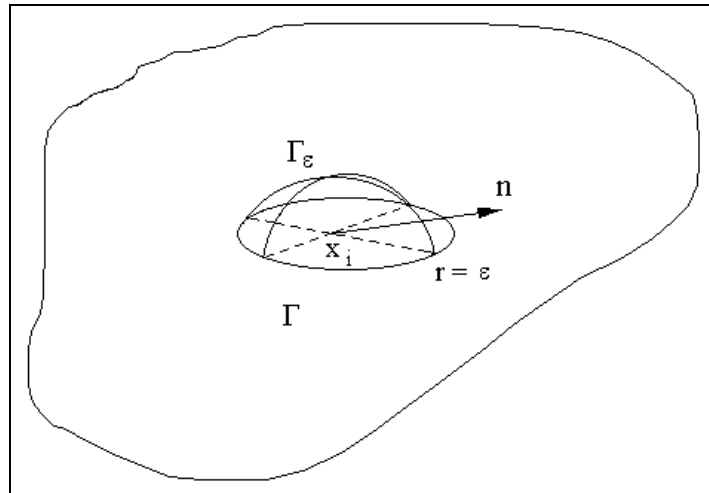


Figure 6.2: Boundary points specialisation of the general integral equation for a three-dimensional domain

At the limit when the radius ε is taken to zero the point x_i becomes a true boundary point and the resulting expression is the specialisation of eq. (6.11.) on Γ . In the three dimensional case we have, before applying any boundary condition:

$$u_i + \int_{\Gamma} u q^* d\Gamma = \int_{\Gamma} q u^* d\Gamma \quad (6.14)$$

Substituting expression (6.12.) in the right-hand side we have:

$$\lim_{\varepsilon \rightarrow 0} \left\{ \int_{\Gamma_\varepsilon} q u^* d\Gamma \right\} = \lim_{\varepsilon \rightarrow 0} \left\{ \int_{\Gamma_\varepsilon} q \frac{1}{4\pi\varepsilon} d\Gamma \right\} = \lim_{\varepsilon \rightarrow 0} \left\{ q \frac{2\pi\varepsilon^2}{4\pi\varepsilon} \right\} \equiv 0 \quad (6.15)$$

whereas taking the limit of the left-hand side yields:

$$\lim_{\varepsilon \rightarrow 0} \left\{ \int_{\Gamma_\varepsilon} u q^* d\Gamma \right\} = \lim_{\varepsilon \rightarrow 0} \left\{ - \int_{\Gamma_\varepsilon} u \frac{1}{4\pi\varepsilon^2} d\Gamma \right\} = \lim_{\varepsilon \rightarrow 0} \left\{ -u \frac{2\pi\varepsilon^2}{4\pi\varepsilon^2} \right\} = -\frac{1}{2} u_i \quad (6.16)$$

The free term produced in eq. (6.16.) must be added to equation (6.11.) obtaining the boundary integral equation generally used in the boundary element method:

$$\alpha u_i + \int_{\Gamma} u q^* d\Gamma = \int_{\Gamma} q u^* d\Gamma \quad \begin{cases} \alpha = 1 & \text{internal nodes} \\ \alpha = \frac{1}{2} & \text{smooth boundary nodes} \end{cases} \quad (6.17)$$

The two-dimensional case is analogous and yields the same results.

6.2.2. The Boundary Element Method

The boundary integral equation (6.17.) must be now discretised to find the values of the boundary nodes used to approximate the exact solution. We only consider the general case of quadratic elements for two- and three-dimensional domains.

The boundary Γ of the domain Ω can be discretised into N elements, each of which is represented in terms of a subset of the nodes used to approximate the unknown field variable u . For three-dimensional domains the elements used are generally of two types: triangular and quadrilateral and both of them can be flat or curved (Fig. 6.3). All variables (potentials, fluxes and co-ordinates) are approximated as a linear interpolation of the corresponding nodal values in terms of a set of functions defined on the elements. These functions, called shape functions, can be quadratic or higher order functions, such as cubic splines or Bézier curves, for both two- and three-dimensional domains.

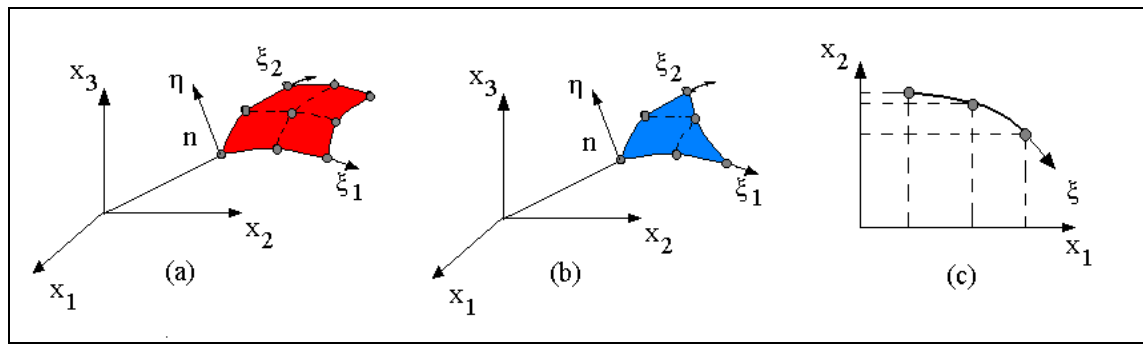


Figure 6.3: Curved (quadratic) elements for two- and three dimensional boundary element problems: (a) quadratic quadrilateral element; (b) quadratic triangular element; (c) quadratic two-dimensional element

In order to deal with curved element in three dimensions, it is necessary to pass from the global Cartesian co-ordinates x_1, x_2, x_3 to a system of oblique co-ordinates, which can be defined using two curvilinear co-ordinates ξ_1 and ξ_2 and the local normal η (Fig. 6.3). The transformation of the field variables can be defined using the Jacobian \mathbf{J} of the two sets of co-ordinates, as follows:

$$\begin{Bmatrix} \frac{\partial u}{\partial \xi_1} \\ \frac{\partial u}{\partial \xi_2} \\ \frac{\partial u}{\partial \eta} \end{Bmatrix} = \begin{bmatrix} \frac{\partial x_1}{\partial \xi_1} & \frac{\partial x_2}{\partial \xi_1} & \frac{\partial x_3}{\partial \xi_1} \\ \frac{\partial x_1}{\partial \xi_2} & \frac{\partial x_2}{\partial \xi_2} & \frac{\partial x_3}{\partial \xi_2} \\ \frac{\partial x_1}{\partial \eta} & \frac{\partial x_2}{\partial \eta} & \frac{\partial x_3}{\partial \eta} \end{bmatrix} \begin{Bmatrix} \frac{\partial u}{\partial x_1} \\ \frac{\partial u}{\partial x_2} \\ \frac{\partial u}{\partial x_3} \end{Bmatrix} = \mathbf{J} \begin{Bmatrix} \frac{\partial u}{\partial x_1} \\ \frac{\partial u}{\partial x_2} \\ \frac{\partial u}{\partial x_3} \end{Bmatrix} \quad (6.18)$$

Differential of volume or area can now be expressed in terms of the new set of oblique co-ordinates by means of the Jacobian \mathbf{J} or the reduced Jacobian \mathbf{G} respectively (Brebbia and Ciskowski 1991):

$$d\Omega = \left| \frac{\partial \mathbf{r}}{\partial \xi_1} \times \frac{\partial \mathbf{r}}{\partial \xi_2} \cdot \frac{\partial \mathbf{r}}{\partial \eta} \right| d\xi_1 d\xi_2 d\eta = |\mathbf{J}| d\xi_1 d\xi_2 d\eta \quad (6.19)$$

$$d\Gamma = \left| \frac{\partial \mathbf{r}}{\partial \xi_1} \times \frac{\partial \mathbf{r}}{\partial \xi_2} \right| d\xi_1 d\xi_2 = |\mathbf{G}| d\xi_1 d\xi_2 \quad (6.20)$$

where the reduced Jacobian \mathbf{G} is the magnitude of the normal vector $\boldsymbol{\eta}$ and can be expressed as:

$$\boldsymbol{\eta} = \frac{\partial \mathbf{r}}{\partial \xi_1} \times \frac{\partial \mathbf{r}}{\partial \xi_2} = (g_1, g_2, g_3) = \left(\frac{\partial x_1}{\partial \eta}, \frac{\partial x_2}{\partial \eta}, \frac{\partial x_3}{\partial \eta} \right) \quad (6.21)$$

and

$$\begin{aligned}
g_1 &= \left(\frac{\partial x_2}{\partial \xi_1} \frac{\partial x_3}{\partial \xi_2} - \frac{\partial x_2}{\partial \xi_2} \frac{\partial x_3}{\partial \xi_1} \right) \\
g_2 &= \left(\frac{\partial x_3}{\partial \xi_1} \frac{\partial x_1}{\partial \xi_2} - \frac{\partial x_1}{\partial \xi_1} \frac{\partial x_3}{\partial \xi_2} \right) \\
g_3 &= \left(\frac{\partial x_1}{\partial \xi_1} \frac{\partial x_2}{\partial \xi_2} - \frac{\partial x_2}{\partial \xi_1} \frac{\partial x_1}{\partial \xi_2} \right) \\
|\mathbf{G}| &= \sqrt{(g_1^2 + g_2^2 + g_3^2)}
\end{aligned} \tag{6.22}$$

For two-dimensional domains the transformation between Cartesian and oblique co-ordinate systems is analogous, with the difference that only one oblique co-ordinate ξ is defined along the element and no normal co-ordinate is necessary.

BIQUADRATIC QUADRILATERAL ELEMENT	QUADRATIC ELEMENT
$u(\xi_1, \xi_2) = \sum_{j=1}^8 \varphi_j u_j = \varphi^j u_j = \boldsymbol{\varphi} \cdot \mathbf{u}$ $\varphi_1 = \frac{1}{4}(\xi_1 + 1)(\xi_2 + 1)(\xi_1 + \xi_2 - 1)$ $\varphi_2 = \frac{1}{4}(\xi_1 - 1)(\xi_2 + 1)(\xi_1 - \xi_2 + 1)$ $\varphi_3 = \frac{1}{4}(1 - \xi_1)(\xi_2 - 1)(\xi_1 + \xi_2 + 1)$ $\varphi_4 = \frac{1}{4}(\xi_1 + 1)(\xi_2 - 1)(\xi_1 - \xi_2 + 1)$ $\varphi_5 = \frac{1}{2}(\xi_1 + 1)(1 - \xi_2^2)$ $\varphi_6 = \frac{1}{2}\xi_1(\xi_2 + 1)(1 - \xi_1^2)$ $\varphi_7 = \frac{1}{2}(\xi_1 - 1)(\xi_2^2 - 1)$ $\varphi_8 = \frac{1}{2}(1 - \xi_2)\xi_2(1 - \xi_1^2)$	$u(\xi) = \sum_{j=1}^3 \varphi_j u_j = \varphi^j u_j$ $\varphi_1 = \frac{1}{2}\xi(\xi - 1)$ $\varphi_2 = \frac{1}{2}\xi(1 + \xi)$ $\varphi_3 = (1 - \xi)(1 + \xi)$

Table 6.1: Interpolation functions for quadratic elements in two and three dimensions

Once the element topology has been defined an approximate expression for the field variable can be found in terms of the nodal values. The interpolation functions for a biquadratic quadrilateral element in three dimensions and a quadratic element in two dimensions are given in Tab. 6.1.

It is now possible to discretise the boundary integral equation (6.17). We can re-write that equation as:

$$c_i u_i + \int_{\Gamma} u q^* d\Gamma = \int_{\Gamma} q u^* d\Gamma \quad (6.23)$$

where the coefficient α valid for smooth boundaries or internal nodes is replaced by a coefficient c_i , which depends on the shape of the boundary and is different from 1/2 for edges or corners on Γ . In general c_i depends on the angle subtended by the corner in radians for two-dimensional elements and steradians for three-dimensional elements. Alternatively, the value of c_i can be determined implicitly from the given boundary conditions.

Now for each nodal point x_i equation (6.23.) can be discretised considering the contribution of each element as follows:

$$c_i u_i + \sum_{j=1}^N \int_{\Gamma_j} u q^* d\Gamma = \sum_{j=1}^N \int_{\Gamma_j} q u^* d\Gamma \quad (6.24)$$

The integrals over the boundary elements Γ_j can then be computed in terms of the interpolation functions. The resulting terms relate the node i where the fundamental solution

is acting to any other node j and are usually called influence coefficients (Brebbia and Ciskowski 1991):

$$\begin{aligned}
 \int_{\Gamma_j} u(\xi_1, \xi_2) q^* d\Gamma &= \int_{\Gamma_j} [\varphi_1(\xi_1, \xi_2) \quad \dots \quad \varphi_8(\xi_1, \xi_2)] q^* d\Gamma \begin{bmatrix} u_1 \\ \dots \\ u_8 \end{bmatrix} = \\
 &= \int_{-1}^1 \int_{-1}^1 [\varphi_1(\xi_1, \xi_2) \quad \dots \quad \varphi_8(\xi_1, \xi_2)] q^* |\mathbf{G}| d\xi_1 d\xi_2 \begin{bmatrix} u_1 \\ \dots \\ u_8 \end{bmatrix} = \\
 &= \begin{bmatrix} h_{ij}^1 & \dots & h_{ij}^8 \end{bmatrix} \begin{bmatrix} u_1 \\ \dots \\ u_8 \end{bmatrix}
 \end{aligned} \tag{6.25}$$

where

$$h_{ij}^k = \int_{-1}^1 \int_{-1}^1 \varphi_k(\xi_1, \xi_2) q^* |\mathbf{G}_j| d\xi_1 d\xi_2 \tag{6.26}$$

and

$$\begin{aligned}
\int_{\Gamma_j} q(\xi_1, \xi_2) u^* d\Gamma &= \int_{\Gamma_j} [\varphi_1(\xi_1, \xi_2) \quad \dots \quad \varphi_8(\xi_1, \xi_2)] u^* d\Gamma \begin{bmatrix} q_1 \\ \dots \\ q_8 \end{bmatrix} = \\
&= \int_{-1}^1 \int_{-1}^1 [\varphi_1(\xi_1, \xi_2) \quad \dots \quad \varphi_8(\xi_1, \xi_2)] u^* |\mathbf{G}| d\xi_1 d\xi_2 \begin{bmatrix} q_1 \\ \dots \\ q_8 \end{bmatrix} = \\
&= \begin{bmatrix} g_{ij}^1 & \dots & g_{ij}^8 \end{bmatrix} \begin{bmatrix} q_1 \\ \dots \\ q_8 \end{bmatrix}
\end{aligned} \tag{6.27}$$

where

$$g_{ij}^k = \int_{-1}^1 \int_{-1}^1 \varphi_k(\xi_1, \xi_2) u^* |\mathbf{G}_j| d\xi_1 d\xi_2 \tag{6.28}$$

The influence coefficients can now be assembled after taking some assumption on the boundary conditions. The potential at a node can be assumed the same for each element sharing that node. The same however cannot be said for the flux, which does not always has a unique value at any one node. The general assembled equation before applying any boundary condition is:

$$c_i u_i + \begin{bmatrix} H_{i1} & \dots & H_{iN} \end{bmatrix} \begin{Bmatrix} u_1 \\ \dots \\ u_N \end{Bmatrix} = \begin{bmatrix} G_{i1} & \dots & G_{iN} \end{bmatrix} \begin{Bmatrix} q_1 \\ \dots \\ q_N \end{Bmatrix} \tag{6.29}$$

In general, if the fluxes are assigned the only unknown variable is the potential at that node. If the potential is assigned, three cases occur (Brebbia and Dominguez 1992):

- the flux is considered to have a unique value for all four elements sharing the node
- the flux is not unique, but three of the four values are assigned
- the flux is not unique and more than one value in different elements is unknown

When only one unknown exists for each node, be it potential or flux, eq. (6.29.) can be recast in a different form moving the unknown values with their coefficients into the left-hand side and the known values into the right-hand side. The resulting system of linear equation can therefore be solved numerically. The integrals in the coefficients h_{ij} and g_{ij} must usually be solved numerically using some higher order method, such as a multipoint Gauss formula.

If more than one unknown for each element appears, then a different approach must be taken, such as the use of discontinuous elements with the nodes shifted inside the element itself (Do Rêgo Silva 1994). Once the balance between equations and unknowns is restored, the system can be solved as before.

Relations (6.25.) and (6.26.) are valid for $i \neq j$. For $i = j$ it is necessary to take into account the term $c_i u_i$. This can be done, as mentioned earlier, either by direct calculation of the coefficient c_i from the angle subtended by the corner if the boundary is not smooth and adding the resulting term to the h_{ii} influence coefficient or by implicit calculation of the influence coefficient itself.

In the former case the following integral equation can be used:

$$c_i = 1 - \frac{1}{4\pi} \int_{\Gamma} \frac{\partial}{\partial n} \frac{1}{r} d\Gamma \quad (6.30)$$

which is valid for any position of the point i . If the point i is on Γ the integral can still be used since the singularity is of the order $1/r$.

In the latter case if a constant potential over the whole boundary is assumed, the condition on total flux across the boundary can be written as:

$$\mathbf{H}\mathbf{I} = \mathbf{0} \quad (6.31)$$

where \mathbf{I} is a vector with unit potential in all nodes. From this condition we have:

$$\sum_{j=1}^N H_{ij} = 0 \quad (6.32)$$

whence

$$H_{ii} = - \sum_{\substack{j=1 \\ j \neq i}}^N H_{ij} \quad (6.33)$$

Eq. (6.29.) can then be cast into matrix form as:

$$\mathbf{H}\mathbf{u} = \mathbf{G}\mathbf{q} \quad (6.34)$$

and then reordered in a linear system of the form:

$$\mathbf{Ax} = \mathbf{f} \quad (6.35)$$

after application of a set of suitable boundary conditions on the values of the potential u and the flux q .

6.3. Boundary Element Formulation of the Helmholtz Equation. Acoustic Radiation and Scattering

The propagation of waves through an elastic medium is governed by the linear wave equation:

$$\nabla^2 u = \frac{1}{c^2} \frac{\partial^2 u}{\partial t^2} \quad (6.36)$$

where $u = u(t)$ represents a velocity potential.

For the time-harmonic case a harmonic expansion can be assumed for the potential u :

$$u(x, t) = u(x) e^{i\omega t} \quad (6.37)$$

and eq. (6.36.) becomes (Helmholtz equation):

$$\nabla^2 u + k^2 u = 0 \quad (6.38)$$

where the wave number k , the angular frequency ω and the sound speed c are related by:

$$k = \frac{\omega}{c} \quad (6.39)$$

For acoustic radiation the potential u must also satisfy the Sommerfield radiation condition at infinity:

$$\lim_{r \rightarrow \infty} \left[r \left(\frac{\partial u}{\partial r} + iku \right) \right] = 0 \quad (6.40)$$

The potential function in eq. (6.38.) is a function of position only. In the absence of volume forces, the velocity potential u is related to the acoustic velocity and pressure by (see also eq. (5.15) with $\varphi = \rho_0 u$ and $s = i\omega$):

$$\begin{aligned} \mathbf{v} &= -\nabla u \\ p &= i\omega \rho_0 u \end{aligned} \quad (6.41)$$

where the equilibrium fluid density ρ_0 is assumed to be constant.

The integral expression equivalent to eq. (6.38.) on the boundary Γ can be derived from the explicit form of the total scattered pressure field introduced in Chapter 5 by application of the reciprocity theorem of the convolution type. From eq. (5.75.) applied to the bounded domain $\Omega \subset \Re^3$ with boundary surface Γ we have:

$$\begin{aligned} \hat{p}(\mathbf{x}', s) = \hat{p}^i(\mathbf{x}', s) - \int_{\mathbf{x} \in \Omega} \left\{ \hat{G}^{\hat{p}\hat{q}}(\mathbf{x}', \mathbf{x}, s) [\hat{\eta}^s(\mathbf{x}, s) - s\kappa] \hat{p}(\mathbf{x}, s) + \right. \\ \left. + \hat{G}^{\hat{p}\hat{f}}(\mathbf{x}', \mathbf{x}, s) [\hat{\xi}^s(\mathbf{x}, s) - s\rho\delta] \hat{p}(\mathbf{x}, s) \right\} dV \quad \mathbf{x}' \in \Re^3 \end{aligned} \quad (6.42)$$

Eq. (6.42.) can be transformed into an equivalent surface source integral equation by applying eq. (5.73) to the source-free incident pressure field $\hat{p}^i(\mathbf{x}', s)$ and the scattered pressure field $\hat{p}^s(\mathbf{x}', s)$. Summing up all the terms we get:

$$\chi_{\Omega'}(\mathbf{x}')\hat{p}(\mathbf{x}', s) = \hat{p}^i(\mathbf{x}', s) + \int_{\mathbf{x} \in \Gamma} \left[\hat{G}^{\hat{p}q}(\mathbf{x}', \mathbf{x}, s) \hat{v}(\mathbf{x}, s) \cdot \mathbf{n} + \hat{G}^{\hat{p}f}(\mathbf{x}', \mathbf{x}, s) \cdot \hat{p}(\mathbf{x}, s) \mathbf{n} \right] d\Gamma \quad \mathbf{x}' \in \mathfrak{R}^3 \quad (6.43)$$

where:

$$\begin{cases} \hat{G}^{\hat{p}q}(\mathbf{x}', \mathbf{x}, s) = s\rho_0 \hat{G}(\mathbf{x}', \mathbf{x}, s) \\ \hat{G}^{\hat{p}f}(\mathbf{x}', \mathbf{x}, s) = -\nabla \hat{G}(\mathbf{x}', \mathbf{x}, s) \end{cases} \quad (6.44)$$

and

$$\hat{G}(\mathbf{x}', \mathbf{x}, s) = \frac{e^{-\frac{s}{c}|\mathbf{x}' - \mathbf{x}|}}{4\pi|\mathbf{x}' - \mathbf{x}|} \quad \mathbf{x}' \neq \mathbf{x} \quad (6.45)$$

The vector \mathbf{n} is the normal vector to the surface Γ in each point \mathbf{x} .

The Green's function $\hat{G}(\mathbf{x}', \mathbf{x}, s)$ is the fundamental solution of the Helmholtz equation (6.38) in three dimensions. As shown in Chapter 5, the integral eq. (6.43) when expressed in terms of the Green's function (6.45) automatically satisfies the Sommerfield radiation condition (6.40).

If we take into account relations (6.39) and (6.41), set $s = i\omega$ and drop the \wedge symbol, we can rewrite eq. (6.43) as:

$$c_i u_i = u^i + \int_{\Gamma} \left[\frac{\partial u}{\partial n} G - u \frac{\partial G}{\partial n} \right] d\Gamma \quad (6.46)$$

with

$$\left\{ \begin{array}{l} c_i = \chi_B(\mathbf{x}'_i) = 1 - \frac{1}{4\pi} \int_{\Gamma} \frac{\partial}{\partial n} \frac{1}{r} d\Gamma \\ \frac{\partial u}{\partial n} = -\mathbf{v} \cdot \mathbf{n} = (\nabla u) \cdot \mathbf{n} \\ G = \frac{e^{-ikr}}{4\pi r} \quad r = |\mathbf{x}' - \mathbf{x}|, \quad \mathbf{x}' \neq \mathbf{x} \\ \frac{\partial G}{\partial n} = \frac{e^{-ikr}}{4\pi r} \left(ik + \frac{1}{r} \right) \frac{\partial r}{\partial n'} \quad r = |\mathbf{x}' - \mathbf{x}|, \quad \mathbf{x}' \neq \mathbf{x} \end{array} \right. \quad (6.47)$$

Eq. (6.46) can now be discretised by taking its value in each node of the boundary element schema, thus obtaining the boundary method matrix form:

$$\mathbf{H}\mathbf{u} = \mathbf{u}^i + \mathbf{G}\mathbf{q} \quad (6.48)$$

where $\mathbf{q} = \frac{\partial \mathbf{u}}{\partial n}$ is the vector of nodal fluxes.

Alternatively, eq. (6.48) can also be expressed in terms of the pressure and the velocity fields on the boundary Γ . Taking into account relationships (6.41) we have:

$$\mathbf{A}\mathbf{p} = \mathbf{p}^i + \mathbf{B}\mathbf{v} \quad (6.49)$$

with

$$\begin{aligned} \mathbf{A} &= \mathbf{H} \\ \mathbf{B} &= -i\omega\rho_0\mathbf{G}_n \end{aligned} \quad (6.50)$$

where the influence coefficients g_{ij} have been modified to include the normal vector \mathbf{n} to the element j in each node k as:

$$g_{ij}^k = \int_{-1}^1 \int_{-1}^1 \varphi_k(\xi_1, \xi_2) n_j^k u^* |\mathbf{G}| d\xi_1 d\xi_2 \quad (6.51)$$

6.4. The Nonuniqueness Problem

The main difficulty of applying BEM to acoustic external problems is the so-called nonuniqueness problem, whereby the solution at certain characteristic frequencies is not unique. The problem is a mathematical one and is related to the boundary integral formulation and not to the physical problem itself.

A simple way of proving the existence of the nonuniqueness of the solution is to compare the boundary integral equation for an exterior Neumann problem (q assigned on Γ) with the boundary integral equation for an interior Dirichlet problem (u assigned on Γ) sharing the same boundary Γ (Brebbia and Ciskowski 1991):

$$c_i u_i + \int_{\Gamma} u q^* d\Gamma = \int_{\Gamma} q u^* d\Gamma + u^i \quad (6.52)$$

$$c_i \sigma_i + \int_{\Gamma} \sigma q^* d\Gamma = -u^i \quad (6.53)$$

Both equations have the same left-hand side member, apart from a change in variable, which is the potential u on the boundary for the exterior problem and the jump in potential σ when taking an internal point x_i to the boundary for the interior problem.

Since the interior formulation does experience a true problem due to the structure eigenfrequencies (resonance frequencies), the exterior domain equation will share the same problem, since it has the same mathematical structure, even though the eigenfrequencies have no physical meaning for an exterior problem and a unique solution actually exists at all frequencies.

There are two major ways of overcoming the nonuniqueness problem, the *Coupled Helmholtz Integral Equation Formulation* (CHIEF) and the *Helmholtz Gradient Formulation* (HGF):

- **CHIEF method:** this formulation, proposed by Schenck (1968), uses the Helmholtz integral equation (6.47) pointing inside the body where $c_i = 0$ as a constraint to be satisfied along with the usual Helmholtz equation. This formulation results in an overdetermined system which can be solved by a least square algorithm, such as the SVD (Singular Value Decomposition) method. One of the difficulties of this formulation is that the internal points used to implement the coupling cannot fall onto the boundary, otherwise the constraint imposed by the second Helmholtz equation leads again to a nonunique solution. The proper choice of the internal

points to use is currently an important research issue, addressed for example by Seybert and Wu (1991)

- **HGF method:** this method has been proposed by Burton and Miller (1971) and consists of a linear combination of the integral Helmholtz equation and its normal derivatives equation. It can be proven that a proper choice of the multiplicative constant of the gradient equation leads to a unique solution at all frequencies. One of the major difficulties of this method is that the normal derivative of the integral equation involves a hypersingular integral. Burton and Miller used a double surface integral to regularise the singularity, but the method is computationally inefficient. More efficient solutions have been proposed by Meyer *et al.* (1978) or De Rego Silva (1994). A partial application of the gradient method has recently been proposed for the solution of structural-acoustic coupling problems, whereby the normal derivative of the integral Helmholtz equation is computed only at a reduced number of points. The method has been proved efficient for both constant (Harris and Amini 1990) and isoparametric (Francis 1991) elements and is used in this research.

6.4.1. The Partial HGF Method

The derivative of eq. (6.46) with respect to the normal direction n' in each point $\mathbf{x}' \in \mathfrak{R}^3$ has the form:

$$c_i \frac{\partial u_i}{\partial n'} = \frac{\partial u^i}{\partial n'} + \int_{\Gamma} \left[\frac{\partial u}{\partial n} \frac{\partial G}{\partial n'} - u \frac{\partial^2 G}{\partial n \partial n'} \right] d\Gamma \quad (6.54)$$

with

$$\frac{\partial^2 G}{\partial n \partial n'} = \frac{1}{4\pi r^3} \left[(3 + ikr - k^2 r^2) \frac{\partial r}{\partial n'} \frac{\partial r}{\partial n} + (1 + ikr) \mathbf{n} \cdot \mathbf{n}' \right] \quad r = |\mathbf{x}' - \mathbf{x}|, \mathbf{x}' \neq \mathbf{x} \quad (6.55)$$

Eq. (6.54) suffers from the same nonuniqueness problem as eq. (6.46), but the characteristic frequencies are different. In the standard HGF formulation, a suitable multiple α of eq. (6.54) is added to eq. (6.47) to build a system with unique solution at all frequencies under the condition that $\text{Im}(\alpha) \neq 0$ (Terai 1980, Meyer *et al.* 1979).

There are three main difficulties in this formulation:

- the presence of hypersingular integrals (of order $\frac{1}{r^2}$) in the derivatives
- the presence of discontinuities in the value of the derivatives when using quadratic isoparametric elements
- the added complexity of having to calculate $2N$ equations for N nodes instead of the standard N equations derived from the boundary integral equation

The hypersingular integrals can be directly evaluated in the sense of Hadamard finite parts (Do Rego Silva 1994) or reduced to singular integrals by applying the integral relationship proposed by Meyer *et al.* (1978):

$$\int_{\Gamma} u \frac{\partial^2 G}{\partial n' \partial n} d\Gamma = \int_{\Gamma} [u(\mathbf{x}) - u(\mathbf{x}')] \frac{\partial^2 G}{\partial n' \partial n} d\Gamma + k^2 u(\mathbf{x}') \int_{\Gamma} (\mathbf{n}' \cdot \mathbf{n}) u d\Gamma \quad (6.56)$$

The problem of discontinuities in the normal derivative across element boundaries when using quadratic isoparametric elements can be overcome by the use of discontinuous elements, whereby the nodes are moved inside the elements and away from the border.

Finally, the problem of the additional overhead of having to calculate the n derivatives of the boundary integral Helmholtz equation can be eased by choosing the centre of each element only as a calculation point. This approach reduces the number of additional equation to approximately $n/3$, since the typical ratio between elements and nodes in a boundary element schema is 1:3.

This approach, referred to as the Partial HGF method, has been proved to yield unique solutions to the scattering problem with quadratic isoparametric elements by D.T.I. Francis of the School of Electronic & Electrical Engineering of the University of Birmingham (1991) and the method used in this research is based on his original code.

Taking therefore the calculation point \mathbf{x}' at the centre of each element and using the integral relationship (6.56) and the boundary conditions (6.41), the resulting normal derivative equation can be discretised as:

$$\sum_{\substack{j=1 \\ j \neq i}}^N (C_{ij} \cdot \mathbf{p}_j - C'_{ij} \cdot \mathbf{p}_i) + C''_{ii} \cdot \mathbf{p}_i + \sum_{j=1}^N C'''_{ij} \cdot \mathbf{p}_i = \sum_{j=1}^N \mathbf{D}_{ij} \cdot \mathbf{v}_j - \frac{1}{2} n' \boldsymbol{\varphi}^0 \cdot \mathbf{v}_i + \frac{\partial p^i(\mathbf{x}')}{\partial n''} \quad (6.57)$$

where \mathbf{p}_k and \mathbf{v}_k are the vectors of nodal values of pressure and velocity in the k^{th} element, $\boldsymbol{\varphi}^0$ is the vector of shape functions calculated in the centre of the element and

$$\left\{ \begin{aligned} C_{ij} &= \int_{-1}^1 \int_{-1}^1 \boldsymbol{\varphi} \frac{\partial^2 G(\mathbf{x}'_i, \mathbf{x})}{\partial n' \partial n} \big| \mathbf{G}_j \big| d\xi_1 d\xi_2 & i \neq j \\ C'_{ij} &= \boldsymbol{\varphi}^0 \int_{-1}^1 \int_{-1}^1 \frac{\partial^2 G(\mathbf{x}'_i, \mathbf{x})}{\partial n' \partial n} \big| \mathbf{G}_j \big| d\xi_1 d\xi_2 & i \neq j \\ C''_{ii} &= \int_{-1}^1 \int_{-1}^1 (\boldsymbol{\varphi} - \boldsymbol{\varphi}^0) \frac{\partial^2 G(\mathbf{x}'_i, \mathbf{x})}{\partial n' \partial n} \big| \mathbf{G}_i \big| d\xi_1 d\xi_2 \\ C'''_{ij} &= k^2 \boldsymbol{\varphi}^0 \int_{-1}^1 \int_{-1}^1 \mathbf{n}' \cdot \mathbf{n} G(\mathbf{x}'_i, \mathbf{x}) \big| \mathbf{G}_j \big| d\xi_1 d\xi_2 \\ \mathbf{D}_{ij} &= -i\omega\rho_0 \int_{-1}^1 \int_{-1}^1 \boldsymbol{\varphi} \mathbf{n}^T \frac{\partial G(\mathbf{x}'_i, \mathbf{x})}{\partial n'} \big| \mathbf{G}_j \big| d\xi_1 d\xi_2 \end{aligned} \right. \quad (6.58)$$

Assembling the coefficients (6.58) that correspond to the same pairs of global nodes, we finally have:

$$\mathbf{C}\mathbf{p} = \frac{\partial \mathbf{p}^i}{\partial n'} + \mathbf{D}\mathbf{v} \quad (6.59)$$

The final system is built by adding to each nodal equation in (6.49) α times the normal derivative equation in (6.59) calculated in the centre of the corresponding element. The coefficient α is taken to be equal to $-ik/m_i$, where m_i is the number of elements sharing node i .

6.5. Structural-Acoustic Coupling

6.5.1. Basic Equations

The usual approach to solving problems involving acoustic radiation and scattering from elastic structures submerged in an infinite fluid medium is to use the coupling of a finite

element model for the elastic structure, which is computationally faster than the equivalent elastodynamic boundary formulation, combined with a boundary element model for the infinite extension of the external fluid medium.

The finite element model is of the form (Zinkiewicz 1971 and the following section for the details):

$$(-\omega^2 \mathbf{M} + i\omega \mathbf{C} + \mathbf{K})\mathbf{u} = \mathbf{f}^r + \mathbf{f}^d \quad (6.60)$$

where \mathbf{M} , \mathbf{C} and \mathbf{K} are the mass, damping and stiffness matrix of the structure respectively, \mathbf{u} is a vector of nodal displacements, \mathbf{f}^r is the load vector corresponding to the external acoustic loading and \mathbf{f}^d is the load vector corresponding to all other forces acting on the structure. Harmonic time dependence of the form $e^{i\omega t}$ is understood for all functions.

The finite element model used is based on M hexahedral element. The nodes of the elements are located at the corners and mid-side positions. As in the boundary element model, all variables are approximated as linear interpolations of their nodal values in terms of a set of quadratic functions in local normalised co-ordinates. The complete set of shape functions is given in table 6.2.

The acoustic load vector can be expressed in terms of the acoustic pressure as (Brebbia and Ciskowski 1991 and next section for the details):

$$\mathbf{f}^r = -\int_{\Gamma} p \mathbf{\Phi} \mathbf{n} \, d\Gamma = -\mathbf{L}p \quad (6.61)$$

BIQUADRATIC HEXAHEDRAL ELEMENT	
$u(\xi_1, \xi_2, \xi_3) = \sum_{j=1}^{20} \varphi_j u_j = \boldsymbol{\varphi}^j \mathbf{u}_j = \boldsymbol{\varphi} \cdot \mathbf{u}$	
$\begin{aligned} \varphi_1 &= \frac{1}{8}(1-\xi_1)(1-\xi_2)(-2-\xi_1-\xi_2-\xi_3) \\ \varphi_2 &= \frac{1}{4}(1-\xi_1^2)(1-\xi_2)(1-\xi_3) \\ \varphi_3 &= \frac{1}{8}(1+\xi_1)(1-\xi_2)(-2-\xi_1-\xi_2-\xi_3) \\ \varphi_4 &= \frac{1}{4}(1+\xi_1)(1-\xi_2^2)(1-\xi_3) \\ \varphi_5 &= \frac{1}{8}(1+\xi_1)(1+\xi_2)(-2+\xi_1+\xi_2-\xi_3) \\ \varphi_6 &= \frac{1}{4}(1-\xi_1^2)(1+\xi_2)(1-\xi_3) \\ \varphi_7 &= \frac{1}{8}(1-\xi_1)(1+\xi_2)(-2-\xi_1+\xi_2-\xi_3) \\ \varphi_8 &= \frac{1}{4}(1-\xi_1)(1-\xi_2^2)(1-\xi_3) \\ \varphi_9 &= \frac{1}{4}(1-\xi_1)(1-\xi_2)(1-\xi_3^2) \\ \varphi_{10} &= \frac{1}{4}(1+\xi_1)(1-\xi_2)(1-\xi_3^2) \end{aligned}$	$\begin{aligned} \varphi_{11} &= \frac{1}{4}(1+\xi_1)(1+\xi_2)(1-\xi_3^2) \\ \varphi_{12} &= \frac{1}{4}(1-\xi_1)(1+\xi_2)(1-\xi_3^2) \\ \varphi_{13} &= \frac{1}{8}(1-\xi_1)(1-\xi_2)(-2-\xi_1-\xi_2+\xi_3) \\ \varphi_{14} &= \frac{1}{4}(1-\xi_1^2)(1-\xi_2)(1+\xi_3) \\ \varphi_{15} &= \frac{1}{8}(1+\xi_1)(1-\xi_2)(-2+\xi_1-\xi_2+\xi_3) \\ \varphi_{16} &= \frac{1}{4}(1+\xi_1)(1-\xi_2^2)(1+\xi_3) \\ \varphi_{17} &= \frac{1}{8}(1+\xi_1)(1+\xi_2)(-2+\xi_1+\xi_2+\xi_3) \\ \varphi_{18} &= \frac{1}{4}(1-\xi_1^2)(1+\xi_2)(1+\xi_3) \\ \varphi_{19} &= \frac{1}{8}(1-\xi_1)(1+\xi_2)(-2-\xi_1+\xi_2+\xi_3) \\ \varphi_{20} &= \frac{1}{4}(1-\xi_1)(1-\xi_2^2)(1+\xi_3) \end{aligned}$

Table 6.2: Interpolation functions for hexahedral quadratic elements three dimensions

where $\boldsymbol{\Phi}$ is the matrix of finite element interpolation functions, \mathbf{L} is a coupling matrix of integral terms that depend on the interpolation function matrix $\boldsymbol{\Phi}$ for both finite and boundary elements, \mathbf{p} is the vector of nodal pressure and \mathbf{n} is normal to the surface Γ pointing outside the acoustic domain.

The two FE and BE equations can be coupled through the relationship between acoustic surface pressure and radiation loading (6.57). The form of the boundary element equation to use is the one derived in the previous section by combining the boundary element

equation (6.49) and its derivative equation (6.59) expressed in terms of the pressure and velocity fields.

There are two main possibilities for linking the FE and BE methods, notably the *structure-variable method* and the *fluid-variable method* (Mathews 1986). In the former method, the BE equation is substituted into the FE equation; in the latter, the reverse substitution is undertaken. In the present case, the structure-variable method is preferred for two main reasons. The first reason is that at frequencies close to the natural resonance frequencies of the scatterer, the FE equation becomes ill conditioned and the use of the structure-variable method has a dampening effect that avoids this problem. The second reason is that it is simpler from a programming point of view to apply external boundary conditions and constraints to the modified FE equation rather than to the modified BE equation and the same code can be used to find the natural frequencies of the structure in the unloaded case.

We can therefore invert the BE equation (6.49), modified with the derivative equation (6.59), with the velocity vector \mathbf{v} replaced in terms of the displacement vector as $i\omega\mathbf{u}$:

$$\mathbf{p} = i\omega\mathbf{A}^{-1}\mathbf{B}\mathbf{u} + \mathbf{A}^{-1}\mathbf{p}^i \quad (6.62)$$

then insert eq. (6.62) in the radiation load eq. (6.61) and finally cast the resulting expression into the FE equation (6.60):

$$(-\omega^2\mathbf{M} + i\omega\mathbf{C} + \mathbf{K})\mathbf{u} = -\mathbf{L}[i\omega\mathbf{A}^{-1}\mathbf{B}\mathbf{u} + \mathbf{A}^{-1}\mathbf{p}^i] + \mathbf{f}^d \quad (6.63)$$

From eq. (6.63) the displacement nodal values \mathbf{u} can finally be computed as:

$$\mathbf{u} = \left[-\omega^2 \mathbf{M} + i\omega(\mathbf{C} + \mathbf{L}\mathbf{A}^{-1}\mathbf{B}) + \mathbf{K} \right]^{-1} (-\mathbf{L}\mathbf{A}^{-1}\mathbf{p}^i + \mathbf{f}^d) \quad (6.64)$$

From the solution for the displacements \mathbf{u} , all other field variables can be worked out using the given constitutive relationships (see for example Francis and Coates 1996).

6.6. Modelling of Absorbing Structures by Means of Viscoelastic Elements

We consider now a viscoelastic body whose material properties can be described using the linear viscoelastic theory introduced in Chapter 3.

Let \mathfrak{B} be a viscoelastic body with relaxation function \mathbf{G} and density ρ , subjected to the body force \mathbf{f} . We define a *dynamic viscoelastic process* for \mathfrak{B} corresponding to \mathbf{G} , \mathbf{f} and ρ , or $\text{DVP}(\mathbf{G}, \mathbf{f}, \rho)$, with the continuity conditions set in Chapter 3 as the set of relationships:

$$\nabla \mathbf{S} + \mathbf{f} = \rho \ddot{\mathbf{a}} \quad (\text{equation of motion}) \quad (6.65)$$

$$\mathbf{E} = \frac{1}{2} [\nabla \mathbf{a} + \nabla \mathbf{a}^T] = \nabla_{\text{sym}} \mathbf{a} \quad (\text{strain-displacement relation}) \quad (6.66)$$

$$\mathbf{S} = \mathcal{L}_{\mathbf{G}}[\mathbf{E}] = \mathbf{G} \oplus \mathbf{E} \quad (\text{Boltzmann relaxation law}) \quad (6.67)$$

where $\mathbf{a} = \mathbf{a}(\mathbf{x}, t)$ is a displacement vector, \mathbf{E} is the strain tensor, \mathbf{S} is the stress tensor, ∇_{sym} is the symmetric divergence operator and the dot notation stands for derivation with respect to time. Equation (6.65) is valid in all interior points of body \mathfrak{B} .

We further consider an elastodynamic problem for the body \mathfrak{B} , occupying a regular domain Ω with surface boundary Γ and subjected to specified body forces \mathbf{f} and surface tractions \mathbf{t} .

We consider a class of arbitrary virtual displacements $\delta\mathbf{a}$, consistent with the external constraints. The virtual work done by the external forces and tractions by effect of the virtual displacements is written as:

$$\delta W = \int_{\Omega} \delta\mathbf{a} \cdot \mathbf{f} d\Omega + \int_{\Gamma} \delta\mathbf{a} \cdot \mathbf{t} d\Gamma \quad (6.68)$$

By using Cauchy's stress formula $\mathbf{t} = \mathbf{S}\mathbf{n}$, where \mathbf{n} is the unit vector normal to the surface Γ , and applying Gauss' theorem, eq. (6.68) can be rewritten as a volume integral:

$$\delta W = \int_{\Omega} \delta\mathbf{a} \cdot \mathbf{f} d\Omega + \int_{\Omega} \nabla \cdot (\delta\mathbf{a}^T \mathbf{S}) d\Omega = \int_{\Omega} \delta\mathbf{a} \cdot \mathbf{f} d\Omega + \int_{\Omega} [\delta\mathbf{a} \cdot \nabla \mathbf{S} + \nabla \delta\mathbf{a} \cdot \mathbf{S}] d\Omega \quad (6.69)$$

The divergence of the virtual displacement vector can be further decomposed in its symmetric $\nabla_{sym} \delta\mathbf{a} = \delta\mathbf{E}$ and deviatoric $\nabla_{dev} \delta\mathbf{a}$ components and noting that the stress tensor \mathbf{S} is symmetric, the virtual work δW can finally be written as:

$$\delta W = \int_{\Omega} \delta\mathbf{a} \cdot \rho \ddot{\mathbf{a}} d\Omega + \int_{\Omega} \delta\mathbf{E} \cdot \mathbf{S} d\Omega \quad (6.70)$$

where the stress equation of motion (6.65) has been used to replace the external actions with the inertia term.

Equating the two expressions (6.68) and (6.70), which is equivalent to equating the external virtual work to the internal variation of kinetic and potential energy, we obtain the variational equation of motion of the body \mathfrak{B} :

$$\int_{\Omega} \delta \mathbf{a} \cdot \mathbf{f} d\Omega + \int_{\Gamma} \delta \mathbf{a} \cdot \mathbf{t} d\Gamma = \int_{\Omega} \delta \mathbf{a} \cdot \rho \ddot{\mathbf{a}} d\Omega + \int_{\Omega} \delta \mathbf{E} \cdot \mathbf{S} d\Omega \quad (6.71)$$

Finally, by incorporating the constitutive relationships (6.66) and (6.67) into the variational equation of motion (6.71) we obtain:

$$\text{Error! Objects cannot be created from editing field codes.} \quad (6.72)$$

Eq. (6.72) can now be discretised using the shape functions defined in the previous section to approximate the displacements \mathbf{a} and their virtual variations. We define therefore the linear interpolation $\mathbf{a} = \Phi \mathbf{u}$ where \mathbf{u} is vector of nodal displacement and rewrite eq. (6.72) as

$$\delta \mathbf{u} \cdot \mathbf{f}_n + \delta \mathbf{u}^T \int_{\Gamma} \Phi^T \mathbf{t} d\Gamma = \delta \mathbf{u}^T \left(\rho \int_{\Omega} \Phi^T \Phi d\Omega \right) \ddot{\mathbf{u}} + \delta \mathbf{u}^T \left[\int_{\Omega} \Phi^T \nabla_{sym}^T (\mathbf{G} \oplus) \nabla_{sym} \Phi d\Omega \right] \mathbf{u} \quad (6.73)$$

or, in view of the fact that the virtual displacements are arbitrary

$$\mathbf{f}^d + \mathbf{f}^r = \left(\rho \int_{\Omega} \Phi^T \Phi d\Omega \right) \ddot{\mathbf{u}} + \left[\int_{\Omega} \Phi^T \nabla_{sym}^T (\mathbf{G} \oplus) \nabla_{sym} \Phi d\Omega \right] \mathbf{u} \quad (6.74)$$

where we have introduced the concentrated load vector \mathbf{f}^l and the radiation load \mathbf{f}^r defined in the previous section.

We consider now an oscillatory displacement process over the viscoelastic body \mathfrak{B} at the real frequency ω :

$$\mathbf{u}(\mathbf{x}, t) = \mathbf{u}(\mathbf{x})e^{i\omega t}, \quad (\mathbf{x}, t) \in \mathfrak{B} \times \mathfrak{R} \quad (6.75)$$

The constitutive relation for strong response functions \mathbf{G} , eq. (6.67), becomes⁴:

$$\begin{aligned} \mathbf{S}(\mathbf{x}, t) &= \left\{ \overset{\circ}{\mathbf{G}}(\mathbf{x}) + \int_0^\infty \dot{\mathbf{G}}(\mathbf{x}, t) e^{-i\omega \tau} d\tau \right\} \nabla_{sym} \mathbf{u} e^{i\omega t} = \\ &= \mathbf{C}^*(\mathbf{x}, \omega) \mathbf{E}(\mathbf{x}) e^{i\omega t}, \end{aligned} \quad (\mathbf{x}, t) \in \mathfrak{B} \times \mathfrak{R} \quad (6.76)$$

where $\mathbf{C}^*(\mathbf{x}, \omega)$ is the *complex modulus*. Dropping the dependence upon the point \mathbf{x} , since we deal with homogenous isotropic materials, $\mathbf{C}^*(\mathbf{x}, \omega)$ is rewritten in terms of its real and imaginary parts as $\mathbf{C}^*(\omega) = \mathbf{C}_1(\omega) + i\mathbf{C}_2(\omega)$, where

$$\mathbf{C}_1(\omega) = \overset{\circ}{\mathbf{G}} + \text{Re} \int_0^\infty \dot{\mathbf{G}}(\tau) e^{-i\omega \tau} d\tau = \overset{\circ}{\mathbf{G}} + \hat{\mathbf{G}}_c \quad (6.77)$$

$$\mathbf{C}_2(\omega) = \text{Im} \int_0^\infty \dot{\mathbf{G}}(\tau) e^{-i\omega \tau} d\tau = \hat{\mathbf{G}}_s \quad (6.78)$$

⁴ Cf. §3.3.8

If we assume the external loads to have the same harmonic dependence on time as the displacement, the equation of motion for the oscillatory displacement field becomes:

$$-\omega^2 \left(\rho \int_{\Omega} \Phi^T \Phi d\Omega \right) \mathbf{u} + \left[\int_{\Omega} \Phi^T \nabla_{sym}^T \mathbf{C}^*(\omega) \nabla_{sym} \Phi d\Omega \right] \mathbf{u} = \mathbf{f}^d + \mathbf{f}^r \quad (6.79)$$

or

$$\left[-\omega^2 \mathbf{M} + \mathbf{K}(\omega) \right] \mathbf{u} = \mathbf{f}^d + \mathbf{f}^r \quad (6.80)$$

where

$$\begin{cases} \mathbf{M} = \rho \int_{\Omega} \Phi^T \Phi d\Omega \\ \mathbf{K}(\omega) = \int_{\Omega} \Phi^T \nabla_{sym}^T \mathbf{C}^*(\omega) \nabla_{sym} \Phi d\Omega \end{cases} \quad (6.81)$$

The matrix $\mathbf{K}(\omega)$ is the frequency dependent viscoelastic stiffness matrix, which defines the viscoelastic finite element. This form of the equation can be computed in each element of the schema. The global form of the FE equation is then assembled by summing up the coefficient that refers to the same global nodes in the complete schema. The integrals are calculated as shown earlier by means of a local co-ordinate transformation.

Eq. (6.80) can now be coupled with the discretised BE model of the radiation load to calculate the displacement of the viscoelastic structure:

$$\mathbf{u} = \left[-\omega^2 \mathbf{M} + i\omega \mathbf{L} \mathbf{A}^{-1} \mathbf{B} + \mathbf{K}(\omega) \right]^{-1} \left(-\mathbf{L} \mathbf{A}^{-1} \mathbf{p}^i + \mathbf{f}^d \right) \quad (6.82)$$

6.7. Conclusions

In this chapter, the boundary element method has been applied to the solution of the integral Helmholtz equation for scattering problems derived from the application of reciprocity theorems. A method of overcoming the nonuniqueness problem typical of this formulation has been presented.

We have shown how the boundary conditions for the problem can be derived from the solution of the variational equation of motion of the scatterer and how to incorporate the two models to obtain a complete expression for the deformation of an elastic body subjected to the radiation loading produced by the acoustic field in the embedding medium.

Finally, the form of the viscoelastic stiffness coefficients have been derived from the linear theory of viscoelasticity and incorporated in the final form of the FE-BE element formulation.

In this chapter, a path started in Chapter 3 comes to its conclusion. The theoretical and experimental results derived and collected so far have lead us to establish a compact and powerful method of analysis of acoustic scattering in the presence of a viscoelastic body immersed in a loading fluid and subjected to a source-free acoustic plane-wave field.

The method will now be put to work in the next chapter, where it will be used to provide a solution to the problem for the case of periodic anechoic tiles and baffles.

References

- BREBBIA, C.A. and CISKOWSKI, R.D. (eds.) (1991), *Boundary Element Methods in Acoustics*, Computational Mechanics Publications, Elsevier Applied Science, London
- BREBBIA, C.A., DOMINGUEZ, J. (1992), *Boundary Elements. An Introductory Course*, Computational mechanics Publications, McGraw-Hill Book Company, Southampton
- BURTON, A.J. and MILLER, G.F. (1971), The Application of Integral Equation Methods to the Numerical Solution of Some Exterior Boundary Value Problems, *Proc. Royal Soc. London A*, 323, 201-210
- CHEN, G.M. and ZHOU, H.W. (1994), Boundary-Element Modelling of Nondissipative and Dissipative Waves, *Geophysics*, 59 (1), 113-118
- COWSAR, L.C. *et al.* (1996), A-Priori Estimates For Mixed Finite-Element Approximations of 2nd-Order Hyperbolic-Equations with Absorbing Boundary-Conditions, *SIAM J. Num. Analysis*, 33 (2), 492-504
- CRUSE, T.A. and RIZZO, F.J. (eds.) (1975), *Boundary-Integral Equation Method: Computational Applications in Applied Mechanics, AMD-Vol. II, A.S.M.E.*
- DI MEGLIO, A. *et al.* (1996), PHOEBE: A 3-Dimensional Transducer Modelling Environment, *Proc. 3rd European Conference on Underwater Acoustics*, Vol. II
- DO RÊGO SILVA, J.J. (1994), *Acoustic and elastic wave scattering using boundary elements*, Southampton: Computational Mechanics Publications
- FRANCIS, D.T.I. (1991), Partial Use of the Helmholtz Gradient Formulation to Obtain Unique Solutions to Acoustic radiation Problems at Characteristic Frequencies, *J. Sound Vib.*, 145, 495-498
- FRANCIS, D.T.I. (1993), A Gradient Formulation of the Helmholtz Integral Equation for Acoustic Radiation and Scattering, *J. Acoust. Soc. Am.*, 93 (4,1), 1700-1708
- Francis, D.T.I., Coates, R.F.W., Acoustic Scattering from Fluid-Filled Shells Using a Combined Finite-Element and Boundary-Element Method, to be published in *Boundary Element Communication*
- GAUL, L. and SCHANZ, M. (1994), Dynamics of Viscoelastic Solids Treated by Boundary Element Approaches in Time-Domain, *Eur. J. Mech., A-Solids*, 13, 43-59
- HARRIS, P.J. and AMINI, S. (1990), *On the Burton and Miller Boundary Integral Formulation of the Exterior Acoustic Problem*, School of Mathematics and Statistics, University of Birmingham, UK, preprint 17/90
- JASWON, M.A. and SYMM, G.T. (1977), *Integral Equation Methods in Potential Theory and Elastostatics*, Academic Press, New York
- MAKIDRAKIS, C.G. (1995), High-Order Fully Discrete Methods for the Equations of Elastic-Wave Propagation with Absorbing Boundary-Conditions, *IMA J. Num. Analysis*, 15 (3), 377-404
- MATHEWS, I.C. (1986), Numerical techniques for three-dimensional steady-state fluid-structure interaction, *J. Acoust. Soc. Am.*, 79, 1317-1325
- MEYER, W.L. *et al.* (1978), Boundary Integral Solutions of Three-Dimensional Acoustic Radiation Problems, *J. Sound Vib.*, 59, 245-262
- SCHENCK, H.A. (1968), Improved Integral Formulation for Acoustic Radiation Problems, *J. Acoust. Soc. Am.*, 44, 41-58
- TERAI, T (1980), On calculation of sound fields around three dimensional objects by integral equation methods, *J. Sound Vib.*, 69, 71-100
- WU, T.W. and SEYBERT, A.F. (1991), A Weighted Residual Formulation for the CHIEF Method in Acoustics, *J. Acoust. Soc. Am.*, 90, 1608-1614
- ZINKIEWICZ, O. C. (1971), *The Finite Element Method in Engineering Science*, McGraw-Hill, London

Chapter 7

Modelling of Acoustic Scattering from Anechoic Viscoelastic Tiles

7.1. Introduction

In the previous chapters, we have been building the various components of a coupled Finite Element-Boundary Element method for the numerical analysis of acoustic scattering from viscoelastic bodies immersed in a loading fluid.

The viscoelastic linear theory has been used to derive the equations of the dynamics of viscoelastic bodies in general and in the special case of oscillatory motion. Then the integral-differential equations describing the acoustic scattering have been derived from the complex frequency-domain reciprocity theorem of the convolution type for both domain and surface problems. The Boundary Element method has been set up from the equivalent surface type

reciprocity equation and the details of the implementation of the numerical method have been discussed. The frequency-dependent boundary conditions for the problem have been determined by coupling the boundary element schema with a finite element schema of the scattering body described in terms of its viscoelastic properties.

In this chapter, the method will be applied to the study of acoustic scattering from complex-shaped tiles. The shape and composition of the tile have been chosen as a natural consequence of the research work carried out during the EC-funded project code-named VERTLINK. The project is described in more details in Chapter 1 and in the annexed papers in Appendix G. The prototype tile is composed of a layer of aluminium, a layer of butyl rubber and a final layer made of a regular grid of circular polyurethane cones. The details of the composition and the reasons behind this choice are discussed in the numerical and experimental results sections.

The simulation environment is first described and its limitations and constraints are discussed. Then the method is validated against a number of examples given in literature of from well-known exact and approximated analytical methods, such as the Rayleigh method of variable separation and Rayleigh-Ganz-Born method introduced in Chapter 5.

The method is then applied to the solution of the acoustic scattering problem from the composite anechoic tile. The dependence of the scattered pressure field from the angle of incidence is investigated as well as the dependence from the cones tip aperture at various frequencies within the range of interest for the VERTLINK project (30-50 kHz).

The numerical results are finally compared with in-tank measurements performed using the immersion method with parametric and standard sources presented in Chapter 4.

7.2. The Simulation Environment

The numerical simulations have been carried out using the WinFEBE computer program, which is presented in details in Chapter 8. WinFEBE is a Windows distributed application written with the purpose of providing a complete analysis environment for finite element-boundary element simulations of acoustic radiation and scattering. The program implements a port of the original DOS program written by D.T.I Francis and others in the Acoustic & Sonar Group of the School of Electronic & Electrical Engineering of the University of Birmingham (Francis 1993).

The original FE-BE algorithm had been modified to include the analysis of frequency-dependent viscoelastic materials and to take advantage the extended memory management features and distributed computing support typical of the Win32 platform. In addition, it has been complemented with a display unit for the visualisation of the models and the output of the results of the numerical analysis in forms of graphs and animated simulations. It also includes a built-in database of elastic, viscoelastic and piezoelectric materials.

The program has been tested during the past two years on several combinations of hardware and operating systems (Windows 95/98, Windows NT 4 and Windows 2000). In its most recent version, it has been implemented on a PC farm composed of five to eight Intel LX440G+ dual-processor machines with two Pentium III 500 MHz processors, 512 MB of internal RAM and an array of 2 to 5 fast SCSI hard disks of different capacity. The computers are remotely controlled from a central console unit that can be used to distribute different analysis tasks (frequency runs or models) to the various computers (nodes) and collect the results for further analysis. A detailed description of the system is given in Chapter 8.

Because of the relative high frequency range investigated in this research, a number of hardware and time constraints must be taken into account. The FE-BE algorithm dictates that

the maximum linear size of all the elements used in the model must not exceed half of the wavelength of the signal in the material or in the surrounding fluid in case of the boundary elements. These constraints are plotted in fig. 7.1 for the frequency range of interest and the different materials used in the simulations.

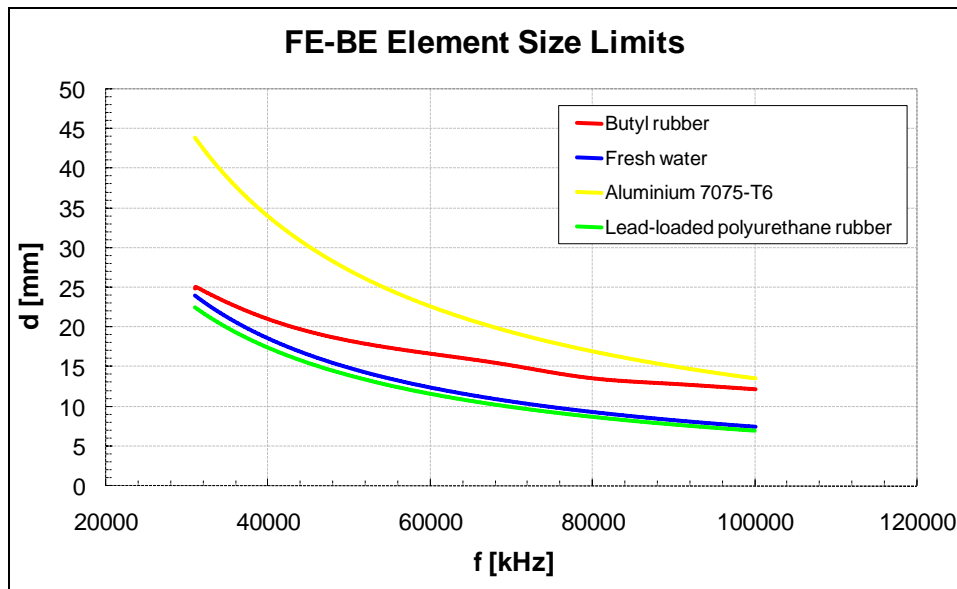


Figure 7.1: FE-BE element size constraints as a function of frequency. The maximum linear dimension must not exceed half a wavelength in all materials

As can be seen, the analysis of a 16x16x5 cm tile (including the grid of cones) made of aluminium, butyl rubber and polyurethane rubber immersed in water requires a maximum linear element size of about 2 cm at 30 kHz and 1 cm at 50 kHz. The number of nodes and elements for these two cases are reported in table 7.1.

According the numerical precision to be used, the memory requirements for these cases are quite substantial. Several tests have been conducted with both single (4-byte) and double (8-byte) precision floating point variables, having respectively 7-8 and 15-16

significant digits. The memory requirements for storing a typical coefficient matrix in these two cases are again reported in table 7.1.

	Nodes	Elements	Memory (single type)	Memory (double type)
f = 30 kHz	FEM 2373	FEM 256	193.3 MB	386.7 MB
	BEM 2114	BEM 704		
f = 50 kHz	FEM 9121	FEM 1024	2.79 GB	5.59 GB
	BEM 8638	BEM 2912		

Table 7.1: Memory requirements for the complete composite tile at two frequencies (FEM = Finite Element Model; BEM = Boundary Element Model)

The matrices evaluated during the analysis, from the mass and stiffness matrices to the coupling \mathbf{L} and the intermediate $\mathbf{L}\mathbf{A}^{-1}\mathbf{B}$ matrices, can both be stored in RAM memory and storage memory (hard disk) using different methods. The latter case practically allows removing model size limitations. However, the time required to store and retrieve values from the hard disk is several orders of magnitude longer than the time required to perform the same operation in RAM. A model of about 500 elements and 1500 nodes would require several days for operations such as the LU decomposition of a corresponding 20.250.000-element matrix (1500 nodes, three displacement components per node).

A compromise has been therefore sought after between model accuracy, frequency range and memory requirements. The largest memory space to be used should not exceed 4 times the available RAM space. With the configuration based on the Intel LX440G+ computers, this amounts to about 2 GB of space, of which 512 MB are stored in RAM (minus the small quota used for operating system functions and loaded programs) and the rest on the disk. The Windows operating systems allows configuring this disk space as an extension of the RAM space. The complete space is called the virtual memory space and as far as the

program is concerned, it can be treated as real RAM memory. This additionally simplifies the program, since it's not necessary to explicitly swap the matrices to disk during their use, but only to store them at the end.

All the models investigated in this research comply with these limitations. Whenever possible, mirror or rotational symmetries have been taken into account in the FE-BE models to reduce the number of elements or increase the upper frequency limit for the same number of elements (smaller element size).

7.3. Validation of the Method

The proposed FE-BE algorithm based on the partial HGF method developed by Francis (1993) has been successfully used in the past to analyse radiation and scattering problems. Several examples can be found in Jarng *et al.* (1990), Francis (1993), Francis (1996). A general review of the possible applications of the program is described in Di Meglio *et al.* (1996).

However, this algorithm has never been used in the particular case of plates or tiles and in the presence of viscoelastic materials. The method has been therefore initially validated by solving a number of problems with known solutions, from either analytical methods or numerical examples reported in the literature. In particular, two cases will be considered, an analytical approximate solution to sound scattering from viscoelastic flat tiles based on the 1st-order Rayleigh-Ganz-Born approximation presented in Chapter 5 and a numerical case of acoustic transmission through epoxy-graphite plates presented by Pates *et al.* (1995).

7.3.1. Case 1: Comparison with the Exact Modal Shapes and with the Rayleigh-Ganz-Born Solution of Sound Scattering for a Simply-Supported Square Plate

We consider the case of a square plate, simply supported along all edges. The exact in-vacuo characteristic frequencies and corresponding modal shapes can be determined by applying the method of variable separation (Rayleigh method) (Leissa 1969). The modal shape of the plate is written as:

$$W(x, y) = X(x)Y(y) \quad (7.1)$$

where the functions $X(x)$ and $Y(y)$ are deflection functions for beams having the same boundary conditions at the edges $x = 0$ and $x = a$ or $y = 0$ and $y = a$ respectively:

$$\begin{cases} X(x) = \sin \frac{(m-1)\pi x}{a} & m = 1, 2, 3, \dots \\ Y(y) = \sin \frac{(n-1)\pi y}{a} & n = 1, 2, 3, \dots \end{cases} \quad (7.2)$$

The characteristic frequencies ω_{mn} are the solutions of the equation

$$\omega^2 - \frac{\pi^4 D(\omega)}{a^4 \rho} \{G_x^4 + G_y^4 + 2[\nu(\omega)H_x H_y + (1 - \nu(\omega))J_x J_y]\} = 0 \quad (7.3)$$

where:

$$D(\omega) = \frac{E(\omega)h^2}{12(1-\nu^2(\omega))}$$

Flexural rigidity
 $E(\omega)$ = storage Young modulus,
 $\nu(\omega)$ = Poisson ratio,
 h = plate thickness

$$G_x = m - 1$$

$$G_y = n - 1$$

for the case of simply supported plate on the four sides

$$H_x = J_x = (m - 1)^2$$

$$H_y = J_y = (n - 1)^2$$

for the case of simply supported plate on the four sides

These relationships, which are in general valid for elastic materials, hold also in the case of linear viscoelastic solids, although in principle eq. (7.3) may have more than one solution for the same values of the modal parameters m and n . The solutions of eq. (7.3) can be found by applying any suitable algorithm for finding the zeros of a non-linear function. In the present case the MATLAB `fzero` function has been used.

We consider a square plate with side $a = 16$ cm and thickness $h = 5$ mm made of butyl rubber with density $\rho = 1800$ kg m⁻³. The characteristic frequencies in vacuo and their modal orders in the range between 30 kHz and 50 kHz are compared in table 7.2.

Rayleigh Method (in-vacuo-simply supported)	FEM-256/BEM-576 (in vacuo-simply supported)
30.614 kHz ($f_{10,6}$)	31.065 kHz
33.631 kHz ($f_{9,8}$)	33.975 kHz
35.338 kHz ($f_{10,7}$)	35.725 kHz
40.176 kHz ($f_{9,9}$)	41.725 kHz
41.110 kHz ($f_{10,8}$)	41.575 kHz
49.091 kHz ($f_{10,9}$)	49.885 kHz

Table 7.2: Comparison of characteristic frequencies (kHz) between analytical solution and coupled finite element-boundary element solution. Between brackets is the modal order

The square plate has been modelled using a mesh of 256 finite elements and 576 boundary elements with size $1.0 \times 1.0 \times 0.5$ cm. The values of the resonance frequencies for the simply supported plate in air and in the fluid-loaded case have been found by examining the maximum value of the averaged displacement of all nodes along the direction of the incoming sound wave (the z axis). The exact and FE-BE modal shapes are shown in figs. 7.2 to 7.4 for the (9,9) mode in air. The FE-BE model shows the deformation along the edges due to the constraints, which the analytical model cannot reproduce. As expected the maximum positive deformation has a phase lag of about 90° ($\phi = -84^\circ$) with respect to the forcing pressure wave.

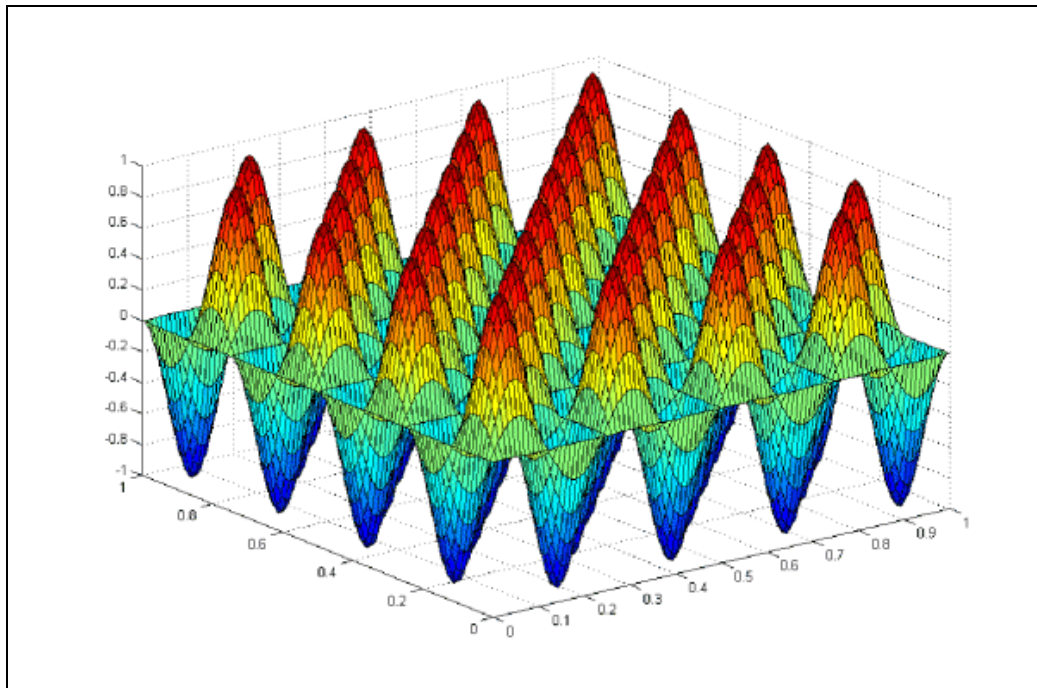


Figure 7.2: Simply-supported square plate. Exact modal shape at 40.176 kHz in vacuum ($f_{9,9}$). The square side is normalised to 1

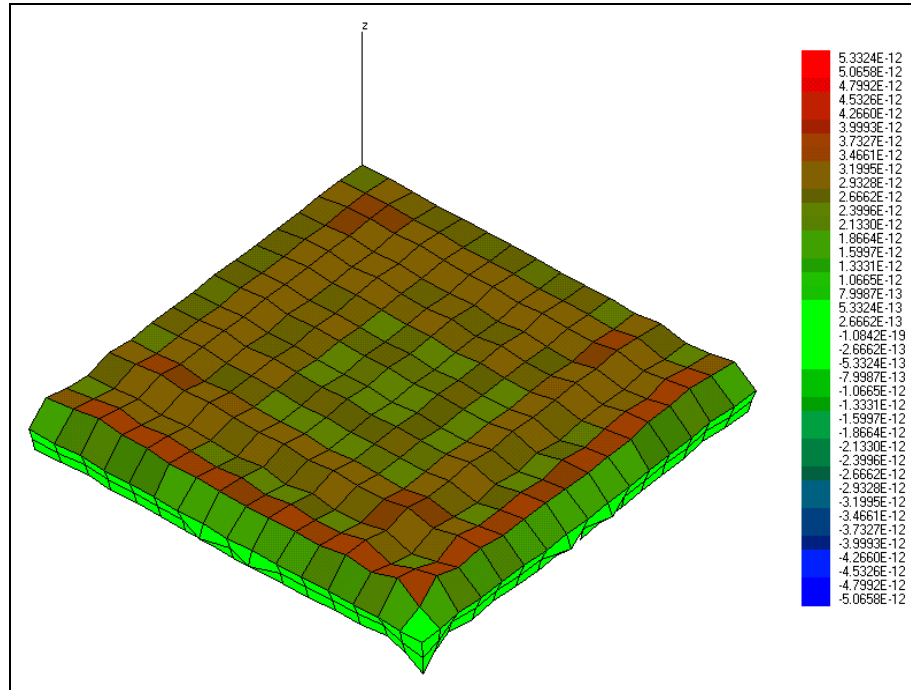


Figure 7.3: Simply-supported square plate in air (quarter model). Maximum positive deformation along the z-axis ($\phi=84$ deg)

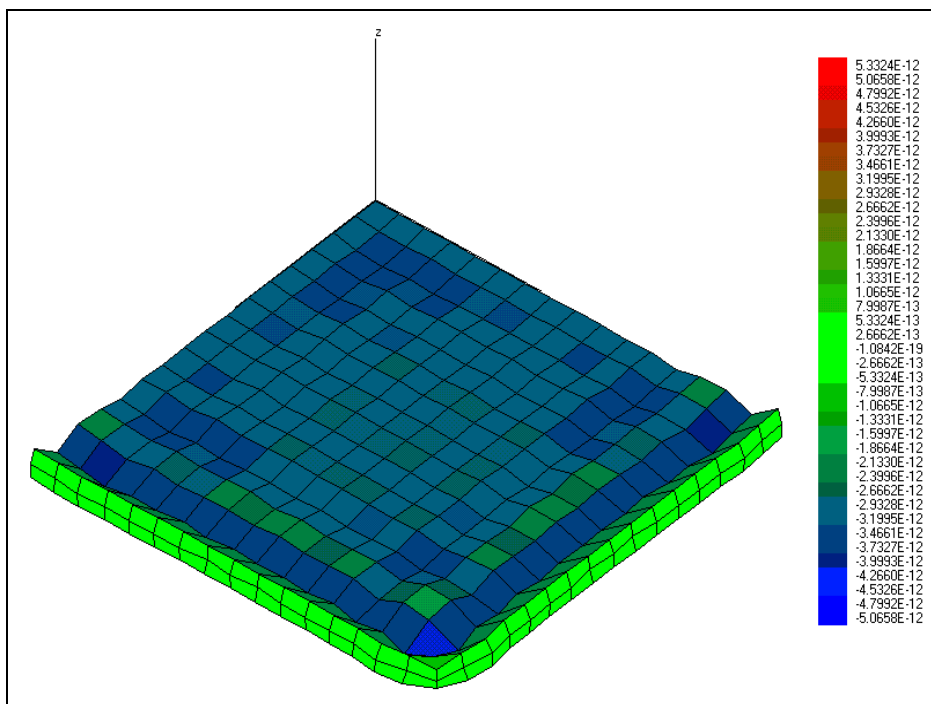


Figure 7.4: Simply-supported square plate in air (quarter model). Maximum negative deformation along the z-axis ($\phi=96$ deg)

The scattered pressure field in air around the same plate obtained by means of the coupled FE-BE model can be compared with the results obtained from the application of the Rayleigh-Ganz-Born method derived in chapter 5. The backscattered pressure fields in air are compared in figs. 7.5 to 7.7 at the three resonance frequencies 31.065 kHz, 41.725 kHz and 49.885 kHz. The results are in good agreement. The difference become noticeable closer for angles close to the plane of the plate, since the FE-BE model incorporates the effect of the physical constraints on the edges. The source direction on the graphs is from 90° (corresponding to normal incidence).

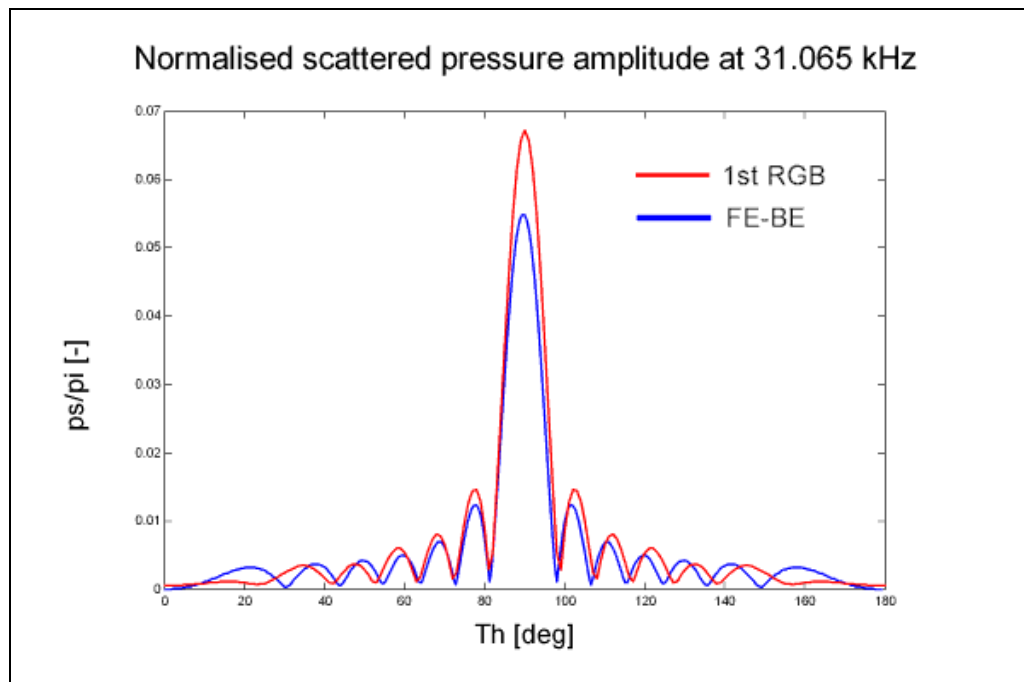


Figure 7.5: Normalised total backscattered pressure field at 31.065 kHz in air. Comparison between the 1st-order RGB solution and the FE-BE solution

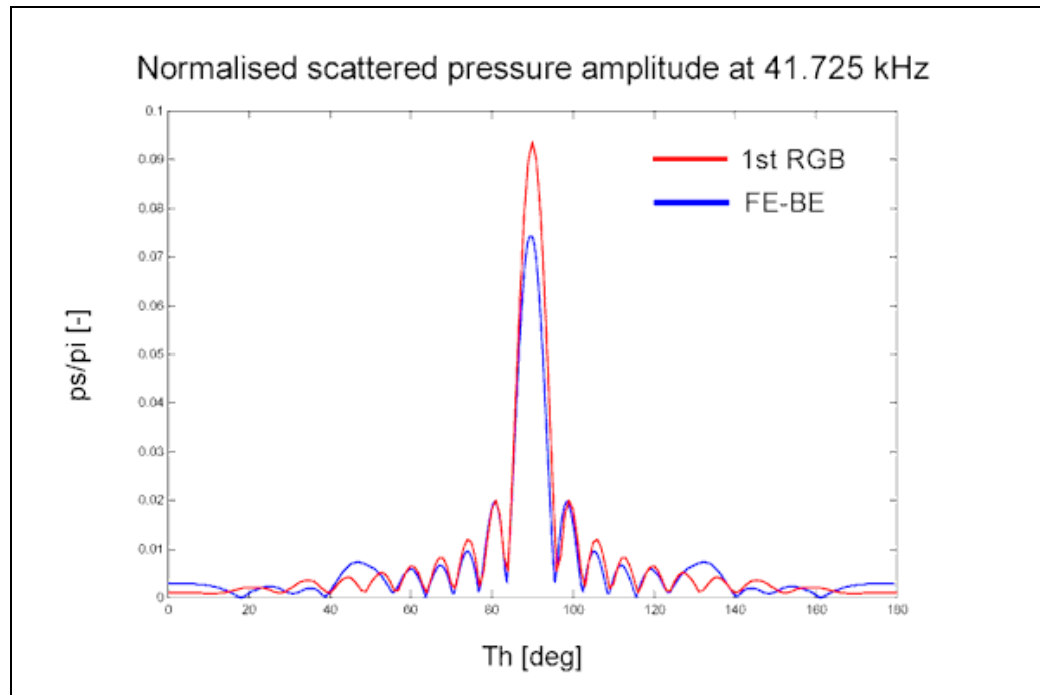


Figure 7.6: Normalised total backscattered pressure field at 41.725 kHz in air. Comparison between the 1st-order RGB solution and the FE-BE solution

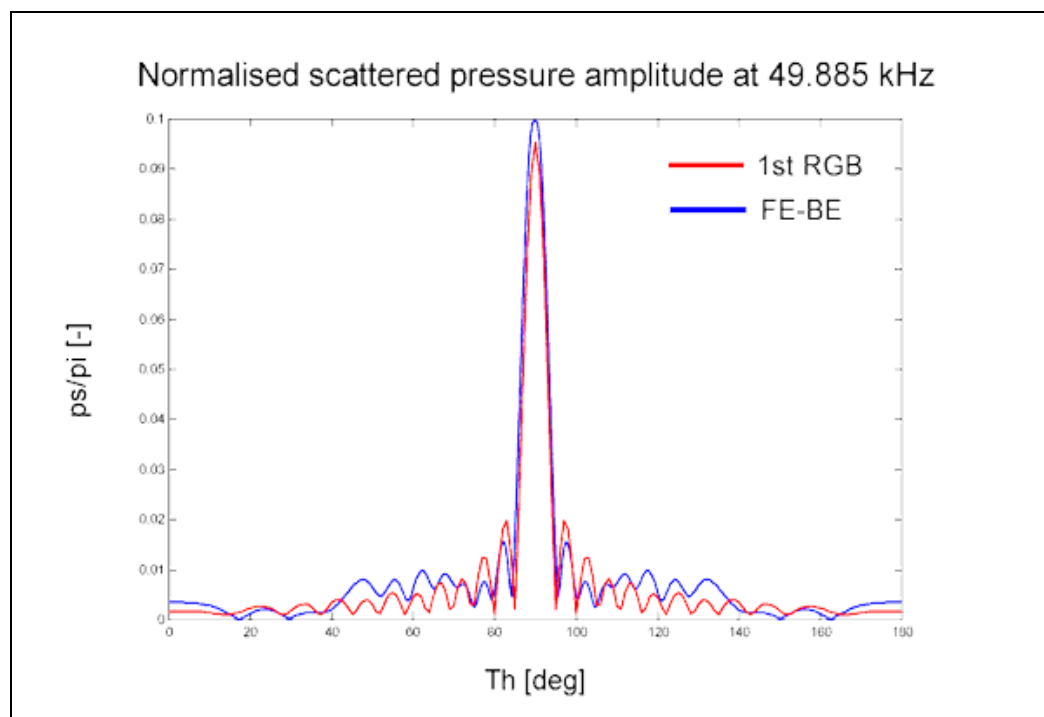


Figure 7.7: Normalised total backscattered pressure field at 49.885 kHz in air. Comparison between the 1st-order RGB solution and the FE-BE solution

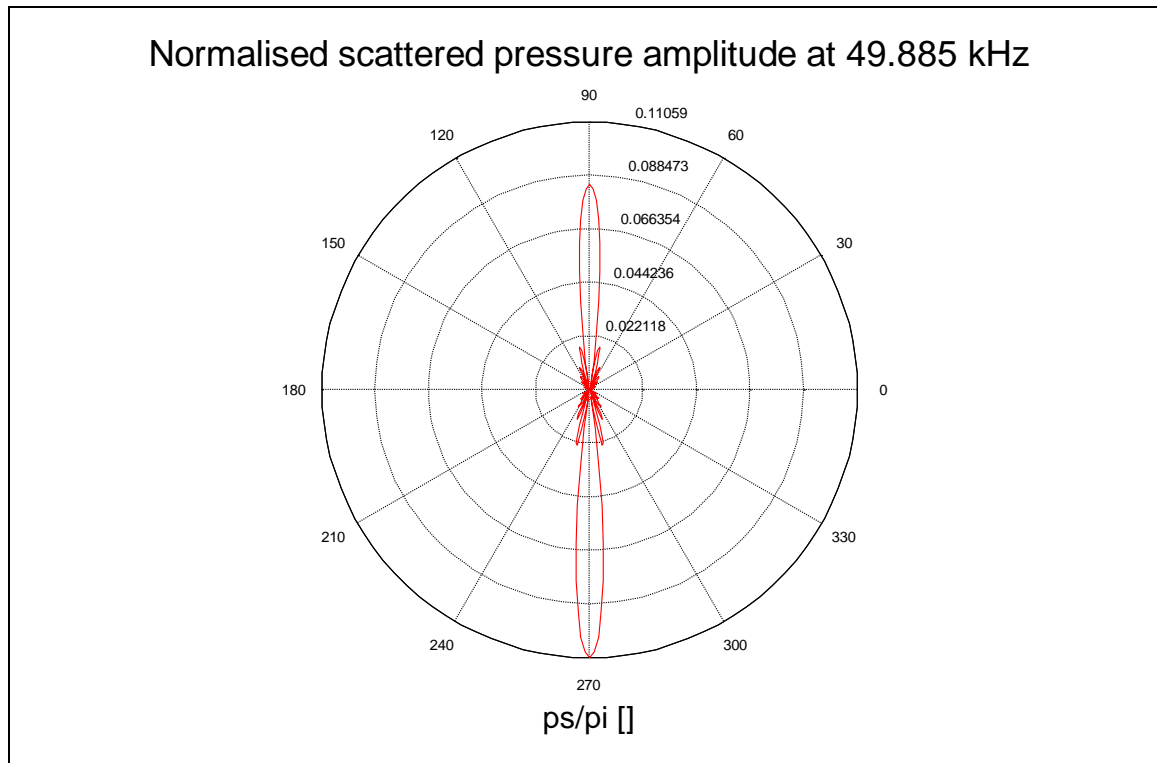


Figure 7.8: Total pressure field around the butyl rubber tile at 49.885 kHz (FE-BE solution)

7.3.2. Case 2: Acoustic Transmission through a Clamped Epoxy-Graphite Plate Facing a Rigid Cavity

In this second case, the coupled FE-BE method is used to investigate the transmission loss of a clamped seven-cross-ply graphite-epoxy rectangular plate facing a rigid-walled closed cavity. The problem is investigated in Pates *et al.* (1995) using their own implementation of the coupled FE-BE method.

In this case, the finite element method is used to find the velocity distribution on the lower side of the plate, the one facing the cavity. The velocity distribution is then used as boundary condition to solve the boundary integral problem inside the cavity. The transmitted pressure is then evaluated at the far end of the cavity. The size of the plate is 30.58 x 15.54 x

0.16 cm. The cavity has the same cross-section as the plate and is 15.54 cm long. The material properties of the graphite-epoxy composite are listed in table 7.3.

E_{11}	15.57e10	Pa
E_{12}	0.807e10	Pa
G_{44}	0.455e10	Pa
ν	0.22	
ρ	1500	kg m ⁻³

Table 7.3: Material properties of graphite-epoxy composite (Pates *et al.* 1995)

The model is made of 64 finite elements and 384 boundary elements. The analysis is carried out in vacuo in the frequency range between 0.05 and 1 kHz. The characteristic frequencies reported by Pates *et al.* are compared to the frequencies determined by the FE-BE method used in this research in table 7.4. The model of the plate an cavity and the modal shape at the first characteristic frequency are printed in figs. 7.9 and 7.10. The transmission loss curves in the proposed range are compared in figs. 7.11 and 7.12.

Pates et al. 1995	FEM-64/BEM-384
~210	207.5
~650	655.0

Table 7.4: Comparison of characteristic frequencies (Hz) (the values in Pates *et al.* (1995) are interpolated from the published graphs in the paper)

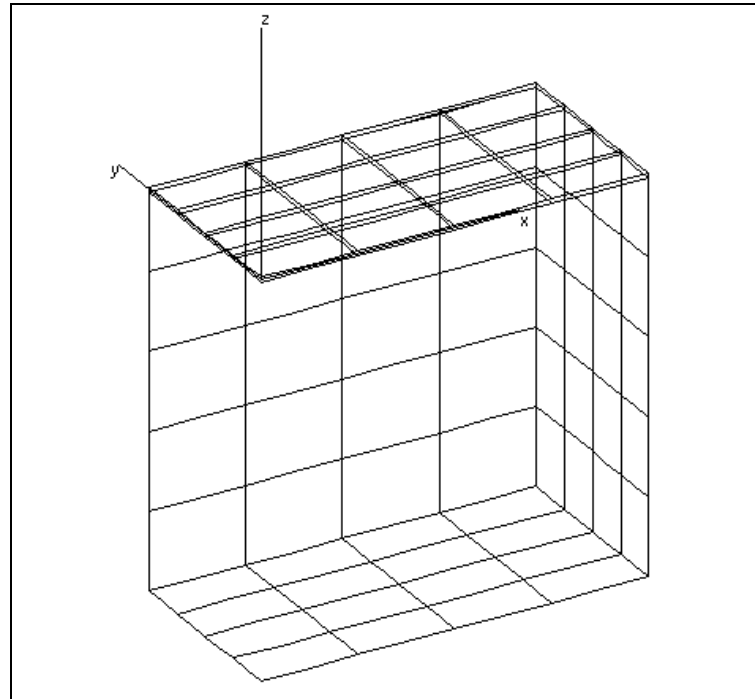


Figure 7.9: Model of the graphite-epoxy plate and acoustic cavity (quarter model)

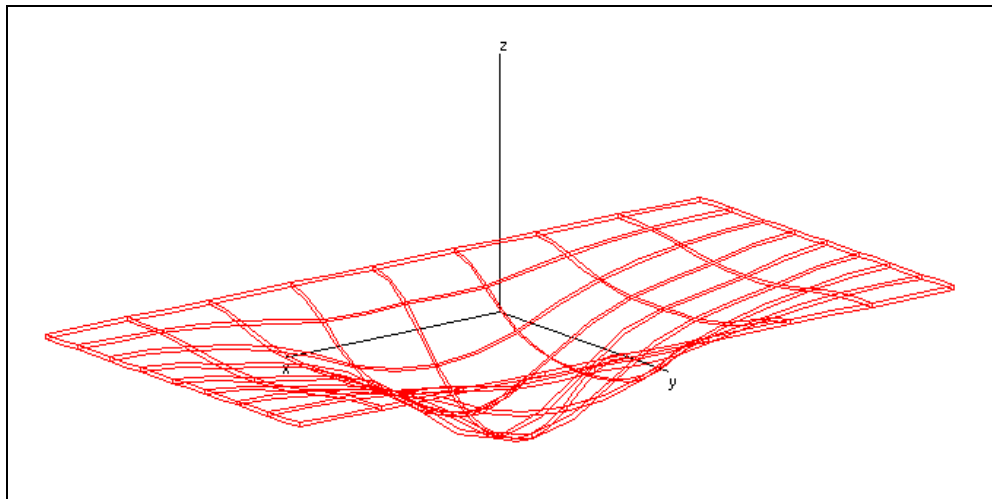


Figure 7.10: First mode shape at 207.5 Hz (f_{22}) of the clamped graphite-epoxy plate

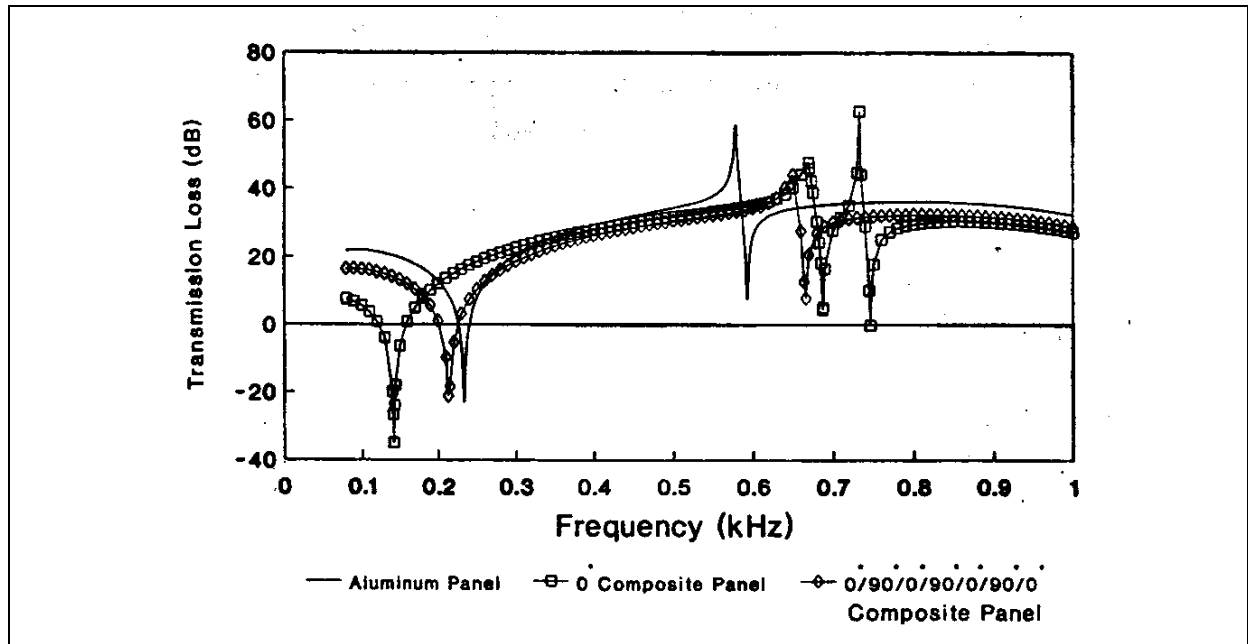


Figure 7.11: Transmission loss for clamped graphite-epoxy panel and rigid cavity reproduced from Pates *et al.* (1995)

Transmission Loss for Clamped Gr/Ep Panel

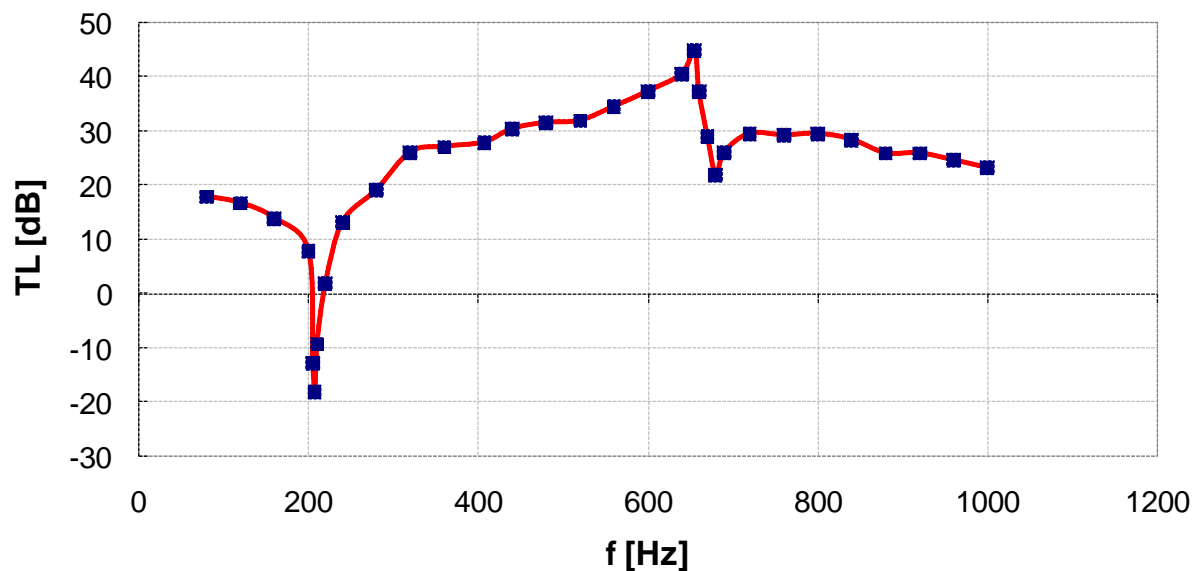


Figure 7.12: Transmission loss for clamped graphite-epoxy panel and rigid acoustic cavity calculated with WinFEBE

7.4. The Anechoic Tile

The anechoic tile was first devised during the research carried out for the VERTLINK project (Jones, Di Meglio, Wang and Aid 1998). The tile is composed of three different layers:

1. A backing layer of aluminium 7075-T6
2. A middle layer of butyl rubber, compounded using the formulation described in Chapter 4
3. An anechoic layer made of a regular grid of circular cones of lead-loaded polyurethane rubber, compounded using the formulation described in Chapter 4,

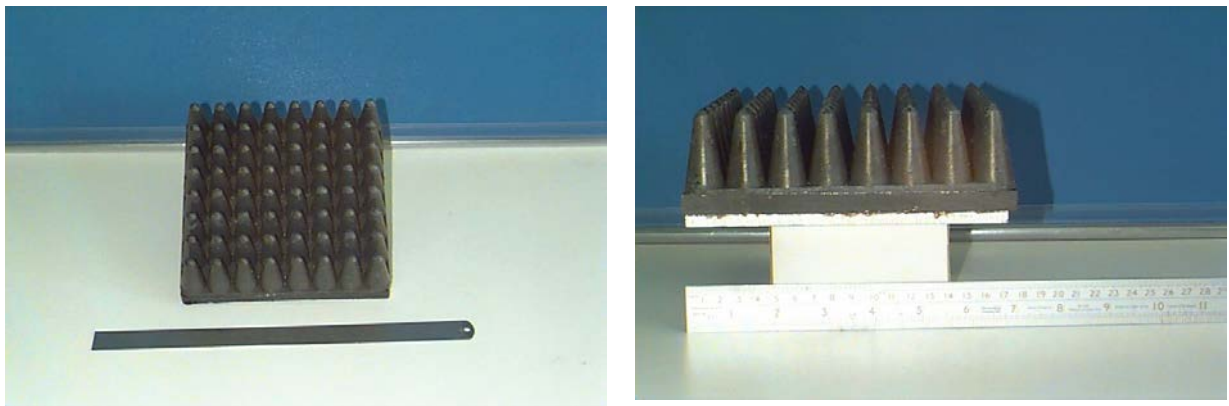
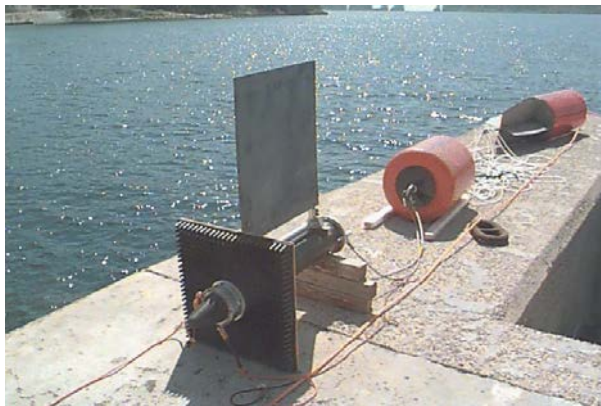


Figure 7.13: Model of the anechoic tile. Left: upper view showing the polyurethane cones; right: side view (on a supporting base) showing the butyl rubber and aluminium layers

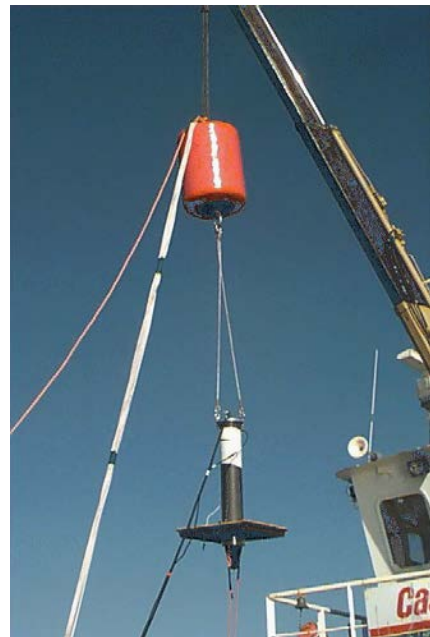
A model of the tile is represented in figs. 7.13. The purpose of the structure was to serve as a prototype for an acoustic screen for underwater floating communications system. In the VERTLINK system, an acoustic receiver is floating below the surface of the sea and

pointing towards the sea-bottom. This unit receives a DPSK-modulated acoustic signal transmitted by a sea-bottom unit and containing environmental data. The efficiency of the surface receiver to detect correctly the signal depends on the surrounding acoustic noise and on the reflections from the near sea surface.

The acoustic baffle is installed above the receiving head of the electro-acoustic transducer (fig. 7.14). The aluminium layer faces upwards and reflects the acoustic noise scattered from the sea surface. The anechoic layer on the other reduces the reflections from the baffle itself and the middle viscoelastic layer absorbs energy out of the signal before it is transmitted on the other side.



(a)



(b)

Figure 7.14: The VERTLINK receiver with the anechoic baffle mounted during the trial in Pilos, Greece in 1997. (a) On the quay with the dorsal stabiliser and the spacing buoys; (b) Deployment from the ship 'Neptune'

The materials for the three layers have been essentially chosen according to two criteria:

1. the general physical properties
2. the technological constraints given by manufacturing processes

The choice of aluminium for the reflecting layer was quite straightforward, because of its high reflection coefficient, availability in form of sheets of any thickness and ease of processing using a standard metal cutting machine.

The butyl rubber was chosen for the absorbing layer because of its high absorption coefficient, resistance to salty water and glues. The base rubber was provided by Exxon Chemical Ltd. in form of white uncured bales and then processed with addition of suitable fillers to get it in form of plane sheets. The details of the composition have been discussed in Chapter 4.

Although the butyl rubber can be easily extruded in form of plane sheets, it is much more complex to obtain small moulded shapes. This constraint led to the choice of the polyurethane rubber for the anechoic grid. The polyurethane rubber can be easily found in form of liquid components that can be mixed, poured in a mould shape and cold-cured in an oven. In particular, the Hyperlast 200 Isocyanate rubber and its C200 Polyol curative were used. The mould shape was made at the milling machine in aluminium, coated to make it smooth and increase surface resilience and greased with silicon oil (Hyperlast Maxsil) to ease extraction of the rubber shape. The mould used to manufacture the tile is shown in fig. 7.15.

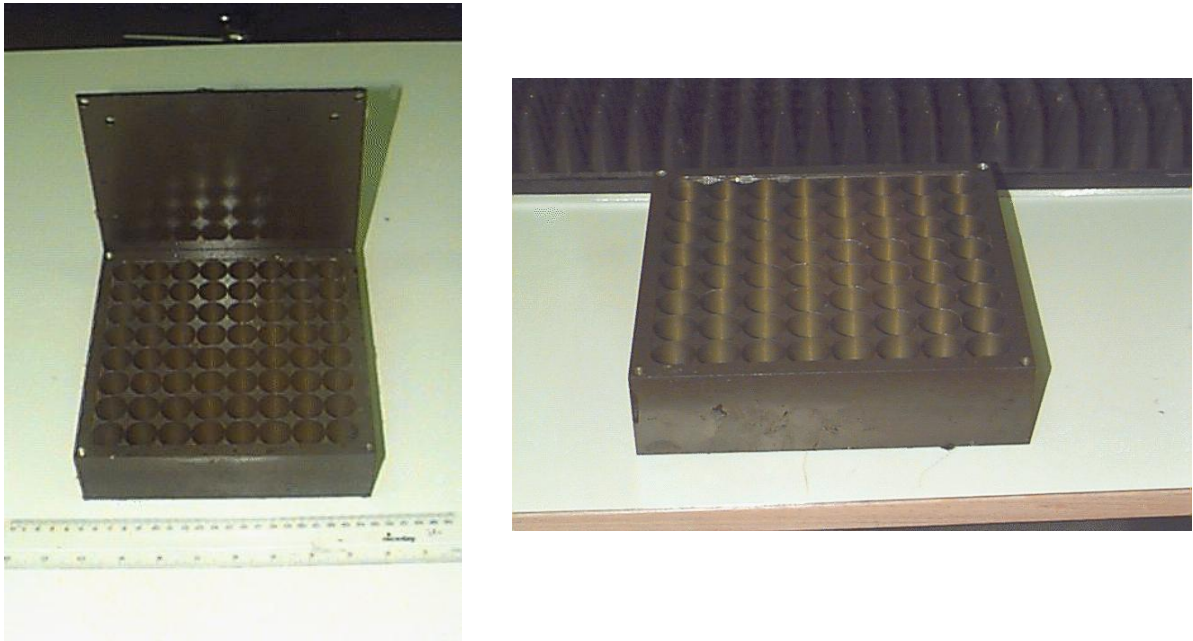


Figure 7.15: The anodised aluminium mould used to manufacture the anechoic cone layer

The layers were finally glued together using high-adhesion, waterproof glue, (Chemlock).

The purpose of the following investigation is to predict the acoustic performance of this kind of composite structure to validate the assumptions made about its behaviour under plane wave scattering conditions.

7.5. FE-BE Analysis Results

A number of different mesh models have been used for the numerical simulations. For normal incidence at 0° and 180° , only a quarter of the model needs to be discretised because of the mirror symmetry with respect to the two planes x - z and y - z (fig. 7.16). For oblique incidence, the mirror symmetry with respect to the vertical plane y - z disappears and one half of the model needs to be discretised (fig. 7.17).

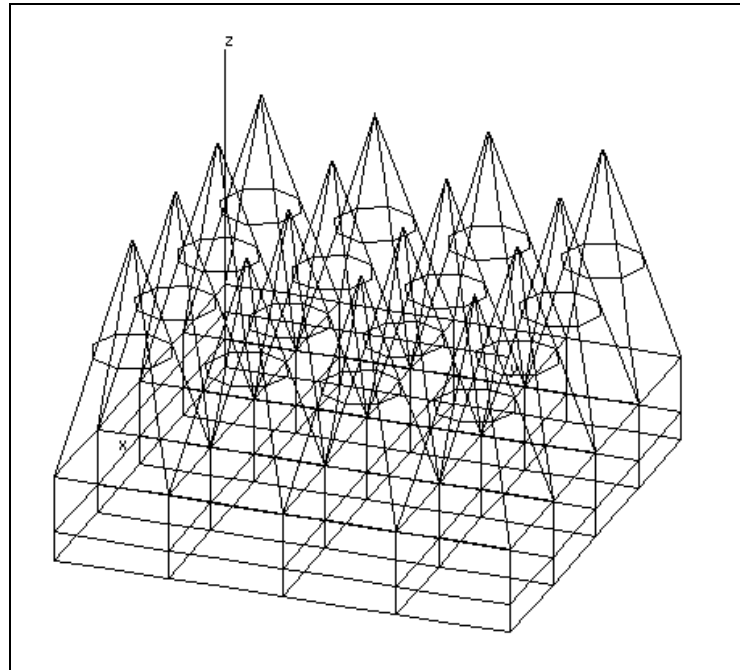


Figure 7.16: Anechoic tile quarter model ($h = 37.5$ mm, wireframe model)

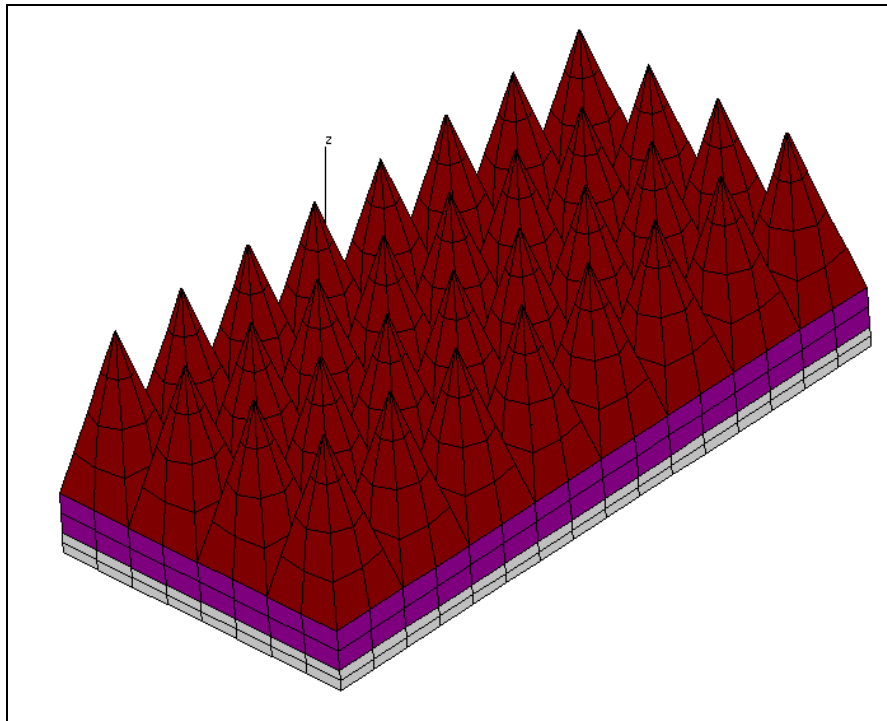


Figure 7.17: Anechoic tile half model ($h = 37.5$ mm, $\theta_0 = 5^\circ$ - solid model)

In the frequency range from 30 kHz to 37 kHz a mesh of 64 finite elements and 192 boundary elements for the quarter model and a mesh of 128 finite elements and 376 boundary elements for the half model have been used. In this case, the elements have a maximum linear size of 20 mm. In the range from 37 kHz to 50 kHz the maximum element size has been reduced to 10 mm and the models have respectively 256 finite elements and 704 boundary elements for normal incidence and 512 finite elements and 1376 boundary elements for oblique incidence.

Simulations of plane wave sound scattering have been investigated for different scattering geometries, namely normal incidence on the anechoic and the reflecting faces, oblique incidence on the anechoic face, side incidence along the rows of cones and with different values of the cone geometrical parameters (height, apex angle and base size). In all cases, the tile is clamped at the corners to reproduce the effect of the constraints due to the mounting bolts.

7.5.1. Form Function of the Anechoic Tile

The field scattered by the tile is expressed in the following sections in terms of a normalised dimensionless form using the concept of form function. Since the shape of the tile varies strongly with orientation, the calculation of the form function can be performed by inserting the average cross section of the tile into the general form function for a three-dimensional body (Chinnery *et al.* 1997).

The general form function can be written as (the geometry of the cone and the scattering configuration is shown in fig. 7.18):

$$f(r, \theta, \phi) = \sqrt{\frac{4\pi r^2}{A}} \frac{p_s(r, \theta, \phi)}{p_i} \quad (7.4)$$

where p_s and p_i are respectively the scattered and incident pressure amplitudes and A is the projected cross-sectional area of the scatterer.

The average projected cross-sectional area for a three-dimensional body is equal to one quarter of the body's surface area. For a square tile of side l , thickness t , cone radius s and height h the average projected area is therefore:

$$\langle A \rangle = \left(\frac{l}{4}\right)^2 + lt + \left(\frac{l}{4s}\right)^2 \pi s \sqrt{s^2 + h^2} \quad (7.5)$$

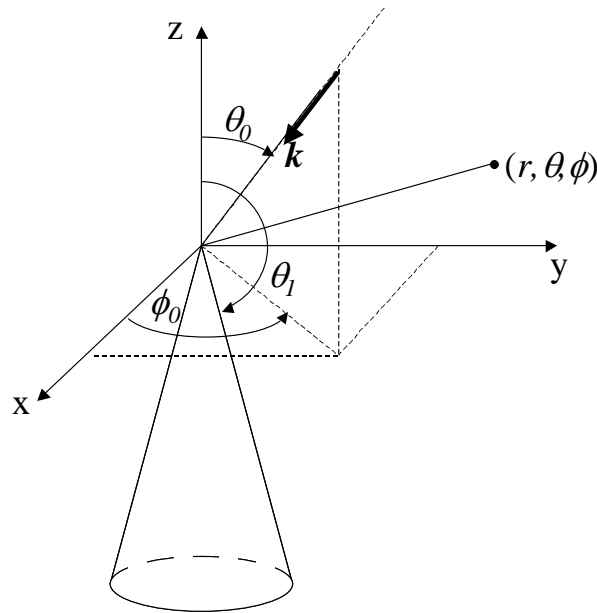


Figure 7.18: Cone and plane wave scattering geometry

In the case of a sphere of radius a , eq. 7.4 can be written as

$$f(r, \theta) = \frac{2r}{a} \frac{p_s(r, \theta)}{p_i} \quad (7.6)$$

It follows that eq. 7.4 for the tile and eq. 7.6 for the sphere are equivalent if

$$a = \frac{l}{2\sqrt{\pi}} \sqrt{1 + 4\frac{t}{l} + \frac{1}{4s} \pi \sqrt{s^2 + h^2}} \quad (7.7)$$

The equivalent radius a defined by eq. 7.7 is used in the following sections to express the frequency dependence of the displacement and pressure response of the anechoic tile.

7.5.2. Determination of the Resonance Frequencies

For structures with high internal damping or immersed in a loading fluid, where the external damping is considerable, the phase of the response with respect to the forcing action can be quite different from the theoretical 90° lag. In the present case, the averaged sum of squares of the displacements is proposed as a suitable measure of the overall deformation (Francis 1995):

$$S = \frac{1}{N^2} \sum_{n=1}^N (a_r \cos \theta - a_i \sin \theta)^2 = \frac{1}{N^2} \sum_{n=1}^N (a_r^2 \cos^2 \theta + a_i^2 \sin^2 \theta - a_r a_i \sin 2\theta) \quad (7.8)$$

where θ is the phase angle during an oscillation period and a_r and a_i are respectively the real and imaginary parts of the displacement. In order to maximise the overall displacement component S , we look for the stationary points of eq. 7.8 with negative second order

derivative. Taking the first derivatives of eq. 7.8, we obtain for the principal denomination of the phase angle θ :

$$\frac{dS}{d\theta} = -\sin 2\theta \sum_{n=1}^N (a_r^2 - a_i^2) - \cos 2\theta \sum_{n=1}^N 2a_r a_i = 0 \Rightarrow \tan 2\theta = \frac{-\sum_{n=1}^N 2a_r a_i}{\sum_{n=1}^N (a_r^2 - a_i^2)} \quad (7.9)$$

The correct quadrant for θ is given by the condition on the second derivative:

$$\frac{d^2S}{d\theta^2} = -\frac{2\cos 2\theta}{\sum_{n=1}^N (a_r^2 - a_i^2)} \left[\left(\sum_{n=1}^N (a_r^2 - a_i^2) \right)^2 + 4 \left(\sum_{n=1}^N 2a_r a_i \right)^2 \right] < 0 \quad (7.10)$$

For condition 7.10 to be true, $\cos 2\theta$ must have the same sign as $\sum_{n=1}^N (a_r^2 - a_i^2)$.

Therefore:

$$\text{if } \sum_{n=1}^N (a_r^2 - a_i^2) > 0, \text{ then } -\pi/2 < 2\theta < \pi/2$$

$$\text{if } \sum_{n=1}^N (a_r^2 - a_i^2) < 0, \text{ then } \pi/2 < 2\theta < 3\pi/2$$

$$\text{if, } \sum_{n=1}^N (a_r^2 - a_i^2) = 0 \text{ then } 2\theta = \pi/2$$

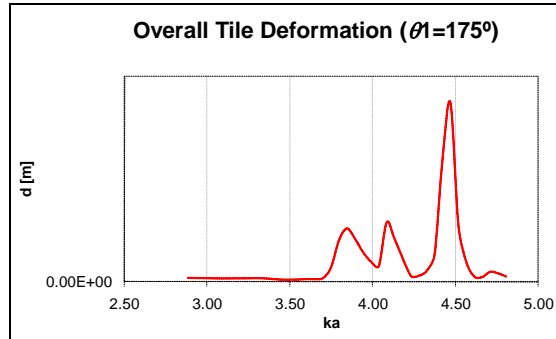
It is necessary to calculate the overall deformation and phase angle for each component of the displacement, since the general motion of each node may not be purely oscillatory, but generically elliptical.

Once the phase and the overall displacement components have been determined as a function of frequency, the resonance frequencies can be identified in correspondence of the peaks of the displacement response. The tile resonance frequencies for different values of the cone apex angle ($\pi\theta_l$) are listed in table 7.8.

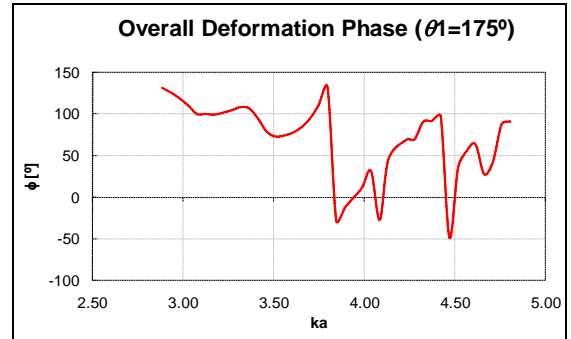
Anechoic tile resonance frequencies (in-vacuo – clamped at the corners)	Anechoic tile resonance frequencies (fluid-loaded – clamped at the corners)			
	5°	15°	25°	35°
15°	5°	15°	25°	35°
--	--	31.5 kHz	31.5 kHz	31.0 kHz
33.06 kHz	--	34 kHz	33.0 kHz	--
38.94 kHz	40.0 kHz	39.5 kHz	40.0 kHz	39.0 kHz
42.06 kHz	43.5 kHz	--	--	45.0 kHz
47.19 kHz	46.5 kHz	49.5 kHz	49.0 kHz	48.0 kHz

Table 7.5: Anechoic tile resonance frequencies

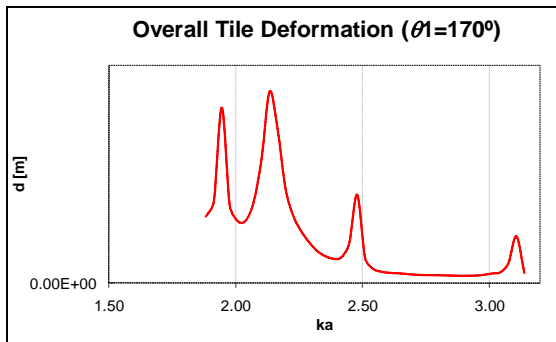
The z-component of the overall displacement for different values of the apex angle is shown in figs. 7.19 and 7.20. The phase of the displacement with respect to the forcing action drops to a negative value in correspondence of each resonance, but is generally quite different from -90° as noted earlier.



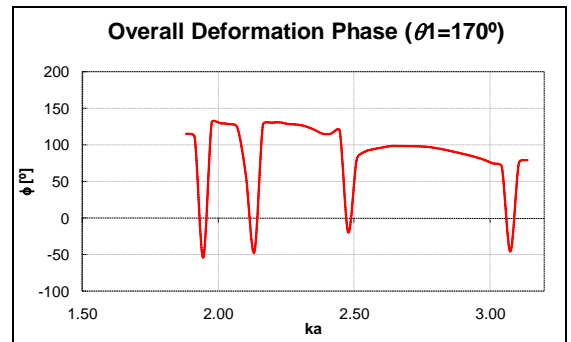
(a1)



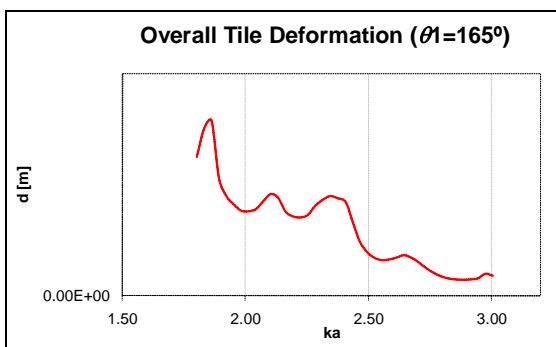
(b1)



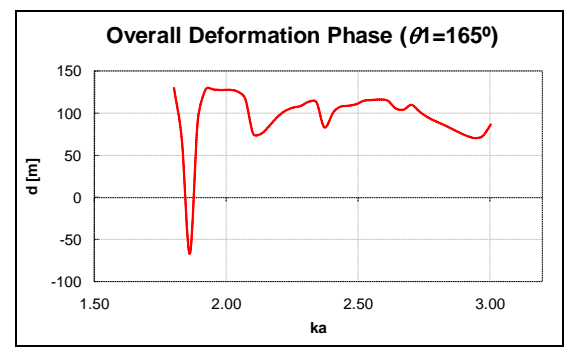
(a2)



(b2)

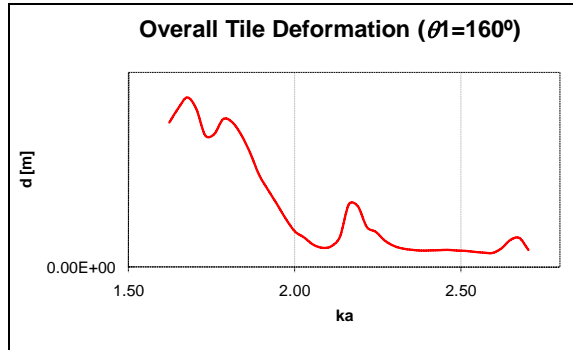


(a3)

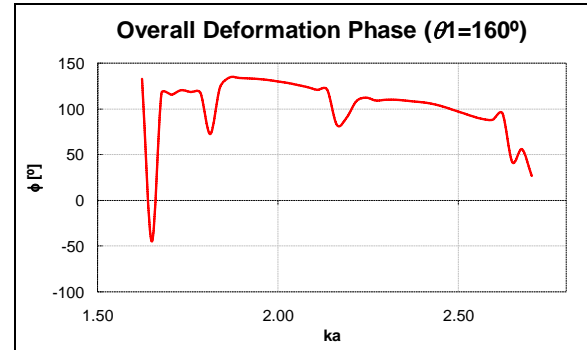


(b3)

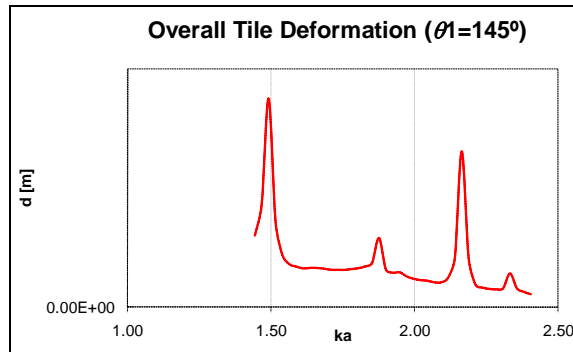
Figure 7.19: Displacement response of the anechoic tile. Series (a): amplitude; series (b): phase



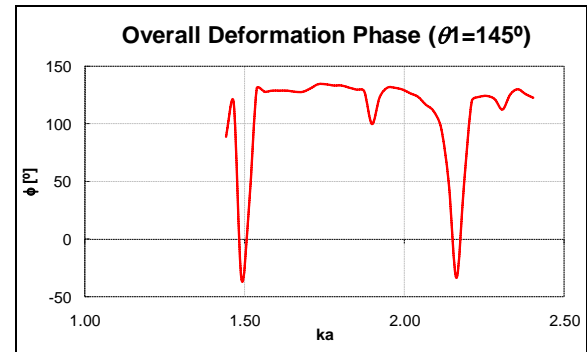
(a4)



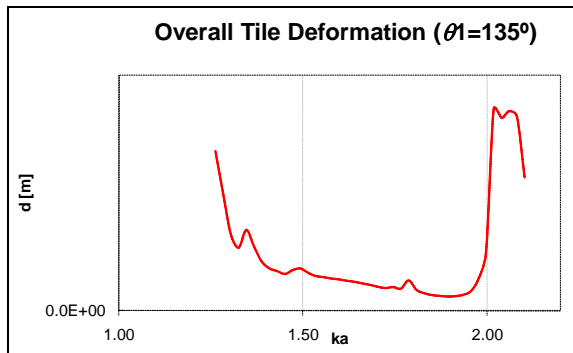
(b4)



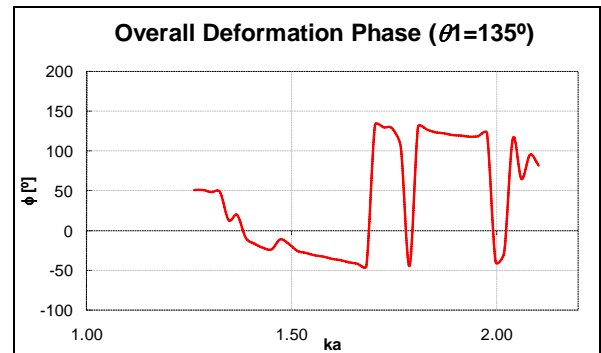
(a5)



(b5)



(a6)



(b6)

Figure 7.20: Displacement response of the anechoic tile. Series (a): amplitude; series (b): phase (continued from previous page)

All the curves show a number of more or less strong resonance peaks. From the analysis of the mode shapes, it can be observed that in the case of thin cones the deformation is greater next to the apex and in the plane perpendicular to the wave propagation direction. The behaviour for thick cones becomes more similar to a plate deformation as the rigidity in the x-y plane increases.

The cones apex actually vibrates in elliptical patterns due to the effect of the plate vibration that changes the relative direction of application of the total force (forcing action and inertia). The components of the cone vibration are related to the distance from the planes of symmetry and the constrained corners. The patterns described by the cone tips on the quarter model are shown in fig. 7.21, whereas the modal shapes for some of the resonance frequencies listed in table 7.5 are shown in figs. 7.22 to 7.25.

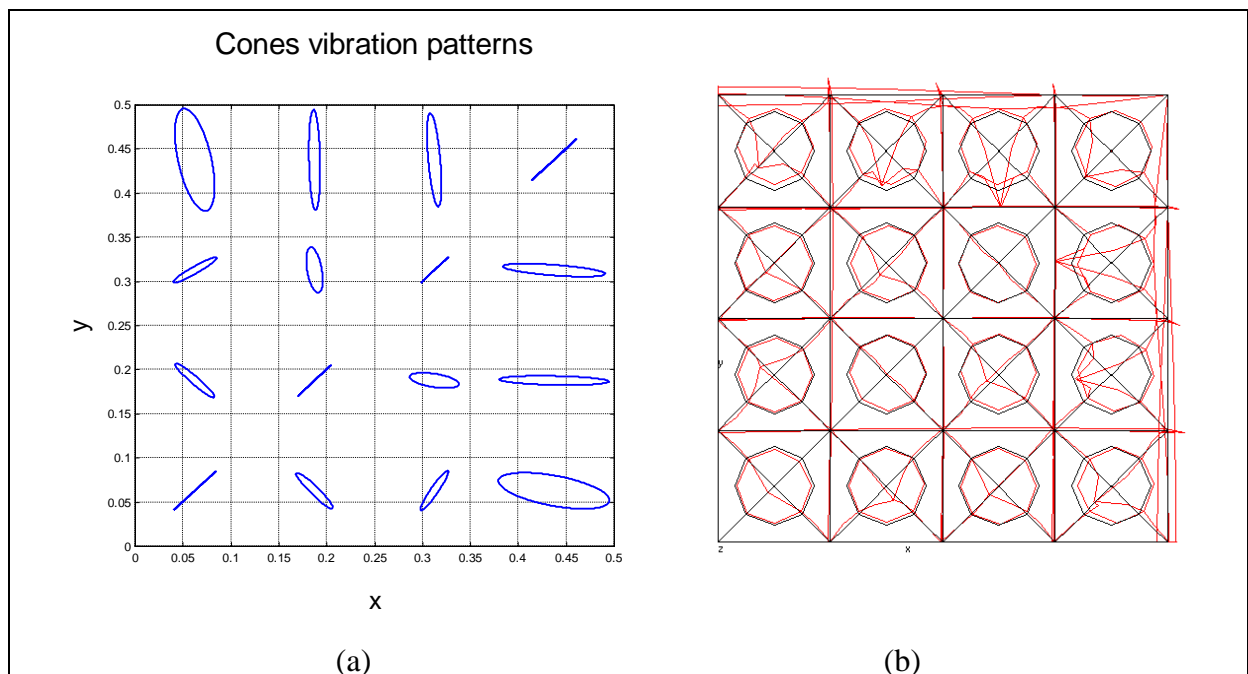


Figure 7.21: Cone tips vibration patterns ($h = 37$ mm, $f = 31.5$ kHz, $ka=1.85$). (a) Tips contours ($l = 1$); (b) tile quarter model, orthogonal projection in the x-y plane (amplification factor = $2.5e12$, — undeformed model, — deformed model)

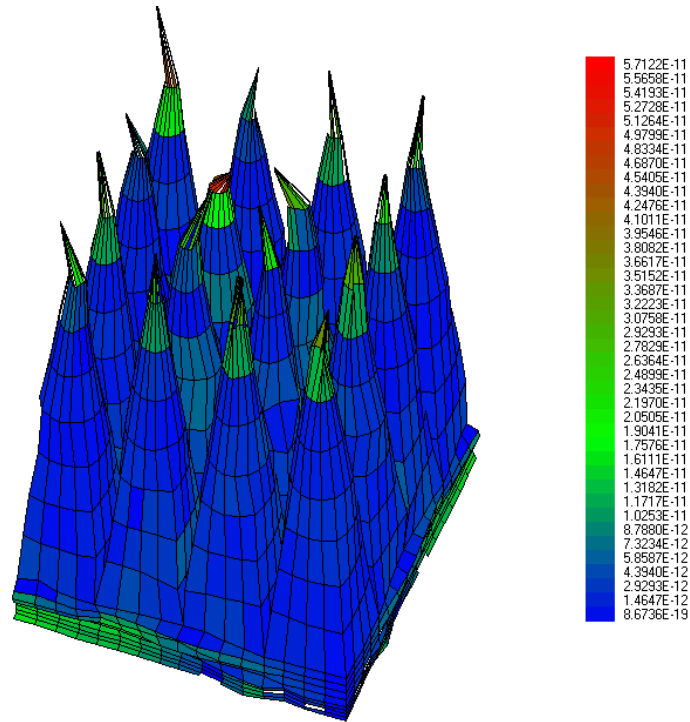


Figure 7.22: Modal shape at $ka = 4.45$, $\theta_1 = 175^\circ$ ($\times 1.25e12$)

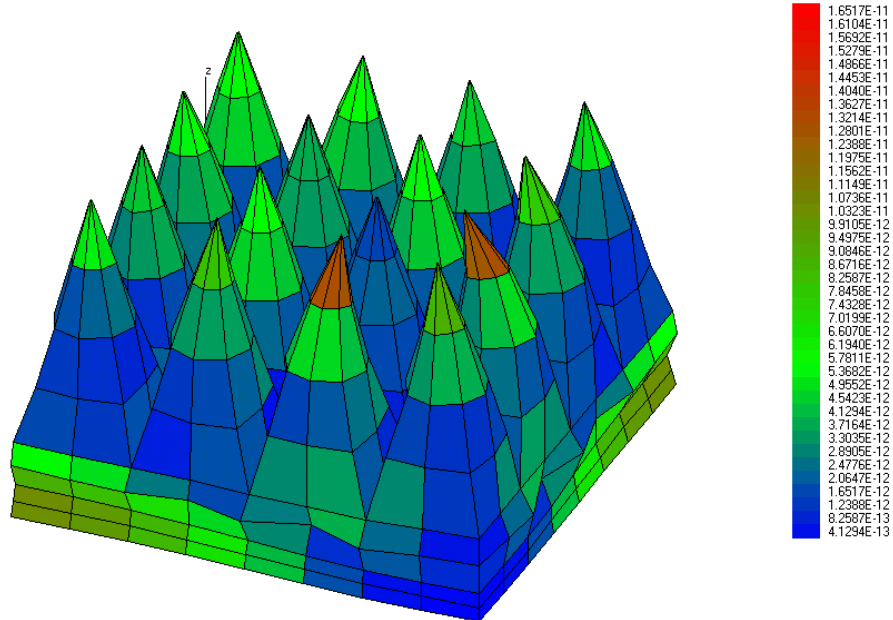
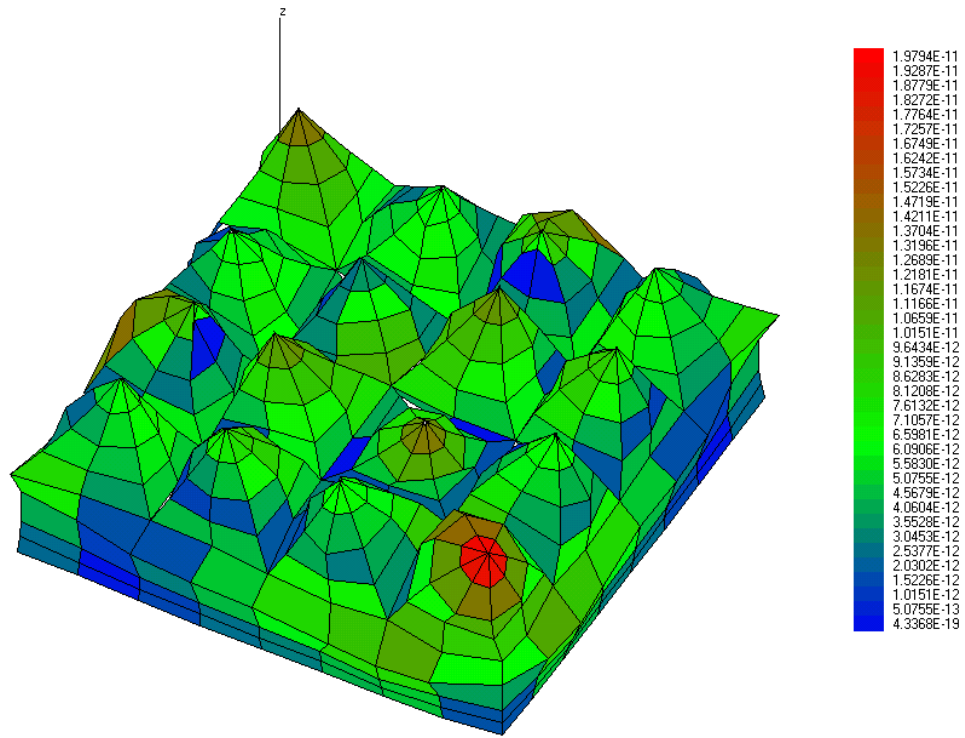
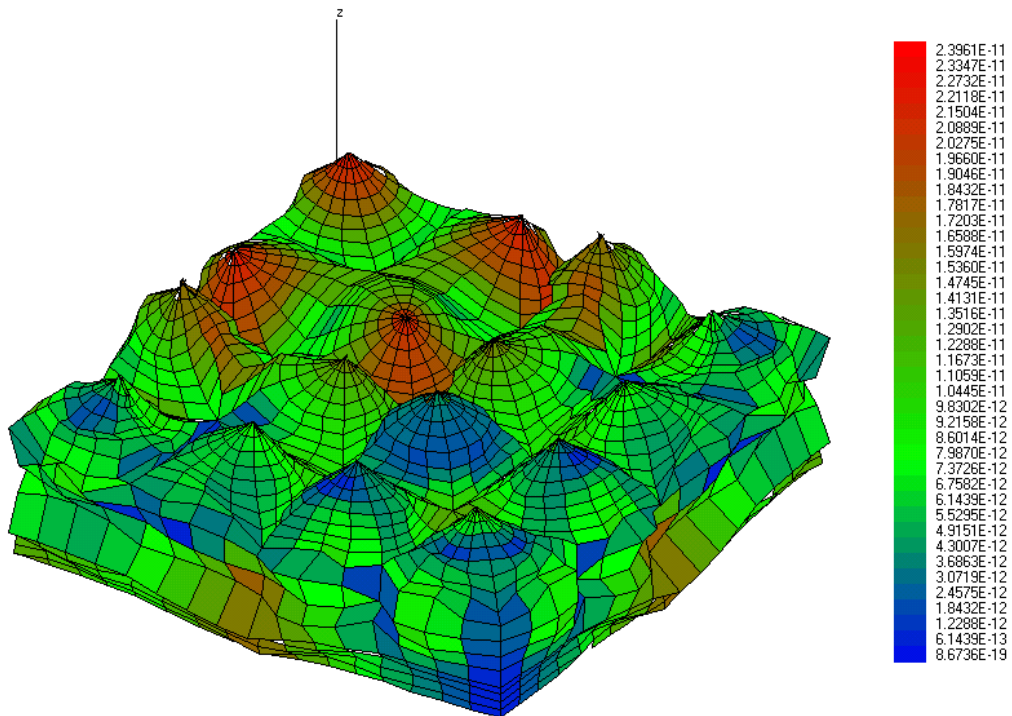


Figure 7.23: Modal shape at $ka = 1.85$, $\theta_1 = 165^\circ$ ($\times 2.5e12$)

Figure 7.24: Modal shape at $ka = 1.49$, $\theta_l = 145^\circ$ ($\times 2.5 \times 10^{12}$)Figure 7.25: Modal shape at $ka = 2.01$, $\theta_l = 135^\circ$ ($\times 2.5 \times 10^{12}$)

7.5.3. Frequency and Polar Response at Normal Incidence on the Anechoic Side

The frequency response for different cone apex angle is show in figs. 7.26 (synoptic view) and 7.27 (single curves). The ‘flat panel’ response refers to a double-layered panel made of butyl rubber and aluminium. The frequency response of the tile as the cone height tends to zero and the cone apex angle tends to 90° ($\theta_l \rightarrow 90^\circ$) becomes closer to the flat panel response.

The different behaviour for different values of the apex angle is examined in more details in §7.5.5.

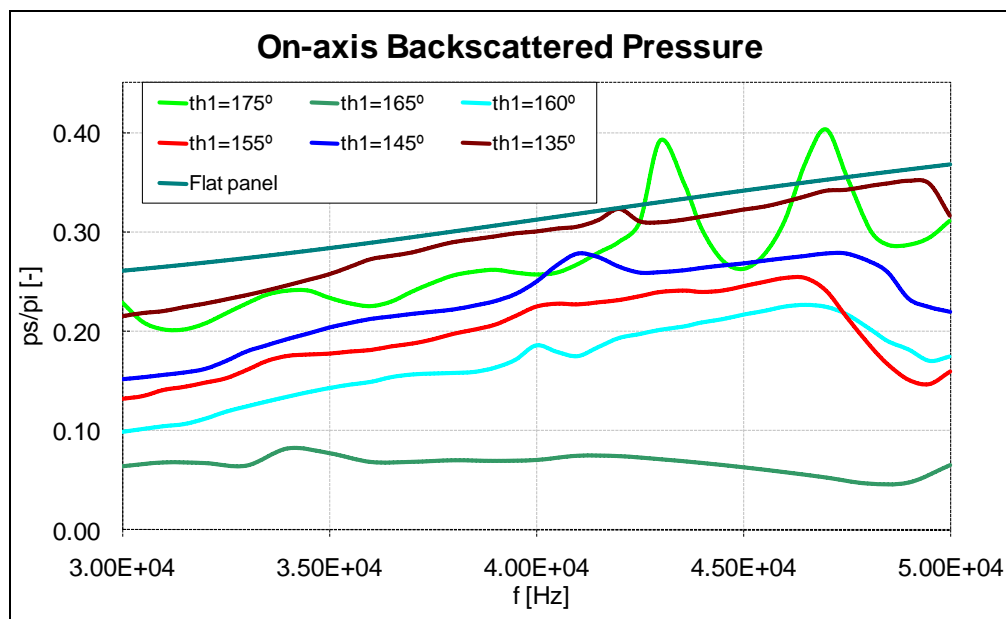


Figure 7.26: On-axis backscattered pressure of the anechoic tile for different values of the cone apex angle

The polar response patterns of the tile for different values of the cone apex angle are shown in figs. 7.28 to 7.30 for some of the resonance frequencies. The scattering patterns are largely dependent of the cone apex angle. The number of pressure amplitude maxima varies with the apex angle, while their position and amplitude vary with the frequency.

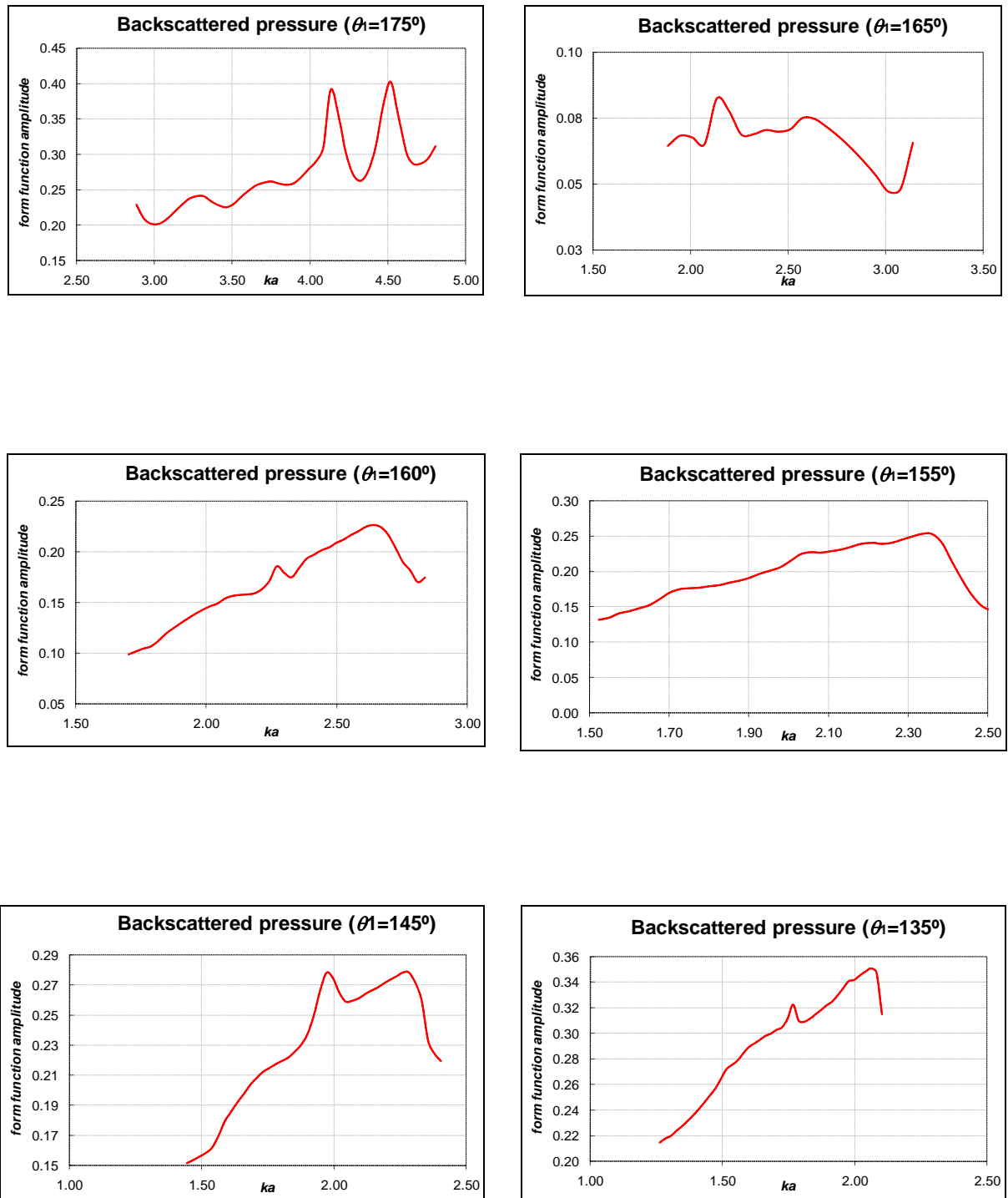


Figure 7.27: Backscattered form function for the anechoic tile at different values of the cone apex angle

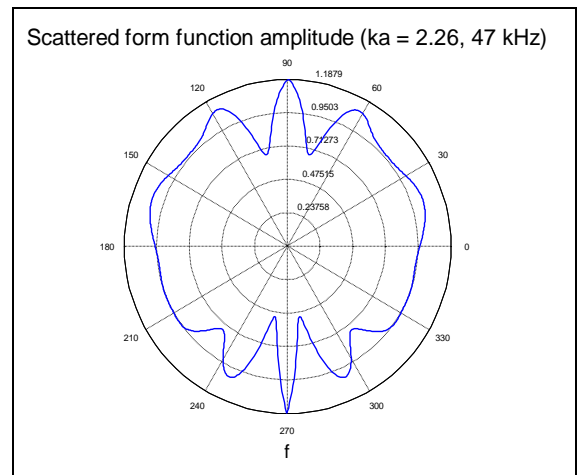
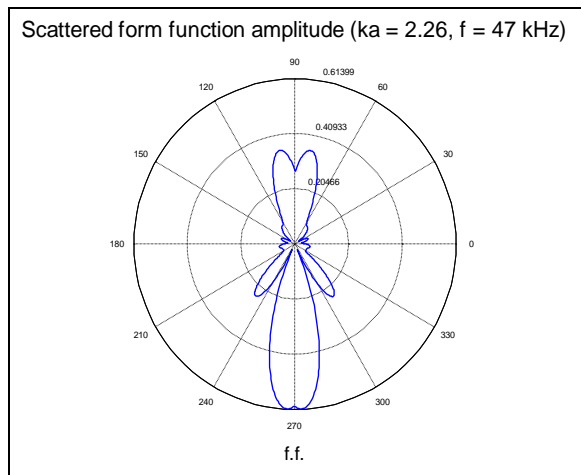
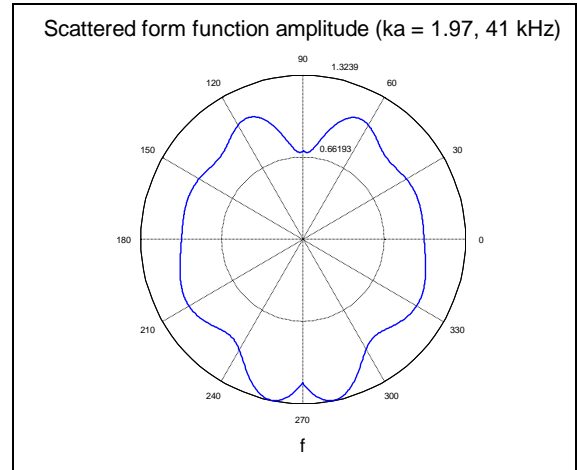
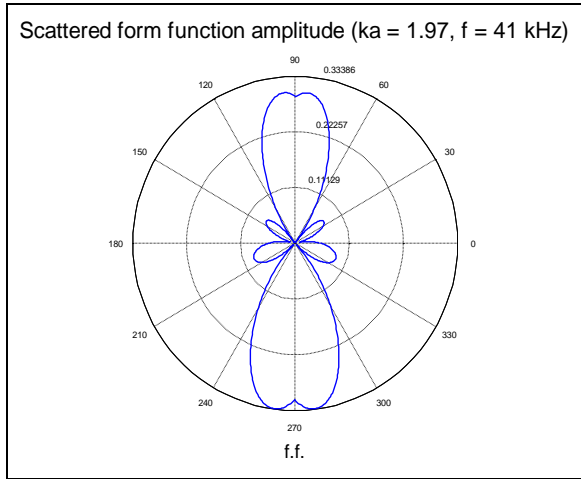


Figure 7.28: Form function polar plots at the displacement resonance frequencies ($\theta_1 = 145^\circ$). Left side scattered form function amplitude; right side: total form function amplitude

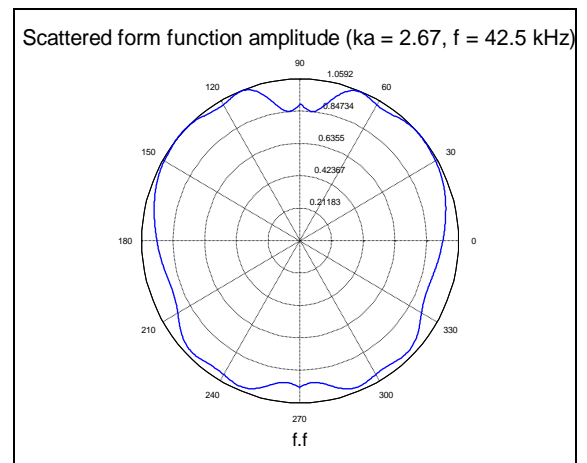
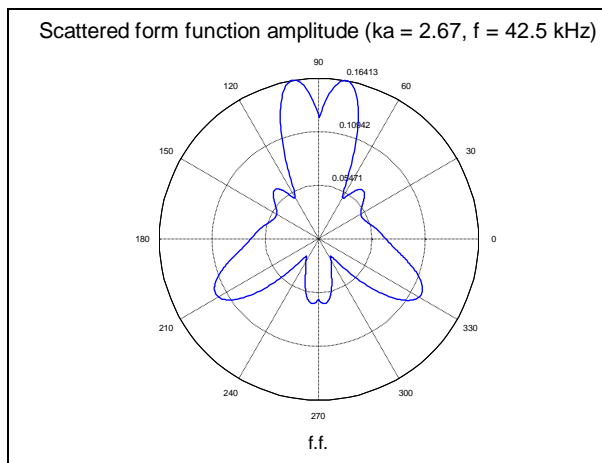
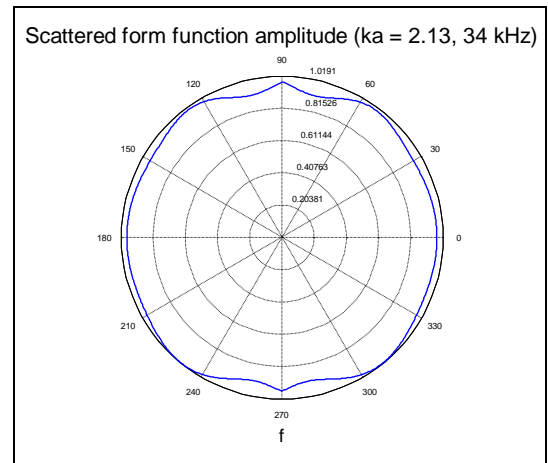
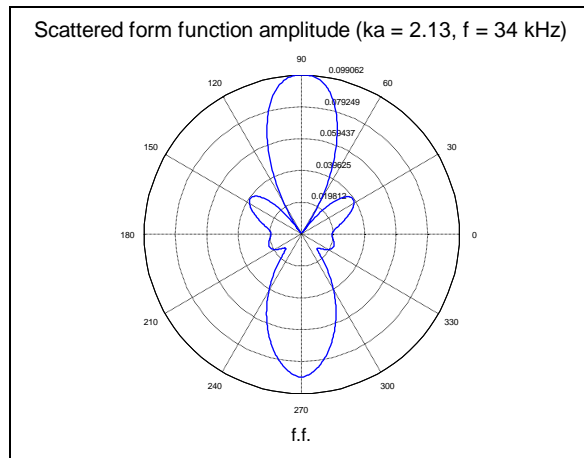


Figure 7.29: Form function polar plots at the displacement resonance frequencies ($\theta_1 = 165^\circ$). Left side: scattered form function amplitude; right side: total form function amplitude

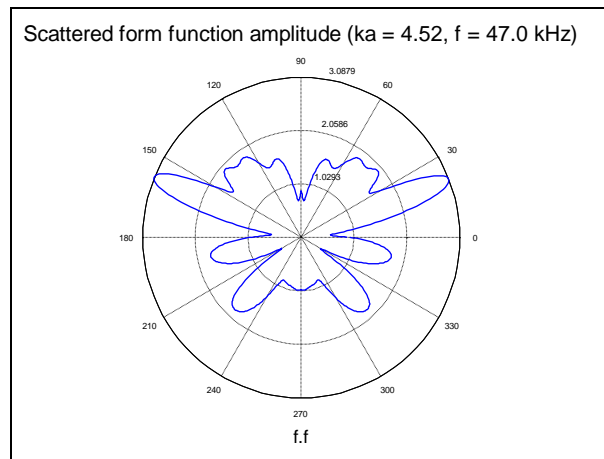
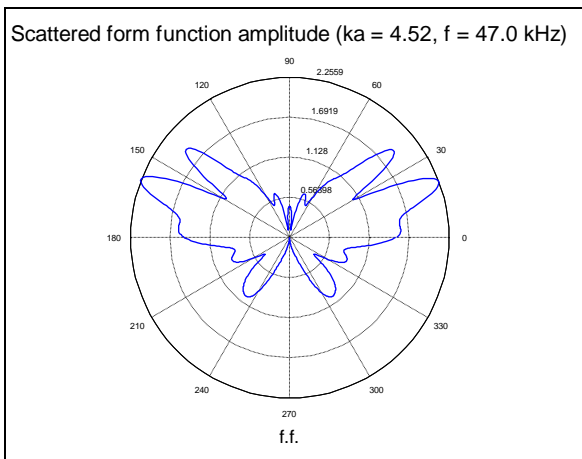
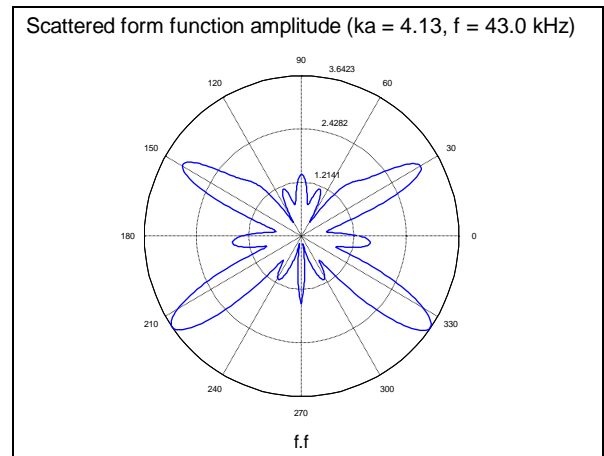
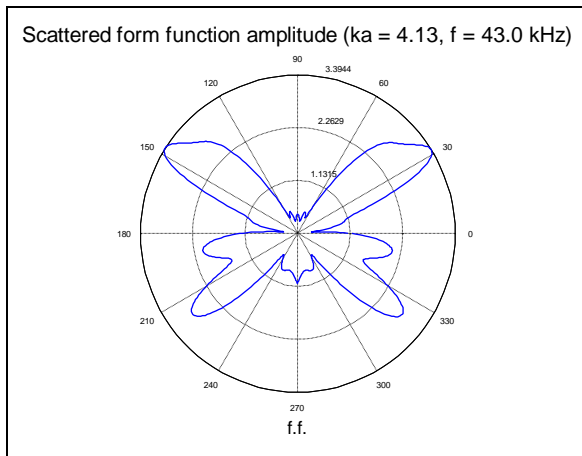


Figure 7.30: Form function polar plots at the displacement resonance frequencies ($\theta_i = 175^\circ$). Left side: scattered form function amplitude; right side: total form function amplitude

The polar plots of the form function show that the scattered signal moves away from the normal to the tile as the cone apex angle decrease. For thin cones, the lobes with the highest amplitude are found in the regions between -60° and 60° and between 120° and 240° , whereas the opposite is true for thick cones.

A possible explanation for this effect can be found in the increase of flexibility of the cones in the plane x-y as the cone apex angle decreases. As previously observed, the tips of the cones describe elliptical rotations with low deformation along the z direction. The sideways deformation is at least of the same order of magnitude if not greater than the deformation of the base plate and could give rise to the sideways scattering.

In addition, as the apex angle exceeds the critical angle for back reflection ($\theta_c = 30^\circ$ or $\theta_l = 150^\circ$, see fig. 7.31), the incident rays are reflected backwards along the direction z only after several reflections against the cone walls, if at all (matching property of the anechoic layer).

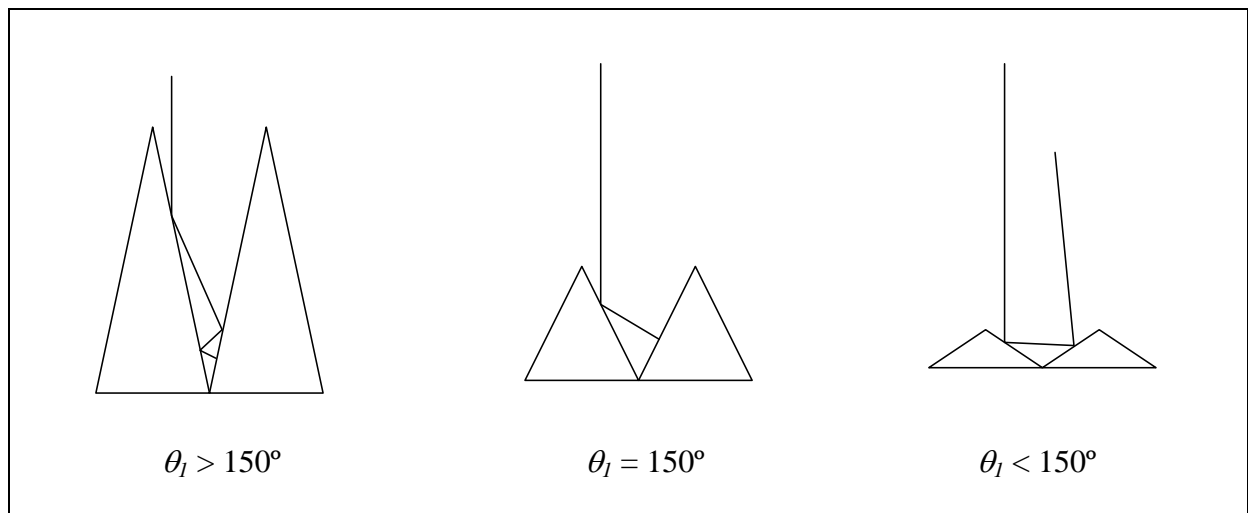


Figure 7.31: Definition of the critical angle of reflection

7.5.4. Dispersion curves

As seen in the previous section, the maxima of the scattered form function vary in amplitude, position and number as frequency and geometry vary.

By plotting the frequency values for each maxima as a function of the angular position and amplitude for a given tile geometry, it's possible to build a graph of dispersion curves that can be used to predict the position of each maxima at any given frequency.

The dispersion plots of the first four maxima for $\theta_l = 145^\circ$ are shown in figs. 7.32 and 7.33 for angular position and amplitude respectively.

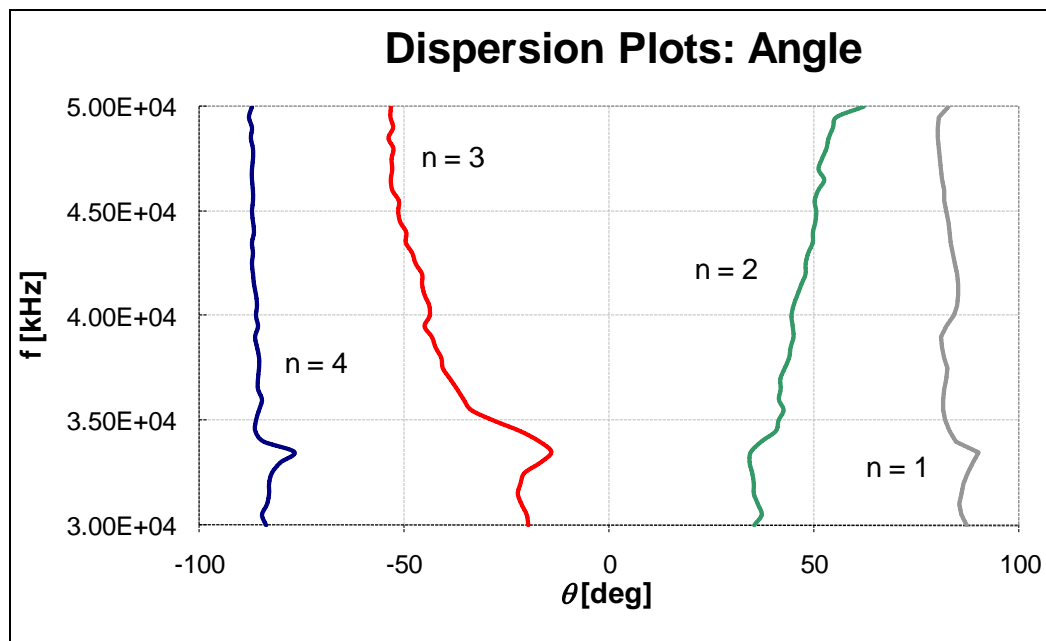


Figure 7.32: Dispersion plots for the first four maxima of the form function: angular position ($\theta_l = 145^\circ$)

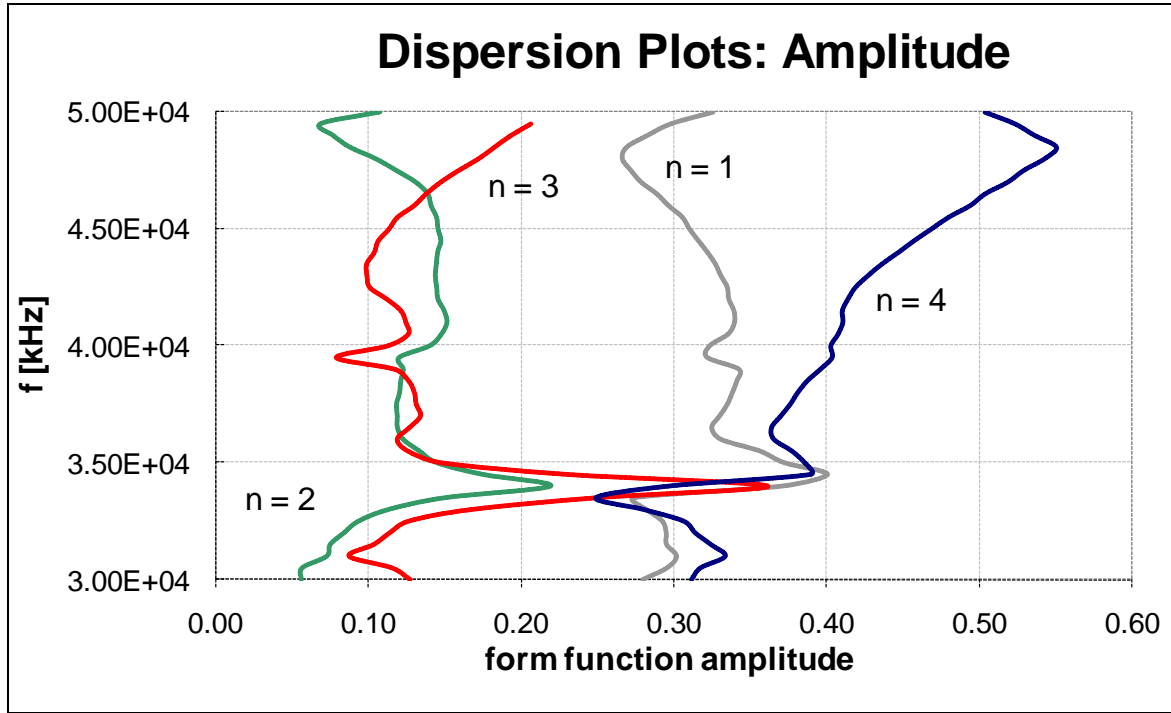


Figure 7.33: Dispersion plots for the first four maxima of the form function: pressure amplitude ($\theta_i = 145^\circ$)

7.5.5. Frequency and Polar Response at Normal Incidence on the Reflecting Side

The response of tile with the signal incident on the reflecting aluminium side has been calculated for the reference case $\theta_i = 165^\circ$.

The backscattered field is shown in fig. 7.34. There is a strong resonance at $ka = 2.13$ ($f = 34.0$ kHz) and minor resonances at $ka = 2.51$ ($f = 40.0$ kHz) and $ka = 2.89$ ($f = 46.0$ kHz).

The polar response corresponding to the resonance at $ka = 2.13$ is plotted in figs. 7.35. It can be observed that in this configuration the scattered field is more similar to what we could expect using a flat panel. The spread of the field to the sides due to the cone vibration is much less pronounced. However, the amplitude of the backscattered field is three times the amplitude of the forward scattered field, which is the desired behaviour.

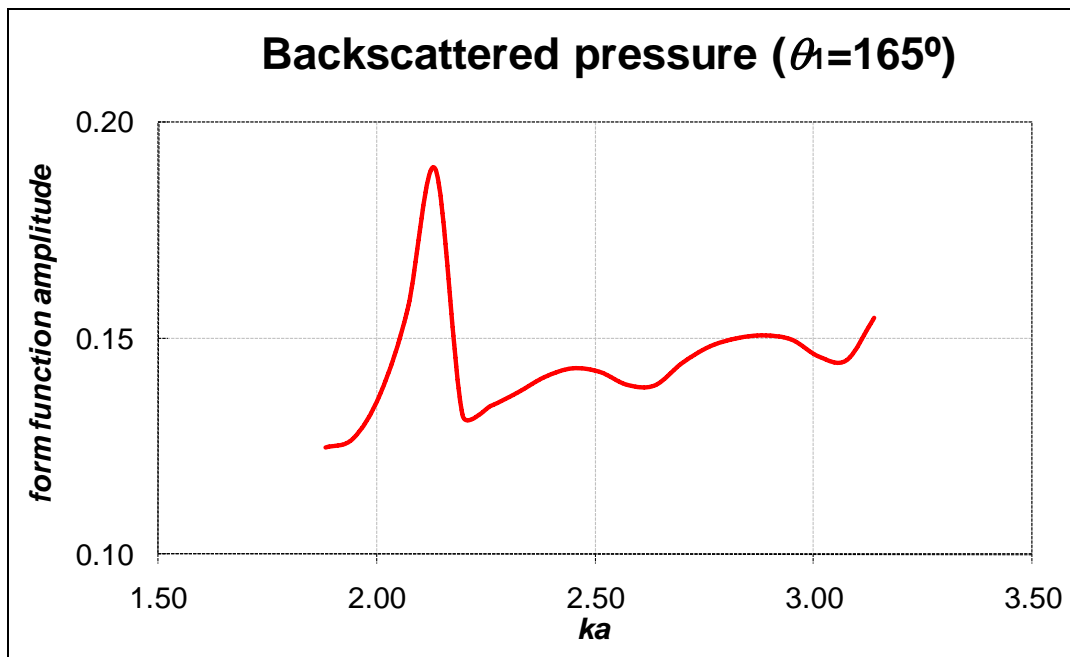
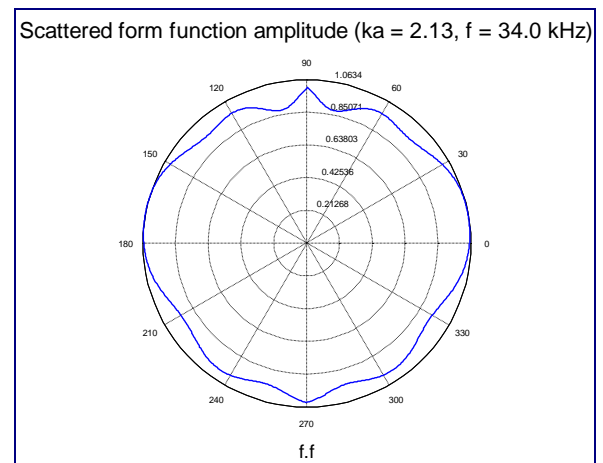
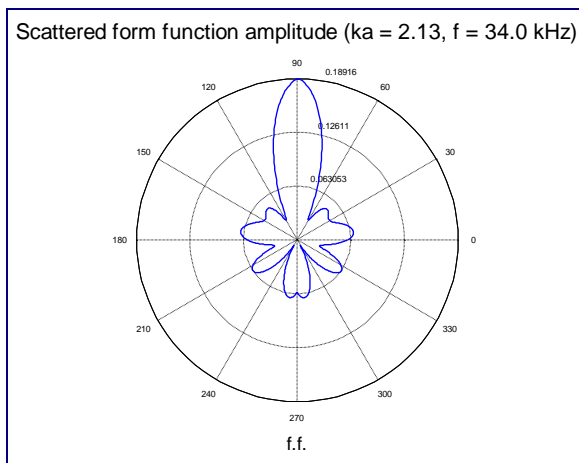


Figure 7.34: Backscattered pressure with signal incident on the reflecting side

Figure 7.35: Form function polar plots at the resonance frequency ($\theta_i = 165^\circ$). Left side: scattered form function amplitude; right side: total form function amplitude

7.5.6. Polar Response at the Characteristic Frequencies at Oblique Incidence on the Anechoic Side

The behaviour of the tile at oblique incidence has been analysed for the reference case $\theta_i = 165^\circ$. The frequency response calculated for incidence $\theta_0 = 15^\circ$, $\theta_0 = 30^\circ$, $\theta_0 = 45^\circ$ is shown in figs. 7.36 to 7.38.

All curves show more or less strong resonance peaks around the value $ka = 2.0-2.5$ ($f = 32.0-40.0$ kHz), which was already present at normal incidence.

The polar response at the values of ka corresponding to the main resonance peaks and off-resonance are shown in figs. 7.39 to 7.41.

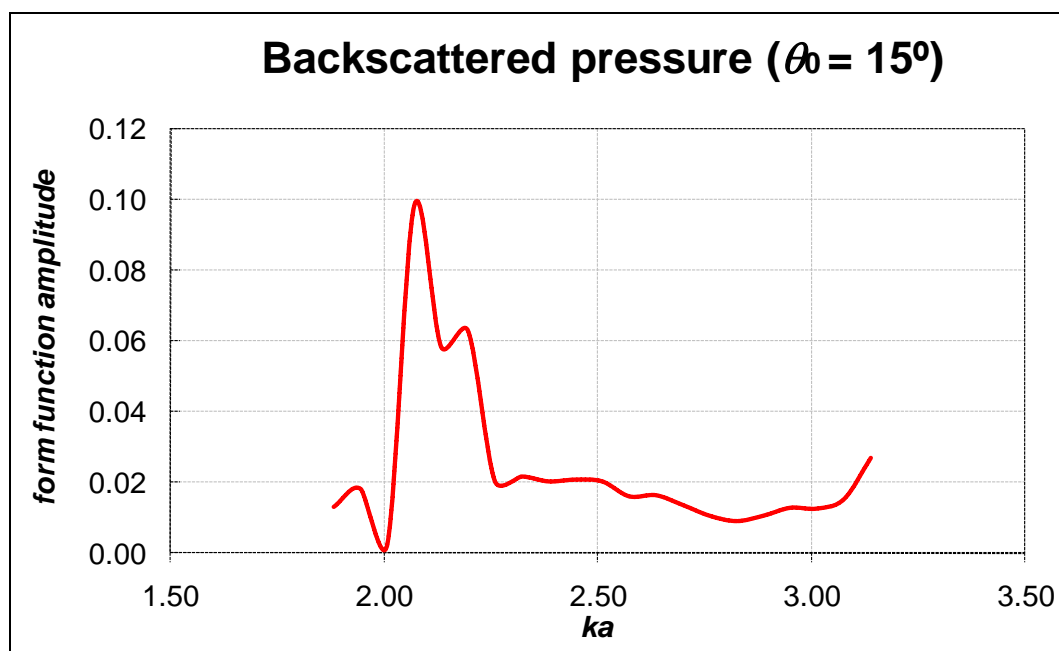
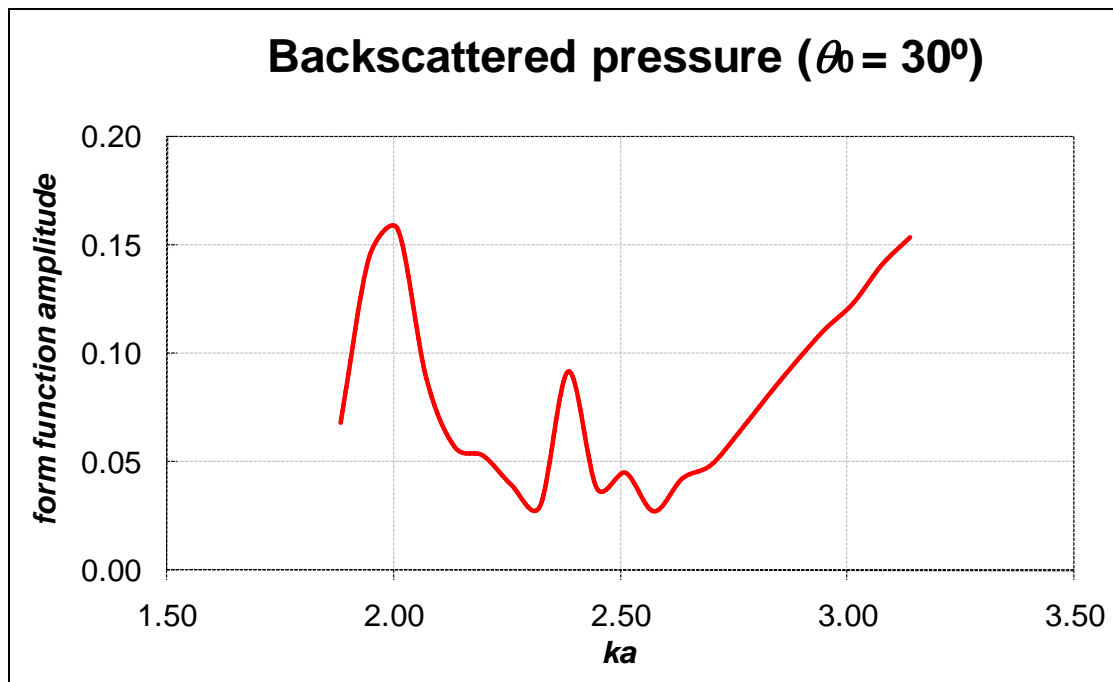
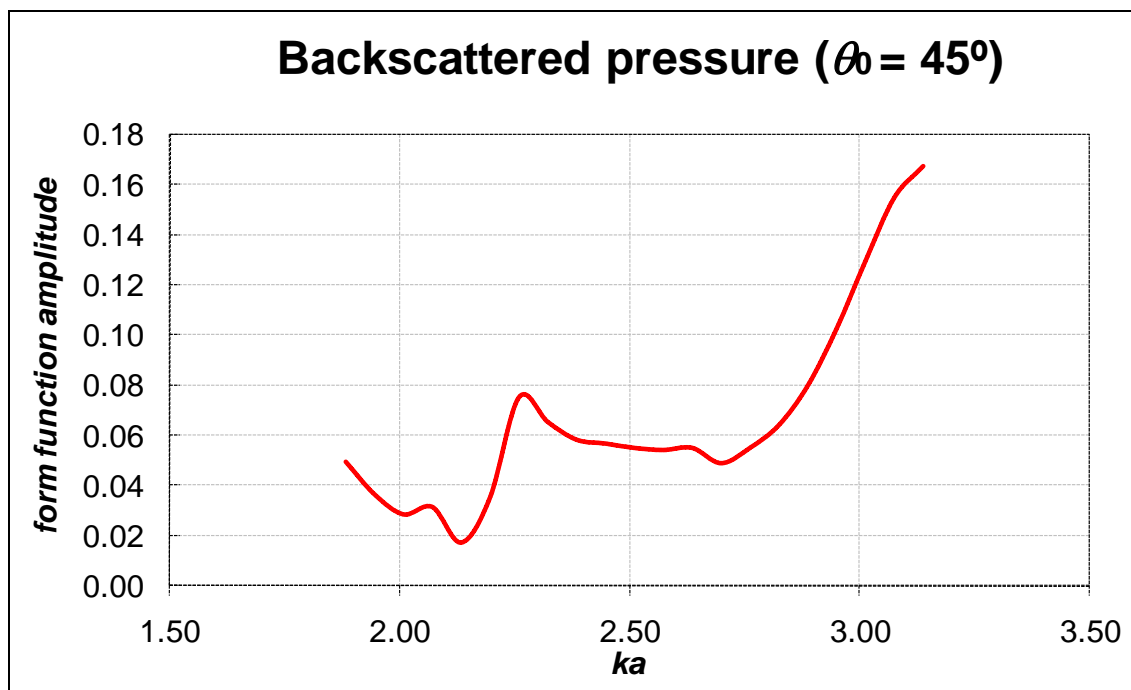


Figure 7.36: Backscattered form function at incidence $\theta_0 = 15^\circ$

Figure 7.37: Backscattered form function at incidence $\theta_0 = 30^\circ$ Figure 7.38: Backscattered form function at incidence $\theta_0 = 45^\circ$

It can be observed that the effect of the resonance and the consequent lateral displacement of the cones is again to spread the scattered field laterally, increasing the amplitude of the secondary lobes. The off-resonance response although deformed is clearly mainly aligned with the normal axis of the tile. To read the plots, it must be noted that the tile is tilted clockwise in the simulations and therefore the incident field forms a negative angle with the scatterer.

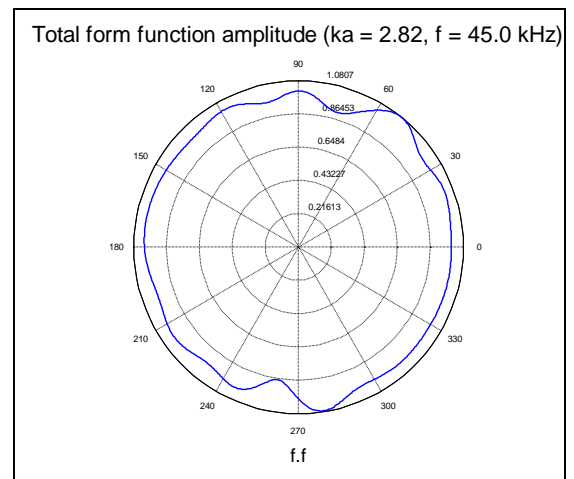
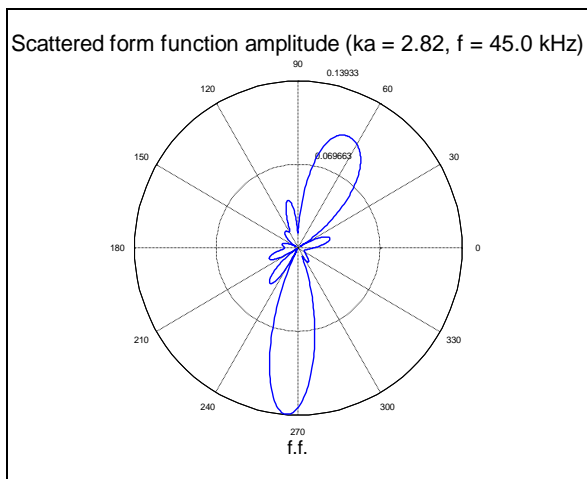
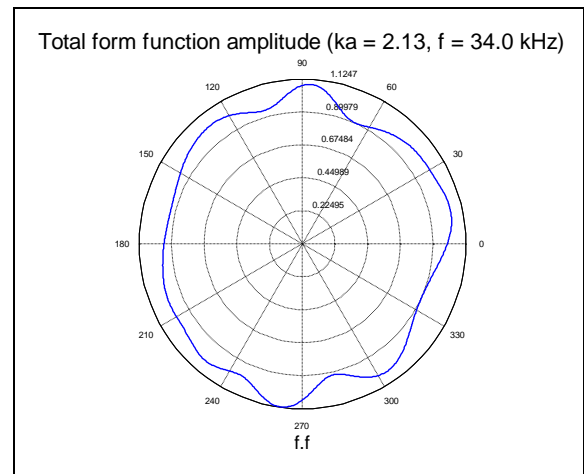
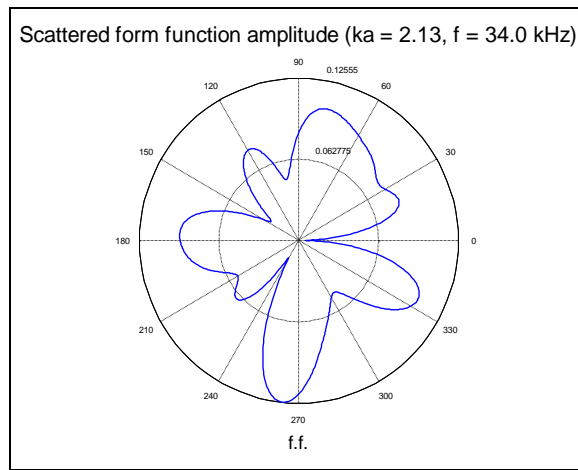


Figure 7.39: Form function amplitude at incidence $\theta_0 = -15^\circ$. Left side: scattered field; right side: total field

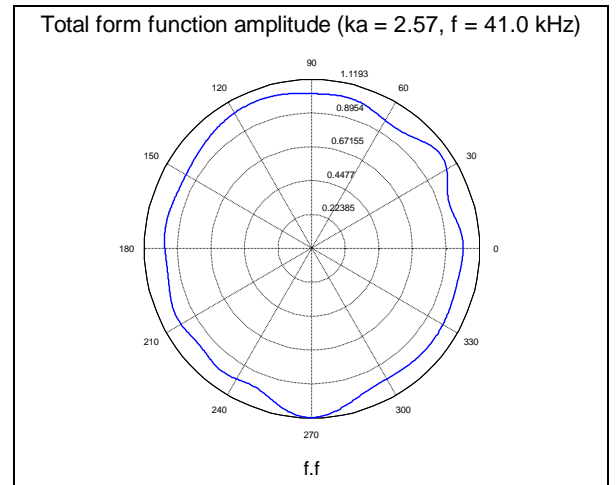
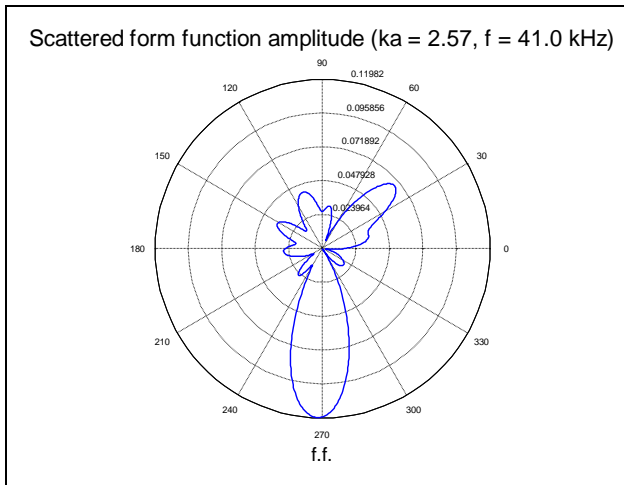
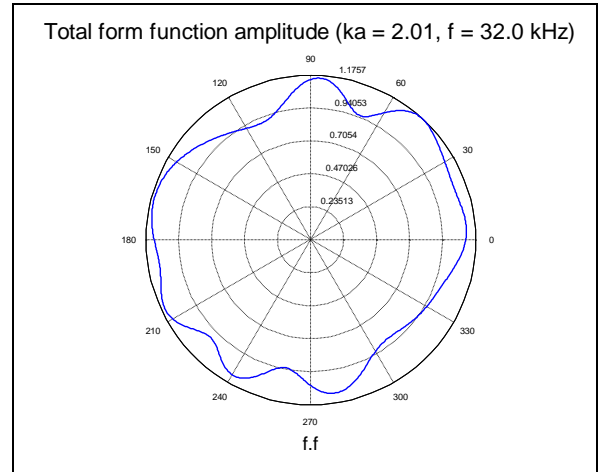
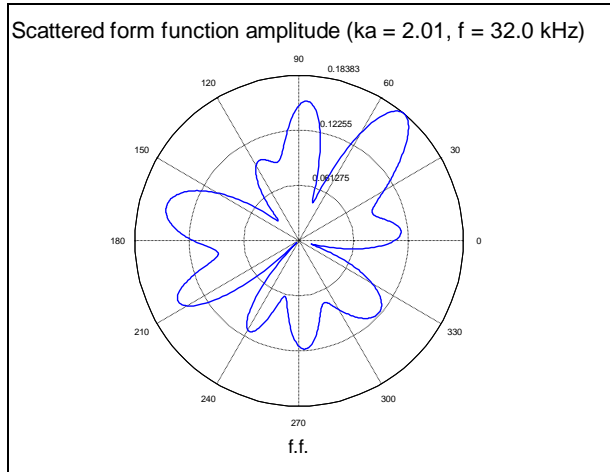


Figure 7.40: Form function amplitude at incidence $\theta_0 = -30^\circ$. Left side: scattered field; right side: total field

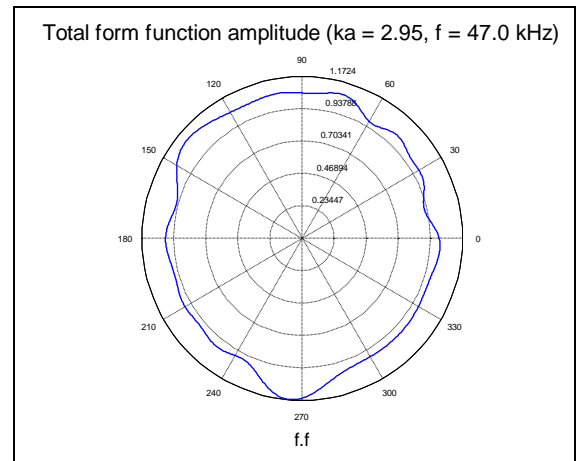
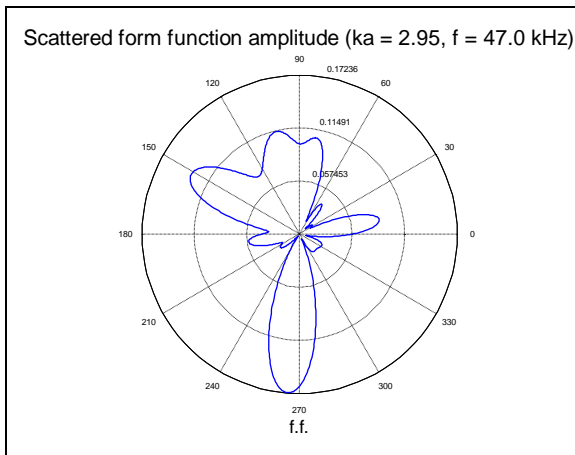
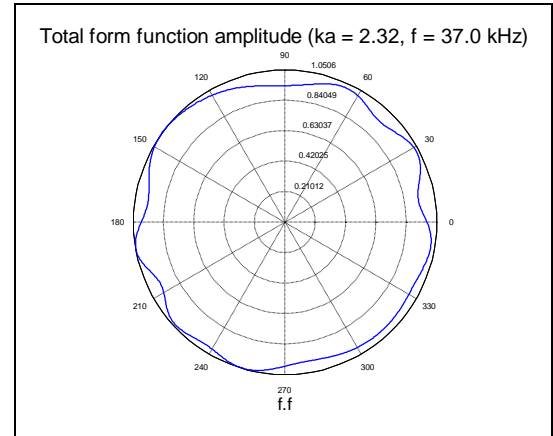
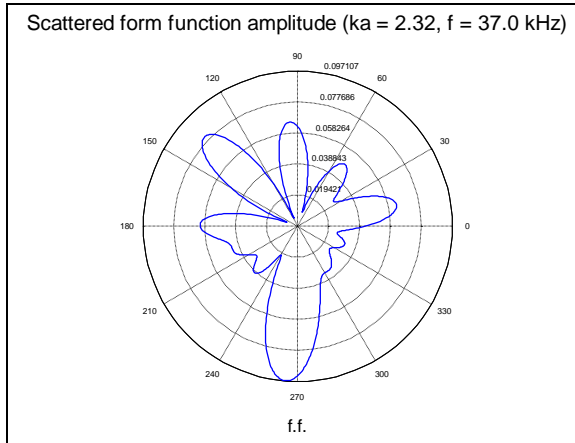


Figure 7.41: Form function amplitude at incidence $\theta_0 = -45^\circ$. Left side: scattered field; right side: total field

A special case of oblique incidence is of course $\theta_0 = 90^\circ$. In this case the incident field is aligned with the rows of cones and additionally the analytical expressions of plane wave scattering (discussed in some more detail in the next section) predict in this case a singularity in the field ($\theta + \theta_0 = \pi$).

The frequency response plotted in fig. 7.42 shows for this case three amplitude peaks at $ka = 2.13$ and $ka = 2.57$ and $ka = 3.01$. The peak in the interval $ka = 2.0$ - 2.5 is present also in this case and it's not only the strongest of the three, but also represent the highest amplitude value found so far in all scattering configurations for this geometry. In addition a 'transparent' point can be observed at $ka = 2.79$ where the backscattered field drops to a very low value.

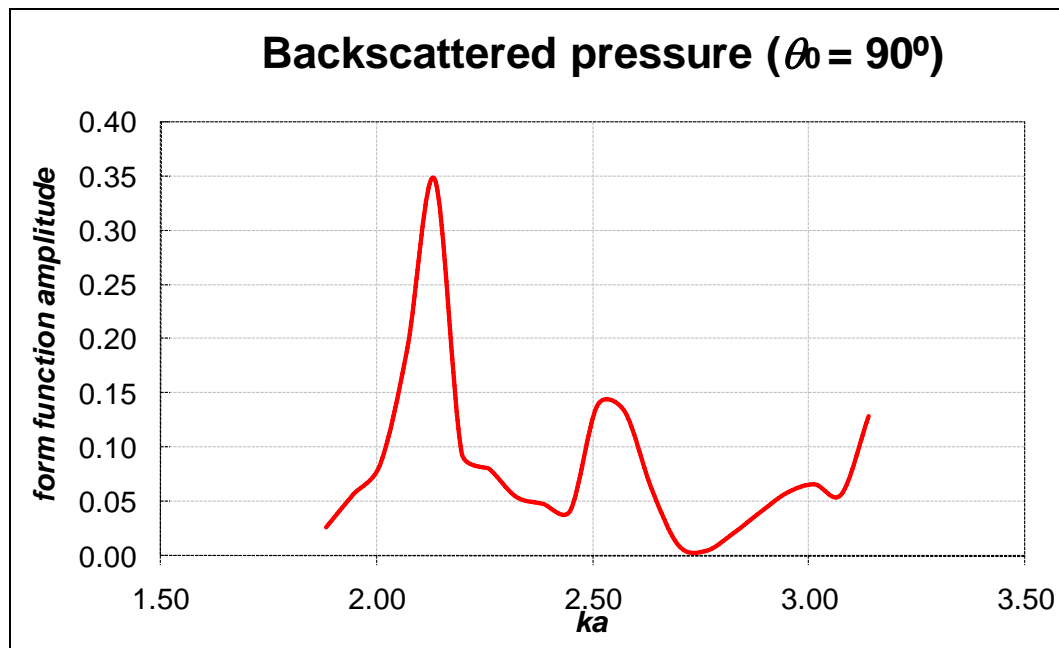


Figure 7.42: Backscattered form function at incidence $\theta_0 = 90^\circ$

The polar plots corresponding to the first peak and the transparent point are plotted in figs. 7.43 and 7.44.

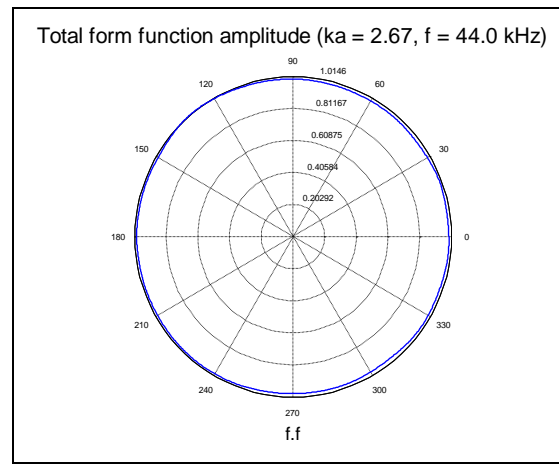
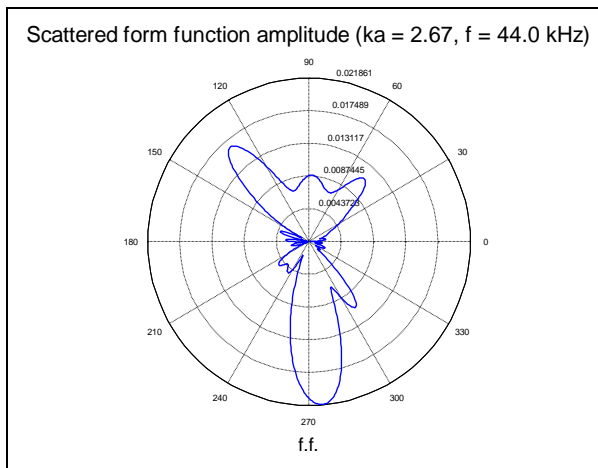
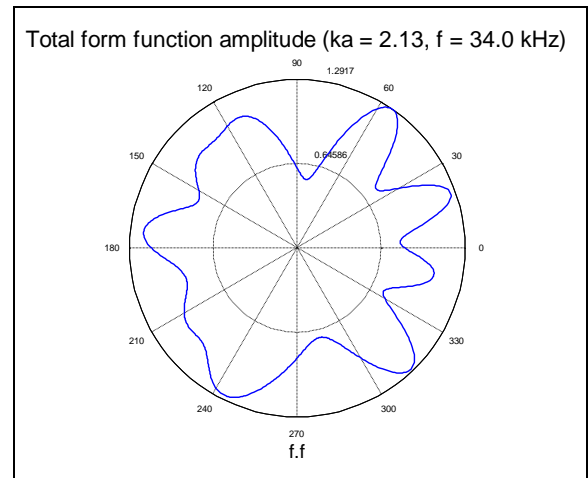
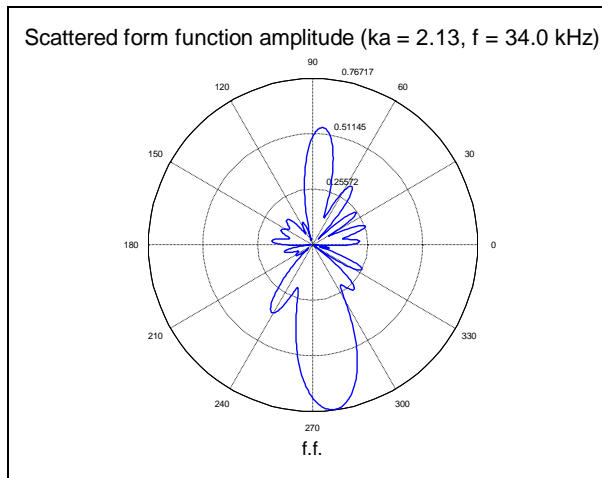


Figure 7.43: Form function amplitude at incidence $\theta_0 = -90^\circ$. Left side: scattered field; right side: total field

7.5.7. Effects of Varying the Cone Apex Angle

As seen in the previous sections, the geometry of the cone making up the anechoic layer has a strong effect on the scattered field and the resonance regime of the tile. In particular, it can be observed that the behaviour in the two regions $\theta_i \rightarrow \pi$ (thin cones) and $\theta_i \rightarrow \pi/2$ (thick cones) is quite different.

The different behaviour can partially be explained from considerations of the special form of the scattered field close to the two limit cases as indeed predicted by analytical expressions available in the case of infinite cones. In the case of infinite soft cones, the scattered field has the appearance of a spherical wave emanating from the tip. For a scalar plane wave and normal incidence ($\theta_0 = 0$), it can be expressed using the analytical form determined by Felsen (Bowman *et al.* 1988):

$$p_s \approx \frac{e^{ikr}}{kr} \left[1 + \sum_{n=1}^{\infty} \frac{1}{(2ikr)^n n!} \prod_{s=1}^n \{s(s-1) + B\} \right] S \quad (7.11)$$

where S is a function of the angles θ and ϕ and the wave vector k , while B is the Beltrami operator:

$$B = \frac{1}{\sin \theta} \frac{\partial}{\partial \theta} \sin \theta \frac{\partial}{\partial \theta} + \frac{1}{\sin^2 \theta} \frac{\partial^2}{\partial \phi^2} \quad (7.12)$$

For thin cones, the function S can be approximated as:

$$S \approx \frac{i}{\log \left[\sin^2 \frac{1}{2} \delta \right]} \frac{1}{\cos \theta + \cos \theta_0} = \frac{i}{\log \left[\sin^2 \frac{1}{2} (\pi - \theta_1) \right]} \frac{1}{\cos \theta + 1} \quad (7.13)$$

The expression for the backscattered field ($\theta = 0$) at normal incidence for thin cones can therefore be written as:

$$p_s^b \approx \frac{e^{ikr}}{kr} \left(\frac{i}{2 \log \left[\sin^2 \frac{1}{2} (\pi - \theta_1) \right]} + \sum_{n=1}^{\infty} \frac{1}{(2ikr)^n n!} \prod_{s=1}^n \left\{ s(s-1) + \frac{i}{2 \log \left[\sin^2 \frac{1}{2} (\pi - \theta_1) \right]} \right\} \right) \quad (7.14)$$

In the case of thick cones, the backscattered field at normal incidence has also been determined by Felsen (Bowman *et al.* 1988):

$$\begin{aligned} p_s^b &\approx -e^{ikr} \sin \theta_1 \left[1 - \sqrt{2\pi} e^{-\frac{1}{4}i\pi} w G(w) \right], & w < 4 \\ p_s^b &\approx \frac{e^{ikr}}{ikr} \frac{1}{(2\theta_1 - \pi)^2}, & w \geq 4 \end{aligned} \quad (7.15)$$

where

$$\begin{aligned} w &= -\sqrt{kr} \cos \theta_1 \\ G(w) &= \frac{2}{\sqrt{\pi}} e^{-2iw^2} \int_{(1-i)_w}^{\infty} e^{-\mu^2} d\mu \end{aligned} \quad (7.16)$$

The backscattered normalised pressure amplitude at the distance $r = 0.5$ m from the apex of the cone derived from expressions 7.14 and 7.15 are plotted in figs. 7.44 and 7.45 as a function of frequency in.

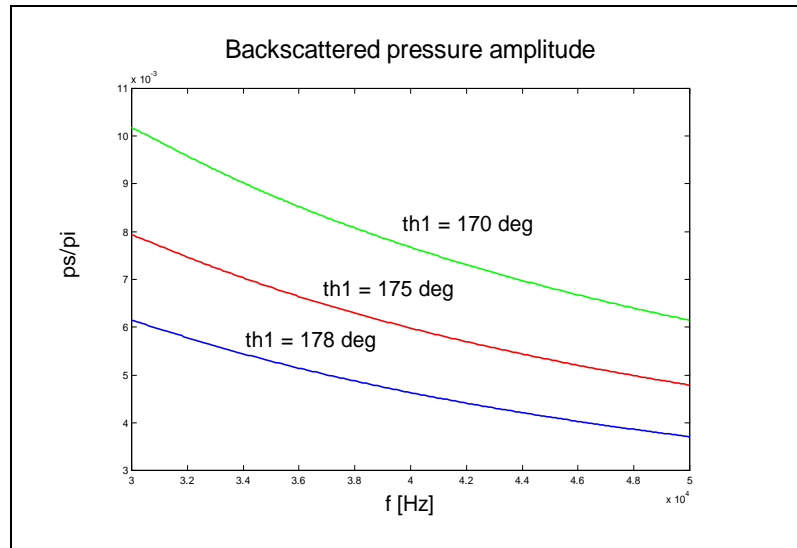


Figure 7.44: Normalised backscattered pressure Vs. frequency for $\theta_1 \sim \pi$

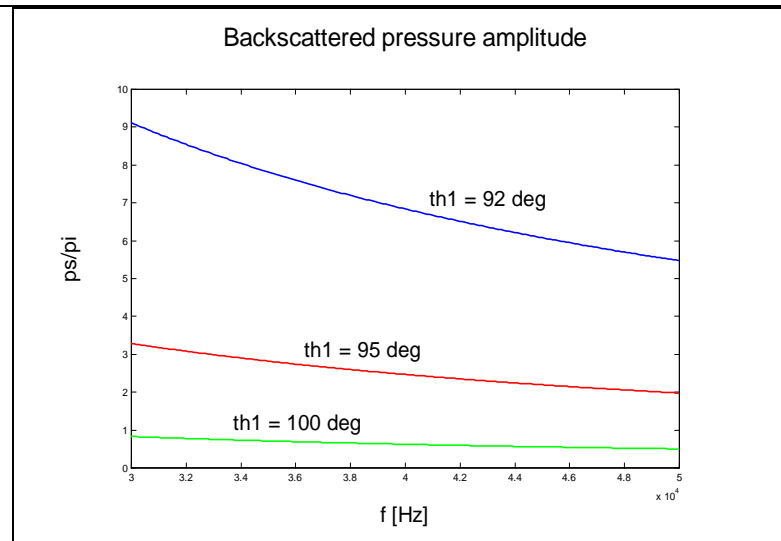


Figure 7.45: Normalised backscattered pressure Vs. frequency for $\theta_1 \sim \pi/2$

7.6. Experimental Comparisons

7.6.1. The Experimental Environment

A model of the tile with apex angle $\theta_l = 165^\circ$ and a complete anechoic baffle have been built and tested in tank.

The tile was suspended in water using an open test rig (see fig. 7.47 and 7.48). An electro-acoustic transducer was placed at one side of the rig in front of the tile. The tile was hanging from a thin metal stripe attached to a motion-controlled step motor and a calibrated hydrophone was used to take measurements of the scattered acoustic field. The general schema of the measurement set-up is represented in fig. 7.46.

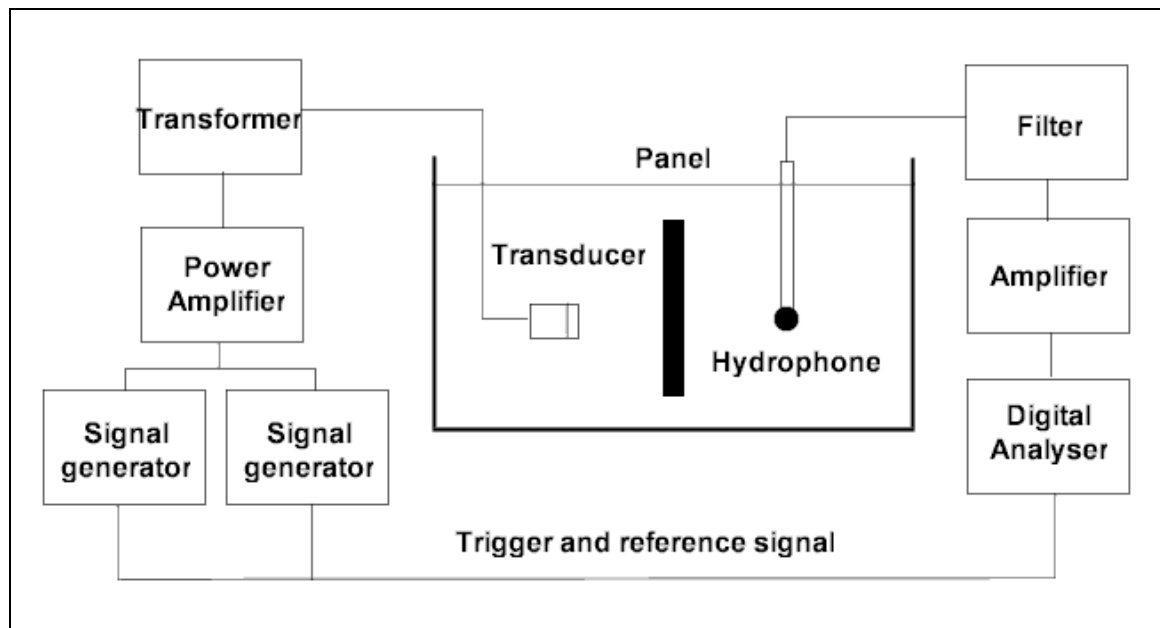


Figure 7.46: General schema of the experimental set up

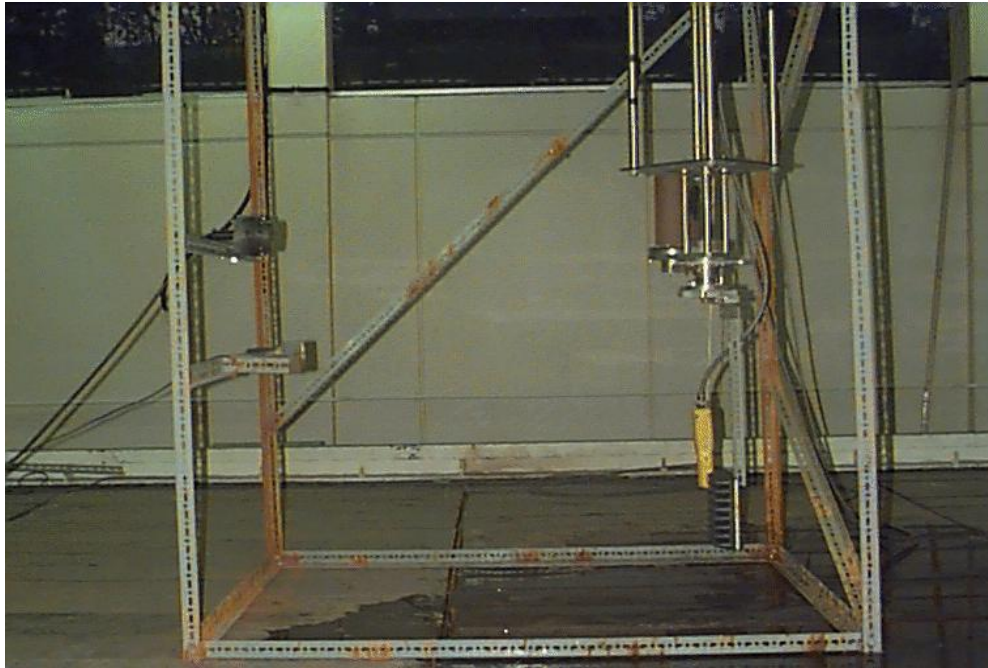


Figure 7.47: Side view of the open test rig. On the left the transducers, on the right the step-motor harness with the tile



Figure 7.48: The open test rig on the wooden cover of the measurement tank at the School of Electronic & Electrical Engineering

A Brüel & Kjaer hydrophone was used in the tests and calibrated in the frequency range between 20 and 50 kHz. The received signal was passed through a passive low-pass filter bank (100 kHz) and then through a signal amplifier. All data was finally recorded using a digital oscilloscope LeCroy 9310.

Three different types of transducers have been used during the experimental measurements. The parametric transducer described in Chapter 4 and Appendix C has been used for most of the tests in the frequency range 30 to 50 kHz. In addition, a number of tests have been made using a tonpilz type transducer and a widebeam transducer provided by the Italian Whitehead Alenia Sistemi Subacquei. The characteristic parameters of the transducers are described in table 7.8.

Characteristic parameters of the test electro-acoustic transducers			
Tonpilz		Widebeam	
Resonance frequency	50.5 kHz	Resonance frequency	38.5 kHz
Material	PZT4	Material	PZT4
Q	4.4	Q	1.5

Table 7.6: Transducers operative parameters (in water)

The signal used for the measurements consisted of a train of pulses generated by one (tonpilz and widebeam transducers) or two HP waveform generators. The typical set up had a burst count of 10 cycles per pulse and a burst rate of 200 Hz.

All measurements have been normalised to the reference signal of the transducer without the tile measured in correspondence of the centre of the tile. In addition, the background signal measured without the target has been subtracted to the measured scattered

signal at the same measurement position in order to obtain the scattered field. The scattered signal obtained in this way was finally used to calculate the form functions.

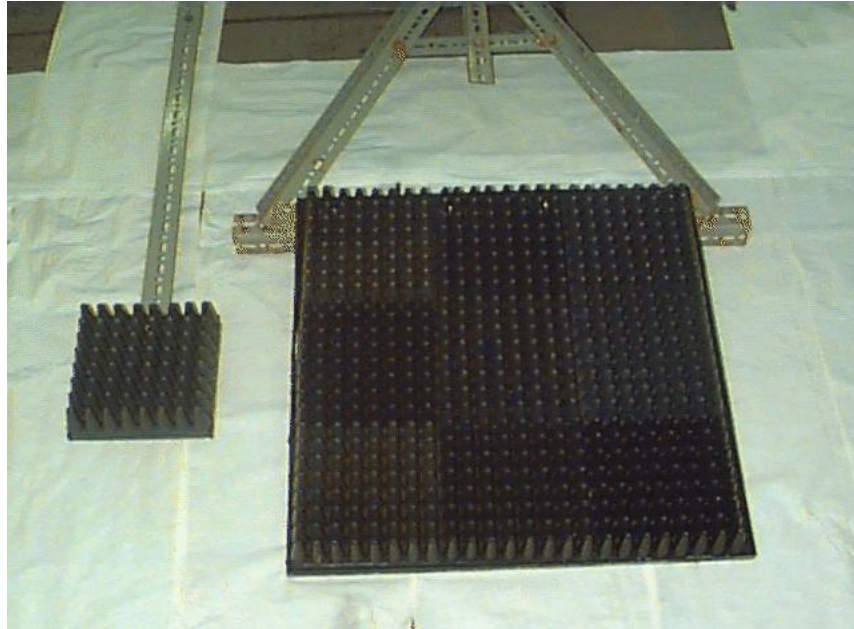


Figure 7.49: The anechoic tile and the complete baffle used during the tests for the VERTLINK project

7.6.2. Results Comparisons

Two sets of test have been performed. First, the frequency response of the tile has been measured at normal incidence for both cases of signal incident on the anechoic side and signal incident on the reflecting side. A second set of tests has successively been carried out to measure the polar response of the tile for different inclinations with respect to the sound wave propagation direction at a number of fixed frequencies.

The agreement between calculated and measured form functions can be considered satisfactory, although the match is not perfect at all points.

The lack of close agreement is most probably due to the presence of the metal bars forming the open rig and the suspension harness where the tile was attached and misalignments or vibrations in the structure itself. It is believed that a tank with absorbing walls and a thinner, more rigid test rig would allow better measurements to be taken.

Some of the calculated and measured form functions are compared in figs. 7.50 to 7.55.

The polar response is measured for the model tile ($\theta_l = 165^\circ$) at the calculated main form function amplitude peaks already shown in section 7.5.3 and 7.5.6.

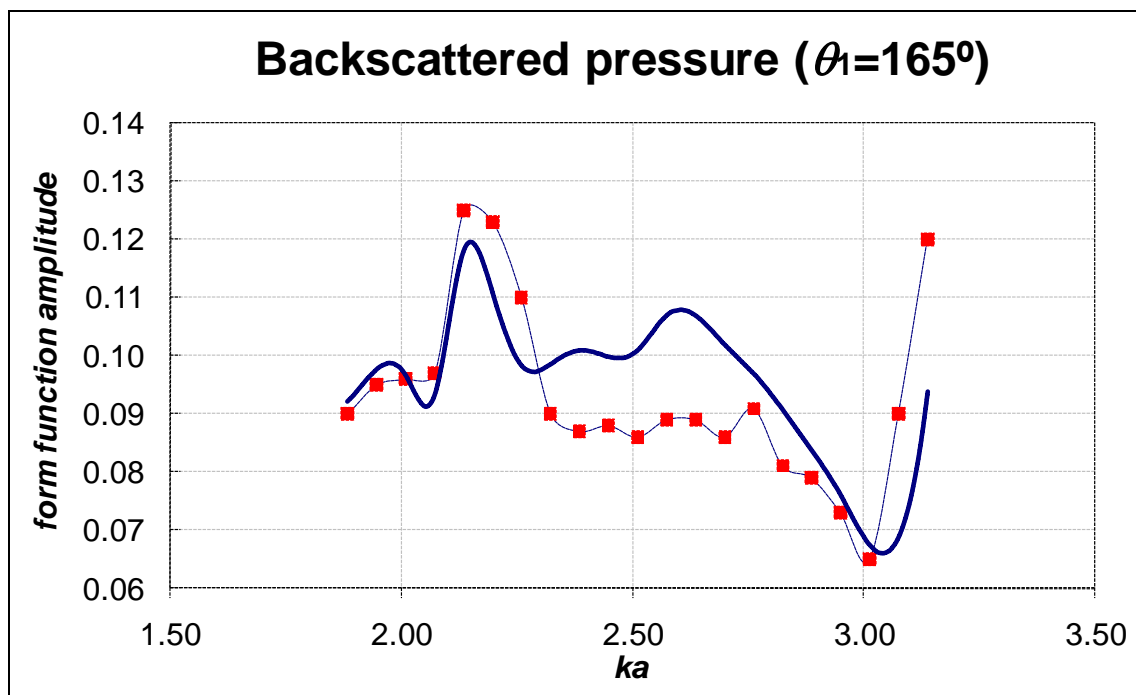


Figure 7.50: Backscattered form function amplitude for the model tile at normal incidence.

— FE-BE, ■ experimental

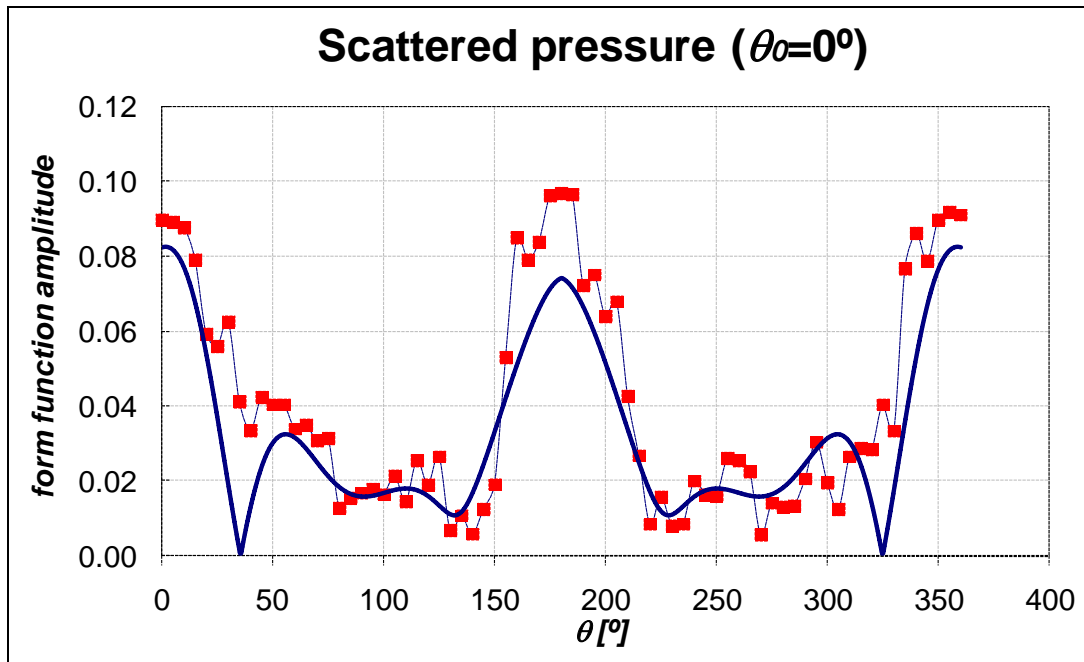


Figure 7.51: Scattered form function amplitude for the model tile at normal incidence, $ka = 2.13$.

— FE-BE, ■ experimental

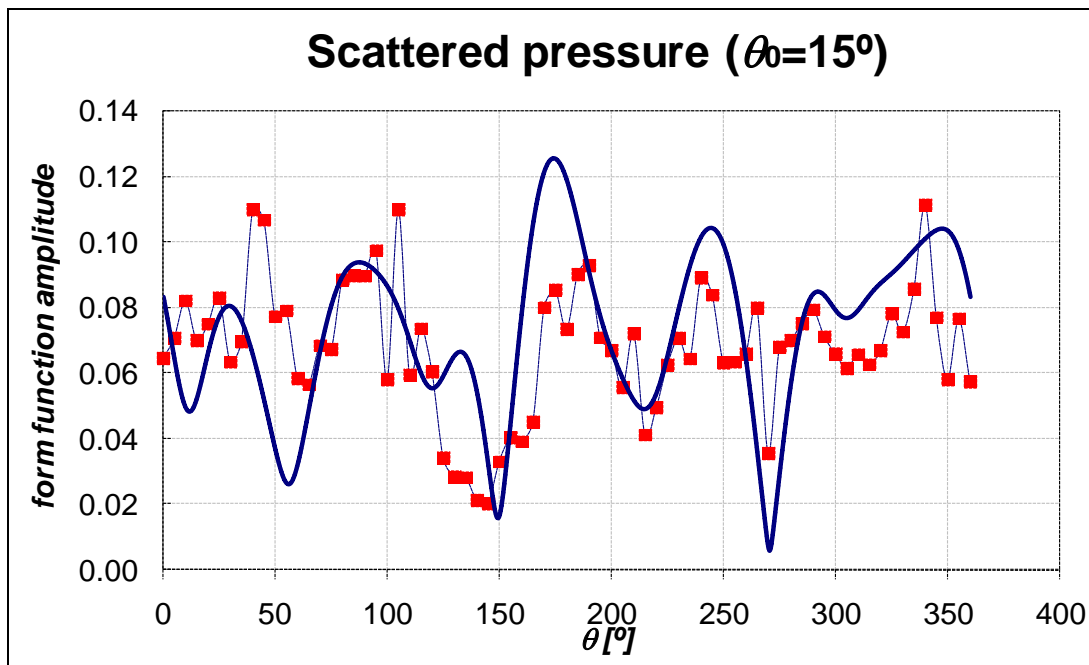


Figure 7.52: Scattered form function amplitude for the model tile at normal incidence, $ka = 2.13$.

— FE-BE, ■ experimental

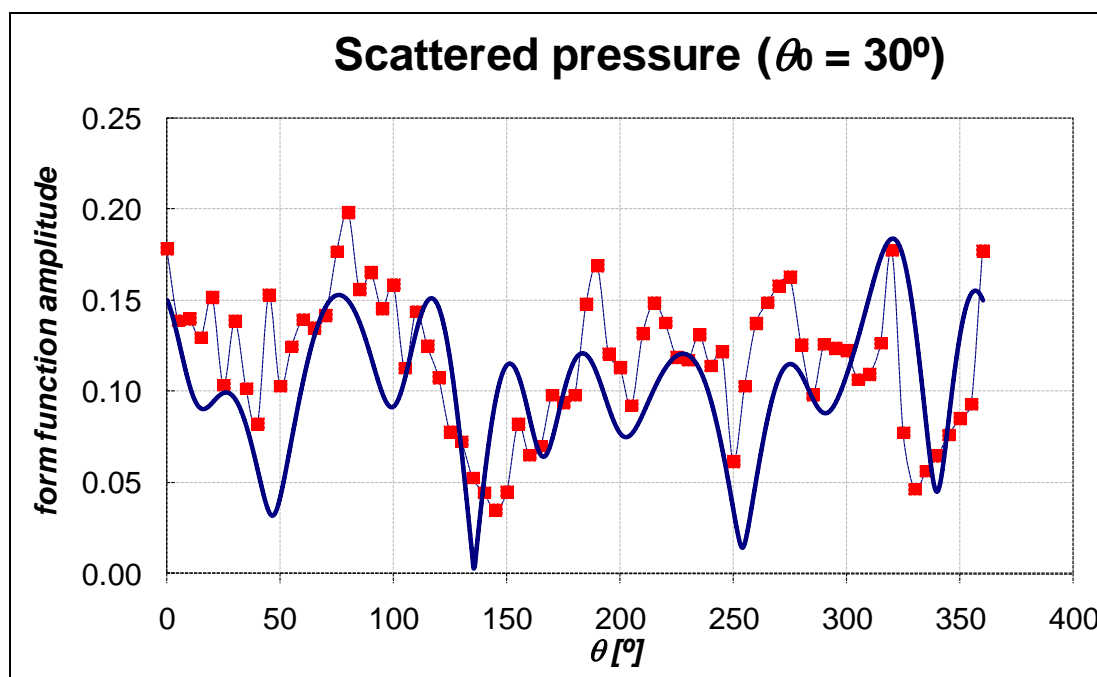


Figure 7.53: Scattered form function amplitude for the model tile at normal incidence, $ka = 2.01$.

FE-BE, ■ experimental

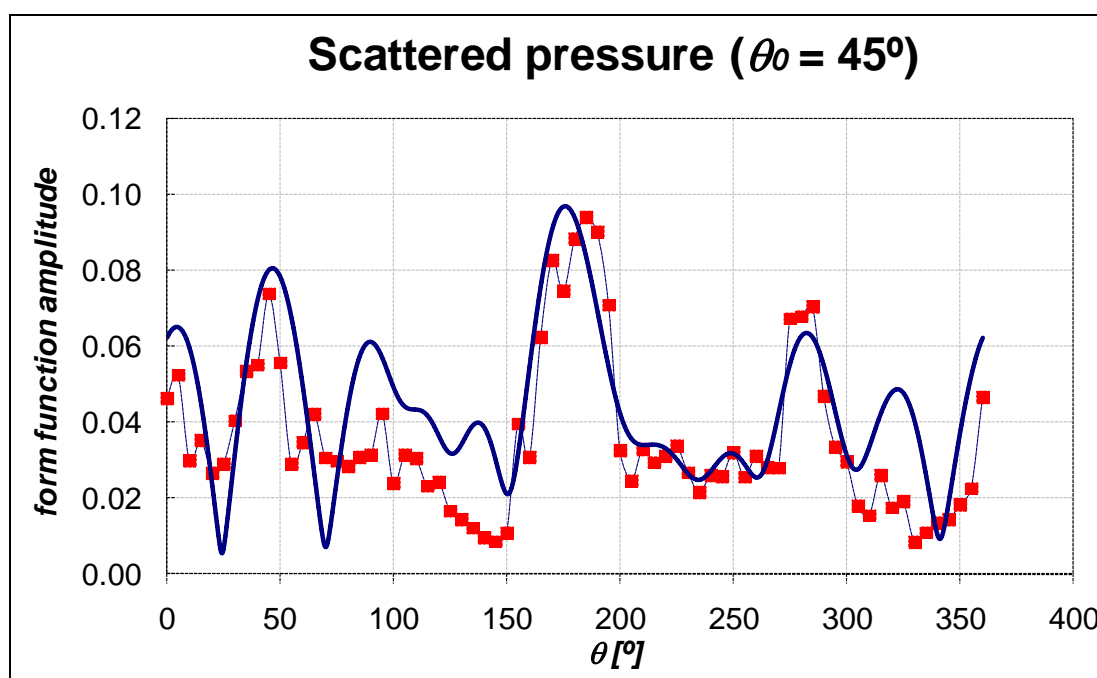


Figure 7.54: Scattered form function amplitude for the model tile at normal incidence, $ka = 2.32$.

FE-BE, ■ experimental

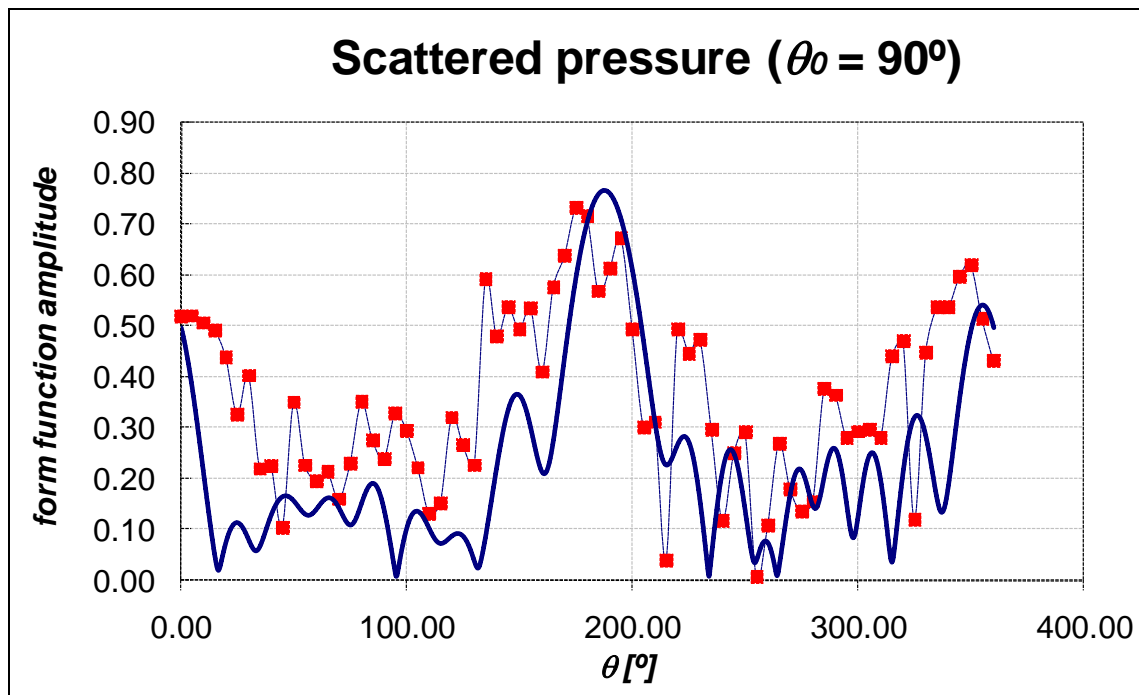


Figure 7.55: Scattered form function amplitude for the model tile at normal incidence, $ka = 2.13$. —

FE-BE, ■ experimental

7.7. References

- BOWMAN, J.J. et al. (1988). *Electromagnetic and acoustic scattering by simple shapes*. Amsterdam: North-Holland
- CHINNERY, P. et al. (1997). Acoustic scattering by non-metallic and metallic cubes in the elastic resonance regime: Experimental measurements and combined finite element/boundary element modeling, *J. Acoust. Soc. Am.*, 102 (1), 60-66
- DI MEGLIO, A. (1996). PHOEBE: a 3-dimensional transducer modelling environment, *Proc. 3rd European Conf. Underwater Acoustics*, II
- FRANCIS, D.T.I (1993). A gradient formulation of the Helmholtz integral equation for acoustic radiation and scattering, *J. Acoust. Soc. Am.*, 93 (4), Pt 1, 1700-1709
- FRANCIS, D.T.I (1996). A combined finite element and boundary element method for submerged structures with internal fluid regions, private communication to be published in *Boundary Elements Communications*
- FRANCIS, D.T.I. (1995). Structural displacements and mode shapes, *private communication*
- JARNG, S.S. et al. (1990). Optimization of sonar transducers using a coupled FE-BE method, *Proc. Inst. Acoustics*, 12 (4), 76-84
- JONES, J., DI MEGLIO, A., WANG, L.S., AID, N. (1998). Underwater Vertical Communication System, *Sea Technology*, 39 (5), 57-62
- LEISSA, A.W. (1969). *Vibration of Plates*, NASA SP-160, Scientific and Technical Information Division,

Office of Technology Utilization, NASA

PATES, C.S. III et al. (1995). Sound-structure interaction analysis of composite panels using coupled boundary and finite element methods, *J. Acoust. Soc. Am.*, 98 (2), Pt. 1, 1218-1221

Chapter 8

Object-Oriented Analysis and Design of a Finite Element-Boundary Element Program

8.1. Introduction

In this final chapter, the finite element-boundary element program used during this research is described in details. The finite element-boundary element algorithm was initially developed in Pascal for the DOS 16-bit platform by Dr. T.I. Francis and others in the Acoustics and Sonar Group of the School of Electronic and Electrical Engineering of the University of Birmingham (Francis 1993).

The program is powerful enough to carry out detailed studies of acoustic radiation and scattering from a variety of objects, including electro-acoustical transducers (Jarng et al. 1990) and object with internal fluid-filled cavities (Francis 1997). However, it suffered from the limitations of the DOS environment, especially memory limitations, and lacked support for viscoelastic materials analysis.

The program has therefore been ported during this research from the DOS platform to the Windows 32-bit platform (win32) and a number of new features have been added. Among these we can list:

- Functions have been added to handle viscoelastic materials and calculate the frequency-dependent stiffness matrix of the scatterer
- The use of the win32 platform allows for better memory management and the possibility of overcoming the strict DOS limitations in terms of memory allocation
- A graphical user interface has been developed, including a powerful set of tools for displaying the FE-BE models and plotting the results of the analysis
- A database of materials has been designed to provide an easy way of selecting among various types of materials, including elastic, viscoelastic and piezoelectric materials
- All the code has been completely revised/rewritten using an object-oriented approach
- A three-tier, client-server model has been developed to allow distributing the load of complex calculations on a farm of computers working simultaneously on different parallel tasks

Although several examples exist in the literature of an object-oriented approach to finite element method programming, as for example in Mackie (1998) and Cross *et al.* (1999), the application of this methodology to boundary elements and acoustic scattering analysis is almost completely unexplored territory (some work on this subject was presented

in 1996 by Haussler Combe as part of a project developed by IBM Germany, see Haussler Combe 1996).

The following sections describe in details the program design process and the features of the WinFEBE program.



Figure 8.1: WinFEBE splash screen (debug version)

8.2. An Overview of Object-Oriented Programming and Design

It is a fact that programming languages have evolved and are constantly evolving by providing explicit support for best practice. Most programming languages have been created by their designer with a specific purpose in mind and they usually offer specific functionality to solve certain tasks. In the beginning, these tasks could be writing a mathematical program (FORTRAN) or being easy to use for educational reasons (PASCAL) or providing special support for data handling (COBOL).

During this process, both the functions and especially the structures of the language are modified. Well nested `gotos` of good Fortran 66 become the `if-then-else` and `for` loops and structures with interface functions become structures with functions or classes in object-oriented terms.

The object-oriented programming (OOP) is often defined as a way to build reusable software components. A class is often represented like an interface connector (IC): input/output specifications, some pins to connect it to the outside world, and nothing else. The IC can be plugged wherever its particular functionality is required with the only need of knowing the I/O specification and not the actual implementation.

OOP is also a way to structure complex programs and encourages programmers to make their types (classes), nouns (objects), and verbs (methods) explicit. Additionally, it allows programming by successive specialization, therefore it becomes possible to implement each behaviour once and then group together related behaviour.

The main difference between procedural and OO programming is that using the former a programmer writes specific code that calls general purpose library routines, whereas using the latter a programmer creates objects that add case-specific intelligence to a generic framework. Because of this OOP behaves like an amplifier and can make good programmers better and bad ones worse. From here stems the need for good design and design tools.

One of the practical benefits of OOP is that old code can use new code, which is much harder than writing new code that uses old code. In fact, a new version of an object can be implemented to provide new functionality and, provided the I/O specifications for the existing interfaces are not changed, old code need not to be modified. The resulting code it's often easier to read, since it is well structured and at a higher level.

Object-oriented programming languages must implement a well-established set of functionalities:

- ***Polymorphism***: similar objects can be treated in the same way. For example, it is possible to ask a box, a sphere, or a pixel for its colour without needing to know what kind of object is answering the question. This leads to property-based algorithms: the programmer knows that the objects being manipulated have certain properties, and ignores everything else about them
- ***Encapsulation***: internals (the implementation) are hidden from the end-user programmer. A class is an interface with invariants, pre-conditions, and post-conditions describing legal states and transitions. It is possible to make arbitrary changes to the implementation (e.g. bug fixes or performance optimisations) without needing to change the code that uses the class
- ***Inheritance***: programmers can implement the next class (child) by adding to (or subtracting from, or mutating) the previous one (parent), thus building on existing functionality and specialising the behaviour
- ***Reflection***: a class knows how to answer questions about its own properties and interfaces (sets of related methods). A caller program can query the class for the proper way of using its functionality, always ensuring to get the proper behaviour out of the class

8.3. The Unified Modelling Language (UML)

Although OOP is a very powerful way of building complex software programs, proper analysis and design become even more important than for procedural programming. Most initial OOP projects were not successful, because the need for a thorough and careful planning that takes most of the allocated time was perceived as an overhead and not as an asset.

The cause of this unbalance was actually due to the lack of design and modelling tools suited to object-oriented programming. Identifiable object-oriented modelling languages began to appear between mid-1970 and the late 1980s as various methodologists experimented with different approaches to object-oriented analysis and design. The number of identified modelling languages increased from less than 10 to more than 50 during the period between 1989-1994. By the mid-1990s, these methods began to incorporate each other's techniques, and a few clearly prominent methods emerged, including the OOSE, OMT-2, and Booch '93 methods.

Finally, the development of UML began in October of 1994 when Grady Booch and Jim Rumbaugh of Rational Software Corporation began their work on unifying the Booch and OMT (Object Modelling Technique) methods. The UML method is currently considered the de facto modelling language for complex software projects (Booch *et al.* 1997).

Object-oriented design is actually an iterative process of further refinements. However at least two main phases can be identified:

- **Analysis:** to formalize the understanding of the problem domain focusing on what, not how: during this phase, no programming

structures should be used (arrays, classes, drop-down menus, etc.). The main techniques in this phase are the **use case diagram**, a story about a single complete interaction between the system and its users or *actors* from a static point of view, and the **sequence diagram**, showing the dynamics of the process and the time ordering of messages.

- **Design:** to specify entities and interactions that implement use cases. During this phase, nouns become objects (classes) and verbs become methods. One of the main techniques in this phase is the **class diagram**, which exactly shows *properties* of the classes and *relationships* between classes

Relationships have a very important role in the design, they are what ties classes together and from them the final structure of the program is shaped. The main types of relationships are:

- **Derivation:** one class specializes another
- **Association:** one class communicates with another
- **Aggregation:** instances of one class contain instances of another

All the entities defined so far (classes, cases, relationships, even comments) have an associated graphic symbol and modifiers or ornaments (see table 8.1). By means of these symbols, it's possible to build a detailed design of a software program, before the actual

implementation starts and with the purpose of knowing exactly what and how to implement. UML is in practice “a graphical language for visualising, specifying, constructing, and documenting the artefacts of a software-intensive system” (Booch et al. 1997).



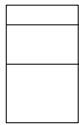

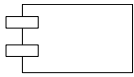
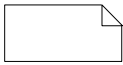

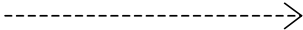
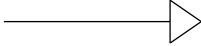

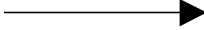
Symbol	Meaning
	Actor
	Use case
	Class
	Interface
	Component
	Note or comment
	Association (with multiplicity)
	Dependency
	Generalisation
	Aggregation
	Message

Table 8.1: UML graphical symbols

8.4. The UML Model of a FE-BE Analysis Program

The WinFEBE UML model has been implemented using two of the main techniques described above, the use case and class diagrams. In this section we describe in general terms the UML diagrams designed during the development of the system. The implementation

details and the meaning of the classes and their methods and properties are discussed in the following sections.

The use case diagram is represented in fig. 8.2. The main FE-BE system is based on four main use cases, Build abstract model, Solve equations, Display results and Store data. Each use case is associated to one or more actors that perform or are subjected to the use case actions.

The four main use cases represented inside the FE-BE Analysis System can be in turn analysed in terms of use cases. We are especially interested in the Solve Equations use case and the Display Results use case. The two subsystems are represented in figs. 8.3 and 8.4 respectively.

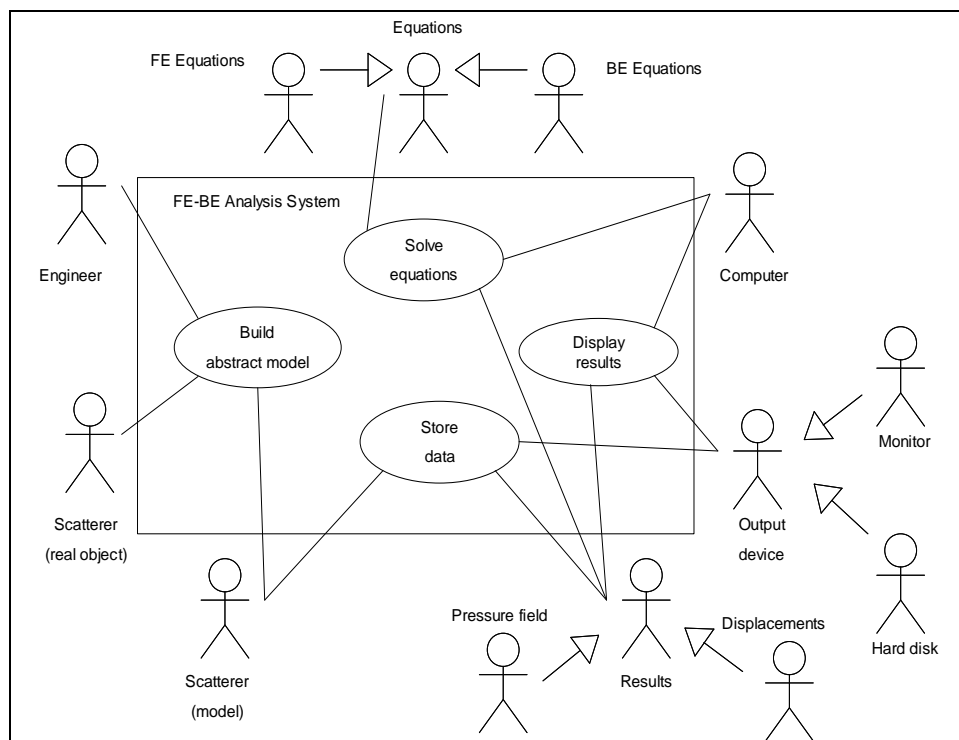


Figure 8.2: The main use case diagram

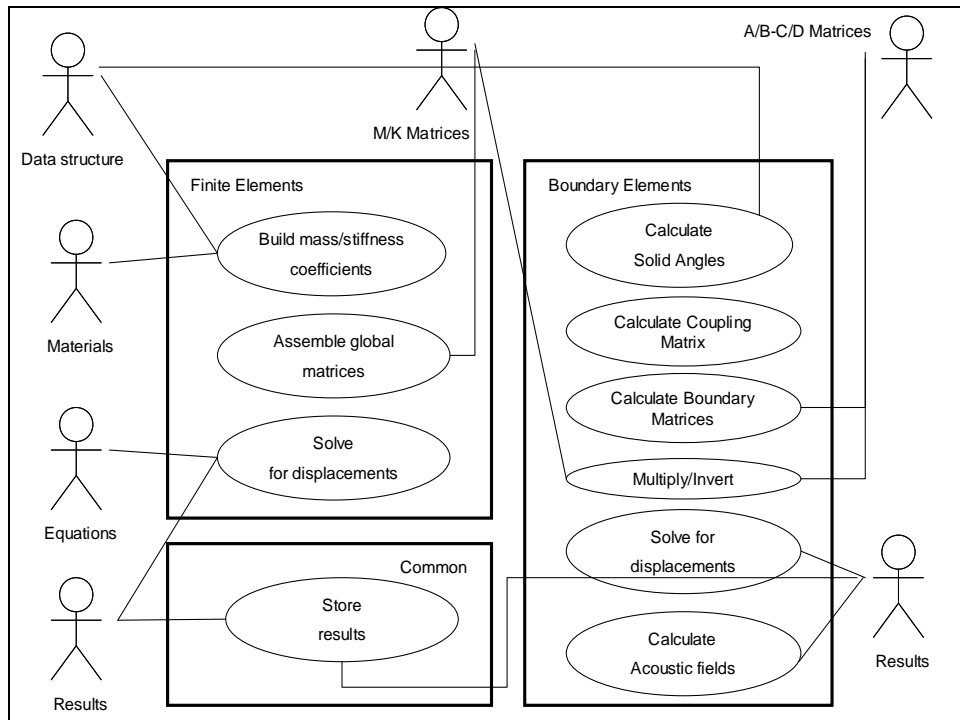


Figure 8.3: The Solve Equations use case diagram

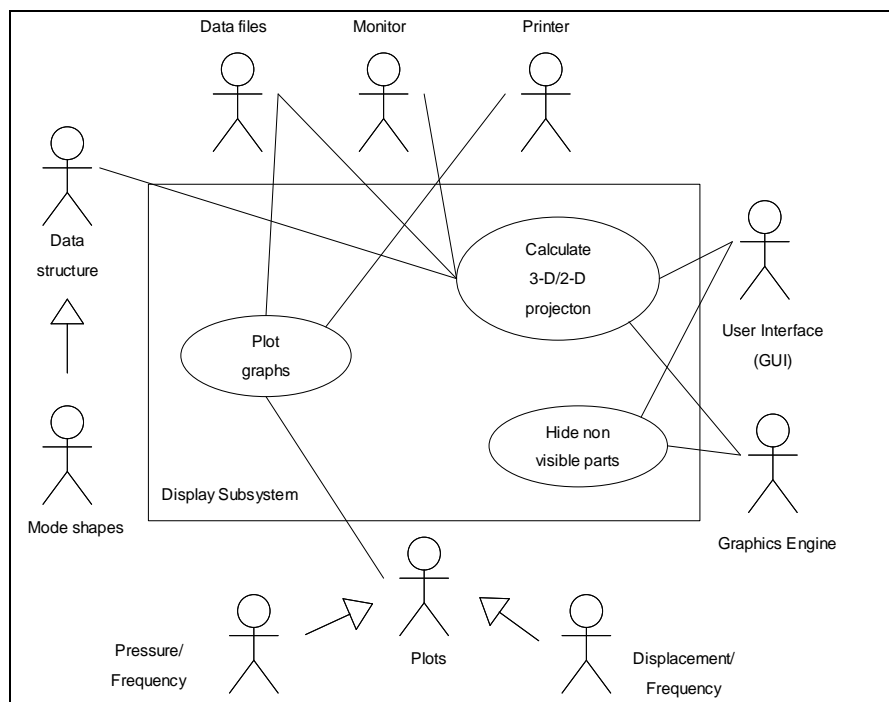


Figure 8.4: The Display Subsystem use case diagram

The class diagram is then used to build a representation of the properties and relationships among all the objects that make up the program structure. The program is designed as a three-tier application, whereby the server part (the real FE-BE program) is remotely controlled by a user application or console and stores data on a network storage device (in our case this is a network-attached hard-disk box with an array of 18GB hard disks).

The console class diagram is represented in fig. 8.5. The class diagrams of the FE-BE server components (data structure, graphics engine and FE-BE algorithm) are represented in figs. 8.6. to 8.8.

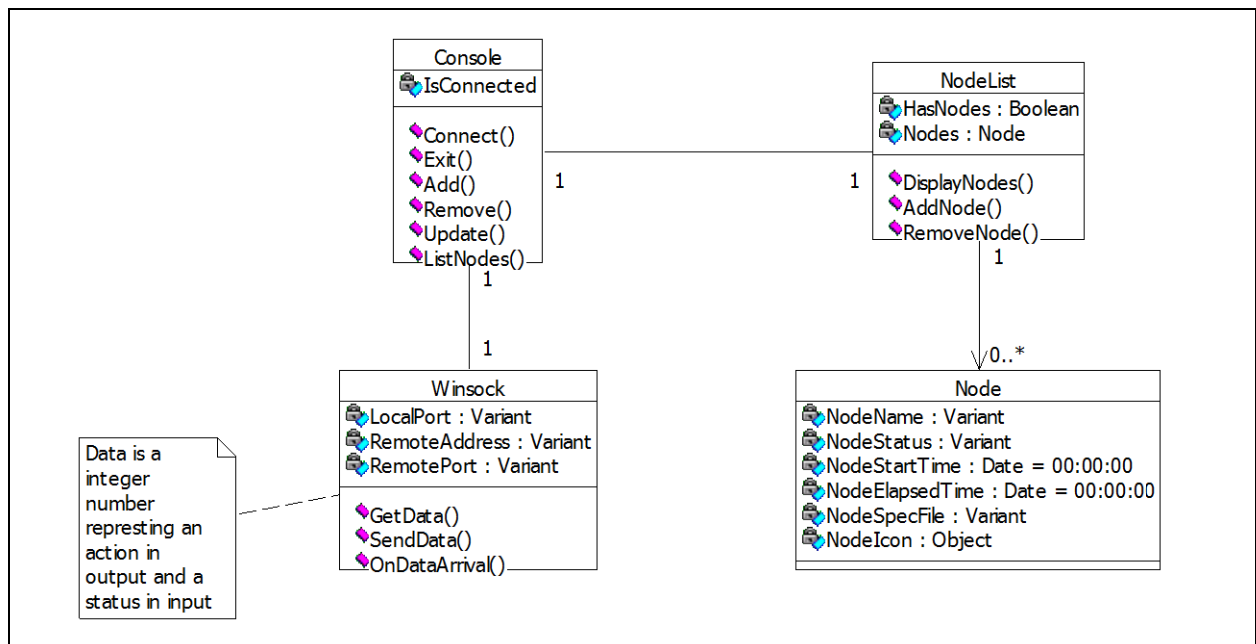


Figure 8.5: The WinFEBE Remote Console class diagram

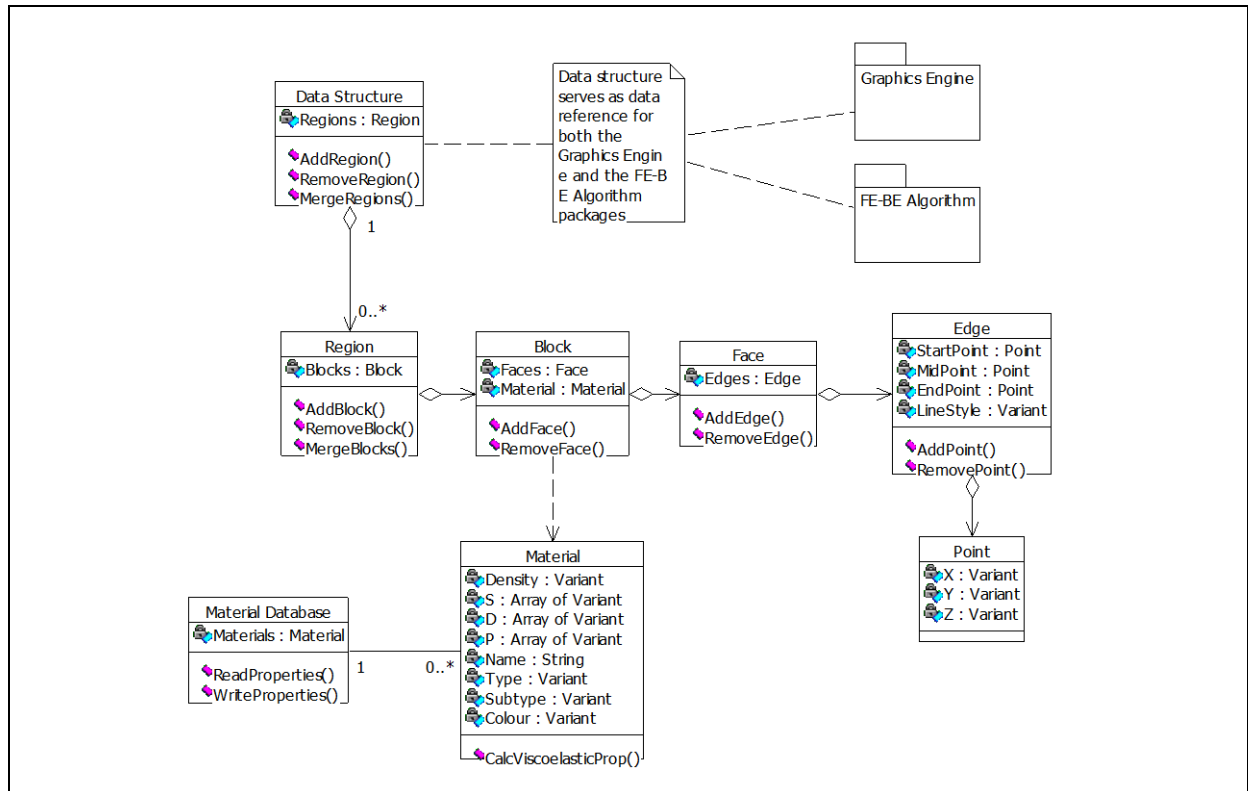


Figure 8.6: The WinFEBE data structure class diagram

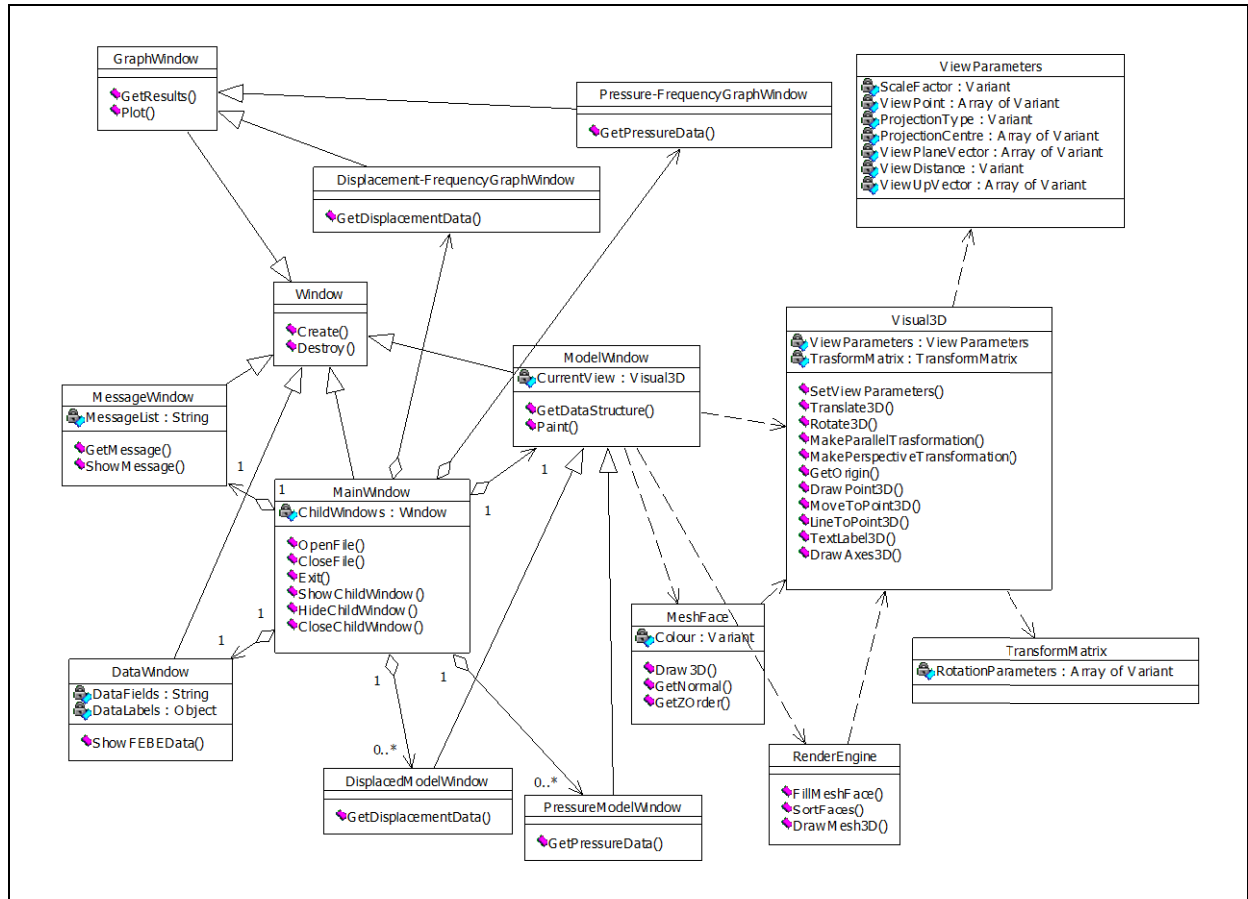
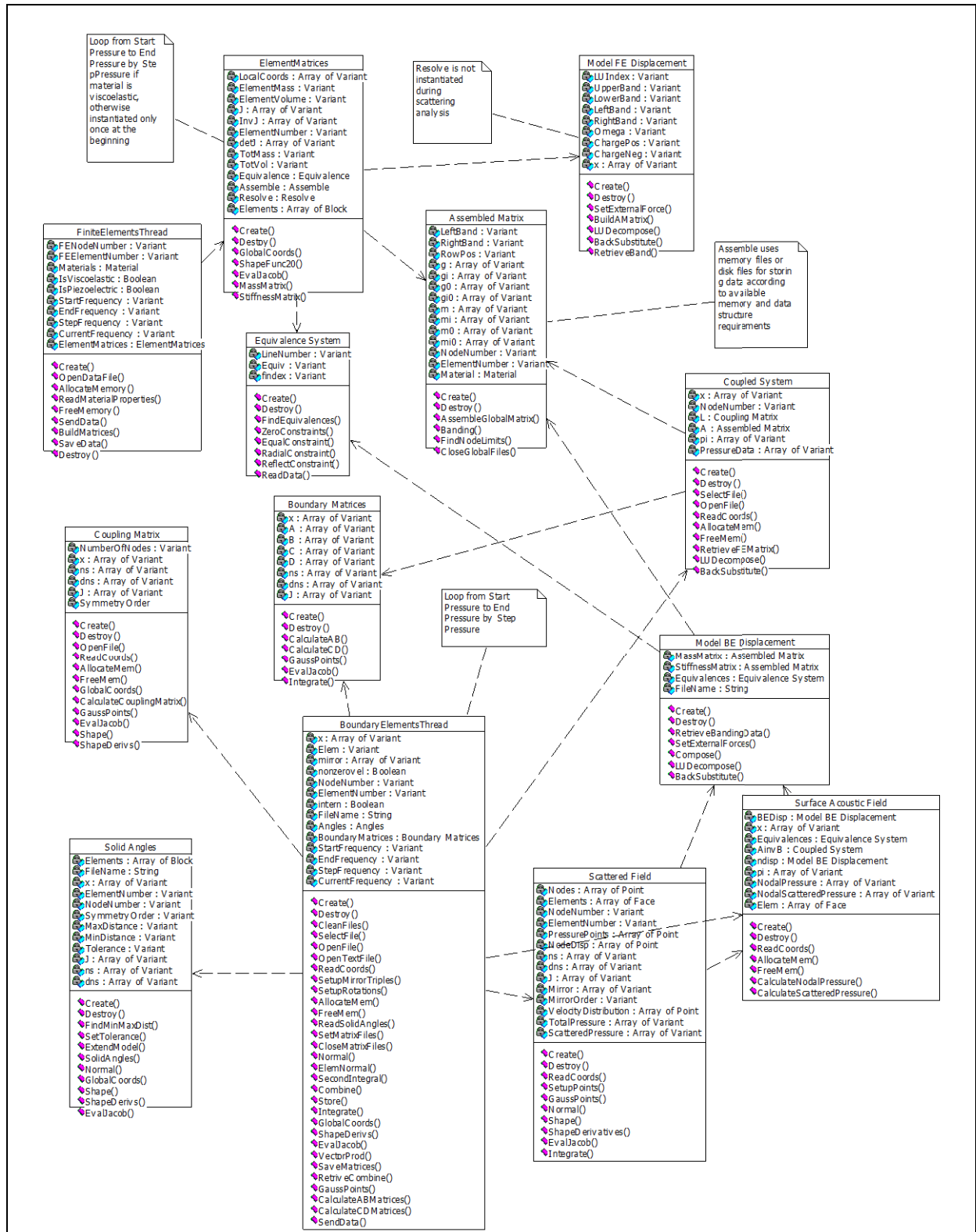


Figure 8.7: The WinFEBE Display and Graphics Engine class diagram



8.5. Model Implementation and Program Structure

8.5.1. *The Programming Language*

The UML model has been implemented using Borland Delphi v.2 and v.3. Delphi is the object-oriented evolution of the traditional Pascal programming language (Calvert 1995). Although it mostly maintains the same clauses and constructs of Pascal, Delphi is based on a completely object oriented model called Borland Object Pascal. All of the core object-oriented techniques are fully implemented in Delphi, such as virtual methods, encapsulation, polymorphism and inheritance.

Additionally, in v.3 the use of pointers and object pointers has been made implicit and therefore hidden from the programmer making the language pointer-safe. This fact, together with a visual development environment, allows writing programs with the same scope as C++, but with the ease of programming of VisualBasic or Java.

8.5.2. *The Graphics User Interface (GUI)*

WinFEBE Graphics User Interface or GUI is based on the so-called iconic model, whereby the user interacts with the program by means of clickable buttons, sliding menus and container windows. The program has been developed for the Win32 platform. It can run on Windows 95/98, Windows NT 4 and Windows 2000 with modest adjustments in the memory management routines.

The program is based on the Windows MDI specification or Multiple Document Interface. A general-purpose main window, the parent window, act as a container for all other windows, providing basic functionalities, such as file input/output, program termination and access to on-line help. All other windows, or child windows, can be started from within the parent container and provide specialised functionality.

Each child window is an object exporting a set of methods for displaying a particular type of information or collecting information. In the initial configuration, after opening a project file, three windows are automatically displayed, the undeformed model window, the data window and the analysis response (message) window (fig. 8.9).

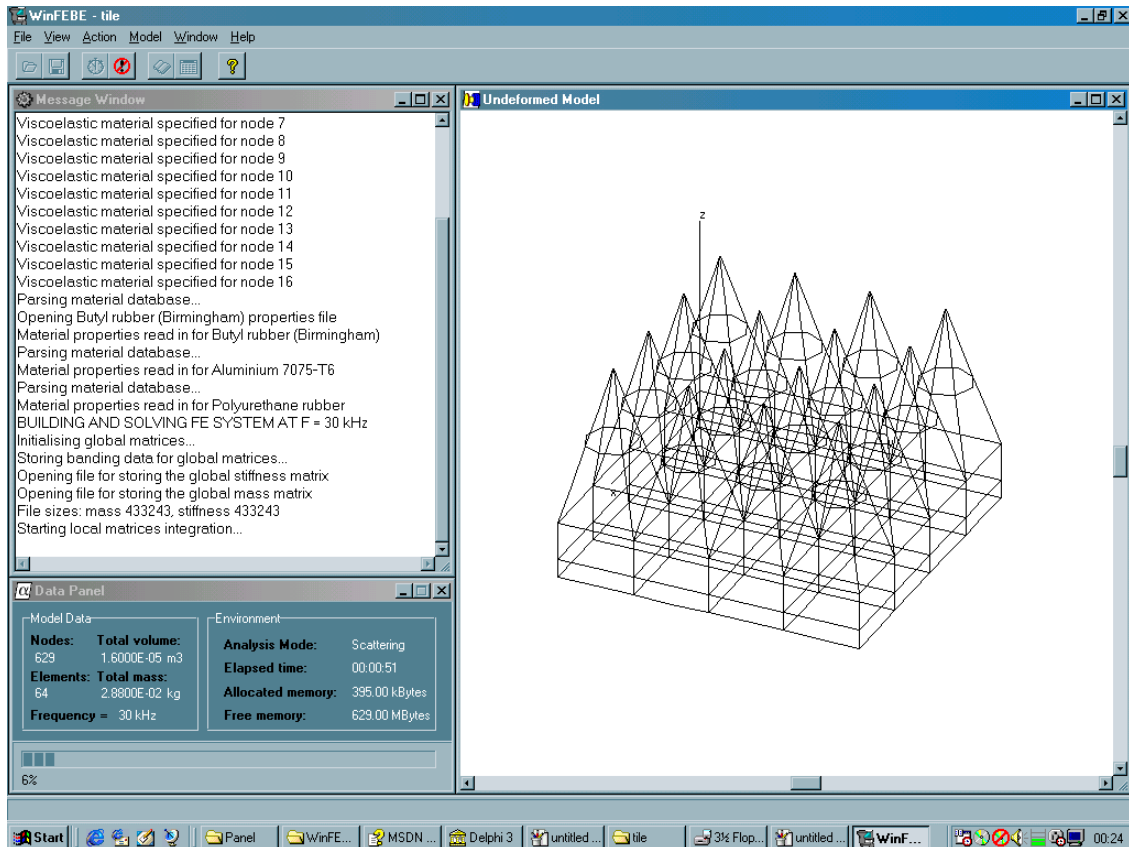


Figure 8.9: The WinFEBE main window displaying the data, message and model child windows

The undeformed model window directly extracts information from the data structure files parsed by the underlying graphics engine to display a 3-dimensional model of the object. This window object exports method to manipulate the properties of the graphics engine to show different views of the model, including a wireframe view and a solid meshed view.

The undeformed window object in turn is the parent object for the deformed model window object. The deformed model window is used to display the displacements of the

nodes of the model and adds new methods to animate the model or magnify/reduce the deformation scale.

A set of plotting windows based on a common plotting window object is finally used in the post-processing part of the program to display the graphs of various physical quantities, such as displacement Vs. frequency or pressure Vs. frequency at a reference node (fig. 8.10).

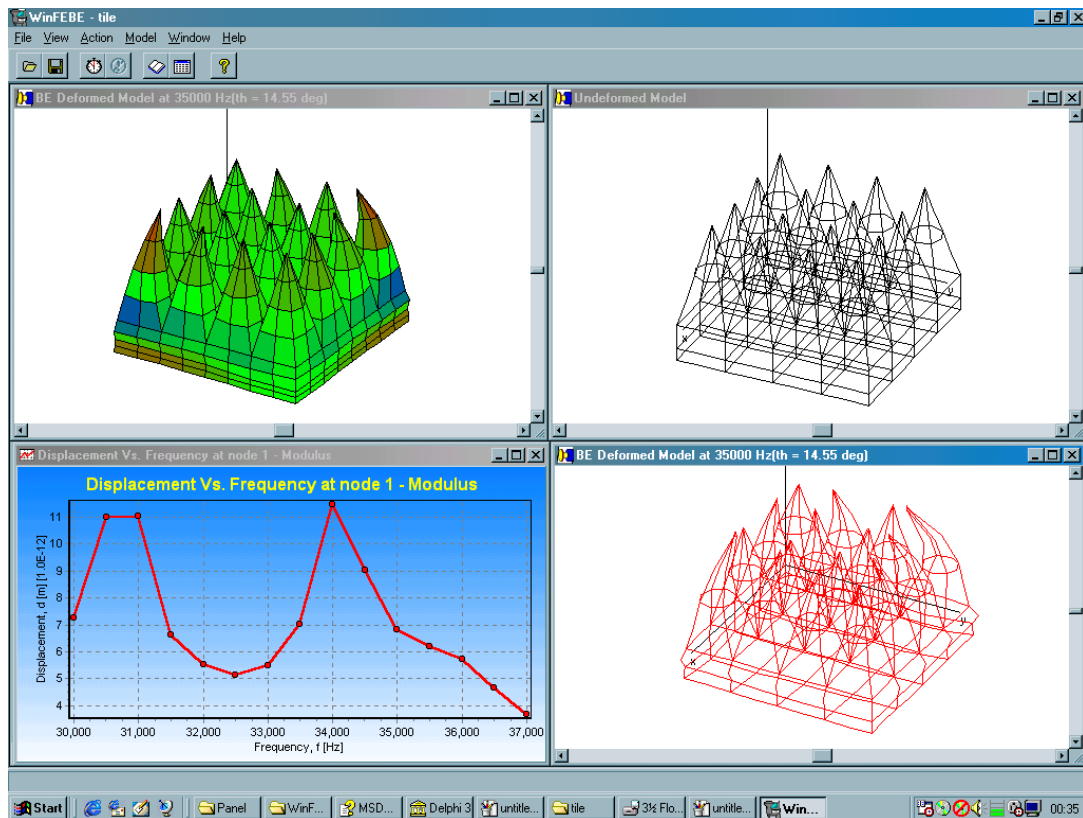


Figure 8.10: The WinFEBE model and graph windows

The material database window is used to browse the material database containing the physical parameter of a number of elastic, viscoelastic and piezo-electric materials to be used in the model. The window can be also used to insert new materials or modify existing ones (fig. 8.11).

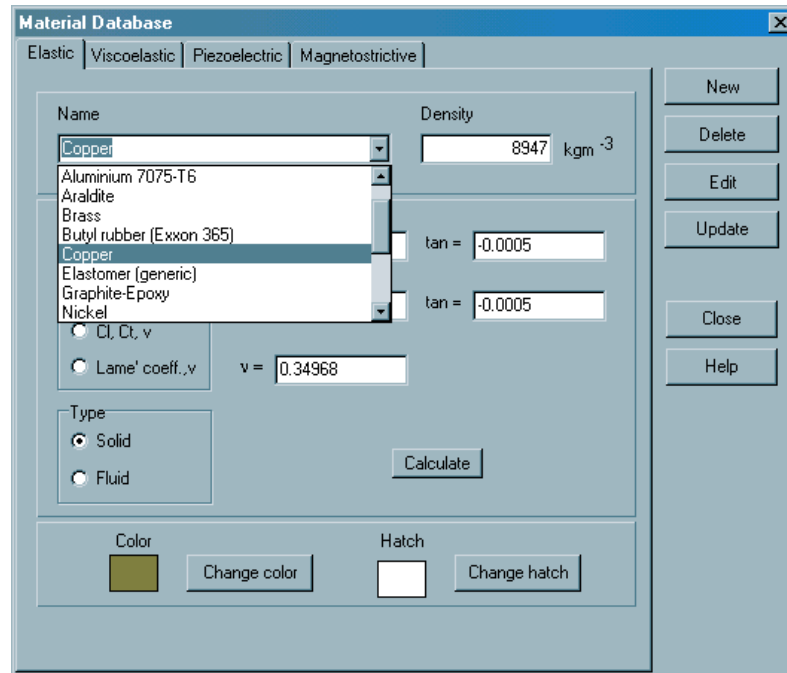


Figure 8.11: The WinFEBE material database dialog

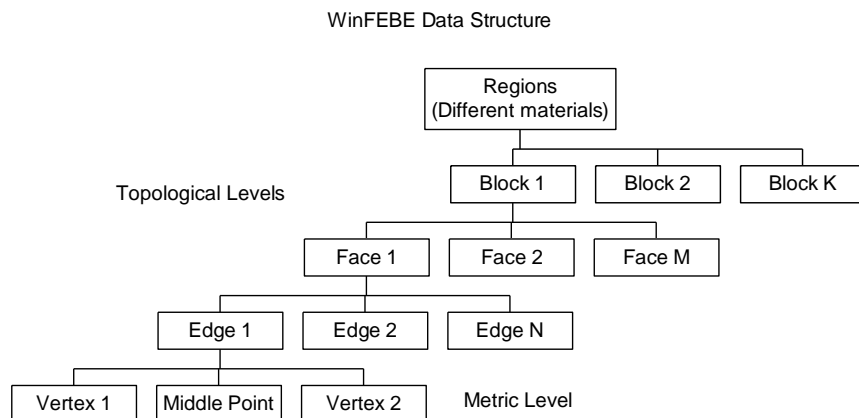
8.5.3. The Graphics Engine

The set of data describing the geometry of an object is usually referred to as the *data structure* of the object. The most common methods used to describe the geometry are (Gardan and Lucas 1985):

- the **boundary representation method**: this is the method most commonly used in the CAD systems. The objects are represented as portions of space closed by a series of surfaces, usually called *facets*. The single facets are given as a list of their constitutive edges and corners. The data structure has the form of a graph, which starts with the topological information and has the metrical information at its base
- the **constructive geometry method**: in this method the objects are defined applying a series of Boolean operators (union, intersection, difference, etc.) to a predefined collection of simple solid objects called *primitives*. The resulting code is more

concise than using the boundary method, but requires frequent re-evaluations of the data to modify or display the objects. The data structure has the form of a Boolean tree, whose branches are the primitives or their descendants and the nodes are the Boolean operators

The data structure used by WinFEBE is implemented using the boundary representation, which is well adapted to the graphic display of simple objects and groups of objects and allows to write simple algorithms to identify points, lines and facets. Additionally, the object-oriented concept of collection is straightforwardly adapted to the graph-like structure of the boundary representation (fig. 8.12).



Each element of the graph is associated with particular topological or metrical information, but not both of them. The main entities of the representation are:

- A. **Regions:** the whole space is ideally subdivided in regions. Each region can be identified with a particular structure or physical medium (for example a transducer with the head in

water and the tail in air can be described as the union of three different regions). However this difference has no consequence on the data structure in itself, but only on the graphic display (different regions are displayed with different patterns or colours)

- B. **Blocks:** each region can be identified with a single block (*object*) or a group of blocks (*structure*). A single blocks must have a unique description of the physical properties. In general the blocks can be primitives (PRISMS, CYLINDERS, CONES, ELLIPSES, etc.) or user-defined entities. WinFEBE implements only rectangular 20-node bricks, which can be directly identified with elements of the finite-element isoparametric schema
- C. **Surfaces:** the blocks are described as collections of surfaces (or facets). Each surface can be a front or a back surface, depending on the direction of its average normal or, which is the same, on the orientation of its edges. Conventionally a front surface has its normal coming out of the screen towards the observer and the edges oriented according to the right-hand or the corkscrew rule. WinFEBE implements 8-node facets, which can be directly identified with element of the boundary element schema.

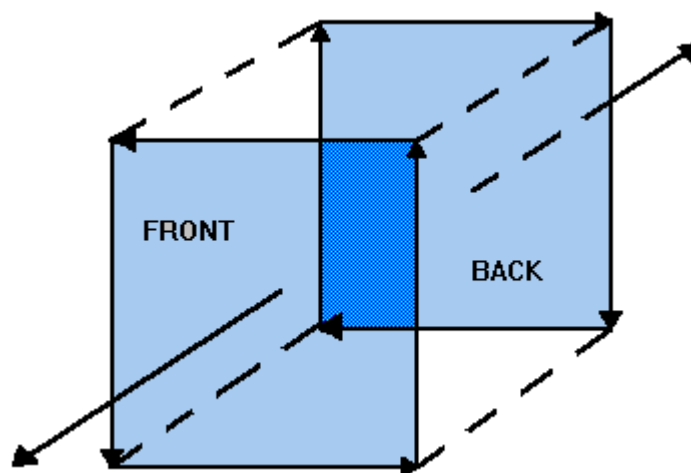


Figure 8.13: The Front/Back Surface Convention

- D. **Edges:** a surface is in turn a collection of edges. The edges are stored in the data structure in the proper order to identify front or back facets. Each edge has two properties, **VISIBLE** and **CLIPFLAG**. These Boolean properties are used by the surface clipping and filling algorithms. WinFEBE implements three-node edges.
- E. **Points:** the entities seen so far are all associated with topological (shape, degree of connectivity, etc.) or geometrical information (degrees of freedom or number of nodes). The point is the only entity of the data structure to be associated with metrical information (position in space). Typically the edges are described by means of two points (straight edges) or a series of points (called *nodes*) used by the parametric equation to describe the shape of the edge

The model is implemented using a series of nested collection objects. A collection is a standard object-oriented way of creating dynamic arrays of other objects.

The complete model is therefore defined as a collection of region objects. Each region is a collection of 20-node block objects. Each block is a collection of surface objects. Each surface is a collection of edge objects. Finally, each edge object simply contains the array of the co-ordinates of its nodes. Each node is given as an index in a general array of co-ordinates, so that each node is only listed once and there are no duplicates.

Each object has a number of properties that can be set at creation time or at run-time to modify the behaviour of the object. For example, the region contains a **COLOUR** or **TEXTURE** property, the facet contains a **VISIBLE** property, and the edge contains a **LINETYPE** property.

Once the data structure of the object has been defined, it must be presented to the graphics user interface. The computer screen or a printed-paper sheet are 2-dimensional

spaces and therefore the graphics engine must include a way of projecting the 3-dimensional objects on a plane. WinFEBE implements a camera-view axonometric projection (fig. 8.14).

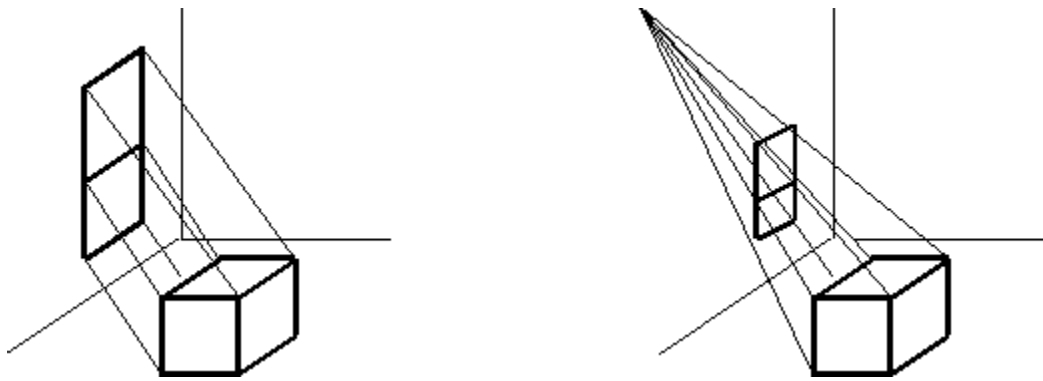


Figure 8.14: Projection methods: orthogonal (left) and axonometric (right)

The camera-view method allows selecting the desired view of the object, front, side, back or any intermediate position. This is done by means of a co-ordinate transformation that maps the 3-D world on a reference plane. The reference plane can be moved around the object and the projection parameters and view reference point can be changed as desired (fig. 8.15).

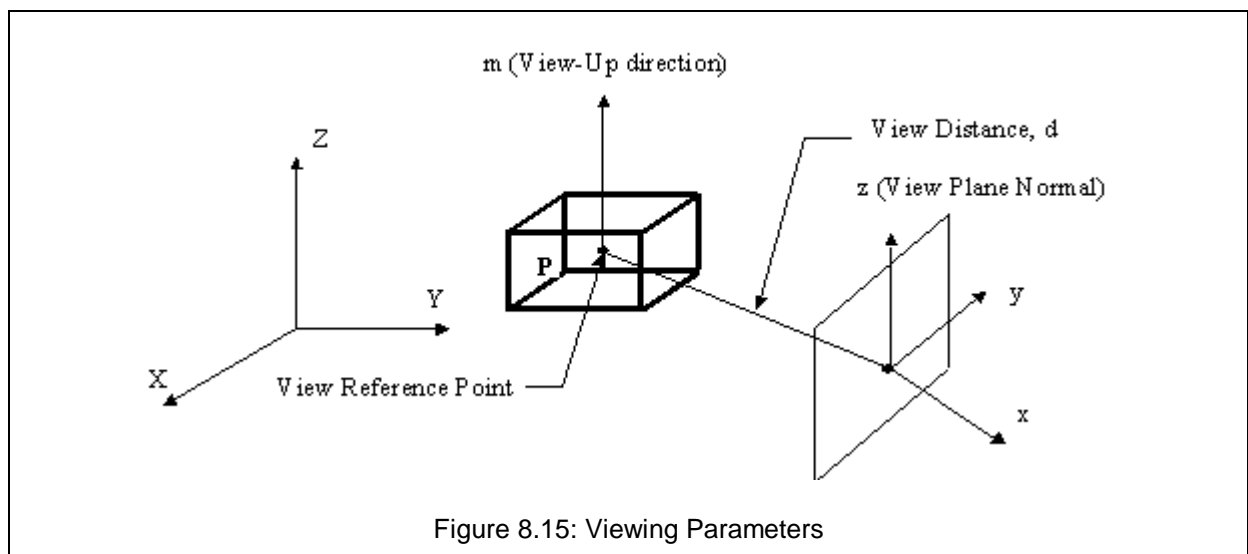


Figure 8.15: Viewing Parameters

Finally, the reference plane is mapped to the screen co-ordinate system. The transformation that maps the two different co-ordinate systems is represented by a roto-translational matrix.

The problem of removing the hidden portions of the drawn objects is not at all a trivial one from a computational point of view. Many algorithms exist to remove or at least conceal the parts of the object that an observer could not see in real life.

The simplest idea is based on the consideration that back faces cannot be seen. Therefore, it is possible to classify each facet in the data structure according to the direction of its normal as projected along the viewing direction (that is perpendicularly to the screen). This can be achieved by calculating the normal vector components in the xyz co-ordinate system and checking the value of the z-component. If this component is not positive, the facet cannot be seen. A useful way to calculate the normal vector components is averaging the values of the facet vertices co-ordinates, using a method proposed by Newell (Newell *et al.* 1972), that gives at the same time an estimate of the projected area of the facet on the three co-ordinate planes:

$$\begin{aligned}
 a &= \sum_{i=1}^n (y_i - y_j)(z_i + z_j) = 2A_{yz} \\
 b &= \sum_{i=1}^n (z_i - z_j)(x_i + x_j) = 2A_{zx} \\
 c &= \sum_{i=1}^n (x_i - x_j)(y_i + y_j) = 2A_{xy}
 \end{aligned}
 \quad j = \begin{cases} 1 & \text{if } i = n \\ i+1 & \text{if } i \neq n \end{cases}
 \quad (8.1)$$

If the $c \leq 0$ the facet is skipped by the graphic engine when displaying the model. Although this approach is very simple and easy to code, it is not sufficient by itself to display

the 3-D objects on the screen, since we must take into account how the front (that is visible) faces overlap and hide each other.

There are four main approaches to the hidden faces removal problem, namely the line approach, the area approach, the scan-line approach and the painter approach. Without going into the details of each method, it suffices here to say that the scan-line method, which examines the rendered scene pixel by pixels to build the final image is certainly the most accurate, but also the most expensive one in computational terms.

The method implemented in the WinFEBE graphic engine is the so-called ‘painter’ method, which is presently considered one of the best compromises between image quality and programming complexity. The basic idea behind the algorithm is that from the observer point of view there is a priority order in the way the facets in the structure hide each other and this order can be used to sort the facets and to display them starting from the farthest one to the one closest to the observer. Each time a new facet is hiding one or more of the previous ones the display is simply painted with the new colour with no need of explicitly calculating the geometry or erasing the hidden areas (fig. 8.16). This approach is named ‘painter’ algorithm because it works in the manner an artist paints an oil picture with different layers of colours.

The idea is credited again to Newell (Newell *et al.* 1972) and has been implemented in many different ways, using frame buffers, geometric data buffers, more or less efficient sorting algorithms and so on. It is very popular because it has average programming complexity (in theory of the order of $N \log N$, where N is the number of facets) and the good results achievable.

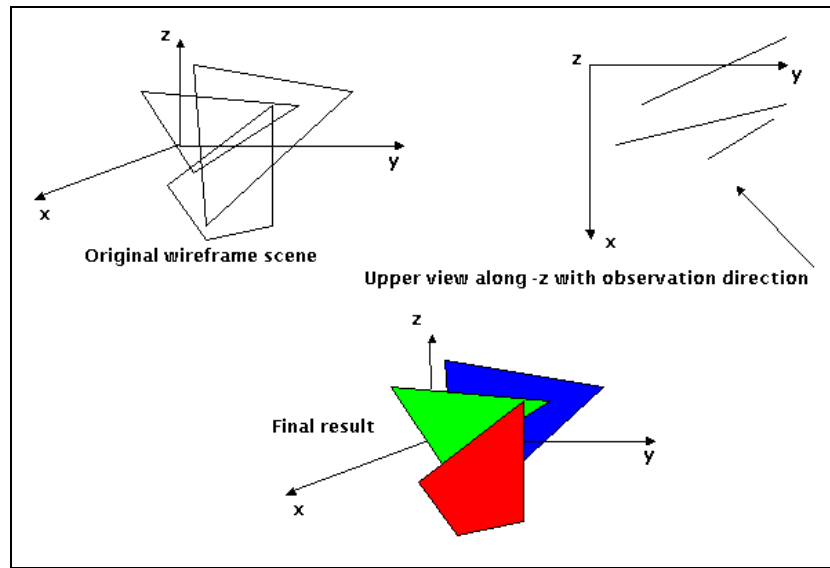


Figure 8.16: The painter algorithm

A drawback of the method is that the facet sorting can start only when all the facets have been stored in memory and it's therefore necessary to completely recalculate and redraw the scene each time even just one of the element is changed, while other algorithm can simply redraw the changed portions and/or screen areas. A bubble-sort type algorithm has been implemented in WinFEBE for the sorting operations ().

8.5.4. The Finite Element and Boundary Element Objects

The Finite Element and the Boundary Element objects are a direct consequence of the boundary representation method used for the data structure. Each 20-node block in the data structure is identified as a Finite Element object and each 8-node surface is in principle identified as a Boundary Element object.

The Finite Element object has a MATERIAL property storing a reference to a material object. The material object in turn exports a set of properties and method to store the physical parameters, such as density and stress tensor components, retrieved from the WinFEBE material database. In case of viscoelastic materials, the material object is exporting a method

to calculate the values of the stress tensor components at any given frequency using a cubic spline algorithm from an array of frequency-value pairs.

The collection of all blocks in the data structure forms the Finite Element Schema object. Additionally, the six surfaces making up each isoparametric finite element have an additional property called the ACTIVE property. The property is set to TRUE if the surface is on the boundary of the domain and to FALSE otherwise. Only the surfaces marked as active are collected in the Boundary Element Schema object.

A special collection of surfaces can be directly linked to a region object to account for the presence of rigid surfaces in the model (housings or rigid cavities).

The data files used by the FE-BE algorithm are built from the FE Schema and the BE Schema objects by parsing the data structure and retrieving the array of common FE-BE nodes and the two sets of FE internal nodes and BE rigid nodes. The common FE-BE nodes are called the active nodes, since they are on the boundary and in contact with the embedding medium and are listed first in the sequence of co-ordinate for both the FE and the BE model.

This approach allows easy modifications of the two schemas. If a new region must be added to the model, the new data structure can be automatically merged with the existing one by identifying and removing the duplicate nodes, extending the existing co-ordinate array with the new nodes and then recalculating the FE and BE schemas.

WinFEBE doesn't contain any means of building the data structure from an arbitrary model, what would be called a meshing tool. It is however possible to obtain a finer model from an existing one by splitting each block in a set of eight blocks and recalculating the schemas from the new co-ordinate array.

8.5.5. The 'Worker' Objects and the Implementation of the FE-BE Algorithm

The FE-BE algorithm is implemented by means of a set of 'worker' objects. Each object can be actually identified as a particular step of the entire algorithm. The advantage of using objects in this case is in the possibility of having the different steps to run as separate processes or threads on the same computer to perform different tasks.

This not only means that the different steps can be performed independently at different times, but also independently at the same time. For example, the Finite Element Analysis object can calculate the global mass and stiffness matrices for a frequency value in the given range, while the Boundary Element Analysis object can work on existing data from the previous calculation.

The latter case has of course really an edge if the program is running on a SMP computer with more than one processor, so that each different thread can be assigned to a different processor.

The structure of the Finite Element and Boundary Element Analysis objects comes directly from the original implementation of the DOS version of the program. The Windows object-oriented version of the algorithm is a port of this original FE-BE algorithm. The latter was already well structured in independent modules contained each one in a different executable file. The worker objects have been therefore modelled on the existing task hierarchy.

The main program is calling the worker objects according to a specified schedule providing the necessary synchronisation. A typical case is, as previously mentioned, a complete run of the FE-BE program for a specified model in a given range of frequencies. The sequence of operations is represented in fig. 8.17 and fig. 8.18.

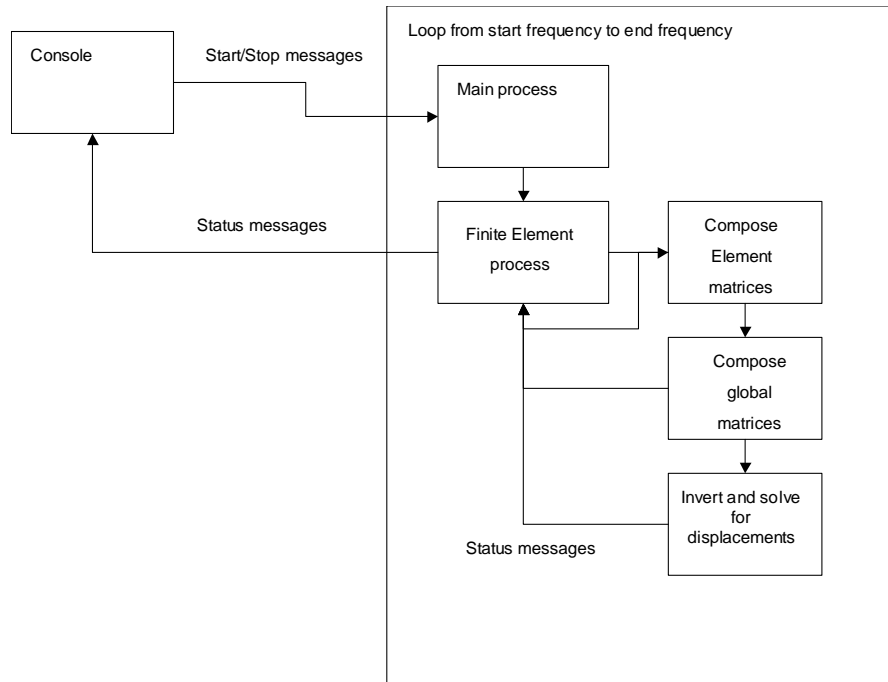


Figure 8.17: The Finite Element algorithm activity diagram

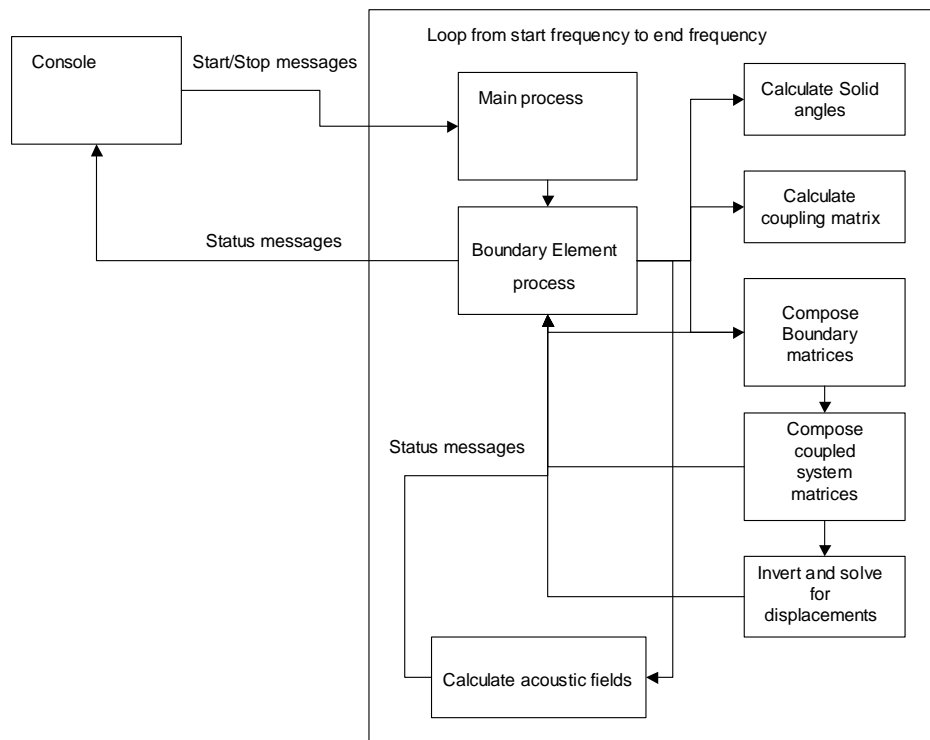


Figure 8.18: The Boundary Element algorithm activity diagram

The inbound and outbound communication messages received and sent by the console and by main program are the glue of the distributed infrastructure used by the program and described in the next section.

8.6. The Supercomputer Model

8.6.1. Client-Server Applications and Distributed Computing

The client-server computing model is currently one of the most dominant paradigms in IT. It has developed during the past 10 years as the computer industry moved from a centralised shared-logic based system to a network of servers and workstation.

In its most recent form a client-server infrastructure can be made of three separate tiers:

1. The Presentation Logic tier
2. The Business Logic tier
3. The Data Access Logic tier

The Presentation logic sits at the user end and allows them to access and manipulate data and information by sending instructions to and receiving results from the business logic tier. The business logic tier receives the instructions, performs a number of specified tasks on the data stored in the data access tier and finally sends back the results of this manipulation (from new information to a simple task execution confirmation).

The client-server model is extremely well suited to distributed computing. A number of tasks can be initiated and controlled from a console application on the client, executed on one or more servers and finally the data stored in a third dedicated device.



Figure 8.19: The WinFEBE computer farm (hosted by the CERN NICE Computing Infrastructure)

In the past few years, this idea has developed in what is currently called the ‘commodity supercomputer’. Farms of several tens (or even hundreds) of CPUs running on out-of-the-shelf commodity PCs can be used to perform complex calculations by distributing simpler independent tasks to each CPU and then collecting and assembling the resulting data. This model is successfully used for example in particle physics to perform lengthy Montecarlo simulations of particle collisions in accelerators (see for example Chen *et al.* 1997 and Joshi *et al.* 1999).

A scaled-down version of this model has been implemented in the WinFEBE program. A task is identified as a single FE or BE calculation at a given frequency on a given model.

The tasks are coordinated by a central console application that can be used to start/stop the task on each individual computer (node); upload/download definition files to/from each node; upgrade the software, etc.

8.6.2. The WinFEBE Console

The WinFEBE console is a Windows applications used to centrally manage the various nodes of the distributed infrastructure. The nodes are displayed as a hierarchical tree (figs. 8.20 and 8.21). For each node it is possible to display information such as name of the node, activity status, start and elapsed time of the current task, task definition file.

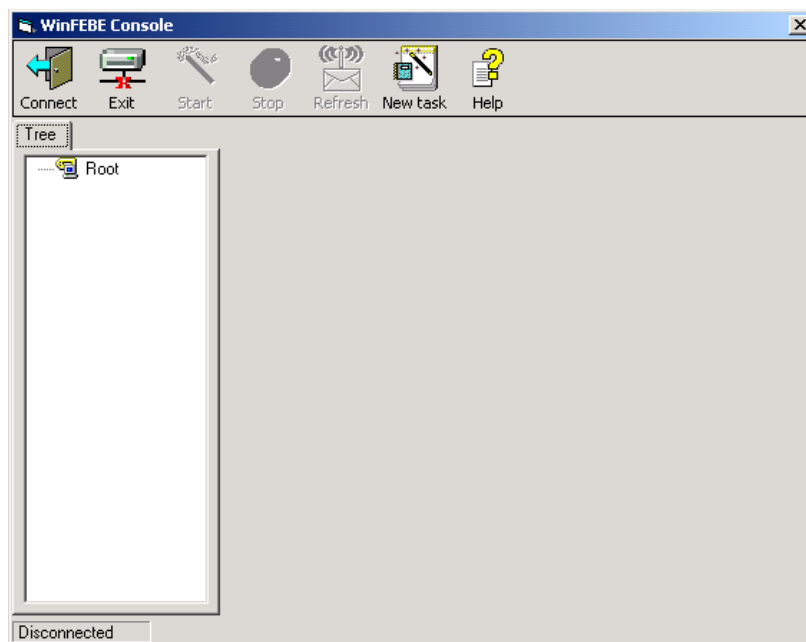


Figure 8.20: The WinFEBE console at start up

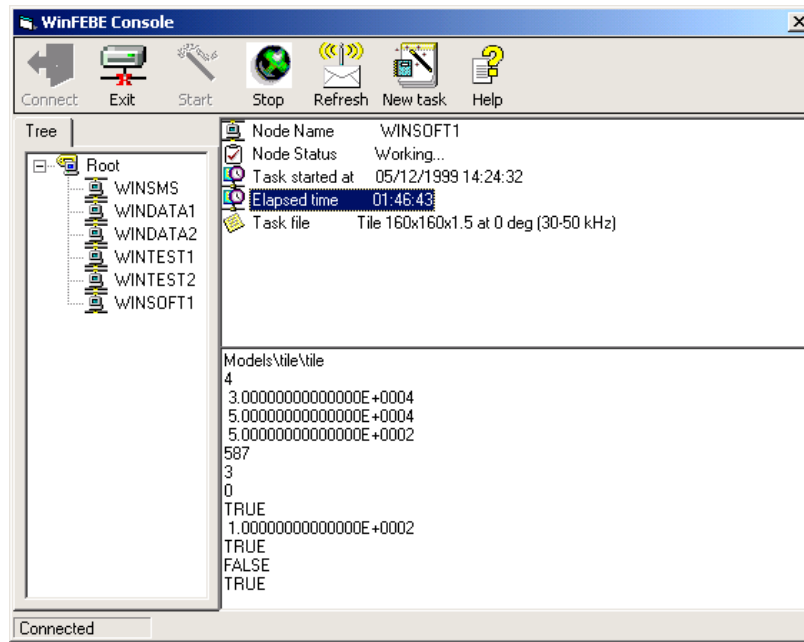


Figure 8.21: The WinFEBE console connected to the nodes

New tasks can be created and uploaded to specified node. In addition, nodes can be added or removed from the structure using the console interface. To add a new node, it's only required to specify the name and/or the IP address of the computer in the local network (fig. 8.22). The necessary server software is automatically downloaded upon the first successful connection and registered in the Windows registry database.

The server program is registered as a DCOM object (Component Object Model) according to the Windows DCOM specification (Grimes 1997). The console can start and stop the object remotely by using standard component instantiation messages.

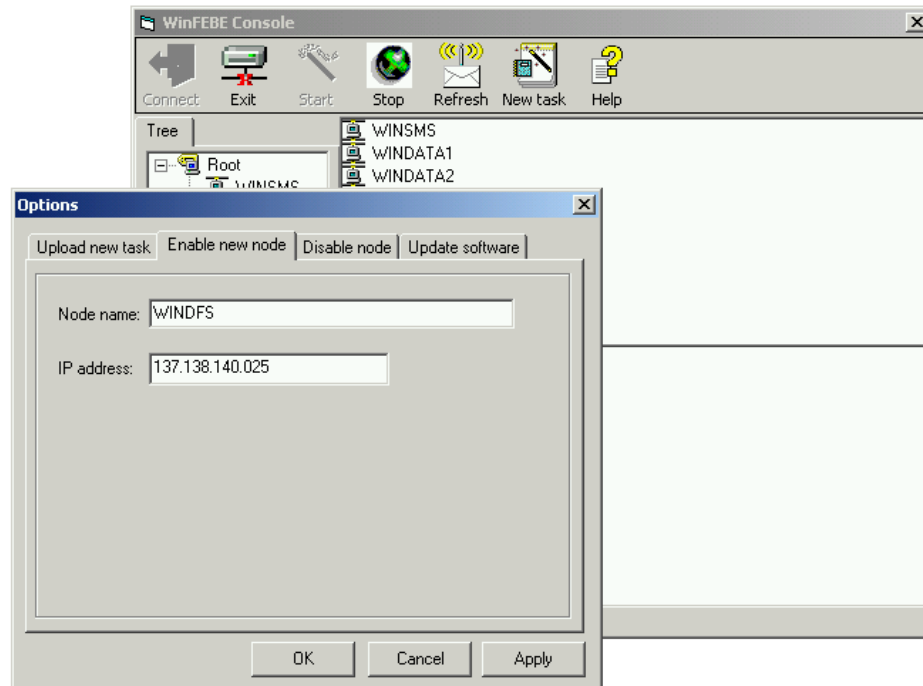


Figure 8.22: The WinFEBE console options dialog to add a new node

8.6.3. The WinFEBE Nodes

The model can include in principle an unlimited number of nodes. A maximum number of seven nodes have been used in this research. The server software runs the given task in automatic mode and periodically listens on a given UDP (User Datagram Protocol) port for incoming messages from the console. At the same time, each server sends periodic messages to the console to notify its status.

The server software is the same as described in the previous sections for the FE-BE algorithm. The process listening on the UDP port runs as a separate thread and doesn't slow down the calculations.

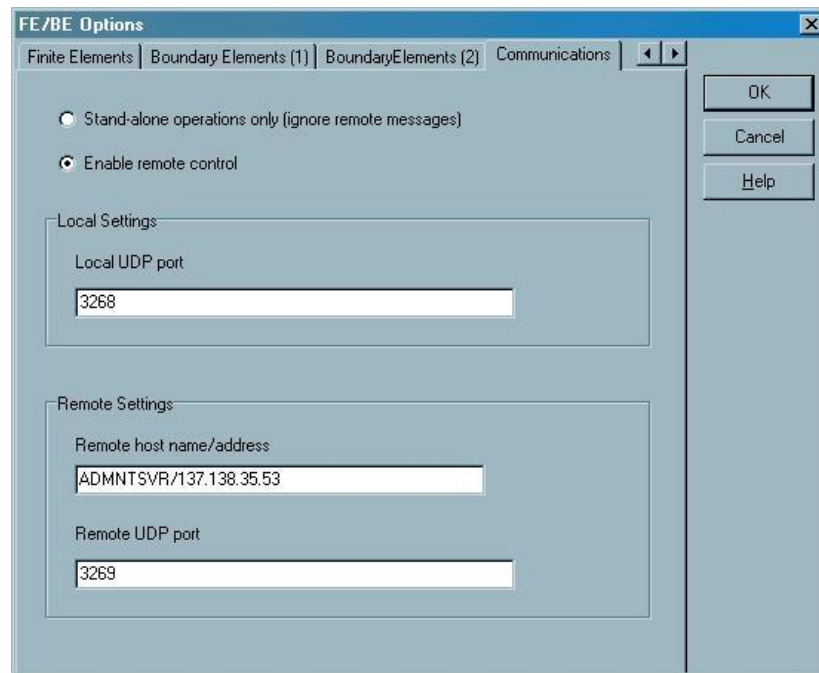


Figure 8.23: The server program communication settings

8.6.4. The Communication Infrastructure

The communication between the console and the nodes is based upon the exchange of UDP packets. Both the client and the server program listen on a default configurable UDP port. Since UDP is a connectionless protocol, there is no protocol-level acknowledgment of reception of a packet. This works well enough on a local network. The client software can resend failed packets after a configurable time-out if no status change packet is received from the target node. The additional advantage is that the console needs not to be running while the nodes send status notification packets. The packets are simply lost and ignored.

There are two types of messages, action messages and status messages. Typically, action messages are sent by the console to the nodes, whereas status messages are sent by the nodes to the console. Some of the possible messages are listed in table 8.2. Messages enclosed in angular brackets are place holders for a specific value such as the time elapsed since start or the bytes of allocated memory.

Message	Category	Message	Category
Start task	Action	Program started	Status
End task	Action	Task started	Status
Suspend task	Action	Task finished	Status
Exit program	Action	<Running time>	Status
Refresh running time	Action	<Allocated memory>	Status
		<Current frequency>	Status
		<Trapped run-time error>	Status

Table 8.2: The client-server UDP messages

8.7. Conclusions

The WinFEBE program presented in this chapter has proved to be a powerful tool for the analysis of acoustic radiation and scattering with a user graphical interface for easy use in Windows. The program is versatile and can be used in many different scenarios, from the study of radiation from electro-acoustical piezoelectric transducers to the investigation of scattering from complex objects.

The use of the distributed client-server infrastructure has helped in reducing one of the most severe drawback of this kind of analysis packages, notably the long time needed to perform high frequency simulations over a wide frequency range, where the number of nodes and elements of the model becomes inevitably larger as the frequency increases.

Some further improvements can be suggested:

- Several low order routines for storing to and retrieving data from disk and a number of mathematical routines (especially for performing complex-valued

operations) are repeated in more than one class as private methods. It would be better to have separate shared libraries

- There is no automated way of generating the data structure from a general description of the objects. The addition of an automatic meshing tool or an import function to retrieve the data structure from industry-standard CAD packages such as AutoCAD would considerably improve the program
- The port of the program to a 64-bit platform system, such as Digital Alpha or the forthcoming Intel Merced processor would further improve floating-point performance and reduce calculation time

8.8. References

- BOOCH, G. *et al.* (1997). *The Unified Modeling Language User Guide*, Addison-Wesley: Reading (MA)
- CALVERT, C. (1995). *DELPHI Unleashed*, Sams Publishing: Indianapolis (IN)
- CHEN, D. *et al.* (1997). QCDSF : a teraflop scale massively parallel supercomputer, *CERN Preprint*
- CROSS, J.T. *et al.* (1999). Why you should consider object-oriented programming techniques for finite element methods, *Int.J. Num. Methods Heat Fluid Flow*, 9 (3), 333-347
- FRANCIS, D.T.I (1993). A gradient formulation of the Helmholtz integral equation for acoustic radiation and scattering, *J. Acoust. Soc. Am.*, 93 (4), Pt 1, 1700-1709
- FRANCIS, D.T.I (1997). A combined finite element and boundary element method for submerged structures with internal fluid regions, private communication
- GARDAN, Y. and LUCAS, M. (1985). *Interactive Graphics in CAD*, Kogan Page
- GRIMES, R. (1997). *DCOM Programming*, WROX Press Ltd.: Birmingham (UK)
- HAUSSLER COMBE, U (1996). Coupling boundary-elements and finite-elements – A structured approach, *Computer Methods in Appl. Mech. Eng.*, 134 (1-2), 117-134
- JARNG, S.S *et al.* (1990). Optimisation of sonar transducers using a coupled FE-BE method, *Proc. Inst. Acoust.*, 12 (4), 57-65
- JOSHI, K. *et al.* (1999). Monte-Carlo Simulations of Globular Cluster Evolution; 1, Method and Test Calculations, *CERN Preprint*

- MACKIE, R.I. (1998). An object-oriented approach to fully interactive finite element software, *Advances in Eng. Software*, 29 (2), 139-149
- NEWELL, M.E. et al. (1972). A new approach to the shaded picture problem, *Proc. ACM National Conf.*

Chapter 9

Summary and Further Work

The work carried out in this research study was first suggested during the preliminary phases of the project VERTLINK. The work has made original contributions in the two main research areas it had to deal with, namely the determination of the physical properties of viscoelastic materials and the analysis, simulation and prediction of the behaviour of complex tiles made of such materials for underwater sound control applications.

The main goal set at the beginning of the work was to find the most efficient way to reduce interference to the signal receiver used in the VERTLINK underwater communication system.

The receiver had to operate in quite harsh conditions since it was deployed near the sea surface where there are two main components of interference.

Two main components of the noise were considered to be of interest:

- 1) The inevitable background noise due to various kind of activities taking place in the marine environment. The effect of this noise could only be overcome

by improving the signal to noise ratio of system by means of a suitable level of transmission power

- 2) The reverberation of the transmitted signal itself on the sea surface bouncing back towards the receiver. It increases with the increase of the transmission power and therefore has to be reduced in a different way

It was therefore decided to investigate the use of a special anechoic baffle to be placed on top of the acoustic receiver. The baffle should have an anechoic side facing the receiver to limit as much as possible to reflection of the incoming signal, a sound absorbing layer and finally a reflecting layer facing the sea surface with the task of reflecting back the reverberation.

Once the project was started, two main areas of investigation were identified:

1. The determination of a suitable material for the sound absorbing layer
2. The numerical analysis of the performance of the structure using a suitable method

Chapter 3 and 4 of this thesis deal with the first identified research area. The choice of some kind of viscoelastic material was thought to be the most cost-effective. The linear theory of viscoelastic was therefore studied and applied to determine the important material parameters to take into account and their special dependency on frequency and temperature. General expressions for the response functions of a generic viscoelastic material were determined with particular attention to the case of vibrational motion.

Once the general analytic expressions for the material parameter were determined, a number of options were investigated to manufacture one or more suitable materials. The technological constraints and the goal to be achieved as described in Chapters 4 and 7 lead to the choice of loaded polyurethane rubber and loaded butyl rubber as the two candidates for the anechoic layer and the absorbing layer.

At this point, it was necessary to measure the effective physical properties of the materials in order to take the appropriate decisions about their final composition. Part of these tests was conducted in collaboration with the Italian Whitehead Alenia Sistemi Subacquei that provided the equipment for testing the samples of loaded polyurethane rubber.

The butyl rubber was tested using the immersion method with parametric transducers. The rubber was moulded in a number of large panels of different density and measurements of the transmission and reflection coefficients were carried out.

The recorded data was finally processed to recover the values of the response functions whose analytic expression as a function of frequency had been determined by means of the linear theory of viscoelasticity.

A novel method was proposed to this effect. The method is based on an adapted form of an optimisation method making use of the analogy between the Hamilton Principle and the form of a functional where the constraints are incorporated using Laplace multipliers (the details are reported in Chapter 4 and Appendix E). The method proved to be efficient and allowed the determination of the complex-valued physical properties of the loaded butyl rubber in the frequency range of the measurements. A paper has been written on this subject and has been submitted to the Journal of the Acoustical Society of America (see Appendix G).

The method can of course be improved. A limitation of the current implementation is the strong dependency on the initial data. If the data used to start the optimisation method (the boundary values) is not a close guess of the real values, the method may fail to converge or converge on a wrong set of values. This could be improved with the addition of some kind of adaptive algorithm to change the boundary values if the method doesn't converge. More investigations are needed about this problem.

After the physical properties of the materials were determined, a suitable method of analysing the proposed structure and predicting its performance had to be chosen. The logical choice was the use of the coupled boundary element/finite element method. There were two main reasons behind this choice. First, the method is now well established as a powerful tool for analysis of sound scattering with fluid loading, thanks to the possibility of calculating the field quantities in the fluid domain by means of the discretisation of the body domain and its border only. Second, a solid expertise already existed inside the Acoustic & Sonar Group and a computer program had been produced and tested before.

However, two main obstacles were left:

1. The FE-BE code didn't include treatment of viscoelastic materials
2. The program was DOS based and as a consequence had memory limitations that had to be overcome to be able to work at the relatively high frequencies specified by the project

Both limitations have been solved during this work. Treatment of viscoelastic materials has been included by means of a special viscoelastic element that recalculates its own material properties as a function of frequency given an analytic expression of the stress

coefficients (for example a spline representation based on the values determined by the Hamilton optimisation method).

The memory limitations have been overcome or at least reduced by porting the program to the Windows environment using an object-oriented programming approach and using a distributed architecture that allows sharing the calculation load on several computers controlled from a central distribution point as described in Chapter 8.

More can be done on this subject, though. The program still has limitations because of the procedural programming style of the original algorithm. A more extensive componentisation of the algorithms and the use of the industry standard DCOM (Distributed Component Object Model) object broker inside the program itself could lead to even faster performance.

Finally, once the material properties had been determined, the analysis tools created and the acoustic baffle geometry decided, the detailed investigation of its performance could be started as fully described in Chapter 7.

The simulations have been carried out on the prototype tile making the complete baffle. The tile behaviour has been studied in details in various scattering configurations and for different values of the geometrical parameters. In addition, a number of experimental measurements have been performed on some of the studied configurations to confirm the quality of the results.

We can therefore draw some conclusions on the results obtained. The tile is behaving as desired in the frequency range of interest. It is possible to identify an optimal range of values for the cones apex angle to get low backscatter and good absorption or matching with the water, in the region beyond the reflection critical angle for the cone, but not too small to avoid the strong lateral spread of the diffracted waves.

The reflecting side is actually able to protect the other side from most of the incoming signal as desired and the performance of the tile doesn't substantially degrade when inclined with respect to the incoming signal. The results are presently being formatted for submission as a journal paper.

The numerical calculation is in good agreement with the experimental measurements. It confirms that the coupled FE-BE method is actually capable of predicting the scattered field in complex configurations.

However, more work can still be done on this subject. Not all the data produced during the simulations has been organised and presented. Most of the interest has been focused on the normal incidence case and a more detailed analysis of the dependence of the tile on the angle of incidence of the signal would provide even more insight into the problem. Additionally, the tile has been always analysed as a whole, but more work could be carried out to try to separate the different components of the scattered field (cone tips, tile lateral edges and so on).

Finally, the experimental results are not (but were not meant to be) exhaustive. More tests can be performed on a wider range of configurations and especially on a broader frequency range.

Appendix A

Relationships among Complex Viscoelastic
Parameters for Isotropic Materials

	<i>Lamé constants λ, μ</i>	<i>Stiffness tensor s_{11}, s_{44}</i>
Young's Modulus, E	$E = \frac{\mu(3\lambda + 2\mu)}{\lambda + \mu}$	$E = \frac{s_{44}(3s_{11} - 4s_{44})}{s_{11} - s_{44}}$
Shear Modulus, G	μ	s_{44}
Poisson's Ratio, ν	$\nu = \frac{\lambda}{2(\lambda + \mu)}$	$\nu = \frac{s_{11} - 2s_{44}}{2(s_{11} - s_{44})}$
Bulk Modulus (adiabatic), K	$K = \lambda + \frac{2}{3}\mu$	$K = s_{11} - \frac{4}{3}s_{44}$
Longitudinal Bulk Modulus, L	$L = \lambda + 2\mu$	$L = s_{11}$

	<i>Response functions G_1, G_2</i>
Young's Modulus, E	$E = \frac{3G_1G_2}{2G_2 - G_1}$
Shear Modulus, G	$\frac{G_1}{2}$
Poisson's Ratio, ν	$\nu = \frac{G_2 - G_1}{2G_2 + G_1}$
Bulk Modulus (adiabatic), K	$K = \frac{G_2}{3}$
Longitudinal Bulk Modulus, L	$\frac{1}{3}(2G_1 + G_2)$

	<i>E, ν</i>	<i>G, ν</i>
s_{11}	$s_{11} = \frac{E(1-\nu)}{(1+\nu)(1-2\nu)}$	$s_{11} = \frac{2G(1-\nu)}{1-2\nu}$
s_{12}	$s_{12} = \frac{E\nu}{(1+\nu)(1-2\nu)}$	$s_{12} = \frac{2G\nu}{1-2\nu}$
s_{44}	$s_{44} = \frac{E}{2(1+\nu)}$	$s_{44} = G$

Bulk Modulus (adiabatic), K	$K = \frac{E}{3(1-2\nu)}$	$K = \frac{2G(1+\nu)}{3(1-2\nu)}$
Longitudinal Bulk Modulus, L	$L = \frac{E(1-\nu)}{(1+\nu)(1-2\nu)}$	$L = \frac{2G(1-\nu)}{1-2\nu}$

Appendix B

Polymer Compounding and Processing Techniques

The mechanical properties of polymeric materials depend heavily on the additional ingredients used during the manufacturing and processing stages and on the manufacturing itself. The choice of the right material to use for a given application is dictated by a number of parameters (Capps 1993):

- dynamic mechanical and/or physical requirements
- environmental resistance
- service lifetime
- processability and ease of fabrication
- cost

For underwater applications, the choice of the base material, the ***gum stock*** is usually dependent on static non-acoustical engineering properties, such as bondability, environmental

resistance or electrical characteristics. The desired acoustical properties can then be attained through the use of specific additives and curing strategies. Since there are no exact ways of determining *a priori* the results of the combination of the many factors occurring in polymer processing, some experience and sometimes a trial and error process are necessary.

9.1. Elastomeric polymers classes

Each base material class usually exhibits a characteristic range of glass transition temperatures (description of polymer states), maxima and bandwidth of the loss factor and slope and bandwidth of the glassy storage modulus. The first step is therefore the choice of the appropriate class of polymers. The most widely used elastomers for underwater applications are (Capps 1993):

- Butyl (IIR) and Chlorobutyl (CIIR) rubbers
- Ethylene-Propylene-Diene Monomer (EPDM)
- Fluorocarbon (CFM) rubbers
- Natural Rubber (NR)
- Nitrile (NBR) rubbers
- Polybutadiene (BD)
- Polychloroprene (Neoprene) (CR) rubbers
- Polyethylene (CSM)
- Polyurethanes (ethylene-propylene and adipic acid copolimers)
- Styrene-Butadiene Rubber (SBR)

For underwater applications, *butyl* and *polyurethane* rubbers are usually chosen.

Butyl rubber and its chlorate version, *chlorobutyl*, have very good oxidation resistance and high tensile strength. They show outstanding permeation resistance to both gases and water and excellent resistance to most acid and bases and to a variety of inorganic salts and inorganic or organic oils. They have excellent dielectric properties and electrical insulation resistance. The high internal damping makes these rubbers very important in shock and vibration absorbing structures.

The four main types of polyurethanes are casting resins, millable rubbers, semi-cured thermosetting resins and thermoplastic materials. Casting resins are the most widely used in underwater applications. They come in liquid castable form especially designed for use as potting compounds or sonar encapsulant. The high compatibility with organic liquid makes this rubber suitable for use with acoustic coupling fluids, such as castor oil. The internal damping is high at low frequencies, but decreases at higher frequencies.

As mentioned in §4.2, the molecular structure of these polymers, based on low molecular weight methacrylates, is especially efficient in the frequency range of interest (10 to 100 kHz).

9.2. Cure systems and Crosslinking

In order to convert a compounded rubber formulation into a suitable material, it must undergo a process called *cure* or *vulcanisation*. It involves the application of heat to cause a reaction of the base polymer with a suitable binding agent to form cross-linking between molecular chains. The compound can be mixed with *accelerators* or *retardants* to obtain the desired degree of cross-linking and to vary the resulting mechanical properties. The most

widely used curing agents are sulphur and sulphur bearing compounds, usually mixed with nitrogen or zinc dioxide as accelerators.

The effect of cross-linking are important on static and dynamic Young's and shear moduli, whereas the bulk compression modulus is usually unaffected by the degree of cross-linking.

9.3. Fillers

The use of fillers widely changes both physical and mechanical properties of polymers. The main effect is that of increasing hardness, stiffness, tensile strength and creep resistance as well as producing higher resistance to abrasion and tear.

The viscoelastic properties are also changed, since the presence of a different phase in the material introduces new dissipation mechanisms, such as molecular friction and phase interface interaction and modification of the polymer chain cross-linking during the curing process (Ferry 1980).

The most widely used filler is the *carbon black powder*. It is used mainly as a strength and hardness modifier, even if viscoelastic properties, especially the loss factor, are also greatly affected because of interaction between the polymer chains and the carbon black particle surface.

Degree of dispersion in the polymer matrix, particle dimension and blending proportions are all factors to be taken into account in the analysis of carbon black effects on elastomer gum base.

Mica and metal fillers are used a means of increasing dissipation in the matrix. This kind of fillers heats up the polymer matrix during the curing process and cause permanent

modifications in the chain cross-linking. Good dispersion is required in order to avoid dishomogeneity in the material.

Changes in material density can be obtained with the use of carbon black or metal fillers to increase its value or air-filled phenolic microspheres to decrease its value. Changes in physical and mechanical properties ought to be expected as well.

9.4. Plasticisers, Processing Aids and Softeners

Various materials are used to increasing processing ease during compounding. Oils in small quantity tend to soften the materials, while larger amount can act as extenders or plasticisers. Plasticisers are used to facilitate the inclusion of fillers during the compounding stage and to reduce internal friction during mechanical processing (extrusion and calendaring). The effect of plasticisers after the curing process tends to vanish, although it usually shifts the glass transition region towards higher frequencies and lower temperatures and at the same time broadens it.

9.5. Antidegradants

Elastomeric materials are subjected to ageing processes during they operating life. Major causes are oxidation by external agents, heating, mechanical fatigue and internal friction. The ageing depends widely on the chemical and physical composition as well as the particular curing process the material underwent to in its initial manufacturing stage.

Antidegradants are destroyed during vulcanisation. Minimum quantities of substances called stabilisers are used before and during curing and processing for protection and storage

purposes. Larger quantities of proper antidegradants are then added after vulcanisation to reduce oxidation, UV light effects and mechanical fatigue and stiffening.

9.6. Manufacturing Processes

Rubber finite products are obtained by extrusion, calendaring or moulding. Moulding is usually the most effective way of obtaining any desired shape from the base gum before curing it.

Great care must be used during the moulding process to avoid the trapping of air bubbles or the formation of cracks inside the material. Moulding can be classified in compression moulding, injection moulding and transfer moulding, depending on the method used to insert the base elastomer into the mould. Compression moulding is also very effective when bonding of the polymer to metal parts is required.

9.7. Adhesion

Bonding of polymer to polymer or polymer to metal is of primary importance in many underwater applications and notably in the manufacturing of transducers or multi-layered structures for sound detection or absorption.

Adhesion between two different substances can be mechanical or chemical. Mechanical bonding acts through the interlocking or physical absorption of the materials and the adhesive across the interface, without chemical modifications. Chemical bonding involves the formation of covalent or ionic bonds between the molecules of the adhesive and the material.

Usually the materials must be treated before bonding. Surface treatments include mechanical polishing, anodisation and the chemical action of acids. Anodised metal surfaces can usually be effectively bonded to machined elastomeric surfaces without the need of treatment with chemical agents. The adhesive must be chosen for each different polymer class. Catalogues of specific commercial adhesive can be found for the bonding of butyl or polyurethane rubbers to metallic surfaces, such as Chemlock 218 or Tyrite.

9.8. Measurements Methods for Hard Polymers

9.8.1. Young's and Shear Moduli

The simplest relationship between force and displacement for a viscoelastic material subjected to harmonic motion can be derived from relation (3.83):

$$F = AC^*(\omega)a = ACae^{i\delta(\omega)} \quad (\text{B.14.})$$

where:

F	= forcing harmonic action complex amplitude
$C^*(\omega) = C_1(\omega) + iC_2(\omega) = Ce^{i\delta(\omega)}$	= generic complex stiffness modulus
a	= generalised scalar complex displacement amplitude
$\delta(\omega)$	= frequency dependent phase lag

A = form factor depending on sample constraints
(clamped-free, clamped-clamped, etc.)

The storage and loss moduli (the real and imaginary part of the complex stiffness modulus) are given by:

$$\begin{cases} C_1 = \frac{F}{Aa} \cos \delta(\omega) \\ C_2 = \frac{F}{Aa} \sin \delta(\omega) \end{cases} \quad (\text{B.15.})$$

9.8.2. Forced Non-Resonant Methods

The forced non-resonant methods rely on the determination of the complex stiffness modulus by means of direct measurements of the quantities F , a and δ at a particular frequency ω .

The methods belonging to this class of technique can usually be applied successfully to frequencies from 0.01 to 1000 Hz for the displacement to be accurately measured by means of mechanical or electrical pick-up devices. The measurable stiffness values range from 10^6 to 10^{10} Pa m⁻². Moreover the critical dimension of the sample has to be smaller than the wavelength of the corresponding elastic wave (longitudinal, flexural or torsional respectively).

The most widely used methods are (Ferry 1980; Read 1978):

- ***progressive wave recorder***: a thin strip of material is clamped at both end and one of the ends is driven by a vibrating head forcing a longitudinal wave to propagate along the sample. A displacement sensor moves along the sample at increasing distance from the head recording the amplitude and phase of the vibration. The storage Young's modulus and loss factor can be calculated from the attenuation per unit length and the wavelength
- ***tensile dynamic viscoelastimeter***: a thin strip or rod of material is clamped at one or both ends and forced to vibrate longitudinally at one end. A strain gauge detects the wave amplitude at the moving end, while a stress gauge detects the force at the clamped end. The storage Young's modulus and loss factor are calculated from displacement, force and phase angle using eq. (4.2). This method has been used to characterise the polyurethane rubber used in the anechoic baffle under investigation
- ***flexural dynamic viscoelastimeter***: this method is based on the same principle as the longitudinal viscoelastimeter, but a flexural vibration is forced in the sample of material Strain and stress are measured at some reference points and the complex modulus is calculated using eq. (4.2). An example of this method for low frequency analysis is the Maxwell's rotating rod schematically represented in fig. 4.2
- ***torsional pendulum***: this method is used to measure the shear modulus. A thin strip of material is suspended from a rigid support and a moment-of-inertia bar is attached at the free end. When the bar is moved from the equilibrium position the whole system oscillates at one of its natural frequencies. The shear modulus and loss factor can be calculated from measurements of the period and decrement of the oscillations. Different frequencies can be obtained changing the length of the sample and/or the mass of the bar. This method has been used to characterise the

polyurethane rubber used in the anechoic baffle under investigation.

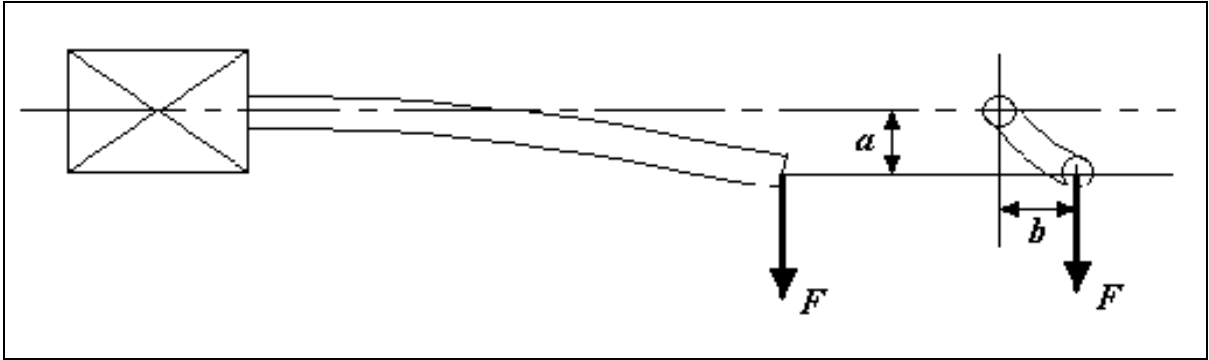


Figure A.1: Maxwell's rotating rod set-up. It is suitable for complex Young's modulus measurements from 10^{-3} to 10^3 Hz (Ferry 1980)

9.8.3. Resonant Methods

When the wavelength of the elastic wave is comparable to the critical dimension of the sample, standing waves can be set up within the sample itself. When a system is vibrating at one of its resonant frequencies (in forced vibrations) or natural frequencies (in free vibrations), then an integral number N of wavelengths will be contained in a sample of length L . In the simple longitudinal or torsional cases the velocity of the wave can be therefore calculated as

$$v = \frac{2L}{N} f \quad (4.16.)$$

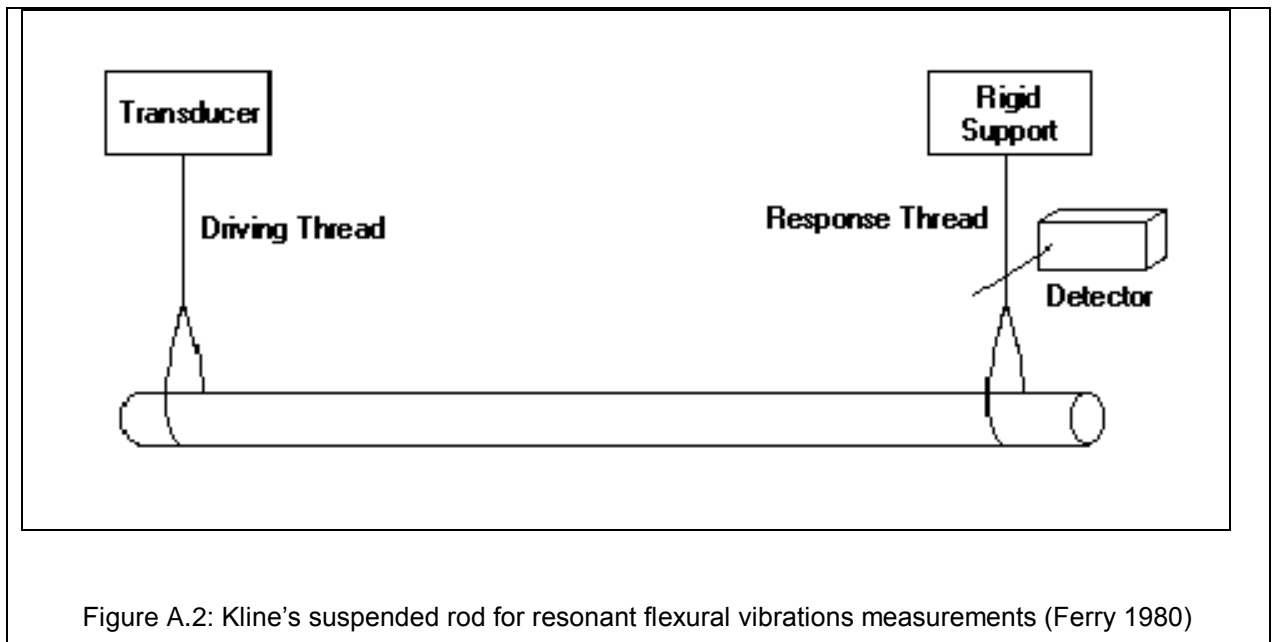
where f is the frequency. In the case of flexural vibrations the relationships is more complex since the waveform depends on the constraints geometry (Ferry 1980; Read 1978).

Calculations of the storage modulus are based on the determination of resonant frequencies or natural frequencies. The loss factor can be calculated as before from the absolute value of the amplitude at resonance for forced vibrations or from the logarithmic decrement for free vibrations.

The range of application for hard viscoelastic solids is of the order of 10 to 5000 Hz.

The most widely used methods are (Read 1978):

- ***vibrating reed***: under this name a number of different techniques is considered. In the commonest configuration a thin rectangular strip is clamped at one end and forced to vibrate transversely. The displacement at the free end gets to a maximum when one of the resonant frequencies is reached. The vibration amplitude can be measured with a capacitance (Ferry 1980). A similar device uses a thin rod suspended at both ends by fine threads. One of the threads is used to propagate a slight oscillatory motion along the rod, whereas the second thread is connected to a displacement detector (Fig. 4.3) (Read 1978)
- ***compound resonance vibration devices***: this method is more complex than the vibrating reed, but is more suitable for high loss polymers, which cannot sustain resonance vibrations on their own. The general principle is that of attaching an additional inertia element to the sample, the properties of which are well known. The resonant frequencies depend on both materials, but the unknown storage modulus and loss factor can be worked out. A simple configuration is made of a thin metal strip coated with the polymer to be tested. The compound strip is displaced from its equilibrium position and the oscillation amplitude, period and decrement are measured.



9.8.4. Bulk and Longitudinal Bulk Moduli

In principle, the information obtained from extensional and shear measurements, as described in the previous section, can be combined to obtain the bulk properties of the material by means of the standard relationships given in Appendix A. However, the subtraction operation is subjected to a strong numerical error and precise results cannot be obtained in this way. Therefore direct measurements of the complex bulk modulus or a combination of shear and longitudinal bulk moduli are often required.

In broad terms the methods to measure the bulk modulus can be split into two classes: methods based on direct measurement of pressure and method based on propagation of longitudinal waves in a confining liquid:

- ***Homogeneous deformation with direct measurement of pressure:*** if a sinusoidally varying pressure is imposed on a sample contained in a cavity whose dimensions are smaller than any wave propagated in the material, the deformation can be assumed to be homogeneous. Under such assumptions two main methods have been developed. In the Philippoff and Brodnyan method (Read 1978) a sample of material is immersed in mercury and compressed by an oil pump. From measurements of the strain of the sample the stress-strain ellipse can be reconstructed and the bulk modulus calculated after correction for the device compliance. In the McKinney, Edelman, Marvin device (Read 1978) the sample is immersed in an inert liquid and a sinusoidally varying pressure is transmitted by a transducer into the cavity, while a second transducer senses the pressure variations in the cavity itself. The complex bulk modulus can be calculated from the complex ratio of input and output voltage after corrections for the device compliance
- ***Homogeneous deformation by longitudinal waves in a confining liquid:*** this method employs either a single sample or a suspension of many small particles. In the first case, the material is immersed in a confining liquid and a longitudinal vibration is propagated in the liquid. The bulk modulus can be calculated from a comparison of the resonant frequency with and without the sample. In the second case small spherical particles in concentration of about 10% by volume are suspended in the liquid. The velocity and attenuation of longitudinal waves can be found to be linearly dependent on the particle concentration. The calculations of bulk modulus are based on theories of wave propagation in biphasic suspensions and can convey highly accurate results (Read 1978)

In the above-described methods, no shear is involved, since the sample is uniformly subjected to the external pressure without appreciable transmission of shear waves. However, if the sample dimension normal to the stress is considerably larger than the wavelength, then the sample experiences both bulk and shear stresses and strain in combinations depending on its shape. In this case, propagation is governed by the longitudinal bulk modulus

$$L^* = K^* + \frac{4}{3} G^* \text{ (cf. Appendix A).}$$

Direct measurements of velocity and attenuation can be made by the passage of a train of pulses sufficiently long to approximate steady-state conditions. Longitudinal bulk and shear measurements can often be accomplished simultaneously by propagating both longitudinal and shear waves in the solid.

The two main methods to investigate the longitudinal bulk modulus are the impedance or the standing wave tube and the ultrasonic immersion method. The latter has been used during this research to characterise the viscoelastic properties of the loaded butyl rubber used in the baffled panel under investigation.

The definition of ultrasonic immersion methods is usually used to refer an experimental set-up in which the sample under measurement is immersed in a volume of fluid large enough to allow the sample to be considered unbounded. This technique has been widely used as a non-destructive method of investigating the longitudinal and shear properties of both isotropic and anisotropic materials (see for example Landel 1958; Rokhlin and Wang 1992; Capps 1993).

Three dominant properties are usually investigated in this way, namely the absorption-dispersion characteristics (that is the complex wave number of the material), the wave velocity and the reflection at the fluid-solid interface. In addition, experiments performed at

both normal and oblique incidence can be used to measure separately the two types of waves that can propagate in a solid material, namely longitudinal and shear waves. This technique allows therefore the determination of two material parameters with one set of measurements.

A limitation of this method can be identified in the difficulty of avoiding edge diffraction from the border of the sample or reflection from the walls of the measurement tank to affect the results. High frequency must generally be used in order to have narrow beam sources and pulsed instead of cw signals are used to avoid the build-up of standing wave in the container. A technique to obtain narrow-beam, low-frequency sources, namely the parametric array, is discussed in the next section. Plane wave propagation is usually assumed, but diffraction correction functions can be used to take into account the frequency spectrum of finite size sources in integral (Humphrey *et al.* 1993; Brekhovskikh 1980) or analytical form (Thompson and Gray 1983; Humphrey 1986).

Three different methods can be used depending on the type of measurements performed:

- ***Transmit-Time or Single Transmission (ST) method:*** in the simplest configuration of this method a panel of the sample material is immersed in a coupling fluid. A transmitter is used to send a series of pulses containing a finite number of cycles of the desired frequency, whereas a second transducer or hydrophone is used to measure the amplitude of the signal in front and on the opposite side of the panel. From a comparison of the flight time and pressure amplitude with and without the panel the sound speed and absorption coefficient of the material can be determined. The length and repetition rate of the pulses must be adjusted to avoid superposition of signals and the set-up of standing waves (Capps 1993). Since the knowledge of such experimental parameters as the thickness of the panel and the geometric set-

up is usually not accurate enough to allow for precise measurements, parameter identification techniques and maximum likelihood estimators based on rational transfer functions have been recently applied to this kind of measurements (Hsu and Hughes 1992; Peirlinckx *et al.* 1993)

- ***Pulse-Echo or Double Transmission (DT) method***: in this type of method, the electro-acoustic transducer is used as both a transmitter and a receiver. A train of pulses is delivered into the sample material and the echoes from the front and back face of the panel are read together with the reflected echo from a standard reflector behind the panel itself. The pulse repetition rate must be short enough to allow the reflected echoes to die away completely before the next pulse is emitted. Both the transmitting and receiving electronics are synchronised. The required information about sound speed and absorption-dispersion of waves in the material can be read from the delay time between pulses and echoes and intensity decrement. Again parametric identification techniques can be used to minimise the effect of uncertainties about thickness, distance and system properties (Zhou *et al.* 1996)
- ***Acoustic interferometry***: this particular method has been developed by McSkimmin *et al.* In the early 1960s. In its simplest form, a pulsed oscillator produces a train of cw pulses with the repetition rate adjusted so to superimpose a echo from a train of pulses with an echo of the next train. In this way, the time delay between pulses is equal to an integer number times twice the distance between transmitter and specimen. The echoes sum up in the receiver giving rise to constructive interference when the transmitted cw pulse is in phase with the echoed cw pulse and a series of maxima can be observed. The condition can be established by varying the pulse repetition rate and information about the input

impedance of the specimen can be inferred.

Appendix C

Transducer equivalent and matching circuit theory

C.1 Matching Circuits

The electrical equivalent of an electro-acoustic transducer can be schematised as:

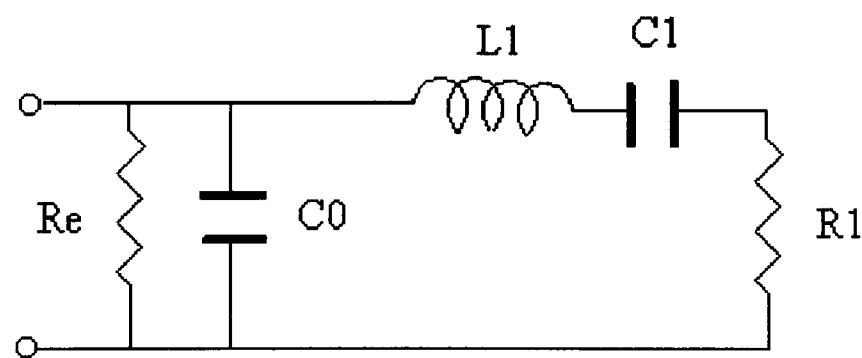


Figure C.1: Schematic diagram of a single resonance transducer equivalent circuit

where

L_1, C_1 = transducer resonance

R_1 = transducer mechanical resistance (internal resistance plus external load)

C_0 = piezoelectric ceramic clamped capacitance

R_e = piezoelectric ceramic internal resistance

The transducer input impedance is:

$$Z_{in} = \frac{R_e \left(R_1 + j\omega L_1 + \frac{1}{j\omega C_1} \right)}{R_e + (1 + j\omega C_0 R_e) \left(R_1 + j\omega L_1 + \frac{1}{j\omega C_1} \right)} \quad (C.1.)$$

At resonance the LC series arm vanishes and the transducer is equivalent to a resistance $R = \frac{R_1 R_e}{R_1 + R_e}$ in parallel to the clamped capacitance C_0 .

The impedance at resonance is therefore:

$$Z_{in} = \frac{R_e R_1}{R_e + R_1 (1 + j\omega C_0 R_e)} \quad (C.2.)$$

The mechanical acoustic efficiency of the transducer at resonance can be calculated from a comparison of the conductance at resonance for air and water loading respectively as:

$$\eta_{ma} = \frac{(G_{ms})_{air} - (G_{ms})_{water}}{(G_{ms})_{air}} \quad (C.3.)$$

The electrical-mechanical efficiency is calculated from the ratio of the conductance in water and the maximum conductance, which can be assumed to be the conductance in air

$$\eta_{em} = \frac{(G_{ms})_{water}}{G_{max}} \cong \frac{(G_{ms})_{water}}{(G_{ms})_{air}} \quad (C.4.)$$

The overall electrical-acoustical efficiency at resonance is therefore:

$$\eta_{ea} = \frac{(G_{ms})_{water}}{(G_{ms})_{air}} \frac{(G_{ms})_{air} - (G_{ms})_{water}}{(G_{ms})_{air}} \quad (C.5.)$$

The input from the power source is maximised when the transducer is a purely resistive load to the power source and the impedance is matched. If the term $\omega C_o R_e$ is negligible compared to unity the input impedance becomes:

$$Z_{in} = \frac{R_e R_1}{R_e + R_1} \quad (C.6.)$$

If the above term is not negligible or maximum efficiency is sought after then a tuning circuit can be added to the equivalent circuit. A single transformer can be used to achieve both aims of tuning out the static capacitance and matching the impedance of the two parts of the circuit, the transducer and the power source.

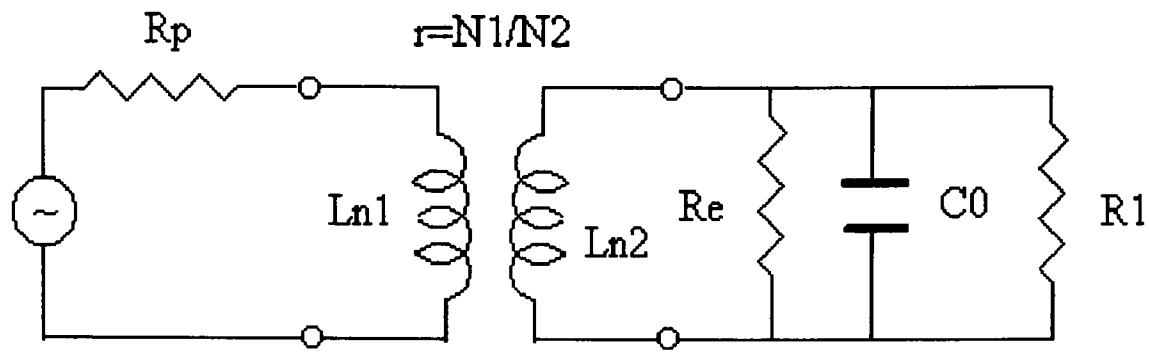


Figure C.2: Schematic diagram of the transducer equivalent circuit at resonance with matching transformer and power source

The transformer ratio r is obtained from the resistance step-up required to match the two portions of the circuit:

$$r = \frac{N_1}{N_2} = \sqrt{\frac{R_{N1}}{R_{N2}}} = \sqrt{\frac{R_p}{\frac{R_1 R_e}{R_1 + R_e}}} \quad (\text{C.7.})$$

where R_p is the known power source resistance and $R = \frac{R_1 R_e}{R_1 + R_e}$ is the measured transducer resistance at resonance.

The number of turns in the secondary inductor must be worked out from the knowledge of the inductance required to match out the clamped capacitance C_0 and the properties of the magnetic core of the transformer. The inductance is:

$$L_{N2} = \frac{1}{\omega_s^2 C_0} \quad (\text{C.8.})$$

whereas the core properties can be found on the manufacturer data sheet and are usually given as the inductance factor A_L :

$$A_L = \frac{\mu_0 \mu_e \cdot 10^6}{\sum \frac{l}{A}} [nH] \quad (C.9.)$$

where

μ_0 = magnetic constant = $4\pi 10^{-7} \text{ Hm}^{-1}$

μ_e = effective core permeability [Hm^{-1}]

$\sum \frac{l}{A}$ = core factor (for non-uniform core shapes)

The number of turns on the secondary inductor is therefore:

$$N_2 = \sqrt{\frac{L_{N2}}{A_L}} \quad (C.10.)$$

where L_{N2} is measured in nH as A_L .

If the parameters are such that the number of turns on the primary is not a feasible number, the alternative is splitting the transformer and the tuning inductor or using just the transformer neglecting the static capacitance.

In this case, the number of turns on the primary can be chosen first according to the principle of completely filling the transformer bobbin with a wire of suitable thickness. The number of turns on the secondary follows from the required transformer ratio.

C.2 Application to the 1 MHz transducer used in the measurement tests

In the acoustic tests of polymer panels a parametric sound source is used. The used transducer is composed of four piezoelectric crystals in the shape of a quarter of a circle. The two pair of opposing crystal can be driven either with the same electrical signal or by the two different primary signals, one for each pair. In the former case the two primary frequencies are electrically mixed, whereas in the latter case the secondary frequency is formed in the water.

In either case, the two pair of crystal are treated as a separate transducer and separately optimised. Both pairs show a resonance frequency of 1.09 MHz with the electrical parameters as shown in Tab. B-1. The conductance/frequency plot and the admittance plot around the resonance for the two pairs are shown in fig. B-3 to B-6 before applying the matching circuit and in fig. xx and xx after optimisation.

	First pair	Second pair
f_s	1.08 MHz	1.08 MHz
C_0	0.37 nF	0.35 nF
R	190 Ω	180 Ω
$(G_{ms})_{air}$	$5.39 \cdot 10^{-3}$ S	$5.50 \cdot 10^{-3}$ S
$(G_{ms})_{water}$	$4.05 \cdot 10^{-3}$ S	$4.18 \cdot 10^{-3}$ S

Tab. C.1: Electrical parameters at resonance for the two ceramic pairs

The transducers efficiency at resonance is:

First pair
 $\eta_{ea} = 0.186$

First pair
 $\eta_{ea} = 0.182$

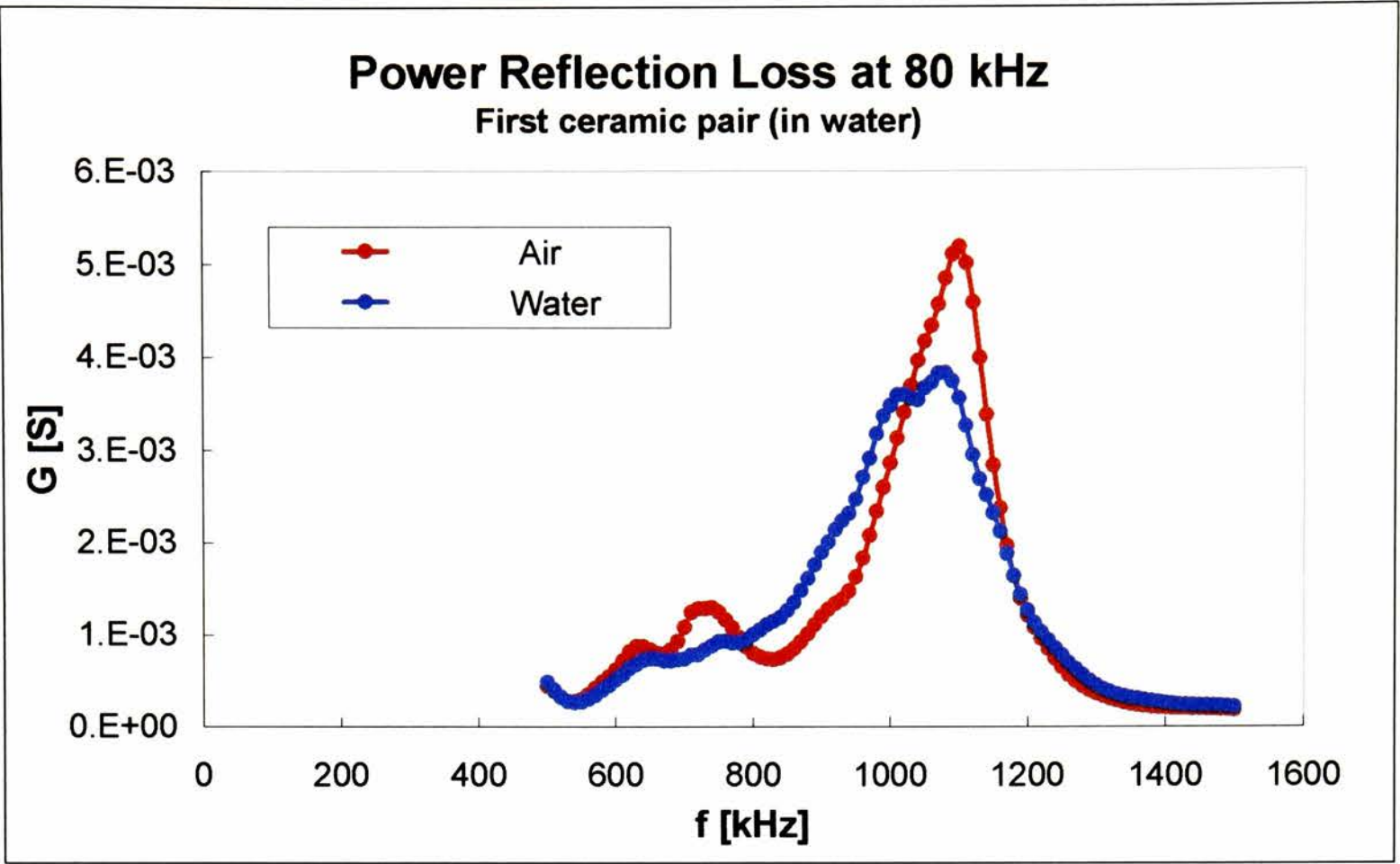


Figure C.3 : Conductance Vs. Frequency for the first ceramic pair around the resonance frequency $f_S = 1.08$ MHz (unmatched)

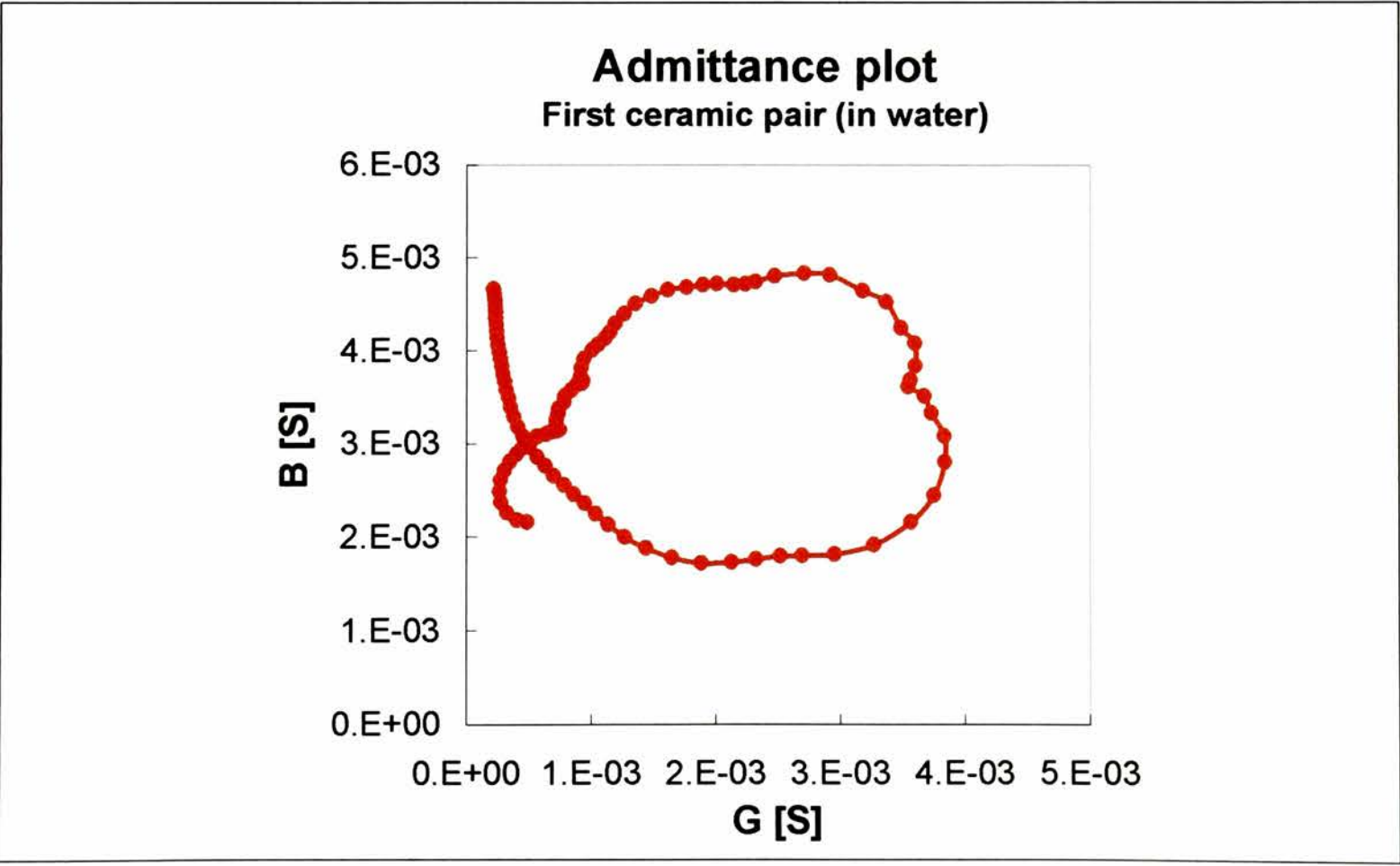


Figure C.4: Admittance plot for the first ceramic pair around the resonance frequency $f_S = 1.08$ MHz (unmatched)

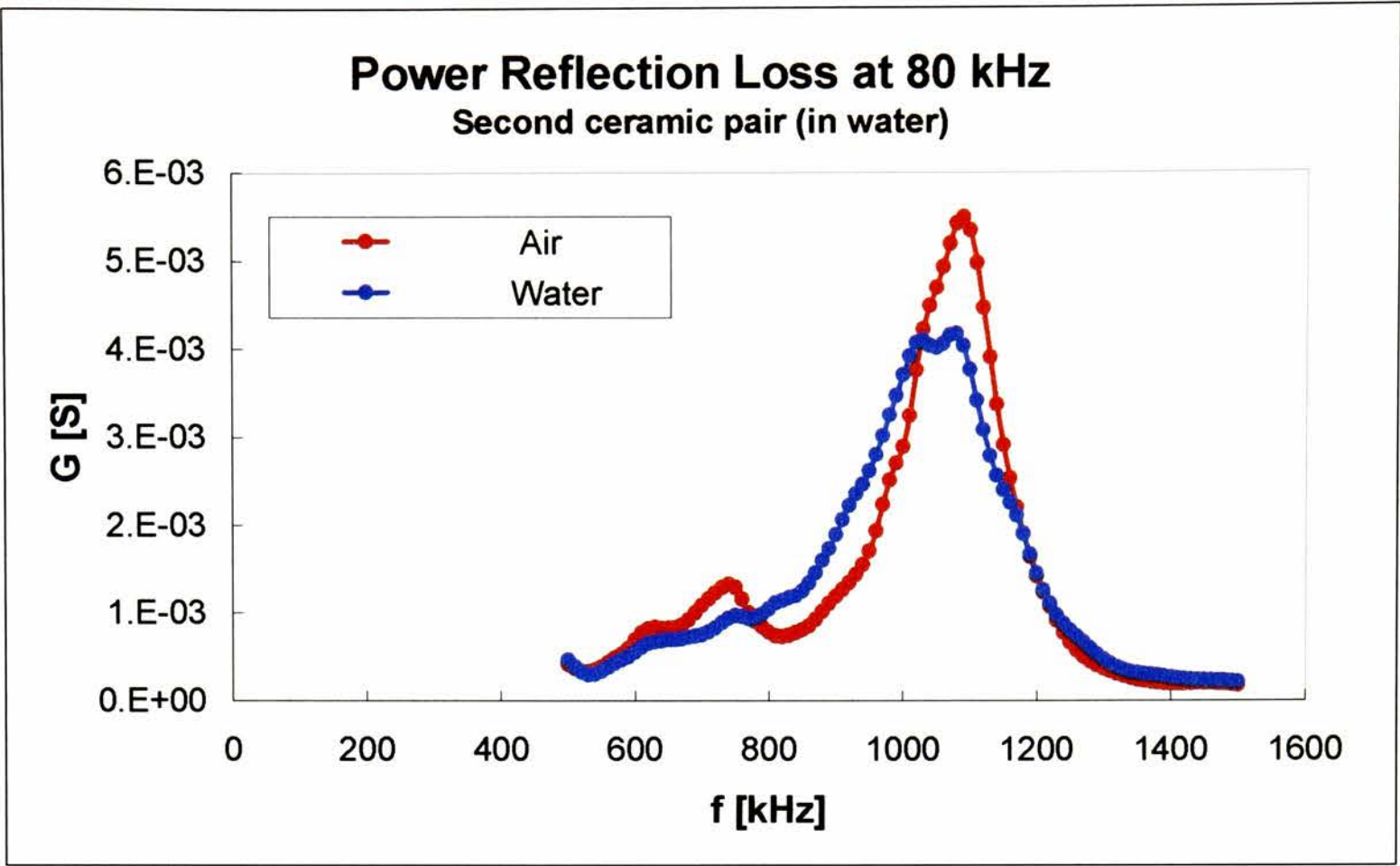


Figure C.5: Conductance Vs. Frequency for the second ceramic pair around the resonance frequency $f_S = 1.08$ MHz (unmatched)

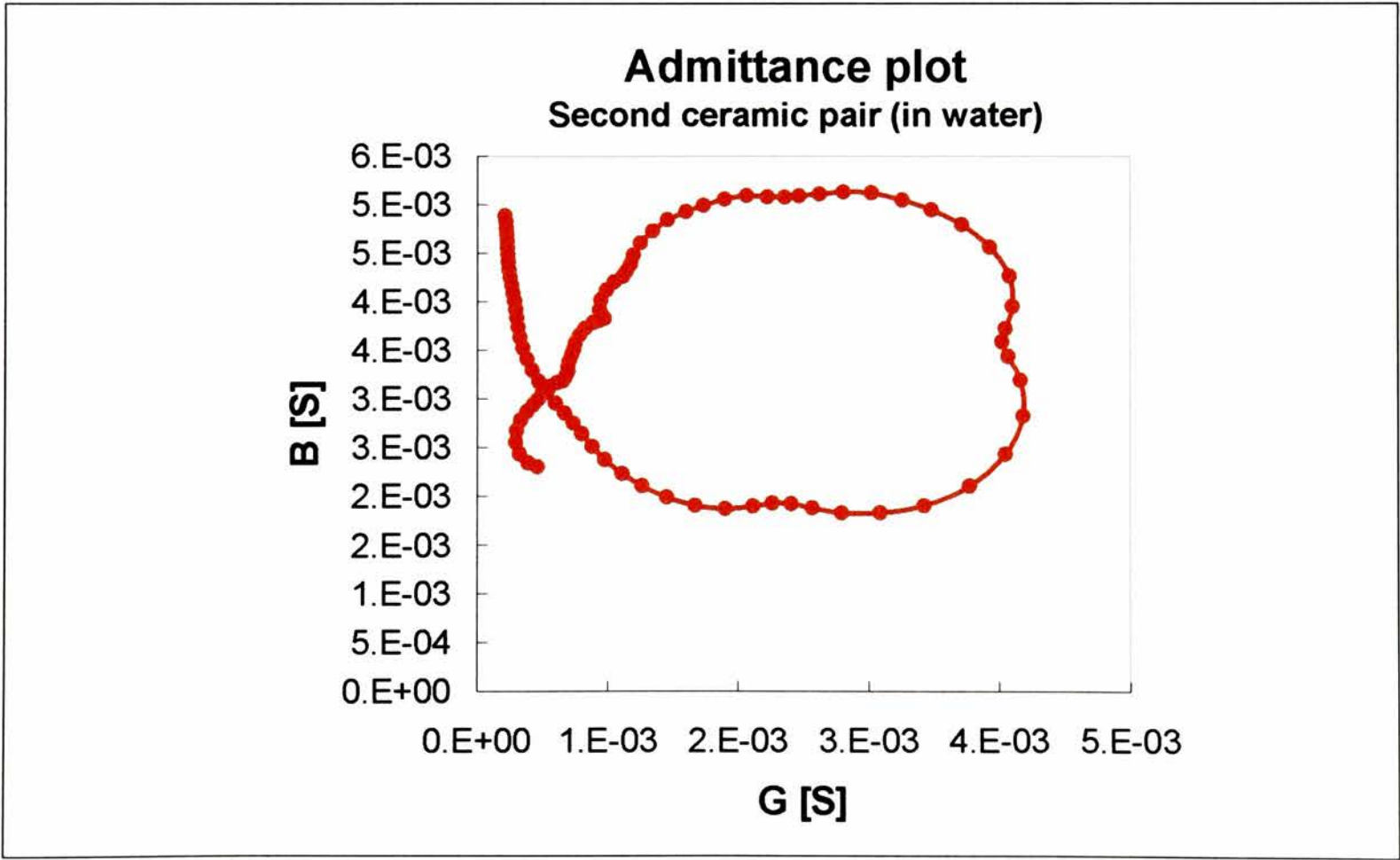


Figure C.6: Admittance plot for the second ceramic pair around the resonance frequency $f_S = 1.08$ MHz (unmatched)

The secondary inductance required to match out the clamped capacitance C_0 is:

First pair :

$$L_{N2} = \frac{1}{\omega_s^2 C_0} = \frac{1}{(2\pi f_s)^2 C_0} = 57.6 \cdot 10^3 \text{ nH} \quad (\text{C.11.})$$

Second pair :

$$L_{N2} = \frac{1}{\omega_s^2 C_0} = \frac{1}{(2\pi f_s)^2 C_0} = 60.9 \cdot 10^3 \text{ nH}$$

The magnetic core chosen for the transformer is a Philips 3F4 MnZn soft ferrite core with a operative frequency range from 50 kHz to 3 MHz. The core shape is an EFD20 with an inductance factor $A_L = 580 \pm 25\%$ with no gap on the core and a clamping force of 40 ± 10 N.

The number of turns on the secondary for both pairs is therefore:

$$N_2 = \sqrt{\frac{L_{N2}}{A_L}} \cong 10 \pm 1 \quad (\text{C.12.})$$

The transformer ratio is:

$$r = \sqrt{\frac{R_p}{\frac{R_1 R_e}{R_1 + R_e}}} \approx 1:7 \quad (\text{C.13.})$$

In principle, it is possible to work out the number of turns on the primary inductor from the required ratio. In this case, the closest match could be achieved with 14 turns on the secondary and 2 turns on the primary. However, this solution is impractical, since it is

usually good practice to have the highest possible density of turns along the bobbin coil former to have a good efficiency and linear behaviour of the transformer.

The alternative method can therefore be used, whereby the transformer and the tuning inductor are split.

The matching inductance can be obtained using the same ferrite core as above with 7-8 turns. The resulting conductance and admittance plots are given in fig. B-7 to B-10.

The transformer ratio in this case doesn't change appreciably after tuning and is achieved by means of two 49-turn layers on the secondary and one 14-turn layer on the primary for both transformers. The wire thickness is chosen so that the two bobbins are uniformly filled. The two layers on the secondary are independently wound around the coil former in the same direction and then added in series using a track on the supporting board.

The measured inductance of the primary and secondary inductors at the transducer resonance frequency f_S are given in Tab. 2:

	First transformer	Second transformer
L_{N1}	0.122 mH	0.135 mH
L_{N2}	5.55 mH	5.65 mH

Tab. C.2: Inductance parameters at the resonance frequency f_S for the two matching transformers

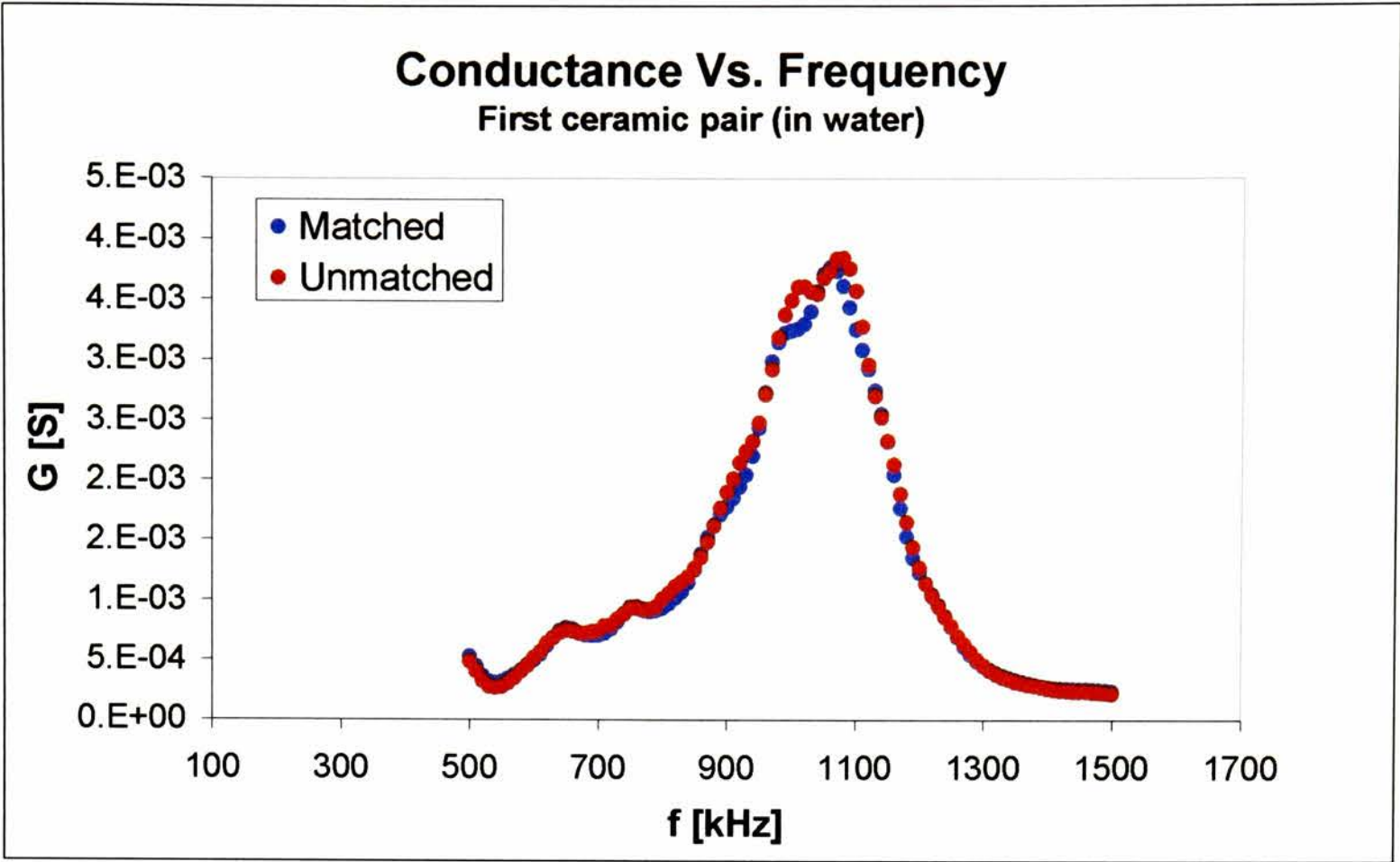


Figure C.7: Conductance Vs. Frequency for the first ceramic pair around the resonance frequency. Comparison between matched and unmatched response

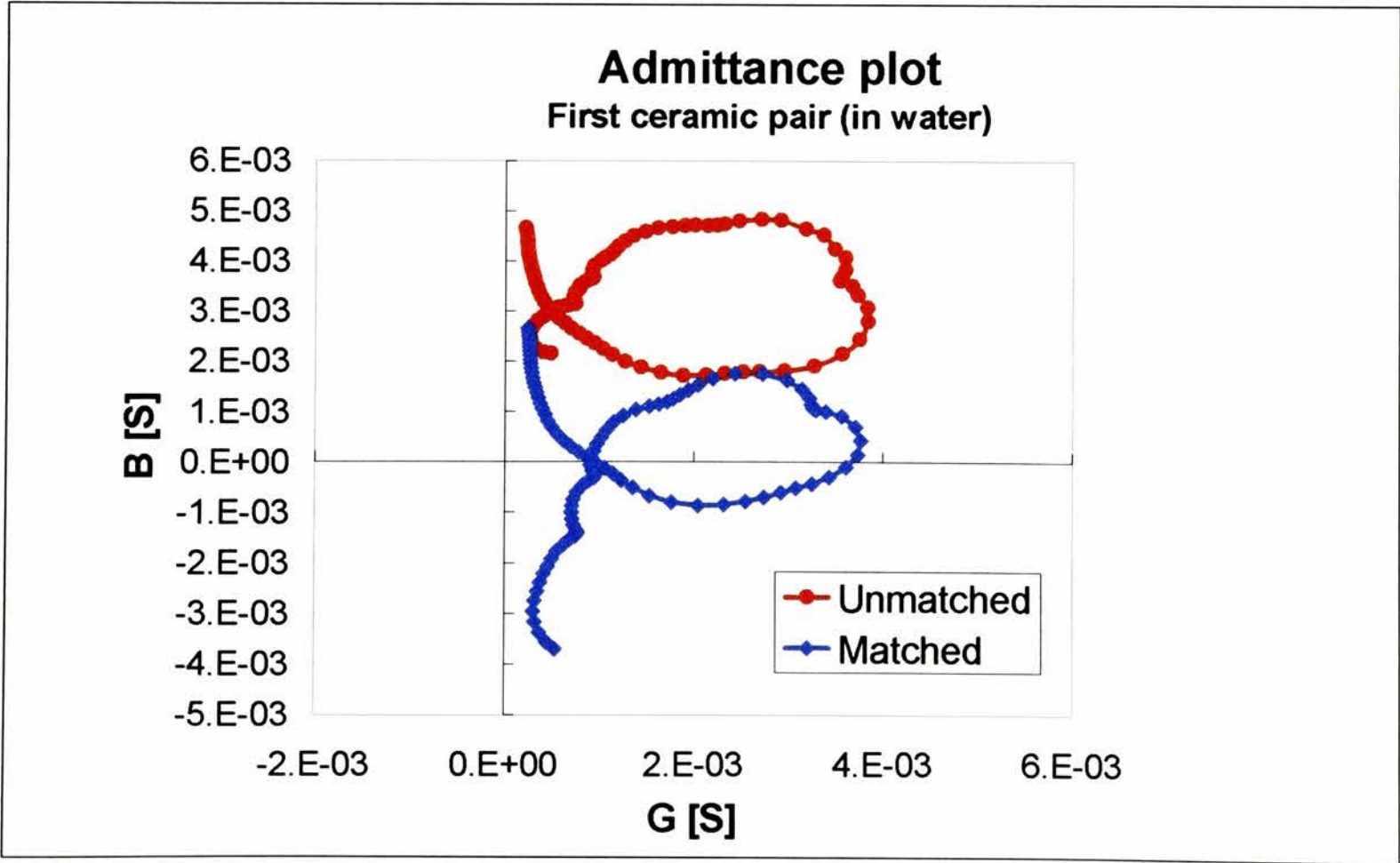


Figure C.8: Admittance plot for the first ceramic pair around the resonance frequency. Comparison between matched and unmatched response

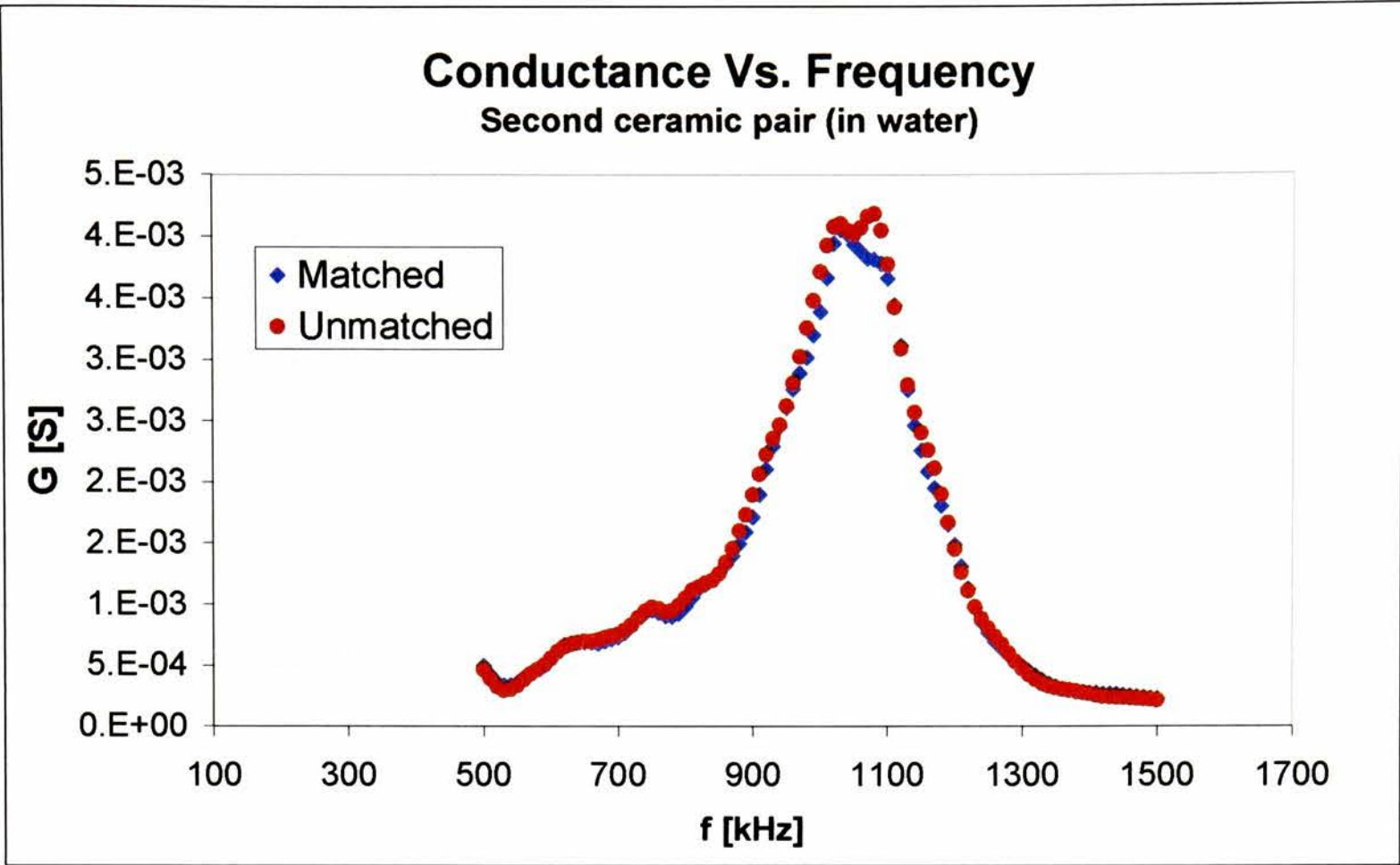


Figure C.9: Conductance Vs. Frequency for the second ceramic pair around the resonance frequency. Comparison between matched and unmatched response

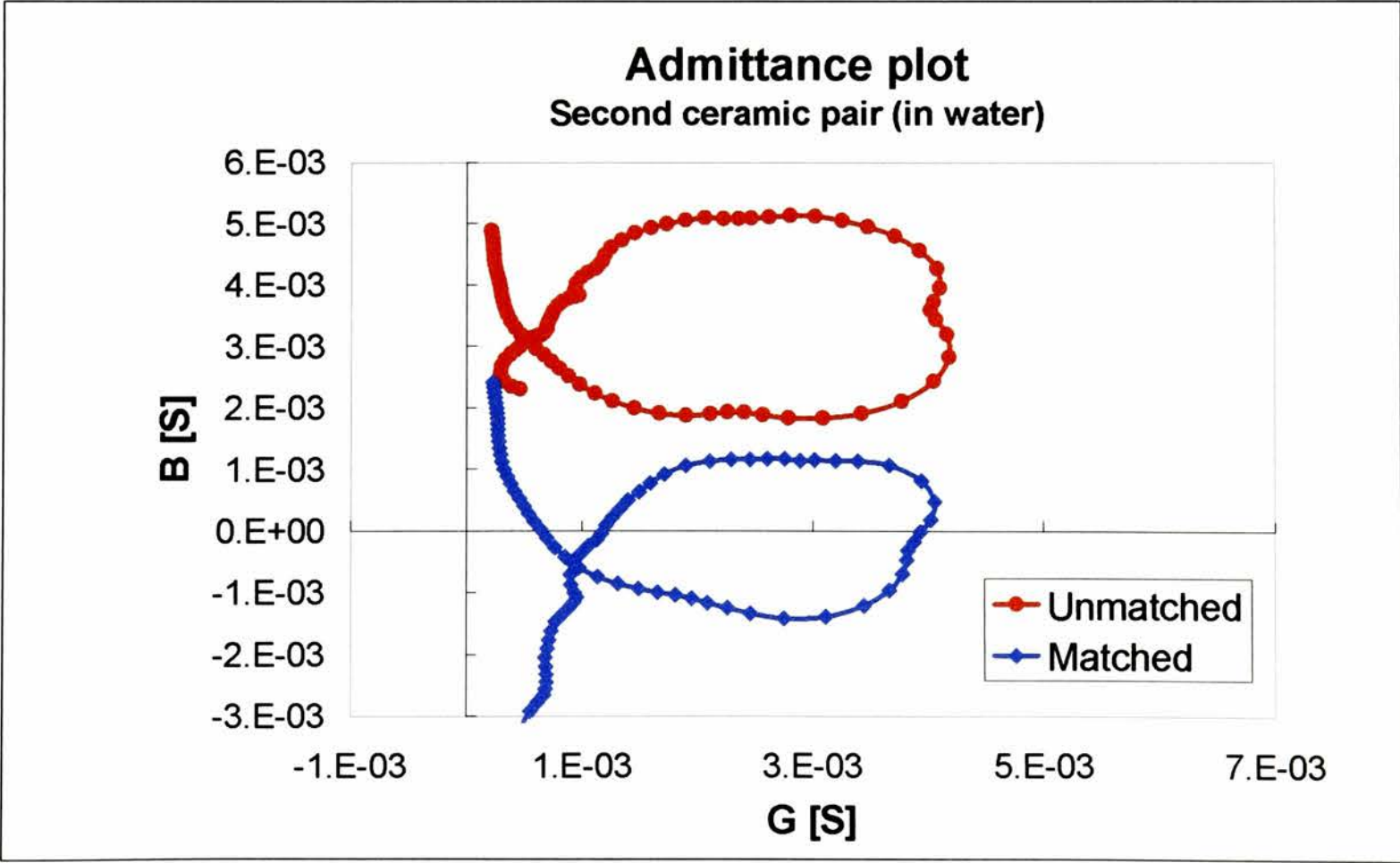


Figure C.10: Admittance plot for the second ceramic pair around the resonance frequency. Comparison between matched and unmatched response



Figure C.11: The test parametric transducer (side view). The aluminium anodised body contains the matching transformers



Figure C.12: The test parametric transducer (front view). The piezoelectric crystals are encased in protective styrcast resin

Appendix D

The Transfer Matrix Method

9.1. Introduction

Modelling and analysis of propagation of plane waves in simple stratified materials can be carried out by means of transfer matrices. The method is quite well established for simple configurations, such as non-depth-depending layers of materials having similar properties and infinite samples subjected to incident plane waves. In this case, the analysis is reduced to the determination of a proper set of physically meaningful independent variables, whose values at the front and at the back of the stratified structure are related by means of the transfer matrix. The matrix depends on the thickness of the single layers and on their properties and it can be recursively evaluated from the basic wave equations.

The method has been investigated in this simple form by means of a computer program written using the MATLAB package and applied to the analysis of stratified materials in two different situations:

- modelling of infinite stratified structures of several different materials (elastic, viscoelastic, porous and fluid layers) subject to one dimensional plane waves and two-dimensional stress state
- modelling of infinite structures made of elastic and viscoelastic layers and subjected to two-dimensional plane waves and three-dimensional stress state

The theory of propagation in stratified media and the methods studied are briefly reported here.

9.2. Modelling of propagation through stratified media including elastic, viscoelastic, porous and fluid

A general stratified medium can be represented as in Fig. C.1. A plane wave is depicted as incident on the left side of the material. Translational invariance is assumed in order to have well defined reflection and transmission coefficients (flows of the external medium, water or air, are not considered).

The plane wave impinging on the left side of the structure is assumed to have pressure $p(A)$ and normal velocity $v_3(A)$ at a point A on the interface in the external fluid and wave number $\underline{k} = \left(\frac{\omega}{c_0} \right) \underline{n}$, where ω is the wave frequency and c_0 the sound velocity in the free fluid. The same applies to a point B in the fluid at the back of the stratified material.

The reflection and transmission coefficients R_a , and T_b for the one-dimensional wave case are therefore related by:

$$\begin{pmatrix} p(A) \\ v_3^f(A) \end{pmatrix} = \begin{bmatrix} a & b \\ c & d \end{bmatrix} \begin{pmatrix} p(B) \\ v_3^f(B) \end{pmatrix} \quad (\text{D.30.})$$

or

$$\begin{pmatrix} 1+R_a \\ (1-R_a)\frac{\cos\theta}{Z_c} \end{pmatrix} = \begin{bmatrix} a & b \\ c & d \end{bmatrix} \begin{pmatrix} T_b \\ T_b\frac{\cos\theta}{Z_c} \end{pmatrix} \quad (\text{D.31.})$$

Since the reciprocity principle applies and $(ac-bd) = 1$, the same relationship is true between R_b , and T_a for the case of a similar plane wave impinging on the right side

The coefficients a , b , c and d depend on the properties of the single layers and on the circular frequency ω and tangential wave number $k_t = k_1 = |\underline{k}| \sin\theta$.

The single layers of materials can be modelled taking into account their constitutive properties as follows:

- **Fluid layers:** in a fluid layer the acoustic field can be described using the pressure p and the velocity component normal to the surface v_3 (the dependence on time t has been removed):

$$\begin{aligned} p(x_3) &= a_1 \exp(-jk_3 x_3) + a_2 \exp(jk_3 x_3) \\ v_3(x_3) &= \frac{k_3}{\omega\rho} [a_1 \exp(-jk_3 x_3) - a_2 \exp(jk_3 x_3)] \end{aligned} \quad (\text{D.32.})$$

where $k_3 = (k_f^2 - k_1^2)^{\frac{1}{2}}$, k_f being the wave number in the fluid. The acoustic field can therefore be determined from the knowledge of two parameters, either the two amplitude parameters a_i or the pressure $p = -\sigma_{33}$ (normal stress) and the velocity component v_3 . The propagation in the layer can therefore be modelled using the matrix form:

$$\begin{Bmatrix} p(A) \\ v_3(A) \end{Bmatrix} = \mathbf{T}_f \begin{Bmatrix} p(B) \\ v_3(B) \end{Bmatrix} \quad (\text{D.33.})$$

where \mathbf{T}_f is the 2x2 transfer matrix

$$\mathbf{T}_f = \begin{bmatrix} \cos(k_3 L_3) & \frac{\omega \rho}{k_3} j \sin(k_3 L_3) \\ \frac{k_3}{\omega \rho} j \sin(k_3 L_3) & \cos(k_3 L_3) \end{bmatrix} \quad (\text{D.34.})$$

and L is the thickness of the fluid layer.

- **Elastic/Viscoelastic solid layers:** in a solid elastic or viscoelastic material two kind of waves can propagate, a dilatational longitudinal wave and rotational shear wave. They can be described using the two displacement potentials φ and $\underline{\psi}$ (time dependence has been omitted):

$$\varphi(x_1, x_3) = a_1 \exp[-j(k_{d3}x_3 + k_1x_1)] + a_1' \exp[j(k_{d3}x_3 - k_1x_1)] \quad (\text{D.35.})$$

$$\psi_2(x_1, x_3) = a_2 \exp[-j(k_{r3}x_3 + k_1x_1)] + a_2' \exp[j(k_{r3}x_3 - k_1x_1)]$$

where $k_{d3} = (k_d^2 - k_1^2)^{\frac{1}{2}}$ and $k_{r3} = (k_r^2 - k_1^2)^{\frac{1}{2}}$, k_d and k_r being the wave numbers of the dilatational and rotational waves in the solid material respectively.

The acoustic field in the solid layer is completely known from the knowledge of the four parameter a_1, a_1', a_2, a_2' or other four equivalent parameters. As for the fluid layer, we can use two components of the stress tensor and two components of the velocity vector. From the potential displacement relations we have:

$$\begin{aligned} v_1 &= j\omega \left[-jk_1(a_1 + a_1')\cos(k_{d3}x_3) - k_1(a_1 - a_1')\sin(k_{d3}x_3) + \right. \\ &\quad \left. k_{r3}(a_2 + a_2')\sin(k_{r3}x_3) + jk_{r3}(a_2 - a_2')\cos(k_{r3}x_3) \right] \\ v_3 &= j\omega \left[-jk_{d3}(a_1 + a_1')\sin(k_{d3}x_3) - k_{d3}(a_1 - a_1')\cos(k_{d3}x_3) + \right. \\ &\quad \left. -jk_1(a_2 + a_2')\cos(k_{r3}x_3) - k_{r3}(a_2 - a_2')\sin(k_{r3}x_3) \right] \\ \sigma_{13} &= G \left\{ 2k_1k_{d3} \left[j(a_1 + a_1')\sin(k_{d3}x_3) - (a_1 - a_1')\cos(k_{d3}x_3) \right] + \right. \\ &\quad \left. (k_{r3}^2 + k_1^2) \left[(a_2 + a_2')\cos(k_{r3}x_3) - j(a_2 - a_2')\sin(k_{r3}x_3) \right] \right\} \quad (D.36.) \\ \sigma_{33} &= \left[-E(k_1^2 + k_{d3}^2) + 2Gk_1^2 \right] (a_1 + a_1')\cos(k_{d3}x_3) + \\ &\quad j \left[E(k_1^2 + k_{d3}^2) - 2Gk_1^2 \right] (a_1 - a_1')\sin(k_{d3}x_3) + \\ &\quad 2jGk_1k_{r3}(a_2 + a_2')\sin(k_{r3}x_3) - 2Gk_1k_{r3}(a_2 - a_2')\cos(k_{r3}x_3) \end{aligned}$$

The matrix propagation model is therefore:

$$\begin{Bmatrix} v_1(A) \\ v_3(A) \\ \sigma_{13}(A) \\ \sigma_{33}(A) \end{Bmatrix} = \mathbf{T}_e \begin{Bmatrix} v_1(B) \\ v_3(B) \\ \sigma_{13}(B) \\ \sigma_{33}(B) \end{Bmatrix} \quad (\text{D.37.})$$

The elements of the single-layer 4x4 matrix \mathbf{T}_e (6x6 for the complete two-dimensional wave case) are reported at the end of the section.

- **Porous solid layers:** porous solid layers can be treated using Biot theory, a Lagrangian model where the stress-strain relationships are derived from a potential energy of deformation. According to Biot theory, three types of waves can propagate in a porous material, due the coupling between the solid frame and the fluid, two dilatational waves and one rotational wave. The acoustic field in the solid frame can be described again using the displacement potentials:

$$\begin{aligned} \varphi(x_1, x_3) &= a_1 \exp[-j(k_{d13}x_3 + k_1x_1)] + a_1' \exp[j(k_{d13}x_3 - k_1x_1)] \\ \varphi(x_1, x_3) &= a_2 \exp[-j(k_{d23}x_3 + k_1x_1)] + a_2' \exp[j(k_{d23}x_3 - k_1x_1)] \\ \psi_2(x_1, x_3) &= a_3 \exp[-j(k_{r3}x_3 + k_1x_1)] + a_3' \exp[j(k_{r3}x_3 - k_1x_1)] \end{aligned} \quad (\text{D.38.})$$

where $k_{d13} = (k_{d1}^2 - k_1^2)^{\frac{1}{2}}$, $k_{d23} = (k_{d1}^2 - k_1^2)^{\frac{1}{2}}$ and $k_{r3} = (k_r^2 - k_1^2)^{\frac{1}{2}}$, k_{d1} , k_{d2} and k_r being the wave numbers of the two dilatational and of the rotational waves in the porous material respectively. The potentials in the solid frame

can be related to the potentials in the fluid by means of set of coefficients μ_i , ($i = 1, 2, 3$).

In this case, six parameters are necessary to completely describe the acoustic field. The expressions for three velocity components and three stress components are as follows (the superscript s stands for solid, whereas the superscript f stands for fluid):

$$\begin{aligned}
 v_1^s &= j\omega \left[\sum_{i=1,2} \left\{ -jk_1(a_i + a_i') \cos(k_{di3}x_3) - k_1(a_i - a_i') \sin(k_{di3}x_3) \right\} + \right. \\
 &\quad \left. k_{r3}(a_2 + a_2') \sin(k_{r3}x_3) + jk_{r3}(a_2 - a_2') \cos(k_{r3}x_3) \right] \\
 v_3^s &= j\omega \left[\sum_{i=1,2} \left\{ jk_{di3}(a_i + a_i') \sin(k_{di3}x_3) - k_{di3}(a_i - a_i') \cos(k_{di3}x_3) \right\} + \right. \\
 &\quad \left. -jk_1(a_2 + a_2') \cos(k_{r3}x_3) - k_{r3}(a_2 - a_2') \sin(k_{r3}x_3) \right] \\
 v_3^f &= j\omega \left[\sum_{i=1,2} \left\{ -jk_{di3}\mu_i(a_i + a_i') \sin(k_{di3}x_3) - k_{di3}\mu_i(a_i - a_i') \cos(k_{di3}x_3) \right\} \right. \\
 &\quad \left. -jk_1\mu_3(a_2 + a_2') \cos(k_{r3}x_3) - k_{r3}\mu_3(a_2 - a_2') \sin(k_{r3}x_3) \right] \\
 \sigma_{13}^s &= G \left\{ 2k_1 \sum_{i=1,2} k_{di3} [j(a_i + a_i') \sin(k_{di3}x_3) - (a_i - a_i') \cos(k_{di3}x_3)] + \right. \\
 &\quad \left. (k_{r3}^2 + k_1^2) [(a_2 + a_2') \cos(k_{r3}x_3) - j(a_2 - a_2') \sin(k_{r3}x_3)] \right\} \quad (D.39.) \\
 \sigma_{33}^s &= \sum_{i=1,2} \left\{ [-(E + Q\mu_i)(k_1^2 + k_{di3}^2) + 2Gk_1^2] (a_i + a_i') \cos(k_{di3}x_3) + \right. \\
 &\quad \left. j[(E + Q\mu_i)(k_1^2 + k_{di3}^2) - 2Gk_1^2] (a_i - a_i') \sin(k_{di3}x_3) \right\} + \\
 &\quad 2jGk_1k_{r3}(a_2 + a_2') \sin(k_{r3}x_3) - 2Gk_1k_{r3}(a_2 - a_2') \cos(k_{r3}x_3) \\
 \sigma_{33}^f &= \sum_{i=1,2} (Q + R\mu_i)(k_1^2 + k_{di3}^2) \left\{ -(a_i + a_i') \cos(k_{di3}x_3) + \right. \\
 &\quad \left. (a_i - a_i') \sin(k_{di3}x_3) \right\}
 \end{aligned}$$

The matrix propagation model is therefore:

$$\begin{Bmatrix} v_1^s(A) \\ v_3^s(A) \\ v_3^f(A) \\ \sigma_{13}^s(A) \\ \sigma_{33}^s(A) \\ \sigma_{33}^f(A) \end{Bmatrix} = \mathbf{T}_p \begin{Bmatrix} v_1^s(B) \\ v_3^s(B) \\ v_3^f(B) \\ \sigma_{13}^s(B) \\ \sigma_{33}^s(B) \\ \sigma_{33}^f(B) \end{Bmatrix} \quad (\text{D.40.})$$

The different behaviours of the layers can now be related using a set of interface matrices, developed from the application of mass and momentum conservation principles. In the following the vector $\underline{V}(A)$ stands for the generic acoustic variables vector in a point A. It is specialised for fluid, elastic and porous solid layers by addition of the superscripts f , e and p respectively.

For fluid-fluid and elastic-elastic contacts the acoustic quantities are constant through the boundary, i.e. $\underline{V}^{f,e}(C) = \underline{V}^{f,e}(D)$ (see Fig. 2.2) between the two layers. The interface matrices reduce to:

$$\begin{aligned} \mathbf{I}_{f,f} \underline{V}^f(C) + \mathbf{J}_{f,f} \underline{V}^f(D) &= 0 \\ \mathbf{I}_{e,e} \underline{V}^e(C) + \mathbf{J}_{e,e} \underline{V}^e(D) &= 0 \end{aligned} \quad (\text{D.41.})$$

where \mathbf{I} is the 2x2 or 4x4 unit matrix respectively for fluid and elastic solid layers and \mathbf{J} is its opposite.

For a porous solid-porous solid contact the boundary conditions on velocity and stress depend on the different porosity of the materials. If Φ_C and Φ_D are the porosity values

respectively in the first and second material then we can use a relationship similar to the ones for fluid and elastic solid contacts, inserting the dependence on porosity in the matrix $\mathbf{J}_{p,p}$:

$$\mathbf{I}_{p,p} \underline{V}^p(C) + \mathbf{J}_{p,p} \underline{V}^p(D) = 0 \quad (\text{D.42.})$$

$$\mathbf{J}_{p,p} = \begin{bmatrix} -1 & 0 & 0 & 0 & 0 & 0 \\ 0 & -1 & 0 & 0 & 0 & 0 \\ 0 & \frac{\Phi_D}{\Phi_C} - 1 & -\frac{\Phi_D}{\Phi_C} & 0 & 0 & 0 \\ 0 & 0 & 0 & -1 & 0 & \frac{\Phi_C}{\Phi_D} - 1 \\ 0 & 0 & 0 & 0 & -1 & 0 \\ 0 & 0 & 0 & 0 & 0 & -\frac{\Phi_C}{\Phi_D} \end{bmatrix} \quad (\text{D.43.})$$

and $\mathbf{I}_{p,p}$ is the 6x6 unit matrix.

The three possible relationships between different materials are summed up as follows:

- **Fluid-Elastic/Viscoelastic solid contact:** the boundary conditions and the boundary transfer matrix relationship are:

$$-p(C) = \sigma_{33}^e(D) \quad 0 = \sigma_{13}^e(D) \quad v_3^f(C) = v_3^e(D)$$

$$\mathbf{I}_{f,e} \underline{V}^f(C) + \mathbf{J}_{f,e} \underline{V}^e(D) = 0 \quad (\text{D.44.})$$

$$\mathbf{I}_{f,e} = \begin{bmatrix} -1 & 0 \\ 0 & 1 \\ 0 & 0 \end{bmatrix} \quad \mathbf{J}_{f,e} = \begin{bmatrix} 0 & 1 & 0 & 0 \\ 0 & 0 & 0 & 1 \\ 0 & 0 & 1 & 0 \end{bmatrix}$$

- **Fluid-Porous solid contact:** the boundary conditions and the boundary transfer matrix relationship are:

$$\begin{aligned}
 v_3^f(C) &= (1-\Phi_D) v_3^{ps}(D) + \Phi_D v_3^{pf}(D) & -\Phi_D p(C) &= \sigma_{33}^{pf}(D) \\
 -(1-\Phi_D) p(C) &= \sigma_{33}^{ps}(D) & 0 &= \sigma_{13}^{ps}(D) \\
 I_{f,p} V^f(C) + J_{f,p} V^p(D) &= 0
 \end{aligned}$$

$$\mathbf{I}_{f,p} = \begin{bmatrix} -1 & 0 \\ 0 & \Phi_D \\ (1-\Phi_D) & 0 \\ 0 & 0 \end{bmatrix} \quad \mathbf{J}_{f,p} = \begin{bmatrix} 0 & (1-\Phi_D) & \Phi_D & 0 & 0 & 0 \\ 0 & 0 & 0 & 0 & 0 & 1 \\ 0 & 0 & 0 & 0 & 1 & 0 \\ 0 & 0 & 0 & 1 & 0 & 0 \end{bmatrix} \quad (\text{D.45.})$$

- **Elastic/Viscoelastic solid-Porous solid contact:** the boundary conditions and the boundary transfer matrix relationship are:

$$\begin{aligned}
 v_3^e(C) &= v_3^{ps}(D) = v_3^{pf}(D) & v_1^e(C) &= v_1^{ps}(D) \\
 \sigma_{13}^e(C) &= \sigma_{13}^{ps}(D) & \sigma_{33}^e(C) &= \sigma_{33}^{ps}(D) + \sigma_{33}^{pf}(D)
 \end{aligned}$$

$$\mathbf{I}_{e,p} V^e(C) + \mathbf{J}_{e,p} V^p(D) = 0$$

$$\mathbf{I}_{f,p} = \begin{bmatrix} 1 & 0 & 0 & 0 \\ 0 & 1 & 0 & 0 \\ 0 & 1 & 0 & 0 \\ 0 & 0 & 1 & 0 \\ 0 & 0 & 0 & 1 \end{bmatrix} \quad \mathbf{J}_{f,p} = \begin{bmatrix} 1 & 0 & 0 & 0 & 0 & 0 \\ 0 & 1 & 0 & 0 & 0 & 0 \\ 0 & 0 & 1 & 0 & 0 & 0 \\ 0 & 0 & 0 & 1 & 0 & 0 \\ 0 & 0 & 0 & 0 & 1 & 1 \end{bmatrix} \quad (\text{D.46.})$$

Using the transfer and interface matrices shown so far, it is possible to model the plane acoustic field in a layered material made of different materials. The matrices must be combined in a convenient form, since they cannot be simply multiplied together.

If L_1, \dots, L_N are N layers of a stratified material the acoustic propagation across the material can be described by the set of relationships:

$$\begin{aligned}
 \mathbf{I}_{i,1} \underline{V}(A) + \mathbf{J}_{i,1} \mathbf{T}_1 \underline{V}(M_2) &= 0 \\
 \mathbf{I}_{1,2} \underline{V}(M_2) + \mathbf{J}_{1,2} \mathbf{T}_2 \underline{V}(M_4) &= 0 \\
 &\dots \\
 \mathbf{I}_{N,o} \underline{V}(M_{2N}) + \mathbf{J}_{N,o} \underline{V}(B) &= 0
 \end{aligned} \tag{D.47.}$$

where A and B are two points respectively on the front (input) and on the back (output) faces of the material and M_2, M_4, \dots, M_{2N} are points on the back faces of each layer inside the material.

The set of equation can be organised in a vector equation of the form:

$$\mathbf{D} \underline{V} = 0 \tag{C.48.}$$

where the vector $\underline{V} = \{\underline{V}(A) \ \underline{V}(M_2) \ \underline{V}(M_4) \ \dots \ \underline{V}(M_{2N}) \ \underline{V}(B)\}$ and the matrix \mathbf{D} is assembled from the set of equation (C.18).

In order to define completely the acoustic field, it is necessary to assign the starting boundary conditions. If we assume that the stratified material is immersed in water and we model the layer of water at the right side as a semi-infinite layer, then its impedance is

$$Z(B) = p(B)/v_3^f(B) = Z_c / \cos \theta \quad (\text{D.49.})$$

where Z_c is the characteristic impedance of the medium. This condition can be added to the previous system inserting the vector $\{0 \dots 0 \ Z(B) - 1\}$ as the bottom line of the matrix **D**. One more condition must be added. If the pressure $p(A)$ at the left side is known, then $p(A) - Z(A)v_3^f(A) = 0$ and we can add the vector $\{0 \dots 0 \ Z(A) - 1\}$ as the top line of matrix **D** the line. In addition this allows us to calculate the impedance $Z(A)$ on the front surface of the material.

From the matrix **D**, the reflection and transmission coefficients can then be calculated as shown previously.

9.3. Single-Layer Transfer Matrix Coefficients for Two-Dimensional Plane waves

Note: the exponential dependence on time t and tangential co-ordinates x_1 and x_3 ,

$e^{j(\omega t - k_1 x_1 - k_3 x_3)}$, is common to all components and is implicitly understood.

$$a_{11} = \cos(k_{L,2}d) + (1-F)[\cos(k_{G,2}d) - \cos(k_{L,2}d)]$$

$$a_{12} = jk_1 \left[\frac{F \sin(k_{L,2}d)}{k_{L,2}} - \frac{2k_{G,2} \sin(k_{G,2}d)}{k_G^2} \right]$$

$$a_{13} = jk_3 \left[\frac{F \sin(k_{L,2}d)}{k_{L,2}} - \frac{2k_{G,2} \sin(k_{G,2}d)}{k_G^2} \right]$$

$$a_{14} = 2k_3 \rho c_G \frac{F}{k_G} [\cos(k_{L,2}d) - \cos(k_{G,2}d)]$$

$$a_{15} = 2k_1 \rho c_G \frac{F}{k_G} [\cos(k_{L,2}d) - \cos(k_{G,2}d)]$$

$$a_{16} = j\rho c_G \left[\frac{k_G F^2}{k_{L,2}} \sin(k_{L,2}d) + \frac{4(k_1^2 + k_3^2)k_{G,2}}{k_G^3} \sin(k_{G,2}d) \right]$$

$$a_{21} = jk_1 \left[\frac{2k_{L,2}}{k_G^2} \sin(k_{L,2}d) - \frac{F}{k_{G,2}} \sin(k_{G,2}d) \right]$$

$$a_{22} = \cos(k_{G,2}d) + 2 \frac{k_1^2}{k_G^2} [\cos(k_{L,2}d) - \cos(k_{G,2}d)]$$

$$a_{23} = 2 \frac{k_1 k_3}{k_G^2} [\cos(k_{L,2}d) - \cos(k_{G,2}d)]$$

$$a_{24} = j\rho c_G k_1 k_3 \left[4 \frac{k_{L,2}}{k_G^3} \sin(k_{L,2}d) + \frac{k_G F^2}{k_{G,2}(k_1^2 + k_3^2)} \sin(k_{G,2}d) - \frac{k_{G,2}}{k_G(k_1^2 + k_3^2)} \sin(k_{G,2}d) \right]$$

$$a_{25} = j\rho c_G \left[4 \frac{k_1^2 k_{L,2}}{k_G^3} \sin(k_{L,2}d) + \frac{k_1^2 k_G F^2}{k_{G,2}(k_1^2 + k_3^2)} \sin(k_{G,2}d) + \frac{k_3^2 k_{G,2}}{k_G(k_1^2 + k_3^2)} \sin(k_{G,2}d) \right]$$

$$a_{26} = a_{15}$$

$$a_{31} = jk_3 \left[2 \frac{k_{L,2}}{k_G^2} \sin(k_{L,2}d) - \frac{F}{k_{G,2}} \sin(k_{G,2}d) \right]$$

$$a_{32} = a_{23}$$

$$a_{33} = \cos(k_{G,2}d) + 2 \frac{k_3^2}{k_G^2} [\cos(k_{L,2}d) - \cos(k_{G,2}d)]$$

$$a_{34} = j\rho c_G \left[4 \frac{k_3^2 k_{L,2}}{k_G^3} \sin(k_{L,2}d) + \frac{k_3^2 k_G F^2}{k_{G,2}(k_1^2 + k_3^2)} \sin(k_{G,2}d) + \frac{k_1^2 k_{G,2}}{k_G(k_1^2 + k_3^2)} \sin(k_{G,2}d) \right]$$

$$a_{35} = a_{24}$$

$$a_{36} = a_{14}$$

$$\begin{aligned}
a_{41} &= \frac{k_3}{\rho c_G k_G} [\cos(k_{L,2}d) - \cos(k_{G,2}d)] \\
a_{42} &= j \frac{k_1 k_3}{\rho c_G k_G} \left[\frac{\sin(k_{L,2}d)}{k_{L,2}} - \frac{\sin(k_{G,2}d)}{k_{G,2}} \right] \\
a_{43} &= j \frac{1}{\rho c_G} \left[\frac{k_3^2}{k_{L,2} k_G} \sin(k_{L,2}d) + \frac{k_{G,2}}{k_G} \sin(k_{G,2}d) + \frac{k_1^2}{k_{G,2} k_G} \sin(k_{G,2}d) \right] \\
a_{44} &= a_{33} \\
a_{45} &= a_{23} \\
a_{46} &= a_{13} \\
a_{51} &= \frac{k_1}{\rho c_G k_G} [\cos(k_{L,2}d) - \cos(k_{G,2}d)] \\
a_{52} &= j \frac{1}{\rho c_G} \left[\frac{k_1^2}{k_{L,2} k_G} \sin(k_{L,2}d) + \frac{k_{G,2}}{k_G} \sin(k_{G,2}d) + \frac{k_3^2}{k_{G,2} k_G} \sin(k_{G,2}d) \right] \\
a_{53} &= a_{42} \\
a_{54} &= a_{32} \\
a_{55} &= a_{22} \\
a_{56} &= a_{12} \\
a_{61} &= j \frac{1}{\rho c_G} \left[\frac{k_{L,2}}{k_G} \sin(k_{L,2}d) + \frac{k_1^2 + k_3^2}{k_{G,2} k_G} \sin(k_{G,2}d) \right] \\
a_{62} &= a_{51} \\
a_{63} &= a_{41} \\
a_{64} &= a_{31} \\
a_{65} &= a_{21} \\
a_{66} &= a_{11}
\end{aligned}$$

$$F = 1 - 2 \frac{k_1^2 + k_3^2}{k_G^2} \quad (\text{D.50.})$$

$$k_L^2 = k_1^2 + k_{L,2}^2 + k_3^2 \quad (\text{D.51.})$$

$$k_G^2 = k_1^2 + k_{G,2}^2 + k_3^2 \quad (\text{D.52.})$$

$$k_1 = k_{L,1} = k_{G,1} \quad (\text{D.53.})$$

$$k_3 = k_{L,3} = k_{G,3} \quad (\text{D.54.})$$

Appendix E

The Hamilton Principle Optimisation Method

(Paper published on *Meccanica*, 32 (6), 1997, pp. 555-565)

Appendix F

Acoustic Field Far-Field Approximation and Relationships among Various Forms of the Green Function for the Scalar and Vector Helmholtz Equation

9.1. Acoustic Field Far-Field Approximation

The far-field approximation of the acoustic field quantities is the leading term of the Taylor expansion of the field equations (5.38):

$$\begin{cases} \hat{p} = \hat{\zeta} \hat{\Phi}^q - \text{div} \hat{\Psi}^f \\ \hat{\mathbf{v}} = \hat{\zeta}^{-1} \hat{\mathbf{f}} - \nabla \hat{\Phi}^q + \hat{\zeta}^{-1} \nabla \text{div} \hat{\Psi}^f \end{cases} \quad (\text{F.1})$$

with the scalar and vector potentials are expressed in terms of the scalar Green function \hat{G} as:

$$\hat{\Phi}^q(\mathbf{x}, s) = \int_{\mathbf{x}' \in \mathcal{D}} \hat{G}(\mathbf{x} - \mathbf{x}', s) \hat{q}(\mathbf{x}', s) dV \quad (\text{F.2})$$

and

$$\hat{\Psi}^f(\mathbf{x}, s) = \int_{\mathbf{x}' \in \mathcal{D}} \hat{G}(\mathbf{x} - \mathbf{x}', s) \hat{f}(\mathbf{x}', s) dV \quad (\text{F.3})$$

where

$$\hat{G}(\mathbf{x}, s) = \frac{e^{-\hat{\gamma}|\mathbf{x}|}}{4\pi|\mathbf{x}|} \quad \forall |\mathbf{x}| \neq 0 \quad (\text{F.4})$$

Expanding the argument $|\mathbf{x} - \mathbf{x}'|$ of the Green function and the Green function as Taylor series to the first order we get the approximated expressions (de Hoop 1995):

$$\begin{aligned} |\mathbf{x} - \mathbf{x}'| &= |\mathbf{x}| - \boldsymbol{\xi} \cdot \mathbf{x}' + O(|\mathbf{x}|^{-1}) \quad \boldsymbol{\xi} = \frac{\mathbf{x}}{|\mathbf{x}|} \quad |\mathbf{x}| \rightarrow \infty \\ \hat{G}(\mathbf{x} - \mathbf{x}', s) &= \frac{e^{-|\hat{\gamma}|\mathbf{x}|}}{4\pi|\mathbf{x}|} e^{i\boldsymbol{\xi} \cdot \mathbf{x}'} \left[1 + O(|\mathbf{x}|^{-1}) \right] \end{aligned} \quad (\text{F.5})$$

The scalar and vector potentials can therefore be expressed as:

$$\begin{cases} \hat{\Phi}^q(\mathbf{x}, s) = \hat{\Phi}^{q\infty}(\boldsymbol{\xi}, s) \frac{e^{-\hat{\gamma}|\mathbf{x}|}}{4\pi|\mathbf{x}|} \left[1 + O(|\mathbf{x}|^{-1})\right] \\ \hat{\Psi}^f(\mathbf{x}, s) = \hat{\Psi}^{f\infty}(\boldsymbol{\xi}, s) \frac{e^{-\hat{\gamma}|\mathbf{x}|}}{4\pi|\mathbf{x}|} \left[1 + O(|\mathbf{x}|^{-1})\right] \end{cases} \quad |\mathbf{x}| \rightarrow \infty \quad (\text{F.6})$$

with

$$\hat{\Phi}^{q\infty}(\mathbf{x}, s) = \int_{\mathbf{x}' \in \mathcal{D}} e^{\hat{\gamma}\boldsymbol{\xi} \cdot \mathbf{x}} \hat{q}(\mathbf{x}', s) dV \quad (\text{F.7})$$

and

$$\hat{\Psi}^{f\infty}(\mathbf{x}, s) = \int_{\mathbf{x}' \in \mathcal{D}} e^{\hat{\gamma}\boldsymbol{\xi} \cdot \mathbf{x}} \hat{q}(\mathbf{x}', s) dV \quad (\text{F.8})$$

The far-field approximation of the acoustic quantities (F.1) can therefore be written as:

$$\begin{cases} \hat{p}(\mathbf{x}, s) = \hat{p}^\infty(\boldsymbol{\xi}, s) \frac{e^{-\hat{\gamma}|\mathbf{x}|}}{4\pi|\mathbf{x}|} \left[1 - O(|\mathbf{x}|^{-1})\right] \\ \hat{\mathbf{v}}(\mathbf{x}, s) = \hat{\mathbf{v}}^\infty(\boldsymbol{\xi}, s) \frac{e^{-\hat{\gamma}|\mathbf{x}|}}{4\pi|\mathbf{x}|} \left[1 - O(|\mathbf{x}|^{-1})\right] \end{cases} \quad |\mathbf{x}| \rightarrow \infty \quad (\text{F.9})$$

where

$$\begin{cases} \hat{p}^\infty = \hat{\zeta} \hat{\Phi}^{q\infty} + \hat{\gamma} \boldsymbol{\xi} \cdot \hat{\Psi}^{f\infty} \\ \hat{\mathbf{v}}^\infty = \hat{\gamma} \boldsymbol{\xi} \hat{\Phi}^{q\infty} + \hat{\eta} \boldsymbol{\xi} \boldsymbol{\xi} \cdot \hat{\Psi}^{f\infty} \end{cases} \quad (\text{F.10})$$

It also results that the far-field amplitude quantities are interrelated by the relationship

$$\begin{cases} -\hat{\gamma}\hat{\xi}\hat{p}^\infty + \hat{\zeta}\hat{v}^\infty = 0 \\ -\hat{\gamma}\hat{\xi} \cdot \hat{v}^\infty + \hat{\eta}\hat{p}^\infty = 0 \end{cases} \quad (\text{F.11})$$

which are typical of uniform plane waves.

9.2. Relationships between Different Forms of the Green Functions for the Helmholtz Equation

The following relationships are reported here as a support of the expressions derived in Chapters 5 for the reciprocity theorems. The demonstration of their validity can be found in (de Hoop 1995):

$$\begin{cases} \hat{p}^{\hat{q}B}(x, x', s) = \hat{G}^{\hat{p}\hat{q}B}(x, x', s) \hat{a}(s) \\ \hat{v}^{\hat{q}B}(x, x', s) = \hat{G}^{\hat{v}\hat{q}B}(x, x', s) \hat{a}(s) \end{cases} \quad (\text{F.12})$$

$$\begin{aligned} \hat{G}^{\hat{p}\hat{q}B}(\mathbf{x}, \mathbf{x}', s) &= \hat{G}^{\hat{p}\hat{q}}(\mathbf{x}', \mathbf{x}, s) \\ \hat{G}^{\hat{v}\hat{q}B}(\mathbf{x}, \mathbf{x}', s) &= -\hat{G}^{\hat{v}\hat{f}}(\mathbf{x}', \mathbf{x}, s) \end{aligned} \quad (\text{F.13})$$

$$\begin{cases} \hat{p}^{\hat{f}B}(x, x', s) = \hat{G}^{\hat{p}\hat{f}B}(x, x', s) \cdot \hat{\mathbf{b}}(s) \\ \hat{v}^{\hat{f}B}(x, x', s) = \hat{G}^{\hat{v}\hat{f}B}(x, x', s) \hat{\mathbf{b}}(s) \end{cases} \quad (\text{F.14})$$

$$\begin{aligned} \hat{G}^{\hat{p}\hat{f}B}(\mathbf{x}, \mathbf{x}', s) &= -\hat{G}^{\hat{v}\hat{q}}(\mathbf{x}', \mathbf{x}, s) \\ \hat{G}^{\hat{v}\hat{f}B}(\mathbf{x}, \mathbf{x}', s) &= \hat{G}^{\hat{v}\hat{f}}(\mathbf{x}', \mathbf{x}, s) \end{aligned} \quad (\text{F.15})$$

9.3. References

DE HOOP, T.A. (1995). *Handbook of Radiation and Scattering of Waves*. London: Academic Press

Appendix G

Tables of Material Properties

The properties of the materials used in the finite element/boundary element modelling are reported here for reference. The following symbols are used in the tables:

- f frequency [Hz]
- ρ density [kg m^{-3}]
- L longitudinal bulk modulus [Pa]
- G shear modulus [Pa]
- c_L longitudinal sound speed [m s^{-1}]
- c_G shear sound speed [m s^{-1}]
- Z longitudinal impedance [MRayl]
- $\text{Re}()$ real part of the complex value
- $\text{Im}()$ imaginary part of the complex value

1. Aluminium 7075–T6

ρ	$\text{Re}(L)$	$\text{Im}(L)$	$\text{Re}(G)$	$\text{Im}(G)$	$\text{Re}(c_L)$	$\text{Im}(c_L)$	$\text{Re}(c_G)$	$\text{Im}(c_G)$	$\text{Re}(Z)$	$\text{Im}(Z)$
2710	3.9E+10	1.2E+08	2.6E+10	8.00E+07	3793.57	210.43	3097.43	171.81	10.28	0.57

2. Butyl rubber

f	ρ	Re(L)	Im(L)	Re(G)	Im(G)	Re(c _L)	Im(c _L)	Re(c _G)	Im(c _G)	Re(Z)	Im(Z)
30000	1800	2.14E+09	3.12E+09	2.28E+08	1.49E+08	1156.24	1395.65	377.23	305.26	2.08	2.51
31000	1800	2.19E+09	3.19E+09	2.32E+08	1.52E+08	1170.106	1410.99	380.88	308.16	2.11	2.54
32000	1800	2.24E+09	3.25E+09	2.36E+08	1.55E+08	1183.152	1425.23	384.26	310.77	2.13	2.57
33000	1800	2.29E+09	3.31E+09	2.4E+08	1.57E+08	1195.52	1438.54	387.40	313.12	2.15	2.59
34000	1800	2.33E+09	3.37E+09	2.44E+08	1.59E+08	1207.345	1451.11	390.37	315.27	2.17	2.61
35000	1800	2.38E+09	3.43E+09	2.47E+08	1.61E+08	1218.756	1463.10	393.19	317.25	2.19	2.63
36000	1800	2.42E+09	3.48E+09	2.51E+08	1.63E+08	1229.875	1474.65	395.90	319.09	2.21	2.65
37000	1800	2.46E+09	3.53E+09	2.54E+08	1.65E+08	1240.822	1485.92	398.56	320.84	2.23	2.67
38000	1800	2.51E+09	3.59E+09	2.58E+08	1.66E+08	1251.712	1497.05	401.18	322.53	2.25	2.69
39000	1800	2.55E+09	3.64E+09	2.61E+08	1.68E+08	1262.658	1508.19	403.81	324.18	2.27	2.71
40000	1800	2.6E+09	3.69E+09	2.64E+08	1.7E+08	1273.767	1519.47	406.48	325.85	2.29	2.74
41000	1800	2.64E+09	3.75E+09	2.68E+08	1.72E+08	1285.128	1531.00	409.22	327.55	2.31	2.76
42000	1800	2.69E+09	3.81E+09	2.72E+08	1.73E+08	1296.758	1542.81	412.03	329.28	2.33	2.78
43000	1800	2.74E+09	3.87E+09	2.75E+08	1.75E+08	1308.657	1554.89	414.91	331.06	2.36	2.80
44000	1800	2.79E+09	3.93E+09	2.79E+08	1.77E+08	1320.824	1567.26	417.86	332.88	2.38	2.82
45000	1800	2.84E+09	3.99E+09	2.83E+08	1.79E+08	1333.258	1579.91	420.87	334.75	2.40	2.84
46000	1800	2.9E+09	4.06E+09	2.88E+08	1.81E+08	1345.958	1592.84	423.95	336.67	2.42	2.87
47000	1800	2.95E+09	4.13E+09	2.92E+08	1.83E+08	1358.923	1606.07	427.09	338.65	2.45	2.89
48000	1800	3.01E+09	4.2E+09	2.96E+08	1.86E+08	1372.15	1619.58	430.30	340.68	2.47	2.92
49000	1800	3.07E+09	4.27E+09	3.01E+08	1.88E+08	1385.638	1633.38	433.57	342.76	2.49	2.94
50000	1800	3.13E+09	4.34E+09	3.05E+08	1.9E+08	1399.384	1647.47	436.89	344.91	2.52	2.97

3. Polyurethane rubber

f	ρ	Re(L)	Im(L)	Re(G)	Im(G)	Re(c _L)	Im(c _L)	Re(c _G)	Im(c _G)	Re(Z)	Im(Z)
30000	2967	3.40E+08	2.87E+08	9.71E+06	8.97E+06	460.79	423.52	77.89	74.87	1.37	1.26
31000	2967	3.74E+08	3.07E+08	1.07E+07	9.60E+06	483.73	438.15	81.77	77.45	1.44	1.30
32000	2967	3.70E+08	3.13E+08	1.06E+07	9.77E+06	480.84	441.95	81.28	78.13	1.43	1.31
33000	2967	3.74E+08	3.07E+08	1.07E+07	9.60E+06	483.73	438.15	81.77	77.45	1.44	1.30
34000	2967	3.79E+08	3.20E+08	1.08E+07	9.99E+06	486.41	447.07	82.22	79.03	1.44	1.33
35000	2967	3.95E+08	3.33E+08	1.13E+07	1.04E+07	496.60	456.43	83.94	80.69	1.47	1.35
36000	2967	3.86E+08	3.26E+08	1.10E+07	1.02E+07	491.48	451.73	83.08	79.85	1.46	1.34
37000	2967	3.95E+08	3.33E+08	1.13E+07	1.04E+07	496.60	456.43	83.94	80.69	1.47	1.35
38000	2967	3.90E+08	3.39E+08	1.11E+07	1.06E+07	493.48	460.36	83.41	81.38	1.46	1.37
39000	2967	4.17E+08	3.23E+08	1.19E+07	1.01E+07	510.43	449.29	86.28	79.42	1.51	1.33
40000	2967	4.54E+08	3.52E+08	1.30E+07	1.10E+07	532.64	468.84	90.03	82.88	1.58	1.39
41000	2967	4.45E+08	3.44E+08	1.27E+07	1.08E+07	527.15	464.01	89.11	82.03	1.56	1.38
42000	2967	4.36E+08	3.37E+08	1.24E+07	1.05E+07	521.72	459.23	88.19	81.18	1.55	1.36
43000	2967	4.40E+08	3.51E+08	1.26E+07	1.10E+07	524.30	468.10	88.62	82.75	1.56	1.39
44000	2967	4.58E+08	3.46E+08	1.31E+07	1.08E+07	535.10	465.17	90.45	82.23	1.59	1.38
45000	2967	4.45E+08	3.44E+08	1.27E+07	1.08E+07	527.15	464.01	89.11	82.03	1.56	1.38
46000	2967	4.63E+08	3.40E+08	1.32E+07	1.06E+07	537.75	461.05	90.90	81.50	1.60	1.37
47000	2967	4.73E+08	3.48E+08	1.35E+07	1.09E+07	543.98	466.38	91.95	82.45	1.61	1.38
48000	2967	4.71E+08	3.28E+08	1.35E+07	1.03E+07	542.73	452.83	91.74	80.05	1.61	1.34
49000	2967	4.93E+08	3.63E+08	1.41E+07	1.13E+07	555.37	476.15	93.87	84.17	1.65	1.41
50000	2967	4.53E+08	3.33E+08	1.29E+07	1.04E+07	532.21	456.29	89.96	80.66	1.58	1.35

Appendix G

Journal Articles and Conference Papers

1. **Di Meglio, A.**, Francis, D.T.I., Coates, R.F.W. (1996). Phoebe: A 3D Transducer Modelling Environment, *Proc. III Eur. Conf. Underwater Acoust.*, Vol. II, Heraklion, Crete, Greece
2. Coates, R.F.W, **Di Meglio, A.**, Peselli, M. (1996). The Modelling of Acoustic Absorbers and Baffle Materials, *Proc. III Eur. Conf. Underwater Acoust.*, Vol. II, Heraklion, Crete, Greece
3. **Di Meglio, A.**, Jones, J.C., Wang, L. S., Francis, D.T.I. (1997). Combined Finite Element-Boundary Element Analysis of Viscoelastic Anechoic Panels for Underwater Applications, *Proc. Oceans '97 Conference MTS/IEEE*, Halifax, Nova Scotia, Canada
4. Jones, J.C., **Di Meglio, A.** Wang, L. S., Coates, R.F.W., Tedeschi, A., Stoner, R.J.(1997). The Design and Testing of a DSP, Half-Duplex, Vertical, DPSK Communication Link, *Proc. Oceans '97 Conference MTS/IEEE*, Halifax, Nova Scotia, Canada

also published as

Jones, J.C., **Di Meglio, A.**, Wang, L.S., Aid, N. (1998). Underwater Vertical Digital Communication System, *Sea Technology*, 39 (5), ,31-36

5. **Di Meglio, A.**, Wang, L.S. (1999). A Variational Method for Identification of Viscoelastic Parameters from Experimental Data, submitted for publication to *J. Acoust. Soc. Am.*